Production of Radionuclides with Medium Energy Protons with the Emphasis on Targetry

by

Christiaan Vermeulen

Dissertation presented for the degree of Doctor of Philosophy in the Faculty of Science at Stellenbosch University

Dr. Gideon F. Steyn (supervisor)
Department of Nuclear Physics
iThemba LABS

Prof. Anthony A. Cowley (co-supervisor)
Department of Physics
Stellenbosch University

April 2014

Declaration

By submitting this dissertation electronically, I declare that the entirety of the work contained therein is my own, original work, that I am the sole author thereof (save to the extent explicitly otherwise stated), that reproduction and publication thereof by Stellenbosch University will not infringe any third party rights and that I have not previously in its entirety or in part submitted it for obtaining any qualification.

Date: .....

Acknowledgements

Foremost, I would like to express my sincere gratitude to my supervisors Dr Deon Steyn and Prof Anthony Cowley for the continuous support of my PhD study and research, for their patience, motivation and enthusiasm. Their guidance helped through the time of research and writing of this thesis. I could not have imagined having better supervisors and mentors for my PhD study.

My sincere thanks also goes to Dr Meiring Nortier, Prof Nico van der Walt, Dr Alexander Hohn, Dr Ferenc Scelezenyi, Dr Zoltan Kovacs and Dr Nick van der Meulen, for their words of encouragement at different times in the process.

I thank my fellow employees at iThemba LABS, many of whom have in some way or another played a significant role in this work.

Also, Dr Sheldon Cooper, for many hours of inspiration and laughs.

Last but not the least, I would like to thank my family: my parents who encouraged me all the time and my wife, Natasja, who has been a rock through all my studies.

Abstract

Production of Radionuclides with Medium Energy Protons with the Emphasis on Targetry

C. Vermeulen

Dissertation: PhD (Physics)

April 2014

The facilities for radionuclide production at iThemba LABS have undergone a number of significant upgrades over the last decade in order to increase the production capacity and to diversify the product portfolio. Central to this effort is a new vertical beam target station (VBTS) and its associated targetry, designed and built to operate at higher proton beam intensities for the large-scale production of relatively long-lived, high-value radionuclides such as ^{22}Na, ^{68}Ge and ^{82}Sr. Along with the VBTS, an existing smaller horizontal beam target station was adapted to accommodate targetry for ^{18}F production, mainly to supply ^{18}F-FDG for use in positron emission tomography (PET). The production capacity was further enhanced by means of a beam splitter to enable bombardments in two target stations simultaneously. This required new developments on several systems, e.g. beam diagnostics, control, interlocking and cooling.

This project brings together a number of different aspects of the upgraded facilities as well as the associated research and development that enable the production of radionuclides in the medium energy region, up to approximately 70 MeV. Investigations were performed on the cooling of the interfacial windows between the cyclotron vacuum and the targets as well as the direct cooling of the targets themselves during intense proton bombardments. For this purpose, empirical as well as computational fluid dynamics (CFD) calculations were performed. In addition, the local radiation shield of the VBTS as well as the beam transport in some of the targetry was investigated by means of Monte Carlo radiation transport calculations.

Excitation functions for the production of various radionuclides in the 66 MeV proton bombardment of ^{192}Os, ^{159}Tb, ^{nat}Gd, ^{155}Gd, ^{152}Gd, ^{93}Nb, ^{nat}Zr and ^{89}Y were measured and compared with theoretical predictions by means of statistical nuclear model calculations as well as the TENDL-2012 library. In particular, the production of ^{186}Re, selected radioterbiums (^{149,152,155}Tb) and radiozirconiums (^{88,89}Zr) is of interest in existing and emerging diagnostic and therapeutic applications in nuclear medicine. A study on ^{28}Mg production in the proton bombardment of ^{nat}Cl using stacked chloride targets was also performed at 200 MeV. This radionuclide is of interest as ^{28}Mg is the only practical radiotracer of Mg. Finally, new targetry for the production of ^{18}F was developed, modelled and optimized for the non-standard degraded beam employed in this particular case.

Uittreksel

Radionukliedproduksie met Medium Energie Protone
met die Klem op Skyfgerei

C. Vermeulen

Proefskrif: PhD (Fisika)

April 2014

Die fasiliteite vir die produksie van radionukliede by iThemba LABS is gedurende die afgelope dekade aansienlik opgegradeer om die produksiekapasiteit te verhoog en om die portfolio van produkte te diversifiseer. Sentraal tot hierdie poging is 'n vertikale-bundel skyfstasie (VBTS) wat gebou is om skywe met hoër intensiteit protonbundels te bombardeer ten einde relatief langlewende, hoë-waarde radionukliede op grootmaat te produseer, insluitende ^{22}Na, ^{68}Ge en ^{82}Sr. Terselfdetyd is 'n bestaande, kleiner horisontale-bundel skyfstasie aangepas om skywe vir die produksie van ^{18}F te huisves, meestal om ^{18}F-FDG vir positronemissietomografie (PET) te lewer. Die produksiekapasiteit is verder verhoog d.m.v. 'n bundeldeler sodat bundel gelyktyding aan twee skyfstasies gelewer kan word. Dit het ontwikkelingswerk vereis aan verskeie stelsels, insluitende diagnostiek, beheer, vergrendeling en verkoeling.

Hierdie projek bring verskeie aspekte bymekaar t.o.v. die opgegradeerde produksiefasiliteite sowel as die geassosieerde navorsing en ontwikkeling benodig vir radionukliedproduksie in die middelenergiegebied tot ongeveer 70 MeV. Die verkoeling van die foelievensters tussen die vakuum van die siklotron en die skyfgerei is ondersoek sowel as die direkte verkoeling van skywe onder intense protonbombardement. Hierdie studie sluit beide empiriese sowel as numeriese vloeidinamika berekeninge in. Verder is die afskerming van die VBTS asook die bundeltransport in verskeie skywe ondersoek m.b.v. Monte Carlo stralingstransport berekeninge.

Opwekkrommes vir die produksie van verskeie radionukliede met protongeïnduseerde reaksies tot en met 66 MeV op ^{192}Os, ^{159}Tb, ^{nat}Gd, ^{155}Gd, ^{152}Gd, ^{93}Nb, ^{nat}Zr en ^{89}Y is gemeet en vergelyk met statistiese kernmodel berekeninge sowel as die TENDL-2012 biblioteek. Die produksie van ^{186}Re, verskeie radioterbiums (^{149,152,155}Tb) en radiozirkoniums (^{88,89}Zr) is van spesifieke belang vir bestaande en toekomstige diagnostiese en terapeutiese toepassings in die kerngeneeskunde. 'n Studie op die produksie van ^{28}Mg in die bombardement van ^{nat}Cl met 200 MeV protone is ook onderneem. In hierdie ondersoek is 'n stapel chloriedskywe gebruik. Die ^{28}Mg is van belang omdat dit die enigste Mg radioisotoop is wat geskik is as 'n radiospoorder van dié element. Laastens is nuwe skyfgerei vir die produksie van ^{18}F ontwikkel, gemodelleer en geoptimiseer vir die nie-standaard afgeremde bundel wat benut word in hierdie geval.

Contents

List of Figures

List of Tables

Chapter 1

Motivation and Outline

1.1 Motivation

Various aspects of the cyclotron production of radionuclides with medium energy protons are discussed with a strong focus on targetry. The work presented here endeavours to bring together several related themes instead of only one well-developed central theme. The content, however, is well constrained by relatively few perspectives. First, most of the research and development (R&D) beam was delivered by the separated-sector cyclotron (SSC) facility of iThemba LABS during a period in its history where the radionuclide production capacity was expanded considerably. This *growth phase* required certain actions and activities which are reflected in this work. Second, there is a pervading Nuclear Medicine perspective, as the main function of the radionuclide production programme at iThemba LABS is to serve the radiomedical community. In addition to single-photon emission computed tomography (SPECT) which has been an established modality in South Africa for several decades, positron emission tomography (PET) became a reality in this country only in 2006 and has shown rapid growth since. While certain therapeutic radionuclides such as radioiodine (^{131}I) for the treatment of thyroid cancer has been around for a long time, new radiopharmaceuticals based on radiometal-labelled biomolecules are becoming increasingly important for targeted radionuclide therapy. Thus, either SPECT, PET or radionuclide therapy will almost always be the underlying motivation for the studies presented here. Third, from a targetry perspective one has to investigate the relevant nuclear reactions, both of the desired radionuclides as well as their co-produced contaminants. The most-recent expansion of the radionuclide production capacity at iThemba LABS was achieved by introducing beam splitting as well as increased beam intensities. Targets that can withstand the higher beam intensities had to be developed. This required an understanding of several other physical processes, most notably the heat generated and radiation emitted during bombardment. From a targetry perspective, one has to provide for proper cooling in a regime of extremely high thermal power densities as well as suitable radiation shielding to bombard and handle targets safely. It is against this backdrop that the work presented here should be seen.

Radionuclides are, of course, not only used in medicine but in a vast array of commercial and non-commercial applications. Relevant cases are highlighted in this work where they overlap with the primary investigation, i.e. the medical application. It also has to be said that the

specific reactions and production routes investigated in this work can be seen as *case studies*, in that the general methodology can be employed in the study of many other radionuclides as well. Typically, if the production of a particular radionuclide has to be established for the first time, one would investigate all the nuclear reactions for its formation and consult the relevant production nuclear data. It is essential to have reliable excitation functions for both the desired radionuclide and the co-produced contaminants. If such data are not available, the correct starting point would be to measure and/or calculate them. From a nuclear data point of view, one would normally assume that nuclides of different elements can be separated, either chemically but sometimes also by a physical means (i.e. volatilization, electromagnetic isotope separation, etc.) The more serious co-produced contaminants, therefore, are those of the same elemental species. Once a reliable set of excitation functions covering the desired energy region is available, one can calculate the corresponding integral yield curves, taking into account growth from precursor decay if required. The next step would be to search for the optimum energy window, namely the region of energy which the target should span to maximize the yield of the radionuclide of choice while minimizing the co-produced contaminants. Quite often, an optimum may not exist but a compromise has to be made which gives a reasonable yield for the desired radionuclide and an acceptably low level of the radio contaminants. This is the only way to find the best production route. Sometimes this is an underestimated step which one really cannot emphasize enough – without good nuclear production data, the investigator is blind. Once the production energy window has been established, the best target material must be selected. Metals often make good targets, however, one may sometimes prefer a compound if the elemental material is chemically reactive. Thus, the physical and chemical properties of candidate target materials must be considered carefully. Their thermal properties, phase transitions (e.g. melting point, boiling point, secondary phase transitions which may lead to volume changes, etc.), reactivity with other materials (e.g. coolants, encapsulation materials, etc.) all need to be taken into account. Finally, prototype targets should be manufactured and tested in actual bombardments. The line of investigation does not usually stop there but may include the chemical processing of the target, further processing of the separated radionuclide into its final form (e.g. solutions ready for injection, labelled compounds, etc.) as well as various stages of quality control and assurance. A development programme may require several iterations of the scheme described above before all requirements are met.

The radionuclides and possible production routes investigated in this work have all been studied at the level of the nuclear data and in some cases extended to the development and testing of new targetry. At the same time, the upgrading of existing bombardment facilities continued as well as the development, construction and commissioning of one new bombardment station, which will be discussed in due course. The developments concerning further processing of irradiated targets have largely been done by others (colleagues in a different division) and are therefore not described in any great detail here.

The advent of new 70 MeV H^- medical cyclotrons is of considerable interest to iThemba LABS, one reason being that the routine production of radionuclides at this laboratory has been based on proton beams of 66 MeV (shared with the neutron therapy programme) since the eighties. Thus, iThemba LABS has been doing R&D work for many years in a comparable

energy and intensity region, in which it now has considerable experience, at a time when a number of other laboratories are being confronted with it for the first time. For this reason, arguments on the results as well as yield predictions are often extended/extrapolated to 70 MeV. According to Schmor [Sch2011] the main driver for these new commercial cyclotrons, such as the IBA Cyclone 70 XP, Best BSCI 70p and CIAE CYCCIAE70, is the production of ^{82}Sr/^{82}Rb and ^{68}Ge/^{68}Ga generators for nuclear medicine. These same generators were indeed the main driver for the new vertical-beam target station (VBTS) at iThemba LABS and, of course, the income that these products can earn for the laboratory.

It is interesting to ponder where the SSC of iThemba LABS fits into the radionuclide production scene, both locally and internationally. According to Lewis and Zetterberg in the CERN Courier of March 2012 [Lew2012], medical-isotope production cyclotron designs went full circle as they were small machines 80 years ago and in recent times returned to the dimensions of their predecessors. An IAEA report of 2006 estimated that, worldwide, there were about 350 cyclotrons at that time, primarily for the production of radionuclides, increasing at a rate of about 50 new cyclotrons per year [IAEA2006]. Lewis and Zetterberg [Lew2012] confirm this growth, estimating the rate between 50 and 60 new cyclotrons per year. So what is driving this growth? The majority of the new machines have operating energies between 10 and 20 MeV and are dedicated to the production of conventional PET radionuclides (mainly ^{11}C and ^{18}F). The arithmetic is fairly simple. By the end of 2014, about 750 medical cyclotrons will be operational around the world. About 75% of these machines will be dedicated to PET. At intermediate energies, the picture will be very different. To the best of our knowledge, only 6 accelerators will contribute to the production of ^{82}Sr for ^{82}Sr/^{82}Rb generators, including the SSC. Interestingly, ^{82}Rb and ^{68}Ga are also PET radionuclides. Over the past decade, ^{82}Rb experienced a growing demand as a PET agent for cardiac perfusion imaging. iThemba LABS positioned itself to take advantage of this demand, regularly exporting ^{82}Sr. The laboratory also exports ^{68}Ge/^{68}Ga generators as well as ^{22}Na in the form of positron emission sources. In addition, iThemba LABS is the sole producer of a number of short-lived medical radionuclides and radiopharmaceutical products in South Africa, regularly supplying ^{67}Ga and ^{123}I to about 60 hospitals and clinics all over the country. It is currently also the only producer of ^{18}F in the Western Cape and the main supplier of ^{18}F-FDG (fluorodeoxyglucose) in both the Eastern and Western Cape provinces. Various other radionuclides can be produced on demand, which will be discussed later.

1.2 Outline

In Chapter 2, an account is given of recent facility upgrades to increase the radionuclide production capacity at iThemba LABS. An overview is given of all the current radionuclide production target stations, their similarities and differences and the role of the latest addition, namely the vertical-beam target station (VBTS), to exploit the high-intensity proton beams delivered by the upgraded SSC. This necessitated a brief history of radionuclide production at iThemba LABS to be included as background information. Aspects of the new high-power targetry for ^{22}Na, ^{68}Ge and ^{82}Sr are discussed as well as the beam splitter, which makes it possible to perform radionuclide production bombardments simultaneously in two irradiation vaults. With

tandem targets in two target stations, the capability now exists to bombard four different targets simultaneously.

Chapters 3 and 4 discuss various aspects of the so-called quadruplet of terbium radionuclides, namely ^{149}Tb, ^{152}Tb, ^{155}Tb and ^{161}Tb. These radionuclides represent α-particle radionuclide therapy, PET, SPECT and β^- radionuclide therapy, respectively. Terbium is the only element in the periodic table that possesses such a unique quadruplet, which represents all the modalities of nuclear medicine. New excitation function measurements relevant to their production are presented as well as *a priori* theoretical predictions based on the geometry-dependent hybrid model (GDH) for pre-equilibrium reactions in combination with the Weisskopf-Ewing evaporation theory for the subsequent equilibrium decay (code ALICE/ASH). The new results are also compared with a relevant nuclear data compilation (TENDL-2012) as well as previously published results, where available. Chapter 3 is dedicated to proton-induced reactions on ^{nat}Gd. Based on the new cross-section measurements on natural target material, estimates are made for certain proton-induced reactions on enriched ^{152}Gd and ^{155}Gd. In a follow-up study, Chapter 4 presents limited new data on ^{152}Gd + p and ^{155}Gd + p to test these predictions as well as extensive new data on the production of Dy radionuclides in Tb + p. This allowed the investigation of the suitability of an indirect production route, ^{159}Tb(p,5n)^{155}Dy$\rightarrow^{155}$Tb, for the production of ^{155}Tb.

In Chapter 5, the production of certain radionuclides of zirconium are investigated. As some targets at iThemba LABS are encapsulated with niobium to prevent them from coming into contact with the cooling water, several ^{93}Nb(p,X)^{88}Zr processes can be exploited to produce the ^{88}Zr/^{88}Y generator as a byproduct. Furthermore, ^{89}Zr found some application in PET. The preparation of ^{88}Zr/^{88}Y generator stock solutions is of particular interest to iThemba LABS. These solutions can, in principle, be produced using targetry of Nb, Y or Zr. It was therefore of interest to compare the production yields obtainable by employing these three elements as target material. Similar to the results presented in Chapters 3 and 4, new experimental excitation functions are compared with ALICE/ASH predictions, the TENDL-2012 compilation as well as available results from the literature. As a byproduct of this work, excitation functions of selected Nb radionuclides in Nb + p have also been extracted as they have relevance in the thin layer activation (TLA) technique, which will be described in more detail later.

A stacked LiCl target developed for the production of ^{28}Mg in spallation reactions induced by 200 MeV protons on ^{nat}Cl is discussed in Chapter 6. The development of a radiochemical separation method formed part of the PhD project of another student [vdM2008] but the modelling of the target, using the Monte Carlo radiation transport code MCNPX, is presented here. Two methods are used to model the proton beam, namely by employing the so-called “cookie cutter cell” and by selecting the “focused beam” option, both sufficient to provide a realistic truncated Gaussian beam profile. The results from high-intensity bombardments on encapsulated LiCl targets are also presented.

Aspects of the production of the therapeutic radionuclide ^{186}Re and a selection of radionuclides of iridium in proton-induced reactions on highly enriched ^{192}Os are investigated in Chapter 7. The study includes new cross-section measurements, integral yield predictions and

comparisons with ALICE/ASH calculations as well as the TENDL-2012 values.

A dedicated ^{18}F production target system for the SSC is described in Chapter 8. In this case, the existing literature production data were found to be sufficient and the focus was therefore exclusively on target development. An elongated, single-cavity boiling water target is described. This target requires an incident beam of 18 MeV, however, the routine production of radionuclides with the SSC is based on a 66 MeV beam. As the SSC is a variable energy cyclotron, it can produce primary beams of 18 MeV, however, such additional energy changes could not be accommodated in the weekly beam schedule. The only viable option was to degrade the 66 MeV down to an average beam energy of 18 MeV, which proved to be challenging. It was found that severe radial spread of the beam reduced the bombardment efficiency to about 20%. A method was subsequently developed to degrade and re-shape the beam in such a way that it was much better matched to the requirements of the target, using the cooling water for most of the degrading. This resulted in a much improved bombardment efficiency. With the aid of the Monte Carlo codes SRIM and MCNPX, the degrader/collimator unit was modelled and refined. The experimentally measured bombardment efficiency for the final design is also compared to the corresponding values obtained from the MCNPX calculations.

In Chapter 9, several aspects of gas cooling of beam window foils are investigated. This work was required by the increase in beam intensity and the need to use thicker foils in the helium-cooled double-foil beam window design of the VBTS. At iThemba LABS, the target bombardment stations are isolated from the beamline vacuum using such windows. Measured convective heat-transfer coefficients are compared with calculations using formulations based on dimensional analysis. For the measurements, an experimental set-up using an electrically heated element was specially developed. Calculations of the radial temperature profiles of the beam windows during bombardment, for all the target stations, are also presented.

Chapter 10 is dedicated to further considerations concerning targetry for high-intensity bombardments. This includes a brief look at radiation shielding of target stations to protect sensitive equipment in the irradiation vaults. Some aspects of targetry not discussed in the preceding chapters, including aspects of target cooling and the limits of what can realistically be achieved in this regard, are presented here.

Finally, a summary and conclusions are presented in Chapter 11. Several appendices are also presented, covering aspects which are relevant to the discussion but where it was felt that a full explanation in the relevant chapters would detract from the main themes. As such, the appendices are not merely a repository for information of secondary importance but rather a space to describe the underlying principles more thorougly, present additional material and extend the discussion.

Chapter 2

Target Stations and Bombardments with High Intensity Beams

2.1 Introduction

The radionuclide production programme of the separated-sector cyclotron facility (SSC) of iThemba LABS received its first test beam in October 1986. Bombardment infrastructure and targetry development continued throughout 1987 and routine production commenced in 1988. At that time, the maximum intensity of the 66 MeV proton beam, shared with the neutron therapy programme, was not foreseen to exceed 100 μA. As a result, the beam delivery and bombardment infrastructure, targetry, and ancillary facilities were designed with this value of 100 μA as a *de facto* upper limit [Mil1989, Haa1992]. This situation remained unchanged during the first decade of operation even though the programme evolved significantly as a result of continuing research and development (R&D) work. For example, in addition to the relatively short-lived radionuclides required by the South African nuclear medicine community for diagnostic procedures, the laboratory also developed targetry and processing methods for the relatively long-lived radionuclides ^{22}Na ($T_{1/2} = 2.603$ y), ^{68}Ge ($T_{1/2} = 270.82$ d) and ^{82}Sr ($T_{1/2} = 25.34$ d) – this will be further elaborated on in due course. As the programme entered its second decade, however, it became abundantly clear that the laboratory would not be able to meet its future obligations in terms of the delivery of radionuclides to a growing client base. An investigation into the available options to address this potential shortfall, in particular towards and beyond the approaching new millennium, pointed towards the need for a substantial increase in the maximum operational beam intensity.

As for any programme sharing the beam at a multi-disciplinary accelerator facility, the radionuclide production programme at iThemba LABS has to contend with unavoidable constraints on the available beam time. A typical weekly operating schedule for the SSC is shown in Fig. 2.1. Briefly, the normal daylight working hours from Mondays to Fridays are dedicated to the treatment of patients undergoing radiotherapy. Experimental nuclear physics is mainly performed during the weekends. This limits the radionuclide production bombardments to mainly the night-time hours, from Monday evenings to Friday mornings. It should also be noted that the time required to change the beam energy (and/or the development of beams of other ion species) is quite significant, therefore it is essential to keep the number of changes

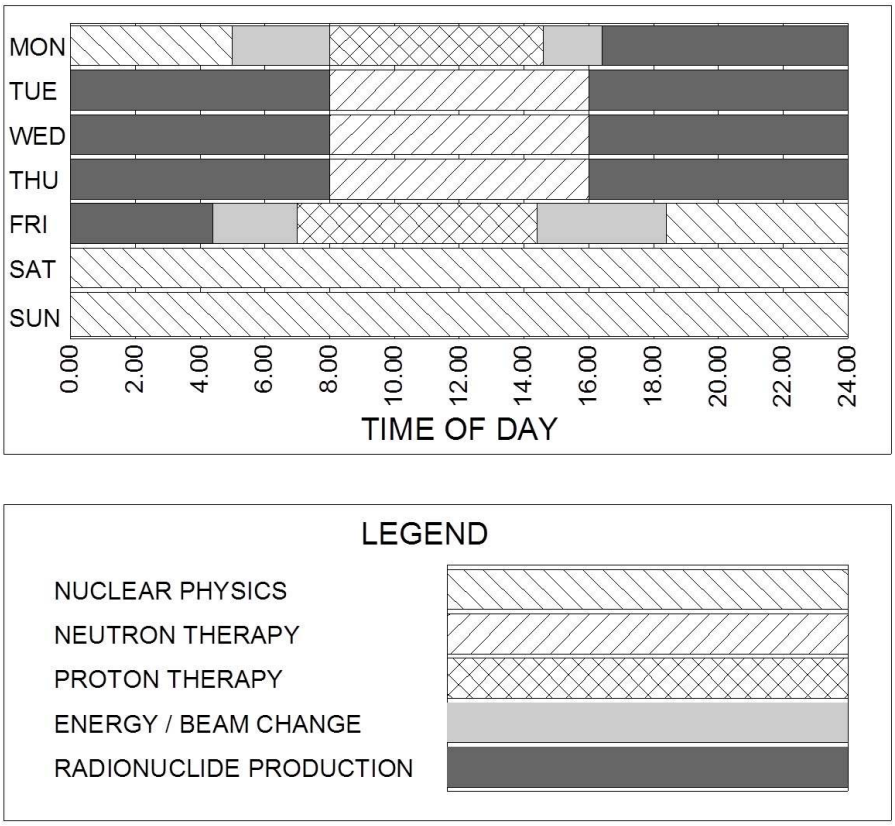

Figure 2.1: A typical weekly beam schedule at iThemba LABS.

as low as possible. It is primarily for this reason that the routine radionuclide production programme utilizes the same proton beam energy of 66 MeV which the radiotherapy programme requires for the generation of their neutron beams. This may, perhaps, seem like an unfortunate limitation for a variable-energy $K = 200$ cyclotron, however, there is an additional benefit over and above the saving of beam time. During the times dedicated for neutron therapy it is often possible to switch the beam to one of the radionuclide production vaults between treatments, e.g. while patients are being set up for treatment. In fact, a rapid beam switching system has been in operation since the early days of beam operations on the SSC, with typical switching times of only a couple of minutes. While this measure would frequently lead to meaningful gains, the total beam time for radionuclide production in a normal week remained in the region 50 to 60 hours. Thus, it was quite clear that a significant increase in the production capacity by manipulating the beam-time allocations to participating programmes was not feasible. Another solution had to be found, in particular one that would propel the production capacity of certain longer-lived, high-value radionuclides well into the terabecquerel regime. Amongst these, ^{68}Ge and ^{82}Sr are especially important as they are precursors (and therefore employed in generators) of ^{68}Ga and ^{82}Rb, respectively, both being important tracers in positron emission tomography (PET) applications (see e.g. [Faß2004, Bai2005, Sch2008, Sch2009] and references therein).

Two main constraints had to be adhered to in the proposed upgrade plan: (1) The existing routine radionuclide production activities had to be continued undisturbed; (2) No additional beam time from the SSC could be requested over and above the normal allocation (see Fig. 2.1).

The decision was therefore made to design and construct a new bombardment station, to be located in a dedicated irradiation vault, as well as targetry which could sustain beam intensities of nominally 250 μA for extended periods of time [Cel2000, Con2005]. In addition, a beam splitter would be designed and constructed which would enable the supply of beam to the new bombardment station as well as one of the existing bombardment stations simultaneously [Fou2005, Nca2005, Con2007]. In order to extract beams of higher intensity, changes and improvements also had to be made to the SSC and one of its injector cyclotrons, a $K = 8$ solid-pole cyclotron (SPC1). Both the SSC and SPC1 had to be supplied with flat-top RF resonators to increase the fraction of the RF phase which can be effectively used for acceleration [Cel2000, Con2005, Nca2005, deV2005]. This would lead to a larger number of protons per beam pulse, however, the pulses would also become longer in spatial extent, requiring an additional buncher [Nca2005] in the transfer beamline connecting SPC1 with the SSC. Furthermore, a host of new beam diagnostics, control and interlocking elements would be required. This included the development of non-destructive beam diagnostic equipment for beam position monitoring [Die2004, Die2008] and current measurement [Kor2008], segmented ionization chambers to detect stray beam [Con2007], and new beam phase measuring equipment for the SSC [Con2006, Con2010].

The aim of this chapter is to give an overview of the entire, now completed upgrade project and to discuss the performance of the new vertical-beam target station (VBTS) and its targetry [Ste2004]. In order to do this, it is useful to discuss the main similarities and differences between all the bombardment stations in use for radionuclide production at iThemba LABS as this sheds light on the overall operational philosophy and the role of the VBTS.

2.2 Production prior to commissioning the VBTS

A total of four high-energy beamlines are currenly dedicated to the radionuclide production programme at iThemba LABS – three horizontal beamlines in one vault and one vertical beamline in another. For many years, only the horizontal beams were available while the space where the vertical-beam vault is now located was being used as a "graveyard" for radioactive waste. It was not a trivial task to clear all that waste out and decontaminate the vault prior to installation of the VBTS. In this section, we would like to briefly describe the infrastructure in the horizontal-beam vault as it strongly influenced the VBTS design.

2.2.1 Target Station 1

The first horizontal-beam target station built at iThemba LABS, referred to as Target Station 1 and often also by its nickname "The Elephant", is a facility for the bombardment of batch targets. At the time of its design and construction, it was foreseen to be the only irradiation facility for routine production purposes in the foreseeable future. It has proved to be very versatile. It has been fully operational since 1987 and is still being used extensively today. Relatively few modifications to the hardware have been made over the years, thus, the description and technical details by Mills *et al.* [Mil1989] are still largely relevant. The beam diagnostics have improved considerably however, and the control system has been upgraded through a num-

ber of iterations. The design of subsequent target stations at iThemba LABS has largely been influenced by the experience gained on Target Station 1, therefore, it is useful to give a brief description of its salient features:

- Target handling is by remote control to limit radiation exposure to staff. Target holders are transferred to and from the target station by means of an electro-pneumatic robot arm. This same robot arm facilitates the transfer of target holders to and from an electrically-driven target transport trolley which moves on rails. In this way, target holders are transported to and from a hot-cell complex, the irradiation vaults and a target loading station as well as a remotely-controlled target storage facility, all connected via a single rail system. The robot arm, transport trolley and part of the rail are shown in Fig. 2.2.

- A thick, multi-layer radiation shield in close proximity to the target suppresses the neutron flux into the vault by around three orders of magnitude. This protects sensitive components inside the vault from radiation damage and prevents excessive neutron activation of the vault and its contents [Mil1989, Ste1992]. The shield has an inner iron layer to effectively slow down fast neutrons to intermediate energies via non-elastic interactions. Neutrons below about 4 MeV are moderated to thermal energies in the middle layer of the shield by elastic scattering with the hydrogen nuclei in the borated paraffin wax, while the boron serves to absorb many of them by thermal neutron capture. An outer lead layer mainly serves to attenuate gamma-rays, especially the 2.2 MeV photons emitted in the capture of thermal neutrons by hydrogen.

- A rotatable target magazine provides versatility to the production programme as several target holders can be loaded into the station prior to a period of intense bombardment. The initial target magazine could accommodate fifteen target holders, however, this was later decided to be an overkill and a replacement magazine which has provision for nine target holders was subsequently fitted. The scaled-down magazine simplified servicing of the station but still provided enough capacity to gain maximum benefit from this feature. Aspects of the standardized target holders will be discussed later.

- The final beam diagnostics prior to the beam reaching the target is located in a diagnostic chamber just upstream of the station (see Fig. 2.2). A four-sector graphite collimator is located in the shielding wall to assist in focusing and centering the beam and to prevent beam from reaching any structures other than the target. These graphite sectors are thick enough to stop the beam. The electric current on each sector is monitored independently as this provides one of the most crucial interlocks to protect the station and beamline from damage caused by a misaligned and/or drifting beam. An overcurrent on a sector will trigger the RF to be switched off within a response time not expected to exceed 30 milliseconds.

- In order to prevent hot spots and to spread the thermal load over a larger surface area of the target, the beam is swept in a circular fashion around the beamline axis. Two small, orthogonal dipole magnets mounted on the outside of the beam pipe is used for

this purpose. The sweep frequency is 450 Hz. The beam sweeping will be discussed in more detail later.

- Targets are irradiated outside the cyclotron and beamline vacuum. A helium-cooled, double-foil Havar window serves to isolate the vacuum from the station. These foils, only a few tens of μm thick, are thin enough to cause minimal degradation to the 66 MeV proton beam [Mil1989, Ste1990].

- An electro-pneumatically controlled pusher arm connects the cooling water to a target holder.

- The entire target station is isolated electrically from earth in order to monitor the beam current and measure the accumulated charge accurately. The entire station, therefore, acts as a Faraday cup. An upper limit set on the beam current is also a crucial parameter provided to the beam interlock system.

For close to a decade, Target Station 1 was the only bombardment facility at iThemba LABS for the routine production of radionuclides. The initial production using batch targets included ^{52}Fe, ^{67}Ga, ^{81}Rb/^{81m}Kr, ^{111}In, ^{123}I and ^{201}Tl [Haa1992]. Later, ^{22}Na, ^{68}Ge and ^{82}Sr became important additions to this list. Nowadays, this target station is still routinely used for the production of mainly five "bread-and-butter" radionuclides, namely ^{22}Na, ^{67}Ga, ^{68}Ge, ^{82}Sr and ^{123}I as interest in some of the other radionuclides have dwindled. A variety of radionuclides for

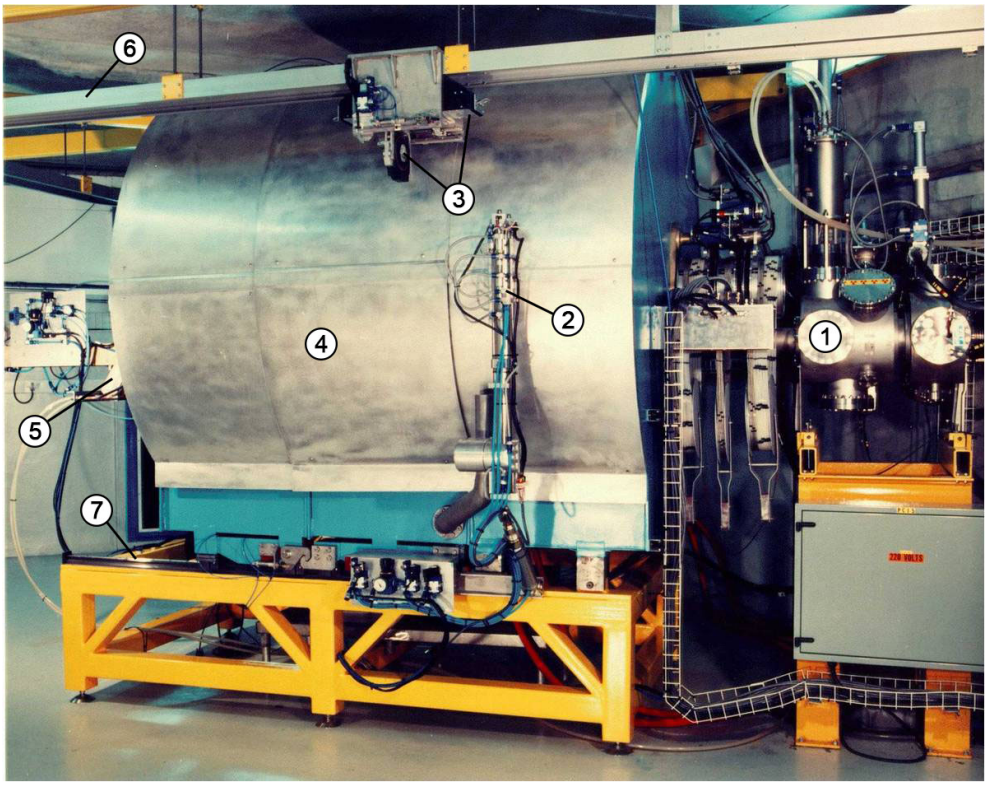

Figure 2.2: Target Station 1 (also called the Elephant) for irradiating batch targets, showing (1) the last diagnostic chamber on a horizontal beamline, (2) robot-arm for target exchanges, (3) a target holder on a target transport trolley, (4) local radiation shield, (5) pusher arm to connect cooling water, (6) rail for target transport, and (7) rail on which part of the shielding can move in order to open the station.

experimental purposes have also been made in ad-hoc bombardments with this facility when required. This includes ^{44}Ti, ^{55}Fe, ^{64}Cu, ^{103}Pd, ^{133}Ba, ^{139}Ce and ^{227}Pa, amongst others.

2.2.2 Target Station 2

A second target station, dedicated to the bombardment of semi-permanent targets, was designed and built at iThemba LABS [Nor1999]. Target Station 2, usually referred to by its nickname "Babe", received first beam in 1996. It is also a shielded and electrically isolated station like Target Station 1 but slightly smaller (see Fig. 2.3). It originally accommodated an in-house developed neon target system for the production of ^{18}F [Nor1996] but this was later replaced with an enriched ^{18}O-water target in order to increase the production yield [Ver2006]. Target Station 2 differs from Target Station 1 in the following ways:

- No beam sweeping is currently done on this station. Instead, the 66 MeV beam is degraded considerably (to nominally 18 MeV for the $H_2{}^{18}O$ target) using mainly the fast-flowing cooling water as the degrader medium, whereafter it is re-shaped with a solid collimator before impinging on the target [Ver2006].
- A target magazine with three positions has been provided to make provision for future expansion, however, this has not yet been utilized as the station only housed one target system at any given time to date. As it is dedicated to semi-permanent targets, there is no robot arm or any service to the rail transport system.
- There is also no electro-pneumatic pusher assembly to connect cooling water to the target(s). Instead, flexible hoses are directly connected to the target system(s) as they are semi-permanent installations.

Figure 2.3: Target Station 2 (also called Babe) for irradiating semi-permanent targets.

It has to be mentioned that the production of ^{18}F with the large separated-sector cyclotron of iThemba LABS has never been envisaged as a permanent measure. The rationale was to stimulate the establishment of PET in South Africa and to provide ^{18}F until such time when the purchase of a dedicated PET cyclotron would be warranted. A small, commercial PET cyclotron with dedicated targetry has since been installed at the Faure premises of iThemba LABS. This cyclotron, operational since 2012, is the third such installation in South Africa and the only one in the Western Cape. While no longer in routine use, the stand-alone $H_2{}^{18}O$ target system in Target Station 2 is still being maintained as a back-up facility. A possible future scenario is that an enriched ^{124}Xe state-of-the-art gas target for the production of ^{123}I with a high radionuclidic purity may also be accommodated in this station. Aspects of production in Target Station 2 are further discussed in Chapter 8.

2.2.3 Experimental beamline

The third beamline in the horizontal-beam vault is dedicated to experimental studies. It is mentioned here for the sake of completeness, in particular since it has been equipped with a specialized target station for the activation of thin targets and/or foil stacks with beams of low intensity. Originally intended for the measurement of recoil ranges in nuclear reactions, this unshielded station is also ideally suited for the measurement of excitation functions, which is essential for choosing the most suitable production route for any given radionuclide and to optimize its targetry. The RERAME-II (REcoil RAnge MEasurements) facility at iThemba LABS [Sze2005] is based on a similar set-up, the original RERAME [Fre1994] at the Laboratorio Nazionale del Sud (LNS) in Catania, Italy. A photograph of the RERAME-II chamber is shown in Fig. 2.4. A vice mechanism for holding the target foils or samples in position as well as a collimator assembly is mounted on the door of the chamber. The door can be opened through 180°, thus bringing parts which are normally inside the chamber to the outside. This allows for rapid and easy removal of targets. A rotatable handle mounted on the door controls the opening and closing of the jaws of the vice, making it easy to accommodate foil stacks or targets of various sizes. The chamber is also equipped with insulated feed-throughs for electrical connections, vacuum connections and a transparent port for viewing a fluorescent beam monitor with a CCD camera. A beryllium oxide (BeO_2) viewer can be placed in the target position for focusing the beam. The entire chamber is electrically isolated from earth and is provided with electron suppression at the beam entrance. This makes it a true Faraday chamber and allows for the absolute measurement of the instantaneous and integrated current (i.e. the cumulative charge.) More detail on the RERAME chamber is given in Appendix A.

2.3 Design features and role of the VBTS

2.3.1 Background

The vertical-beam target station (VBTS) was specifically designed for the production of longer-lived radionuclides with increased beam intensities. It is currently used for the large-scale production of ^{22}Na, ^{68}Ge and ^{82}Sr with beam currents of typically 250 μA, but bombardments up to 300 μA have been demonstrated. A photograph of the VBTS is shown in Fig. 2.5. A direct

Figure 2.4: The RERAME-II irradiation chamber with the door in an open position. The collimator and vice assemblies are mounted on the door. The guide rods on which the jaws of the vice move ensure positional accuracy. The beamline connects to the chamber on the left of the picture.

comparison with Fig. 2.2 shows that the philosophy of the VBTS is very similar to that of Target Station 1. Both stations are used for the bombardment of batch targets. A schematic side view of the VBTS is shown in Fig. 2.6.

The vertical-beam vault is located on a lower level than the horizontal-beam vault. In fact, the 90° bending magnet is situated on the same level as the horizontal-beam target stations (see Fig. 2.6) with most of the vertical beamline located in a channel through the thick concrete roof shielding of the vertical-beam vault. Severe space limitations, especially in the vertical direction, made this quite a challenging project. There was no space, for example, to provide this vault with a neutron shutter as has been done for all the other vaults of the SSC facility. Nevertheless, the completed VBTS proved to be functional and reliable, albeit with some components located in hard-to-reach places. Inexplicably, it has also not acquired a nickname like the other target stations. The design of the building preceded the decision to place a shielded target station in that location, therefore, it has to be said that if one could start the project from scratch, it would be prudent to specify a much larger vault. We feel that it is necessary to point this out as the discerning reader may be mystified about the lay-out of this facility. In order to maximize the distance between the sweeper magnets and the target due to ion-optical considerations, the target is located very close to the floor of the vault. Consequently, there was no space for a support frame which could be electrically isolated from earth, such as those of the other target stations. In fact, the rails on which the two halves of the radiation shield move are recessed into the vault floor. Without electrical isolation the station cannot function like a Faraday cup, therefore another solution had to be found to measure the beam current and accumulated charge. The relatively small distance between the sweeper magnets and the

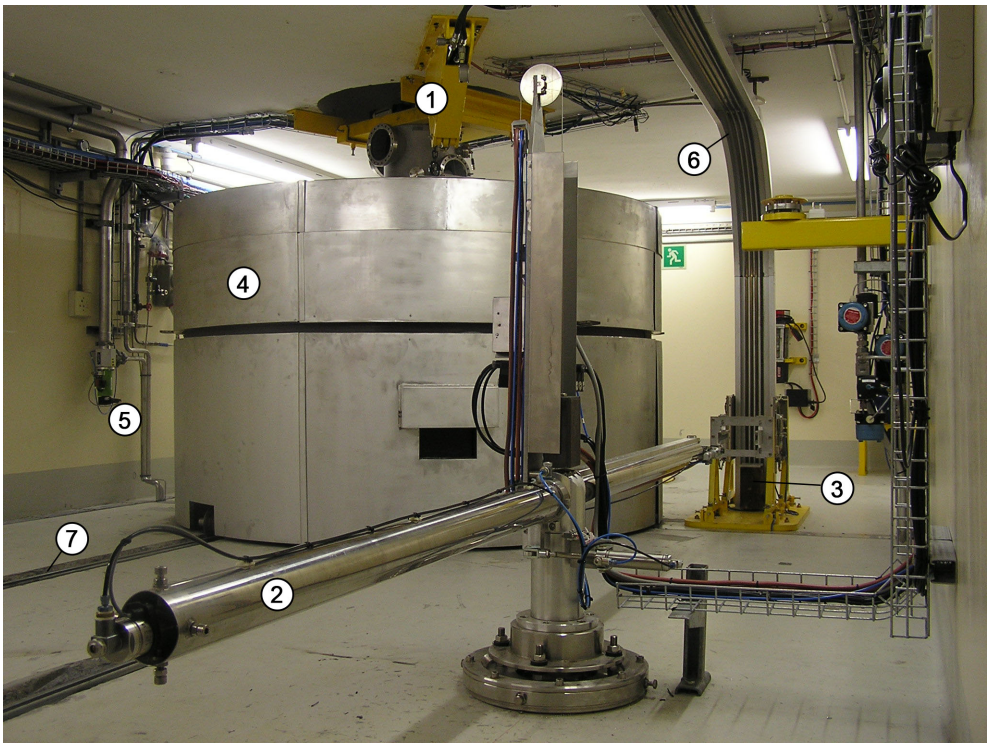

Figure 2.5: The vertical-beam target station (VBTS), showing (1) the diagnostic chamber on the vertical beamline, (2) robot-arm for target exchanges, (3) target transport trolley terminus, (4) local radiation shield, (5) cooling-water lines, (6) rail for target transport, and (7) rail on which one sector of the shielding can move in order to open the station. An idea of scale can be obtained by noting that the vault roof is only 2 m above the floor.

target also required a revised strategy as the required sweep radius could not be achieved with the type of magnets used on Target Station 1. This will be discussed in more detail later. The VBTS also differs from Target Station 1 in that it lacks a target magazine – there simply was not enough space to fit one. This is fortunately not very serious, however, as targets for long-lived radionuclides are less frequently exchanged. In the following paragraphs, aspects of the targetry will be discussed first, followed by the matching requirements for the beam.

2.3.2 Targetry

The targetry developed for the VBTS is strongly influenced by the methodology used by the Brookhaven Linac Isotope Producer (BLIP) as well as the Isotope Production Facility (IPF) at Los Alamos National Laboratory (LANL) in the USA (see e.g. [Mau1983, Mau1990, Med2012, Nor2004, Nor2007] and references therein). The targets are disc shaped and completely surrounded by fast-flowing cooling water (i.e. a 4π cooling geometry). Sensitive target materials that should not come directly into contact with the cooling water (e.g. materials with a low melting point, water-soluble compounds like salts, substances that readily corrode in water, etc.) are clad (encapsulated) in thin metal jackets (capsules) with a sufficiently high melting point and/or other desired properties (e.g. chemical inertness to the target material). The reader is referred to Ref. [Ste2008a] for details on capsule manufacturing, sealing of the capsules by modern welding techniques (e.g. laser welding and electron-beam welding under vacuum) and the promising method of neutron radiography to investigate their integrity. Four types of target have been developed for the VBTS:

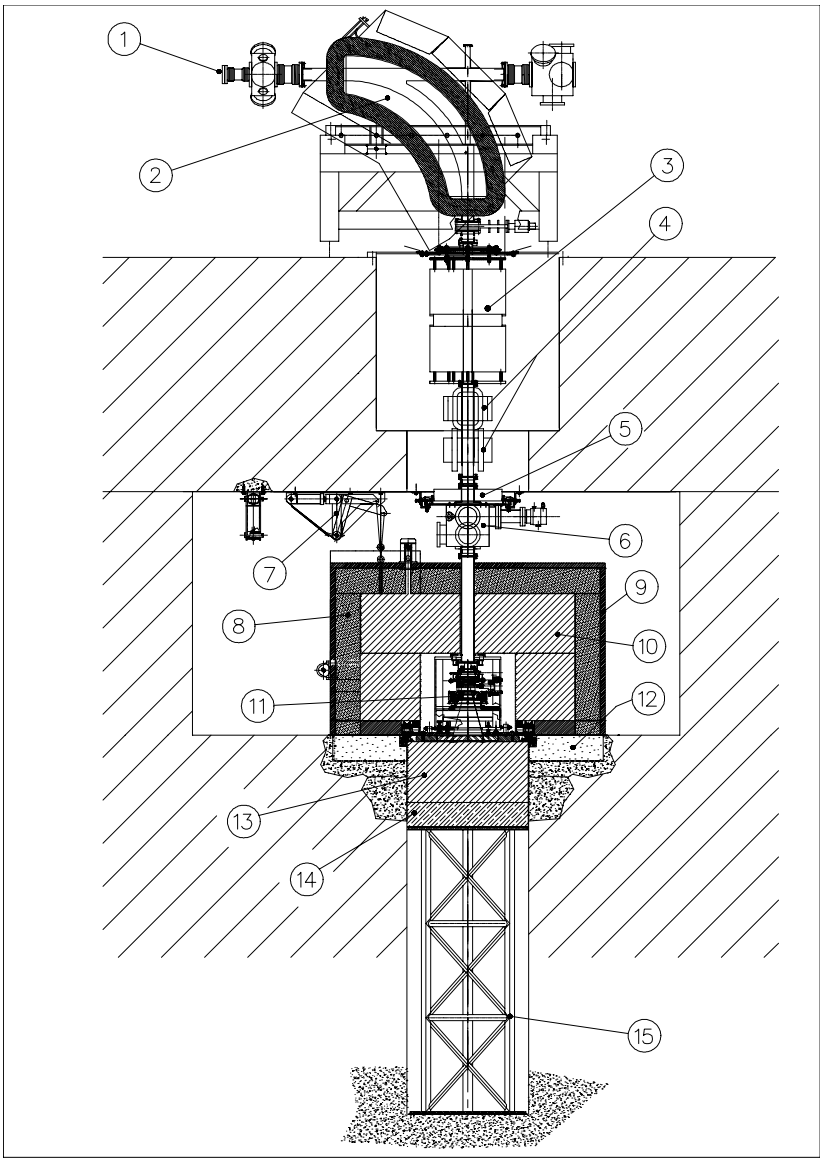

Figure 2.6: Schematic side view of the vertical beam target station (VBTS) showing (1) a section of the horizontal beamline, (2) 90° bending magnet, (3) a set of quadrupoles for final focusing, (4) orthogonal sweeping magnets for circular sweeping of the beam, (5) a set of orthogonal steering magnets, (6) diagnostic chamber, (7) a mechanism to lift a section of the shielding during target exchanges, (8) borated paraffin-wax middle layer of shield, (9) outer lead layer of shield, (10) inner iron layer of shield, (11) the target, (12) below floor-level water tanks containing 4% ammonium pentaborate solution, (13) forward iron shield, (14) forward borated paraffin-wax shield, and (15) support tower.

- Natural metallic gallium cladded with niobium for the production of ^{68}Ge. Two nuclear reactions contribute, namely ^{69}Ga(p,2n)^{68}Ge (which is dominant) and ^{71}Ga(p,4n)^{68}Ge. Gallium has a melting point of only 29.78 °C, thus during bombardment it is in a molten state inside the niobium capsule which, due to its high melting point of 2468 °C, remains in a solid state. Niobium is chosen specifically for its high resistance to chemical attack by molten gallium. (Selective volatilization [vdM2011] is used to recover the ^{68}Ge from the irradiated Ga.)

- Natural metallic rubidium cladded with grade 316 stainless steel for the production of ^{82}Sr. The relevant nuclear reactions are ^{85}Rb(p,4n)^{82}Sr and ^{87}Rb(p,6n)^{82}Sr. Rubidium also has a low melting point of 38.89 °C and is in a molten state during bombardment, while

the stainless steel (melting point of about 1400°C) remains solid. These targets are used for the large-scale production of ^{82}Sr.

- Natural RbCl compressed salt tablets encapsulated in niobium. This is an alternative target to the one described above for the production of ^{82}Sr [vdM2013] and is rather infrequently employed, mainly to produce relatively small quantities for local use.
- Natural magnesium cladded with niobium for the production of ^{22}Na with a high radionuclidic and radiochemical purity, mainly used in positron emission sources.

In principle, target discs can be stacked behind each other and irradiated together in series if the beam energy is high enough to penetrate through the stack to the last disc at the back. The 66 MeV proton beam only allows meaningful tandem targetry, in contrast to the three-target stacks typically utilized at the 100 MeV proton beam facility of the IPF at Los Alamos. Figure 2.7 compares tandem targets for the production of ^{82}Sr/^{68}Ge in Target Station 1 and the VBTS. As can be seen in the figure, they are similar in thickness but different in diameter – 22 mm outer diameter for Target Station 1 and 40 mm for the VBTS. It is the larger surface area of the VBTS targets which allows them to be bombarded with a higher beam current, simply because there is more water-cooled surface to remove the heat from. Roughly, one would expect the thermal performance in terms of the maximum beam current that these targets can handle to scale linearly with the cooled surface area, and this is indeed what we found in practice. There is a proviso, however, namely that the beam should be properly spread, e.g. by sweeping, as will be discussed later. The relevant excitation functions for this particular case are shown in Fig. 2.8. The vertical dashed lines indicate typical production energy windows. It is clear that each energy window nicely contains the maximum of the relevant excitation function. This is a very good example of a successful tandem configuration, with one radionuclide being produced in a higher-energy slot (^{82}Sr) and one in a lower-energy slot (^{68}Ge). Some energy regions are not

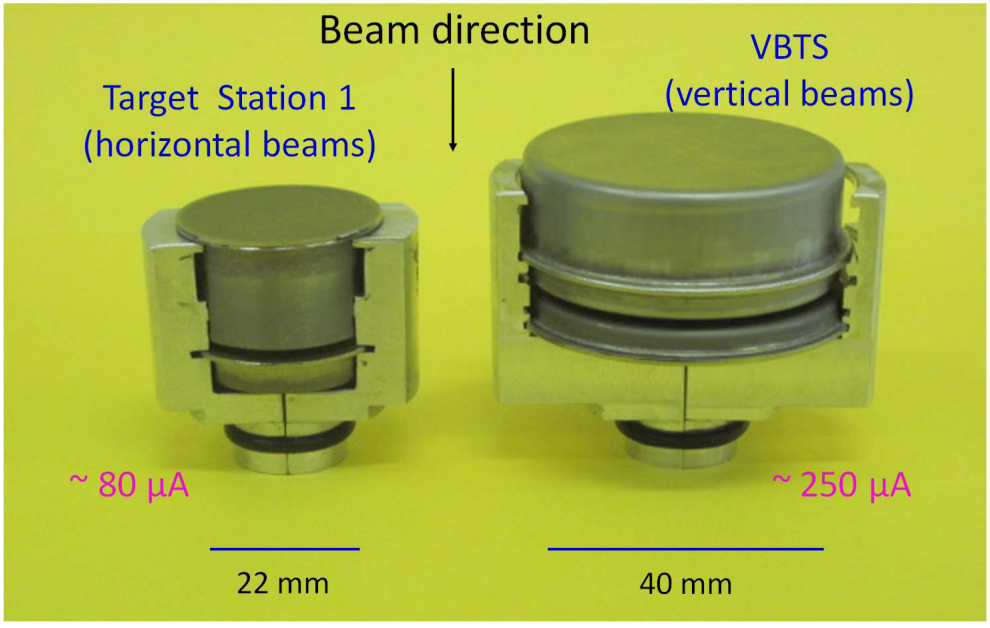

Figure 2.7: Tandem targets for the production of ^{82}Sr and ^{68}Ge. Note the gap for a 1 mm thick fast-flowing water layer between the two encapsulated discs.

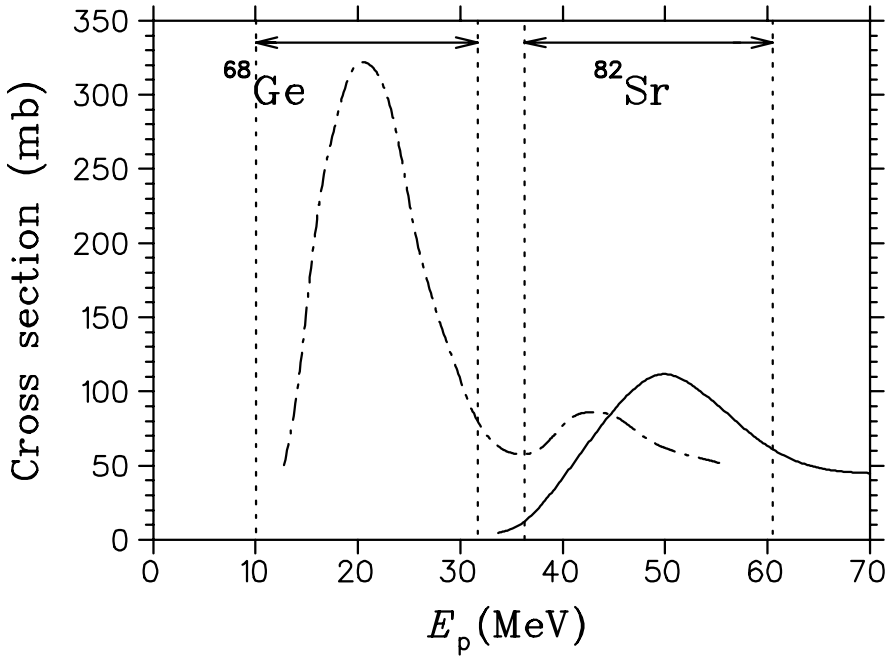

Figure 2.8: Excitation functions for the production of ^{82}Sr and ^{68}Ge. The curves are spline fits through the data of IAEA-Tecdoc-1211 [Gul2001]. Typical energy windows in a tandem target are indicated by the dashed vertical lines.

available for production purposes due to the presence of the cladding materials and cooling-water layers. The thickness of the cooling-water layers is nominally 1 mm. Such thin water layers are employed to reduce the size of "dead regions in energy" (so-called dead layers) and they also help to achieve a high linear velocity of the cooling water. This will be discussed in more detail in Chapter 10.

In Fig. 2.9 the target holders of Target Station 1 and the VBTS are compared, while Fig. 2.10 shows an exploded schematic view of a loaded target holder. The outer dimensions of the VBTS target holders had to be made the same as those of Target Station 1 in order to be compatible with the target transport trolley and other existing target handling infrastructure. The dimensions of the inner cavities are different, however, due to the different target diameters to be accommodated. The holders used in Target Station 1 have two inlet and two outlet water ports each, while those used in the VBTS have double this number (i.e. four inlet and four outlet ports, respectively) because more cooling is required at higher beam intensities. During bombardment, the cooling-water flow through each port is nominally 30 L/min at an inlet pressure of about 10 bar and at room temperature. In the case of the VBTS, this gives a linear flow velocity of about 16 m/s and 480 exchanges of the water volume in the target holder per second. The relatively high flow rate is required to suppress surface boiling as the thermal power density is rather large because of the limited available surface area to cool from. It is essential to prevent reaching or exceeding the critical heat flux (CHF) where the development of steam becomes significant enough to effectively isolate the cooling water from making proper contact with the hot target surfaces, as such conditions lead to rapid burnout. In fact, the CHF is an increasing function of the fluid velocity in subcooled flow conditions [Cel1992]. VBTS targets have already been operated at a thermal load just above 20 kW, conditions under which they become quite hot objects and thermally close to CHF. This is why such a large

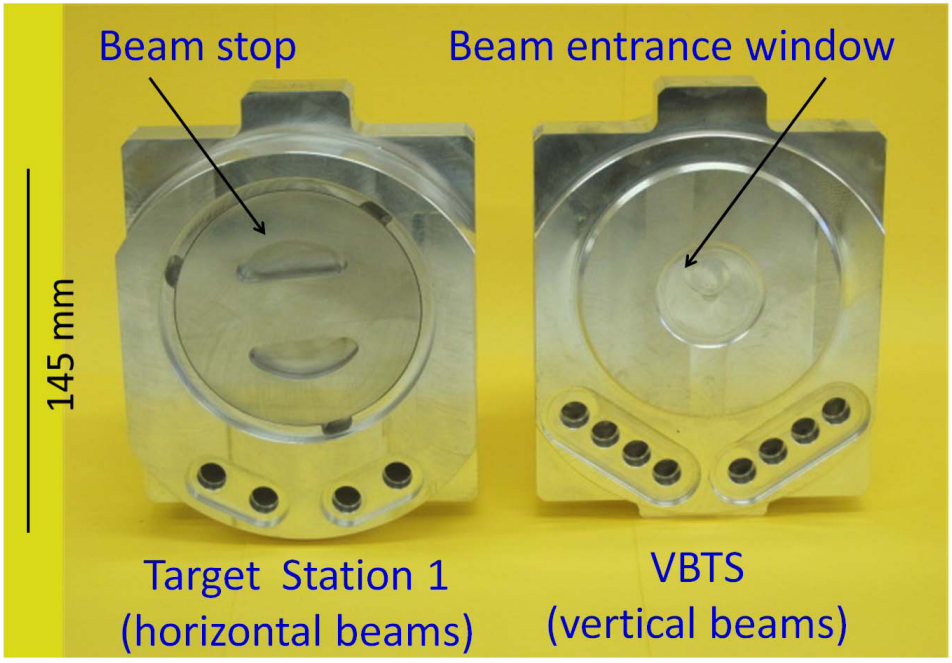

Figure 2.9: Latest generation of target holders used in Target Station 1 and the VBTS. Note that the VBTS version has twice the number of inlet and outlet cooling-water ports.

number of cooling-water exchanges per second is desirable – as steam develops it should be flushed out as rapidly as possible. We will return to the matter of high heat fluxes and CHF in Section 2.3.4.

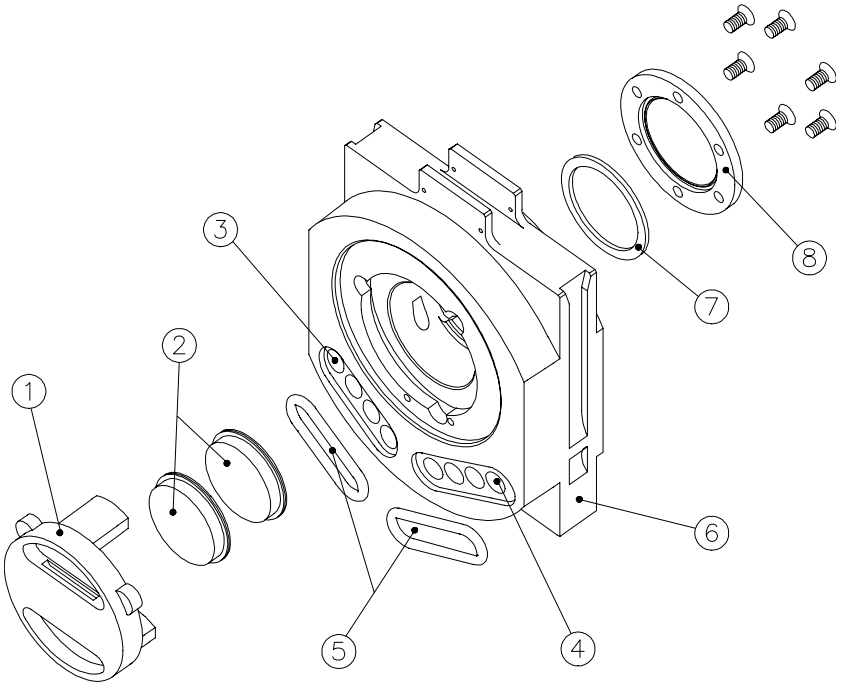

Figure 2.10: Exploded view of a tandem target holder, showing (1) beamstop, (2) two target discs behind each other, (3) cooling-water inlet ports, (4) cooling-water outlet ports, (5) molded rubber seals, (6) aluminium target-holder body, (7) metal seal, and (8) beam entrance window.

A further advantage of a high flow rate is that the convective heat-transfer coefficient increases with increasing linear velocity of the coolant. This usually follows a power law, namely

$h \propto v^x$ where x is known to have a value near 0.8 when water is the coolant. While some numerical heat-transfer calculations have been performed and are useful, these cannot predict how hot, chemically-reactive materials will behave in an intense proton beam. The importance of experimentation and practical experience should therefore never be underestimated. Niobium, for example, is not completely inert and chemical attack by molten gallium is often thought to be responsible for target failure. A recent study [Bac2013] found a correlation between the crystaline properties of the niobium (grain size and uniformity) and target failure of Nb-encapsuled Ga targets, suggesting that stock and/or supplier selection may be important to improve their survival probability. We mention this just to emphasize the complexity of issues surrounding high-power targetry. At iThemba LABS, we did experience some target failures and they do still happen occasionally. Such events can be rather painful. Fortunately, only very rarely did any collateral damage to equipment result from a target failure at our facilities. Interestingly, the modes and frequency of target failure seem to be about the same for the VBTS and Target Station 1 and in terms of reliability the two stations seem to behave similarly.

One difference between the target holders shown in Figs. 2.9 and 2.10 concerns the beam entrance window. These windows used to be manufactured separately and bolted on (see Fig. 2.10) using soft copper seals to obtain a waterproof assembly. While generally quite reliable, occasionally one would leak. A recent test batch of target holders was made on a state-of-the-art CNC (computer numeric control) milling machine in such a way that the beam entrance window remained as an integral part of the target holder body. These holders, shown in Fig. 2.9, are now being evaluated in actual productions runs. One last point concerning targetry that we would like to make is that state-of-the-art targets as described above cannot be made without modern machine tools – an appropriate CNC mill and associated quality control to accurately cut the quite complex faces of the target holders and electron-beam welding under vacuum to clad targets are both absolutely essential. We have also started leveraging 3D printing to rapidly prototype the designs of targetry components that are complex and expensive to manufacture. As we do not have any of these apparatus in-house at iThemba LABS, a significant part of the target manufacturing has to be outsourced at present.

2.3.3 Vertical beamline and beam sweeping

As shown in Fig. 2.6, a single bending magnet with zero degree entrance and exit angles bends the beam from the horizontal direction into the vertical direction. The beam then passes through two quadrupole magnets for final focusing. Below the last quadrupole the two orthogonal sweeper magnets are located. Two orthogonal steering magnets are located below the last sweeper magnet. There used to be only one steerer magnet as small adjustments to the bending magnet current was used for steering in the orthogonal direction. While this worked quite well and the method was used for several years, a second steerer magnet was recently added for the sake of more flexibility and to simplify the beam set-up procedure. A diagnostic chamber is located just below the steerer-magnet assembly. This chamber contains a harp and a Faraday cup for measuring the beam position and current, respectively, as well as a capacitive probe to measure the beam current in a non-destructive manner. The harp and Faraday cup can only be put into the beam at relatively low beam intensities (up to approx-

imately 1 μA) and is essential during the initial stages of setting up the beam. With higher beam intensities, the currents on the four sectors of the entrance collimator provide the beam position information in the region of the target. This collimator is sandwiched in-between (and in close proximity to) the target and the double-foil Havar beam window assembly.

Intensity profiles of 66 MeV proton beams at iThemba LABS have been measured many times and can normally be reproduced satisfactorily with a Gaussian truncated at a width of twice the full width at half maximum (2 $\times$ FWHM). An example is shown in Fig. 2.11, obtained by analyzing an autoradiogram made on radiochromic film with an open source version of the software package DoseLab [Dem2000]. As will be shown below, the circular sweeping (wobbling) of a well-defined beam on a sensible sweep radius results in a significantly better distribution of the thermal load than simply defocusing the beam to the same overall size. There is a proviso, however, namely that the sweep frequency should also be sensible and matched to the time structure of the beam. In this regard, we would like to quote from the Proceedings of the First Workshop on Targetry and Target Chemistry [Bec1985] where the following statement was made during a discussion on the thermal properties of target foils: *"The Louvain group observed that beam wobbling was effective only in the case when the beam strike was swept at a frequency (kHz) far greater than the reciprocal of the thermal rise time. Beam sweeping at mains frequency (50–60 Hz) is analogous to slowly moving a concentrated blowtorch over a thin plate."* Furthermore, the thermal rise time increases with increasing target volume and decreases with increasing surface area from which cooling takes place.

Transient heat-transfer calculations have been performed for typical beams incident on the 25 μm Havar foils used on the beam-window assemblies of the horizontal-beam target stations as well as the 50 μm outer (atmosphere side) and 75 μm inner (vacuum side) Havar foils in the case of the VBTS. Rise times between 30 and 40 milliseconds are typical but they can be lower if

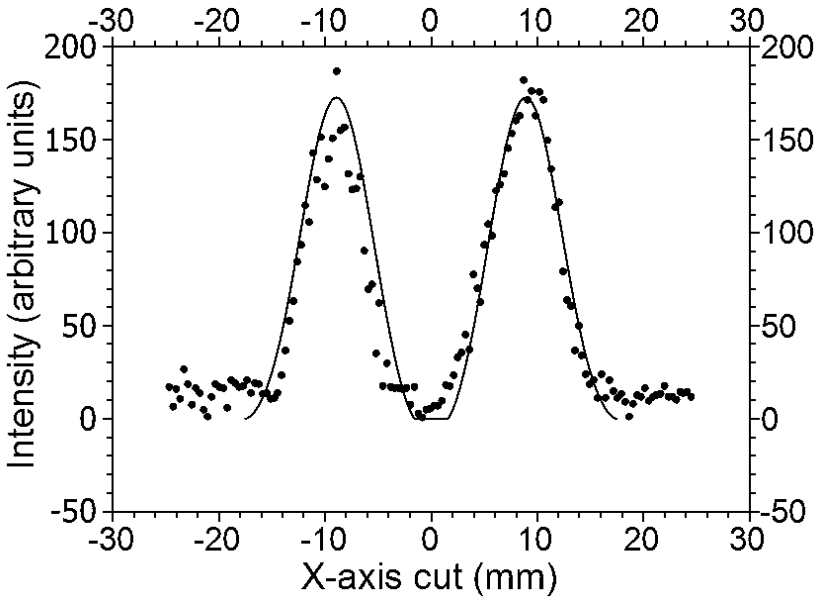

Figure 2.11: Measured VBTS beam profile (symbols) obtained from an autoradiogram analyzed with the DoseLab software (see text). The curve is a cross section through a rotating Gaussian function truncated at 2 $\times$ FWHM.

the beam is sharply focused. For these thin windows, the "Louvain criterion" suggests a sweep frequency of at least several hundred Hz. In the case of Target Station 1, the sweeper magnets are located on the outside of the standard beam pipe and the sweep frequency is 450 Hz. This is close to an upper limit for that set-up as the power loss due to eddy currents in the stainless steel beam pipe (which is proportional to the thickness of the pipe, the third power of its radius and the square of the frequency) becomes too severe at higher frequencies [Fou2005]. Nevertheless, 450 Hz has proved to be sufficient for that station over many years of operation.

In the case of the VBTS, however, a sweep system similar to that of Target Station 1 could not be used as the distance between the sweeper magnets and the target (only about 2 m – see Fig. 2.6) was too small to reach the desired sweep radius. The problem could be solved by making that section of the beamline from a non-conducting material. A ceramic Al_2O_3 beam pipe (720 mm long, 96 mm outer diameter and 5.5 mm wall thickness) with a thin conductive layer evaporated on to the inner surface allows effective penetration of the magnetic field but prevents charge accumulation if hit by beam particles [Fou2005]. Moreover, the use of low-loss ferrite material for the yoke and pole pieces of the magnets allows us to operate the VBTS with a sweep frequency of 3 kHz. As these magnets are located in a region which is normally quite inaccessible and highly radioactive, air-cooled magnet coils are used to eliminate possible water leaks from more conventional water-cooled conductors. More specifically, water-cooled conductors would have had to be quite thin to limit eddy current losses, leading to quite a high coolant differential pressure, which was what concerned the developers most. Technical details of these novel magnets can be found in a paper by Fourie *et al.* [Fou2005].

A convenient way to investigate the efficacy of the beam sweeping is to study the temperature profiles on the Havar foils under different bombardment conditions. Our approach was to first obtain the best choice of the beam and sweep diameters from steady-state calculations and then to perform the transient calculations for the optimal case with different sweep frequencies. Calculated beam power-density profiles and the corresponding temperature profiles on a VBTS Havar foil are shown in Fig. 2.12. (The details of these calculations will be discussed in Chapter 9.) The beam current was fixed at 300 μA and because the inner foil is thicker (75 μm) and gets hotter than the outer foil (50 μm) it was chosen for this part of the study. A conservative value of $h = 0.2$ W cm^{-2} K^{-1} was taken for the convective heat-transfer coefficient of the helium. (This was the topic of a separate study by Steyn *et al.* [Ste2012] and will be elaborated on in Chapter 9.) Furthermore, the overall diameter of the spreaded/swept beam was fixed at 30 mm, which is realistic albeit slightly smaller than the 36 mm aperture of the four-sector collimator. As can be expected, a too small beam diameter as well as a too-small sweep diameter both lead to non-optimal situations. The bombardment conditions are much better when the beam diameter (assuming a Gaussian truncated and renormalized to give a width of 2 $\times$ FWHM) is similar to the sweep diameter. This is in agreement with with findings at TRIUMF [Ste1994]. It was found that the maximum temperature reaches a minimum of $\sim$ 200 °C with a beam diameter of 13 mm and a sweep diameter of 17 mm. Thus, the optimum is found with a sweep diameter of about 30% larger than the beam diameter. The results of transient calculations for this case are shown in Fig. 2.13, where the differential temperature of the hottest node, expressed as a percentage of the corresponding steady-state temperature, is

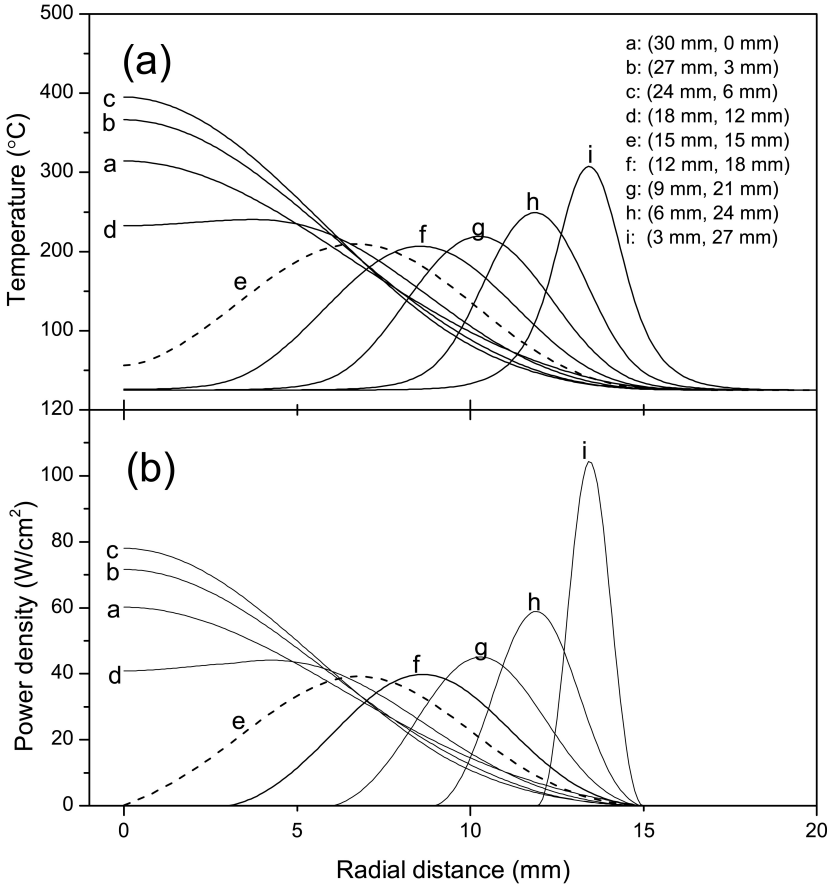

Figure 2.12: (a) Calculated temperature and (b) power-density curves for a 75 μm thick Havar window foil of the VBTS under bombardment with a 300 μA swept Gaussian beam. The beam and sweep diameters are varied according to (beam, sweep) as indicated. The overall diameter of the swept beam is kept at a constant value of 30 mm. The dashed line denotes the case where the beam and sweep diameters are equal, which is close to the optimal combination of (13 mm, 17 mm) – see text.

plotted versus the sweep frequency. As can be seen from the figure, the thermal "ripple effect" is less than 1% at 3 kHz.

To conclude the discussion on beam sweeping, we would like to comment on the argument sometimes made that such sweeping is not essential as the same can be achieved by defocusing. This is, of course, not true, as clearly illustrated by Fig. 2.12. Moreover, to develop an optimally defocused beam and maintain it over a long bombardment is also not easy. It is impractical to "shrink" a high-intensity beam from a too-large diameter as it may hit uncooled structures and cause damage. Increasing the beam diameter by defocusing inevitably introduces stages where the beam diameter is "too small". In our opinion, it is much more sensible to provide beam sweeping and to implement an interlock condition where a minimum sweep diameter must be present before the beam intensity may exceed a set limit, determined by safety considerations. Figure 2.14 shows beam conditions that can damage the Havar foils (reaching temperatures close to the melting point) and perhaps better illustrates the power of beam sweeping than does Fig. 2.12. Having been used as entrance and exit windows on gas targets as well as vacuum windows on beamlines for decades, Havar retains 75% of its tensile strength at room temperature up to 500 °C [Sch2012] and it has been reported to perform well under bombardment conditions up to 700 °C [Nit1976]. As can be seen in Figs. 2.12 and 2.14,

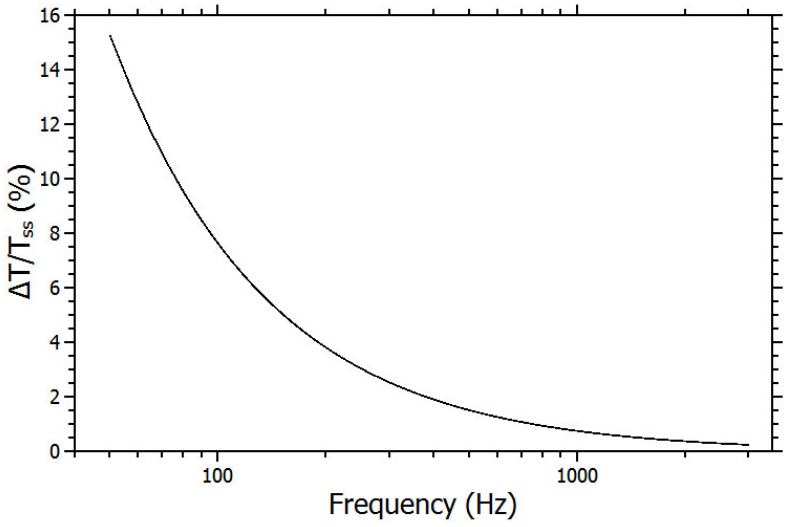

Figure 2.13: Temperature variation versus sweep frequency, expressed as a percentage of the steady state temperature, of the hottest node on a 50 μm thick VBTS Havar window foil under bombardment with an optimized swept Gaussian beam (i.e. a beam diameter of 13 mm and a sweep diameter of 17 mm – see text) at a beam current of 300 μA.

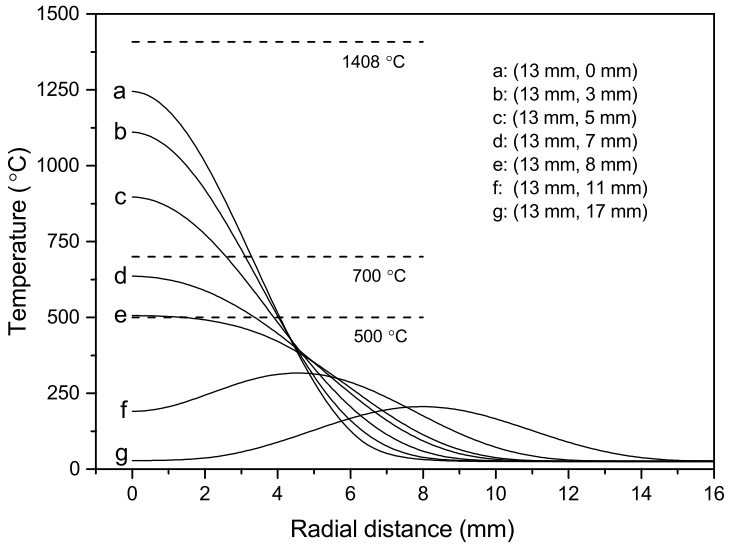

Figure 2.14: Temperature curves for a 75 μm Havar window of the VBTS under bombardment with a swept Gaussian beam. The beam diameter is kept constant at a value of 13 mm but the sweep diameter is varied as indicated. The melting point of Havar is 1408 °C but the maximum operational temperature is considered to be 700 °C (see text).

VBTS windows operate well below these temperatures if the beam is properly set up. Lastly, the longevity of these windows can be impressive but they do ultimately fail. Fortunately, Havar windows very rarely fail catastrophically but usually give an early warning by developing a pin-hole leak, therefore, either a deterioration of the beamline vacuum or an increased leakage of the helium cooling gas is observed. As they become very radioactive, a rapid removal and replacement strategy is essential to limit the radiation dose to staff.

2.3.4 High heat fluxes

At iThemba LABS, the encapsulated gallium targets which are bombarded in the lower-energy slot of a VBTS target holder are the most at risk. Questions are often asked about their thermal performance, especially after a target failure. It is certainly true that they experience the highest heat fluxes due to the presence of the Bragg peak, however, are these failures primarily "thermal failures"? The question is relevant as in some cases molten niobium was found in the target holder after a failure. Given that the majority of targets are fine after bombardment, why are there signs of melting in only a few cases and under similar bombardment conditions?

A somewhat simplified thermal model of such a target disc may shed light on these issues, as long as all assumptions are conservative. For the sake of the argument, it is necessary to borrow a few concepts which will be explained in more detail in Chapters 9 and 10. Here we consider forced convection cooling from the two flat surfaces normal to the axial direction but neglect cooling from the curved radial surface. The molten gallium is considered to be static, i.e. mixing by free convection is neglected and heat transfer in the body of the target is by conduction only. A realistic Gaussian beam profile is chosen: 13 mm beam diameter and 17 mm sweep diameter, which is close to the best case in Fig. 2.12. Similar to the approach of Ref. [Nor1995], the Sieder-Tate equation is used to estimate the convective heat-transfer coefficient, using the hydraulic diameter of an internal flow passage as the characteristic length in the Nusselt and Reynolds numbers. A constant linear flow velocity of 16 m/s is assumed for the cooling water with an entrance temperature of 25 °C. A beam current of 250 μA corresponds to about 8 kW deposited by the beam in this target disc alone. For this case, the power-density profile is shown in Fig. 2.15. It is significant that a level of 1 kW/cm^2 is exceeded – Celata *et al.* [Cel1992], for example, considers a heat flux of 0.8 kW/cm^2 already as "very high" and suggests forced convection cooling at subcooled flow boiling conditions as most appropriate for cooling.

It has to be mentioned that a convective heat-transfer coefficient calculated from any empirical equation such as the Sieder-Tate is somewhat uncertain. It does not, for example, take any nucleate boiling into account. Many authors, including Celata *et al.* [Cel1992], comment on how nucleate boiling in subcooled flow conditions can be an efficient technique to increase the rate of heat transfer, as long as critical heat flux (CHF) is avoided. Above CHF the convective heat-transfer coefficient drops sharply and rapid catastrophic burnout becomes highly probable.

Calculations were performed using the finite difference approach with the target disc divided into 300 radial and 40 axial nodes. The Bragg peak is located inside the target disc as the beam is stopped completely. The axial intensity distribution of the beam was calculated using the well-known computer code SRIM [Zie2013]. Here we mention only the relevant maximum temperatures:

- Maximum temperature H_2O/Nb boundary – 167 °C,
- Maximum temperature Ga/Nb boundary – 296 °C,
- Maximum inner temperature – 846 °C.

The predicted maximum inner temperature is considerably lower than the boiling point of gallium (2403 °C). This is a satisfactory result, in particular as neglecting free convection of the molten gallium yields an overestimation. Should conditions have been such that the gallium starts to boil, the resulting pressure build-up is likely to deform the target capsule and it may rupture. Deformed target capsules (e.g. evidence of local bulging) have, for example, been observed in encapsuled salt targets, both at iThemba LABS and Los Alamos (see, e.g. [Bac2013] and references therein). This is usually a serious situation at iThemba LABS, as the 1 mm cooling-water layers become constricted, negatively affecting or even disrupting target cooling. Such deformed targets usually show failure in the region where the beam strikes. In the present case, however, one may conclude that primary thermal failure is unlikely under the chosen bombardment conditions.

Target failures may be the result of corrosive effects, which may be dependent on temperature but if so its precise nature is not clear. It has been reported by the Los Alamos group [Bac2013] that the majority of their failures occurred outside the high beam intensity region and, in fact, at the coldest areas of the capsules. In some cases this mode of failure has also been observed at iThemba LABS. While inconclusive, some indications suggest that the problem is not related to corrosive effects but something else. Reference [Bac2013] suggests localized stress as a possibility, leading to cracks in the Nb capsules but this idea is still under investigation. Occasionally a cracked weld seam has been observed at iThemba LABS but this mode of failure is quite rare.

It is interesting to keep the beam diameter the same as above but to gradually reduce the sweep diameter. The boiling point of gallium is reached at a sweep diameter of about 7 mm

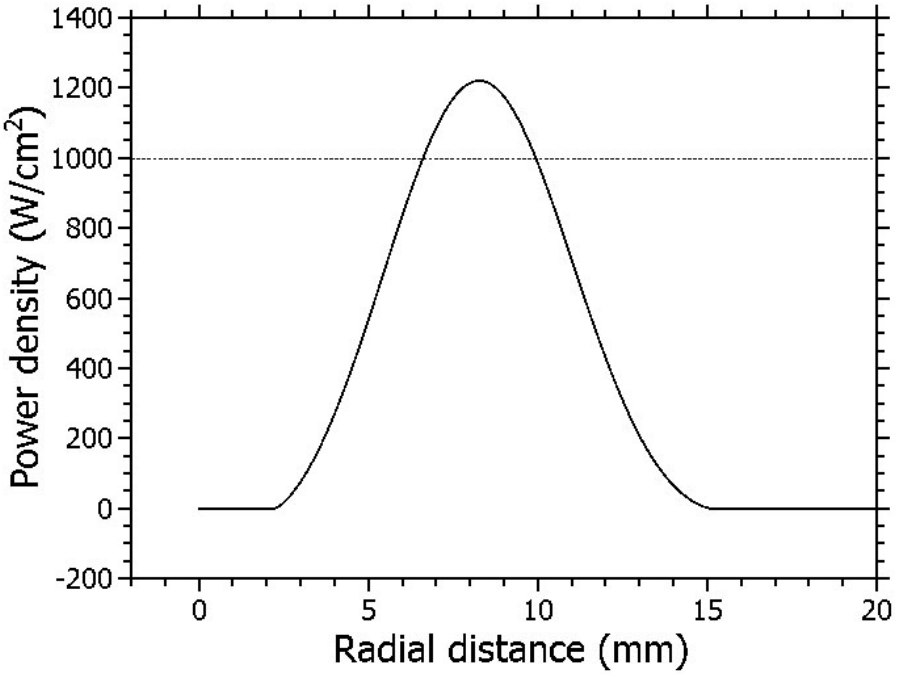

Figure 2.15: The power-density curve for a Ga target under bombardment at a level of 8 kW in the lower-energy slot of a VBTS target holder. The diameter of the truncated Gaussian beam is 13 mm and the sweep diameter is 17 mm.

under these conditions. Towards smaller sweep radii the situation gets rapidly worse. We believe that should the sweeping fall away completely while the beam remains on target at this level, catastrophic thermal failure is not merely a possibility – it is a certainty. On the other hand, such an event should manifest in the logged values collected during the bombardment, thus, we know that this is not an explanation for the majority of failures.

The visual evidence suggests that signs of melting of the niobium and capsule deformation (bulging out) are linked. In two interesting cases, both targets in the tandem configuration were lost when they actually touched, melted and fused together. As the cooling water layers are only 1 mm thick, capsule deformation can rapidly lead to compromised cooling. This suggests that capsule melting is not the primary reason for target failure but happens at a later stage in the sequence of events, essentially after the target has already failed.

To conclude this section, we would like to make two statements concerning the target discs in the higher-energy slot. Firstly, both the encapsulated rubidium and magnesium targets proved to be very reliable. We have seen several target failures where they survived when the gallium target in the lower-energy slot perished, but the converse has not been observed. The trouble always seem to start in the lower-energy slot. Secondly, failed rubidium targets do not lead to explosions and collateral damage. Initially, we were very concerned about what would happen if molten rubidium would get into contact with cold cooling water, especially because of the rapid release of hydrogen from the subsequent chemical reaction. It turns out that the hydrogen is effectively removed by the cooling water to a header tank from where it escapes via a flexible connection to the exhaust stack of the air handling system.

2.4 Beam splitter

A schematic diagram of the beam splitter, which makes it possible to irradiate targets in both radionuclide production vaults simultaneously, is shown in Fig. 2.16. It is based on a similar system at the Paul Scherrer Institute (PSI) and uses an electrostatic channel and a septum magnet to obtain two beams.

Since the beam delivered by the SSC is more stable in the vertical direction than the horizontal direction, it is first rotated through 90° before passing through the electrostatic channel. A set of five quadrupole magnets are used for this purpose, all turned through 45° with respect to the orientation that is normally used [Con2007]. The angle between the deflected beam and the main beam is 16° at the exit of the septum magnet. Figure 2.17 shows the beam profile just in front of the electrostatic channel and 100 mm behind it. A clear separation between the main and deflected beams is evident. More information can be found in [Con2007, Con2010] and references therein.

2.5 Flat-top RF resonators

Flat-top RF resonators have been installed on the light-ion injector cyclotron (SPC1) and the SSC. They are fixed-frequency resonators tuned for operation only when high-intensity 66 MeV beams are required. In the case of the injector cyclotron, a fifth harmonic of 81.8 MHz is

superimposed on the main RF resonators by small additional resonators which are capacitively coupled to the main resonators. Shown in Fig. 2.18, the two flat-top resonators are mounted perpendicularly on to the main resonators. A different approach was followed for the SSC as space and cost limitations had to be taken into account. A single half-wave resonator, fitted into one of the valley vacuum chambers, operates at a frequency of 49.12 MHz, which is the third harmonic of the fundamental RF frequency. The principle is illustrated in Fig. 2.19. Technical details can be found in [Nca2005, deV2005] and references therein.

2.6 Diagnostic equipment

2.6.1 Non-destructive beam current measurement

As already mentioned, the VBTS and its targetry are grounded and cannot function as a Faraday cup for the measurement of beam current and integrated charge. Instead, the current is measured non-destructively using a capacitive probe, located in its diagnostic chamber, in conjunction with digital signal processing. This system has been replicated in two other positions along the high-energy beamline as well. This allows the comparison of the beam current in three positions with the added advantages of reduced activation and beam loss at those other locations.

The capacitive probes deliver high-frequency signals consisting of a train of pulses induced by individual beam bunches, with a typical pulse length of 2 ns. These probes have a coaxial design, shown in Fig. 2.20. The beam passes through a hollow cylindrical conductor, inducing signals with an excellent signal-to-noise ratio once the beam intensity gets above a few μA. (Note that these probes are not useful for beam currents below about 1 μA.) Prior investigations showed that probe signals can contain significant contaminant first harmonic pick-up from the RF-systems but that excellent proportionality exist between the amplitudes of several of the higher harmonics (i.e. from the frequency components of the signals) and the beam current. Unfortunately, there is also a dependence on pulse length, which may vary depending on the

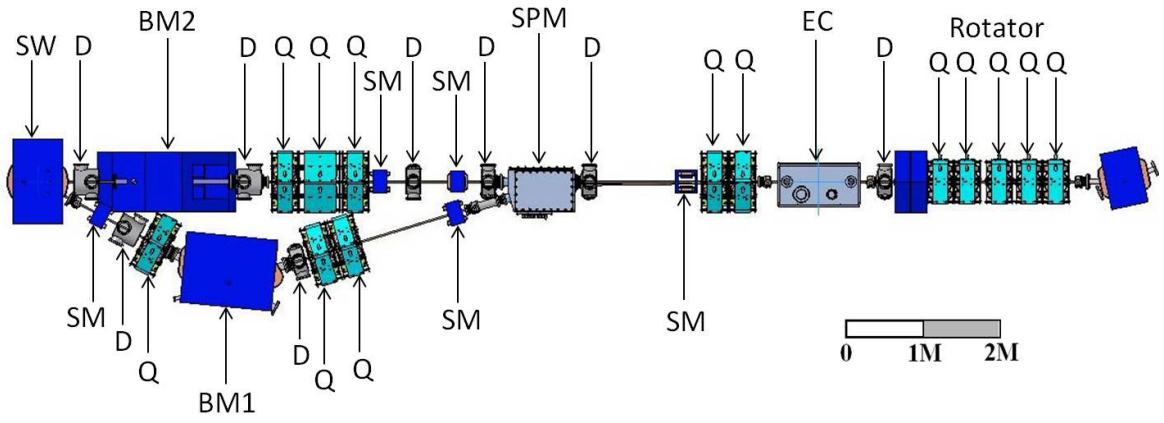

Figure 2.16: Layout of the beam splitter. The beam is incident from the right. The main components are the electrostatic channel (EC), the septum magnet (SPM), a 45° horizontal bending magnet (BM1), the 90° bending magnet for deflecting the beam into the vertical beamline (BM2), and the switcher magnet of the horizontal-beam vault (SW). Q, SM and D designate quadrupole magnets, steering magnets and diagnostic chambers, respectively. The first five quadrupoles on the right constitute the 90° beam rotator.

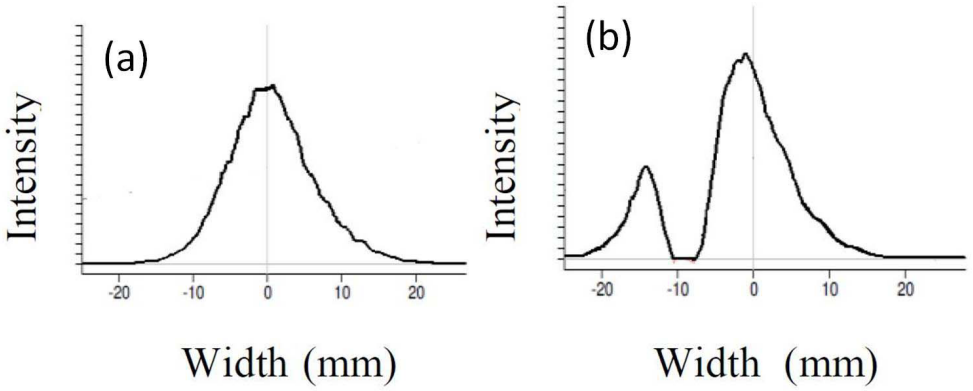

Figure 2.17: (a) The beam profile in front of the electrostatic channel and (b) 100 mm behind the channel.

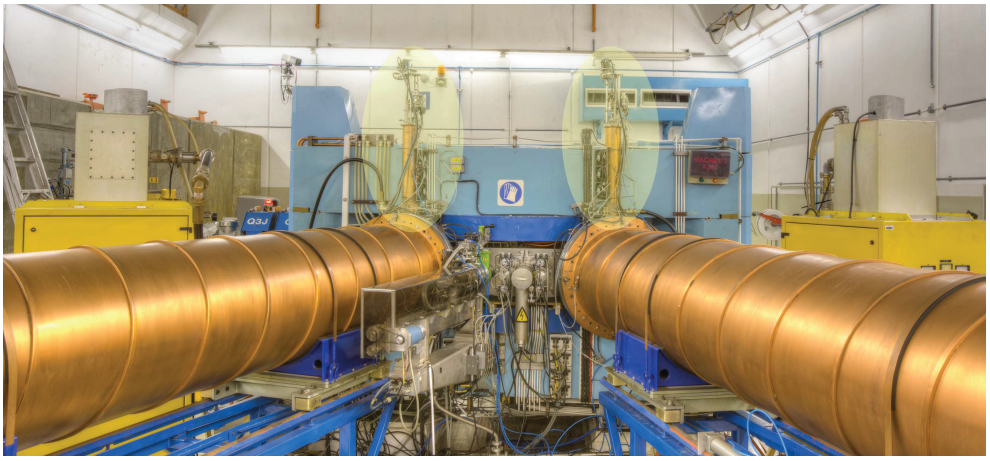

Figure 2.18: Photograph showing the flat-top RF resonators (highlighted) mounted onto the main RF resonators of the light-ion injector cyclotron (SPC1).

beam tune. This makes an absolute calibration problematic if the total intensity is based on a single harmonic component. Evaluation of the full signal was found to be more accurate. In the final system, the probe signals are digitally analyzed using a PC-based digital oscilloscope card, which can perform analog to digital conversions at a rate of 5×10^9 samples per second with 8-bit resolution. Signals in time slots of about 32 RF periods can be stored in one shot and analyzed with a sophisticated signal-processing algorithm. First, the signals are cleaned from RF pick-up and then the exact beginning and end points of the individual pulses are determined. Next, the individual pulse signals are integrated twice between these beginning and end points. This is done repeatedly for 200 successive captures and the values obtained are averaged, filtered and converted to a beam intensity by multiplying with a calibration factor. This factor is determined by comparison with measurements in a high-intensity beam stop as well as Faraday cups in the injection beamline. The continuous monitoring of the beam intensity in several positions is very valuable and by time stamping and logging these values together with those of other diagnostic equipment, one has valuable information to analyze and help understand abnormal events and/or problems. Extensive technical details can be found in the paper by Kormány *et al.* [Kor2008].

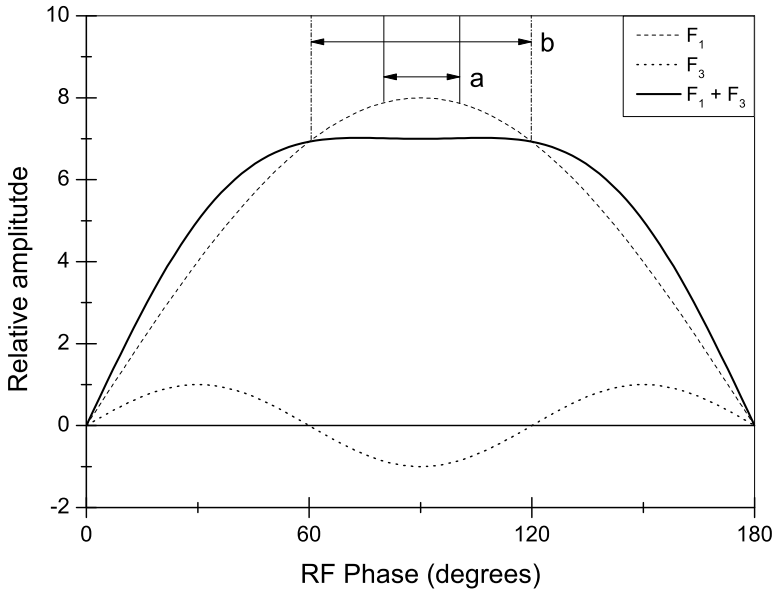

Figure 2.19: Principle of RF flat topping. A third harmonic is superimposed on the main RF frequency, leading to a larger effective fraction (i.e. b > a) of the RF phase suitable for acceleration.

2.6.2 Non-destructive beam position monitors

Two kinds of non-destructive beam position monitors have been implemented on the SSC. The first uses light emitted by residual gas in a cyclotron beamline [Die2008], while the second kind, implemented on the high-energy isotope production beamlines, is based on a variant of the capacitive probe described above but segmented [Die2004] to contain four electrodes, mounted coaxially inside a cylindrical copper housing (see Fig. 2.21). Variation in pulse length is not an issue in this case as signals from the four electrodes are affected similarly and only the ratios of their amplitudes are important. The third and fourth harmonics of the picked-up signals are therefore used in the analysis to determine the beam position. Calibration of these monitors have been performed on an xy-table with the beam simulated by a conducting rod. The voltages on each electrode were measured as a function of x- and y-displacement from the center line of the monitor. From the measured data, at intervals of 0.5 mm covering an area of 1600 mm^2, a look-up table has been compiled for each monitor. Comparisons have also been made with information from standard harps in measurements with beam. The sensitivity and stability of these robust units were found to be a fraction of a millimeter, exceeding the required characteristics by far. The continuous monitoring capabilities of these devices make them powerful diagnostic tools and the logging of values together with those of other diagnostics provide a valuable history of the beam. References [Con2005, Die2004] can be consulted for further technical details.

2.6.3 Stray-beam monitors

Air-filled ionization chambers, similar in design to those of PSI, were installed at approximately 2 m intervals along the high-energy beamlines leading to the radionuclide production vaults to detect stray beam hitting the beam pipe. These monitors are ring-shaped or annular in

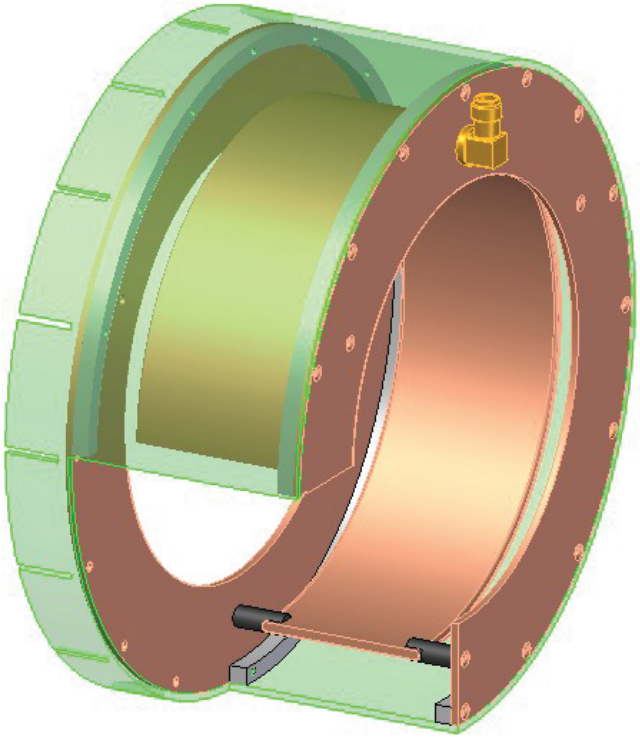

Figure 2.20: A coaxial capacitive probe for the non-destructive measurement of the beam current with a section removed to show the internal structure. The inner diameter of the Cu electrode is 116 mm, thickness 2 mm and length 46 mm.

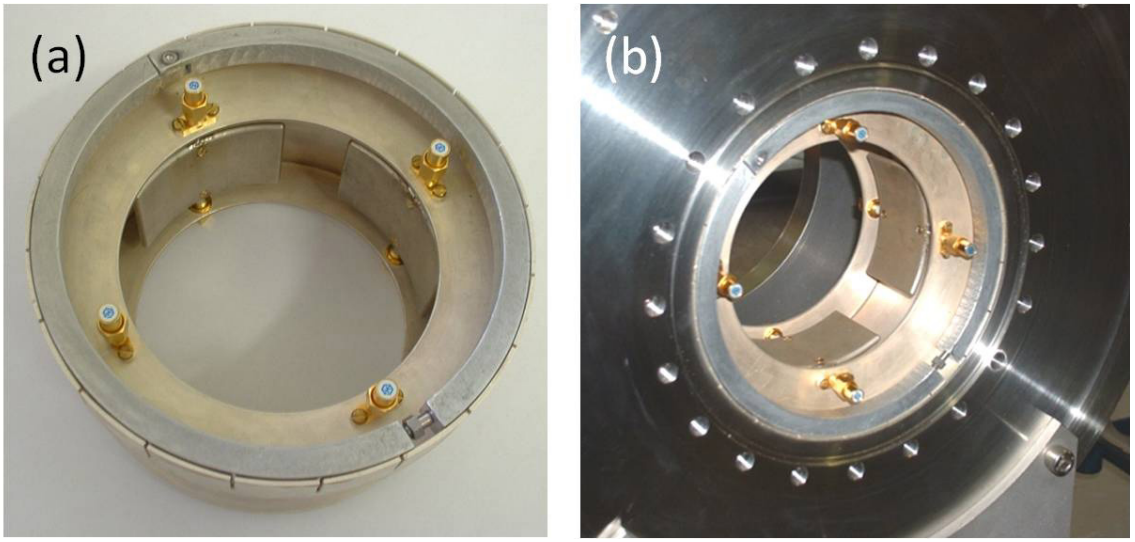

Figure 2.21: (a) A coaxial beam position monitor. (b) A beam position monitor mounted inside an opened diagnostic chamber.

design and fit over the outside of the beamline (see Fig. 2.22). They have four sectors each to give some idea of whether stray particles hit the top, bottom, left or right side of the beamline. Further detail on their design and read-out electronics can be found in the paper by Conradie *et al.*. [Con2007]. These detectors now form part of the safely-interlock system during beam operations in the radionuclide production vaults.

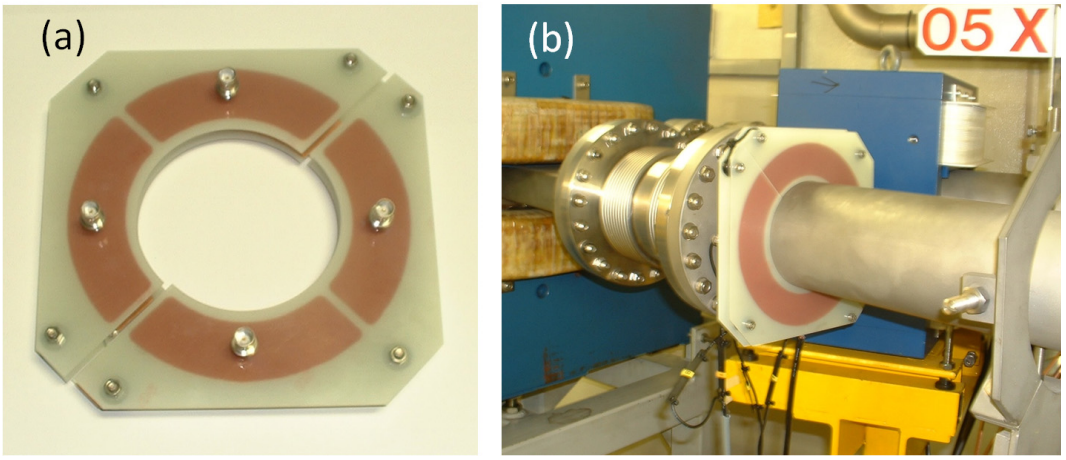

Figure 2.22: (a) A four-sector stray-beam monitor. (b) A stray-beam monitor mounted around a high-energy beamline.

2.7 Safety interlock system

The safety interlock system (SIS) for the radionuclide production facilities had to be expanded to include all three bombardment stations individually but also two bombardment stations simultaneously for split-beam operation. Initially the old hardware solution relied on a Programmable Logic Controller using a Logic Ladder. Problems faced by the old system included:

- The old interlock system could not handle two beamlines simultaneously without operator overrides.
- There was a lack of space on the physical interlock crate to add more complex interlock handling.
- The system sent one signal to the main cyclotron interlock system and thus could not show and store individual failure modes to aid troubleshooting.

A new system was built around a Safety Interlock SABus Card (manufactured at iThemba LABS) via a PCI card in a dedicated PC. A "Heartbeat" signal from this PC is also monitored by the main cyclotron interlock system. A GUI running in the isotope production control room shows line statuses and faults. The system can now log both previous alarm histories as well as override histories. In addition to direct monitoring of the field devices for flow of both helium and cooling water, the system also receives interlock signals from the LabVIEW-based beam monitoring PCs for the horizontal- and vertical-beam vaults and associated stations. The beam monitoring systems have to monitor the current falling on the four-sector carbon collimator and send a trip signal if the value reaches more than 1.2 μA on any sector. The second critical parameter is the overcurrent limit to protect targets from temperature induced damage. A third condition is monitored on Target Station 2, namely the pressure in the water-filled target for ^{18}F production. The sweep radius has been hard-wired separately as an additional safety feature. Shown in Fig. 2.23 is a screenshot of the beam monitoring system page for split-mode operation of the VBTS and one of the horizontal target stations.

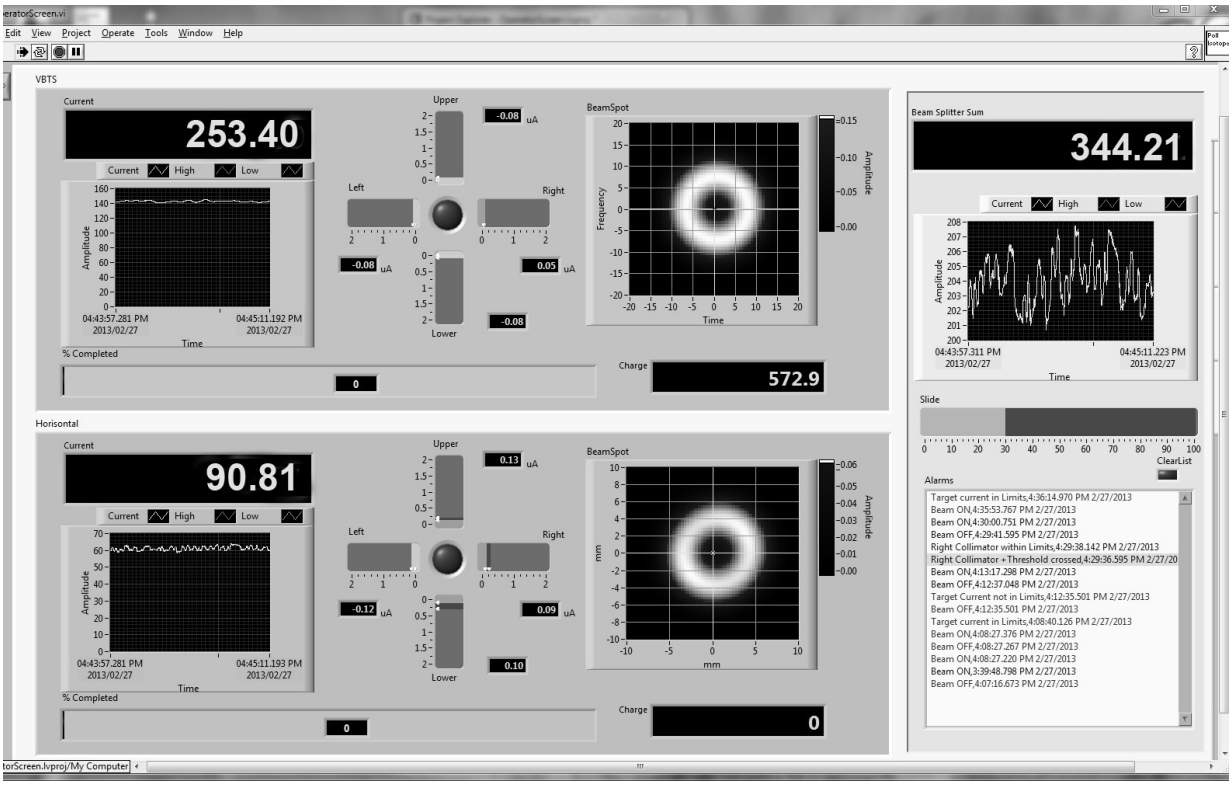

Figure 2.23: Screenshot of the safety interlock system (SIS) page for split-beam operation of the VBTS and a horizontal-beam target station.

2.8 Conclusion

This chapter, a shortened version of which has been converted to a technical paper and published [Ste2013], gives an overview of the radionuclide production target stations at iThemba LABS with particular emphasis on the VBTS and its targetry, developed to utilize the increased beam intensities delivered by the SSC. Several upgrades to the SSC facility made this possible, the most important being the addition of flat-top RF resonators. Operation with increased beam intensities also required new beam diagnostics. The non-destructive beam current and beam position monitors as well as the stray-beam monitors offer continuous monitoring and display, their logs provide valuable beam history information for fault finding and signals can be interlocked when required. Recent developments improved the integration between beam monitoring and the safety interlock system. The beam splitter provides more flexibility and increased capacity as two target stations can receive beam simultaneously. Thus, it is possible to irradiate four targets simultaneously when tandem targets are loaded in both the VBTS and Target Station 1.

By and large, the various upgrades have proven to be successful. iThemba LABS has a very active radionuclide production programme and is one of very few facilities in the world providing longer-lived, high-value radionuclides such as ^{22}Na, ^{68}Ge and ^{82}Sr on a continuing basis. While the programme is largely robust, there are some weaknesses. One weakness is its location, i.e. the large distance to some of its most important clients. Another weakness, which potentially should be easier to address, is the in-house lack of some of the necessary high technology infrastructure required to manufacture state-of-the-art targetry. Many tar-

getry components, in particular those that require accurate CNC milling and electron-beam (EB) welding, have to be sourced out. This complicates quality control and to some extent hampers further development work. Self sufficiency in targetry manufacture is certainly recommended for any radionuclide production programme at higher energies for which targetry are not commercially available. It should finally be mentioned that some development work is always continuing and changing operational demands necessitates ongoing evolution of the radionuclide production programme.

Chapter 3

Radionuclides of Tb in Proton-Induced Reactions on ^{nat}Gd

3.1 Introduction

The chemical labelling of macromolecules such as monoclonal antibodies and peptides with radiometals is at the cutting edge of current research in the detection and treatment of aggressive metastatic diseases. This is possible because these compounds can be chosen to be highly specific to malignant cell populations. Much has been written in recent times around the use of diagnostic-therapeutic pairs or so-called "theranostic" agents, where different isotopes of the same element can be labelled to a specific macromolecule and serve the functions of diagnostic and therapeutic agent respectively. In some cases it may even be desirable to combine the two agents in the same application to allow detection of metastases, monitoring of treatment efficacy, and detection of progression or recurrence. According to Kircher *et al.* [Kir2012], the use of these modalities strengthens the worldwide trend towards personalised medicine, where the diagnosis and treatment are tuned to be very specific to the individual. Zevalin^{TM} and Bexxar^{TM} are two examples of radioimmunotherapy agents that have, together with radiolabelled peptide products like Octreoscan^{TM}, according to Goldsmith [Gol2010] and Weiner [Wei2001], already found widespread commercial use in the radiomedical field. Radiometal-labelled disease-targeting radiopharmaceuticals are therefore set to become the next revolution in Nuclear Medicine.

Several lanthanide group radioelements have been identified as increasingly important role-players in the ever expanding field of labelled compounds (see e.g. Uusijärvi *et al.* [Uus2006]). Radiolanthanides with half-lives of several days which are both useful in combination with tumor targeting antibodies due to their low β^- energies, as well as being able to be produced with high radionuclidic purity, are quite rare. Only ^{143}Pr ($T_{1/2}$ = 13.6 d, E_{β^-} = 315 keV), ^{149}Pm ($T_{1/2}$ = 2.2 d, E_{β^-} = 366 keV), ^{161}Tb ($T_{1/2}$ = 6.9 d, E_{β^-} = 155 keV), ^{166}Ho ($T_{1/2}$ = 1.1 d, E_{β^-} = 711 keV) and ^{177}Lu ($T_{1/2}$ = 6.7 d, E_{β^-} = 133 keV) more or less match these criteria [Rös2007, Ma1996, Pil2003].

Another plus for the lanthanides is the fact that they can be readily bound to conjugate biomolecules of human serum albumin (HSA) as shown by Zeisler *et al.* [Zei1999] and Rösch

[Rös2000]. The radionuclide pair ^{140}Nd/^{140}Pr, in particular, can be used to combine radionuclide therapy and PET, since the longer-lived parent ^{140}Nd ($T_{1/2} = 3.37$ d) is a pure Auger electron emitter while the short-lived daughter ^{140}Pr ($T_{1/2} = 3.4$ min) is a positron emitter. A strong accumulation of HSA-DTPA labelled with the ^{140}Nd/^{140}Pr *in vivo* generator in Morris hepatomas in rats was reported by Zeisler [Zei1999], while the use of PET made it possible to follow the protein metabolism of the tumours for several days.

Terbium is even more unique amongst the lanthanides in that it offers a set of radionuclides which are potentially suitable for diagnosis using SPECT (^{155}Tb, $T_{1/2} = 5.32$ d) and PET (^{152}Tb, $T_{1/2} = 17.5$ h). For targeted radionuclide therapy, both ^{149}Tb ($T_{1/2} = 4.1$ h) and ^{161}Tb ($T_{1/2} = 6.9$ d) seem to be promising. Very few *in vivo* applications of Tb-radionuclides have been reported, particularly using ^{149,152,155,161}Tb [Abb2000, Bec2004, All1996, Bey2004, Leh2011]. This shortage can be chiefly ascribed to the general lack of well established production methods. Allen and Blagojevic [All1996] already pointed out in 1996 that ^{149}Tb may be a good candidate for targeted radiotherapy because of its relatively low-energy α-particle emissions. Unfortunately, its location is quite far from the line of stability, with no easily accessible production paths leading to its formation.

Subsequently, Beyer *et al.* [Bey2004] demonstrated direct evidence for single cancer cell kill using ^{149}Tb-rituximab, the ^{149}Tb obtained via spallation reactions by 1.4 GeV protons on a tantalum target in conjuction with on-line isotope separation at the ISOLDE facilty of CERN. The half-life, chemical properties and beta energy of ^{161}Tb are similar to that of the already useful ^{177}Lu as shown by Pillai *et al.* [Pil2003]. Indeed, Lehenberger *et al.* [Leh2011] recently suggested ^{161}Tb as an alternative for ^{177}Lu due to the fact that the former radionuclide also emits a significant amount of conversion and Auger electrons. A greater therapeutic effect may therefore be expected compared to ^{177}Lu. These authors produced ^{161}Tb-DOTA-Tyr3-octreotate of similar quality and stability to ^{177}Lu-DOTA-Tyr3-octreotate, employing the ^{160}Gd(n,γ)^{161}Gd$\rightarrow$^{161}Tb reaction on 98.2% enriched ^{160}Gd in a reactor.

The relevant part of the Karlsruhe Chart of the Nuclides is shown in Fig. 3.1 and the possible proton-induced reactions leading to the formation of ^{149,152,155,161}Tb are presented in Table 3.1. When the natural isotopic composition of the target nucleus as well as the reaction threshold energies are taken into account, only a few processes stand out as having a practical potential for production using medium or low energy particle accelerators. It is immediately evident that the cyclotron production of ^{149}Tb will be severely hampered by the low natural abundances of ^{152}Gd (0.20%) and ^{154}Gd (2.18%). In the case of ^{161}Tb, the neutron capture reaction ^{160}Gd(n,γ)^{161}Gd followed by β^- decay to ^{161}Tb would make this radionuclide ideally suitable for production in a nuclear reactor. On the other hand, a study of proton-induced reactions on ^{nat}Tb may yield useful information on the production possibilities of ^{152g}Tb and ^{155}Tb. Besides the detailed experimental work that included the measurement of cross sections for the formation of ^{151,152,153,154m,155,156,160}Tb presented in this chapter, theoretical calculations were also performed for all contributing reactions.

The radionuclide ^{152g}Tb is a suitable candidate for PET studies as the 17% branching ratio for positron emission is reasonable and the mean positron energy of 1.1 MeV is quite accept-

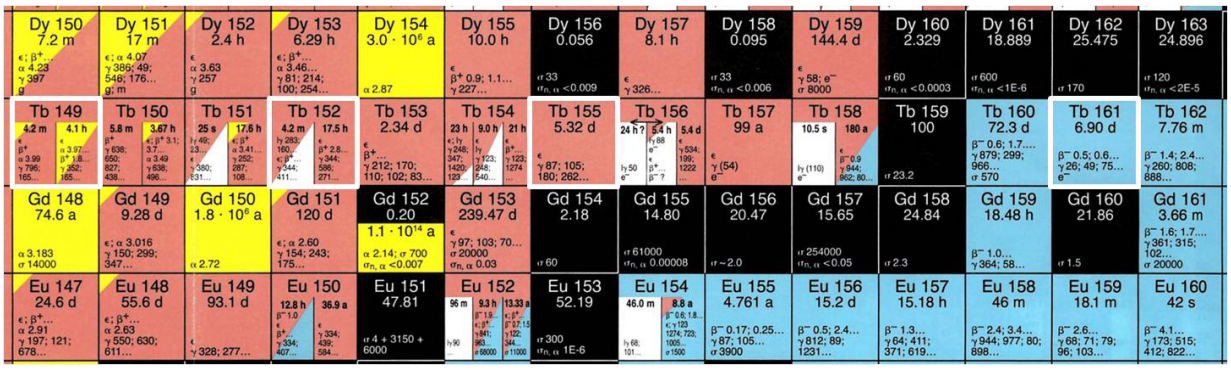

Figure 3.1: Relevant part of the Karlsruhe Chart of the Nuclides, showing the medically important radionuclides of Tb with white frames. With permission © Nucleonica GmbH 2012.

Table 3.1: Proton-induced reactions for formation of the quadruplet of Tb radionuclides.

Reaction	Q value (MeV)	Natural Isotopic Abundance[a]
^{152}Gd(p,4n)^{149}Tb	-28.21 MeV	0.20%
^{154}Gd(p,6n)^{149}Tb	-43.36 MeV	2.18%
^{155}Gd(p,7n)^{149}Tb	-49.80 MeV	14.80%
^{156}Gd(p,8n)^{149}Tb	-58.33 MeV	20.47%
^{152}Gd(p,n)^{152}Tb	-4.77 MeV	0.20%
^{154}Gd(p,3n)^{152}Tb	-19.91 MeV	2.18%
^{155}Gd(p,4n)^{152}Tb	-26.35 MeV	14.80%
^{156}Gd(p,5n)^{152}Tb	-34.89 MeV	20.47%
^{157}Gd(p,6n)^{152}Tb	-41.25 MeV	15.65%
^{158}Gd(p,7n)^{152}Tb	-49.18 MeV	24.84%
^{160}Gd(p,9n)^{152}Tb	-62.58 MeV	21.86%
^{154}Gd(p,γ)^{155}Tb	4.83 MeV	2.18%
^{155}Gd(p,n)^{155}Tb	-1.61 MeV	14.80%
^{156}Gd(p,2n)^{155}Tb	-10.14 MeV	20.47%
^{157}Gd(p,3n)^{155}Tb	-16.50 MeV	15.65%
^{158}Gd(p,4n)^{155}Tb	-24.44 MeV	24.84%
^{160}Gd(p,6n)^{155}Tb	-37.83 MeV	21.86%
^{160}Gd(p,γ)^{161}Tb	6.81 MeV	21.86%

[a]Taken from Firestone & Eckström [Fir2004].

able. Only one previous data set relevant to its production, however, could be found in the literature. Excitation functions for $^{152(m+g)}$Tb together with ^{154m}Tb and ^{154g}Tb were previously measured by Challan *et al.* up to 17 MeV [Cha2007].

Of the radioterbiums, ^{155}Tb seems to be the most promising candidate for diagnostic imaging using SPECT. The gamma energies of 87 and 105 keV are ideal for most SPECT cameras. The relatively longer half-life of 5.3 days should allow slower metabolic processes to be followed successfully. Only thick-target yields for natural targets have been reported previously by Dmitriev *et al.* [Dmi1989].

The relative scarcity of data at medium energies on the formation of the radioterbiums in proton-induced reactions on Gd prompted this investigation of ^{nat}Gd + p up to 66 MeV. As natural Gd has seven stable isotopes, one cannot reasonably expect it to be suitable as a target

material for radionuclidically pure products. The objective was therefore not necessarily to investigate the usefulness of ^{nat}Gd as a production target material, but merely to employ it in an initial experimental investigation to identify the most useful reactions. This approach can only really be successful if good agreement between the measured data and theoretical calculations can be obtained. If sufficiently good overall agreement for a particular radionuclide formed in ^{nat}Gd + p has been obtained, one can with some measure of confidence employ the specific calculations for the individual Gd target nuclei to make yield predictions for enriched targets. The rationale is that once the most suitable reactions have been identified, further experimental work on enriched target materials would be required. As a point of departure for this approach, it was considered only necessary to obtain good shape agreement between the measured and the calculated excitation functions as an overall renormalisation would *inter alia* be permissible.

The work presented in this chapter have been performed in a collaboration between researchers from iThemba LABS, the Cyclotron Department of ATOMKI in Debrecen, Hungary and the National Institute of Radiological Sciences (NIRS) in Chiba, Japan. It was agreed to measure excitation functions simultaneously at iThemba LABS and NIRS, in the same energy region, and to publish the results together. This would allow the immediate comparison of new data in a region where information from the literature was largely non-existent. A paper on this work has subsequently been published (Vermeulen *et al.* [Ver2012]).

3.2 Experimental method

The stacked-foil activation technique (see Appendix A) was employed to measure the excitation functions of radionuclides produced in ^{nat}Gd + p from threshold up to 66 MeV. Three separate irradiations were performed, one at the separated-sector cyclotron facility of iThemba LABS and two at the AVF-930 isochronous cyclotron facility of NIRS in Chiba, Japan.

3.2.1 Irradiations at iThemba LABS

At iThemba LABS, the stack consisted of high-purity Gd foils of 25.2 mg/cm^2 thickness (99.9%, New Metals, UK) and groups of 28.9 mg/cm^2 thick Cu degrader foils (99.9%, Goodfellow, UK) as required to obtain well-spaced proton energies across the entire energy region of interest. High-purity Al foils of 3.24 mg/cm^2 thickness (99.999%, Goodfellow, UK) and Ti foils of 11.5 mg/cm^2 thickness (99.999%, Goodfellow, UK) were incorporated as monitor foils as an independent check on the accumulated proton charge and beam energy. The thicknesses of all the foils used in these experiments were accurately determined by weighing. The foil stack was bombarded in an accurately calibrated Faraday chamber mounted at the end of an external beam line.

The irradiation chamber is based on the design of the RERAME (REcoil RAnge MEasurements) facility of the Laboratory Nazionale del Sud (LNS) in Catania, Italy, suitable for many kinds of activation studies. More detail is given in Chapter 2 and Appendix A.

The beam was collimated to a spot of 4 mm in diameter. The average beam current was 50 nA and the irradiation time was 3 h. The beam current and accumulated charge were

measured with a Brookhaven Instruments Corporation Model 1000C current integrator. The current and charge values were also logged in 1 second intervals to an analysis computer. As the Faraday chamber was evacuated to the same vacuum as the beam line, the first foil of the stack received the full extracted beam energy of nominally 66.0 MeV. The beam energy was accurately measured using a calibrated 90° bending magnet.

3.2.2 Irradiations at NIRS

The higher energy experimental stack consisted of 17 high-purity Gd foils of 18.49 mg/cm^2 thickness (99.9%, Goodfellow, UK) and groups of Co (99.9%, Goodfellow, UK) and Au (99.9%, Goodfellow, UK) degrader foils. The Co foils were used above 32 MeV and the Au foils below this energy. The thicknesses of the Co foils varied between 235.85 and 239.41 mg/cm^2 while the Au foils had a uniform thickness of 100.69 mg/cm^2. Titanium foils of 4.58 mg/cm^2 thickness (99.999%, Goodfellow, UK) were used as monitor foils to accurately determine the accumulated proton charge.

The lower energy experimental stack consisted of 9 high-purity Gd foils of which the first five were 18.49 mg/cm^2 thick (99.9%, Goodfellow, UK) and the next four were 6.8 mg/cm^2 thick (99.9%, Goodfellow, UK) to suit the lower energy part of the stack. Only Au degrader foils (99.9%, Goodfellow, UK) of 100.69 mg/cm^2 were used in this stack. Titanium foils of 14.08 mg/cm^2 thickness (99.999%, Goodfellow, UK) were used as monitor foils to accurately determine the accumulated proton charge, in addition to independent measurement with an electronic current integrator. Both stacks were irradiated at the end of an external beam line of the AVF-930 isochronous cyclotron. The beam spot was focussed to 4 mm in diameter. The calibrated Faraday chamber was separated from the beam line vacuum by an entrance window foil during both runs. The extracted beam energies were determined accurately by magnetic deflection. The beam energies were 70.2 and 30.1 MeV, respectively. Due to the presence of an entrance window and the composition of the stacks, the incident energies on the first Gd foils had slightly degraded values of 66.7 and 29.4 MeV, respectively. The first irradiation lasted for 1.5 h at an average beam current of 50 nA. The second irradiation lasted for 3.8 h with an average beam current of 70 nA.

3.2.3 Radionuclide assays

After bombardment, the activated foils were repeatedly measured individually by means of standard off-line γ-ray spectrometry. In all three experiments, accurately calibrated HPGe detectors were used. At iThemba LABS, the detector had a relative efficiency of 18% and a resolution of 1.8 keV FWHM at 1.33 MeV. The photo-peak areas were determined by means of the quantitative Canberra Genie 2000 analysis software in conjunction with a Canberra DSA 1000 multi-channel analyser system. At NIRS, the detector had a relative efficiency of 30% and a resolution of 2.1 keV FWHM at 1.33 MeV. The photo-peak areas were determined by means of quantitative analysis software (supplied by Laboratory Equipment, Japan). The efficiency curves for these detectors were determined in all cases by using standard calibrated γ-ray sources traceable to either the BIPM or NIST.

3.2.4 Data analysis

The cross sections of the observed activation products were derived from their measured γ-ray emissions using decay data from the online compilation of Firestone and Eckström [Fir2004]. The γ-lines used to identify the nuclides of interest are listed in Table 3.2. The activation formula, as explained in Appendix A, was used in all these calculations. Corrections were made for decay losses during and after bombardment, as well as during counting.

Table 3.2: Investigated Tb radionuclides and their decay properties used for experimental cross-section determinations[a].

Nuclide	Half-life	Decay mode	γ-rays (keV)	Intensity (%)
^{149}Tb	4.118 h	$\epsilon+\beta^+$: 83.3% α: 16.7%	352.24	29.43
^{151}Tb	17.609 h	$\epsilon+\beta^+$: 100%	251.86 287.35	26.3 28.3
^{152}Tb	17.5 h	$\epsilon+\beta^+$: 100%	271.13 344.27 586.26	8.6 65.0 9.4
^{153}Tb	2.3 d	$\epsilon+\beta^+$: 100%	212.00	31.0
^{154m2}Tb	22.7 h	$\epsilon+\beta^+$: 98.2% IT: 1.8%	225.94 346.64	26.8 69.0
^{155}Tb	5.32 d	ϵ: 100%	180.10 367.23	7.45 1.48
^{156}Tb	5.35 d	$\epsilon+\beta^+$: 100%	199.21 356.42 534.32	40.9 13.6 66.6
^{160}Tb	72.3 d	β^-: 100%	966.17 1177.96	25.1 14.9

[a]Taken from Firestone & Eckström [Fir2004].

Even though the accumulated charge was directly measured in all the experiments by means of calibrated current integrators, the excitation function of ^{48}V extracted from the Ti monitor foils served as a consistency check. The standard ^{48}V excitation function data recommended by the IAEA [Gul2001] was used. The agreement with the recommended curve is excellent, as shown in Fig. 3.2. For all the stacks, the beam flux measured by direct integration agreed to within 5% with the values determined from the monitor foils sets.

Corrections for beam current losses due to nonelastic nuclear interactions were made according to the prescription and tables of Janni [Jan1982]. This is described in more detail in Appendix B. The computer code, STACK, used to calculate the average proton energy in each foil is based on the stopping power formulae of Anderson and Ziegler [And1977]. These values agree very well with the newer compilation by Berger [Ber2004]. A number of independent checks at the higher energies were also performed using the Monte Carlo code SRIM of Ziegler

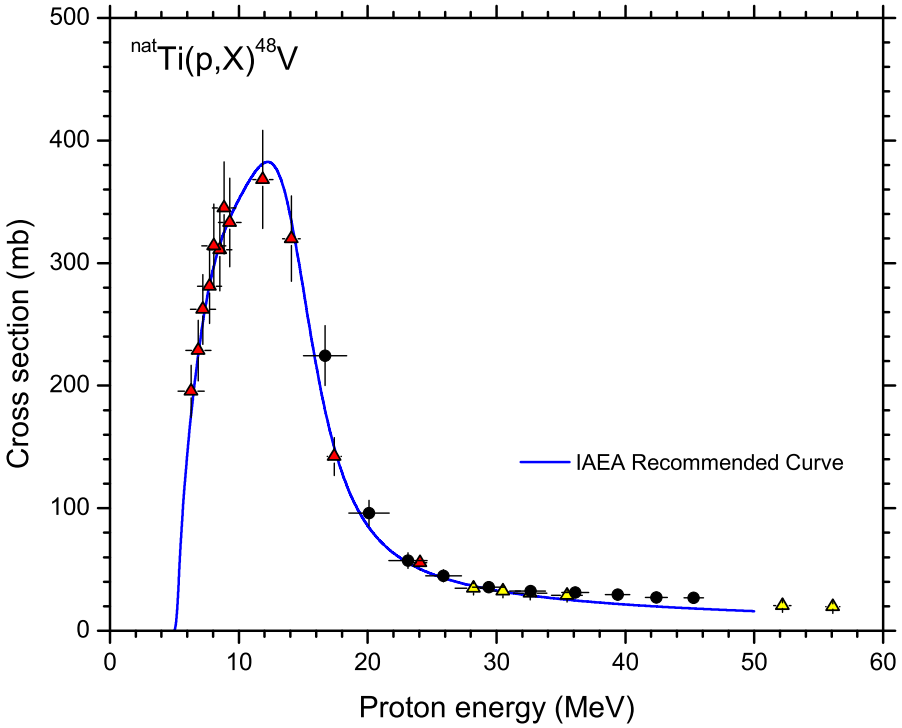

Figure 3.2: Monitor excitation function for the production of ^{48}V in the bombardment of Ti with protons. Black circles: this work (iThemba LABS). Red triangles: this work (NIRS Stack 1). Yellow triangles: this work (NIRS Stack 2).

and Biersack [Zie2006] and found to be consistent with the proton energy values determined from the published stopping power tables.

The total uncertainties in the measured cross sections were obtained by summing all the contributing uncertainties in quadrature and are expressed with a 1σ (68%) confidence level. A variable component includes the uncertainty due to counting statistics and photo-peak integration as well as the uncertainty associated with the beam-loss correction. The latter did not exceed 1.6%. The systematic uncertainty is estimated to be about 7%, including the uncertainty in beam current integration (3%), detector efficiency (5%), counting geometry (1%), decay corrections (2%) and foil thickness (3%) [ISO1995]. The uncertainty in energy of each measured data point was estimated from the uncertainty in incident beam energy, foil thickness and energy straggling in the stack. This is described in more detail in Appendix C.

3.3 Theoretical calculations

In this work, theoretical excitation functions were calculated using the Geometry Dependent Hybrid (GDH) model as implemented in the code ALICE/ASH [Bro2006]. Various evolutions of the ALICE code appeared since the early seventies and, to the best of our knowledge, ALICE/ASH is still the latest official release of the code based on the original non-Monte Carlo approach in solving the statistical model equations. Since 2010, a series of ALICE codes based on a Monte Carlo approach were released by the Los Alamos National Laboratory (LANL), the latest being ALICE 2012. While the new Monte Carlo version will be explored in our future work, for the purposes of this thesis project it was decided to focus on ALICE/ASH.

The ALICE/ASH calculations were performed using the recommended values for the input parameters according to the comments in the preamble to the code [Bro2006]. Level densities were calculated according to the generalized superfluid model (GSM). The normal pairing shift was selected. Experimental nuclidic masses were used where available, else calculated using the built-in Myers and Swiatecki mass formula of the code. A level density parameter of $a = A/9$ and an initial energy bin size of 0.5 MeV were specified. The calculations were performed within the frame of the GDH model for the pre-equilibrium emission of protons and neutrons. The subsequent evaporation during the equilibrium stage was calculated according to the Weiskopf-Ewing formalism as implemented in the code. The evaporated particles included protons, neutrons, deuterons and α-particles. To avoid the known scatter in the high energy "tail" regions of some of the excitation functions, especially in the case of the (p,n) reactions, we adopted the practice of performing sets of calculations, varying the energy bin size (parameter *ED* in the code) from 0.4 to 0.6 MeV in steps of 0.01 MeV, followed by taking the arithmetic average over all sets. This has been reported on extensively in a previous paper [Sze2010]. In cases where the scatter was not problematic, an energy bin size of 0.5 MeV was adopted. More information and a complete set of parameters are presented in Appendix D.

Separate sets of calculations were performed for all the stable Gd isotopes as target nuclei. The excitation functions for ^{nat}Gd + p were obtained by weighing all these individual excitation functions with their respective natural abundances followed by summing.

In addition to the ALICE/ASH predictions, the measured excitation functions are also compared with the relevant cross sections compiled in the TENDL-2012 library [Kon2012, Kon2013]. TENDL is a nuclear data library which provides the output of the TALYS Nuclear Model Code System for both basic physics and applications. It contains evaluations for seven types of incident particles, including protons, for all isotopes with half-lives longer than 1 second (about 2400 isotopes) up to 200 MeV. An acronym for "TALYS Evaluated Nuclear Data Library", TENDL endeavours to provide nuclear data for all nuclides, complete in terms of open reaction channels, secondary ejectile distributions and covariance data. Calculations are progressively refined in terms of the adjustable parameters in the TALYS code based on available experimental data and, in some cases, the model-based data may even be overruled by the measured data. The TALYS code contains a suite of nuclear reaction models in a single code system and is widely used as a *nuclear data tool*, in the sense that it can generate nuclear data for all open reaction channels, the majority of which cannot be directly investigated experimentally as those target nuclei are unstable. The first version of TALYS (version 1.0) was released in 2004 and the latest official version (1.4) in 2011. Target mass numbers can vary between 12 and 339. It treats n, γ, p, d, t, ^{3}He and α-particles as projectiles and ejectiles, and incorporates modern implementations for the optical model, level densities, direct reactions, compound reactions, pre-equilibrium reactions, fission reactions, together with a large nuclear structure database. Being a significantly larger code system than ALICE, it was interesting to find some of the ALICE subroutines directly incorporated into TALYS. In this study, the TENDL-2012 data are treated in the same way as other relevant published information and we do not attempt to either interpret and/or refine it. In particular, we were curious to know how trustworthy this library is for practical radionuclide production applications.

3.4 Results and discussion

The measured cross sections for the production of the Tb radionuclides are presented in Table 3.1 as well as Figs. 3.3 through 3.6. All the cross-section values are for the direct production of the particular radionuclides.

3.4.1 The ^{nat}Gd(p,xn)^{151}Tb process

At proton energies up to 66 MeV, ^{151}Tb is formed by several nuclear reactions: ^{152}Gd(p,2n), $Q = -11.94$ MeV; ^{154}Gd(p,4n), $Q = -27.08$ MeV; ^{155}Gd(p,5n), $Q = -33.52$ MeV; ^{156}Gd(p,6n), $Q = -42.05$ MeV; ^{157}Gd(p,7n), $Q = -48.41$ MeV and ^{158}Gd(p,8n), $Q = -56.35$ MeV.

In addition to the ground state ($T_{1/2} = 17.6$ h), one metastable state ($T_{1/2} = 25$ s) is also populated during the activation. The metastable state decays rapidly to the ground state by internal transition (IT). Due to the short half-life of the metastable state, only the cumulative ground state could be measured in these experiments. The results are presented in Fig. 3.3. The energies where cross-section values are not presented are due to the following reasons: The region from 11.6 to 6.66 MeV falls below the calculated threshold for this reaction and between 28.1 and 31.5 MeV long counting times (beyond $2\times$ the half-life of ^{151}Tb) lead to a significant growth of ^{155}Tb from ^{155}Dy decay with γ-lines which disturb the measured peak. The excitation function shows a peak at about 20 MeV (with a maximum of 2.5 mb) and increases continuously from about 30 MeV onwards. The maximum value is around 100 mb at 66 MeV.

Figure 3.3 also compares the experimental results with the ALICE/ASH predictions and TENDL-2012. Both satisfactorily reproduce the position of the peak of the excitation function and its magnitude. As far as we know, these are the first cross-section data for this nuclear process reported in the literature.

3.4.2 The ^{nat}Gd(p,xn)^{152}Tb process

Proton bombardment of natural Gd at 66 MeV opens six reaction channels that form ^{152}Tb, namely ^{152}Gd(p,n), $Q = -4.77$ MeV; ^{154}Gd(p,3n), $Q = -19.91$ MeV; ^{155}Gd(p,4n), $Q = -26.35$ MeV; ^{156}Gd(p,5n), $Q = -34.89$ MeV; ^{157}Gd(p,6n), $Q = -41.25$ MeV and ^{158}Gd(p,7n), $Q = -49.18$ MeV.

Just like the previous nuclear process, one relatively short-lived metastable state ($T_{1/2} = 4.3$ m) is also populated during the irradiation and it decays mostly to the ground state ($T_{1/2} = 17.5$ h, $IT = 79\%$). Taking into account our measuring set-up, we could only extract the excitation function of the ground state after the complete decay of the directly-formed m1 state.

The new cross sections for the ^{nat}Gd(p,xn)$^{152(0.79m+g)}$Tb process are presented in Fig. 3.3. The excitation function has a local maximum of about 1 mb at 12 MeV and increases from 22 MeV onwards towards a plateau, with a value of about 100 mb at 66 MeV. Only one previous author [Cha2007] was found who reported cross sections for this process up to 18 MeV. Their results are also shown in Fig. 3.3. Both the present data and the results of Challan *et al.* show good agreement with the theoretical calculation. It should be noted, however, that beyond 30 MeV the ALICE/ASH results seem to be systematically lower than the experimental data and TENDL-2012 but the disagreement is relatively small.

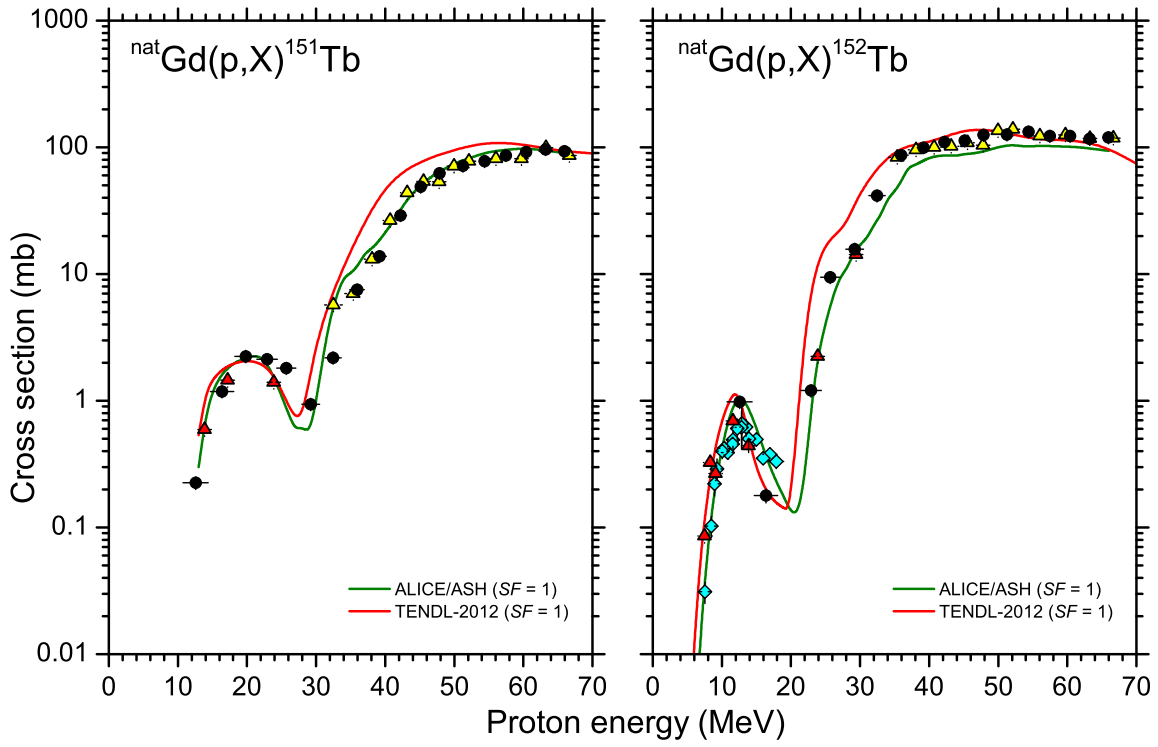

Figure 3.3: Excitation functions for the production of ^{151,152}Tb in the irradiation of ^{nat}Gd with protons. Black circles: this work (iThemba LABS). Red triangles: this work (NIRS Stack 1). Yellow triangles: this work (NIRS Stack 2). Blue diamonds: Challan *et al.* [Cha2007]. The curves are the results from ALICE/ASH calculations [Bro2006] and the TENDL-2012 library [Kon2012, Kon2013], as indicated. Scale factors applied to the theoretical predictions are indicated by *SF* (see text).

3.4.3 The ^{nat}Gd(p,xn)^{153}Tb process

The following reactions are relevant to the formation of ^{153}Tb: ^{152}Gd(p,γ), $Q = 3.89$ MeV; ^{154}Gd(p,2n), $Q = -11.25$ MeV; ^{155}Gd(p,3n), $Q = -17.68$ MeV; ^{156}Gd(p,4n) $Q = -26.22$ MeV; ^{157}Gd(p,5n) $Q = -32.58$ MeV and ^{158}Gd(p,6n), $Q = -41.25$ MeV. The contribution of the first reaction to the production of ^{153}Tb is almost negligible.

Looking at the decay mode, ^{153}Tb is a very simple radioisotope. It has no prominent metastable states and thus only the ground state needs to be considered during the analysis. It has a half-life of 2.34 d and decays by EC (100%) to ^{153}Gd. Prior to our study, no cross-section data were reported in the literature for this process as far as we know. Our measured values are presented in Fig. 3.4. The excitation function increases over the investigated energy region up to about 42 MeV and then decreases very slowly. No substantial peaks are observable. The maximum value is around 190 mb at about 42 MeV.

Figure 3.4 also compares the experimental results with the ALICE/ASH predictions. The calculation satisfactorily reproduces the shape of the experimental excitation function but overpredicts the cross section. Note that in Fig. 3.4 the theoretical curve has been renormalized to the experimental data to effect a better comparison (normalization factor $SF = 0.7$). In contrast, the TENDL 2102 curve reproduces the data quite well quantitatively up to about 55 MeV, whereafter it has a much steeper decreasing slope than observed experimentally. In fact, this steep fall-off towards higher energies is evident in several other cases as well, as will be seen below.

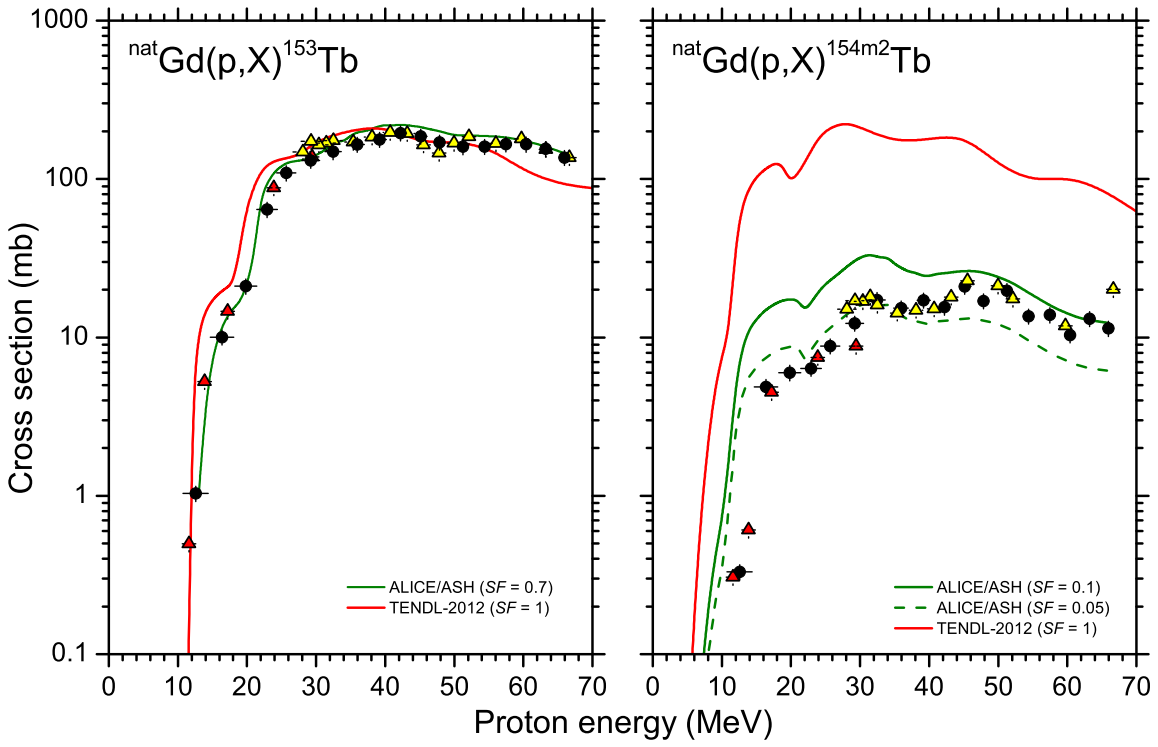

Figure 3.4: Excitation functions for the production of ^{153,154m2}Tb in the irradiation of ^{nat}Gd with protons. Black circles: this work (iThemba LABS). Red triangles: this work (NIRS Stack 1). Yellow triangles: this work (NIRS Stack 2). See also caption to Fig. 3.3.

3.4.4 The ^{nat}Gd(p,xn)^{154}Tb process

Five reactions form ^{154}Tb on ^{nat}Gd in the investigated energy region: ^{154}Gd(p,n), $Q = -4.33$ MeV; ^{155}Gd(p,2n), $Q = -10.77$ MeV; ^{156}Gd(p,3n), $Q = -19.31$ MeV; ^{157}Gd(p,4n), $Q = -25.67$ MeV and ^{158}Gd(p,5n), $Q = -33.60$ MeV.

Besides the ground state ($T_{1/2} = 21.4$ h) two prominent metastable states, usually denoted by m1 and m2, are also populated during the irradiation, having $T_{1/2}$ of 9.4 h and 22.7 h, respectively. The m1 state decays ($EC = 78\%$) to ^{154}Gd as well as feeding the ground state ($IT = 22\%$) of ^{154}Tb, while the m2 state decays predominantly ($EC = 98\%$) to ^{154}Gd. During this experiment, it was only possible to extract data for the m2 state. As with the preceding process, cross sections for this process are reported for the first time, to the best of our knowledge. The experimental results are shown in Fig. 3.4 together with the results of the ALICE/ASH calculations. The ALICE/ASH prediction seems to describe the shape of the data set fairly well, however, the large overprediction is expected as the calculation is for ^{154}Tb in total, i.e. a calculation for the particular metastable state only is not possible with the particular code used. A scale factor of $SF = 0.05$ (the dashed curve in Fig. 3.4) was employed on the relevant ALICE/ASH predictions to estimate physical yields for ^{154m2}Tb. This will be discussed in more detail later. Likewise, the TENDL-2012 values are for the total ^{154}Tb production, explaining the overprediction in the figure. Nevertheless, the overall shape is satisfactory and similar to the ALICE/ASH result until about 50 MeV, at which point the steeper decline towards larger energies becomes prominent.

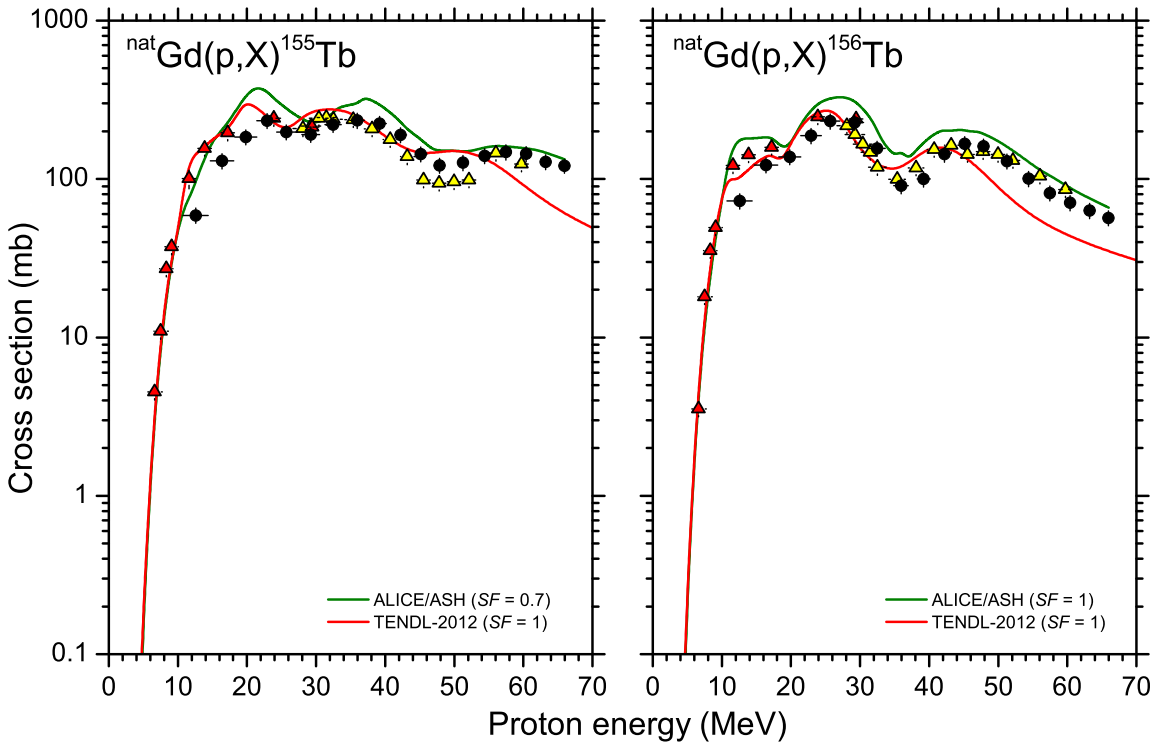

Figure 3.5: Excitation functions for the production of ^{155,156}Tb in the irradiation of ^{nat}Gd with protons. Black circles: this work (iThemba LABS). Red triangles: this work (NIRS Stack 1). Yellow triangles: this work (NIRS Stack 2). See also caption to Fig. 3.3.

3.4.5 The ^{nat}Gd(p,xn)^{155}Tb process

Among the five possible reactions on ^{nat}Gd which form ^{155}Tb, namely ^{154}Gd(p,γ), $Q = 4.83$ MeV; ^{155}Gd(p,n), $Q = -1.61$ MeV; ^{156}Gd(p,2n), $Q = -10.14$ MeV; ^{157}Gd(p,3n), $Q = -16.50$ MeV and ^{158}Gd(p,4n), $Q = -24.44$ MeV, only the last four contribute dominantly to its formation with protons up to 66 MeV. In this case, only the ground state ($T_{1/2} = 5.3$ d) has a significant half-life, making the cross-section evaluation quite easy.

New cross-section values for the ^{nat}Gd(p,x)^{155}Tb process are shown in Fig. 3.5. The ALICE/ASH calculations reproduce the shape of the excitation function quite well but a scale factor of $SF = 0.7$ has been adopted to deal with a general overprediction. In contrast, the TENDL-2012 values reproduce the experimental data quite well up to about 50 MeV, followed by an underprediction towards higher energies due to the too-steep drop-off described before.

3.4.6 The ^{nat}Gd(p,xn)^{156}Tb process

The activation of ^{nat}Gd with protons opens five reaction channels that produce ^{156}Tb below 66 MeV: ^{155}Gd(p,γ), $Q = 5.31$ MeV; ^{156}Gd(p,n), $Q = -3.23$ MeV; ^{157}Gd(p,2n), $Q = -9.59$ MeV; ^{158}Gd(p,3n), $Q = -17.52$ MeV and ^{160}Gd(p,5n) $Q = -30.92$ MeV. The contribution of the ^{155}Gd(p,γ) reaction to the formation of ^{156}Tb is almost negligible.

Although two longer-lived metastable states (m1 and m2) are populated during the irradiation with $T_{1/2}$ of 1.02 d and 5 h, respectively, both decay to the ground state ($T_{1/2} = 5.4$ d). In this work, we measured the ground state after sufficient time was allowed for the metastable states to decay to negligible levels.

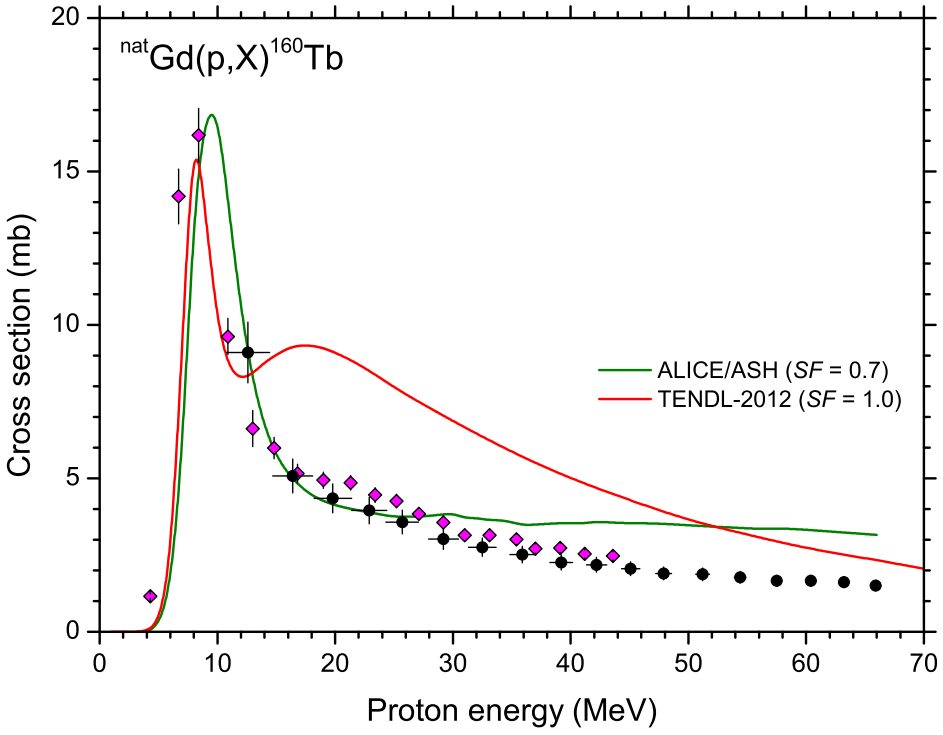

Figure 3.6: Excitation function for the production of ^{160}Tb in the irradiation of ^{nat}Gd with protons. Black circles: this work (iThemba LABS). Red diamonds: Birattari *et al.* [Bir1973]. See also caption to Fig. 3.3.

The experimental results are shown in Fig. 3.5, together with the results of the ALICE/ASH calculations and TENDL-2012. It is evident that the ALICE/ASH calculations reproduce the experimental results quite well, however, it seems to overpredict the measured values by about 25% beyond the onset part of the first peak. The TENDL-2012 values are found to be in good agreement up to about 42 MeV, followed by the now familiar underprediction toward higher energies. Based on these results, the excitation function clearly has three prominent peaks, at about 14, 25 and 44 MeV.

3.4.7 The ^{nat}Gd(p,n)^{160}Tb process

Only the ^{160}Gd(p,n)^{160}Tb ($Q = -0.89$ MeV) nuclear reaction forms ^{160}Tb. The ground state has a relatively long half-life of 72.3 d while no metastable states have half-lives long enough to affect its population.

In Fig. 3.6, the new results are compared with the published experimental data of Birattari *et al.* [Bir1973]. The present results are in good agreement with these literature values in the overlapping energy region. The ALICE/ASH calculations overpredicts the cross-section maximum (by about 30%) and gives a different energy value for its position, shifted by about 2 MeV. Note that in Fig. 3.6 this theoretical curve has been renormalized to the experimental data to effect a better comparison (normalization factor $SF = 0.7$). The TENDL-2012 values describe the low-energy peak better, both in terms of its position and height, but then show a broad second peak at about 18 MeV which is completely unexpected for a single mono-isotopic (p,n) reaction and is most probably unphysical.

3.4.8 Integral yield calculations

Integral yields (also called thick-target yields – see Appendix E for the relevant equations) were derived for the ^{152}Gd(p,n)^{152}Tb, ^{155}Gd(p,n)^{155}Tb and ^{155}Gd(p,4n)^{152}Tb processes and possible co-produced contaminants, utilizing the scaled (where necessary) ALICE/ASH cross-section predictions and assuming 100% enriched targets. These results are shown in Fig. 3.7.

In the case of ^{152}Gd(p,n)^{152}Tb, the (p,2n) reaction leading to the ground state of ^{151}Tb will introduce a significant radiocontamination above about 12 MeV, in particular as ^{151g}Tb and ^{152g}Tb have similar half-lives. From threshold up to 12 MeV should, however, provide a radionuclidically pure ^{152}Tb product with an estimated physical yield of about 49 MBq/μAh (1.3 mCi/μAh).

Similarly, in the case of ^{155}Gd(p,n)^{155}Tb the (p,2n) reaction leading to ^{154m2}Tb, ^{154m1}Tb and ^{154g}Tb will introduce significant radiocontamination above about 11 MeV (Fig. 3.7 shows ^{154m2}Tb only). The energy window from threshold up to 11 MeV should provide a radionuclidically pure ^{155}Tb product, with an estimated physical yield of about 5.6 MBq/μAh (0.15 mCi/μAh).

In the case of ^{155}Gd(p,4n)^{152}Tb, several (p,xn) reactions will lead to significant radiocontamination, as shown in Fig. 3.11. This is, of course, not unexpected. Nevertheless, an energy window from threshold up to 66 MeV will provide a very large physical yield, estimated to exceed 1200 MBq/μAh (32.43 mCi/μAh). It might be interesting to investigate this production route in conjunction with electromagnetic isotope separation.

By and large, the (p,n) reaction on enriched ^{152}Gd and ^{155}Gd targets appears to be the most simple (perhaps also most useful) for ^{152}Tb and ^{155}Tb production, respectively, and the estimated yields seem to be very reasonable for commercial production purposes. The low natural abundance of ^{152}Gd (0.2%) is, of course, problematic but the much higher abundance of ^{155}Gd (14.8%) should be sufficient for enrichment to a high level.

3.5 Conclusion

Measured cross sections for the production of several Tb radionuclides in ^{nat}Gd + p have been presented as well as corresponding calculations with the code ALICE/ASH and a comparison with the relevant data of TENDL-2012. This information was used to make estimations of ^{152g}Tb and ^{155}Tb physical yields. Clearly, without the use of electromagnetic isotope separation techniques, radionuclidically pure productions will require the use of the (p,n) reaction only and highly enriched targets with careful selection of the production energy window. This is a challenging region on the chart of the nuclides where nature is not very accommodating towards large-scale accelerator production of Tb radionuclides via (p,xn) reactions. Reactions using other light ions do not seem to yield any real advantage. As with the spallation reaction utilized for producing ^{149}Tb at CERN, electromagnetic isotope separation can, in principle, be used to collect the radionuclide of choice. This is an avenue that requires further investigation.

The present study yielded useful information but unfortunately the natural abundance of ^{152}Gd was too small to induce sufficient quantities of ^{149}Tb in the target foils, thus, those photo-peaks could not be detected above background in the γ-ray spectra. It was clear that measurements on enriched targets would be required to study that radionuclide.

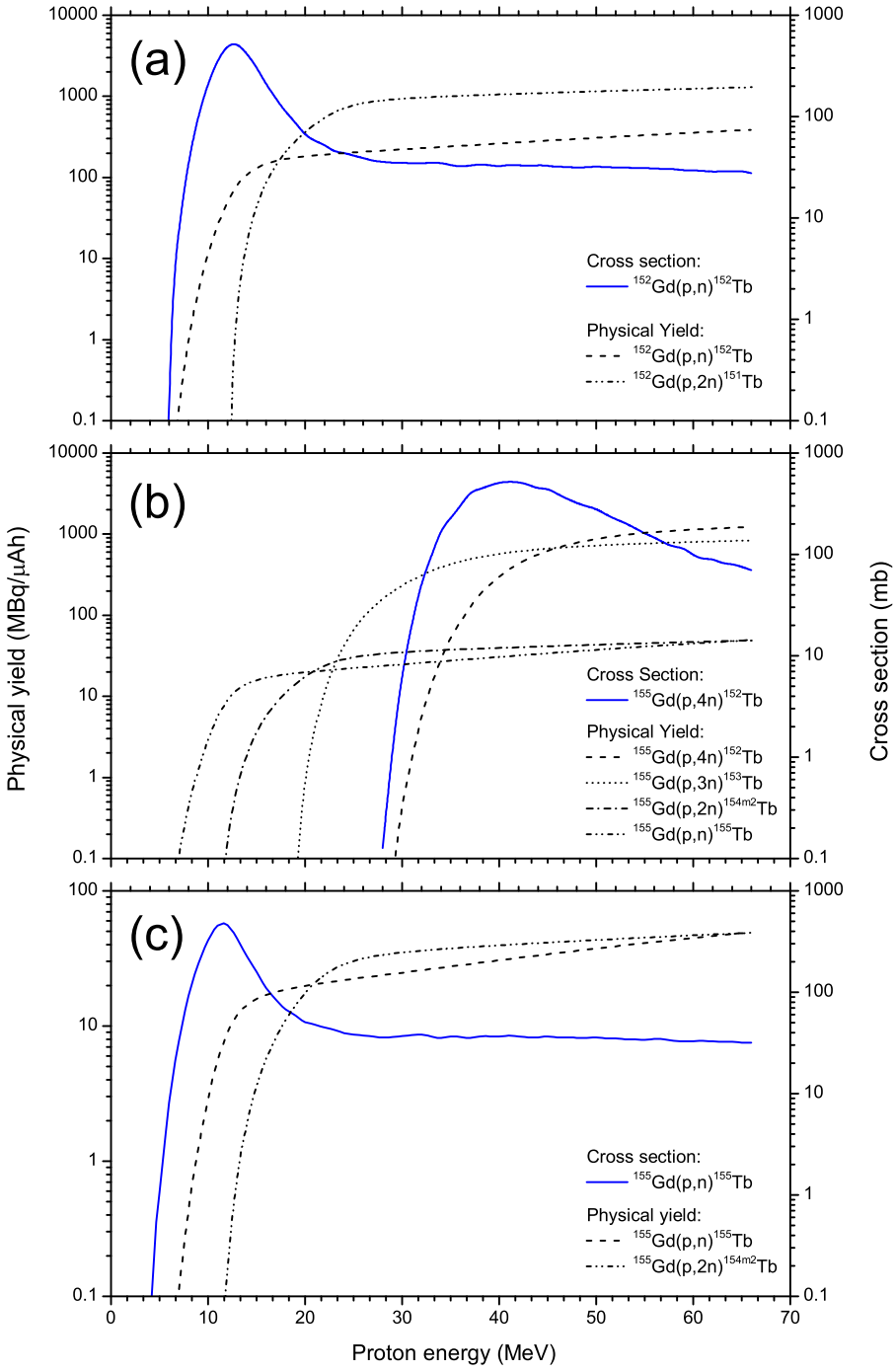

Figure 3.7: Calculated excitation functions and corresponding physical yields for the production of ^{152}Tb via the ^{152}Gd(p,n) reaction (a) and the ^{155}Gd(p,4n) reaction (b) as well as for ^{155}Tb via the ^{152}Gd(p,n) reaction (c). Physical yields for co-produced Tb contaminants are also shown, as indicated. A 100% enrichment of the ^{152}Gd and ^{155}Gd targets is assumed.

Following the experimental work on ^{nat}Gd + p presented in this chapter, some further experimental work was pursued on enriched ^{152}Gd + p and ^{155}Gd + p as well as ^{nat}Tb + p. In the following chapter, data for the (p,4n) reaction on enriched ^{152}Gd and ^{155}Gd for the production of ^{149}Tb and ^{152}Tb, respectively, are presented as well as the indirect production of ^{155}Tb via ^{155}Dy decay in proton-induced reactions on natural Tb. In the case of the (p,4n) reaction on enriched Gd targets, the requirement for electromagnetic isotope separation is assumed while the indirect reaction path ^{159}Tb(p,5n)^{155}Dy$\rightarrow$^{155}Tb may be an alternative for the production of ^{155}Tb in a radionuclidically pure form.

Table 3.3: Measured cross sections for the production of the denoted radionuclides in the irradiation of ^{nat}Gd with protons.

Proton energy (MeV)	Cross section[a] (mb)						
	^{151}Tb	^{152}Tb	^{153}Tb	^{154m2}Tb	^{155}Tb	^{156}Tb	^{160}Tb
6.63 ± 0.99					$(4.52 \pm 0.51) \times 10^{+1}$	$(3.54 \pm 0.39) \times 10^{+0}$	
7.52 ± 0.95		$(8.56 \pm 1.01) \times 10^{-2}$			$(1.09 \pm 0.13) \times 10^{+1}$	$(1.80 \pm 0.20) \times 10^{+1}$	
8.34 ± 0.92		$(3.25 \pm 0.39) \times 10^{-1}$			$(2.71 \pm 0.30) \times 10^{+1}$	$(3.53 \pm 0.39) \times 10^{+1}$	
9.11 ± 0.89		$(2.66 \pm 0.31) \times 10^{-1}$			$(3.73 \pm 0.42) \times 10^{+1}$	$(4.93 \pm 0.54) \times 10^{+1}$	
11.60 ± 0.79		$(6.92 \pm 0.77) \times 10^{-1}$	$(4.97 \pm 0.55) \times 10^{-1}$	$(3.06 \pm 0.34) \times 10^{-1}$	$(1.00 \pm 0.14) \times 10^{+2}$	$(1.22 \pm 0.14) \times 10^{+2}$	
12.56 ± 1.83	$(2.25 \pm 0.26) \times 10^{-1}$	$(9.78 \pm 1.09) \times 10^{-1}$	$(1.04 \pm 0.12) \times 10^{+0}$	$(3.31 \pm 0.37) \times 10^{-1}$	$(5.90 \pm 0.65) \times 10^{+1}$	$(7.26 \pm 0.79) \times 10^{+1}$	$(9.10 \pm 0.99) \times 10^{+0}$
13.86 ± 0.70	$(5.93 \pm 0.65) \times 10^{-1}$	$(4.40 \pm 0.04) \times 10^{-1}$	$(5.26 \pm 0.58) \times 10^{+0}$	$(6.08 \pm 0.67) \times 10^{-1}$	$(1.56 \pm 0.18) \times 10^{+2}$	$(1.42 \pm 0.16) \times 10^{+2}$	—
16.39 ± 1.70	$(1.19 \pm 0.13) \times 10^{+0}$	$(1.79 \pm 0.23) \times 10^{-1}$	$(1.00 \pm 0.11) \times 10^{+1}$	$(4.87 \pm 0.56) \times 10^{+0}$	$(1.30 \pm 0.15) \times 10^{+2}$	$(1.23 \pm 0.14) \times 10^{+2}$	$(5.08 \pm 5.52) \times 10^{+0}$
17.21 ± 0.56	$(1.45 \pm 0.18) \times 10^{+0}$	—	$(1.46 \pm 0.16) \times 10^{+1}$	$(4.50 \pm 0.49) \times 10^{+0}$	$(1.96 \pm 0.22) \times 10^{+2}$	$(1.59 \pm 0.18) \times 10^{+2}$	—
19.83 ± 1.59	$(2.24 \pm 0.25) \times 10^{+0}$	—	$(2.10 \pm 0.23) \times 10^{+1}$	$(5.99 \pm 0.68) \times 10^{+0}$	$(1.84 \pm 0.21) \times 10^{+2}$	$(1.38 \pm 0.15) \times 10^{+2}$	$(4.35 \pm 0.48) \times 10^{+0}$
22.90 ± 1.49	$(2.12 \pm 0.23) \times 10^{+0}$	$(1.20 \pm 0.14) \times 10^{+0}$	$(6.41 \pm 0.70) \times 10^{+1}$	$(6.37 \pm 0.70) \times 10^{+0}$	$(2.34 \pm 0.26) \times 10^{+2}$	$(1.88 \pm 0.21) \times 10^{+2}$	$(3.95 \pm 0.43) \times 10^{+0}$
23.90 ± 0.29	$(1.40 \pm 0.16) \times 10^{+0}$	$(2.24 \pm 0.25) \times 10^{+0}$	$(8.79 \pm 0.96) \times 10^{+1}$	$(7.49 \pm 0.82) \times 10^{+0}$	$(2.41 \pm 0.27) \times 10^{+2}$	$(2.47 \pm 0.27) \times 10^{+2}$	—
25.68 ± 1.39	$(1.81 \pm 0.21) \times 10^{+0}$	$(9.43 \pm 1.03) \times 10^{+0}$	$(1.09 \pm 0.12) \times 10^{+2}$	$(8.82 \pm 0.97) \times 10^{+0}$	$(1.98 \pm 0.22) \times 10^{+2}$	$(2.32 \pm 0.26) \times 10^{+2}$	$(3.57 \pm 0.39) \times 10^{+0}$
28.08 ± 1.44	—	—	$(1.48 \pm 0.17) \times 10^{+2}$	$(1.51 \pm 0.17) \times 10^{+1}$	$(2.08 \pm 0.23) \times 10^{+2}$	$(2.17 \pm 0.24) \times 10^{+0}$	—
29.22 ± 1.28	$(9.41 \pm 1.01) \times 10^{-1}$	$(1.58 \pm 0.18) \times 10^{+1}$	$(1.31 \pm 0.15) \times 10^{+2}$	$(1.23 \pm 0.14) \times 10^{+1}$	$(1.91 \pm 0.21) \times 10^{+2}$	$(2.28 \pm 0.25) \times 10^{+2}$	$(3.02 \pm 0.33) \times 10^{+0}$
29.26 ± 1.40	—	—	$(1.73 \pm 0.19) \times 10^{+2}$	$(1.71 \pm 0.19) \times 10^{+1}$	$(2.16 \pm 0.24) \times 10^{+2}$	$(1.91 \pm 0.21) \times 10^{+2}$	—
29.41 ± 0.14	—	$(1.42 \pm 0.16) \times 10^{+1}$	$(1.38 \pm 0.15) \times 10^{+2}$	$(8.80 \pm 0.97) \times 10^{+0}$	$(2.13 \pm 0.24) \times 10^{+2}$	$(2.40 \pm 0.27) \times 10^{+2}$	—
30.38 ± 1.37	—	—	$(1.65 \pm 0.18) \times 10^{+2}$	$(1.69 \pm 0.19) \times 10^{+1}$	$(2.42 \pm 0.27) \times 10^{+2}$	$(1.65 \pm 0.18) \times 10^{+2}$	—
31.46 ± 1.33	—	—	$(1.69 \pm 0.19) \times 10^{+2}$	$(1.81 \pm 0.20) \times 10^{+1}$	$(2.45 \pm 0.27) \times 10^{+2}$	$(1.48 \pm 0.16) \times 10^{+2}$	—
32.51 ± 0.30	$(2.19 \pm 0.25) \times 10^{+0}$	$(4.16 \pm 0.46) \times 10^{+1}$	$(1.49 \pm 0.17) \times 10^{+2}$	$(1.73 \pm 0.20) \times 10^{+1}$	$(2.20 \pm 0.24) \times 10^{+2}$	$(1.56 \pm 0.17) \times 10^{+2}$	$(2.76 \pm 0.30) \times 10^{+0}$
35.36 ± 1.30	$(7.02 \pm 0.79) \times 10^{+0}$	$(8.36 \pm 0.92) \times 10^{+1}$	$(1.71 \pm 0.19) \times 10^{+2}$	$(1.43 \pm 0.16) \times 10^{+1}$	$(2.37 \pm 0.26) \times 10^{+2}$	$(9.97 \pm 1.09) \times 10^{+1}$	—
35.94 ± 1.20	$(7.54 \pm 0.83) \times 10^{+0}$	$(8.69 \pm 0.95) \times 10^{+1}$	$(1.66 \pm 0.18) \times 10^{+2}$	$(1.53 \pm 0.17) \times 10^{+1}$	$(2.34 \pm 0.26) \times 10^{+2}$	$(9.06 \pm 0.99) \times 10^{+1}$	$(2.52 \pm 0.28) \times 10^{+0}$
38.10 ± 1.06	$(1.31 \pm 0.15) \times 10^{+1}$	$(9.58 \pm 1.04) \times 10^{+1}$	$(1.84 \pm 0.20) \times 10^{+2}$	$(1.49 \pm 0.17) \times 10^{+1}$	$(2.07 \pm 0.23) \times 10^{+2}$	$(1.18 \pm 0.13) \times 10^{+2}$	—
39.20 ± 1.11	$(1.38 \pm 0.15) \times 10^{+1}$	$(9.96 \pm 1.08) \times 10^{+1}$	$(1.78 \pm 0.20) \times 10^{+2}$	$(1.72 \pm 0.19) \times 10^{+1}$	$(2.24 \pm 0.25) \times 10^{+2}$	$(1.00 \pm 0.11) \times 10^{+2}$	$(2.26 \pm 0.25) \times 10^{+0}$

[a]The error values listed include a systematic uncertainty which is estimated to be 7% (see text).

Continued on next page

Table 3.3: Table continues from previous page.

Proton energy (MeV)	Cross section[a] (mb)						
	^{151}Tb	^{152}Tb	^{153}Tb	^{154m2}Tb	^{155}Tb	^{156}Tb	^{160}Tb
40.73 ± 0.95	$(2.65 \pm 0.29) \times 10^{+1}$	$(9.97 \pm 1.09) \times 10^{+1}$	$(1.97 \pm 0.22) \times 10^{+2}$	$(1.52 \pm 0.17) \times 10^{+1}$	$(1.78 \pm 0.19) \times 10^{+2}$	$(1.53 \pm 0.17) \times 10^{+2}$	—
42.23 ± 1.03	$(2.91 \pm 0.32) \times 10^{+1}$	$(1.10 \pm 0.13) \times 10^{+2}$	$(1.95 \pm 0.22) \times 10^{+2}$	$(1.55 \pm 0.17) \times 10^{+1}$	$(1.90 \pm 0.21) \times 10^{+2}$	$(1.43 \pm 0.16) \times 10^{+2}$	$(2.19 \pm 0.24) \times 10^{+0}$
43.21 ± 0.86	$(4.38 \pm 0.48) \times 10^{+1}$	$(1.02 \pm 0.12) \times 10^{+2}$	$(1.94 \pm 0.22) \times 10^{+2}$	$(1.80 \pm 0.20) \times 10^{+1}$	$(1.38 \pm 0.15) \times 10^{+2}$	$(1.63 \pm 0.18) \times 10^{+2}$	—
45.12 ± 0.95	$(4.89 \pm 0.54) \times 10^{+1}$	$(1.13 \pm 0.13) \times 10^{+2}$	$(1.86 \pm 0.21) \times 10^{+2}$	$(2.10 \pm 0.23) \times 10^{+1}$	$(1.44 \pm 0.16) \times 10^{+2}$	$(1.67 \pm 0.19) \times 10^{+2}$	$(2.06 \pm 0.23) \times 10^{+0}$
45.56 ± 0.77	$(5.37 \pm 0.59) \times 10^{+1}$	$(1.09 \pm 0.12) \times 10^{+2}$	$(1.64 \pm 0.18) \times 10^{+2}$	$(2.27 \pm 0.25) \times 10^{+1}$	$(9.88 \pm 1.08) \times 10^{+2}$	$(1.43 \pm 0.16) \times 10^{+2}$	—
47.80 ± 0.87	$(5.36 \pm 0.59) \times 10^{+1}$	$(1.04 \pm 0.12) \times 10^{+2}$	$(1.46 \pm 0.16) \times 10^{+2}$	—	$(9.43 \pm 1.03) \times 10^{+1}$	$(1.49 \pm 0.16) \times 10^{+2}$	—
47.89 ± 0.80	$(6.23 \pm 0.68) \times 10^{+1}$	$(1.26 \pm 0.14) \times 10^{+2}$	$(1.71 \pm 0.19) \times 10^{+2}$	$(1.70 \pm 0.19) \times 10^{+1}$	$(1.22 \pm 0.14) \times 10^{+2}$	$(1.61 \pm 0.18) \times 10^{+2}$	$(1.90 \pm 0.21) \times 10^{+0}$
49.99 ± 0.68	$(7.13 \pm 0.78) \times 10^{+1}$	$(1.35 \pm 0.15) \times 10^{+2}$	$(1.68 \pm 0.19) \times 10^{+2}$	$(2.12 \pm 0.23) \times 10^{+1}$	$(9.63 \pm 1.07) \times 10^{+1}$	$(1.43 \pm 0.16) \times 10^{+2}$	—
51.23 ± 0.73	$(7.15 \pm 0.78) \times 10^{+1}$	$(1.26 \pm 0.14) \times 10^{+2}$	$(1.60 \pm 0.18) \times 10^{+2}$	$(1.97 \pm 0.22) \times 10^{+1}$	$(1.27 \pm 0.14) \times 10^{+2}$	$(1.30 \pm 0.15) \times 10^{+2}$	$(1.87 \pm 0.21) \times 10^{+0}$
52.11 ± 0.59	$(7.76 \pm 0.85) \times 10^{+1}$	$(1.39 \pm 0.16) \times 10^{+2}$	$(1.85 \pm 0.21) \times 10^{+2}$	$(1.75 \pm 0.19) \times 10^{+1}$	$(9.89 \pm 1.09) \times 10^{+1}$	$(1.31 \pm 0.14) \times 10^{+2}$	—
54.41 ± 0.67	$(7.76 \pm 0.85) \times 10^{+1}$	$(1.33 \pm 0.15) \times 10^{+2}$	$(1.60 \pm 0.18) \times 10^{+2}$	$(1.36 \pm 0.15) \times 10^{+1}$	$(1.40 \pm 0.16) \times 10^{+2}$	$(1.00 \pm 0.11) \times 10^{+2}$	$(1.77 \pm 0.20) \times 10^{+0}$
56.02 ± 0.50	$(8.14 \pm 0.89) \times 10^{+1}$	$(1.23 \pm 0.14) \times 10^{+2}$	$(1.68 \pm 0.19) \times 10^{+2}$	—	$(1.46 \pm 0.16) \times 10^{+2}$	$(1.04 \pm 0.12) \times 10^{+2}$	—
57.46 ± 0.55	$(8.64 \pm 0.94) \times 10^{+1}$	$(1.23 \pm 0.14) \times 10^{+2}$	$(1.66 \pm 0.19) \times 10^{+2}$	$(1.39 \pm 0.16) \times 10^{+1}$	$(1.48 \pm 0.17) \times 10^{+2}$	$(8.16 \pm 0.89) \times 10^{+1}$	$(1.66 \pm 0.18) \times 10^{+0}$
59.73 ± 0.42	$(8.16 \pm 0.89) \times 10^{+1}$	$(1.25 \pm 0.14) \times 10^{+2}$	$(1.80 \pm 0.20) \times 10^{+2}$	$(1.18 \pm 0.13) \times 10^{+1}$	$(1.24 \pm 0.13) \times 10^{+2}$	$(8.56 \pm 0.93) \times 10^{+1}$	—
60.38 ± 0.45	$(9.17 \pm 1.01) \times 10^{+1}$	$(1.23 \pm 0.14) \times 10^{+2}$	$(1.66 \pm 0.18) \times 10^{+2}$	$(1.03 \pm 0.12) \times 10^{+1}$	$(1.44 \pm 0.16) \times 10^{+2}$	$(7.08 \pm 0.77) \times 10^{+1}$	$(1.66 \pm 0.19) \times 10^{+0}$
63.20 ± 0.36	$(9.65 \pm 1.05) \times 10^{+1}$	$(1.17 \pm 0.13) \times 10^{+2}$	$(1.55 \pm 0.17) \times 10^{+2}$	$(1.31 \pm 0.15) \times 10^{+1}$	$(1.29 \pm 0.14) \times 10^{+2}$	$(6.31 \pm 0.69) \times 10^{+1}$	$(1.62 \pm 0.18) \times 10^{+0}$
63.26 ± 0.32	$(9.97 \pm 1.09) \times 10^{+1}$	$(1.17 \pm 0.13) \times 10^{+2}$	$(1.54 \pm 0.17) \times 10^{+2}$	—	—	—	—
65.93 ± 0.36	$(9.34 \pm 1.02) \times 10^{+1}$	$(1.19 \pm 0.13) \times 10^{+2}$	$(1.37 \pm 0.15) \times 10^{+2}$	$(1.14 \pm 0.13) \times 10^{+1}$	$(1.21 \pm 0.12) \times 10^{+2}$	$(5.68 \pm 0.62) \times 10^{+1}$	$(1.51 \pm 0.17) \times 10^{+0}$
66.68 ± 0.30	$(8.60 \pm 0.94) \times 10^{+1}$	$(1.18 \pm 0.13) \times 10^{+2}$	$(1.36 \pm 0.15) \times 10^{+2}$	$(2.01 \pm 0.22) \times 10^{+1}$			

[a]The error values listed include a systematic uncertainty which is estimated to be 7% (see text).

Chapter 4

Radionuclides of Tb in Proton-Induced Reactions on ^{152,155}Gd and ^{nat}Tb

4.1 Introduction

In the January 2013 issue of the CERN Courier, an article appeared with the following title: *Terbium: a new "Swiss army knife" for nuclear medicine* [CERN2013]. It refers to the work of Müller *et al.* [Mül2012] on a preclinical study of new tumour-targeting radiopharmaceuticals labelled with the quadruplet of Tb radionuclides introduced in Chapter 3. Excellent results were obtained with a folate-based targeting agent containing a DOTA chelator for binding the Tb to the biomolecule. Both PET (^{152}Tb) and SPECT (^{155}Tb) imaging of folate receptor (FR)-positive human tumours xenografted into mice were shown to be of high quality. In addition, the same compound labelled with the therapeutic Tb radionuclides (^{161}Tb and ^{149}Tb) demonstrated impressive statistics of remission of the disease. While independent studies were performed with the α-particle emitter (^{149}Tb) and the β^- emitter (^{161}Tb), the authors speculated that cocktails of these two isotopes to optimize the efficacy of the treatment might be an intriguing option, which required further systematic investigation.

Except for the reactor produced ^{161}Tb, the large-scale production of any of the other radioterbiums, with a radionuclidic purity suitable for medical use, has not yet been demonstrated. In one of the earlier studies in the literature, Levin *et al.* [Lev1981] demonstrated the photonuclear production of ^{155}Tb via the reaction ^{156}Tb(γ,n)^{155}Dy$\rightarrow^{155}$Tb, using bremsstrahlung with a maximum energy of 25 MeV at an electron accelerator. A radionuclidic purity > 99.9% could be obtained, which is substantially higher than possible with a cyclotron. While their electron beam current was rather low and the corresponding yield relatively small, these authors speculated about large-scale production possibilities with future electron accelerators having orders of magnitude higher beam intensities. A number of studies investigated the use of ^{12}C beams. Allen *et al.* [All2001] and Zaitseva *et al.* [Zai2003] studied the ^{nat}Nd(^{12}C,xn)^{152}Dy$\rightarrow^{152}$Tb and ^{nat}Nd(^{12}C,xn)^{149}Dy$\rightarrow^{149}$Tb reactions, respectively. While useful yields could be obtained, the end product inevitably contained a mixture of Tb radionuclides. This is clearly a general problem when charged-particle induced reactions are utilized, even on highly enriched targetry. Electromagnetic isotope separation, such as used at the ISOLDE facility of CERN for the collection of radioterbiums produced in proton-induced spallation reactions, may yet be the

only feasible way to ensure a radionuclidic purity close to 100%. Indeed, it is interesting to contemplate this possibility with nuclear reactions at much lower energies, using much smaller equipment than ISOLDE, as an option for large-scale production in a dedicated facility.

As part of a project financially supported by the Swiss–South African Joint Research Program (JRP 12), iThemba LABS was approached by researchers from the Paul Scherrer Institute (PSI) to collaborate on measuring production cross sections for the direct formation of ^{149,152,155}Tb in ^{152,155}Gd + p as well as for the indirect formation of ^{155}Tb via the decay of its precursor ^{155}Dy in ^{159}Tb + p. Some target materials were supplied by PSI. This includes ^{152}Gd (0.2% natural abundance) enriched to 30.60% and ^{155}Gd (14.8% natural abundance) enriched to 99.82%. In contrast, natural Tb is mono-isotopic ^{159}Tb (100%).

The relevant part of the Karlsruhe Chart of the Nuclides has already been presented in Fig. 3.1 and Table 3.1 is still relevant for the proton-induced reactions on ^{152}Gd and ^{155}Gd. For Tb + p, the relevant nuclear reactions are presented in Table 4.1.

As already seen in Chapter 3, Mother Nature is not very friendly in this part of the periodic table and to achieve these radionuclides in a radionuclidically pure form, and not only in a no-carrier-added (NCA) form, is complicated. The work presented here can be seen as a follow-up study on the work presented in Chapter 3, although it has started some time before publication of the ^{nat}Gd + p results. The measurements have been performed at iThemba LABS in collaboration with ATOMKI and PSI. Cross sections are presented for ^{153,155,157,159}Dy, ^{153,154m2,155,156}Tb and ^{151,153}Gd in Tb + p as well as for ^{152}Gd(p,4n)^{149}Tb and ^{155}Gd(p,4n)^{152}Tb.

Table 4.1: Relevant proton-induced reactions for direct formation of the observed Dy, Tb and Gd radionuclides.

Reaction	Q value (MeV)
^{159}Tb(p,n)^{159}Dy	-1.148 MeV
^{159}Tb(p,3n)^{157}Dy	-17.04 MeV
^{159}Tb(p,5n)^{155}Dy	-33.45 MeV
^{159}Tb(p,7n)^{153}Dy	-49.60 MeV
^{159}Tb(p,p3n)^{156}Tb	-23.66 MeV
^{159}Tb(p,d2n)^{156}Tb	-21.43 MeV
^{159}Tb(p,tn)^{156}Tb	-15.17 MeV
^{159}Tb(p,p4n)^{155}Tb	-30.57 MeV
^{159}Tb(p,d3n)^{155}Tb	-28.34 MeV
^{159}Tb(p,t2n)^{155}Tb	-22.09 MeV
^{159}Tb(p,p5n)^{154m2}Tb	-39.73 MeV
^{159}Tb(p,d4n)^{154m2}Tb	-37.51 MeV
^{159}Tb(p,t3n)^{154m2}Tb	-31.25 MeV
^{159}Tb(p,p6n)^{153}Tb	-46.65 MeV
^{159}Tb(p,d5n)^{153}Tb	-44.42 MeV
^{159}Tb(p,t4n)^{153}Tb	-38.16 MeV
^{159}Tb(p,α3n)^{153}Gd	-15.99 MeV
^{159}Tb(p,2p5n)^{153}Gd	-44.30 MeV
^{159}Tb(p,α5n)^{151}Gd	-30.84 MeV
^{159}Tb(p,2p7n)^{151}Gd	-59.89 MeV

4.2 Experimental method

4.2.1 Irradiations and radionuclide assays

Three foil stacks were irradiated at iThemba LABS which, for the sake of the discussion of this chapter only, will be referred to as Stacks 1, 2 and 3. Most of the detail of Section 3.2 and Appendix A is again relevant, therefore, only salient aspects not treated elsewhere are presented here.

Stacks 1 and 2 contained thin targets prepared from oxides of Gd and Tb using the sedimentation technique developed by Rösch *et al.* [Rös1993]. Gadolinium trioxide (Gd_2O_3) and tetraterbium heptaoxide (Tb_4O_7) powders were obtained from Isoflex USA and Koch Chemicals Ltd., respectively. Due to limited quantities of the enriched Gd powder, only relatively few targets could be made. In each case, fine powder of the target material was sedimented onto a 26 μm thick Ti backing and covered with a 10 μm thick Al foil. The diameter of a sediment layer was 13 mm, defined by the inner diameter of the sedimentation cells used. The thicknesses of the sediment layers varied between 1.4 and 4.4 mg/cm^2 but nominally 2.5 mg/cm^2 for Tb_4O_7, 4 mg/cm^2 for $^{152}Gd_2O_3$ and 1.5 mg/cm^2 for $^{155}Gd_2O_3$. As before, the thickness of each target sediment and target foil was determined accurately by weighing. Stack 1 contained seven ^{152}Gd and seven Tb targets while Stack 2 contained seven ^{155}Gd targets, covering the energy region 30–62 MeV. The target foils were interspersed with Cu monitor foils of nominally 108 mg/cm^2 thickness (99.99%, Goodfellow, UK) as well as Cu and Al degrader foils of various thicknesses, as required. Just prior to the bombardment, it was decided to degrade the 66 MeV proton beam by a few MeV to better match the expected energy region of the (p,4n) reaction for ^{152,155}Gd + p. This was done with a single Cu degrader. At that time, future irradiations of similar stacks at a beam energy of 30 MeV were planned, to cover the lower energy region of the excitation functions for reactions with thresholds below this value. Unfortunately, due to unforseen cyclotron problems, that opportunity as planned was lost at iThemba LABS. These lower energy studies still have to be performed – it is now being planned for the second half of 2014, possibly at Jülich. As the data sets for (p,xn) reactions where $x < 4$ are still incomplete, only results for the (p,4n) reactions in ^{152,155}Gd + p are presented at this stage.

Stack 1 had another inherent limitation, namely that the ^{152}Gd targets only had an enrichment level of 30.60%. The content of the other stable Gd isotopes are as follows: ^{154}Gd (9.3%), ^{155}Gd (18.1%), ^{156}Gd (14.8%), ^{157}Gd (8.6 %), ^{158}Gd (11%) and ^{160}Gd (7.6%). Although not ideal, these measurements are nevertheless expected to provide useful information for the important reaction ^{152}Gd(p,4n)^{149}Tb, while the interpretation of several of the other (p,xn) reactions may be rather complicated. In the case of the ^{155}Gd targets, no such complication is expected as the level of enrichment was 99.82%.

The decision to irradiate a third stack containing metallic Tb foils was made later. This was done, in part, as a check on the results from the Tb_4O_7 sediment targets. Results from experiments using the sedimentation technique sometimes show unusually large scatter, which could potentially be a problem in stacked-foil experiments having so few targets as Stacks 1 and 2. The scatter is thought to be a result of sediment targets being rather fragile, sometimes

suffering damage either before or during bombardment. A second reason was that for ^{159}Tb + p, almost no excitation function data could be found in the literature, which made it an interesting study in its own right. Also, because of the delay in the investigation of the lower energy region, it was decided to design Stack 3 to cover the entire energy region down to the threshold of the (p,n) reaction. Normally, we prefer not to degrade the 66 MeV beam so far down due to the increasing energy uncertainty with increasing penetration depth in the stack. On the other hand, the lower energy region for Tb + p could always be re-investigated later with a lower energy incident beam (e.g. 30 MeV), should compelling reasons exist to do so. Stack 3 consisted of elemental Tb foils of nominally 18.6 mg/cm^2 thickness (99%, Goodfellow Metals, UK), Cu monitor foils of nominally 45.8 mg/cm^2 (99.9%, Goodfellow, UK) throughout the stack, as well as Ti monitor/degrader foils of nominally 115 mg/cm^2 in the region between 20 and 35 MeV. A selection of Al and Cu foils of various thicknesses were used as degraders.

The radionuclide assays were performed using off-line HPGe γ-ray spectrometry as described in Section 3.2.3. In addition to the coaxial detectors used for our normal γ-ray spectrometry, a planar HPGe detector with a 10 mm thick Ge crystal was used to assay the 58 keV γ-ray of ^{159}Dy and the 97 keV γ-ray of ^{153}Gd. This was done because the planar detector has a higher efficiency and a significantly lower Compton background for these low-energy γ-rays.

4.2.2 Data analysis

As before, the cross sections of the observed activation products were calculated from their measured γ-ray emissions using decay data from the online compilation of Firestone and Eckström [Fir2004]. The γ-lines used for the radionuclide identification and quantification are listed in Table 3.2 for Tb, and Table 4.2 for Dy and Gd radionuclides. Further details can be found in Section 3.2.4 and Appendices A, B and C.

Table 4.2: Investigated Dy and Gd radionuclides and their decay properties used for experimental cross-section determinations[a].

Nuclide	Half-life	Decay mode	γ-rays (keV)	Intensity (%)
^{153}Dy	6.4 h	$\epsilon + \beta^+$: 99.99%	213.75	10.9
^{155}Dy	9.9 h	$\epsilon + \beta^+$: 100%	226.92	68.4
^{157}Dy	8.14 h	$\epsilon + \beta^+$: 100%	326.16	92.0
^{159}Dy	144.4 d	ϵ: 100%	58.00	2.22
^{151}Gd	124.0 d	ϵ: 100%	153.60	6.20
			243.28	5.60
^{153}Gd	240.4 d	ϵ: 100%	97.43	29.0
			103.18	21.1

[a]Taken from Firestone & Eckström [Fir2004].

The results for the ^{nat}Cu(p,x)^{62}Zn monitor reaction are shown in Fig. 4.1 for all three stacks, together with the standard excitation function recommended by the IAEA [Gul2001]. For the experimental cross sections of this study, the logged beam currents from the electronic current

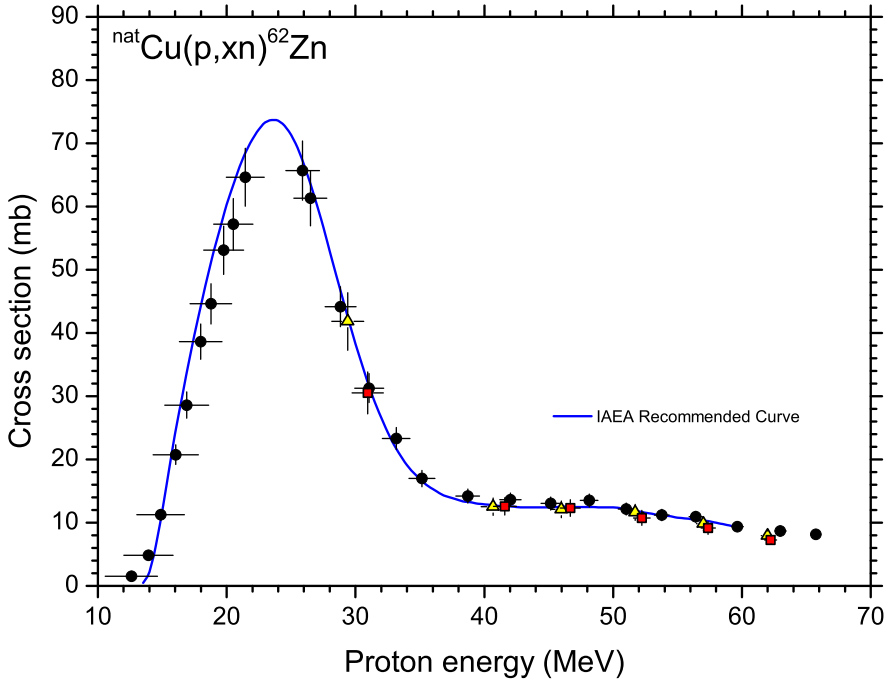

Figure 4.1: Monitor excitation function for the production of ^{62}Zn in the bombardment of ^{nat}Cu with protons. Yellow triangles: this work (Stack 1). Red squares: this work (Stack 2). Black circles: this work (Stack 3 – see text for details).

integrator were used. The measured cross sections reproduce the recommended curve satisfactorily, therefore, there was no need to make any corrections from the accumulated charge values extracted from the monitor reaction measurements. A similar quality of agreement was found for the ^{nat}Ti(p,x)^{48}V monitor reaction.

4.3 Theoretical calculations

Theoretical cross sections have been calculated with the code ALICE/ASH. Comparisons have also been made with the values of the TENDL-2012 library. This has already been described in detail in Section 3.3. It should be noted that where cumulative cross sections are presented, such as for ^{159}Tb(p,X)^{155}Tb which contains a component from the decay of the precursor ^{155}Dy, the following expression have been used (cf. [Par1991]):

$$\sigma_D^{cum} = \sigma_D^{dir} + \epsilon \left[\frac{\lambda_P}{\lambda_P - \lambda_D} \right] \sigma_P^{dir}, \tag{4.1}$$

where σ_D^{cum} is the cumulative cross section of the daughter nuclide, σ_D^{dir} is the cross section for the direct formation of the daughter nuclide, σ_P^{dir} is the cross section for the direct formation of the parent nuclide, ϵ is the branching ratio for decay of the parent to the daughter nuclide, with λ_P and λ_D the decay constants of the parent and daughter nuclides, respectively.

4.4 Results and discussion

The results from Stacks 1 and 2 (i.e. the $^{152}Gd_2O_3$, $^{155}Gd_2O_3$ and $^{159}Tb_4O_7$ sediment targets) are presented in Table 4.3. The results from Stack 3 (i.e. the Tb metal foils) are presented in

Tables 4.4, 4.5 and 4.6. The excitation functions are shown in Figs. 4.2 through 4.8 and the derived physical yield curves and related quantities in Figs. 4.9 through 4.12.

4.4.1 The ^{152}Gd(p,4n)^{149}Tb reaction

Because the $^{152}Gd_2O_3$ targets only had a 30.6% level of enrichment of ^{152}Gd, several other reactions also contributed to the direct formation of ^{149}Tb, such as ^{154}Gd(p,6n)^{149}Tb ($Q = -43.36$ MeV) and ^{155}Gd(p,7n)^{149}Tb ($Q = -49.80$ MeV). The ^{152}Gd(p,4n)^{149}Tb ($Q = -28.21$ MeV) reaction, however, is expected to dominate the excitation function. The measured data are shown in Fig. 4.2, scaled for targets of 100% enrichment. Comparisons are made with ALICE/ASH predictions for the (p,4n) reaction on its own, as well as the sum of the contributions from the (p,4n), (p,6n) and (p,7n) reactions mentioned above, weighed according to the relative ^{152}Gd, ^{154}Gd and ^{155}Gd abundances in the target material, respectively. The ALICE/ASH predictions overestimate the cross sections considerably and have been renormalized (with a scale factor of $SF = 0.30$) for purposes of comparison with the experimental data. One can clearly see in the figure that both ALICE/ASH curves reproduce the shape of the excitation function quite well, even though the data points are rather few. The excitation function peaks at about 250 mb at an energy of 42 MeV. Also, the contributions from the (p,6n) and (p,7n) reactions are indeed small and feature only towards higher energies, above about 55 MeV. Figure 4.2 also shows the TENDL-2012 values for the (p,4n) reaction, which are also substantially larger than the measured values and have been renormalized to the measured data for purposes of comparison (scale factor $SF = 0.39$). The TENDL-2012 data do not reproduce the shape of the experimental excitation function nearly as well as the ALICE/ASH predictions and appear to be shifted towards lower energies by about 4–5 MeV.

4.4.2 The ^{155}Gd(p,4n)^{152}Tb reaction

Concerning the measurements, only the (p,4n) reaction on ^{155}Gd contributed significantly to ^{152}Tb formation as the ^{155}Gd enrichment level was close to 100%. The experimental cross sections are shown in Fig. 4.3, together with ALICE/ASH predictions and the relevant TENDL-2012 values. The ALICE/ASH and TENDL-2012 values both underestimate the excitation function and have therefore been renormalized to the measurements for purposes of comparison (scale factors $SF = 1.7$ and $SF = 1.3$, respectively). Both predictions are somewhat shifted relative to the measurements – TENDL-2012 towards lower energies and ALICE/ASH towards higher energies. The blue curve is a spline fit through the measured data, used for calculating the integral yield curve, which will be presented later. The excitation function reaches a maximum of about 900 mb at energy of about 39 MeV.

4.4.3 The ^{159}Tb(p,7n)^{153}Dy reaction

The ^{159}Tb(p,7n)^{153}Dy ($Q = -49.6$ MeV) reaction could only be observed in three of the Tb metal foils of Stack 3, at the highest energies, as shown in Fig. 4.4. It is presented here for completeness only. Both ALICE/ASH and TENDL-2012 do not reproduce the onset of the excitation function in the threshold region very well, therefore, a spline fit (blue curve) through the mea-

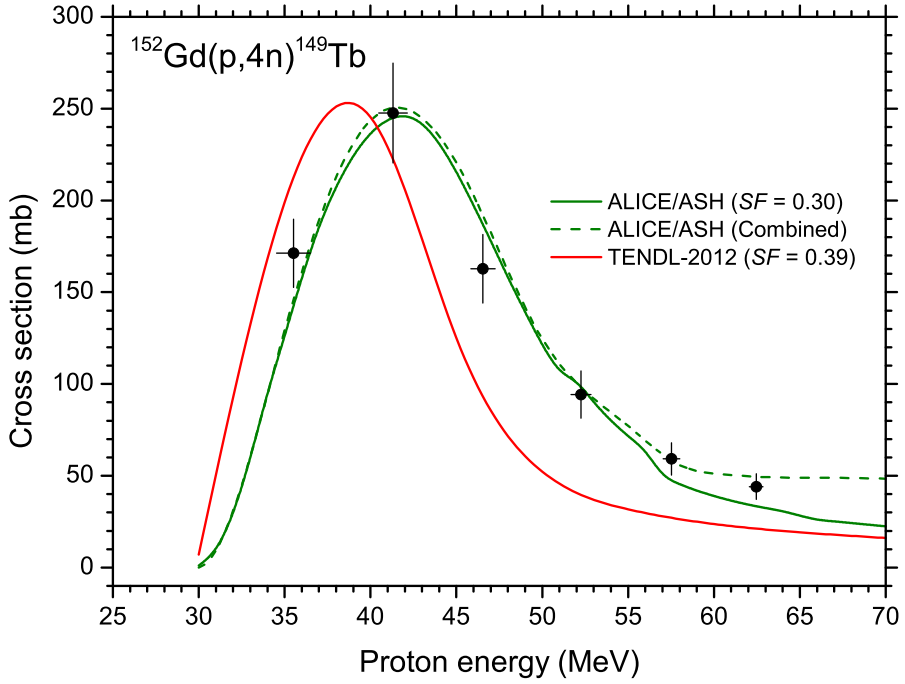

Figure 4.2: Excitation function for the production of ^{149}Tb in the irradiation of ^{152}Gd with protons. Black circles: this work (Stack 1). The solid curves show the results from ALICE/ASH calculations [Bro2006] and the TENDL-2012 library [Kon2012, Kon2013] for the (p,4n) reaction on ^{152}Gd only, as indicated, while the dashed green curve also includes co-produced contributions from the (p,6n) reaction on ^{154}Gd and the (p,7n) reaction on ^{155}Gd (see text). Note that the dashed green curve has been raised slightly relative to the solid green curve to make it visible in the region of energy where the two curves overlap.

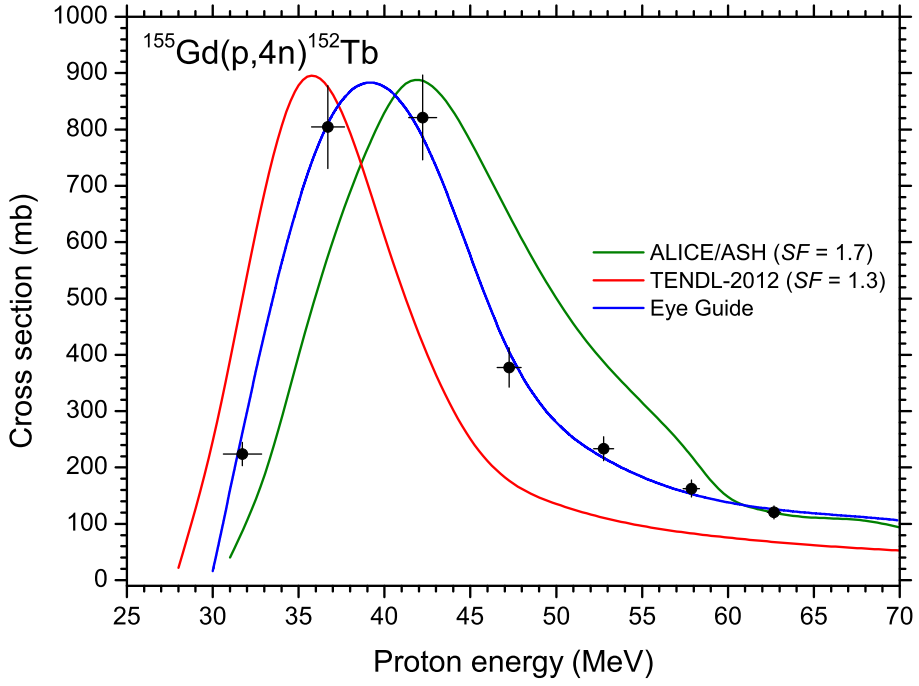

Figure 4.3: Excitation function for the production of ^{152}Tb in the irradiation of ^{155}Gd with protons. Black circles: this work (Stack 2). See also caption to Fig. 4.2.

sured data, extrapolated to 70 MeV, has been used to calculate the physical yield curve. This will be further discussed later.

Table 4.3: Measured cross sections for the production of Tb and Dy radionuclides in the irradiation of ^{152,155}Gd and ^{nat}Tb with protons – results from Stacks 1 and 2.

Proton energy (MeV)	Cross section (mb)			
	^{152}Gd(p,4n)^{149}Tb	^{155}Gd(p,4n)^{152}Tb	^{159}Tb(p,5n)^{155}Dy	^{159}Tb(p,3n)^{157}Dy
31.73 ± 1.11	–	$(2.24 \pm 0.21) \times 10^{+2}$	–	–
35.69 ± 0.98	–	–	–	$(3.73 \pm 0.34) \times 10^{+2}$
35.52 ± 0.99	$(1.71 \pm 0.19) \times 10^{+2}$	–	–	–
36.71 ± 0.96	–	$(8.04 \pm 0.74) \times 10^{+2}$	–	–
41.31 ± 0.84	$(2.48 \pm 0.27) \times 10^{+2}$	–	–	–
41.46 ± 0.83	–	–	$(1.80 \pm 0.17) \times 10^{+2}$	$(2.03 \pm 0.19) \times 10^{+2}$
42.22 ± 0.82	–	$(8.21 \pm 0.75) \times 10^{+2}$	–	–
46.55 ± 0.71	$(1.63 \pm 0.19) \times 10^{+2}$	–	–	–
46.69 ± 0.71	–	–	$(5.07 \pm 0.47) \times 10^{+2}$	$(1.33 \pm 0.12) \times 10^{+2}$
47.25 ± 0.70	–	$(3.77 \pm 0.35) \times 10^{+2}$	–	–
52.25 ± 0.58	$(9.43 \pm 1.28) \times 10^{+1}$	–	–	–
52.38 ± 0.58	–	–	$(5.52 \pm 0.51) \times 10^{+2}$	$(1.12 \pm 0.10) \times 10^{+2}$
52.76 ± 0.57	–	$(2.33 \pm 0.21) \times 10^{+2}$	–	–
57.52 ± 0.48	$(5.92 \pm 0.88) \times 10^{+1}$	–	–	–
57.64 ± 0.48	–	–	$(4.16 \pm 0.38) \times 10^{+2}$	$(1.05 \pm 0.10) \times 10^{+2}$
57.87 ± 0.47	–	$(1.63 \pm 0.15) \times 10^{+2}$	–	–
62.46 ± 0.39	$(4.41 \pm 0.69) \times 10^{+1}$	–	–	–
62.58 ± 0.39	–	–	$(2.10 \pm 0.19) \times 10^{+2}$	$(8.79 \pm 0.82) \times 10^{+1}$
62.68 ± 0.39	–	$(1.20 \pm 0.12) \times 10^{+2}$	–	–

4.4.4 The ^{159}Tb(p,5n)^{155}Dy reaction

In the case of the ^{159}Tb(p,5n)^{155}Dy ($Q = -33.45$ MeV) reaction, both the ALICE/ASH prediction, the TENDL-2012 data and the experimental data agree reasonably well in magnitude at the maximum of the excitation function. However, as shown in Fig. 4.4, the TENDL-2012 results seem to be systematically shifted towards lower energies, while the ALICE/ASH prediction is shifted towards higher energies. There is also good agreement in shape between the ALICE/ASH prediction and the measurements, the main difference being the approximately 2 MeV shift. In contrast, the TENDL-2012 excitation function shows a significantly narrower width in the peak region. While not perfect, the overall agreement between the measurements from Stacks 1 and 3 is acceptable – the majority of the experimental points from the two data sets agree within the experimental uncertainties. This is very reassuring. The excitation function reaches a maximum of about 520 mb at 48 MeV. As before, the blue "eye-guide" curve is a spline fit used for calculating integral yields.

4.4.5 The ^{159}Tb(p,3n)^{157}Dy reaction

The results for the ^{159}Tb(p,3n)^{157}Dy ($Q = -17.04$ MeV) reaction are shown in Fig. 4.5. As the measured cross sections span several orders of magnitude, the figure is presented on a log scale. The agreement with the ALICE/ASH prediction is very satisfactory, both in absolute magnitude and in shape, while the TENDL-2012 values are somewhat lower with the peak position shifted towards the lower energy side by about 4 MeV. The overall agreement between

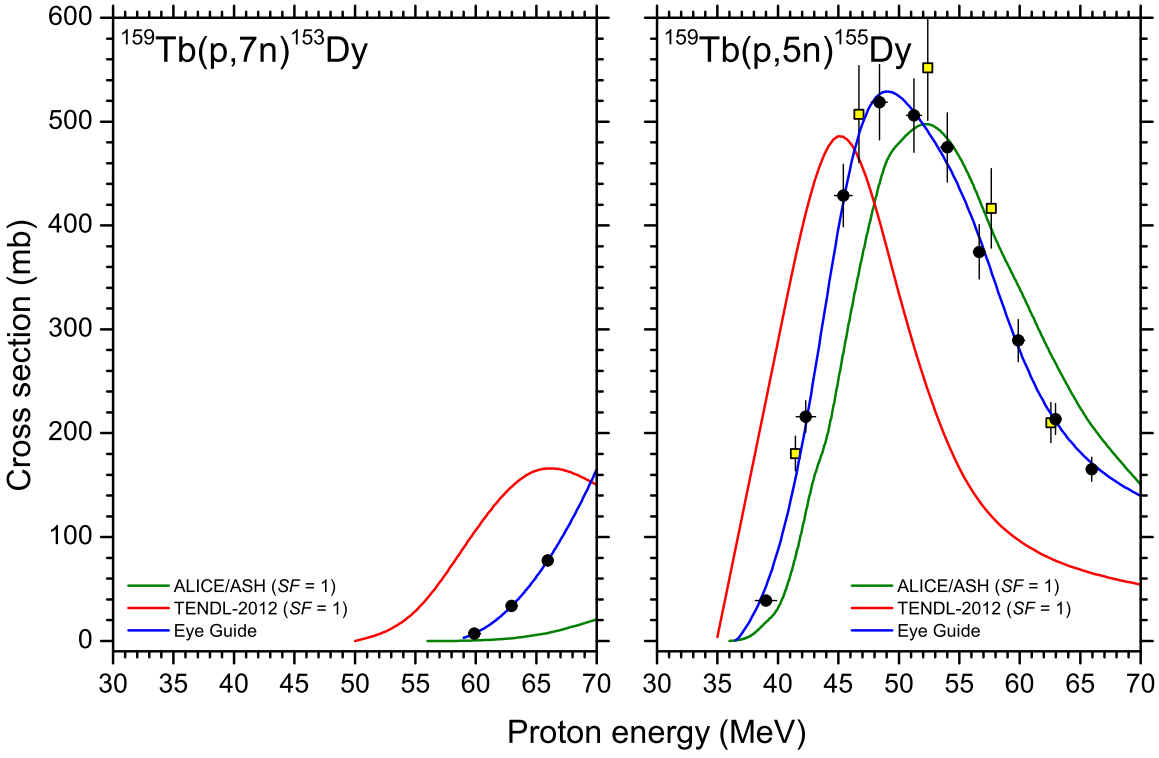

Figure 4.4: Excitation functions for the production of ^{153,155}Dy in the irradiation of ^{159}Tb with protons. Black circles: this work (Stack 3). Yellow squares: this work (Stack 1). See also caption to Fig. 4.2.

the measurements from Stacks 1 and 3 is also acceptable. The excitation function reaches a maximum of just over 1000 mb at about 27 MeV. The blue "eye-guide" curve is a spline fit.

4.4.6 The ^{159}Tb(p,n)^{159}Dy reaction

Figure 4.5 also shows the results for the ^{159}Tb(p,n)^{159}Dy ($Q = -1.148$ MeV) reaction. The excitation function peaks just over 100 mb at an energy of about 10.4 MeV. The agreement with the only set of previously published data found in the literature, by Hassan *et al.* [Has2007], is reasonable. By and large, the agreement with the ALICE/ASH prediction and TENDL-2012 values is poor, particularly in the tail regions towards higher energies where large overpredictions are observed in both cases. We also noted a strange anomaly in the (p,n) data of TENDL-2012 for a range of target nuclei. There is a notable but spurious second local maximum towards higher energies, which is not characteristic of (p,n) reactions. This observation was further investigated and is separately discussed in Appendix F. The blue "eye-guide" curve is a spline fit through the experimental cross sections of this work only.

4.4.7 The ^{159}Tb(p,X)^{153}Tb process

Several reaction channels are open for the formation of ^{153}Tb ($T_{1/2} = 2.3$ d) e.g. ^{159}Tb(p,p6n)^{153}Tb ($Q = -46.65$ MeV), ^{159}Tb(p,d5n)^{153}Tb ($Q = -44.42$ MeV), ^{159}Tb(p,t4n)^{153}Tb ($Q = -38.16$ MeV) as well as indirectly via the the decay of the precursor ^{153}Dy ($T_{1/2} = 6.4$ h). The measurements were performed after the complete decay of the shorter-lived precursor and the resulting cross sections are therefore cumulative. The measurements are presented in Fig. 4.6, as well as the

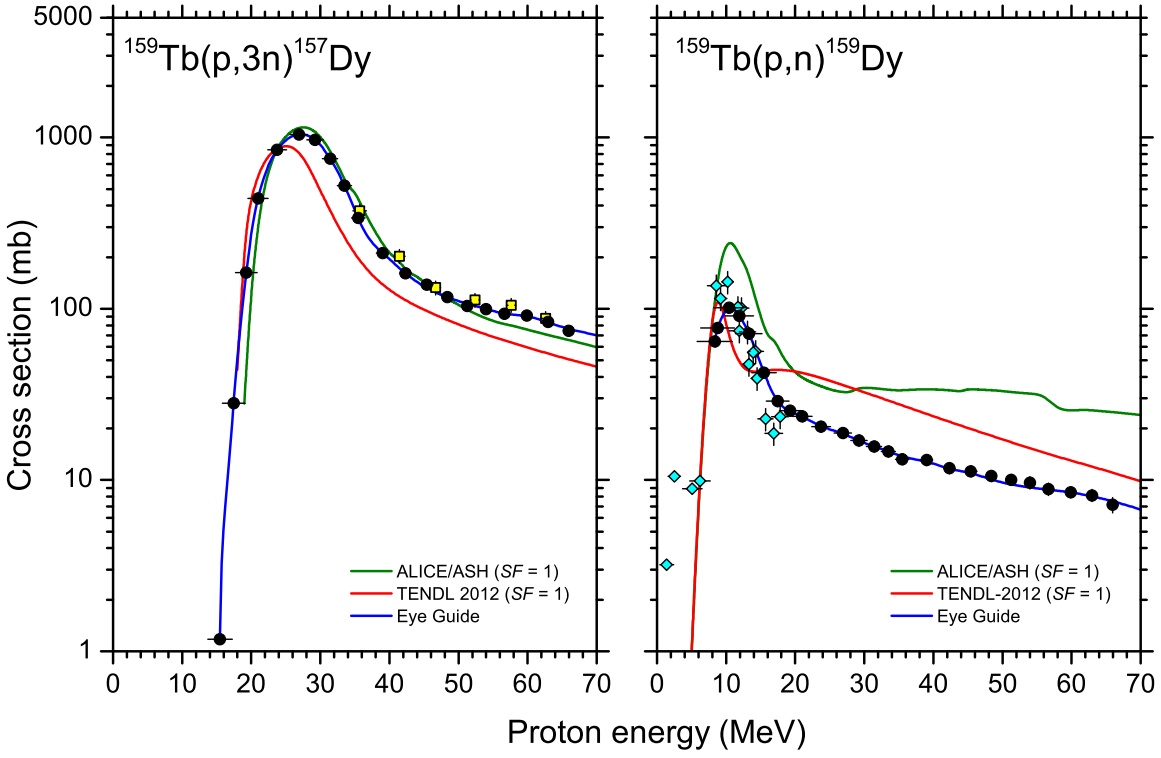

Figure 4.5: Excitation functions for the production of ^{157,159}Dy in the irradiation of ^{159}Tb with protons. Black circles: this work (Stack 3). Yellow squares: this work (Stack 1). Blue diamonds: Hassan *et al.* [Has2007]. See also caption to Fig. 4.2.

ALICE/ASH and TENDL-2012 predictions. It is impossible to make a judgment on the quality of the theoretical predictions as the measurements reflect only the steep slope near an effective threshold somewhat above 50 MeV. It seems, however, as if the TENDL-2012 values are shifted towards lower energies and the ALICE/ASH values towards higher energies. Neither curves can be successfully scaled to the data, therefore, the scale factors were kept at a value of $SF = 1$. This may be an indication that energy shifts are more likely than over- and underpredictions.

4.4.8 The ^{159}Tb(p,X)^{154m2}Tb process

Similar to the discussion of Section 3.4.4, it was only possible to extract cross sections for the m2 state. Both the ALICE/ASH and TENDL-2012 curves had to be scaled considerably for purposes of making a comparison with the measurements ($SF = 0.075$), as shown in Fig. 4.6. In this particular case, the cross sections are for the direct production of ^{154m2}Tb due to the very long half-life of the precursor, ^{154}Dy ($T_{1/2} = 3 \times 10^6$ y). While the relevant reaction Q-values are all below 40 MeV (^{159}Tb(p,p5n)^{154m2}Tb, $Q = -39.93$ MeV; ^{159}Tb(p,d4n)^{154m2}Tb, $Q = -37.51$ MeV; ^{159}Tb(p,t3n)^{154m2}Tb, $Q = -31.25$ MeV) no ^{154m2}Tb were detected below 53 MeV. It is difficult to make a conclusive judgement about the agreement between the experimental measurements and the theoretical predictions. It seems, however, that the TENDL-2012 values reproduce the shape of the excitation function better in this case, albeit with an order of magnitude overprediction.

Table 4.4: Measured cross sections for the production of Dy radionuclides in the irradiation of ^{nat}Tb with protons.

Proton energy (MeV)	Cross section (mb)			
	^{153}Dy	^{155}Dy	^{157}Dy	^{159}Dy
8.35 ± 2.53	–	–	–	$(6.45 \pm 0.46) \times 10^{+1}$
8.76 ± 2.45	–	–	–	$(7.73 \pm 0.55) \times 10^{+1}$
10.43 ± 2.22	–	–	–	$(1.01 \pm 0.07) \times 10^{+2}$
11.91 ± 2.06	–	–	–	$(9.10 \pm 0.64) \times 10^{+1}$
13.28 ± 1.94	–	–	–	$(7.16 \pm 0.51) \times 10^{+1}$
15.47 ± 1.78	–	–	$(1.17 \pm 0.11) \times 10^{+0}$	$(4.23 \pm 0.30) \times 10^{+1}$
17.45 ± 1.66	–	–	$(2.81 \pm 0.20) \times 10^{+1}$	$(2.89 \pm 0.21) \times 10^{+1}$
19.28 ± 1.56	–	–	$(1.63 \pm 0.11) \times 10^{+2}$	$(2.54 \pm 0.18) \times 10^{+1}$
20.98 ± 1.48	–	–	$(4.41 \pm 0.31) \times 10^{+2}$	$(2.36 \pm 0.17) \times 10^{+1}$
23.75 ± 1.37	–	–	$(8.47 \pm 0.59) \times 10^{+2}$	$(2.05 \pm 0.15) \times 10^{+1}$
26.89 ± 1.25	–	–	$(1.04 \pm 0.07) \times 10^{+3}$	$(1.90 \pm 0.14) \times 10^{+1}$
29.21 ± 1.17	–	–	$(9.70 \pm 0.68) \times 10^{+2}$	$(1.70 \pm 0.13) \times 10^{+1}$
31.41 ± 1.11	–	–	$(7.53 \pm 0.53) \times 10^{+2}$	$(1.57 \pm 0.11) \times 10^{+1}$
33.49 ± 1.04	–	–	$(5.23 \pm 0.37) \times 10^{+2}$	$(1.47 \pm 0.11) \times 10^{+1}$
35.48 ± 0.99	–	–	$(3.38 \pm 0.24) \times 10^{+2}$	$(1.32 \pm 0.09) \times 10^{+1}$
39.01 ± 0.89	–	$(3.90 \pm 0.28) \times 10^{+1}$	$(2.11 \pm 0.15) \times 10^{+2}$	$(1.31 \pm 0.09) \times 10^{+1}$
42.31 ± 0.81	–	$(2.16 \pm 0.15) \times 10^{+2}$	$(1.61 \pm 0.11) \times 10^{+2}$	$(1.18 \pm 0.09) \times 10^{+1}$
45.42 ± 0.74	–	$(4.29 \pm 0.30) \times 10^{+2}$	$(1.38 \pm 0.10) \times 10^{+2}$	$(1.13 \pm 0.08) \times 10^{+1}$
48.39 ± 0.67	–	$(5.19 \pm 0.36) \times 10^{+2}$	$(1.17 \pm 0.08) \times 10^{+2}$	$(1.05 \pm 0.08) \times 10^{+1}$
51.25 ± 0.61	–	$(5.06 \pm 0.35) \times 10^{+2}$	$(1.04 \pm 0.07) \times 10^{+2}$	$(1.00 \pm 0.07) \times 10^{+1}$
54.00 ± 0.55	–	$(4.75 \pm 0.33) \times 10^{+2}$	$(9.97 \pm 0.70) \times 10^{+1}$	$(9.65 \pm 0.80) \times 10^{+0}$
56.65 ± 0.50	–	$(3.75 \pm 0.26) \times 10^{+2}$	$(9.37 \pm 0.66) \times 10^{+1}$	$(8.86 \pm 0.72) \times 10^{+0}$
59.87 ± 0.44	$(6.97 \pm 0.71) \times 10^{+0}$	$(2.89 \pm 0.20) \times 10^{+2}$	$(9.15 \pm 0.64) \times 10^{+1}$	$(8.46 \pm 0.59) \times 10^{+0}$
62.97 ± 0.36	$(3.36 \pm 0.25) \times 10^{+1}$	$(2.14 \pm 0.15) \times 10^{+2}$	$(8.37 \pm 0.59) \times 10^{+1}$	$(8.14 \pm 0.66) \times 10^{+0}$
65.95 ± 0.30	$(7.75 \pm 0.55) \times 10^{+1}$	$(1.65 \pm 0.12) \times 10^{+2}$	$(7.45 \pm 0.52) \times 10^{+1}$	$(7.16 \pm 0.72) \times 10^{+0}$

4.4.9 The ^{159}Tb(p,X)^{155}Tb process

The excitation function of ^{155}Tb ($T_{1/2} = 5.42$ d) contains contributions which are directly produced (^{159}Tb(p,p4n)^{155}Tb, $Q = -30.57$ MeV; ^{159}Tb(p,d3n)^{155}Tb, $Q = -28.34$ MeV; ^{159}Tb(p,t2n)^{155}Tb, $Q = -22.09$ MeV) as well as an indirectly produced contribution via the decay of a shorter-lived precursor, ^{155}Dy ($T_{1/2} = 9.9$ h). These measurements were performed after the decay of the precursor, thus, the resulting cross sections are cumulative. As shown in Fig. 4.7, the data span several orders of magnitude and are therefore plotted on a log scale. The agreement with the ALICE/ASH prediction is satisfactory, both in shape and absolute magnitude, although the theoretical values are shifted towards higher energies by about 2 MeV. In contrast, the TENDL-2012 values are shifted somewhat towards lower energies and underestimate the maximum cross section. The excitation function peaks at a value of about 670 mb at 51 MeV.

4.4.10 The ^{159}Tb(p,X)^{156}Tb process

As discussed in Section 3.4.6, two relatively long-lived metastable states, ^{156m1}Tb ($T_{1/2} = 1.02$ d) and ^{156m2}Tb ($T_{1/2} = 5$ h) both decay to the ground state of ^{156}Tb ($T_{1/2} = 5.4$ d). The measurements were performed after the near complete decay of the metastable states. There is no

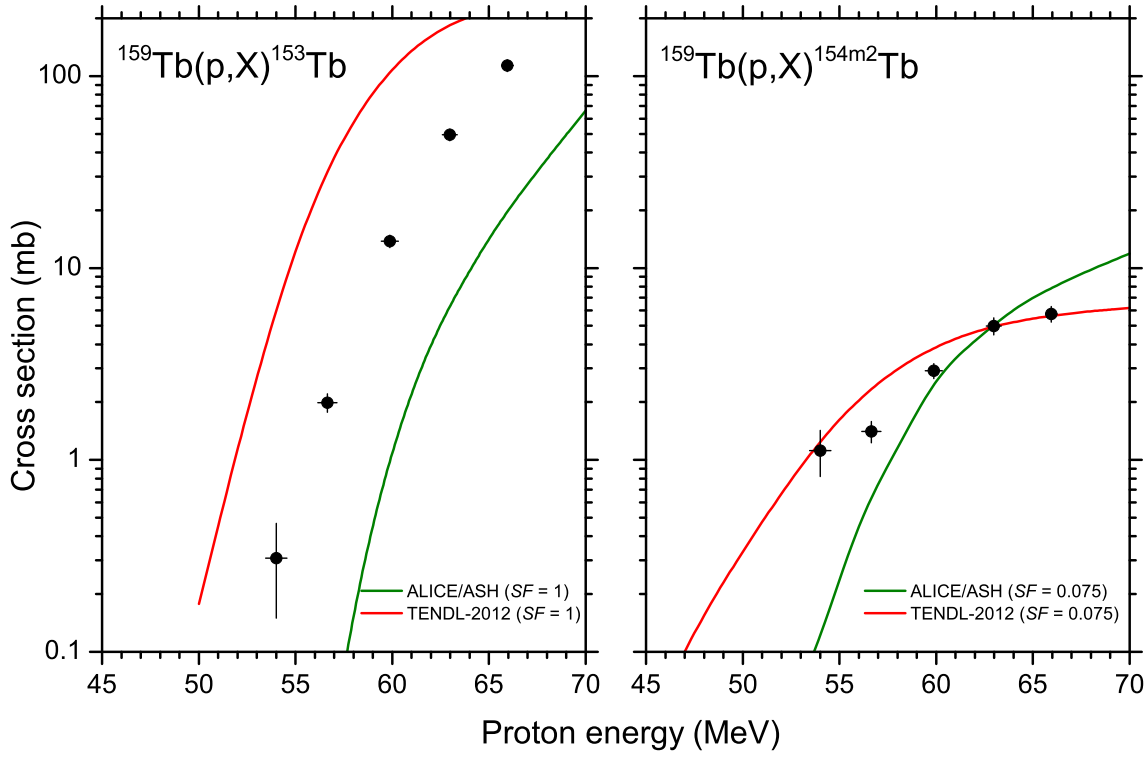

Figure 4.6: Excitation functions for the production of ^{153,154m2}Tb in the irradiation of ^{159}Tb with protons. Black circles: this work (Stack 3). See also caption to Fig. 4.2.

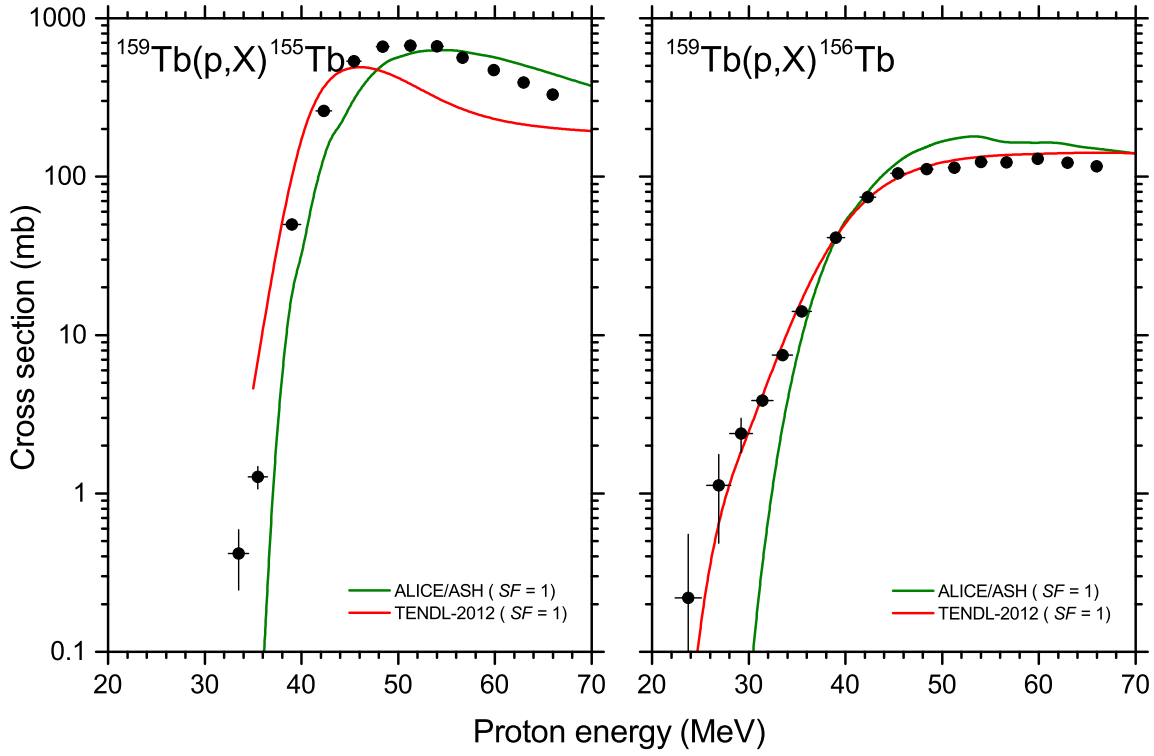

Figure 4.7: Excitation functions for the production of ^{155,156}Tb in the irradiation of ^{159}Tb with protons. Black circles: this work (Stack 3). See also caption to Fig. 4.2.

Dy precursor (^{156}Dy is stable). The experimental results are shown in Fig. 4.7, together with the ALICE/ASH calculations and the TENDL-2012 values. The TENDL-2012 results are in excellent agreement with the measured data. The ALICE/ASH prediction seems to start at a too-high threshold and also slightly overpredicts the excitation function maximum.

Table 4.5: Measured cross sections for the production of Tb radionuclides in the irradiation of ^{nat}Tb with protons.

Proton energy (MeV)	Cross section (mb)			
	^{153}Tb	^{154m2}Tb	^{155}Tb	^{156}Tb
23.75 ± 1.37	–	–	–	$(2.19 \pm 3.33) \times 10^{-1}$
26.89 ± 1.25	–	–	–	$(1.12 \pm 0.64) \times 10^{+0}$
29.21 ± 1.17	–	–	–	$(2.39 \pm 0.59) \times 10^{+0}$
31.41 ± 1.11	–	–	–	$(3.86 \pm 0.29) \times 10^{+0}$
33.49 ± 1.04	–	–	$(4.18 \pm 1.72) \times 10^{-1}$	$(7.46 \pm 0.54) \times 10^{+0}$
35.48 ± 0.99	–	–	$(1.27 \pm 0.21) \times 10^{+0}$	$(1.41 \pm 0.10) \times 10^{+1}$
39.01 ± 0.89	–	–	$(4.99 \pm 0.36) \times 10^{+1}$	$(4.11 \pm 0.29) \times 10^{+1}$
42.31 ± 0.81	–	–	$(2.61 \pm 0.18) \times 10^{+2}$	$(7.41 \pm 0.52) \times 10^{+1}$
45.42 ± 0.74	–	–	$(5.34 \pm 0.37) \times 10^{+2}$	$(1.05 \pm 0.07) \times 10^{+2}$
48.39 ± 0.67	–	–	$(6.63 \pm 0.46) \times 10^{+2}$	$(1.12 \pm 0.08) \times 10^{+2}$
51.25 ± 0.61	–	–	$(6.73 \pm 0.47) \times 10^{+2}$	$(1.14 \pm 0.08) \times 10^{+2}$
54.00 ± 0.55	$(3.08 \pm 1.59) \times 10^{-1}$	$(1.12 \pm 0.30) \times 10^{+0}$	$(6.65 \pm 0.47) \times 10^{+2}$	$(1.24 \pm 0.09) \times 10^{+2}$
56.65 ± 0.50	$(1.99 \pm 0.22) \times 10^{+0}$	$(1.41 \pm 0.18) \times 10^{+0}$	$(5.63 \pm 0.39) \times 10^{+2}$	$(1.23 \pm 0.09) \times 10^{+2}$
59.87 ± 0.44	$(1.38 \pm 0.10) \times 10^{+1}$	$(2.92 \pm 0.26) \times 10^{+0}$	$(4.71 \pm 0.33) \times 10^{+2}$	$(1.30 \pm 0.09) \times 10^{+2}$
62.97 ± 0.36	$(4.95 \pm 0.35) \times 10^{+1}$	$(4.99 \pm 0.51) \times 10^{+0}$	$(3.92 \pm 0.27) \times 10^{+2}$	$(1.23 \pm 0.09) \times 10^{+2}$
65.95 ± 0.30	$(1.14 \pm 0.08) \times 10^{+2}$	$(5.76 \pm 0.55) \times 10^{+0}$	$(3.30 \pm 0.23) \times 10^{+2}$	$(1.16 \pm 0.08) \times 10^{+2}$

Table 4.6: Measured cross sections for the production of Gd radionuclides in the irradiation of ^{nat}Tb with protons.

Proton energy (MeV)	Cross section (mb)	
	^{151}Gd	^{153}Gd
33.49 ± 1.17	–	$(2.36 \pm 0.22) \times 10^{-1}$
35.48 ± 1.11	–	$(9.67 \pm 0.70) \times 10^{-1}$
39.01 ± 1.04	–	$(4.57 \pm 0.32) \times 10^{+0}$
42.31 ± 0.99	–	$(8.80 \pm 0.62) \times 10^{+0}$
45.42 ± 0.89	–	$(1.17 \pm 0.08) \times 10^{+1}$
48.39 ± 0.81	–	$(1.44 \pm 0.10) \times 10^{+1}$
51.25 ± 0.74	–	$(8.92 \pm 0.63) \times 10^{+0}$
54.00 ± 0.68	$(9.06 \pm 1.14) \times 10^{-1}$	$(8.83 \pm 0.62) \times 10^{+0}$
56.65 ± 0.50	$(1.59 \pm 0.15) \times 10^{+0}$	$(8.34 \pm 0.56) \times 10^{+0}$
59.87 ± 0.46	$(5.71 \pm 0.41) \times 10^{+0}$	$(2.07 \pm 0.15) \times 10^{+1}$
62.97 ± 0.39	$(9.26 \pm 0.65) \times 10^{+0}$	$(3.98 \pm 0.28) \times 10^{+1}$
65.95 ± 0.30	$(1.11 \pm 0.08) \times 10^{+1}$	$(7.80 \pm 0.55) \times 10^{+1}$

4.4.11 The ^{159}Tb(p,X)^{151}Gd process

Only a few values could be measured above 50 MeV, dominated by the ^{159}Tb(p,α5n)^{151}Gd ($Q = -30.84$ MeV) reaction as the ^{159}Tb(p,2p7n)^{151}Gd ($Q = -59.89$ MeV) is not contributing significantly in this energy region. The results are shown in Fig. 4.8. The ALICE/ASH prediction is reasonable while the TENDL-2012 values are shifted towards lower energies.

4.4.12 The ^{159}Tb(p,X)^{153}Gd process

As shown in Fig. 4.8, the contributions of both the ^{159}Tb(p,α3n)^{153}Gd ($Q = -15.99$ MeV) and ^{159}Tb(p,2p5n)^{153}Gd ($Q = -44.30$ MeV) reactions are clearly visible. The sharp rise starting just below 60 MeV is from the latter reaction, which is not well described by the ALICE/ASH predictions, nor by TENDL-2012. This kind of behaviour in an excitation function is not unusual and has been described before, e.g. for the ^{68}Zn(p,X)^{64}Cu reaction, where the contributions from the ^{68}Zn(p,αn)^{64}Cu and the ^{68}Zn(2p,3n)^{64}Cu reactions show a similar trend [Sze2005].

4.4.13 Integral yield calculations

Thick-target yields (see Appendix D) for ^{149}Tb and ^{152}Tb, derived from the ^{152}Gd(p,4n)^{149}Tb and ^{155}Gd(p,4n)^{152}Tb excitation functions, respectively, are shown in Fig. 4.9. Note that these are *physical yields*. In the case of ^{149}Tb, the scaled ALICE/ASH prediction shown in Fig. 4.2 (solid green curve) was used for this purpose, while the eye-guide curve in Fig. 4.3 was used for ^{152}Tb. With an energy window of 66 MeV down to threshold (about 30 MeV), a physical yield of 2556 MBq/μAh (69.1 mCi/μAh) can be expected for ^{149}Tb and 1924 MBq/μAh (52.0 mCi/μAh)

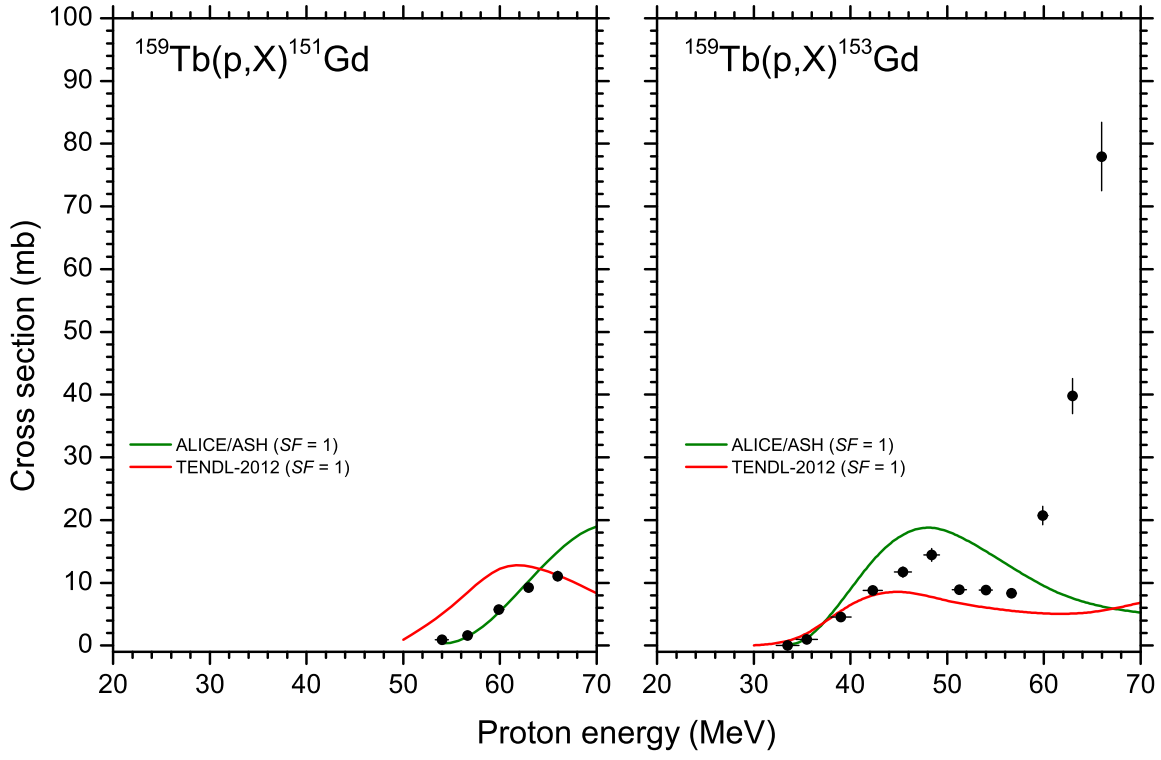

Figure 4.8: Excitation functions for the production of ^{151,153}Gd in the irradiation of ^{159}Tb with protons. Black circles: this work (Stack 3). See also caption to Fig. 4.2.

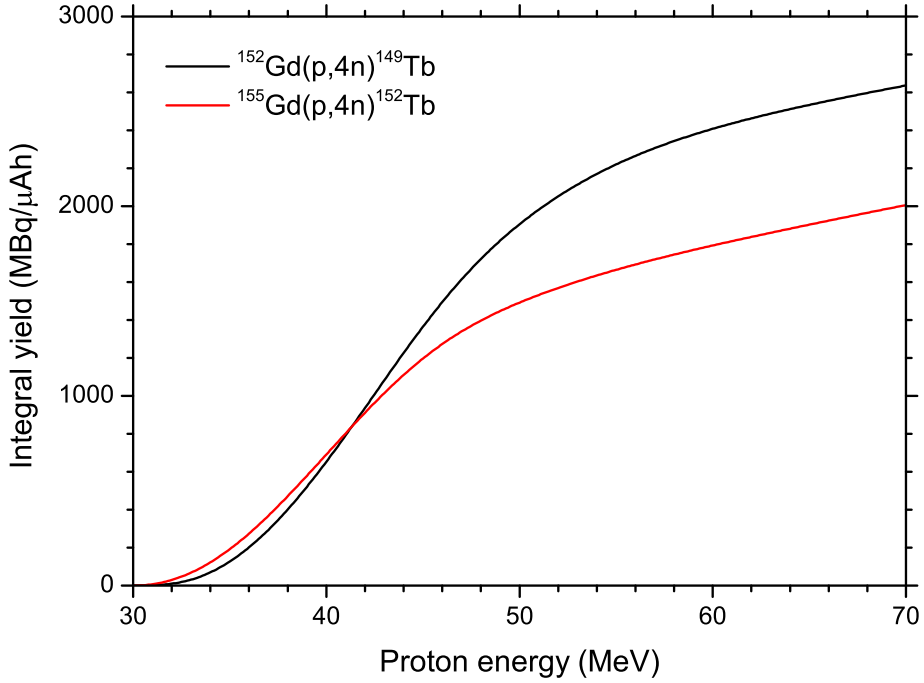

Figure 4.9: Integral physical yields for the production of ^{149}Tb and ^{152}Tb via (p,4n) reactions on targets of ^{152}Gd and ^{155}Gd, respectively. A 100% enrichment of the targets is assumed.

for ^{152}Tb from the above (p,4n) reactions, respectively. These are very high yields but, unfortunately, do not lead to radionuclidically pure products, as already mentioned. The value for ^{152}Tb is higher than the rather conservative estimate of 1200 MBq/μAh (32.4 mCi/μAh) from the ^{nat}Gd + p study (see Section 3.4.8).

Thick-target yields for ^{153,155,157,159}Dy in Tb +p, derived from spline fits through the measured excitation function data (the blue curves in Figs. 4.4 and 4.5) are shown in Fig. 4.10. It is evident that the ^{155}Tb produced via ^{155}Dy decay will contain the decay products of a considerable amount of ^{157}Dy as well, in any energy window. However, ^{157}Tb is long-lived with a half-life of 71 y [Fir2004], therefore only low levels of ^{157}Tb activity are to be expected in the final product. The yield of ^{159}Dy is quite low as it is also quite long-lived ($T_{1/2} = 144.4$ d) and furthermore it decays to stable ^{159}Tb, thus, it is no contributor to any radiocontaminant. Nevertheless, stable Tb will affect labelling efficiency, which should be taken into consideration. Lastly, ^{153}Dy will contribute ^{153}Tb as a radiocontaminant but only above 59 MeV.

To produce ^{155}Tb via ^{155}Dy decay would require two chemical separations. The Dy should be separated from the Tb target material as soon as possible after the end of bombardment (EOB). An optimum waiting time would then be required to allow for maximum growth of ^{155}Tb, followed by a second chemical separation to isolate the Tb from the remaining Dy. In order to evaluate this production route, one needs to investigate the growth and decay characteristics of all the relevant Dy radionuclides on a common time line. It is also necessary to make some assumptions on the duration of the chemical separations. Let $t = 0$ be the time when an isolated quantity of pure ^{155}Dy starts to decay. The growth and decay curve (see Appendix G for the relevant equations) of ^{155}Tb formed via the decay of the ^{155}Dy is shown in Fig. 4.11,

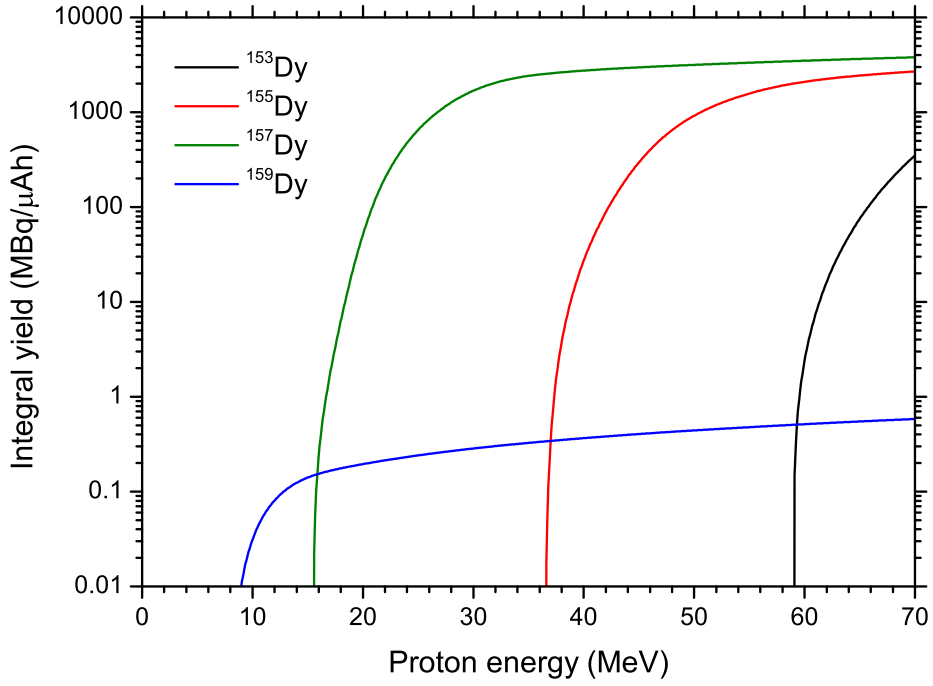

Figure 4.10: Integral physical yields for the production of ^{153,155,157,159}Dy in the proton bombardment of ^{159}Tb (natural Tb).

where $A_d(t)$ denotes the activity of the daughter at time t and $A_m(0)$ denotes the activity of the mother radionuclide at time $t = 0$. The curve reaches a maximum at $t = 39.6$ h, which should be close to the optimum waiting time after the first chemical separation before performing the second chemical separation, depending on the effective duration of the separation procedure. The dashed line in Fig. 4.11 shows the points in time where the ^{155}Tb activity reaches 90% of the maximum. These times are $t = 21.6$ h and $t = 72.5$ h during the periods of net growth and net decay, respectively. This is rather convenient, as it indicates that there is an interval of many hours during which the second chemical separation can be performed. A FORTRAN code developed previously [Ste2006] was adapted to follow the growth and decay of all the produced Dy radionuclides on a time line, taking the durations of chemical separations into account. In fact, the bombardment time, waiting times and processing times are all variables. Different production scenarios can therefore be investigated. The code calculates the yield and radionuclidic purity as well as the ^{155}Tb purity as a percentage of all Tb nuclei produced.

As an example of the kind of results one can obtain, the conditions of Table 4.7, which we consider to be realistic, will be used in the following calculations. A bombardment time of 10 h is just over one half-life of the mother radionuclide, ^{155}Dy. Waiting time 1 is the time interval between EOB and the start of the first chemical separation and includes tasks such as the removal of the target from the beamline, transport to a reception hot cell, decapsulation and transfer of the irradiated material to a processing hot cell. The actual ion-exchange procedure of the chemical separations is assumed to have a duration of 1 h each. Waiting time 2 is the period required for the accumulation of ^{155}Tb from ^{155}Dy decay and is taken as 39 h. Waiting time 3 is a short period between the end of the second chemical separation and the reference time, allowing for the removal of the product from the hot cell and performing a measurement

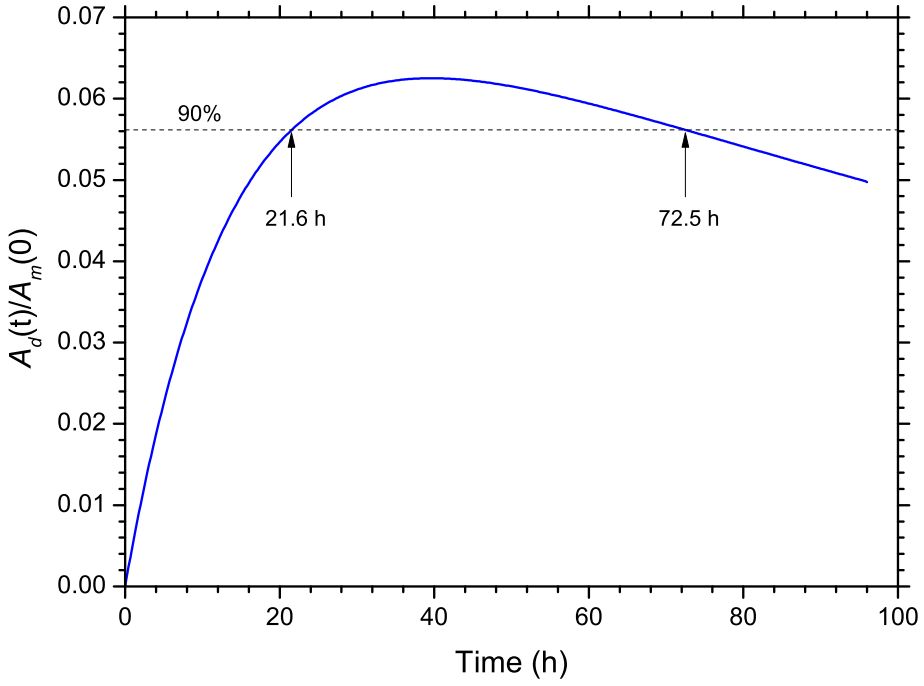

Figure 4.11: Growth and decay of ^{155}Tb formed in the decay of ^{155}Dy. A_d and A_m denote daughter and mother activities, respectively (see text).

of the activity. The exit energy of the energy window is taken as 35 MeV and the entrance energy is varied between 50 and 70 MeV. The results are shown in Fig. 4.12, plotted versus the entrance proton energy. The yield rises from 39.8 GBq (1074 mCi) at an incident energy of 50 MeV to 116.6 GBq (3151 mCi) at an incident energy of 70 MeV. It is evident that this production route is suitable for the production of Ci quantities of ^{155}Tb. The radionuclidic purity is better than 99.9% at all incident energies below 60 MeV but decreases monotonically above 60 MeV to a value of about 88% at 70 MeV. The number of ^{155}Tb nuclei, expressed as a percentage of all produced Tb nuclei, has a value of 57.5% at 40 MeV, increasing towards higher energies until reaching a maximum of 68.1% at 62 MeV, then decreases slightly to a value of 65.4% at 70 MeV. The relevant equations to calculate yields from precursor decay are presented in Appendix H.

It is evident that this indirect production route can provide high yields of ^{155}Tb with excellent radionuclidic purity, however, nuclei of other stable and long-lived Tb species are also produced. This reduces the purity in terms of the fraction of all Tb nuclei produced, which may affect the labelling efficiency.

4.5 Electromagnetic isotope separation

Electromagnetic (EM) isotope separation (also called EM mass separation) may be the only method to obtain highly radionuclidically pure ^{149}Tb. The same applies to ^{152}Tb if the high-yield (p,4n) reaction is utilized. It is, therefore, interesting to contemplate the possibility of using EM isotope separation as the technology of choice to remove isotopic impurities. Recently, Lapi *et al.* [Lap2010] and D'Auria *et al.* [DAu2013] demonstrated efficient EM isotope separation

Table 4.7: Production conditions used for calculating the ^{155}Tb yield via ^{155}Dy decay in the proton bombardment of a thick ^{159}Tb target.

Production step	Duration (h)
Bombardment time	10.0
Waiting time 1	0.5
Chemical separation 1[a]	1.0
Waiting time 2	39.0
Chemical separation 2[b]	1.0
Waiting time 3	0.5
Exit proton energy: 35 MeV	
Incident proton energy: Variable in range 50 - 70 MeV	

[a] ^{155}Dy from ^{159}Tb target matrix
[b] ^{155}Tb from recovered ^{155}Dy

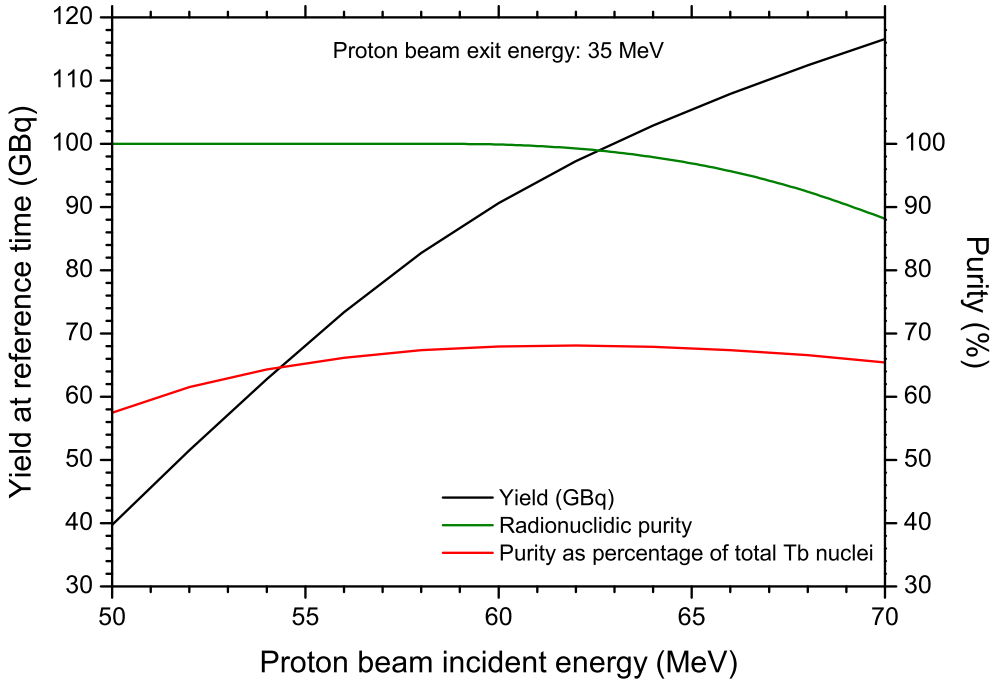

Figure 4.12: Production yield, radionuclidic purity, and purity as a percentage of total Tb nuclei produced of ^{155}Tb via ^{155}Dy decay in the proton bombardment of a thick Tb target, plotted as a function of incident beam energy. The exit proton energy is 35 MeV. The production conditions are those of Table 4.7.

for ^{99}Mo. These authors also speculate about using EM isotope separation for many other medically important radionuclides, some of which can be produced in sufficient quantities via reactions such (n,γ) and (γ,n) but which result in products with a low specific activity. While the principles of EM isotope separation are well known for many decades, practical issues remain, e.g. ion source reliability and efficiency as well as the challenges associated with handling high levels of radioactivity after extensive operation at high beam intensities.

It is not far-fetched to believe that should ^{149}Tb prove to be important enough to nuclear medicine at some time in the future, the present engineering problems, which preclude large-

scale productions with good radionuclidic purity, will be solved. This happened before, e.g. in the case of ^{18}F. Furthermore, future dedicated facilities may be small and compact, in stark contrast to the large spallation + ISOL facilities such as ISOLDE at CERN. A possible scenario may include a commercial 70 MeV cyclotron, such as the IBA Cyclone 70 XP, Best BSCI 70p or CIAE CYCCIAE70 [Sch2011] in conjunction with a compact EM isotope separator, such as that of the Ion Source Test Facility (ISTF) at TRIUMF [DAu2013]. This last-mentioned facility is a fantastic step in the right direction and may be ideally suited for proof-of-principle studies. In fact, prior chemical processing of batch targets may provide feedstock of already relatively high specific activity for the EM separator system, which will then provide the final purifying step. Sufficient quantities of pure ^{152}Tb and ^{155}Tb would also be collected, probably simultaneously with the ^{149}Tb, depending on the chosen target material.

4.6 Conclusion

Measured cross sections for the ^{152}Gd(p,4n)^{149}Tb, ^{155}Gd(p,4n)^{152}Tb, ^{159}Tb(p,xn)^{153,155,157,159}Dy, ^{159}Tb(p,X)^{153,154m2,155,156}Tb and ^{159}Tb(p,X)^{151,153}Gd reactions have been presented. In the case of ^{159}Tb + p, cross sections for various Tb and Gd radionuclides have also been extracted, some directly produced and others cumulatively. Integral yields for ^{149}Tb and ^{152}Tb in the proton bombardment of enriched Gd targets have been calculated, as well as the yield and purity to be expected from the indirect production route ^{159}Tb(p,5n)^{155}Dy$\rightarrow$^{155}Tb. It is shown that excellent yields can readily be obtained with a commercial 70 MeV cyclotron, however, EM isotope separation may be the only way to achieve ^{149,152,155}Tb products with a high level of radionuclidic purity and the desired specific activity. Furthermore, it is speculated that dedicated, compact facilities for their production may be feasible. However, this would require a great deal of further experimental investigation and development work. A facility such as the ISTF at TRIUMF may be ideally suited to pursue such studies.

Concerning nuclear data needs, a consistent experimental investigation of the ^{152}Gd(p,n)^{152}Tb and ^{155}Gd(p,n)^{155}Tb reactions is still lacking. This will require ^{152}Gd + p and ^{155}Gd + p stacked-foil experiments in the energy region from the respective (p,n) reaction thresholds up to about 30 MeV. At the time of writing, we initiated a discussion with staff of the Forschungszentrum Jülich about the possibility to measure these cross sections using their new 30 MeV IBA cyclotron. That laboratory is also the experts in making targets using the sedimentation technique. The idea was well received but no commitments have yet been made.

Chapter 5

Radionuclides of Zr and Nb in Proton-Induced Reactions on ^{89}Y, ^{93}Nb and ^{nat}Zr

5.1 Introduction

The radionuclide ^{90}Y ($T_{1/2} = 64$ h, $\beta^- = 100\%$, $E_{\beta^-} = 2.3$ MeV) has become increasingly important over the last two decades for targeted radiotherapy through the use of ^{90}Y-labelled antibodies or by being incorporated into microspheres. Verel *et al.* [Ver2003], for example, reported that ^{90}Y has attractive β^- emissions for therapy but lacks associated photon emissions for imaging of *in-vivo* bio-distributions. The broad bremsstrahlung spectrum also makes it difficult to accurately quantify the delivered dose using SPECT, which is required for determining the therapeutic efficacy of ^{90}Y. While ^{111}In and ^{99m}Tc are routinely used as SPECT imaging surrogates for ^{90}Y dosimetry, PET imaging is superior in terms of sensitivity, spatial resolution and accuracy of quantification. PET is therefore ideal to perform *in-vivo* dosimetry in targeted radiotherapy. Several studies have shown that ^{89}Zr ($T_{1/2} = 78.41$ h) is one of the most attractive PET imaging surrogates for ^{90}Y, e.g. Avlia-Rodriguez *et al.* [Avi2006]. Furthermore, quantitative ^{89}Zr immuno-PET is used as a scouting procedure prior to radio-immunotherapy with ^{90}Y-labelled antibodies, while ^{88}Y finds application as a substitute for ^{90}Y in the development of labelled compounds. This is facilitated by the availability of ^{88}Y in carrier-free form via the ^{88}Zr/^{88}Y generator system reported by Taylor *et al.* [Tay1991] and Faßbender *et al.* [Faß2004].

On the diagnostic side, ^{89}Zr has shown great promise as a PET probe for imaging the ^{89}Zr-labelled anti-CD147 monoclonal antibody expression in pancreatic cancer and has the potential to select appropriate patients with CD147-expressing tumours who could gain benefit from anti-CD147 therapy [Sug2013]. Also, cardiovascular molecular imaging can be used for the detection of rupture-prone intra-vascular plaques. Specifically, heterogeneous ^{89}Zr-radiolabelled Bevacizumab, a monoclonal anti-vascular endothelial growth factor (VEGF)-A, can depict VEGF levels corresponding to the angiogenic status in tumours. This suggested its potential use in carotid endarterectomy (CEA) specimens. Golestani *et al.* [Gol2013], for example, reported that uptake within plaques was first observed *ex-vivo* in these specimens and the results suggest that noninvasive imaging of VEGF, using ^{89}Zr-Bevacizumab, could provide clinicians with a new and perhaps better diagnostic tool in the determination of individuals with a higher risk for cardiovascular events.

It is also prudent to look at possible industrial applications of the radioniobiums. To this end, an interesting industrial application of radionuclides is the thin layer activation (TLA) method. This method is a versatile tool for studying the wear and corrosion of moving components in mechanical systems. Thin surface layers (in the micrometer to millimeter range) of mainly parts made of metals and alloys are activated by direct irradiation with appropriate charged particle beams. A powerful aspect of the method is that the process propagation times associated with wear and corrosion can be quantified without having to disassemble the machine being assayed or, in most cases, not even having to stop it [Dit2006]. As Nb is a ubiquitous additive in a large number of high-strength and high temperature steels as well as an important component in many nickel-based super-alloys, it follows that some isotopes of Nb could be suitable for direct activation TLA probing of wear and corrosion on these materials.

For an isotope to be useful for TLA it has to fulfil a number of requirements, depending on the application. First, it should have a half-life that is long enough to allow it to be followed for a period ranging from days to months in the case of wear measurements, and up to a number of months or years in the case corrosion measurements. Second, it should have γ-ray emissions of sufficiently high energy to allow *in situ* measurement of the activated components, having to pass through other structures in the machine being studied. Finally, it should have high enough production cross sections to allow fast activation of the component without longer-lived radionuclides being formed excessively as a result of a longer bombardment time. Two radioniobiums, ^{91m}Nb ($T_{1/2} = 60.86$ d) and ^{92m}Nb ($T_{1/2} = 10.25$ d), fulfil the requirements for wear measurements and have been evaluated for application in thin-layer activation (TLA) studies of machine components made of alloys containing niobium [Dit2008].

With proton beams in the region up to 70 MeV, various radio-zirconiums can be successfully produced using ^{89}Y and/or ^{93}Nb as target materials and ^{88}Zr can also be produced from the bombardment of ^{nat}Zr itself. Since ^{88}Zr serves as the mother isotope of the ^{88}Zr/^{88}Y generator, the carrier Zr from the target does not create a purity problem. At Los Alamos National Laboratory in the USA, for example, ^{88}Zr was recovered for several years as a byproduct from proton activated Nb target capsules irradiated at iThemba LABS [Faß2004]. An aim of the present work was to better quantify yields in this process as Nb has increasingly become the encapsulation material of choice in high-intensity targetry for many other radionuclides. While tantalum has a higher corrosion resistance, niobium is much easier to work, i.e. weld, machine and form. Nowadays, people look seriously at the recovery of useful radionuclides from target capsules, beam dumps and shielding materials. In some cases, such “byproduct” radionuclides have proved to be a valuable resource and a means to recover some production costs. This also serves to streamline the handling of the nuclear waste associated with these materials as well as to reduce the cost of disposal of said waste.

Prior to 2008, the available excitation function data for ^{89}Y + p and ^{93}Nb + p were very limited and fragmented, with large discrepancies between the various sets of measurements in some cases. In recent times, more or less concurrently, various groups measured new data sets for these reactions, expanding the available database significantly and resolving many of the discrepancies. The work by Ditroi *et al.* [Dit2008, Dit2009] on ^{93}Nb + p and Khandaker *et*

al. [Kha2012] on ^{89}Y + p, in the energy region relevant to the present study, deserves a special mention in this regard. In this work, we present new excitation function data for the energy region 30–66 MeV. It was planned to also measure new data below 30 MeV at iThemba LABS but because of the new results published by other authors, which covered the lower-energy region satisfactorily, it was decided to discontinue that part of the investigation. We compare our results with selected data sets only, mainly concentrating on the newer studies as the above authors did comparisons with the older work. Comparisons are also made with ALICE/ASH predictions and the relevant data from the TENDL-2012 library.

One objective of this study was to investigate the feasibility of using tandem niobium/yttrium targetry to optimize ^{88}Zr and ^{89}Zr yields. Another objective was to compare the different production routes suitable for ^{88}Zr/^{88}Y generators.

The relevant part of the Karlsruhe Chart of the Nuclides is shown in Fig. 5.1 and the possible proton-induced reactions leading to the formation of the measured Nb and Zr isotopes, as well as their Q-values, are listed in Table 5.1.

5.2 Experimental method

5.2.1 Irradiations and radionuclide assays

Three foil stacks were irradiated at iThemba LABS for this set of experiments. As before, most of the detail of Section 3.2 and Appendix A also applies to this section, therefore only salient aspects are presented here. The activities induced in the foils were repeatedly measured using conventional off-line γ-ray spectroscopy, using two calibrated HPGe detector systems simultaneously. Only the strongest γ-lines available were used for quantifying the activities of individual radionuclides, as summarized in Table 5.2.

The first stack was employed to measure the excitation functions of radionuclides produced in ^{93}Nb + p and ^{89}Y + p between 30 and 66 MeV. It consisted of foils of Nb and Y (nominally

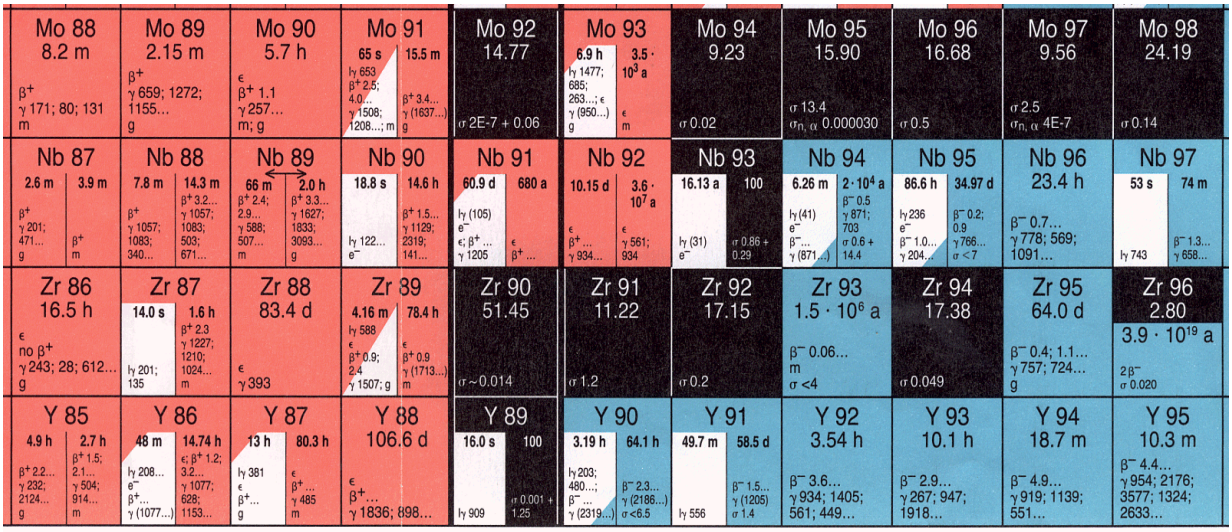

Figure 5.1: Relevant part of the Karlsruhe Chart of the Nuclides, showing the target materials Nb, Zr and Y as well as the radionuclides relevant to this study. With permission © Nucleonica GmbH 2012.

Table 5.1: Relevant proton-induced reactions for direct formation of the observed Zr and Nb radionuclides.

Reaction	Q value (MeV)	Reaction	Q value (MeV)
^{89}Y(p,4n)^{86}Zr	-34.74 MeV	^{93}Nb(p,αn)^{89}Zr	-5.545 MeV
^{89}Y(p,3n)^{87}Zr	-25.29 MeV	^{93}Nb(p,dt)^{89}Zr	-23.13 MeV
^{89}Y(p,2n)^{88}Zr	-12.93 MeV	^{93}Nb(p,ptn)^{89}Zr	-25.36 MeV
^{89}Y(p,n)^{89}Zr	-3.615 MeV	^{93}Nb(p,^{3}He2n)^{89}Zr	-26.12 MeV
		^{93}Nb(p,2dn)^{89}Zr	-29.39 MeV
^{93}Nb(p,α4n)^{86}Zr	-36.67 MeV	^{93}Nb(p,pd2n)^{89}Zr	-31.62 MeV
^{93}Nb(p,2t2n)^{86}Zr	-48.00 MeV	^{93}Nb(p,2p3n)^{89}Zr	-33.84 MeV
^{93}Nb(p,dt3n)^{86}Zr	-54.25 MeV		
^{93}Nb(p,pt4n)^{86}Zr	-56.48 MeV		
^{93}Nb(p,^{3}He5n)^{86}Zr	-57.24 MeV		
^{93}Nb(p,2d2n)^{86}Zr	-60.51 MeV		
		^{93}Nb(p,nt)^{90}Nb	-20.28 MeV
^{93}Nb(p,α3n)^{87}Zr	-27.22 MeV	^{93}Nb(p,d2n)^{90}Nb	-26.54 MeV
^{93}Nb(p,2tn)^{87}Zr	-38.55 MeV	^{93}Nb(p,p3n)^{90}Nb	-28.76 MeV
^{93}Nb(p,dt2n)^{87}Zr	-44.81 MeV		
^{93}Nb(p,pt3n)^{87}Zr	-47.03 MeV		
^{93}Nb(p,^{3}He4n)^{87}Zr	-47.79 MeV		
^{93}Nb(p,2d3n)^{87}Zr	-51.06 MeV		
^{93}Nb(p,pd4n)^{87}Zr	-53.29 MeV	^{93}Nb(p,t)^{91}Nb	-8.235 MeV
		^{93}Nb(p,dn)^{91}Nb	-14.49 MeV
^{93}Nb(p,α2n)^{88}Zr	-14.86 MeV	^{93}Nb(p,p2n)^{91}Nb	-16.72 MeV
^{93}Nb(p,2t)^{88}Zr	-26.20 MeV		
^{93}Nb(p,dtn)^{88}Zr	-32.45 MeV		
^{93}Nb(p,pt2n)^{88}Zr	-34.68 MeV		
^{93}Nb(p,^{3}He3n)^{88}Zr	-35.44 MeV		
^{93}Nb(p,2d2n)^{88}Zr	-38.71 MeV	^{93}Nb(p,d)^{92}Nb	-6.606 MeV
^{93}Nb(p,pd3n)^{88}Zr	-40.93 MeV	^{93}Nb(p,pn)^{92}Nb	-8.831 MeV
^{93}Nb(p,2p4n)^{88}Zr	-43.16 MeV		

25 μm thick, $>$99.9% purity, supplied by Goodfellow, UK). The Nb and Y were interspersed with Cu and Al degraders as well as Cu and Ti monitor foils. The bombardment lasted 2 hours at a nominal beam current of 50 nA.

The second stack contained thick Nb discs (0.41 g/cm^2, $>$99.9% purity, supplied by Goodfellow, UK). A single 50 μm thick Cu monitor foil preceded the Nb discs and the beam was stopped in the last Nb disc. This stack served to directly measure the thick-target yield curves for ^{93}Nb + p reaction products completely. After bombardment, these thicker discs were assayed in the same way as the foils. Attenuation losses of the γ-rays, however, are not negligible for such thick targets (i.e. as compared to the case of thin foils). Attenuation losses were taken into account by computing detector efficiency corrections using the Monte Carlo radiation transport code MCNPX [Pel2011a] and an exact simulation of the target (as a source) and the detector system.

A third stack contained Zr foils to investigate the ^{nat}Zr + p processes with the production of ^{88}Zr being the focus of this work. It consisted of Zr foils (0.01795g/cm^2, >99.9% purity, supplied by Goodfellow, UK) interspersed with Cu and Al degraders as well as Cu and Ti monitor foils, similar to the first stack.

One thick target, consisting of an Y_2O_3 disc encapsulated in Al, was also bombarded with a 66 MeV proton beam. The Y_2O_3 (>99.99%, Alfa Aesar, UK) compressed well in a hydraulic press, which is not always the case for oxides. The target thickness was 1.91 g/cm^2, covering the energy window from 65.0 MeV down to 50.7 MeV. It served as an integral test of the integral yield curves derived for the ^{89}Y(p,2n)^{88}Zr and ^{89}Y(p,n)^{89}Zr reactions, in addition to investigating the target making using this particular compound.

Table 5.2: Investigated Zr and Nb radionuclides and their decay properties used for experimental cross-section determinations[a].

Nuclide	Half-life	γ-rays (keV)	Decay mode	Intensity (%)
^{86}Zr	16.5 h	242.80	$\epsilon + \beta^+$: 100%	95.84%
^{87}Zr	1.68 h	1226.94	$\epsilon + \beta^+$: 100%	2.80%
^{88}Zr	83.4 d	392.87	ϵ: 100%	97.3%
^{89}Zr	3.27 d	908.96	$\epsilon + \beta^+$: 100%	100%
^{90}Nb	14.6 h	1129.22	$\epsilon + \beta^+$: 100%	92.70%
^{91m}Nb	60.86 d	1204.77	IT : 93% $\epsilon + \beta^+$: 7%	2.9%
^{92m}Nb	10.15 d	934.46	$\epsilon + \beta^+$: 100%	99.0%

[a]Taken from Firestone & Ekström [Fir2004].

The uncertainties in counting statistics were mostly well below 1%, thus insignificant in comparison with other experimental uncertainties, except near reaction thresholds and in the case of the relatively short-lived ^{87}Zr ($T_{1/2}$ = 1.68 h) where long counting times could not be afforded. Systematic uncertainties were similar to that of Section 3.2.4, with a total of about 7%. The uncertainty in the proton energy value of each data point was calculated taking into account the uncertainty in the incident beam energy, foil thickness and straggling, as discussed in Appendix C. These values ranged from ± 0.3 to 1.1 MeV.

The results for the ^{nat}Cu(p,X)^{62}Zn monitor reaction are shown in Fig. 5.2 for the first and third stacks, as well as the standard excitation function recommended by the IAEA [Gul2001]. For the experimental cross sections of this study, the logged beam currents from the electronic current integrator were used. The measured cross sections reproduce the recommended curve satisfactorily, therefore, there was no need to make any corrections from the accumulated charge values extracted from the monitor reaction measurements. A similar quality of agreement was found for the ^{nat}Ti(p,X)^{48}V monitor reaction as shown in Fig. 5.2.

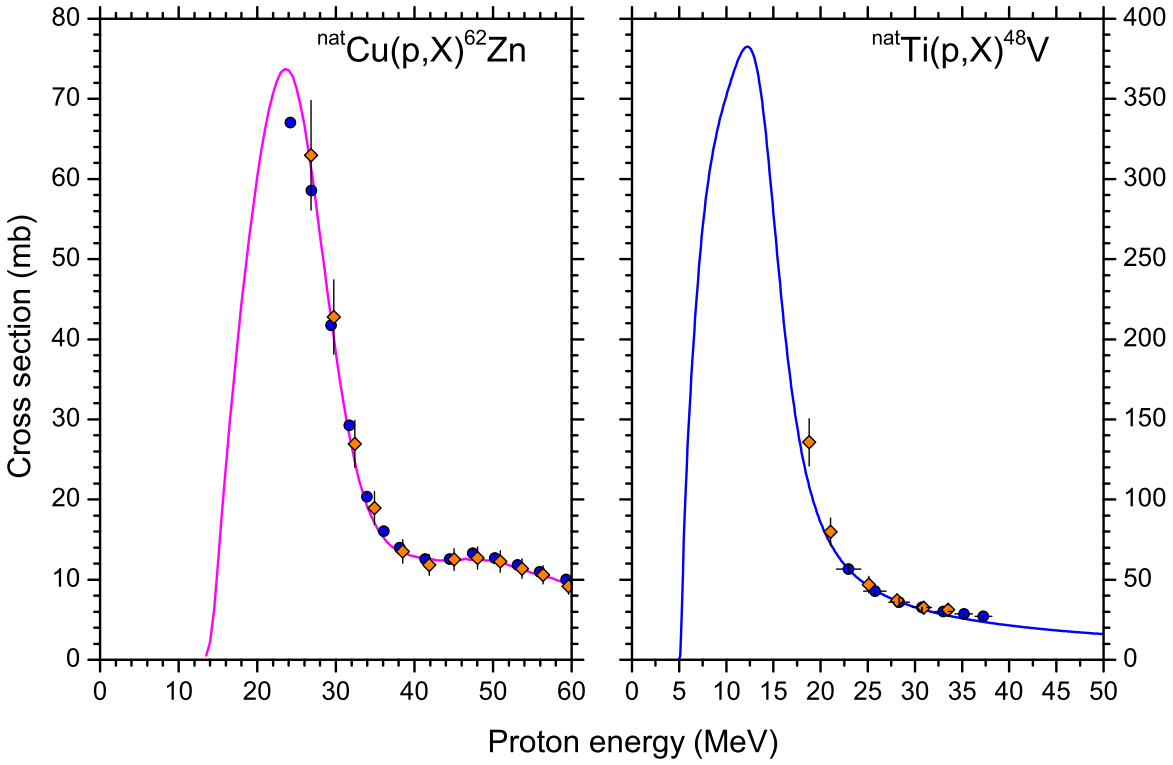

Figure 5.2: Excitation functions of the ^{nat}Cu(p,X)^{62}Zn and ^{nat}Ti(p,X)^{48}V monitor reactions. Blue circles are for the first stack. Orange diamonds are for the third stack. Curves: IAEA recommended data.

5.3 Results and discussion

5.3.1 The ^{89}Y(p,4n)^{86}Zr reaction

In Fig. 5.3, our measured data shows excellent agreement with both Uddin *et al.* [Udd2005] and Michel *et al.* [Mic1997] as well as the couple of points from Khandaker *et al.* [Kha2012]. Both the ALICE/ASH and TENDL 2012 curves had to be scaled up ($SF = 2.4$ and 1.55, respectively) but the overall agreement in shape is very good. The TENDL data, however, is shifted towards lower energies. This shift is seen seen in almost all our comparisons.

5.3.2 The ^{93}Nb(p,X)^{86}Zr process

The excitation function of ^{86}Zr ($T_{1/2} = 16.5$ h) contains contributions from the following channels: ^{93}Nb(p,α4n)^{86}Zr, $Q = -36.67$ MeV; ^{93}Nb(p,2n2t)^{86}Zr, $Q = -48.00$ MeV; ^{93}Nb(p,dt3n)^{86}Zr, $Q = -54.25$ MeV; ^{93}Nb(p,pt4n)^{86}Zr, $Q = -56.48$ MeV; ^{93}Nb(p,^{3}He5n)^{86}Zr, $Q = -57.24$ MeV and ^{93}Nb(p,2d2n)^{86}Zr, $Q = -60.51$ MeV. Very little data exists in the energy region of our measurements. Michel *et al.* [Mic1997] has the most complete data set and our data correspond well with these measurements. Only two other corresponding points were found from Ditrói *et al.* [Dit2008] and one from Titarenko *et al.* [Tit2011]. The ALICE/ASH curve, when scaled up twofold, fits the data very well in shape. The TENDL-2012 curve seems to have the right shape but shifted in energy. The data are presented in Fig. 5.3.

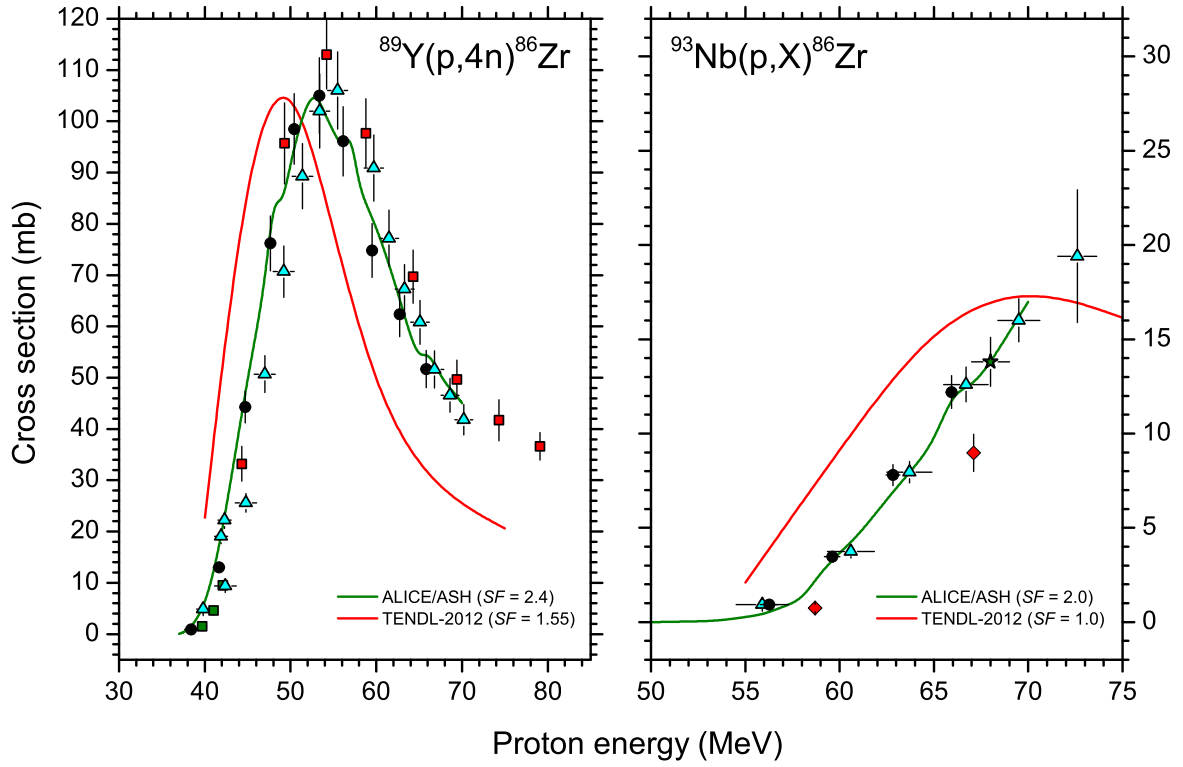

Figure 5.3: Excitation functions for the production of ^{86}Zr in the bombardment of ^{89}Y and ^{93}Nb with protons, respectively. Black circles: this work. Red squares: Uddin *et al.* [Udd2005]. Red diamonds: Ditrói *et al.* [Dit2008]. Green squares: Khandaker *et al.* [Kha2012]. Cyan triangles: Michel *et al.* [Mic1997]. Green stars: Titarenko *et al.* [Tit2011].

5.3.3 The ^{89}Y(p,3n)^{87}Zr reaction

Only three sets of data are available in the literature for the ^{89}Y(p,3n)^{87}Zr reaction. West *et al.* [Wes1993] and Saha *et al.* [Sah1966] reported good data sets and even the couple of points from Levkovskij [Lev1991] agrees very well with our data. The ALICE/ASH and TENDL-2012 curves were scaled up slightly but show good agreement with all the measured data sets.

5.3.4 The ^{93}Nb(p,X)^{87}Zr process

The reaction channels open for ^{93}Nb(p,X)^{87}Zr are as follows: ^{93}Nb(p,α3n)^{87}Zr, $Q = -27.22$ MeV; ^{93}Nb(p,2tn)^{87}Zr, $Q = -38.55$ MeV; ^{93}Nb(p,dt2n)^{87}Zr, $Q = -44.81$ MeV; ^{93}Nb(p,pt3n)^{87}Zr, $Q = -47.03$ MeV; ^{93}Nb(p,^{3}He4n)^{87}Zr, $Q = -47.79$ MeV; ^{93}Nb(p,2d3n)^{87}Zr, $Q = -51.06$ MeV; ^{93}Nb(p,pd4n)^{87}Zr, $Q = -53.29$ MeV. Only the two data points of Titarenko *et al.* [Tit2011] were found for this process. The measured points are shown in Fig. 5.4 and shows good agreement with Titarenko. The TENDL-2012 data had to be scaled by a factor $SF = 2.8$ to overlap with the measured data but the shape seems to be satisfactory, albeit shifted towards lower energies by about 3 MeV. Better overall agreement is found in the case of the ALICE/ASH prediction but with a scale factor of $SF = 1.5$.

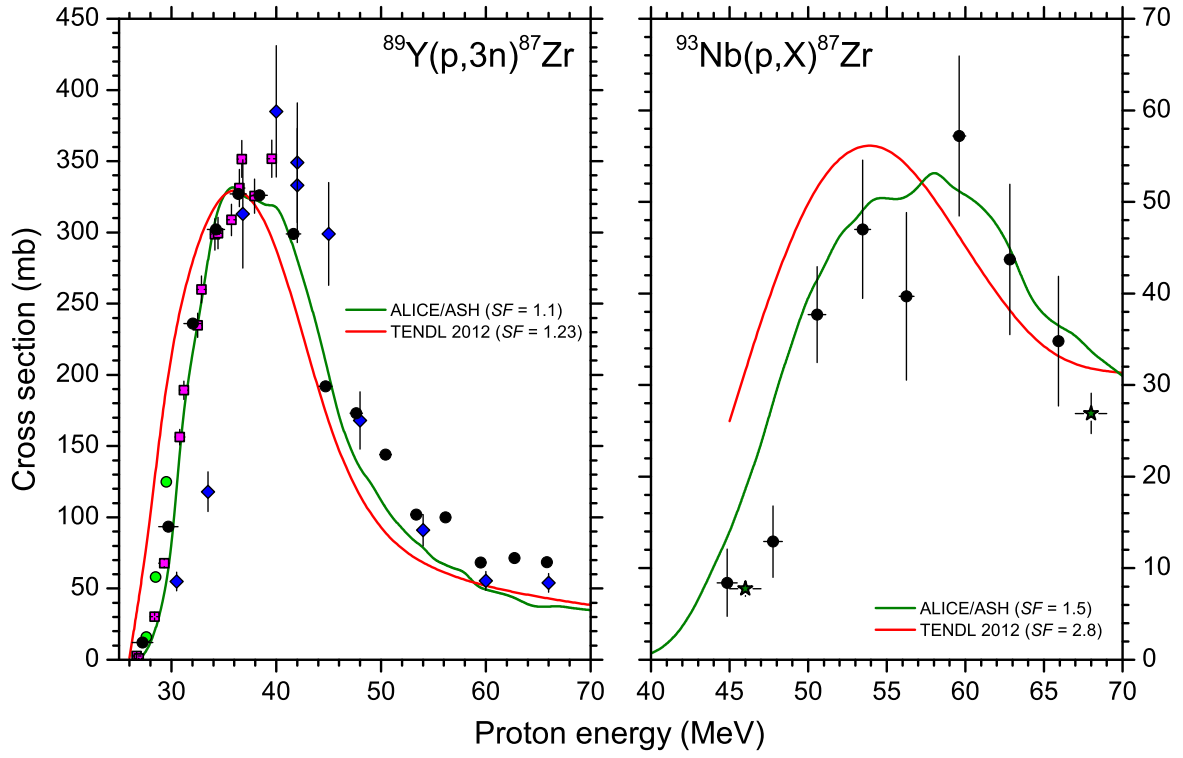

Figure 5.4: Excitation functions for the production of ^{87}Zr in the bombardment of ^{89}Y and ^{93}Nb with protons, respectively. Black circles: this work. Green stars: Titarenko *et al.* [Tit2011]. Magenta squares: West *et al.* [Wes1993]. Blue diamonds: Saha *et al.* [Sah1966]. Green circles: Levkovskij [Lev1991].

5.3.5 The ^{89}Y(p,2n)^{88}Zr reaction

Excellent agreement was found between our data and the latest, well measured data sets available in the literature for the ^{89}Y(p,2n)^{88}Zr reaction [Udd2005, Oma2009, Tar2005, Mus1998, Mic1997, Kha2012], as shown in Fig. 5.5. The ALICE/ASH and TENDL-2012 curves reproduce the data quite well, although both seem to peak slightly lower. A polynomial was fitted to the data to serve as an eye guide, which was also employed to calculate the integral yield curve.

5.3.6 The ^{93}Nb(p,X)^{88}Zr process

Many reaction channels are open for the ^{93}Nb(p,X)^{88}Zr process: ^{93}Nb(p,α2n)^{88}Zr, $Q = -14.86$ MeV; ^{93}Nb(p,2t)^{88}Zr, $Q = -26.20$ MeV; ^{93}Nb(p,dtn)^{88}Zr, $Q = -32.45$ MeV; ^{93}Nb(p,pt2n)^{88}Zr, $Q = -34.68$ MeV; ^{93}Nb(p,^{3}He3n)^{88}Zr, $Q = -35.44$ MeV; ^{93}Nb(p,2d2n)^{88}Zr, $Q = -38.71$ MeV; ^{93}Nb(p,pd3n)^{88}Zr, $Q = -40.93$ MeV; ^{93}Nb(p,2p4n)^{88}Zr, $Q = -43.16$ MeV. The excitation function is shown in Fig. 5.5. Our data peaks slightly lower than most other authors and the agreement with Michel *et al.* [Mic1997] is perhaps slightly better. The eye guide curve, which was chosen to more closely follow the present data, was used in calculating the integral yield curve. The ALICE/ASH prediction shows good agreement with the measured data but TENDL-2012 underpredicts the lower energy side and overpredicts the higher energy side.

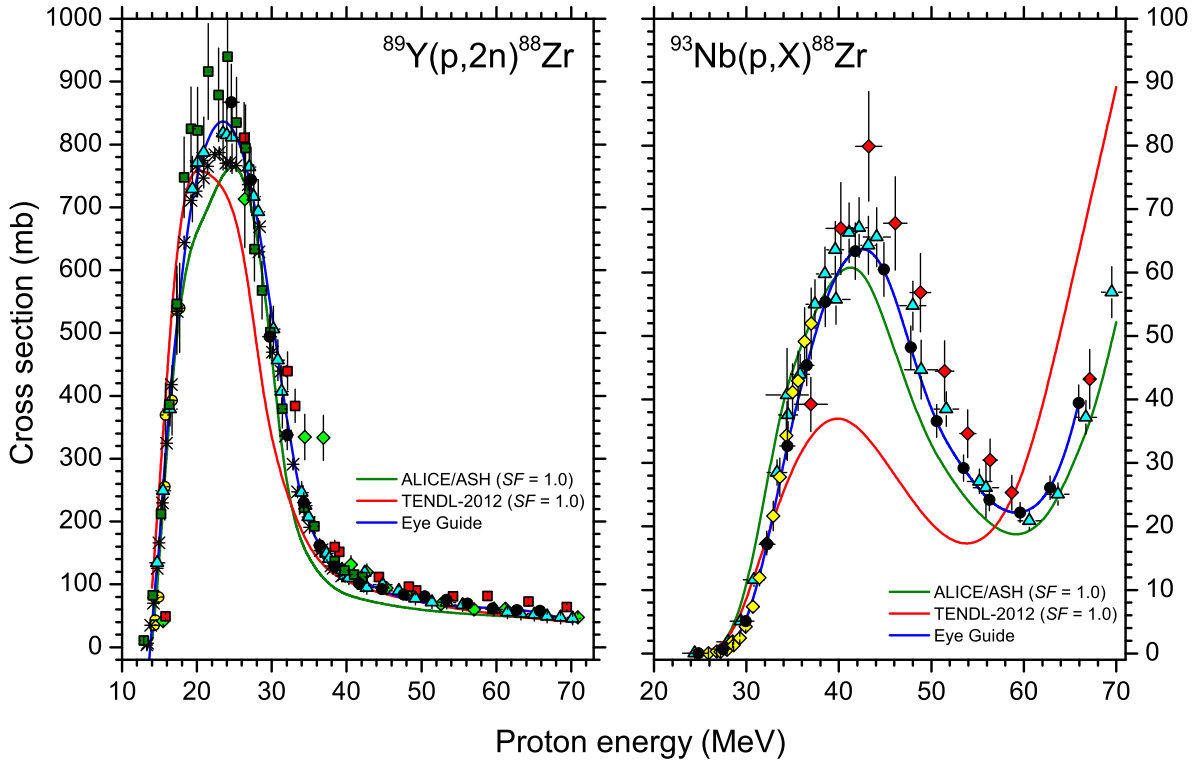

Figure 5.5: Excitation functions for the production of ^{88}Zr in the bombardment of ^{89}Y and ^{93}Nb with protons, respectively. Black circles: this work. Red squares: Uddin *et al.* [Udd2005]. Yellow circles: Omara *et al.* [Oma2009]. Green diamonds: Tárkányi *et al.* [Tar2005]. Asterisks: Mustafa *et al.* [Mus1998]. Red diamonds: Ditrói *et al.* [Dit2008]. Yellow diamonds: Ditrói *et al.* [Dit2009]. Cyan triangles: Michel *et al.* [Mic1997]. Green squares: Khandaker *et al.* [Kha2012].

5.3.7 The ^{nat}Zr(p,X)^{88}Zr process

In the case of the ^{nat}Zr(p,X)^{88}Zr process, our measurements agree very well with the experimental data of Michel *et al.* [Mic1997] as well as with slightly scaled up ALICE/ASH and TENDL-2012 curves ($SF = 1.1$, see Fig. 5.6). The data of both Uddin *et al.* [Udd2008] and Khandaker *et al.* [Kha2009] seem to be significantly lower. The quite large disagreement between the measurements of Michel and the other two authors was part of the motivation for the present measurements. It was felt that, in order to make a sensible comparison of the various production routes for ^{88}Zr, it was necessary to get clarity on this particular excitation function. It is indeed strange that the available data seem to coalesce into two groups. Perhaps it is significant that the Khandaker data of 2009 were measured at the same facility where the Uddin data of 2008 originated from. Admittedly, this is not an explanation for their excellent agreement while differing significantly with the other data sets.

Note that a large body of excitation functions were extracted from the γ-ray spectra collected for ^{nat}Zr + p, however, only the results for ^{88}Zr production are considered to be relevant here. The main focus of this chapter is the production of selected radionuclides of Zr, which cannot be produced in a carrier-free form from Zr targets. Since ^{88}Zr is used in a generator system for the supply of ^{88}Y in a carrier-free form, the ^{nat}Zr(p,X)^{88}Zr process is relevant to the present discussion. A manuscript on the full data set is in an advanced stage of preparation (at the

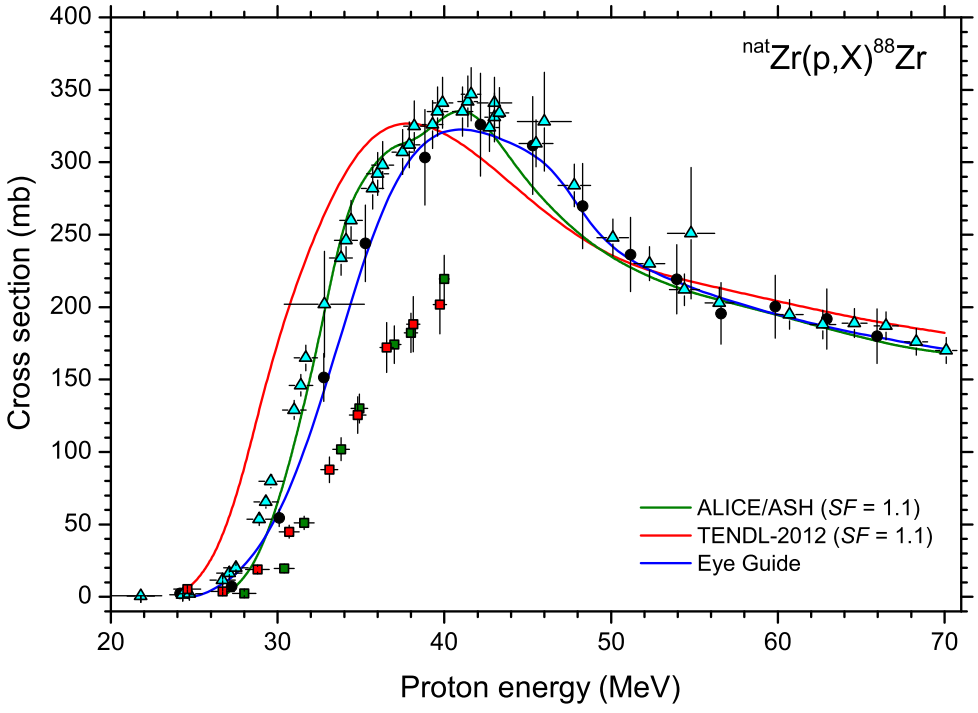

Figure 5.6: Excitation function for the production of ^{88}Zr in the bombardment of ^{nat}Zr with protons. Black circles: this work. Red squares: Uddin *et al.* [Udd2008]. Cyan triangles: Michel *et al.* [Mic1997]. Green squares: Khandaker *et al.* [Kha2009].

time of writing) but most of that work is considered to fall outside the scope of this thesis. By and large, the ^{nat}Zr + p work addressed another issue, related to the TLA method. As Zr is an important element in many alloys, it was necessary to resolve some serious discrepancies in the database for ^{nat}Zr + p.

5.3.8 The ^{89}Y(p,n)^{89}Zr reaction

In the case of the ^{89}Y(p,n)^{89}Zr reaction, the ALICE/ASH prediction as well as the TENDL-2012 curve agrees very well with our data. The agreement with the measurements of other authors is generally good, as shown in Fig. 5.7.

5.3.9 The ^{93}Nb(p,X)^{89}Zr process

For the ^{93}Nb(p,X)^{89}Zr process, similar to ^{93}Nb(p,X)^{88}Zr, a large number of reaction channels are open in the investigated energy region: ^{93}Nb(p,αn)^{89}Zr, $Q = -5.545$ MeV; ^{93}Nb(p,dt)^{89}Zr, $Q = -23.13$ MeV; ^{93}Nb(p,ptn)^{89}Zr, $Q = -25.36$ MeV; ^{93}Nb(p,^{3}He2n)^{89}Zr, $Q = -26.12$ MeV; ^{93}Nb(p,2dn)^{89}Zr, $Q = -29.39$ MeV; ^{93}Nb(p,pd2n)^{89}Zr, $Q = -31.62$ MeV; ^{93}Nb(p,2p3n)^{89}Zr, $Q = -33.84$ MeV. The measured excitation function as well as literature data are shown in Fig. 5.7. Our data joins smoothly with the lower energy data set of Ditrói *et al.* [Dit2009]. Both the ALICE/ASH code and TENDL-2012 values underpredict the higher energy side of the excitation function but show excellent agreement from about 40 MeV down to threshold.

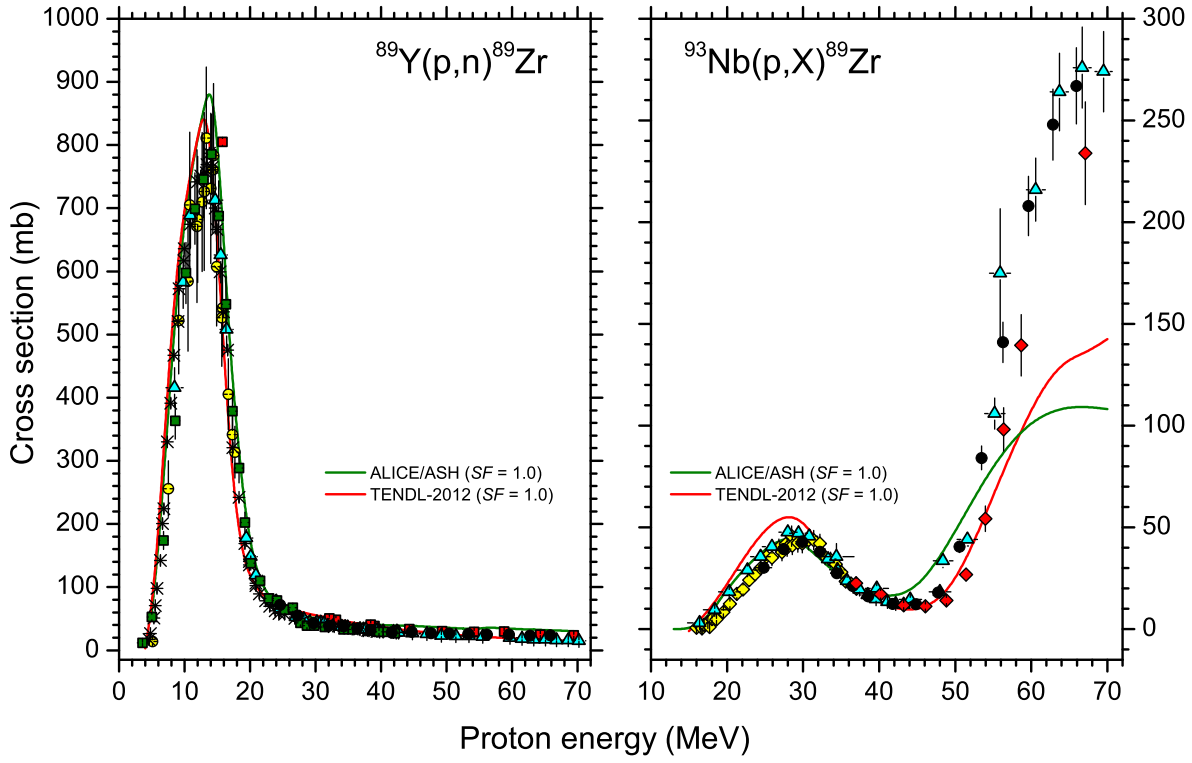

Figure 5.7: Excitation functions for the production of ^{89}Zr in the bombardment of ^{89}Y and ^{93}Nb with protons, respectively. Black circles: this work. Red squares: Uddin *et al.* [Udd2005]. Yellow circles: Omara *et al.* [Oma2009]. Asterisks: Mustafa *et al.* [Mus1998]. Red diamonds: Ditrói *et al.* [Dit2008]. Yellow diamonds: Ditrói *et al.* [Dit2009]. Cyan triangles: Michel *et al.* [Mic1997]. Green squares: Khandaker *et al.* [Kha2012].

5.3.10 The ^{93}Nb(p,X)^{90}Nb process

The excitation function for the ^{93}Nb(p,X)^{90}Nb process is shown in Fig. 5.8. The data of Michel *et al.* [Mic1997] peak somewhat higher than our data but the overall agreement is good. The prediction of ALICE/ASH and the TENDL-2012 data both reproduce the shape of the excitation function quite well but had to be scaled up by factors of $SF = 1.17$ and $SF = 1.6$, respectively.

5.3.11 The ^{93}Nb(p,X)^{91m}Nb process

The open reaction channels for ^{93}Nb(p,X)^{91m}Nb are as follows: ^{93}Nb(p,t)^{91m}Nb, $Q = -8.235$ MeV; ^{93}Nb(p,dn)^{91m}Nb, $Q = -14.49$ MeV; ^{93}Nb(p,p2n)^{91m}Nb, $Q = -16.72$ MeV. Quite a large discrepancy was found between our measurements and previously reported experimental data, shown in Fig. 5.8. The values of this work are considerably lower than the values of Michel *et al.* [Mic1997] as well as the 2009 data of Ditrói *et al.* [Dit2009], by about a factor of 2 at the peak. Careful scrutiny could not resolve this difference. This is rather surprising, taken into account that the same decay data were used in all the studies. While the 2009 values of Ditrói are in agreement with the data of Michel in the overlapping energy region, there is a curious disagreement with the 2008 data of Ditrói *et al.* [Dit2008] at higher energies. There seems to be a drop of the excitation function towards a threshold that is more than 10 MeV higher than the expected threshold (red diamonds in Fig. 5.8). We scrutinized this data set in both the original

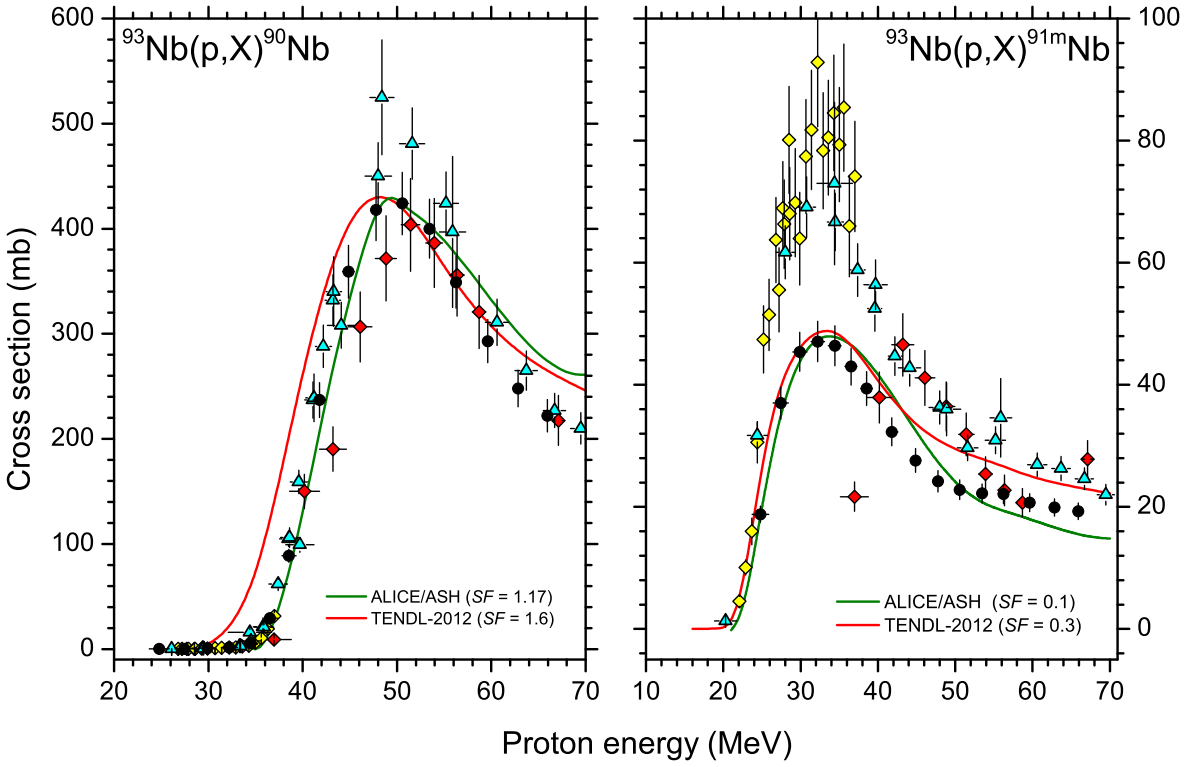

Figure 5.8: Excitation functions for the production of ^{90}Nb and ^{91m}Nb, respectively, in the bombardment of ^{93}Nb with protons. Black circles: this work. Red diamonds: Ditrói *et al.* [Dit2008]. Yellow diamonds: Ditrói *et al.* [Dit2009]. Cyan triangles: Michel *et al.* [Mic1997].

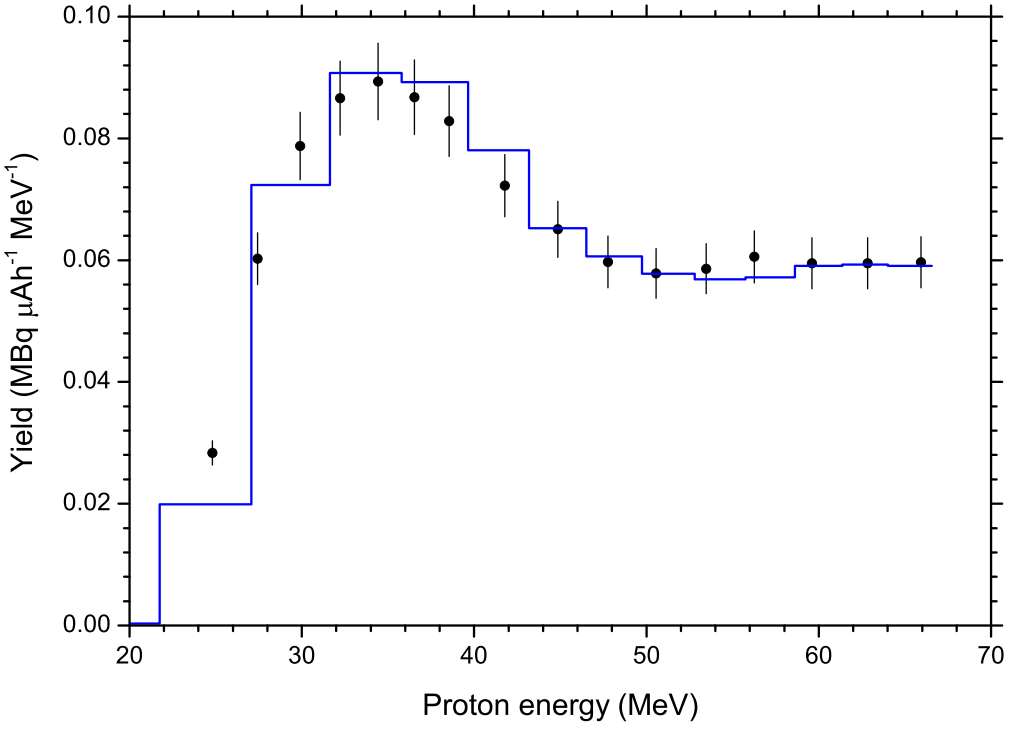

Figure 5.9: Differential yields of ^{91m}Nb in the bombardment of ^{93}Nb with protons, extracted from the two experimental stacks irradiated in this work. Solid Circles: thin Nb foils. Histogram: thick Nb discs.

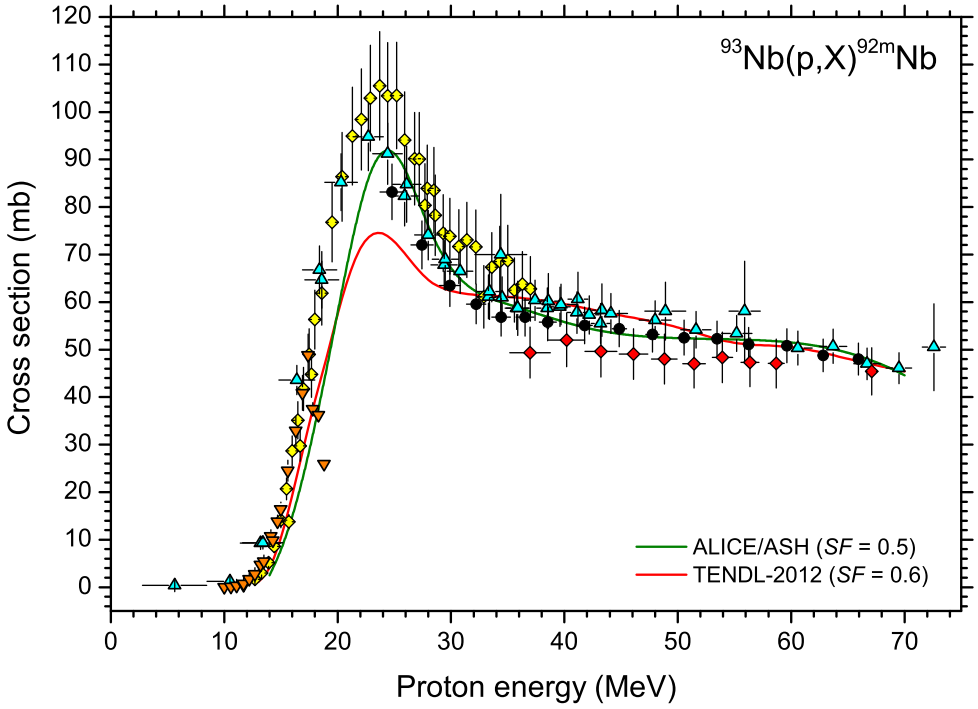

Figure 5.10: Excitation function for the production of ^{92m}Nb in the bombardment of ^{93}Nb with protons. Black circles: this work. Red diamonds: Ditrói *et al.* [Dit2008]. Yellow diamonds: Ditrói *et al.* [Dit2009]. Cyan triangles: Michel *et al.* [Mic1997]. Orange triangles: Avila Rodrigues *et al.* [Avi2008].

paper and the relevant EXFOR entry to make sure that it was not mistakenly the data of a deuteron-induced reaction, which those authors also investigated. Such a mistake, however, does not seem to have been made.

In a further attempt to shed light on this discrepancy, the corresponding differential yields from both irradiated stacks of this work have been compared. Point data (extracted from the thin Nb foils) and values in larger energy intervals (extracted from the thicker Nb discs, plotted as a histogram) are shown in Fig. 5.9. Overall good agreement is evident. The enigma thus stands. The fact that the ALICE/ASH code intrinsically predicts the total of ground and metastable contributions, the curve had to be scaled down considerably in Fig. 5.8 ($SF = 0.1$) but the overall shape agreement is very good. The TENDL-2012 data also had to be scaled aggressively ($SF = 0.3$) which is rather unexpected, given that the underlying TALYS calculations pertain to the particular metastable state only in this case.

5.3.12 The ^{93}Nb(p,X)^{92m}Nb process

The open channels for the ^{93}Nb(p,X)^{92m}Nb process are ^{93}Nb(p,d)^{92m}Nb, $Q = -6.606$ MeV and ^{93}Nb(p,pn)^{92m}Nb, $Q = -8.831$ MeV. The data are shown in Fig. 5.10. Both the TENDL-2012 and ALICE/ASH curves were scaled down to fit the data ($SF = 0.5$ and $SF = 0.6$, respectively). The shape agreement is quite good in the case of ALICE/ASH and reasonable for TENDL-2012. The agreement with previous data is not perfect but reasonable. Interestingly, the two sets of data by Ditrói *et al.* [Dit2008, Dit2009] for a higher and a lower energy region, respectively, do not join smoothly. Our data seem to bisect these two data sets.

5.3.13 Thick-target yields

Production of ^{88}Zr as a byproduct from ^{93}Nb + p

The thick-target yield curve derived from the excitation function (see Appendix E), as well as measured values, are presented in Fig. 5.11 for the production of ^{88}Zr from ^{93}Nb + p. This process was one of the major focus points of this study, in order to better quantify the ^{88}Zr that can be extracted as a byproduct from other radionuclide productions. This can be achieved by processing the used Nb target capsules, as already mentioned. The useful energy windows covered by the Nb encapsulation in the VBTS for a tandem Mg/Ga target arrangement as well as a tandem RbCl/Ga arrangement in Target Station 1 are presented in Table 5.3. It is clear that especially in the case of the VBTS (the grey bars in Fig. 5.11 highlight the energy windows), it is possible to recover a significant amount of ^{88}Zr. At the rate of 0.847 Mbq/μAh and assuming a 200 μA proton beam intensity, a production rate of 819 MBq/h (4.58 mCi/h) is obtained, which is substantial for such a relatively long-lived radionuclide. These targets are typically bombarded over a period of two weeks to an accumulated charge of 20 000 μAh, resulting in a ^{88}Zr yield between 14 000 MBq (378 mCi) and 15 000 MBq (405 mCi) at EOB, depending on the decay losses within the particular beam history. These beam histories are very fragmented as the beam is shared between several users and the allocated beam to the radionuclide production programme has to be utilized for the production of a range of radionuclides.

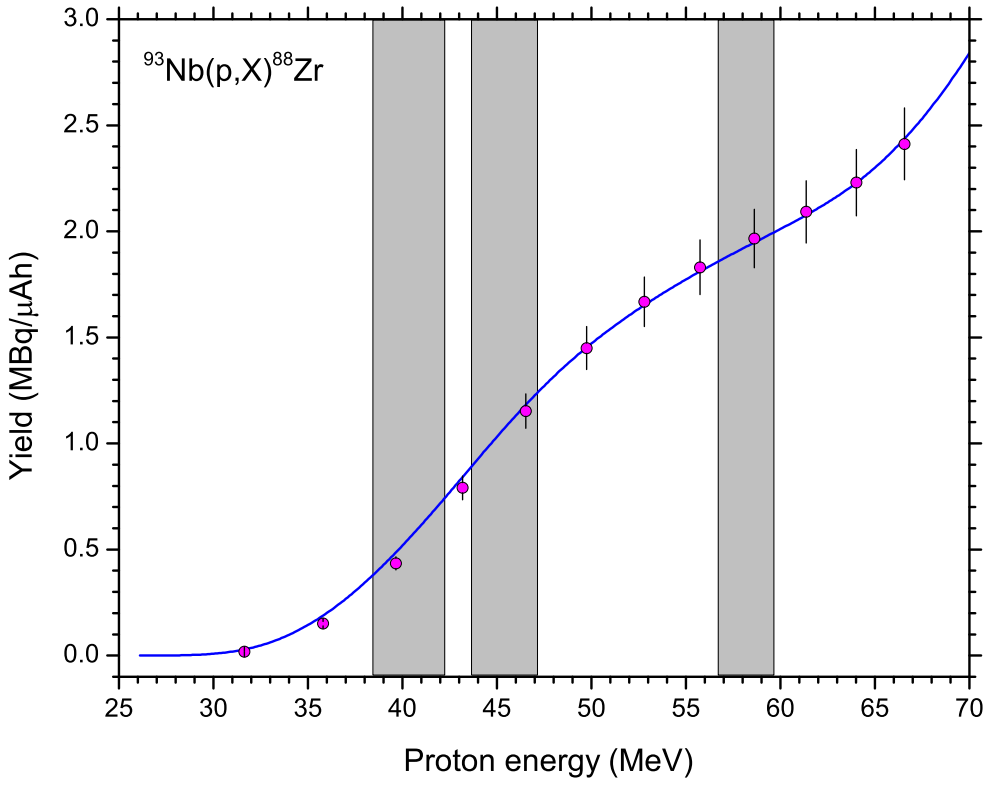

Figure 5.11: Integral physical yield for the production of ^{88}Zr in the proton bombardment of ^{93}Nb. The curve was derived from the measured excitation function. The symbols are the values obtained from the thick Nb discs. The grey bars show the energy windows for a VBTS Mg/Ga tandem target where ^{88}Zr is formed in the Nb capsule walls.

Table 5.3: Physical yields of ^{88}Zr from Nb encapsulation in typical iThemba LABS production targets bombarded with 66 MeV protons.

E-in (MeV)	E-Out (MeV)		Physical Yield (Mbq/μAh)
^{88}Zr – VBTS (vertical beam)			
59.65	56.71		0.136
47.14	43.66		0.347
42.24	38.44		0.364
		Total	0.847
^{88}Zr – Target Station 1 (horizontal beam)			
62.33	60.64		0.086
35.43	31.04		0.148
29.15	26.10		0.004
		Total	0.238

Dedicated production of ^{88}Zr from Y + p, Y_2O_3 + p, Zr + p and Nb + p

Fig. 5.12 shows the thick-target yields for ^{88}Zr for all the investigated target materials. At iThemba LABS, we are somewhat hesitant to use elemental yttrium in high-power targetry due to its chemical reactivity. During machining, turnings of Y often ignite in air, making it a

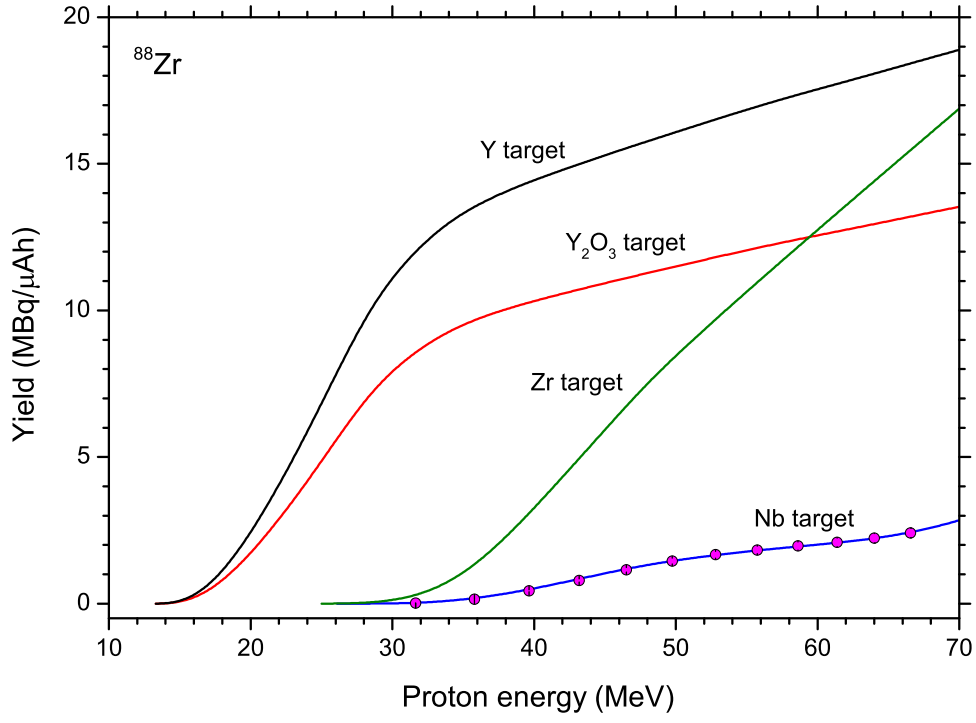

Figure 5.12: Integral physical yields for the production of ^{88}Zr in the bombardment of Y, Y_2O_3, Zr and Nb with protons.

rather dangerous material to work with. Finely divided Y powder can be extremely dangerous (i.e. when used for purposes of target manufacture by powder compression) since it combusts spontaneously in air. For this reason, it was decided to use a more stable compound of Y as target material. At iThemba LABS, compressed yttrium oxide (Y_2O_3) discs, encapsulated in Al, have been tested successfully as production targets. It has a high melting point of 2410 °C. In addition, Y_2O_3 can be readily dissolved in water or dilute acid, facilitating easy separation via ion-exchange chromatography. It has to be said, however, that elemental Y foil targets have been employed by several other authors (e.g. [Woo2013] and references therein) but at significantly lower beam intensities. The feasibility of thicker Y discs as targets in the context of the present application was not investigated.

It is clear that when it becomes necessary to generate a larger amount of ^{88}Zr activity in a dedicated production run within a shorter time frame, Nb is not the target material of choice. From a nuclear data perspective, it will be better to use Y_2O_3 targets in the energy window below about 35 MeV and natural Zr above this energy. Note that the ^{88}Zr/^{88}Y generator system consists of a stock solution, from which the ^{88}Y is separated from time to time by conventional ion-exchange chromatography. In this case, the separation of ^{88}Y is not affected by stable Zr in the stock solution. The stock solution is recovered after the load step on to the resin column. All Zr are washed from the column before elution of the ^{88}Y. The ^{88}Zr yield predicted for a tandem target consisting of a natural Zr disk in the higher-energy slot and an Al-encapsulated Y_2O_3 in the lower-energy slot, such that the average energy of protons entering the Y_2O_3 material is 35 MeV, is 21.9 MBq/μAh.

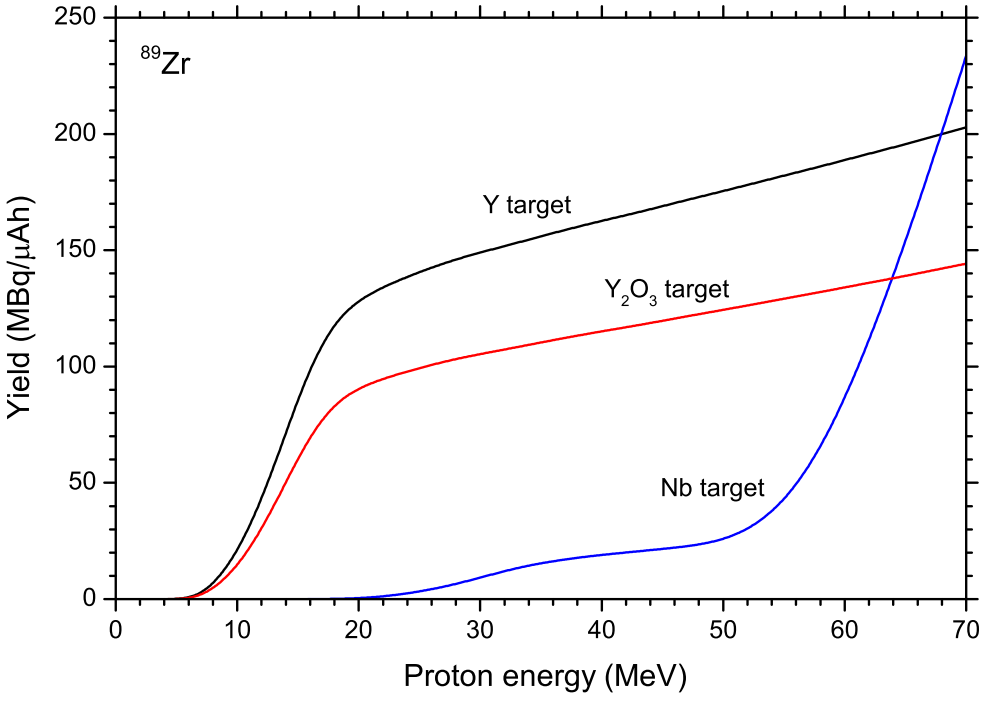

Figure 5.13: Integral physical yields for the production of ^{89}Zr in the bombardment of Y, Y_2O_3 and Nb with protons.

Dedicated production of ^{89}Zr from Y + p, Y_2O_3 + p and Nb + p

In Fig 5.13, the ^{89}Zr yields from the investigated target materials is presented for Y + p, Y_2O_3 + p and Nb + p. From a ^{89}Zr yield perspective, it is evident that Y_2O_3 is the target material of choice below about 50 MeV and Nb above this energy. Niobium may therefore be considered as a tandem target partner for Y_2O_3, also because Nb discs have far superior thermal properties than thick Al-encapsulated Y_2O_3 targets (in particular concerning their longevity in high-intensity bombardments). The choice, however, depends on the level of ^{88}Zr contamination that the particular application can tolerate (which, in non-human studies, is normally not important). Production of radionuclidically pure ^{89}Zr (i.e. no ^{88}Y contamination) will only be possible in a very small energy window on Y_2O_3 targets; about 6–14 MeV.

5.4 Conclusion

The excitation function database for the most important radionuclides produced in the ^{89}Y + p and ^{93}Nb + p processes now seems to be consistent. It was shown that significant quantities of ^{88}Zr can be produced as a byproduct from activated Nb target capsules. For dedicated productions of ^{88}Zr for use as ^{88}Y generators, an Y_2O_3/Zr tandem target will optimize the yield, which will be about a factor 5 higher than with a thick Nb target. For the ^{93}Nb(p,X)^{91m}Nb process, a significant discrepancy in the literature could not be resolved. We could find only two excitation function data points on ^{93}Nb(p,X)^{87}Zr in the literature and have expanded the currently known data set significantly for this case. The cross sections and yields of both ^{88}Zr and ^{89}Zr have now been satisfactorily determined experimentally and the productions for medical applications can thus be planned with confidence. A selection of this work have already been published [Ste2011].

Table 5.4: Measured cross sections for the production of Nb and Zr radionuclides in the irradiation of ^{93}Nb with protons.

Proton energy (MeV)	Cross section[a] (mb)						
	^{90}Nb	^{91m}Nb	^{92m}Nb	^{86}Zr	^{87}Zr	^{88}Zr	^{89}Zr
24.80 ± 1.06	$(6.29 \pm 1.80) \times 10^{-02}$	$(1.88 \pm 0.13) \times 10^{+01}$	$(8.32 \pm 0.58) \times 10^{+01}$	–	–	$(1.73 \pm 0.57) \times 10^{-02}$	$(3.02 \pm 0.21) \times 10^{+01}$
27.44 ± 0.98	$(1.98 \pm 0.22) \times 10^{-01}$	$(3.70 \pm 0.26) \times 10^{+01}$	$(7.20 \pm 0.50) \times 10^{+01}$	–	–	$(6.60 \pm 2.20) \times 10^{-01}$	$(3.94 \pm 0.28) \times 10^{+01}$
29.90 ± 0.92	$(6.98 \pm 0.55) \times 10^{-01}$	$(4.54 \pm 0.32) \times 10^{+01}$	$(6.35 \pm 0.45) \times 10^{+01}$	–	–	$(5.10 \pm 0.43) \times 10^{+00}$	$(4.29 \pm 0.30) \times 10^{+01}$
32.22 ± 0.86	$(1.50 \pm 0.11) \times 10^{+00}$	$(4.71 \pm 0.33) \times 10^{+01}$	$(5.96 \pm 0.42) \times 10^{+01}$	–	–	$(1.72 \pm 0.12) \times 10^{+01}$	$(3.80 \pm 0.27) \times 10^{+01}$
34.42 ± 0.82	$(5.38 \pm 0.38) \times 10^{+00}$	$(4.64 \pm 0.33) \times 10^{+01}$	$(5.68 \pm 0.40) \times 10^{+01}$	–	–	$(3.27 \pm 0.23) \times 10^{+01}$	$(2.75 \pm 0.19) \times 10^{+01}$
36.53 ± 0.78	$(2.95 \pm 0.21) \times 10^{+01}$	$(4.30 \pm 0.30) \times 10^{+01}$	$(5.68 \pm 0.40) \times 10^{+01}$	–	–	$(4.54 \pm 0.32) \times 10^{+01}$	$(2.13 \pm 0.15) \times 10^{+01}$
38.54 ± 0.74	$(8.88 \pm 0.62) \times 10^{+01}$	$(3.94 \pm 0.28) \times 10^{+01}$	$(5.58 \pm 0.39) \times 10^{+01}$	–	–	$(5.54 \pm 0.39) \times 10^{+01}$	$(1.62 \pm 0.11) \times 10^{+01}$
41.78 ± 0.68	$(2.37 \pm 0.17) \times 10^{+02}$	$(3.23 \pm 0.23) \times 10^{+01}$	$(5.51 \pm 0.39) \times 10^{+01}$	–	–	$(6.34 \pm 0.45) \times 10^{+01}$	$(1.25 \pm 0.09) \times 10^{+01}$
44.85 ± 0.63	$(3.59 \pm 0.25) \times 10^{+02}$	$(2.76 \pm 0.20) \times 10^{+01}$	$(5.44 \pm 0.38) \times 10^{+01}$	–	$(8.41 \pm 3.66) \times 10^{+00}$	$(6.05 \pm 0.43) \times 10^{+01}$	$(1.22 \pm 0.09) \times 10^{+01}$
47.77 ± 0.59	$(4.18 \pm 0.29) \times 10^{+02}$	$(2.42 \pm 0.17) \times 10^{+01}$	$(5.32 \pm 0.37) \times 10^{+01}$	–	$(1.29 \pm 0.39) \times 10^{+01}$	$(4.82 \pm 0.34) \times 10^{+01}$	$(1.80 \pm 0.13) \times 10^{+01}$
50.56 ± 0.55	$(4.24 \pm 0.30) \times 10^{+02}$	$(2.28 \pm 0.16) \times 10^{+01}$	$(5.25 \pm 0.37) \times 10^{+01}$	–	$(3.77 \pm 0.52) \times 10^{+01}$	$(3.66 \pm 0.26) \times 10^{+01}$	$(4.05 \pm 0.28) \times 10^{+01}$
53.46 ± 0.51	$(4.00 \pm 0.28) \times 10^{+02}$	$(2.22 \pm 0.16) \times 10^{+01}$	$(5.23 \pm 0.37) \times 10^{+01}$	–	$(4.70 \pm 0.76) \times 10^{+01}$	$(2.92 \pm 0.21) \times 10^{+01}$	$(8.42 \pm 0.59) \times 10^{+01}$
56.26 ± 0.47	$(3.49 \pm 0.25) \times 10^{+02}$	$(2.21 \pm 0.16) \times 10^{+01}$	$(5.11 \pm 0.36) \times 10^{+01}$	$(9.19 \pm 1.23) \times 10^{-01}$	$(3.97 \pm 0.92) \times 10^{+01}$	$(2.42 \pm 0.17) \times 10^{+01}$	$(1.41 \pm 0.10) \times 10^{+02}$
59.61 ± 0.41	$(2.93 \pm 0.21) \times 10^{+02}$	$(2.07 \pm 0.15) \times 10^{+01}$	$(5.08 \pm 0.36) \times 10^{+01}$	$(3.46 \pm 0.27) \times 10^{+00}$	$(5.72 \pm 0.87) \times 10^{+01}$	$(2.22 \pm 0.16) \times 10^{+01}$	$(2.08 \pm 0.15) \times 10^{+02}$
62.83 ± 0.36	$(2.48 \pm 0.17) \times 10^{+02}$	$(1.99 \pm 0.14) \times 10^{+01}$	$(4.88 \pm 0.34) \times 10^{+01}$	$(7.80 \pm 0.56) \times 10^{+00}$	$(4.37 \pm 0.82) \times 10^{+01}$	$(2.61 \pm 0.19) \times 10^{+01}$	$(2.48 \pm 0.17) \times 10^{+02}$
65.93 ± 0.30	$(2.22 \pm 0.16) \times 10^{+02}$	$(1.93 \pm 0.14) \times 10^{+01}$	$(4.80 \pm 0.33) \times 10^{+01}$	$(1.22 \pm 0.09) \times 10^{+01}$	$(3.48 \pm 0.71) \times 10^{+01}$	$(3.95 \pm 0.28) \times 10^{+01}$	$(2.67 \pm 0.19) \times 10^{+02}$

[a]The error values listed include a systematic uncertainty which is estimated to be 7% (see text).

Table 5.5: Cross sections for the production of Zr radionuclides in the irradiation of ^{89}Y with protons.

Proton energy (MeV)	Cross section[a] (mb)			
	^{89}Y(p,4n)^{86}Zr	^{89}Y(p,3n)^{87}Zr	^{89}Y(p,2n)^{88}Zr	^{89}Y(p,n)^{89}Zr
24.58 ± 1.07	–	–	$(8.67 \pm 0.61) \times 10^{+02}$	$(7.17 \pm 0.51) \times 10^{+01}$
27.24 ± 0.98	–	$(1.21 \pm 0.34) \times 10^{+01}$	$(7.44 \pm 0.52) \times 10^{+02}$	$(5.48 \pm 0.39) \times 10^{+01}$
29.71 ± 0.92	–	$(9.35 \pm 0.99) \times 10^{+01}$	$(4.94 \pm 0.35) \times 10^{+02}$	$(4.28 \pm 0.30) \times 10^{+01}$
32.04 ± 0.86	–	$(2.36 \pm 0.20) \times 10^{+02}$	$(3.38 \pm 0.24) \times 10^{+02}$	$(3.90 \pm 0.28) \times 10^{+01}$
34.25 ± 0.82	–	$(3.02 \pm 0.25) \times 10^{+02}$	$(2.30 \pm 0.16) \times 10^{+02}$	$(3.82 \pm 0.27) \times 10^{+01}$
36.37 ± 0.78	–	$(3.27 \pm 0.26) \times 10^{+02}$	$(1.62 \pm 0.11) \times 10^{+02}$	$(3.48 \pm 0.25) \times 10^{+01}$
38.39 ± 0.74	$(8.91 \pm 1.61) \times 10^{-01}$	$(3.26 \pm 0.28) \times 10^{+02}$	$(1.28 \pm 0.09) \times 10^{+02}$	$(3.23 \pm 0.23) \times 10^{+01}$
41.64 ± 0.68	$(1.30 \pm 0.09) \times 10^{+01}$	$(2.99 \pm 0.24) \times 10^{+02}$	$(1.02 \pm 0.07) \times 10^{+02}$	$(2.84 \pm 0.21) \times 10^{+01}$
44.71 ± 0.63	$(4.43 \pm 0.31) \times 10^{+01}$	$(1.92 \pm 0.20) \times 10^{+02}$	$(9.24 \pm 0.65) \times 10^{+01}$	$(2.93 \pm 0.22) \times 10^{+01}$
47.63 ± 0.59	$(7.62 \pm 0.53) \times 10^{+01}$	$(1.73 \pm 0.16) \times 10^{+02}$	$(8.38 \pm 0.59) \times 10^{+01}$	$(2.71 \pm 0.22) \times 10^{+01}$
50.43 ± 0.55	$(9.85 \pm 0.69) \times 10^{+01}$	$(1.44 \pm 0.17) \times 10^{+02}$	$(8.07 \pm 0.57) \times 10^{+01}$	$(2.64 \pm 0.21) \times 10^{+01}$
53.34 ± 0.51	$(1.05 \pm 0.07) \times 10^{+02}$	$(1.02 \pm 0.10) \times 10^{+02}$	$(7.55 \pm 0.53) \times 10^{+01}$	$(2.61 \pm 0.21) \times 10^{+01}$
56.14 ± 0.46	$(9.61 \pm 0.67) \times 10^{+01}$	$(9.99 \pm 1.43) \times 10^{+01}$	$(6.92 \pm 0.49) \times 10^{+01}$	$(2.47 \pm 0.20) \times 10^{+01}$
59.50 ± 0.41	$(7.48 \pm 0.52) \times 10^{+01}$	$(6.82 \pm 0.87) \times 10^{+01}$	$(6.16 \pm 0.44) \times 10^{+01}$	$(2.47 \pm 0.20) \times 10^{+01}$
62.72 ± 0.36	$(6.24 \pm 0.44) \times 10^{+01}$	$(7.13 \pm 0.94) \times 10^{+01}$	$(5.91 \pm 0.42) \times 10^{+01}$	$(2.34 \pm 0.17) \times 10^{+01}$
65.83 ± 0.30	$(5.17 \pm 0.36) \times 10^{+01}$	$(6.85 \pm 0.66) \times 10^{+01}$	$(5.80 \pm 0.41) \times 10^{+01}$	$(2.40 \pm 0.17) \times 10^{+01}$

[a]The error values listed include a systematic uncertainty which is estimated to be 7% (see text).

Table 5.6: Cross sections for the production of ^{88}Zr in the irradiation of ^{nat}Zr with protons.

Proton energy (MeV)	Cross section[a] (mb)
	^{nat}Zr(p,X)^{88}Zr
24.10 ± 1.08	$(2.34 \pm 0.26) \times 10^{+00}$
27.25 ± 0.98	$(7.19 \pm 0.78) \times 10^{+00}$
30.10 ± 0.93	$(5.46 \pm 0.59) \times 10^{+01}$
32.76 ± 0.87	$(1.52 \pm 0.17) \times 10^{+02}$
35.27 ± 0.79	$(2.44 \pm 0.27) \times 10^{+02}$
38.83 ± 0.75	$(3.03 \pm 0.33) \times 10^{+02}$
42.16 ± 0.66	$(3.26 \pm 0.35) \times 10^{+02}$
45.30 ± 0.62	$(3.12 \pm 0.34) \times 10^{+02}$
48.29 ± 0.57	$(2.70 \pm 0.29) \times 10^{+02}$
51.17 ± 0.53	$(2.36 \pm 0.26) \times 10^{+02}$
53.94 ± 0.50	$(2.19 \pm 0.24) \times 10^{+02}$
56.60 ± 0.45	$(1.96 \pm 0.21) \times 10^{+02}$
59.84 ± 0.40	$(2.00 \pm 0.22) \times 10^{+02}$
62.95 ± 0.36	$(1.92 \pm 0.21) \times 10^{+02}$
65.94 ± 0.30	$(1.80 \pm 0.19) \times 10^{+02}$

[a]The error values listed include a systematic uncertainty which is estimated to be 7% (see text).

Chapter 6

Production of ^{28}Mg in the Bombardment of LiCl Targets with Protons

6.1 Introduction

The element magnesium is an essential nutrient for all living organisms. The radionuclide ^{28}Mg has been employed as a radiotracer of magnesium since the second half of the previous century (Sheline and Johnson [She1953]) and found wide application in the study of absorption, retention and excretion in metabolic processes (cf. Martin and Bauer [Mar1962]; Mendelson *et al.* [Men1965]; Kniffen *et al.* [Kni1972]; Watson *et al.* [Wat1979]; Verhas *et al.* [Ver2002]) as well as in animal and human physiology (cf. Schimansky [Sch1973]; Schwartz *et al.* [Sch1981]; Iwata *et al.* [Iwa1992]; Heijnen *et al.* [Hei1996]). Since ^{28}Mg ($T_{1/2} = 20.9$ h) is its only radionuclide with a half-life longer than 10 minutes, it has regularly been employed in quantitative studies of Mg bioavailability in agriculture and nutrition (cf. Verhas *et al.* [Ver2002]; Bohn [Boh2003], and references therein). Its mode of decay is 100% by β^-- emission (Firestone and Eckström [Fir2004]) with several intense γ-lines suitable for γ-ray spectrometry, which will be discussed later.

The present investigation concerns the cyclotron production of ^{28}Mg with protons in the energy region 50–200 MeV. The various possible production routes have already been discussed in a thesis of a colleague (N. P. van der Meulen [vdM2008] as well as in a paper (Steyn *et al.* [Ste2008b]) in which new experimental cross sections and integral yields were reported for the ^{nat}Cl(p,X)^{28}Mg process. The last-mentioned work also provided a summary on alternative production routes that employ projectiles other than protons. In the case of protons, the work of Lundqvist and Malmborg [Lun1979] deserves a special mention. These authors investigated the production of carrier-free ^{28}Mg and ^{24}Na in proton-induced reactions on natural targets of Si, P, S, Cl, Ar and K in the energy region 50–180 MeV. It was shown that only the ^{nat}P(p,X)^{28}Mg process has higher cross sections for ^{28}Mg formation than ^{nat}Cl(p,X)^{28}Mg (about 30% higher at 150 MeV). Unfortunately, many compounds of phosphorus decompose at relatively low temperatures, rendering them unsafe to use as target materials. In fact, we could not identify a single suitable compound with a relatively high P content as well as good thermal stability. The conclusion was that ^{nat}Cl + p was the production route of choice and LiCl was the target material of choice based on thermal stability and Cl content [Ste2008b]. The relevant part of

the Karlsruhe Chart of the Nuclides is shown in Fig. 6.1. The energy region of the present study is determined by the fact that the effective threshold of the ^{nat}Cl(p,X)^{28}Mg process is about 50 MeV and the maximum proton beam energy available at iThemba LABS is 200 MeV. As will be shown, proton energies significantly above 66 MeV are required to produce ^{28}Mg in meaningful quantities as the residual nucleus is rather far removed from the relevant Cl target nuclei (see Fig. 6.1). A part of this study was to establish what the prospects for ^{28}Mg production would be at iThemba LABS and to investigate the options for production targetry.

LiCl has excellent thermal properties for targetry, including a melting point of 605 °C and a boiling point of 1325 °C. A yield of about 80% of the ^{nat}Cl + p theoretical maximum can also be expected. The problem with a large energy window, such as 50–200 MeV, is that a single LiCl target would be about 148 mm (30.6 g/cm^2) thick. Such a thick target would be impractical and virtually impossible to cool sufficiently during a high-intensity bombardment. A solution was suggested in our previous paper [Ste2008b], namely to stack several thinner, encapsulated LiCl targets behind each other and to provide each individual target with fast flowing cooling water in a 4π geometry. In this way, the total surface area to cool from can be increased radically, albeit with the loss of some production yield due to the capsule walls

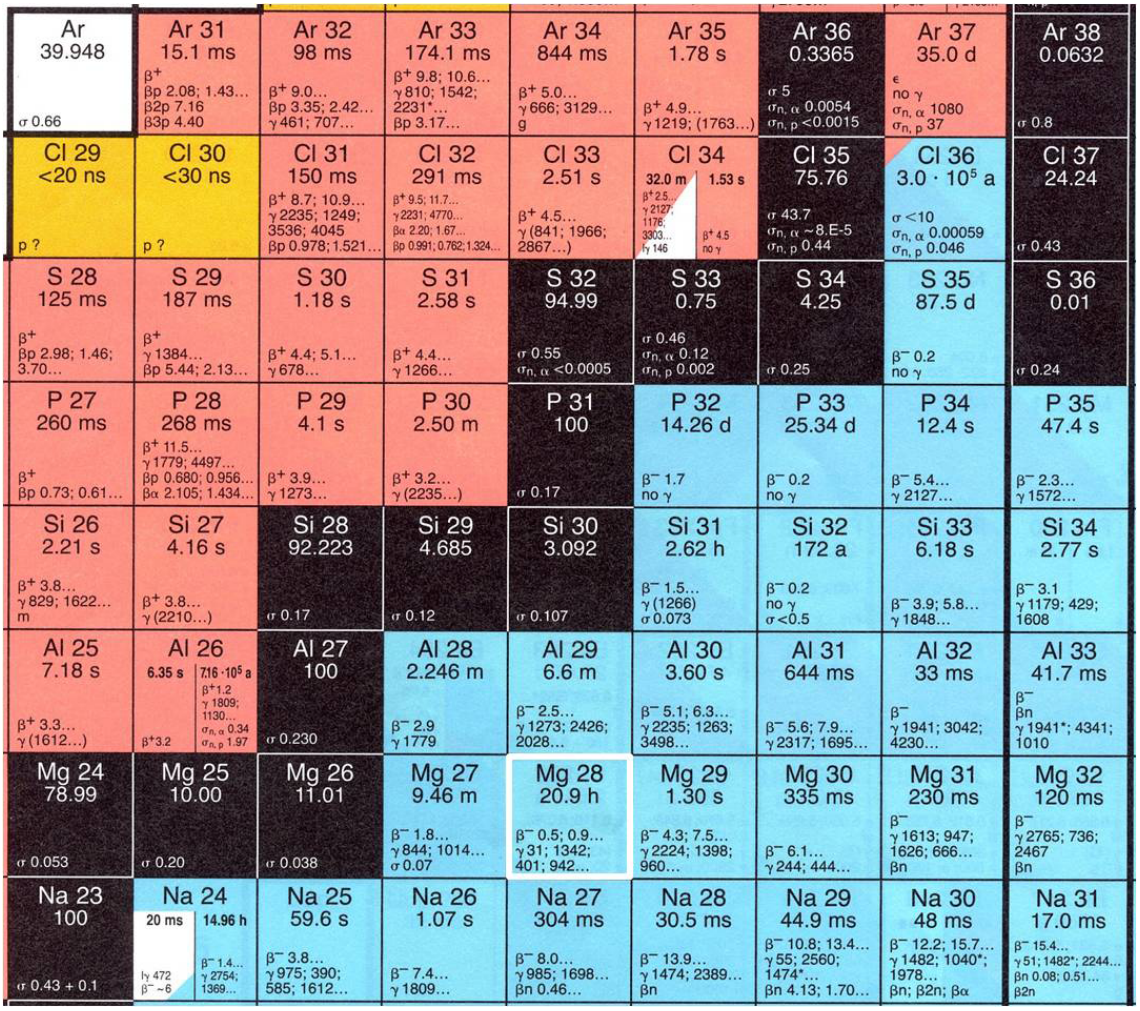

Figure 6.1: Relevant part of the Karlsruhe Chart of the Nuclides, showing the location of ^{28}Mg in a white frame. With permission © Nucleonica GmbH 2012.

and cooling water "dead layers". This concept is, of course, nothing new – the Brookhaven Linac Isotope Producer (BLIP), for example, has bombarded stacks of multiple targets since 1973 (Mausner *et al.* [Mau1990]). The BLIP targets are relatively large, however. Mausner *et al.* reported compressed salt discs of 4.5 and 7 cm in diameter, enclosed in stainless steel capsules with Inconel windows. Compressed KCl and RbCl targets were developed for the production of ^{28}Mg and ^{82}Sr, respectively, and it was reported that the BLIP was the only supplier of ^{28}Mg in North America at that time.

In order to reduce the amount of irradiated target material that needed to be processed, it was decided to limit the diameter of individual target discs to 20 mm at iThemba LABS, albeit with some beam losses towards the back of the stack due to the radial beam spread caused by multiple Coulomb scattering inside the target material. The adopted philosophy is that some outscattering of protons can be tolerated, as long as these losses are not too severe. Another reason why target discs of 20 mm in diameter would be attractive was because such targetry would be compatible with the existing infrastructure for target handling, bombardment and batch processing in the production of short-lived radionuclides, as well as with existing methods for encapsulation and decapsulation in our laboratory. We report here on an experimental target holder designed to irradiate a stack of encapsulated LiCl targets with a 200 MeV proton beam. In addition, the individual targets were compatible with the standard production target holders in use on the horizontal-beam target station (Target Station 1) for bombardments with 66 MeV protons (Steyn *et al.* [Ste2013]).

The work reported here had three clearly defined objectives: First, to determine the outscattering losses of a 200 MeV proton beam experimentally in an actual target stack, as well as by means of Monte Carlo modelling using the radiation transport code MCNPX (Pelowitz [Pel2011a]). Second, to investigate individual target performance in bombardments with moderately intense beams, employing a 66 MeV proton beam. Third, to develop a separation chemistry using the activated target material obtained from these bombardments. This proof-of-concept study would assist in deciding on a production regimen. In addition, production yields would be obtained which could be compared with expectations based on the already completed nuclear data study. The choice of these two beam energies was influenced by the capabilities of the present cyclotron infrastructure as well as with the weekly beam schedule of the separated-sector cyclotron (SSC) at iThemba LABS. The 200 MeV beams are regularly produced for proton therapy. The 66 MeV beams are used for the routine production of radionuclides and for neutron therapy. Some of the ancillary infrastructure necessary to produce beams of high intensity (e.g. flat-top RF resonators, bunchers, etc.) has been designed and implemented for 66 MeV beams only and not for any other proton energies at this stage. Thus, the SSC cannot produce 200 MeV beams of high intensity without further development. The current work should therefore be seen as a proof-of-concept study and not one aimed at establishing a large-scale production facility for ^{28}Mg at iThemba LABS based on a 200 MeV proton beam. Production yields achievable with the SSC at its current level of evolution, for different target and beam configurations, are also reported. It should be clarified that only the first two objectives mentioned above are presented in this thesis. The third objective, namely the development of a separation chemistry, was included in the thesis project of van der Meulen [vdM2008].

6.2 Nuclear data

Van der Meulen [vdM2008] reported the excitation function for the ^{nat}Cl(p,X)^{28}Mg process, derived from measured integral yield data. This is the inverse procedure normally followed, namely to derive the integral yield curve from microscopic cross sections obtained in stacked-foil experiments. The reason for this approach was simply the difficulty in making thin foils or samples from a chloride salt. For the initial ^{nat}Cl + p measurements, proton beams of 200, 100 and 66 MeV were employed to bombard stacks of thick targets of NaCl. Whereas the integral yield curve is normally obtained by a numerical integration of the excitation function (folded with the inverse of the stopping power), the excitation function can, in principle, be found by means of a numerical differentiation of the integral yield curve. It is also important to point out that the monitor foil results of that study confirmed that outscattering losses from those stacks were negligible. Results from that study were also published [Ste2008b].

The excitation function determined experimentally at iThemba LABS [vdM2008, Ste2008b] is shown in Fig. 6.2, together with the data of Lundqvist and Malmborg [Lun1979], TENDL-2012 and the ALICE/ASH prediction. The ALICE/ASH and TENDL-2012 results are considerably lower but have approximately the right shape. The excitation function rises monotonically from threshold and flattens out towards higher energies, with no prominent structures or peaks. This is typical for spallation reactions (see e.g. Cugnon [Cun2012]). Note that in addition to the neutron emission, numerous charged particles have to be emitted to reach Mg from Cl + p. This kind of process is only possible at these energies for the lighter target nuclei, which have relatively low Coulomb barriers. The contributing reactions include the following: ^{35}Cl(p,6p2n)^{28}Mg, $Q = -66.58$ MeV; ^{37}Cl(p,6p4n)^{28}Mg, $Q = -85.47$ MeV; ^{35}Cl(p,α4p)^{28}Mg, $Q = -38.29$ MeV; ^{37}Cl(p,α4p2n)^{28}Mg, $Q = -57.18$ MeV. If the above Q-values as calculated with the QCalc Q-value calculator of the Brookhaven National Laboratory [Pri2012] can be trusted, cluster emission is pretty much a given below 68.5 MeV. Thus, the effective experimental threshold near 50 MeV may be an indication that cluster emission is significant. The cross sections are very low – below 0.2 mb at 200 MeV. This is already an indication that the large-scale production of this radionuclide will be considerably difficult, if not precluded. Nevertheless, it is useful to quantify the production capability and assess the various options.

6.3 Investigation with 200 MeV protons

6.3.1 Target stack

Ten LiCl target tablets were prepared by compaction of anhydrous LiCl powder ($>$99%, supplied by Merck) in a hydraulic press. The powder was freeze dried for 48 hours prior to compaction. Each tablet had a diameter of 20 mm and a thickness of 2.74 g/cm^2. The compressed tablets were baked in a vacuum oven overnight at 200 °C to ensure that any remaining moisture and/or volatile substances were removed, before being sealed in Al capsules with 0.5 mm thick entrance and exit windows. The encapsulated targets fitted inside a specially made target holder which located each target precisely, so that the spacing between them provided for cooling water layers of 1 mm thickness. The Al entrance window of the target holder had a

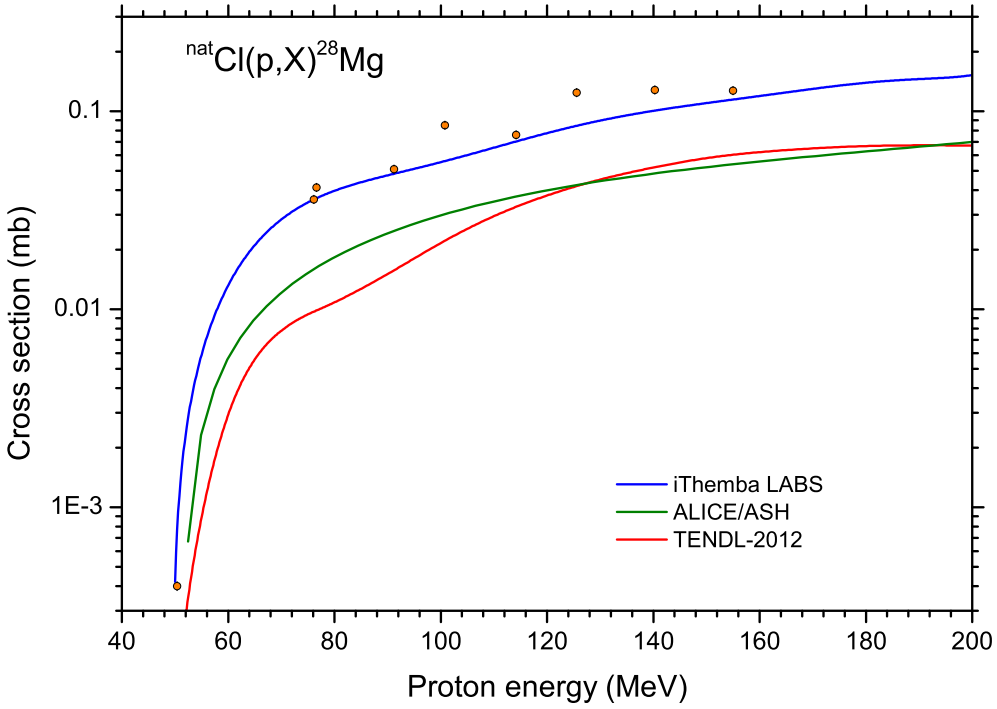

Figure 6.2: Excitation function for the production of ^{28}Mg in the bombardment of ^{nat}Cl with protons. Blue curve: excitation function derived from measured thick-target yields at iThemba LABS [vdM2008, Ste2008b]. Symbols: Lundqvist and Malmborg [Lun1979].

thickness of 1 mm. Cooling water was circulated through the target holder during bombardment at a flow rate of about 5 L/min, as shown schematically in Fig. 6.3. The water was taken from the same chiller unit that supplied cooling water to the beamline magnets and had a temperature of nominally 16 °C. A Ni monitor foil was placed directly behind the last target (i.e. target no. 10) inside the cooling water layer at the back of the target holder. This foil had a diameter of 30 mm and was included to measure the radial intensity distribution of the beam at that location after the bombardment.

The target stack was irradiated with a proton beam of nominally 200 MeV inside the evacuated RERAME II activation chamber at iThemba LABS (see Chapter 2 and Appendix A). The incident beam was not collimated in this case but focused to a relatively small spot of about 3 mm in diameter at the front of the target holder. The collimator unit remained in place but was supplied with a 16 mm aperture through which the beam could be focused cleanly. The focusing was aided using a BeO viewer on which a crosshair scale was drawn. The spot size was also confirmed by means of an autoradiogram prior to bombarding the stack. The duration of the bombardment was about 80 minutes at a beam current of nominally 100 nA. The accumulated charge was 133.34 nAh (480.02 μC) when the bombardment was stopped.

Monte Carlo modelling of the beam and target stack was performed using the radiation transport code MCNPX 2.7.0 (Pelowitz, [Pel2011a]). Initially, the incident beam was specified in the source definition to have a Gaussian radial intensity distribution with a full width at half maximum (FWHM) value of 1.5 mm. The beam was truncated using a so-called "cookie cutter cell" so that it had a well defined width of 3 mm. (Another scenario will be discussed later). It has been shown in several previous investigations that the radial intensity distribution of un-

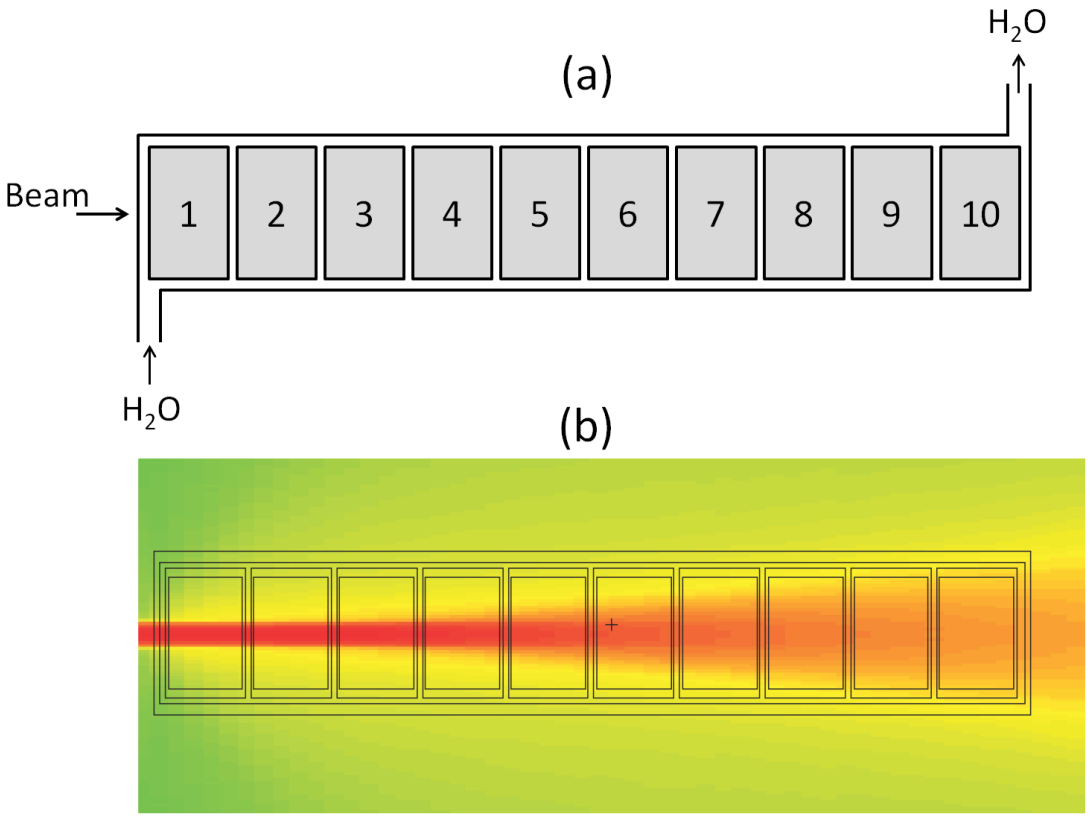

Figure 6.3: (a) Schematic diagram of the 200 MeV experimental LiCl target stack, and (b) MCNPX model with a superimposed graphical display of the calculated proton flux obtained from a mesh tally.

collimated beams from the SSC can be very successfully represented by a Gaussian function truncated at 2 $\times$ FWHM (see e.g. Fig. 2.11 as well as Steyn *et al.* [Ste2013] for a recent measurement). Protons were tracked as they traversed the target stack and no variance reduction was performed. The results presented in this work were obtained by following the histories of 1×10^6 source protons in each run. This was sufficient to pass the relevant statistical tests of the code. The proton flux averaged over each LiCl target cell was obtained by appropriately defined flux tallies. A mesh tally that completely surrounded the target stack was used to obtain a graphical display of the proton flux. This is also shown in Fig. 6.3, overlaid on top of the target geometry as defined in the input to the code. A second mesh tally was defined which surrounded the Ni monitor foil only. This provided the radial flux density distribution of protons traversing the Ni foil.

6.3.2 Radionuclide assays

After bombardment, each individual LiCl target was decapsulated and dissolved in a 75 mL ammonium chloride solution at a pH of 8. This was the load solution required by the radiochemical separation procedure. A 10 mL sample of each solution was sealed in a standard serum vial, which served as a counting source for accurately measuring the induced activity. The rest of the solution was used to develop the radiochemical separation procedure mentioned above. The ^{28}Mg activities were determined by off-line γ-ray spectrometry using the 941.7 keV (38.3%) and 1342.3 keV (52.6%) γ-lines (Firestone and Eckström [Fir2004]). An accurately calibrated HPGe detector with a relative efficiency of 18% and a resolution of 1.8 keV at 1.33

MeV, connected to a SILENA EMCA 2000 multi-channel analyzer, was used for all activity measurements. With the exception of the source prepared from target no. 10, which contained very little ^{28}Mg activity, the statistical uncertainties were small compared to systematic uncertainties. The latter include uncertainty estimates as follows: beam current integration (3%), detector efficiency (5%), source fraction volume measurement (1%) and counting geometry (1%).

In the case of the Ni monitor foil, the radionuclide of interest was ^{57}Ni ($T_{1/2} = 35.6$ h), which was measured after completing the ^{28}Mg measurements. Since the objective was to derive the radial beam intensity distribution at that position in the stack, a vertical strip of 2 mm width was cut from the foil and further divided into ten pieces, each 3 mm long. These smaller 2×3 mm^2 foil fragments were first individually weighed before being mounted on larger aluminium frames to make their handling easier. The activity of each source prepared in this way was assayed for its 1377.63 keV (81.7%) γ-line (Firestone and Eckström [Fir2004]). As only the shape of the distribution was required, the specific activities of the sources were first derived in units of Bq/mg and then renormalized relative to the strongest source.

6.3.3 Results and discussion

The total ^{28}Mg activity determined experimentally for each target and the predicted activity based on the previously published nuclear data study (Steyn *et al.* [Ste2008b]) for the respective energy windows, as indicated, are presented in Table 6.1. All values pertain to the end of bombardment (EOB). The ratios of measured and predicted activities are also included in Table 6.1 and are shown in Fig. 6.4. As can be seen from the figure, targets 1 through 8 have ratios consistent with unity within the measured uncertainties, from which one can conclude that outscattering losses of protons were insignificant for these targets. The situation is very different for targets 9 and 10, thus, outscattering losses seem to have been significant for those two targets.

Results from the MCNPX calculations are also shown in Fig. 6.4. In this case, each value on the y-axis (histogram) is the ratio of the proton flux averaged over the volume of that particular LiCl target and the incident proton flux. It is, however, necessary to take the beam intensity attenuation due to non-elastic nuclear interactions into account. It has been well known for many decades that the radial spread (divergence) of a charged particle beam is mainly caused by multiple Coulomb scattering inside the target material and that at energies below about 500 MeV/nucleon, the effect of other processes on beam divergence is secondary (cf. Litton *et al.* [Lit1968]). For this reason, beam losses by outscattering and beam losses by non-elastic nuclear interactions are largely uncoupled. The proton flux ratio, J_i/J_0 , where $1 \leq i \leq 10$ is an index for the target number in the stack (see Fig. 6.3 and Table 6.1) and J_0 is the incident proton flux, is therefore multiplied by the inverse of the beam attenuation factor due to non-elastic nuclear interactions in each target ($1/P_i$). Values for P_i were obtained from the tables and the relevant formula by Janni [Jan1982]:

$$P_i = 1 - P(E_0, \bar{E}_i), \tag{6.1}$$

where E_0 is the incident proton energy, $\bar{E}_i$ is the median energy of the energy window of LiCl target no i, and $P(E_0, \bar{E}_i)$ is the non-elastic nuclear interaction probability of a proton traversing

Table 6.1: Measured and predicted ^{28}Mg activities in LiCl target stack.

Target no.	Energy window (MeV)	Activity[1] (kBq)		Ratio
		Measured	Predicted[2]	
1	199.5 → 189.7	152.07 ± 9.35	149.59	1.017 ± 0.063
2	188.3 → 178.1	139.68 ± 8.69	139.48	1.001 ± 0.062
3	176.6 → 166.0	119.85 ± 7.46	126.29	0.949 ± 0.059
4	164.4 → 153.3	109.76 ± 6.84	110.54	0.993 ± 0.062
5	151.6 → 139.7	98.95 ± 6.18	96.28	1.028 ± 0.064
6	137.9 → 125.2	82.31 ± 5.18	81.18	1.014 ± 0.064
7	123.3 → 109.4	64.10 ± 4.11	63.31	1.012 ± 0.065
8	107.3 → 91.8	45.68 ± 2.99	46.06	0.992 ± 0.065
9	89.3 → 71.1	23.13 ± 1.60	31.92	0.725 ± 0.050
10	69.1 → 45.6	1.81 ± 0.35	7.76	0.233 ± 0.045
TOTAL	199.5 → 45.6	837.34	852.41	0.982

[1]Activity at EOB. Bombardment duration 80 min.
Accumulated charge 133.34 nAh (480.02 μC).

[2]Using production data from Steyn *et al.* [Ste2008b].

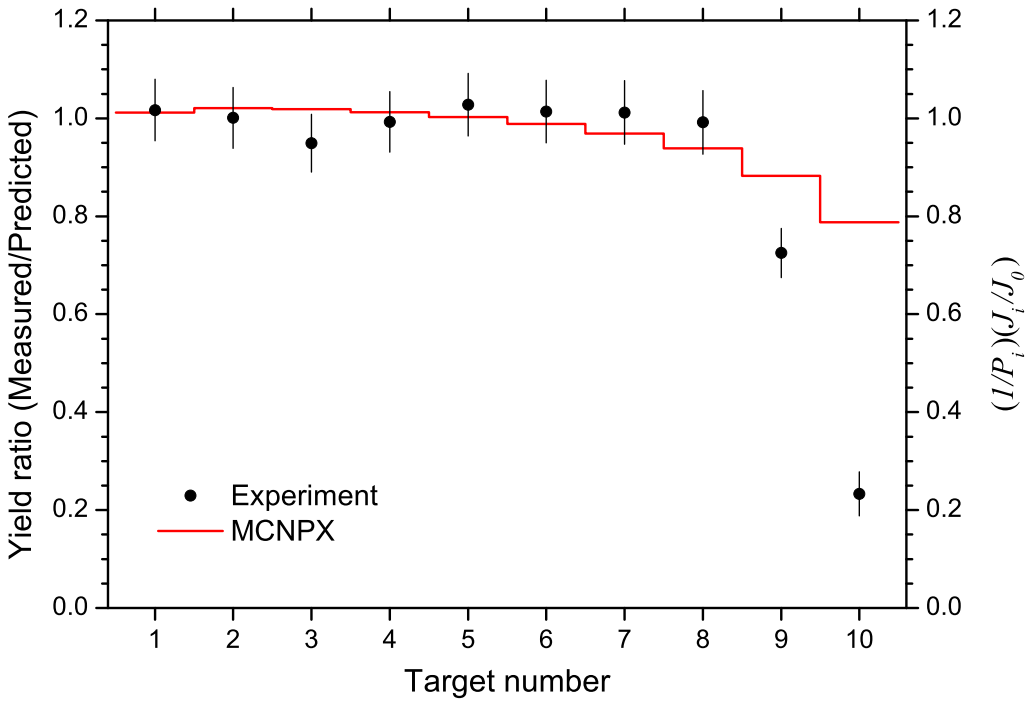

Figure 6.4: (a) Black circles: Ratio of measured and predicted yields for each LiCl target at EOB. Histogram: Ratio of average proton flux in each LiCl capsule (corrected for beam attenuation due to non-elastic nuclear interactions) and the incident flux (see text).

the target stack when its energy has degraded to a value of $\bar{E}_i$ from its initial value of E_0 (also see Appendix B). The quantity $(1/P_i)(J_i/J_0)$, plotted in Fig. 6.4 for all $1 \leq i \leq 10$, should be consistent with unity if outscattering losses are insignificant but values less than 1 should be an indicator of outscattering beam loss. Lower values are indeed found for targets 9 and 10 but to a lesser extent than obtained from the experimentally determined activity ratios.

Figure 6.5 compares the radial beam intensity distributions as deduced from the ^{57}Ni activity induced in the Ni monitor foil, and from the MCNPX calculations, respectively. In the case of the measurements, the normalized specific activity is plotted versus the position of the centre of each foil fragment. The radial uncertainty was taken as 1/3 of the length of a foil fragment. The proton flux density distribution obtained from an MCNPX mesh tally, normalized relative to the maximum value, is plotted as a histogram in Fig. 6.5. The MCNPX distribution has a Gaussian shape and is somewhat narrower than the measured distribution.

The differences between the measurements and the MCNPX predictions are not unexpected. The larger width of the experimentally determined radial beam intensity distribution shown in Fig. 6.5 can be explained by two physical processes that have not been taken into account in this particular MCNPX simulation. The first is the fact that an actual charged particle beam has non-zero transverse emittance and will always contain some angular divergence. This is discussed later. The second is that the actual beam is never perfectly stationary and some movement of the beam spot will occur over the course of the bombardment. Some movement of the beam from the SSC is almost always observed on the BeO viewer although it is usually small. The combined effect of beam movement and angular divergence will certainly increase the radial beam spread. The narrower MCNPX radial distribution is compatible with the smaller outscattering losses predicted from the MCNPX simulation, in particular targets 9 and 10, as shown in Fig. 6.5. Also, the energy straggling increases with increasing penetration depth, becoming quite significant at positions 9 and 10 in the stack. This increases the overall energy uncertainty at the back of the stack, which can lead to differences between measured and predicted yields.

In the final release of the MCNPX code (March 2011), a focused beam source option was implemented [Pel2011b]. The reason why the cookie cutter cell option was used instead of the focused beam option is because the latter option was not available when the initial modelling was done. Recently, the calculations were repeated using the focused beam source option. A discussion on these latter calculations is presented at the end of this chapter.

It is interesting to look at the cumulative ^{28}Mg yields obtained from the 200 MeV target stack (see Table 6.1). The measured cumulative production yield from all ten targets is 6.28 MBq/μAh at EOB. The corresponding expected yield derived from the previously published nuclear data (Steyn *et al.* [Ste2008b]) is 6.39 MBq/μAh, thus very good overall agreement is obtained. Should one discard the last two targets in the stack, the total measured yield is 6.09 MBq/μAh at EOB. Thus, eight targets give a cumulative yield of about 97% of that for ten targets. From a production point of view, it is clearly not worthwhile having the last two targets in the stack. One may also consider to further reduce the number of targets in the stack. The corresponding percentages (relative to the total of all ten targets) are as follows: seven targets (92%); six targets

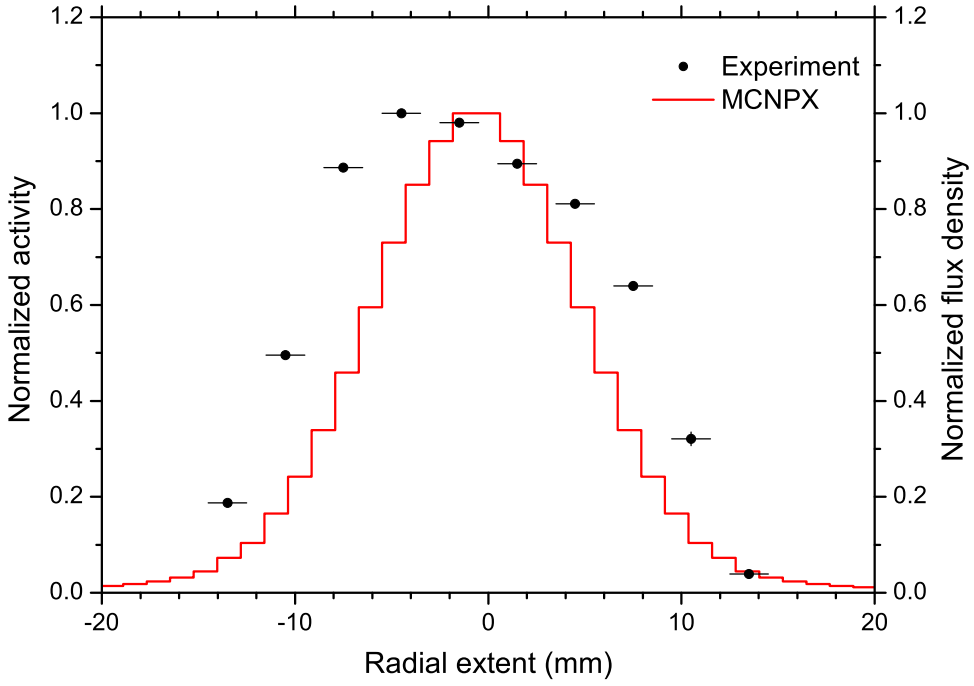

Figure 6.5: Radial distributions of measured ^{59}Ni activity in the Ni monitor foil (solid symbols) and proton flux density calculated with MCNPX (histogram) at the exit of LiCl target no. 10. Both distributions have been renormalized relative to their respective maxima for purposes of comparison. Error bars are shown only where they exceed the symbol size.

(84%); five targets (74%); four targets (62%); three targets (49%). From a practical point of view, a stack consisting of six or seven encapsulated targets may be the most sensible choice for a 200 MeV production target system.

6.4 Investigation with 66 MeV protons

Several Al-encapsulated LiCl targets were bombarded with 66 MeV protons to obtain ^{28}Mg solution for the radiochemical investigation. Unfortunately, a meticulous record on some of these bombardments were not kept. For this reason, it was recently decided to make a new batch of targets and test them thoroughly in the Elephant. At the time of writing, two bombardments have been completed in this new investigation. The two Al-encapsulated LiCl targets were individually bombarded in a standard production target holder with 66 MeV proton beams of 65 and 90 μA, respectively. The bombardment with 65 μA beam intensity lasted one hour and the second bombardment at 90 μA lasted two hours. Since these were relatively high beam intensities, it was necessary to make provision for the expansion of the LiCl salt when it melted. It is expected that the bulk of the LiCl will be in a molten state during a bombardment. The expansion due to the solid-to-liquid phase transition is quite substantial, of the order of 37%, based on the data of Delobbe-Lussier [Del2013]. The LiCl tablets consisted of 7.0 g compressed powder each, equivalent to a thickness of 2.23 g/cm^2 during bombardment. The Al capsules had just the right amount of extra space inside to accommodate the expected expansion. The tablets were sealed inside the capsules under vacuum. The energy window of the molten LiCl was $61.5 \rightarrow 40.5$ MeV and for the whole encapsulated target it was $62.6 \rightarrow 38.9$ MeV. The corre-

sponding thermal loads were 1.54 and 2.13 kW with beams of 65 and 90 μA, respectively. The heat was effectively removed with fast-flowing cooling water, as described in Chapter 2.

Both targets looked fine after the bombardment with no visible evidence of damage. After decapsulation and dissolution, counting sources in serum vials were prepared from a fraction of the target solution in each case, as described in the previous section. The yields obtained (1.8 and 5.0 MBq) are in agreement with the expected yields, within the experimental uncertainty. Clearly, the production rate is very small with a 66 MeV proton beam and a significantly higher beam energy is required to obtain a useful yield. The main aim of the bombardments at 66 MeV, however, was to investigate the thermal performance of the targets. The fact that they can withstand thermal loads in excess of 2 kW is a very reassuring result.

The choice of capsule material was discussed prior to the bombardment. It was decided to use Al for the initial work and to change to Nb only if problems were experienced. As these targets seem to behave well with Al encapsulation, it is not deemed necessary to expand the investigation to Nb encapsulation at this stage.

To conclude this section, it is worth mentioning that many of the chlorides can, in principle, serve as target materials for ^{28}Mg production. The question on how these targets behave in high-intensity bombardments is relevant. At iThemba LABS, encapsulated RbCl targets with a geometry and construction similar to the LiCl targets described above have been employed for several years to produce ^{82}Sr under a contract for the DOE in the United States. About 30 of these targets were bombarded with beams of about 90 μA to accumulated charges of 10 000 μAh or more. This is ample proof that chloride targets in a molten state can withstand extended bombardments under conditions where the beam power density is large (of the order of 1 kW/cm^2 – see also Section 2.3.4).

6.5 Production prospects at iThemba LABS

According to the staff of the Accelerator Department of iThemba LABS, the SSC can currently produce 200 MeV proton beams up to a maximum intensity of only about 2 μA. This translates into a production rate of about 12 MBq/h for a full stack of targets, which is rather limiting. It is also impossible at present to transport a 200 MeV proton beam to the radionuclide production vaults as some beam transport elements were only designed for a maximum of 100 MeV, most notably the switcher magnet which selects between therapy and radionuclide production. The cyclotron staff are confident that 100 MeV proton beams of 50 μA can be delivered to the radionuclide production stations with the present infrastructure. This will give a production rate of about 30 MBq/h (i.e. just short of 1 mCi/h). It is, therefore, possible to make relatively small quantities of ^{28}Mg with the SSC, useful for experimental purposes. Bulk production, however, is not presently a possibility.

6.6 Further Monte Carlo modelling

The development of the MCNP (Monte Carlo N-Particle) code system progressed through numerous convoluted stages (including name changes) spanning many decades and it is, in fact,

still under development. In 1995, a split occurred amongst the developers and two versions of the code emerged, MCNP4 and MCNPX. The separate development of MCNP and MCNPX persisted until 2011. Eventually, the two development teams joined forces again with the release of MCNP6. This short summary does not do justice to the rather rich history of MCNP, nevertheless, what is important here is to mention that the focused beam source option was implemented only in the final release of MCNPX [Pel2011b] after having been promised to users for some time. The code cannot transport the beam through electric and magnetic fields and depends on essential accelerator beam parameters as input. The beam is assumed to be transported through a field-free drift region between the exit of the last focusing magnet system and the target. The relevant beam emittance values in two orthogonal directions to the beam direction have to be specified in the input as well as the drift length (in cm) and spot size (in FWHM) on the target. Estimates for these parameters were supplied by the Accelerator Department: $\epsilon_x = 14$ π-mm-mrad, $\epsilon_y = 5$ π-mm-mrad with a drift length of $L = 150$ cm. The beam spot on target was assumed to be circular. Calculations were performed for several values of the beam spot size, as summarized in Table 6.2 for the last LiCl target in the 200 MeV stack, where they are compared with the corresponding results obtained using the cookie cutter cell option.

With a beam spot FWHM of 1.5 mm, the focused beam and cookie cutter options essentially give the same results. By increasing the beam spot FWHM to 5 mm and 8 mm, respectively, the ouscattering losses increase somewhat, as expected. The losses are slightly larger when the cookie cutter cell option is used, which is rather unexpected. For all practical purposes, however, the differences in the results obtained with the two beam options are not significant.

6.7 Conclusion

At iThemba LABS, a ^{28}Mg production rate of about 30 MBq/h is possible with the existing Elephant infrastructure and a 100 MeV proton beam on a stack of three encapsulated LiCl targets. This is sufficient for producing relatively small quantities for experimental purposes but bulk production is not a possibility. The loss of beam by outscattering in a relatively long stack of relatively small targets was investigated experimentally with a 200 MeV beam, as well as by means of Monte Carlo simulations with the radiation transport code MCNPX. These results clearly show that outscattering losses are not serious. In principle, the yield can be increased about fourfold if the intensity of 200 MeV beams can be increased to about 50 μA. In principle, such a capability can be developed, should such a need arise in future.

Table 6.2: Ratio of proton flux in LiCl target no. 10 relative to the incident 200 MeV beam flux, corrected for beam attenuation due to non-elastic nuclear interactions.

Beam spot FWHM (mm)	$\frac{1}{P_{10}}\left(\frac{J_{10}}{J_0}\right)$	
	Focused beam	Cookie cutter cell
1.5	0.79	0.79
5.0	0.77	0.76
8.0	0.73	0.70

Chapter 7

Radionuclides of Ir and Re in Proton-Induced Reactions on ^{192}Os

7.1 Introduction

The radionuclide ^{186}Re has been described as an ideal radionuclide for radioimmunotherapy because of its suitable decay properties ($E_{\beta^- max}$ = 1.07 MeV, β^- = 92.53%, $T_{1/2}$ = 3.7183 d) [Fir2004, Zhu1997]. For its no-carrier-added production with accelerated charged particles, the ^{186}W(p,n)^{186}Re and ^{186}W(d,2n)^{186}Re nuclear reactions were studied in some detail [Tar2006, Tar2007a, Tar2003]. Since tungsten is not a mono-isotopic element (the amount of ^{186}W in natural tungsten is only 28.6%), for practical productions both methods require highly enriched (>99%) ^{186}W target material to decrease the yields of the longer-lived undesirable rhenium radio-contaminants [i.e. ^{183}Re ($T_{1/2}$ = 70 d), ^{184m}Re ($T_{1/2}$ = 169 d), ^{184g}Re ($T_{1/2}$ = 38 d)] [Fir2004]. Even if 100% enriched ^{186}W material is used, the formation of ^{184}Re via the ^{186}W(p,3n)^{184}Re (Q = −15.21 MeV) and the ^{186}W(d,4n)^{184}Re (Q = −17.44 MeV) reactions limits the useful production energy windows from the relevant thresholds up to 15.3 and 17.6 MeV, respectively, for the (p,n) and (d,2n) reactions [Pri2012]. An additional disadvantage of the deuteron-induced reaction is the limited availability of deuteron beams for radionuclide production purposes in recent years.

This chapter reports the results of an investigation into a possible alternative production method based on the ^{192}Os(p,α3n)^{186}Re nuclear reaction. We measured the excitation function of this process for the first time from its threshold energy (E_{thr} = 13.37 MeV) up to 66 MeV.

A literature study revealed that charged particle induced nuclear reactions on ^{192}Os have also been studied to some extent for the production of the therapy-relevant radionuclide ^{192}Ir and some isotopes of Pt. The main motivation for these works was to evaluate alternative production methods for these radionuclides. Hilgers *et al.* [Hil2005] compared reactor and cyclotron production of ^{192g}Ir ($T_{1/2}$ = 78.83 d) used in brachytherapy. They measured the excitation function of the ^{192}Os(p,n)^{192g}Ir reaction up to 20 MeV. The aim was also the same in the work of Tàrkànyi *et al.* [Tar2007b], however, these authors investigated the ^{192}Os(d,2n)^{192g}Ir process for production purposes. Qaim *et al.* [Qai2009] investigated the ^{192}Os(^{3}He,4n) reaction in some detail for the production of ^{191}Pt ($T_{1/2}$ = 2.8 d). This radionuclide has found application both in therapy and in environmental studies (cf. Tinker *et al.* [Tin1991], Bonardi *et al.* [Bon1998]).

Since our bombarding energy was relatively high, i.e. 66 MeV, we were able to observe the presence of several iridium radionuclides ($^{188\rightarrow192}$Ir) in the activated ^{192}Os samples. The excitation functions for their formation in ^{192}Os + p nuclear reactions are useful for the following reasons:

1. The new data for the ^{192}Os(p,n)^{192}Ir reaction not only can validate the previous results [Hil2005] but also extend the database up to 66 MeV.

2. Since the ^{186,187,188,189,190}Ir radioisotopes are potential contaminants in the case of ^{192}Ir production, the knowledge of their excitation functions can be used to calculate practical production parameters for ^{192}Ir (i.e. irradiation time, energy window, cooling time, etc.)

3. No earlier cross-section data could be found in the literature for ^{186,187,188,189,190}Ir produced via ^{192}Os + p reactions. Also, the MENDL-2P data library [Shu1988] has no entry for Os + p reactions, a further indication that experimental data were not available for comparison with theoretical predictions at that time.

It was decided, therefore, to also extract cross sections for the ^{192}Os(p,n)^{192}Ir, ^{192}Os(p,3n)^{190}Ir, ^{192}Os(p,4n)^{189}Ir, ^{192}Os(p,5n)^{188}Ir, ^{192}Os(p,6n)^{187}Ir and ^{192}Os(p,7n)^{186}Ir nuclear reactions from their respective thresholds up to 66 MeV. Additionally, the experimental data are compared with predictions using the code ALICE/ASH and the TENDL-2012 library. The relevant part of the Karlsruhe Chart of the Nuclides is shown in Fig. 7.1.

7.2 Experimental method

The stacked-foil activation technique (see Appendix A) was employed to measure the excitation functions of the ^{192}Os(p,xn)^{186,187,188,189,190,192}Ir and ^{192}Os(p,X)^{186}Re nuclear reactions from threshold up to 66 MeV. Two separate irradiations were performed, one at the separated-sector

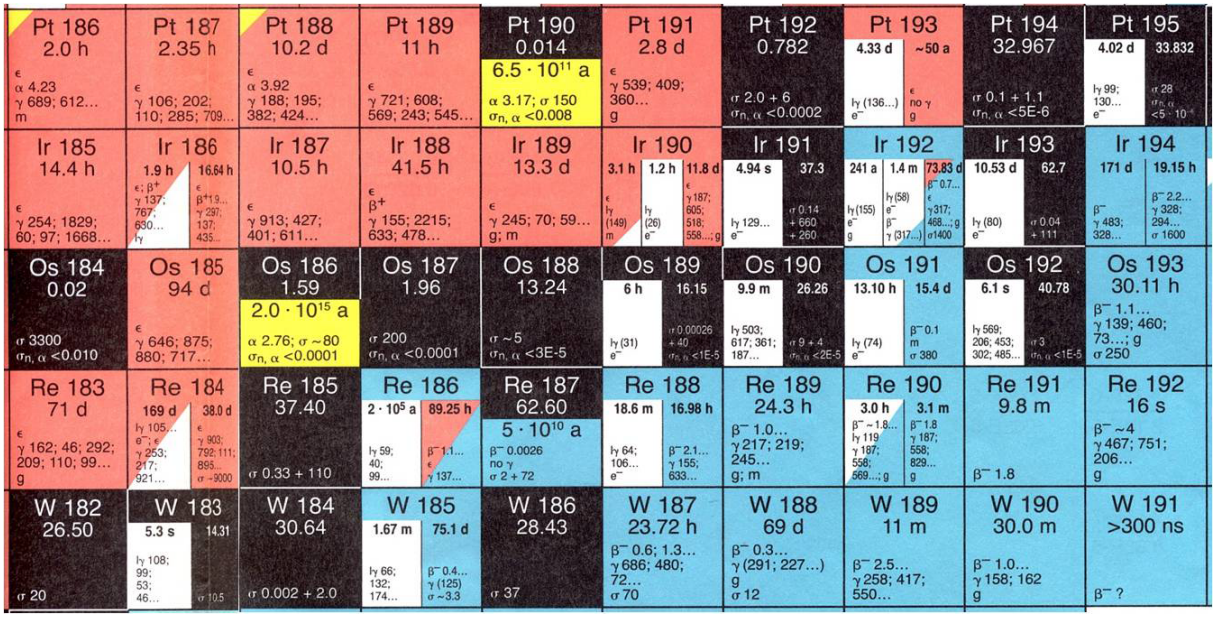

Figure 7.1: Relevant part of the Karlsruhe Chart of the Nuclides, showing the relevant Ir, Os, Re and W nuclides. With permission © Nucleonica GmbH 2012.

cyclotron facility of iThemba LABS and one at the MGC-20 cyclotron of ATOMKI. The investigated energy region was 66 $\rightarrow$ 12 MeV at iThemba LABS, and in the additional experiment at ATOMKI the ^{192}Os(p,n)^{192}Ir reaction was studied at lower energies, namely 16.9 $\rightarrow$ 7.7 MeV.

7.2.1 Target Preparation

The enriched ^{192}Os (> 99%, Trace Sciences International, Richmond Hill, Canada) targets were prepared by electro-deposition using a method based on the work of Chakrabarty *et al.* [Cha2001], which substitutes the tedious and dangerous OsO_4 process [Stu1983] with a more controllable volatilization of Os metal as $OsCl_4$. The isotopic composition of the enriched Osmium is listed in Table 7.1. A sketch of the electrolytic cell, designed to simultaneously produce four targets, is shown in Fig. 7.2. It consisted of a cylindrical Teflon chamber (35 mm in diameter and 50 mm high) with an axial Pt rod in the centre as the anode. Thin Cu substrates, serving both as cathodes and target backings, were made of 50 μm thick Cu foil (> 99%, Goodfellow, UK), each with a diameter of 12 mm. These foils were mounted in tight-fitting cavities on the wall of the cylinder. The diameter of the electro-deposited Os layers was 10 mm. A brief description of the electro-deposition procedure is as follows:

The Cu backing foils were first washed with acetone, then with 0.5 M HNO_3 and finally with distilled water before being dried with acetone, in order to remove all surface impurities. Each target backing mounted on the electrolytic cell was supported by a 1 mm thick copper disc, all electrically connected to form the cathode. Metallic ^{192}Os (68.7 mg of grey metal powder)

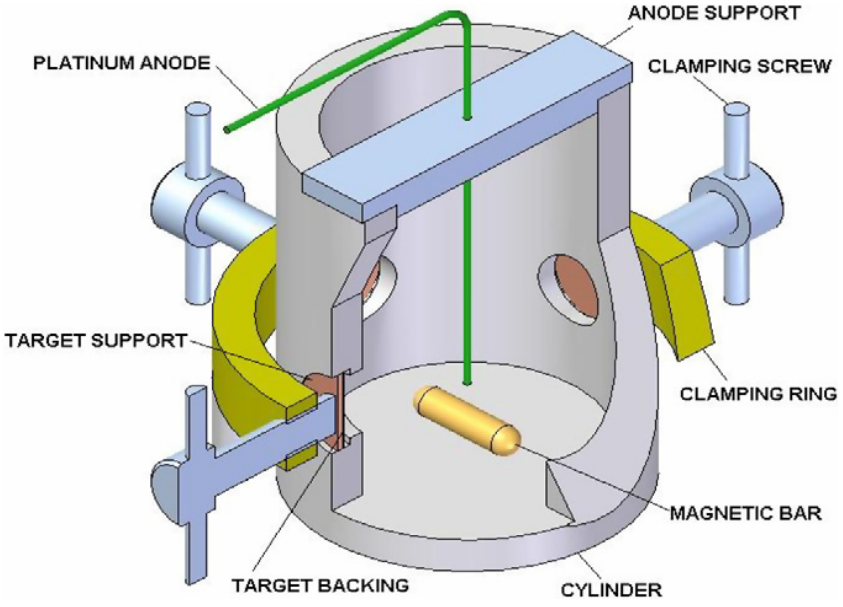

Figure 7.2: Sketch of the electrolytic cell used for preparing the enriched ^{192}Os targets.

Table 7.1: Isotopic composition of the enriched osmium target material[a].

Isotope	^{184}Os	^{186}Os	^{187}Os	^{188}Os	^{189}Os	^{190}Os	^{192}Os
Enrichment (%)	< 0.005	< 0.005	< 0.005	0.101 ± 0.01	0.160 ± 0.01	0.344 ± 0.01	99.395 ± 0.019

[a]Supplied by Trace Sciences International, Richmond Hill, Canada.

was transferred into a 10 mL flat-bottomed test tube with a magnetic stirrer bar placed inside. The test tube was connected to a condenser and through the condenser to a 50 mL receiver flask containing 5 mL of distilled water, so that a closed system for dissolution/distillation was obtained. A small quantity of *aqua-regia* (5 mL) was added to the test tube before it was closed using a glass stopcock, followed by heating on a hot plate while stirring. After the complete dissolution of the Os powder, the heating temperature was slowly increased further until the whole solution containing the Os in the tube was distilled as $OsCl_4$ and collected into the receiver. Then the test tube and the condenser were washed repeatedly with small fractions (about 2 mL each) of distilled water. These washings were also transferred to the receiver flask and the solution was finally diluted with more distilled water until an acidic solution of 30 mL was obtained. This solution was then used as the stock solution for the electro-deposition of 16 Os targets (four batches of 4 targets each).

During the first three electro-deposition runs, 8 mL of stock solution was used to prepare the electrolytic bath for each run. To each fraction of stock solution was added 720 mg sulphamic acid and 2080 mg Na_2HPO_4 to act as buffer. The pH value was adjusted to 10–12 by adding 10 M NaOH, giving a total bath volume of 30 mL in all cases. During this step the colorless solution changed to a pale yellow color. Analytical grade reagents were used throughout this work and were obtained from Merck (SA) Pty. Ltd. or Sigma-Aldrich GmbH.

During each electro-deposition run, the temperature of the bath was maintained between 80 and 90 °C while the current was typically around 450 mA. The potential typically varied in the range 5.3–5.8 V. In the first and second runs, 1 h electro-deposition times resulted in an average of 2.5 mg ^{192}Os deposited onto the copper backings. To obtain even thicker targets, the time of electro-deposition was then increased to 2 h. The average electro-deposition mass obtained on each backing was 4.00 mg in the third run. For the fourth and last run, the remaining stock solution (6 mL) with 2 h electro-deposition time resulted in an average ^{192}Os mass per backing of 3.3 mg, which was consistent with the previous results. The surface uniformity of the deposits was investigated using an optical microscope and appeared to be of high quality.

7.2.2 Irradiations at iThemba LABS

The electroplated ^{192}Os targets were activated in a stacked-foil arrangement in the RERAME II irradiation chamber at iThemba LABS. For this run, all 16 Os targets were irradiated. The general details of Section 3.2 and Appendix A are again applicable, therefore only salient features are highlighted here.

The samples were interspersed with different monitor and energy degrader foils. Cu target backings and beam intensity monitors with nominal thicknesses of 50 and 9.5 μm, respectively, as well as Al energy degraders and beam intensity monitors with nominal thicknesses of 1200 μm and 50 μm were supplied by Goodfellow, Cambridge, UK. Their individual thicknesses were accurately determined by weighing. The incident proton energy was 66.5 MeV as measured using a calibrated analysis dipole magnet. The beam current fluctuated between 60 and

100 nA during the bombardment, which lasted for 2.55 h. The current was logged at 1 second intervals for the duration of the run.

7.2.3 Irradiations at ATOMKI

The difficulty in making the targets, amongst other reasons, led to the decision to re-use the same foils in Debrecen for the lower energy bombardment. A long "cooling time" of 1.6 y was applied between the two stack irradiations for the Ir radioisotopes of interest formed during the first irradiation to completely decay, with one exception, namely the long-lived metastable state of ^{192}Ir, i.e. ^{192m2}Ir ($T_{1/2} = 241$ y). This half-life is too long to affect any of the experimental results, however, even though it decays by *IT*(100%). For this run only 8 samples were used. The incident proton energy was 17.5 MeV as measured using the two-probe relative phase difference method [Kor1994]. This method has an intrinsic accuracy of better than 0.1%. The beam current was around 60 nA and the irradiation lasted for 4.5 h.

Although the accumulated charges were measured directly by means of well calibrated current integrators, IAEA recommended monitor reactions were also employed as consistency checks [Gul2001]. In Faure, the ^{nat}Al(p,X)^{24}Na and ^{nat}Cu(p,X)^{62}Zn processes were used for this purpose while in Debrecen the ^{nat}Cu(p,n)^{65}Zn monitor reaction was used. The beam fluxes determined by direct integration agreed well (within 5%) with the monitor reaction results. In Fig. 7.3, the measured cross sections of ^{65}Zn, ^{62}Zn and ^{24}Na are compared with the recommended IAEA curves. These results also verify the calculated average proton energy values for all foils throughout the stacks, obtained by means of the stopping-power compilation of Anderson and Ziegler [And1977].

7.2.4 Data analysis

After the bombardments, the activated samples were individually measured by means of off-line γ-ray spectrometry. The decay data of the Ir radioisotopes were taken from the Nudat 2.5 database [Kin1996]. The energies and branching ratios used in this work for analysis are listed in Table 7.2. Spectra from each sample were collected several times. The measuring times were progressively increased to obtain sufficient statistics for Ir radioisotopes with longer half-lives. The measurements were performed nondestructively using calibrated HPGe detectors at both laboratories, having relative efficiencies of 15% (Faure) and 10% (Debrecen). Both detectors had a resolution of 1.8 keV FWHM at 1.33 MeV.

The peak-area analysis was done using dedicated software, Silena EMCA 2000 version 2.03.0 in Faure and the FGM program [Sze1985] in Debrecen. The cross sections were calculated by applying the well-known activation formula (see Appendix A). The total uncertainties in the measured cross sections were obtained by summing all the contributing uncertainties in quadrature and are expressed with 1σ (68%) confidence level. A variable component includes the uncertainty due to counting statistics and photo-peak integration as well as the uncertainty associated with the beam-loss correction. The latter did not exceed 2%. Systematic uncertainties were similar to that of Section 3.2.4, estimated to be about 7% in total for the

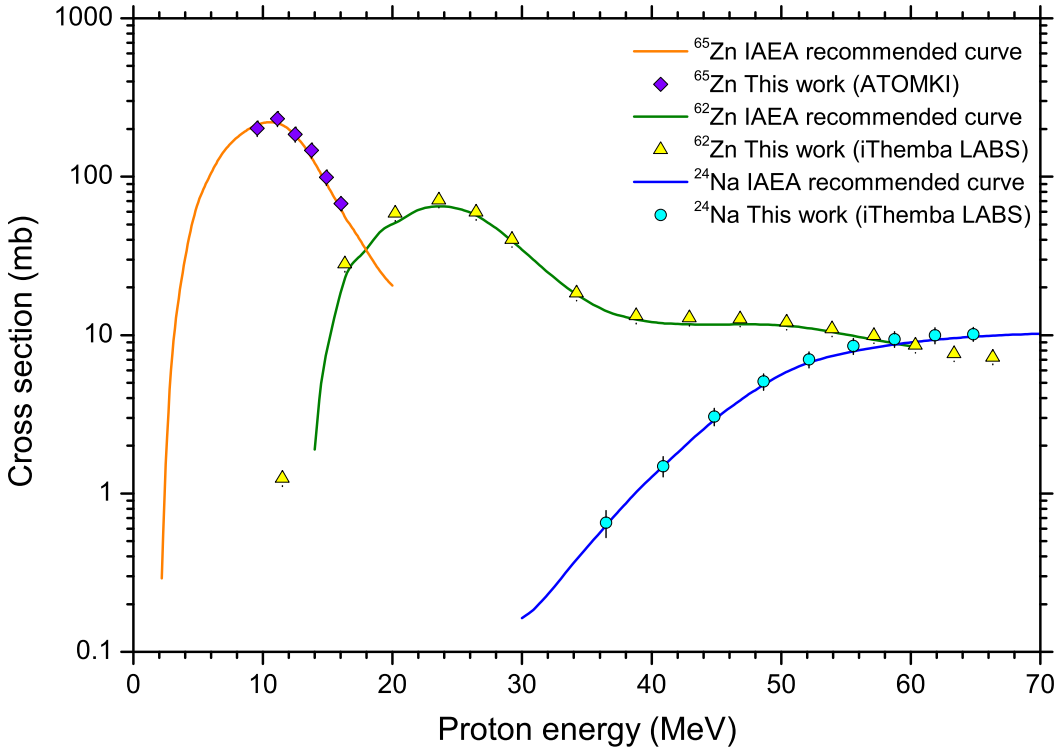

Figure 7.3: Excitation functions of the ^{nat}Cu(p,X)^{62}Zn and ^{nat}Al(p,X)^{24}Na and ^{nat}Cu(p,n)^{65}Zn monitor reactions.

Table 7.2: Investigated Ir and Re radionuclides and their decay characteristics[a] as well as their respective Q-values[b].

Nuclide	Half-life	Production Reaction	Q-value (MeV)	γ-rays (keV)	Intensity (%)
^{186g}Ir	16.64 h	^{192}Os(p,7n)^{186}Ir	-45.92	137.16	41.0%
				296.90	62.3%
				434.84	33.9%
				773.28	8.9%
^{187}Ir	10.5 h	^{192}Os(p,6n)^{187}Ir	-37.47	427.12	4.12%
				610.68	3.93%
				912.95	4.79%
^{188}Ir	41.5 h	^{192}Os(p,5n)^{188}Ir	-30.60	155.03	29.7%
				477.99	15.0%
				632.99	18.0%
^{189}Ir	13.2 d	^{192}Os(p,4n)^{189}Ir	-22.42	245.09	6.0%
^{190}Ir	11.78 d	^{192}Os(p,3n)^{190}Ir	-16.05	557.99	30.1%
				605.21	39.9%
^{192}Ir	73.83 d	^{192}Os(p,n)^{192}Ir	-1.83	316.51	82.81%
				468.07	47.83%
^{186}Re	3.718 d	^{192}Os(p,α3n)^{186}Re	-13.30	137.16	9.42%

[a]Taken from Nudat 2.5 [Kin1996] but compared with Firestone & Eckström [Fir2004].
[b]Calculated using QCalc [Pri2012].

radio-iridiums. Unfortunately, ^{186}Re has only one measurable γ-line at 137.157 keV (9.42%) which was disturbed by the 136.474 keV γ-line of ^{57}Co (10.68%) that is produced in the copper backing. The MCA program used was able to fit the two overlapping peaks in this energy region but this increased the total uncertainty up to 16%. The energy uncertainties have been calculated as described in Appendix C.

7.3 Results and discussion

7.3.1 The ^{192}Os(p,7n)^{186}Ir reaction

One prominent metastable state, ^{186m}Ir ($T_{1/2}$ = 1.90 h) decays by $EC + \beta^+$ (75%) to stable ^{186}Os and by IT (25%) to the ground state of ^{186}Ir ($T_{1/2}$ = 16.64 h). The cross sections for the ^{192}Os(p,7n)$^{186(0.25m+g)}$Ir reaction are presented in Fig. 7.4. As the (p,7n) reaction peaks above 66 MeV, our new data (6 points) only cover the onset part of the excitation function curve. In the investigated energy region, the ALICE/ASH calculation reproduces the experimental results quite well, whereas the TENDL-2012 library shows the now familiar shift towards lower energies but reproduces the shape rather well.

7.3.2 The ^{192}Os(p,6n)^{187}Ir reaction

The short-lived metastable state, ^{187m}Ir ($T_{1/2}$ = 30.3 ms) decays completely to the ground state (IT = 100%). This ground state ($T_{1/2}$ = 10.5 h) decays further by EC (100%) to ^{187}Os. Our only data (8 cross sections) are shown in Fig. 7.4. The excitation function curve for the ^{192}Os(p,6n)$^{187(m+g)}$Ir reaction peaks at about 55 MeV with a maximum just below 580 mb. The ALICE/ASH calculation describes the onset part of the experimental curve well, however, it has a higher maximum at 740 mb and somewhat overpredicts the measured values beyond 54 MeV. The TENDL-2012 values are closer to the measured data in this case but it is still very slightly shifted towards lower energies.

7.3.3 The ^{192}Os(p,5n)^{188}Ir reaction

From the point of view of the decay mode, ^{188}Ir is a rather simple. There are no prominent metastable states, thus only the ground state needs to be considered in the analysis. It has a half-life of 41.5 h and decays by EC (100%) to ^{188}Os. The excitation function curve has a maximum of 880 mb at 44.5 MeV. Only our data (10 data points) are available for this reaction in the literature in the investigated energy region, as shown in Fig. 7.5. The theoretical calculation by means of ALICE/ASH also predicts the position of the maximum at the same energy but with a lower value (780 mb). TENDL-2012 shows good agreement in shape as well but has an even lower peak for the cross-section maximum.

7.3.4 The ^{192}Os(p,4n)^{189}Ir reaction

In addition to the ground state of ^{189}Ir ($T_{1/2}$ = 13.2d), one metastable state ^{189m}Ir ($T_{1/2}$ = 13.3 ms) is also populated during this process. It decays rapidly to the ground state by IT (100%),

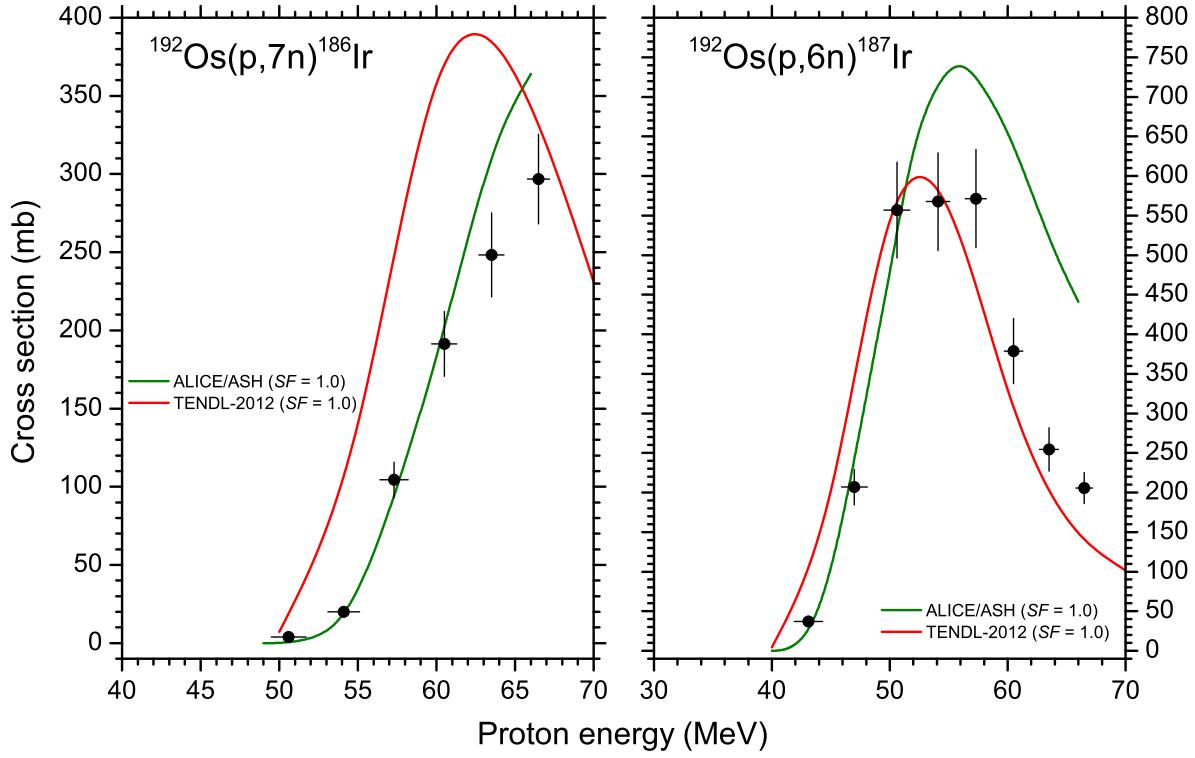

Figure 7.4: Excitation functions for the production of ^{186}Ir and ^{187}Ir in the bombardment of ^{192}Os with protons. Black circles: this work.

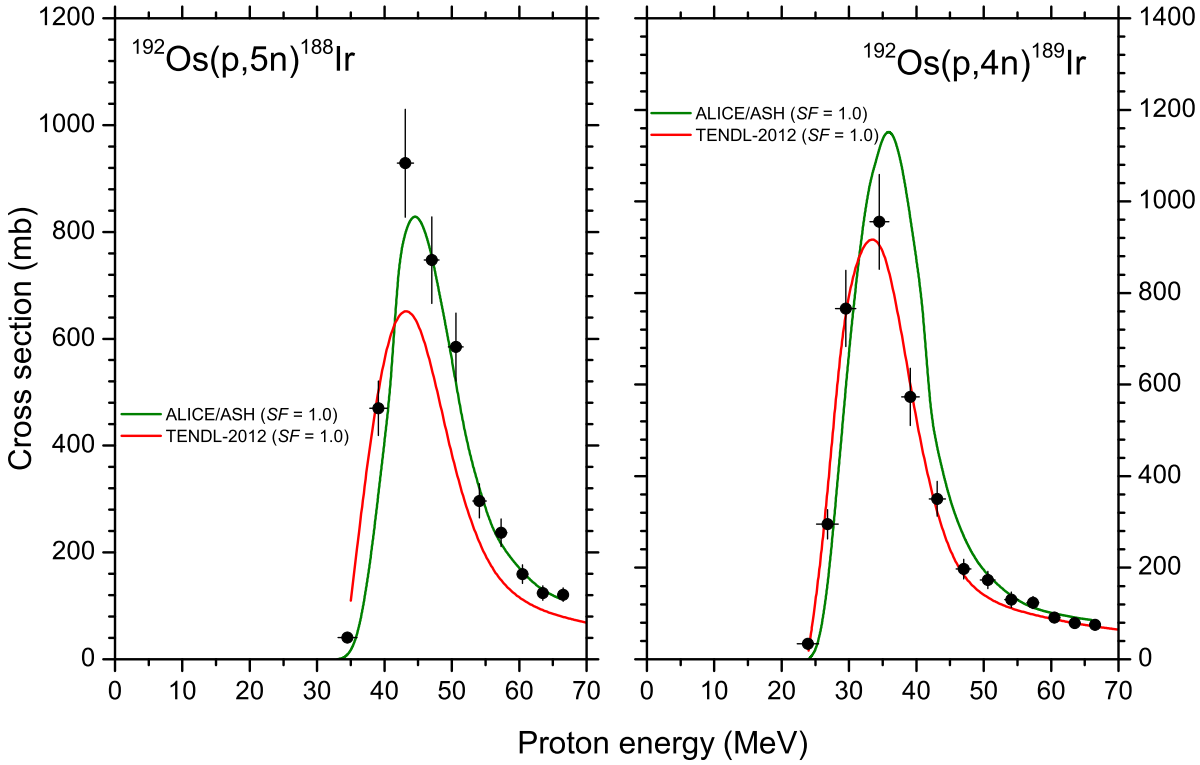

Figure 7.5: Excitation functions for the production of ^{188}Ir and ^{189}Ir in the bombardment of ^{192}Os with protons. Black circles: this work.

therefore the cumulative ^{189}Ir ground state cross sections are measured. The ground state feeds the metastable state, ^{189m}Os ($T_{1/2} = 5.8$ h) which also decays by IT (100%) to the ground state of ^{189}Os. As with the previous reaction, we also report here cross-section values for the first time (see Fig. 7.5). Our excitation function curve for the ^{192}Os(p,4n)$^{189(m+g)}$Ir reaction shows a peak (960 mb) at about 34 MeV. The ALICE/ASH theoretical excitation function also behaves similarly; it predicts a maximum value of 1120 mb at 35 MeV. It should be noted, however, that beyond the peak the ALICE/ASH results are systematically higher than the experimental data. The TENDL-2012 library predicts the excitation function extremely well in this case.

7.3.5 The ^{192}Os(p,3n)^{190}Ir reaction

Two relatively short-lived metastable states of ^{190}Ir are formed via the (p,3n) reaction: ^{190m1}Ir ($T_{1/2} = 1.2$ h) and ^{190m2}Ir ($T_{1/2} = 3.23$ h). The m1 state decays by IT (100%) to the ground state of ^{190}Ir ($T_{1/2} = 11.78$ d) while the m2 state decays predominantly to ^{190}Os ($T_{1/2} = 9.9$ m) by electron capture ($EC = 94.4\%$). Unfortunately, the m2 state also populates ^{190m1}Ir by IT (5.6%). On the other hand, the ground state of ^{190}Ir also feeds ^{190}Os. Since we had relatively long cooling times before the activity measurements (> 15 h), it was only possible to extract the excitation function of the ground state after the complete decay of the directly-formed m1 and m2 states. Note, however, that the contribution of the m2 metastable state is only 5.6% in this case.

Prior to our study, no cross-section data for the ^{192}Os(p,3n)$^{190(m1+0.056m2+g)}$Ir process had

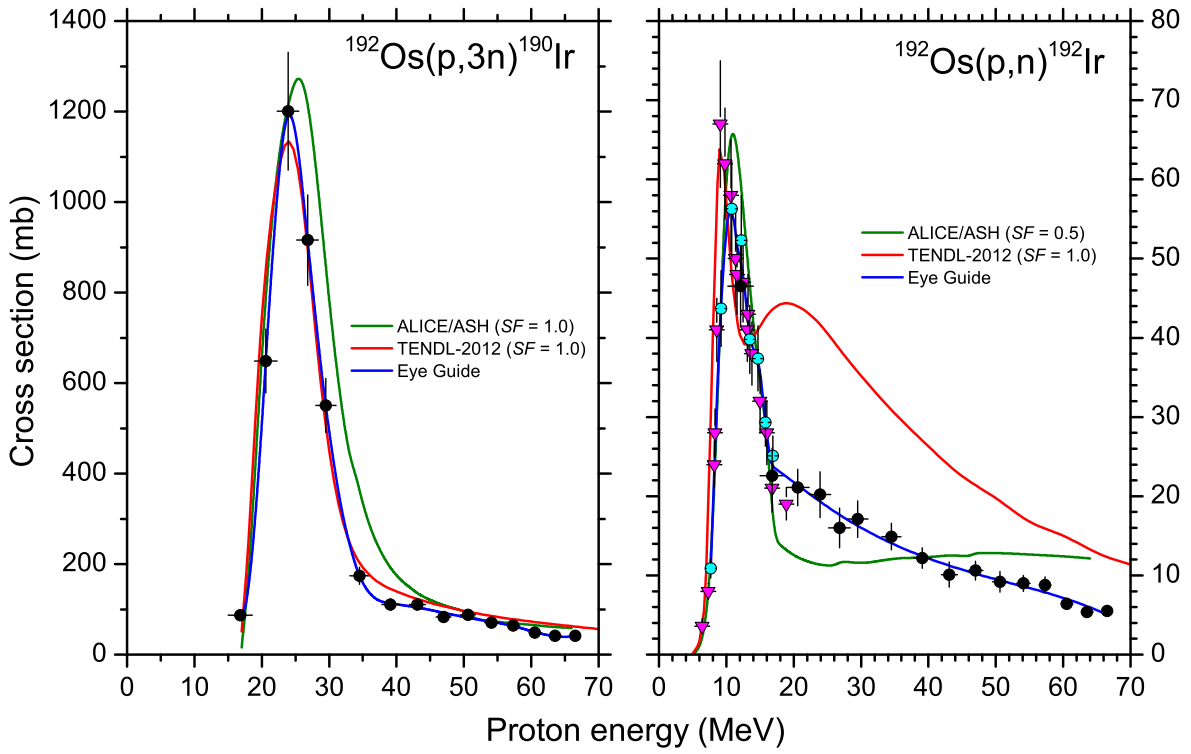

Figure 7.6: Excitation functions for the production of ^{190}Ir and ^{192}Ir in the bombardment of ^{192}Os with protons. Black circles: this work, iThemba LABS. Blue circles: This work, ATOMKI. Red triangles: Hilgers *et al.* [Hil2005].

been reported in the literature. Our measured values (15 data points) are presented in Fig. 7.6. The excitation function curve for this reaction peaks at about 24 MeV with a maximum of 1180 mb. The ALICE/ASH calculation also reproduces both the position and the maximum (25 MeV and 1220 mb) of the excitation function curve quite well. Naturally, because the theoretical calculation cannot distinguish the isomeric states explicitly and contain them all, the experimental curve is expected to be lower than the calculated one. In the case of TENDL-2012, however, the calculated curve is still lower than the measured data.

7.3.6 The ^{192}Os(p,n)^{192}Ir reaction

The ^{192}Os(p,n)^{192}Ir reaction populates several long-lived isomers of ^{192}Ir. Two metastable states, ^{192m1}Ir ($T_{1/2}$ = 1.45 m) and ^{192m2}Ir ($T_{1/2}$ = 241 y) decay predominantly by internal transition (IT = 99.98% and 100%, respectively) to the ground state, ^{192g}Ir ($T_{1/2}$ = 73.831 d). Due to the decay scheme of ^{192}Ir and our technical limitations, it was impossible to separately measure the excitation functions of these three isomers. In addition to the long half-life of the m2 state, making an activity measurement difficult, its strongest γ-line at 155.16 keV (0.0974%) is also too weak for successful off-line γ-ray analysis. Taking into account our measuring set-up, we could only extract the excitation function of the ground state after the complete decay of the directly-formed m1 state. As the duration of the bombardment was very short in comparison with the ^{192m2}Ir half-life, the contribution from its decay to the ground state yield was negligible.

Our systematic study resulted in 24 new cross-section values for the ^{192}Os(p,n)$^{192(m1+g)}$Ir reaction up to 66 MeV from the two experiments (16 from Faure and 8 from Debrecen). Our data shows a maximum of 56 mb at about 11 MeV. As is evident in Fig. 7.6, the present results are in good agreement with the data of Hilgers *et al.* [Hil2005]. Based on the two measurements, the database for this reaction seems to be consistent and can be used for estimating the available $^{192(m1+g)}$Ir yield in practical applications. Figure 7.6 also compares the experimental results with the ALICE/ASH predictions and TENDL-2012. The ALICE/ASH calculation correctly reproduces the position of the peak of the excitation function (at 11 MeV) but overpredicts the cross-section maximum by about a factor of two (note that in Fig. 7.6 the ALICE/ASH curve has been renormalized to the experimental data to effect a better comparison; $SF = 0.5$). One possible reason for the overprediction may be the fact that the calculation also contains some contribution attributed to the m2 metastable state, which is absent in the experimental data. However, based on the results of Hilgers *et al.* [Hil2005], this contribution is relatively small and cannot completely explain the relatively large discrepancy. The TENDL-2012 curve reproduces the primary peak well but shows a strange bump with a second maximum around 20 MeV. This anomaly has been explored further and is considered in Appendix F.

Hilgers *et al.* investigated the production possibility of ^{192g}Ir via the (p,n) reaction. They suggested using the 16 $\rightarrow$ 8 MeV energy window to prevent the formation of other, contaminating Ir radioisotopes. Having an incident proton energy higher than 16 MeV, the formation of ^{190}Ir ($T_{1/2}$ = 11.78 d, $Q = -16.05$ MeV) is possible in the target. From the point of view of any practical production, the presence of this radioisotope would be undesirable. Since we also measured cross sections for the ^{192}Os(p,3n)$^{190(m1+0.056m2+g)}$Ir reaction, we could calculate the

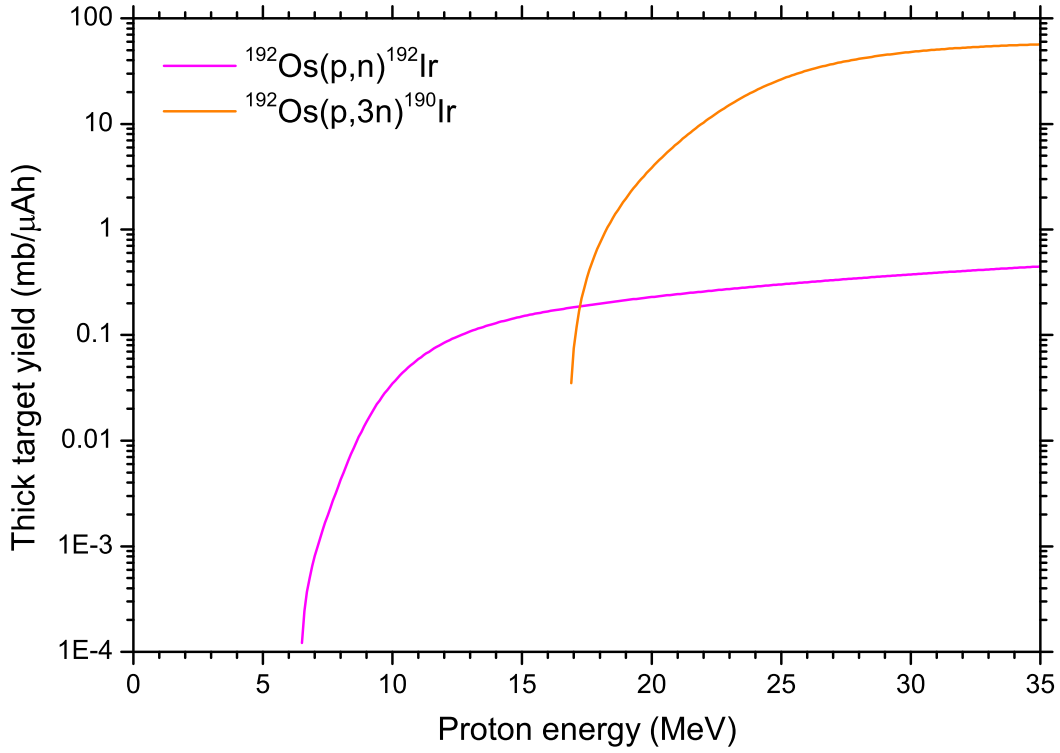

Figure 7.7: Integral physical yields for the production of ^{190}Ir and ^{192}Ir in the bombardment of ^{192}Os with protons.

integral yield of ^{190}Ir. The results are shown in Fig. 7.7, together with the calculated yields for ^{192}Ir. It can be concluded that the maximum incident bombarding proton energy must be kept strictly below 16.14 MeV otherwise a large amount of ^{190}Ir will be present at the end of bombardment (EOB). For example, at 17 MeV the ^{190}Ir contamination is already around 70%. This value will be unacceptable for practical production purposes. Although the ^{190}Ir/^{192}Ir activity ratio will decrease as a function of cooling time, it remains quite high even after one half-life of ^{192}Ir (2.2% after 78.83 d).

7.3.7 The ^{192}Os(p,X)^{186}Re process

The measured cross-section data for the ^{192}Os(p,X)^{186}Re ($T_{1/2} = 3.718$ d) nuclear process are presented in Table 7.3 and Fig. 7.8. This excitation function is dominated by the ^{192}Os(p,α3n)^{186}Re reaction, showing a maximum of about 82 mb at 24 MeV. The increase of the tail part of the curve is due to the contributions of other reactions which also form ^{186}Re, mainly via the ^{192}Os(p,2p5n)^{186}Re ($Q = -41.60$ MeV) reaction. The values of the TENDL-2012 library completely fail to reproduce the excitation function in the peak region.

Based on the results of our measurements, integral thick-target yields were also calculated for the production of ^{186}Re up to the threshold energy ($E_{thr} = 27.3$ MeV) of the ^{192}Os(p,α5n)^{184}Re reaction. This reaction produces the first longer-lived rhenium radio-contamination via this method. Therefore the available "longer-lived contamination free" yield is 7.76 MBq/μAh (0.21 mCi/μAh) in the energy region 13.4 $\rightarrow$ 27.3 MeV. The results can be seen in Fig. 7.9. For comparison we have also reproduced in Fig. 7.9 the thick-target yields of the ^{186}W(p,n) and

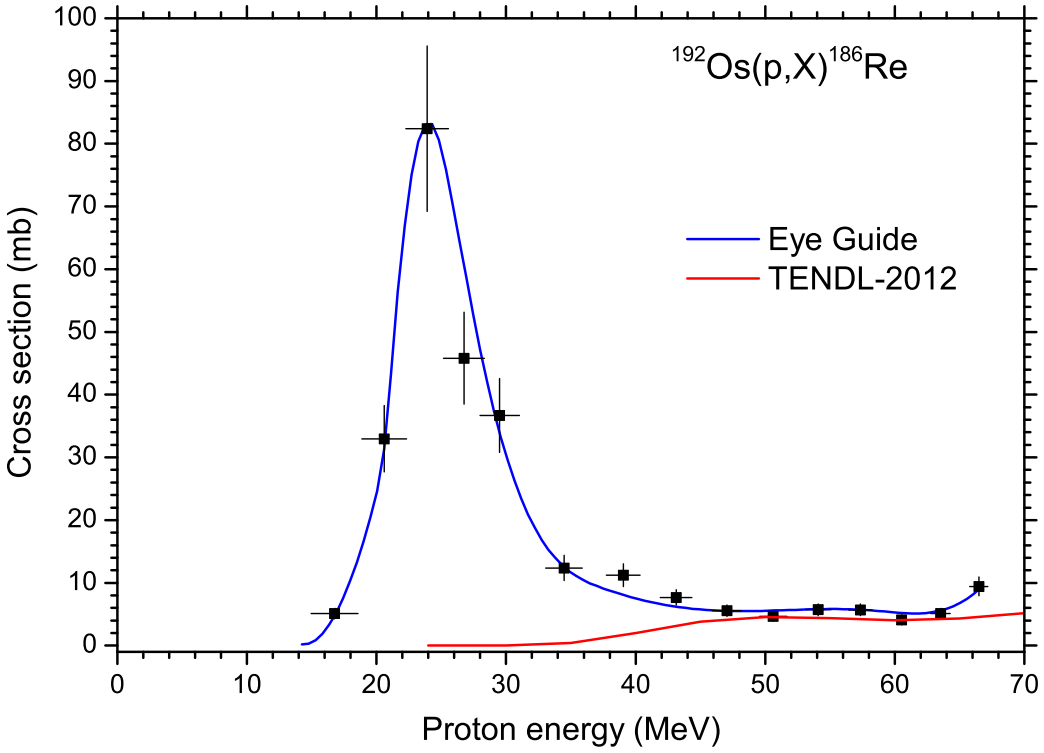

Figure 7.8: Excitation function for the production of ^{186}Re in the bombardment of ^{192}Os with protons.

^{186}W(d,2n) reactions up to their earlier-mentioned 15.3 and 17.6 MeV useful upper energies, respectively. These yield calculations were taken from the IAEA database [Gul2001]. As can be seen from Fig. 7.9, the ^{192}Os(p,α3n) reaction provides double the "longer lived contamination free" yield of the ^{186}W(p,n) reaction. However, if one has a multiparticle accelerator in this energy region, the ^{186}W(d,2n) process clearly seems to be the method of choice. A possible drawback of the ^{192}Os(p,X)^{186}Re method is the co-production of ^{189}Re ($T_{1/2} = 24.3$ h) and ^{188}Re ($T_{1/2} = 17$ h) via the ^{192}Os(p,α)^{189}Re ($Q = 6.96$ MeV) and the ^{192}Os(p,αn)^{188}Re ($Q = -0.072$ MeV) reactions, respectively. Due to their low threshold energies, the bulk of the ^{189}Re and ^{188}Re activities are formed below 14 MeV, therefore, the end of bombardment (EOB) total radio-rhenium contamination level could be significantly reduced if the production window is strictly kept at the energy region between 27.3 and 14 MeV. Additionally, using a proper cooling period, the contamination will automatically decrease below to required level.

The above discussion requires some clarification concerning the spectroscopy of ^{186}Re and the radio-contaminants ^{188}Re and ^{189}Re. Unfortunately, the useful characteristic γ-lines from the decay of these radionuclides are also present in the decay of ^{186}Ir, ^{188}Ir and ^{189}Ir, respectively. In the case of ^{186}Re, the problem was not serious as ^{186}Ir formation essentially only takes place above 50 MeV (see Fig. 7.4), which is above the main energy region of interest for ^{186}Re. Also, data for ^{186}Ir could be extracted without any disturbance from ^{186}Re by using the 296.90 keV γ-line (branching ratio 62.3% for ^{186}Ir but only 0.000053% for ^{186}Re). Furthermore, several days after EOB the much shorter-lived ^{186}Ir ($T_{1/2} = 16.64$ h) has decayed substantially compared to ^{186}Re ($T_{1/2} = 3.718$ d) and relatively long counting times produced reasonably good statistics for ^{186}Re using the 137.16 keV (9.42%) γ-line. The values above 50 MeV could be

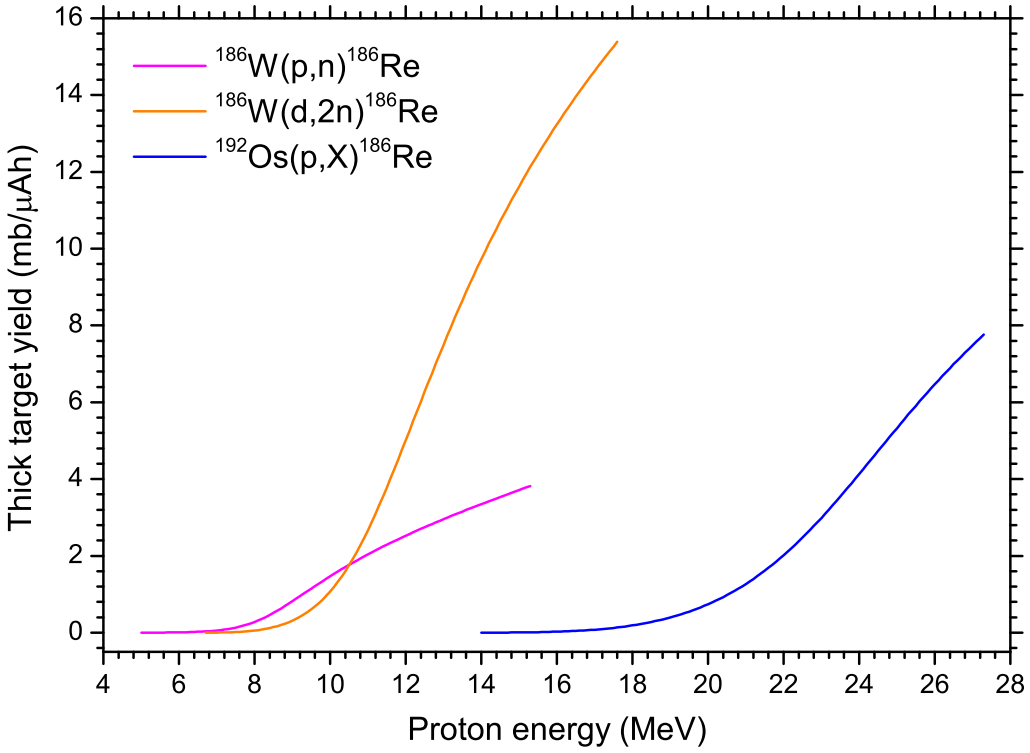

Figure 7.9: Calculated integral thick-target yields for the ^{186}W(p,n)^{186}Re, ^{186}W(d,2n)^{186}Re and ^{192}Os(p,α3n)^{186}Re reactions.

corrected by subtracting relatively small contributions from ^{186}Ir to those photo-peaks. In the cases of ^{188}Re ($T_{1/2}$ = 17 h) and ^{189}Re ($T_{1/2}$ = 24.3 h), the levels of contamination from the longer-lived ^{188}Ir ($T_{1/2}$ = 41.5 h) and ^{189}Ir ($T_{1/2}$ = 13.2 d), respectively, were far more severe in much larger overlapping energy regions. The situation worsened as a function of time. Similar "sweet spots" in terms of waiting time, such as for the assay of ^{186}Re, were simply not there for ^{188}Re and ^{189}Re. It finally became evident that to extract their excitation functions, chemical separation of the Ir from the Re would be required.

7.4 Conclusion

Excitation functions have been reported for the first time for the ^{192}Os(p,3n)^{190}Ir, ^{192}Os(p,4n)^{189}Ir, ^{192}Os(p,5n)^{188}Ir, ^{192}Os(p,6n)^{187}Ir and ^{192}Os(p,7n)^{186}Ir nuclear reactions up to 66 MeV. We have also extended the database of the ^{192}Os(p,n)^{192}Ir reaction with 24 new values up to this energy. The previous data by Hilgers *et al.* [Hil2005] below 24 MeV have also been experimentally confirmed for the first time. Based on the present yield calculations, the ^{190}Ir contamination level in ^{192}Ir productions can be evaluated as a function of energy. We also compared our results with predictions by means of the geometry-dependent hybrid model code ALICE/ASH as well as the TENDL-2012 library and found fair agreement for the majority of the reactions investigated.

According to the present results, the production of ^{186}Re via the ^{192}Os(p,α3n)^{186}Re reaction seems to be marginally superior in terms of yield than the ^{186}W(p,n)^{186}Re method in the case of accelerators capable of accelerating protons up to 30 MeV. Additionally, this method may be useful to co-produce the therapeutically relevant ^{192}Ir radioisotope if a stacked target

configuration is used. We have to say, however, that we were somewhat disappointed with the rather low cross sections extracted for the ^{192}Os(p,X)^{186}Re process. It was hoped that the study would reveal somewhat higher values than what was eventually found, in order to justify a sufficient waiting time for decay of the shorter-lived ^{188}Re and ^{189}Re contaminants to acceptably low levels. Nevertheless, relatively large batch productions are possible (provided sufficient ^{192}Os target material can be located at an affordable price). A significant advantage over the ^{186}W(p,n)^{186}Re reaction, however, could not be shown. With a 30 MeV commercial cyclotron (30 MeV for proton beams) with a 15 MeV deuteron-beam capability installed, the ^{186}W(d,n)^{186}Re reaction is, without any doubt, the production route of choice.

Table 7.3: Measured cross-sections for the ^{192}Os(p,X)^{186}Re process.

Proton energy (MeV)	Cross section (mb)
16.8 ± 1.8	$(5.10 \pm 0.80) \times 10^{+0}$
20.6 ± 1.7	$(3.29 \pm 0.53) \times 10^{+1}$
23.9 ± 1.6	$(8.24 \pm 1.32) \times 10^{+1}$
26.8 ± 1.6	$(4.58 \pm 0.73) \times 10^{+1}$
29.5 ± 1.5	$(3.67 \pm 0.59) \times 10^{+1}$
34.5 ± 1.4	$(1.24 \pm 0.20) \times 10^{+1}$
39.1 ± 1.3	$(1.12 \pm 0.18) \times 10^{+1}$
43.1 ± 1.2	$(7.70 \pm 1.20) \times 10^{+0}$
47.0 ± 1.1	$(5.60 \pm 0.90) \times 10^{+0}$
50.6 ± 1.1	$(4.60 \pm 0.70) \times 10^{+0}$
54.1 ± 1.0	$(5.70 \pm 0.90) \times 10^{+0}$
57.3 ± 0.9	$(5.60 \pm 0.90) \times 10^{+0}$
60.5 ± 0.8	$(4.20 \pm 0.70) \times 10^{+0}$
63.5 ± 0.8	$(5.10 \pm 0.80) \times 10^{+0}$
66.5 ± 0.7	$(9.40 \pm 1.50) \times 10^{+0}$

[a]The error values listed include a 7% estimated systematic uncertainty (see text).

Table 7.4: Measured cross sections for the production of radio-iridium isotopes in the irradiation of ^{192}Os with protons.

Proton energy (MeV)	Cross section[a] (mb)					
	^{192}Ir	^{190}Ir	^{189}Ir	^{188}Ir	^{187}Ir	^{186}Ir
7.7 ± 0.7	$(1.09 \pm 0.12) \times 10^{+1}$	–	–	–	–	–
9.2 ± 0.6	$(4.37 \pm 0.48) \times 10^{+1}$	–	–	–	–	–
10.8 ± 0.6	$(5.63 \pm 0.61) \times 10^{+1}$	–	–	–	–	–
12.1 ± 1.9	$(4.65 \pm 0.51) \times 10^{+1}$	–	–	–	–	–
12.2 ± 0.5	$(5.23 \pm 0.57) \times 10^{+1}$	–	–	–	–	–
13.5 ± 0.5	$(3.98 \pm 0.43) \times 10^{+1}$	–	–	–	–	–
14.7 ± 0.4	$(3.74 \pm 0.41) \times 10^{+1}$	–	–	–	–	–
15.8 ± 0.4	$(2.93 \pm 0.30) \times 10^{+1}$	–	–	–	–	–
16.8 ± 1.8	$(2.26 \pm 0.35) \times 10^{+1}$	$(8.68 \pm 0.94) \times 10^{+1}$	–	–	–	–
16.9 ± 0.3	$(2.51 \pm 0.25) \times 10^{+1}$	–	–	–	–	–
20.6 ± 1.7	$(2.11 \pm 0.23) \times 10^{+1}$	$(6.49 \pm 0.71) \times 10^{+2}$	–	–	–	–
23.9 ± 1.6	$(2.02 \pm 0.29) \times 10^{+1}$	$(1.20 \pm 0.13) \times 10^{+3}$	$(3.38 \pm 0.37) \times 10^{+1}$	–	–	–
26.8 ± 1.6	$(1.60 \pm 0.25) \times 10^{+1}$	$(9.16 \pm 1.00) \times 10^{+2}$	$(2.95 \pm 0.32) \times 10^{+2}$	–	–	–
29.5 ± 1.5	$(1.71 \pm 0.23) \times 10^{+1}$	$(5.51 \pm 0.60) \times 10^{+2}$	$(7.66 \pm 0.83) \times 10^{+2}$	–	–	–
34.5 ± 1.4	$(1.49 \pm 0.17) \times 10^{+1}$	$(1.74 \pm 0.19) \times 10^{+2}$	$(9.55 \pm 1.04) \times 10^{+2}$	$(4.04 \pm 0.47) \times 10^{+1}$	–	–
39.1 ± 1.3	$(1.22 \pm 0.13) \times 10^{+1}$	$(1.11 \pm 0.12) \times 10^{+2}$	$(5.73 \pm 0.62) \times 10^{+2}$	$(4.70 \pm 0.51) \times 10^{+2}$	–	–
43.1 ± 1.2	$(1.01 \pm 0.16) \times 10^{+1}$	$(1.10 \pm 0.12) \times 10^{+2}$	$(3.50 \pm 0.38) \times 10^{+2}$	$(9.29 \pm 1.01) \times 10^{+2}$	$(3.69 \pm 0.40) \times 10^{+1}$	–
47.0 ± 1.1	$(1.06 \pm 0.12) \times 10^{+1}$	$(8.32 \pm 0.90) \times 10^{+1}$	$(1.97 \pm 0.21) \times 10^{+2}$	$(7.47 \pm 0.81) \times 10^{+2}$	$(2.07 \pm 0.23) \times 10^{+2}$	–
50.6 ± 1.1	$(0.92 \pm 0.13) \times 10^{+1}$	$(8.82 \pm 0.96) \times 10^{+1}$	$(1.73 \pm 0.19) \times 10^{+2}$	$(5.85 \pm 0.64) \times 10^{+2}$	$(5.57 \pm 0.61) \times 10^{+2}$	$(0.38 \pm 0.06) \times 10^{+1}$
54.1 ± 1.0	$(0.90 \pm 0.10) \times 10^{+1}$	$(7.03 \pm 0.72) \times 10^{+1}$	$(1.30 \pm 0.17) \times 10^{+2}$	$(2.97 \pm 0.32) \times 10^{+2}$	$(5.68 \pm 0.62) \times 10^{+2}$	$(2.01 \pm 0.22) \times 10^{+1}$
57.3 ± 0.9	$(0.88 \pm 0.10) \times 10^{+1}$	$(6.41 \pm 0.70) \times 10^{+1}$	$(1.24 \pm 0.13) \times 10^{+2}$	$(2.37 \pm 0.26) \times 10^{+2}$	$(5.71 \pm 0.62) \times 10^{+2}$	$(1.04 \pm 0.11) \times 10^{+2}$
60.5 ± 0.8	$(0.64 \pm 0.07) \times 10^{+1}$	$(4.88 \pm 0.53) \times 10^{+1}$	$(9.11 \pm 0.99) \times 10^{+1}$	$(1.59 \pm 0.17) \times 10^{+2}$	$(3.79 \pm 0.41) \times 10^{+2}$	$(1.91 \pm 0.21) \times 10^{+2}$
63.5 ± 0.8	$(0.54 \pm 0.06) \times 10^{+1}$	$(4.13 \pm 0.45) \times 10^{+1}$	$(7.89 \pm 0.86) \times 10^{+1}$	$(1.24 \pm 0.14) \times 10^{+2}$	$(2.55 \pm 0.28) \times 10^{+2}$	$(2.48 \pm 0.27) \times 10^{+2}$
66.5 ± 0.7	$(0.55 \pm 0.06) \times 10^{+1}$	$(4.15 \pm 0.45) \times 10^{+1}$	$(7.51 \pm 0.82) \times 10^{+1}$	$(1.21 \pm 0.12) \times 10^{+2}$	$(2.06 \pm 0.20) \times 10^{+2}$	$(2.97 \pm 0.29) \times 10^{+2}$

[a]The error values listed include a systematic uncertainty which is estimated to be 7% (see text).

Chapter 8

Targets for ^{18}F Production at iThemba LABS

8.1 Historical perspective

Fluorine-18 production targets using enriched $H_2{}^{18}O$ have gone though a number of iterations since the seminal paper by Ruth and Wolf [Rut1979] in the late seventies outlined the usefulness of enriched water as the target material of choice for ^{18}F production. The target development can be roughly broken up into four overlapping generations of targets that have played specific roles as the field of PET scanning developed and demanded more and more of this radionuclide for clinical work. In 1991 Guillaume *et al.* [Gui1991] published a review of existing data and some practical and technical recommendations for the routine production were put forward. The reviewed targets and the relevant references are shown in Table 8.1. (Note that some of the values listed by Guillaume *et al.* for saturation conditions have been converted by us to a one hour bombardment at a beam current of 1 μA to make direct comparisons possible between the listed methods.) This is still a representative collection of the relevant reactions. As can be seen from the table, the target nucleus is either ^{16,18}O or ^{20}Ne (see the relevant part of the Karlsruhe Chart of the Nuclides in Fig. 8.1). Several oxygen and neon gas-target systems were developed but once $H_2{}^{18}O$ became freely available, the liquid water targets became the technology of choice. It is evident from the table that the yield from ^{18}O is significantly higher than from ^{20}Ne as the target nucleus. From then until the present, almost all commercial targets have been of the Generation II type (see below) and the only real major change has been the move from Ag to Nb or Ta as the material of the target body (or insert) in direct contact with the enriched water.

Two further comments concerning Table 8.1 need to be made. First, gas targets (both $^{18}O_2$ and Ne) required prefluorination and/or some other passivation scheme of the inner target surfaces in order to successfully extract ^{18}F after bombardment. In addition to the added carrier, reduced extraction efficiencies were not uncommon. Eventually, most of the initial proponents of the gas targetry also migrated to water targets. Second, the reactor production of ^{18}F is only of academic interest. A review by Vera Ruiz [Ver1988] indicated that useful yields could be obtained with Li salts having a sufficient ^{16}O content but that the practical problems were significant. Here, two reactions are exploited together, namely ^{6}Li(n,^{3}H)^{4}He to produce the tritium required for the ^{16}O(^{3}H,n)^{18}F reaction.

Table 8.1: Different ^{18}F production modes reported prior to the early nineties [Gui1991].

Reaction	Target	E^a (MeV)	Thick target yield^b (mCi/μAh)	Main form	Reference
^{18}O(p,n)^{18}F	$^{18}O_2$	14	68.1		[Rut1979]
	$^{18}O_2$	10	47.3	$[^{18}F]F_2$	[Nic1984]
	$H_2{}^{18}O$	16	34.7	$[^{18}F]F^-$	[Kil1985]
^{20}Ne(d,α)^{18}F	^{20}Ne	14	29.0		[Cas1980]
	Ne + 0.1% F_2	14	14.3	$[^{18}F]F_2$	[Cas1980]
	Ne + 0.18% F_2	11.2	10	$[^{18}F]F_2$	[Ble1986]
	Ne + 15% H_2	11.2	10	$[^{18}F]HF$	[Ble1986]
	Ne + 6.7% H_2	11.2	8	$[^{18}F]F^-$	[Ble1986]
^{20}Ne(d,X)^{18}Ne^c	Ne + 10% H_2	6.3	3.5	$[^{18}F]HF$	[Dah1983]
^{16}O(α,d)^{18}F	H_2O	30	1.1	$[^{18}F]F^-$	[Cla1966]
		48	7.0	$[^{18}F]F^-$	[Lin1973]
^{16}O(α,2n)^{18}Ne^c	O_2	40	14	$[^{18}F]HF$	[Noz1968]
^{16}O(^{3}He,p)^{18}F	H_2O	41–14	7	$[^{18}F]F^-$	[Fit1977]
^{16}O(^{3}He,n)^{18}Ne^c	H_2O	36	7.6	$[^{18}F]F^-$	[Knu1983]
^{20}Ne(^{3}He,αn)^{18}Ne^c	Ne + 2% H_2	27.5	5–7	$[^{18}F]HF$	[Cro1978]
		n Flux ($cm^{-2} \cdot s^{-1}$)	Yield^e (mCi/h)		
^{16}O(^{3}H,n)^{18}F^d	Li_2CO_3	3×10^{13}	78	$[^{18}F]F^-$	[Ver1988]
	^{6}LiOH.H_2O	3×10^{13}	250	$[^{18}F]F^-$	[Ver1988]

[a] Energy window down to the reaction threshold unless otherwise indicated.
[b] One hour experimental irradiation at a beam current of 1 μA.
[c] The precursor ^{18}Ne decays to ^{18}F with a half-life of 1.67 s.
[d] Reactor produced: ^{3}H produced via the ^{6}Li(n,^{3}H)^{4}He reaction.
[e] One hour activation time in neutron field.

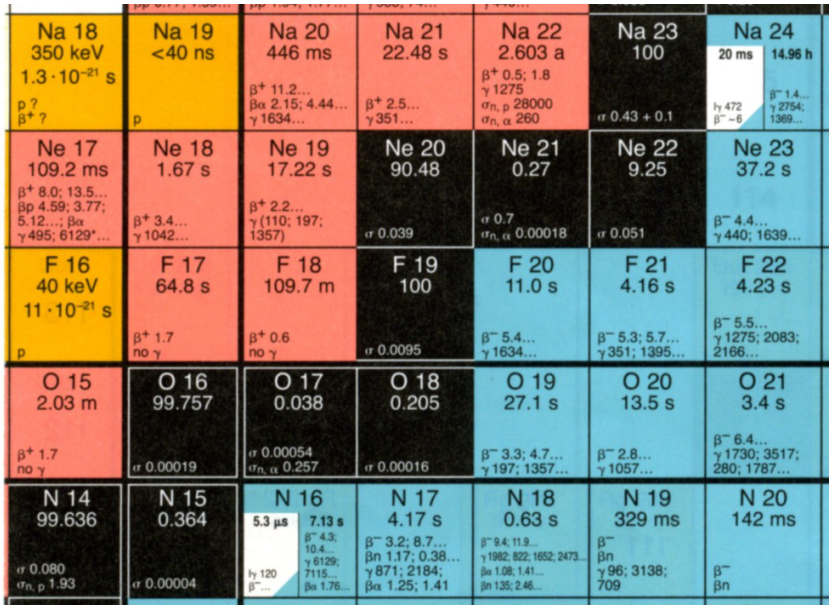

Figure 8.1: Relevant part of the Karlsruhe Chart of the Nuclides for the production of ^{18}F. With permission © Nucleonica GmbH 2012.

8.1.1 Generation 0 targets – earlier times

Generation 0 targets primarily consisted of non-enriched water bounded by very thin entrance and exit beam windows on either side of the water volume. These targets were usually thin since the bombarding particles were either low energy deuterons or ^{3}He, resulting in small stopping lengths. A few target designs, however, had relatively large volumes (i.e. several mL of water).

8.1.2 Generation I targets

Generation I targets were characterized by small volumes of enriched $H_2{}^{18}O$ water (typically significantly less than 1 mL) constrained by very thin beam windows. An external high gas pressure (usually helium between 10 and 20 bar) was usually supplied to the water cavity to suppress boiling. Very small volumes were necessary because of the relative scarcity of the enriched water in the early eighties as well as its prohibitive cost at that time.

8.1.3 Generation II targets

In the late eighties and into the nineties and beyond, target volumes were creeping up to and over 1 mL as the demand for ^{18}F increased and the enriched water became more readily available commercially. The level of enrichment also improved dramatically from about 20–30% to more than 90% during this period. Generation II targets, such as the one shown in Fig. 8.2, operate in the boiling regime. With the boiling targets, an increase in yield by an order of magnitude could be achieved. The elongated (or enlarged) shape of the target cavity is important as it prevents burn-through, a problem which sometimes happened in first-generation targets which were typically much thinner and thus would not stop the proton beam when a significant amount of steam bubbles formed. While an external gas pressure is sometimes employed, this is normally omitted as the boiling water under saturation conditions self-regulates its pressure, the value of which is directly proportional to the thermal load from the beam.

8.1.4 Other recent concepts

A small number of radical design targets have been developed over the years. Arguably the most successful of these is the thermosyphon target [Sto2010] that utilizes a separated pressurized cavity to allow for fluid volume changes while maintaining a full target cavity. This results in an increased beam intensity tolerance and thus increased yields. It has to be said, however, that some people argue that well-designed, elongated boiling water cavities can achieve yields comparable to thermosyphon targets with the added benefit of simplicity of design. The jury is not yet out on this question, to our knowledge, therefore the reluctance to label the thermosyphon concept as “Generation III” at this time. Other concepts include the flow-through targets [Dos2008] and $^{18}O_2$ gas targets of various designs.

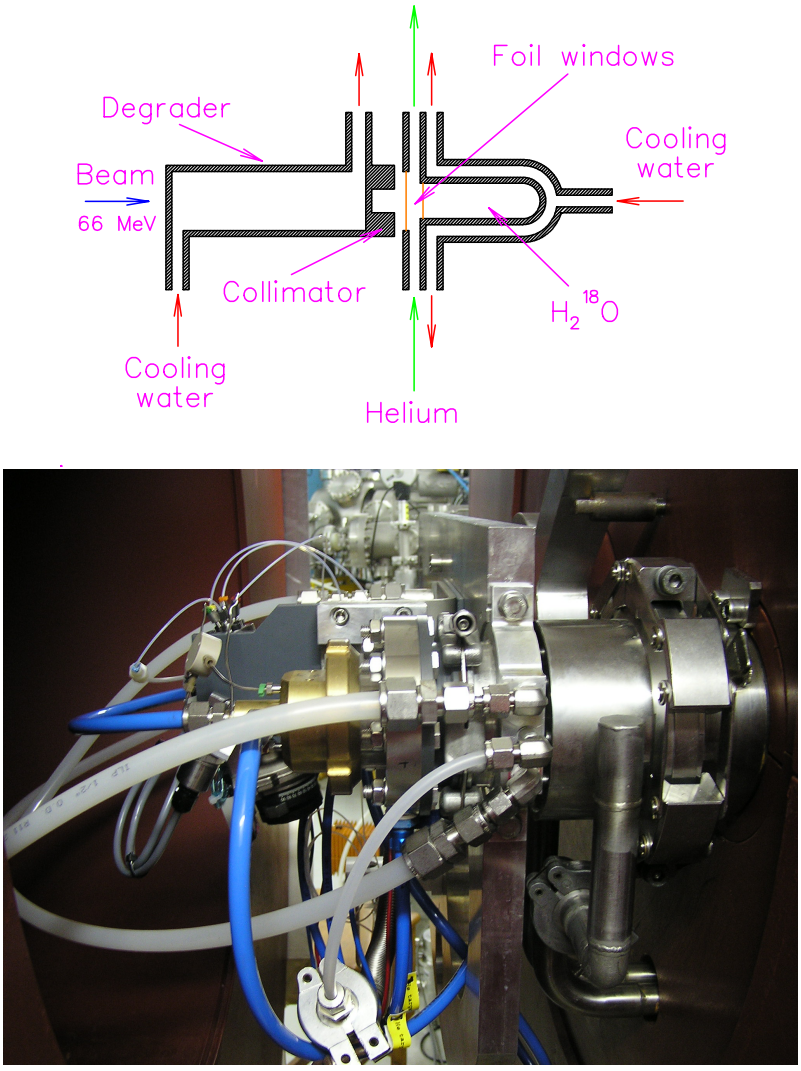

Figure 8.2: TOP: Simplified schematic diagram of the enriched ^{18}O-water target in use at iThemba LABS for the routine production of ^{18}F. This is an example of a Generation II target. BOTTOM: Side view of the iThemba LABS ^{18}O-water target. Note that the beam is incident from the right.

8.2 The iThemba LABS case

8.2.1 Background

In 2005, iThemba LABS was tasked to establish an ^{18}F-FDG production facility to catalyze the introduction of PET in South Africa. To this end a grant was applied for and received from the so-called "Innovaton Fund" of the NRF to cover the construction of a production clean room for FDG, the purchase of a commercial water target and the building of a beam splitter to allow the bombardment of the water target without interrupting the rest of the radioisotope production programme.

The Ion Beam Applications SA (IBA) standalone target (SAT) system was selected, since this was considered to be the most compatible to incorporate into the existing bombardment station (see Fig. 8.3), which was originally built for semi-permanent targets and was used to accommodate an experimental Ne gas target for the small-scale production of [^{18}F]F_2 for experimental puposes [Nor1999]. This bombardment station is situated at the end of a 30 meter long beamline, containing 10 quadrupole magnets for beam focusing along this distance. There

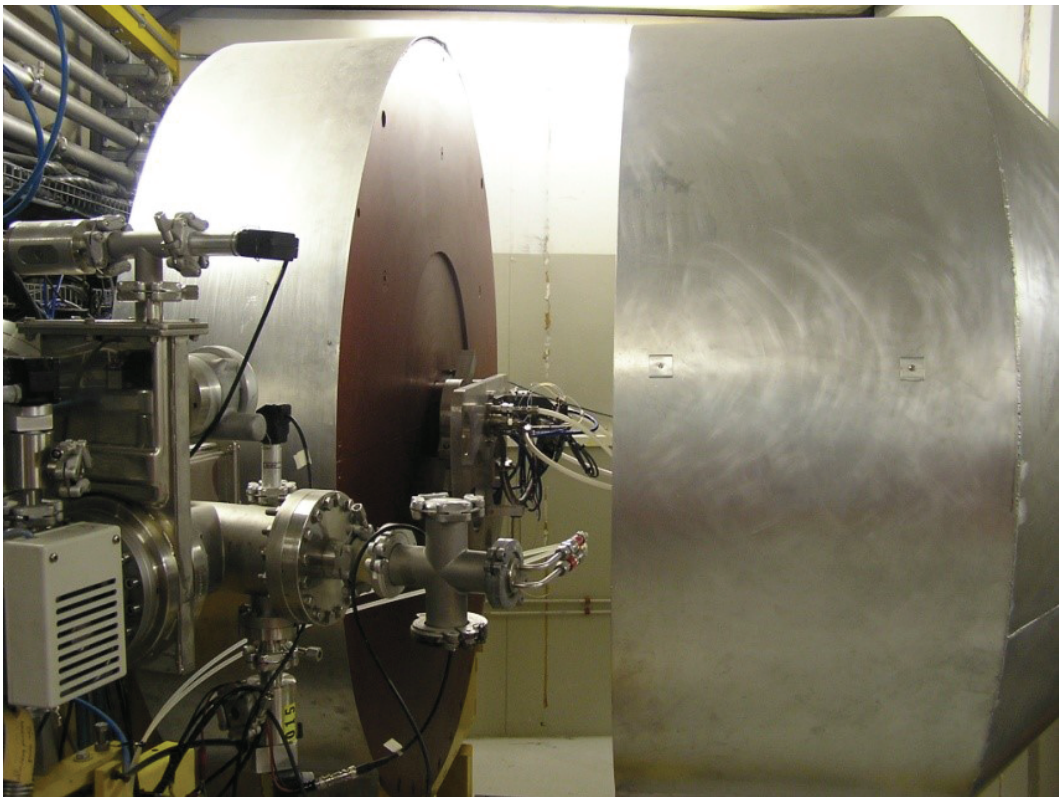

Figure 8.3: The bombardment station at iThemba LABS dedicated to the production of ^{18}F using a modified $H_2{}^{18}O$ target from IBA. The station is shown in the open position.

is a diagnostic chamber 1 meter ahead of the target, containing a harp for beam alignment as well as a Faraday cup.

The SAT system requirement set by IBA was for 18 MeV protons delivered to an area no larger than a circle of 11 mm diameter. The tight schedule on cyclotron utilization meant that energy changes between 18 and 66 MeV, four times per week, was simply not possible (an energy change translates to 4-6 h of downtime). The routine production beam of 66 MeV would thus have to be degraded and shaped to accommodate this target geometry and energy specification. This type of degrading had been done before at the Paul Sherrer Institute [Hus1985]. To achieve the optimal energy and beam size, a degrader/collimator unit was designed and built at iThemba LABS (see Fig. 8.4).

As mentioned before and discussed in detail in Chapter 9, all targetry at iThemba LABS is separated from the beam line vacuum by means of a helium-cooled double-foil Havar window. The water targetry is no exception. The direct proton activation of the window and degrader system as well as the secondary neutron activation of the immediate vicinity is far more severe than what is typical for a PET facility. The target is therefore well shielded during bombardment, similar to all the other radionuclide production targets at iThemba LABS. The degrader/collimator unit was designed for easy and rapid removal. The unit is water cooled to dissipate the heat generated by degrading the proton beam from 66 MeV down to 18 MeV.

A first prototype degrader/collimator unit was installed and autoradiography was used to determine the shape of the transmitted beam (see Fig. 8.5). The initial results looked very promising and therefore the IBA target and collimator assembly was added to the bombardment

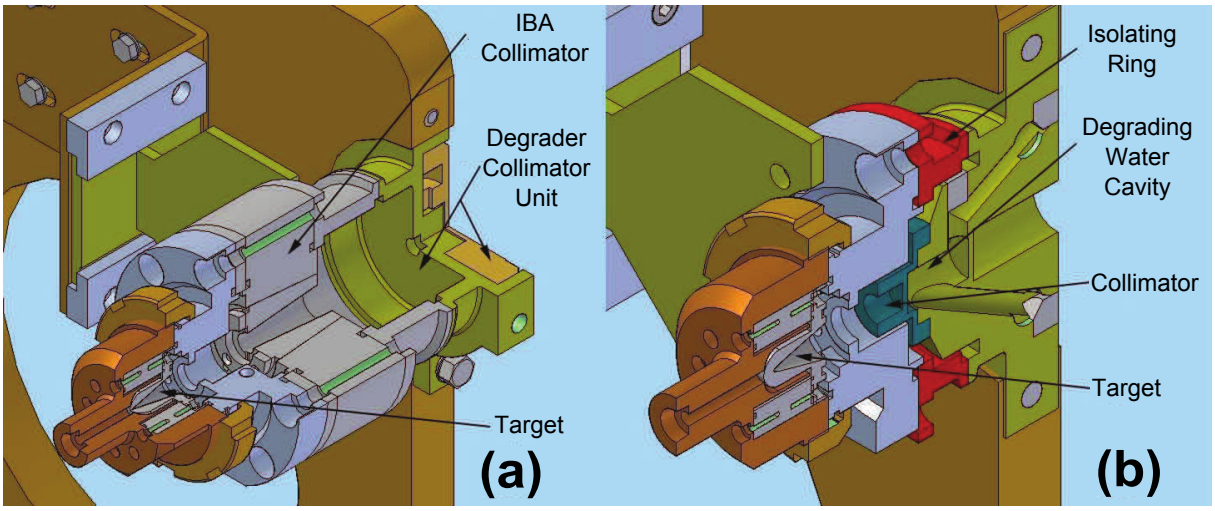

Figure 8.4: (a) Design of the initial degrader/collimator unit coupled to the IBA collimator and target. (b) Design of the final degrader/collimator unit. Note that the original IBA collimator shown in (a) has been discarded in (b).

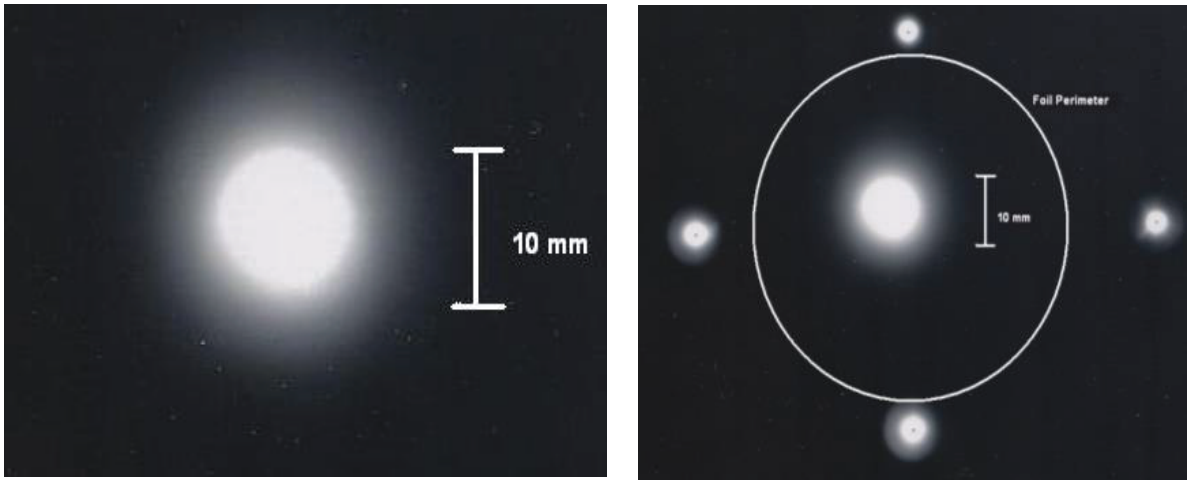

Figure 8.5: Autoradiograms of beam shape at the exit of the initial degrader/collimator unit.

station. Unfortunately, it was found to be impossible to get more than 20% of the incident beam into the water cavity. When simulating the beam divergence from the double-foil window to the target cavity entrance using the SRIM code [Zie2006] (see Fig. 8.6a), it was discovered that the radial beam spread was simply too large, resulting in significant losses (of about 80%) in the various materials in front of the target and in particular the original IBA entrance collimator (see Fig. 8.5a). A total redesign of the target assembly was thus deemed necessary at this point.

8.2.2 The new integrated degrader/collimator unit

Estimates based on a Monte Carlo simulation of the beam, degrader and target geometry, using the SRIM code, quantitatively reproduced the low bombardment efficiency. The relevant beam profile is shown in Fig. 8.6 (a) [Zie2006]. The problem could only be solved by completely rebuilding the SAT system. This was confirmed by further SRIM simulations of alternative designs. The original IBA collimator was permanently removed in order to allow the target cavity to be as close to the degrader/collimator unit as possible, thereby minimizing the effect

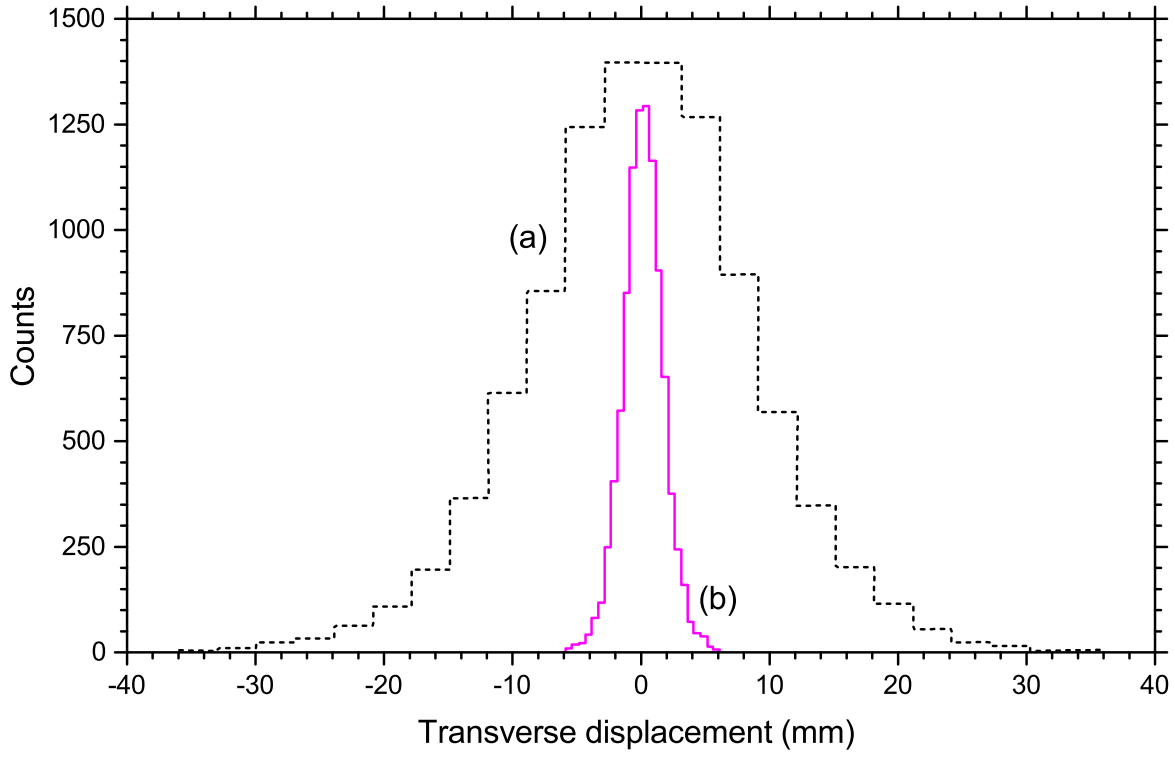

Figure 8.6: The beam profile at the entrance to the target-water cavity, as calculated using the SRIM code for (a) the initial degrader/collimator design and (b) the final degrader/collimator design.

of beam divergence. The distance between the beam exit from the degrader/collimator unit and the target entry window foil was effectively reduced from 136.8 mm to 21.7 mm. The design of the new integrated degrader/collimator unit was also changed to utilize the cooling water for most of the energy degradation, now in close proximity to the target cavity. These changes resulted in a significantly smaller beam spread (see Fig. 8.6) and consequently a much better interaction of the beam with the target volume.

The flow channels in the unit are set in such a way that the cooling water will always be in contact with the two axial aluminium walls (or windows) required to contain the water. This allows for effective cooling and avoids any dead flow areas in the water cavity. The degrader/collimator unit is electrically isolated from the target to allow independent measurement of the beam intensity on these two components. The principle of the degrader/collimator unit is best depicted schematically at the top of Fig. 8.2.

During the first bombardment with the new assembly, it was possible to relatively quickly achieve an 80% to 20% ratio of beam current measured on the target and degrader/collimator unit, respectively. It was clear that the shape of the beam in the target cavity was now acceptable, however, we needed to be sure that the other beam characteristics were good as well.

Figure 8.7 (a) shows the target mounted in the dedicated bombardment station (the radiation shield is in an open position) while (b) shows the station ready for bombardment (i.e. a closed shield).

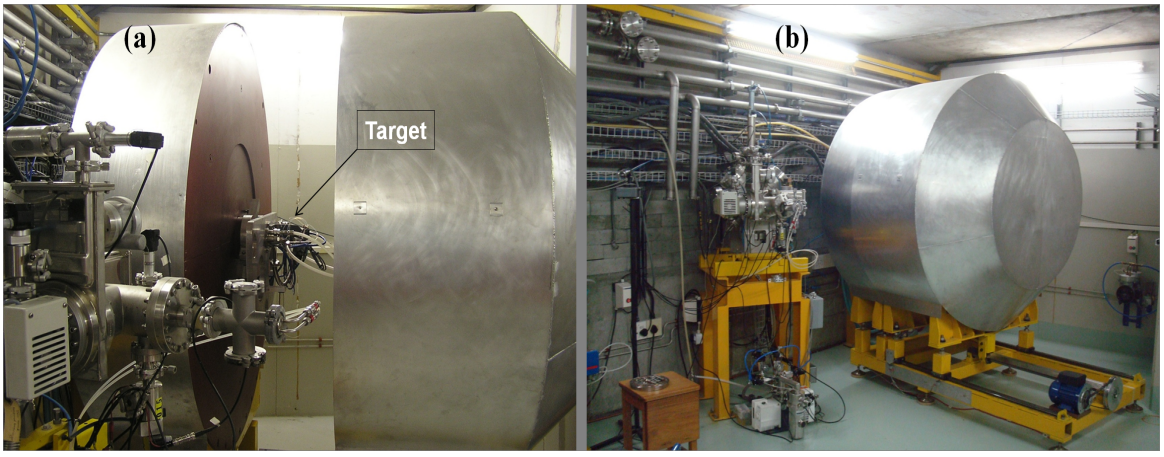

Figure 8.7: (a) Enriched water target mounted in the dedicated bombardment station (Babe). (b) Station ready for bombardment. The beam is incident from the left.

8.2.3 Determination of the beam energy and profile

To measure the average energy of the beam entering the target water cavity, a stack of Cu monitor foils was activated with the degraded beam with the aim of using the standard ^{nat}Cu(p,X)^{65}Zn monitor reaction as set out in IAEA Tecdoc 1211 [Gul2001]. By placing the foils in the beam stop provided by IBA for setting up the target, it was possible to measure the energy in the exact spot where the target cavity would be situated. The results are shown in Fig. 8.8.

It is clear that the mean energy of the degraded beam has the desired value of nominally 18 MeV within the experimental uncertainty. Some slight discrepancies between the standard

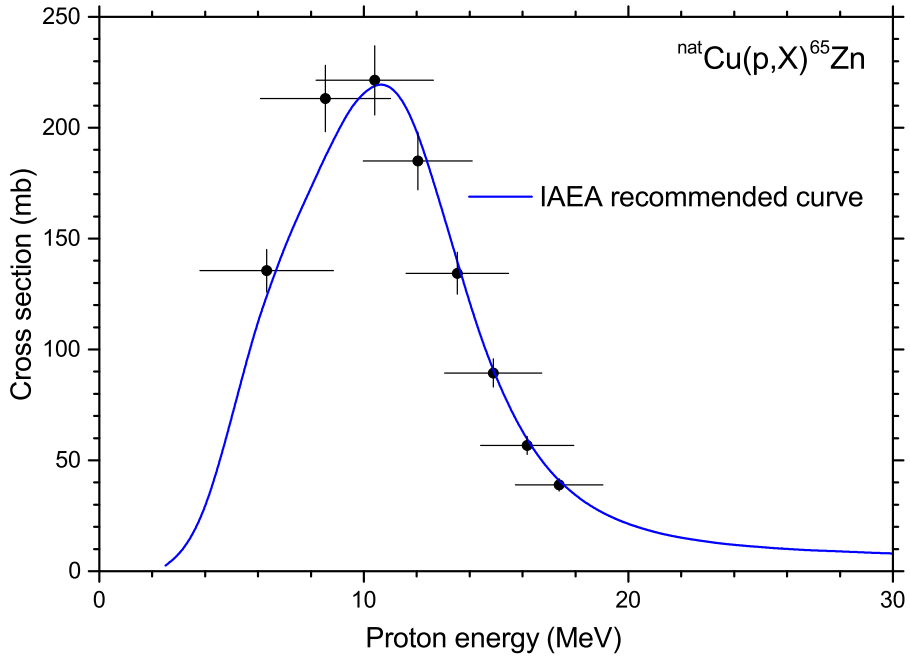

Figure 8.8: Foil stack measurement of the beam energy in the target cavity. The curve represents a standard ^{nat}Cu(p,X)^{65}Zn monitor excitation function [Gul2001] while the symbols represent the measurements performed at iThemba LABS. The large energy uncertainties are due to the fact that the 66 MeV incident beam is significantly degraded.

excitation function and the measurements can be expected due to the straggling through the degrading materials, which leads to an increasing energy spread as a function of penetration depth. We find it remarkable that such an excellent level of agreement is still obtained at such a large penetration depth.

For determining the beam profile, the most activated foil in the foil stack was cut into a matrix of 49 pieces and each piece was counted individually using standard off-line γ-ray spectrometry. In order to achieve accurate measurement of the very small amounts of long-lived radioactivity in these foil fractions, the HPGe detector of the environmental analysis laboratory at iThemba LABS was used. This detector is shielded with "older" lead that has a very low natural radioactivity content. The number of counts per square mm of a characteristic photo-peak of ^{65}Zn (the 1115 keV γ-line) was plotted versus the matrix dimensions. To reproduce a projected beam profile with positional information, a 3D polynomial fit was applied to the matrix of counts per foil piece using the Origin 9.1 data analysis software package. Where X and Y denote the position axes and Z the counts in the photopeak area, a projection of the 3D fit onto the XY-plane yields the 2D profile shown in Fig. 8.9. A well-defined beam spot is evident (as well as a slight beamline misalignment that was subsequently corrected). It has to be said that the method described above was rather cumbersome. When this work was done, we were not yet familiar with the analysis method using autoradiograms in conjunction with the DoseLab software package (see Section 2.3.3 and [Dem2000]) which was adopted in later studies.

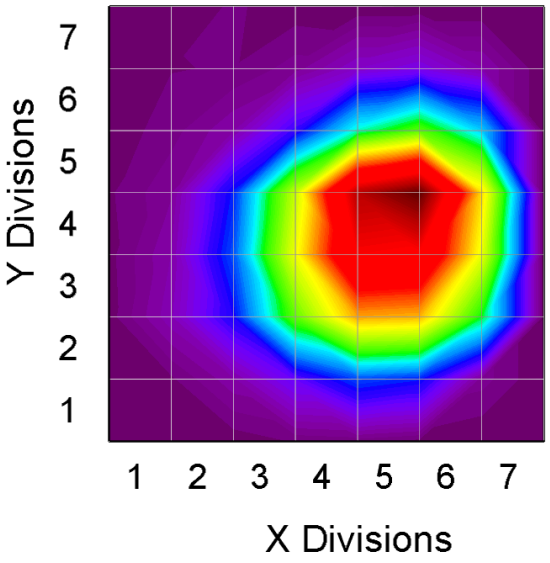

Figure 8.9: The beam profile as measured by counting individual parts of one of the monitor foils in conjunction with a polynomial fit (see text) over the foil matrix to reconstruct the beam shape and position.

8.2.4 Target operational behaviour

At iThemba LABS, measurements of the target pressure versus the beam current were performed on the modified IBA 2.3 mL single-cavity boiling target. A calibrated piezoresistive transducer with a response time of about 1 ms is a component of the beam interlock system

and was used for the pressure measurements. An EG&G CD 1010 current digitizer was used to measure the beam current. These values were logged on a PC using the LabVIEW code for data acquisition. The results are compared in Table 8.2 with corresponding values supplied by IBA for this target, the latter measured during bombardment with a primary proton beam of nominally 18 MeV. While the values at iThemba LABS are marginally lower, the agreement is satisfactory and a clear indication that the degrading and reshaping of the 66 MeV beam is successful.

Table 8.2: Target pressure versus beam current as measured by IBA and iThemba LABS.

Beam Current μA	Target pressure[a] IBA[b] (bar)	Target pressure[a] iThemba LABS[c] (bar)
5	1.0	1.0
10	1.5	1.5
15	2.5	2.1
20	4.0	3.5
25	6.0	5.5
30	10.0	9.5
35	18.0	17.0
40	30.0	27.9

[a]Gauge pressure.
[b]Employing a primary beam of 18 MeV.
[c]Employing a 66 MeV primary beam degraded to nominally 18 MeV.

The most important test, however, is the comparison of the production yield with expectations based on published production data. Production yields obtained with the target system described above have generally been found to be in good agreement with values based on evaluated integral yield data from the paper by Takács *et al.* [Tak2003], which superseded the IAEA-Tecdoc-2011 [Gul2001] evaluation (see Fig. 8.10). This is further evidence that possible negative effects such as bulk vaporization in the target cavity do not lead to burn-through of the beam.

Figure 8.10 should be viewed with some caution. It seems to indicate that an increase in beam energy is beneficial as it leads to a higher yield (i.e. considering a target length sufficient to reach the effective reaction threshold of about 4 MeV). The critical beam parameter, however, is not the beam current but the beam power dissipated in the target water. The integral yield per unit energy deposited by the beam is plotted versus the beam energy in Fig. 8.11. The integral yield curve plotted with these units is no longer monotonically increasing but instead shows a peak with a maximum at about 14 MeV. Thus, the optimal beam entrance energy into the water cavity is in fact 14 MeV. Since some window material is required upstream to contain the water, the optimal incident beam energy should be $\Delta E + 14$ MeV, where ΔE is the effective energy width of the window.

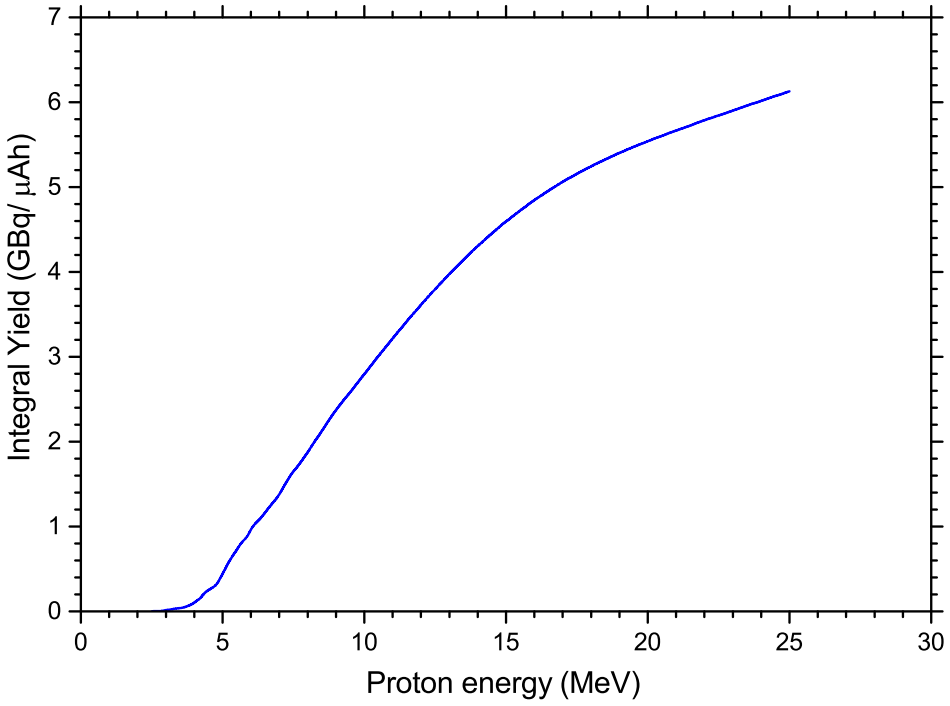

Figure 8.10: Integral yield curve for the production of ^{18}F in the bombardment of ^{18}O with protons. The evaluated data for the ^{18}O(p,n)^{18}F reaction were taken from [Tak2003].

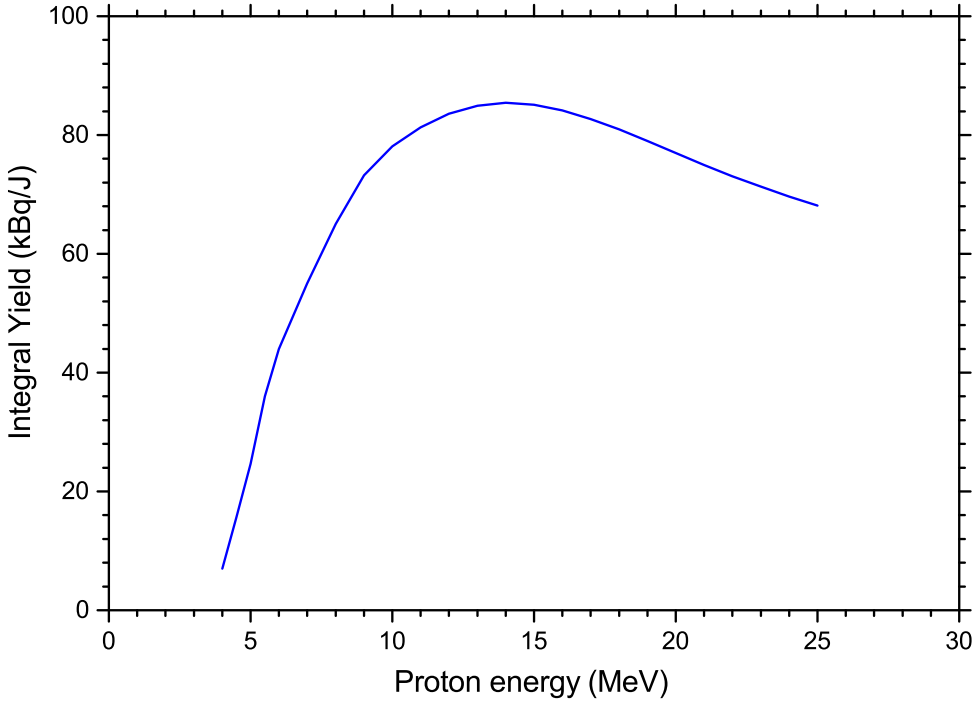

Figure 8.11: Integral yield per unit energy deposited by the beam versus the beam energy for the production of ^{18}F in the bombardment of ^{18}O with protons. The evaluated data for the ^{18}O(p,n)^{18}F reaction were taken from [Tak2003].

8.3 A saturation boiling model for an elongated water target operating at high pressure

Boiling or Generation II targets have now been around for the better part of twenty years. There are still some debates and open questions, however, in particular whether a second cavity for condensation cooling (i.e. a condenser) separated from the target cavity could enhance the target performance (see e.g. Chatwin-Davies *et al.* [Cha2006]). Note that the IBA target employed at iThemba LABS only has a single, elongated cavity (i.e. no separate condenser or reflux cavity). Instead the target is cold filled to only three-quarters full to allow for expansion as the water density drops with increasing temperature. It is certainly true that in large systems (e.g. boiling nuclear reactors) a separate condenser stage can be used with great efficacy. On the scale of a small target which contains only around 2–5 mL of violently boiling water, however, the clean separation of the steam from the liquid and the subsequent return of the condensate to the target cavity from a separate condenser are difficult to successfully implement. In contrast, targets with single cavities are simpler (see e.g. Buckley [Buc2006]) and generally work well.

In a recent study by Alvord *et al.* [Alv2008], it was pointed out that elevated pressures and temperatures in excess of the saturation conditions may exist during bombardment, however, as long as the rate of condensation matches the rate of vaporization, the bulk of the system should remain at saturation. Bulk boiling, enhanced by radiation-induced nucleation, provides a rapid mixing mechanism within the small target cavity. Superheated regions are therefore likely to form but also likely to disappear rapidly (on the scale of a few milliseconds). One concern may be unstable behaviour, e.g. rapid cycles of bulk vaporization and condensation, which my lead to large pressure fluctuations. This has been observed in boilers of various kinds and should be avoided in targets as it may destroy the thin foil entrance window. Due to the presence of fast mixing, a simple model can be formulated which assumes the target water to have a constant temperature. A second simplification is to neglect the temperature difference across the target chamber wall (1 mm thick niobium) which is justified because this wall is quite thin. A further assumption is that a single convective heat-transfer coefficient applies which is constant over the entire water-cooled surface. By writing down the energy balance between the beam heating and the convection cooling (Newton's law of cooling) and rearranging terms, one gets the following equation:

$$T_w = \left(\frac{\Delta E}{hA}\right) I_b + T_0 \tag{8.1}$$

where T_w is the target-water temperature, ΔE is the beam energy window, A is the water-cooled surface, h is the convective heat-transfer coefficient, I_b is the beam current and T_0 is the bulk temperature of the cooling water. The only unknown is the convective heat-transfer coefficient, however, h only acts as a scaling factor and does not affect the shape of the T_w versus I_b curve.

Assuming saturation conditions, the relationship between the pressure, P, of the target water and its temperature, T_w, is uniquely known from the steam tables [Steam2013]. In fact, the pressure of a contained liquid at saturation constitutes an excellent thermometer. Figure 8.12 shows a plot of P versus I_b, where h has been adjusted until a good fit with the

measurements was obtained. An effective heat-transfer coefficient of $h = 0.49$ W cm^{-2} °C^{-1} was extracted in this way. Figure 8.13 shows the characteristic curve of pressure versus temperature for water at saturation. The good agreement in shape is taken as evidence that the majority of the system operates at saturation conditions.

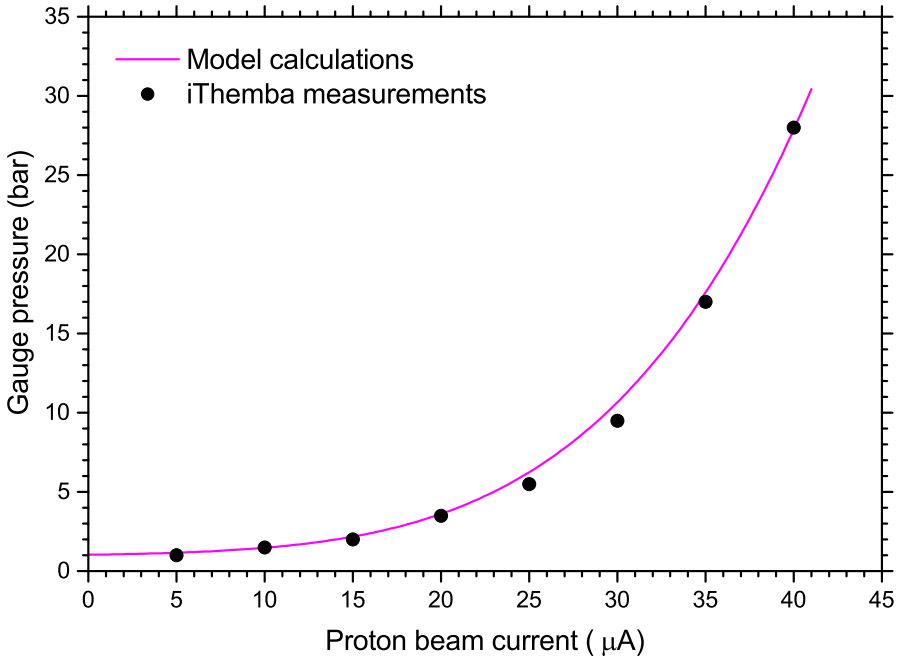

Figure 8.12: Pressure inside the 2.3 mL water target versus the proton beam current. The symbols are the measurements performed at iThemba LABS while the solid curve is a calculation using Eq. 8.1.

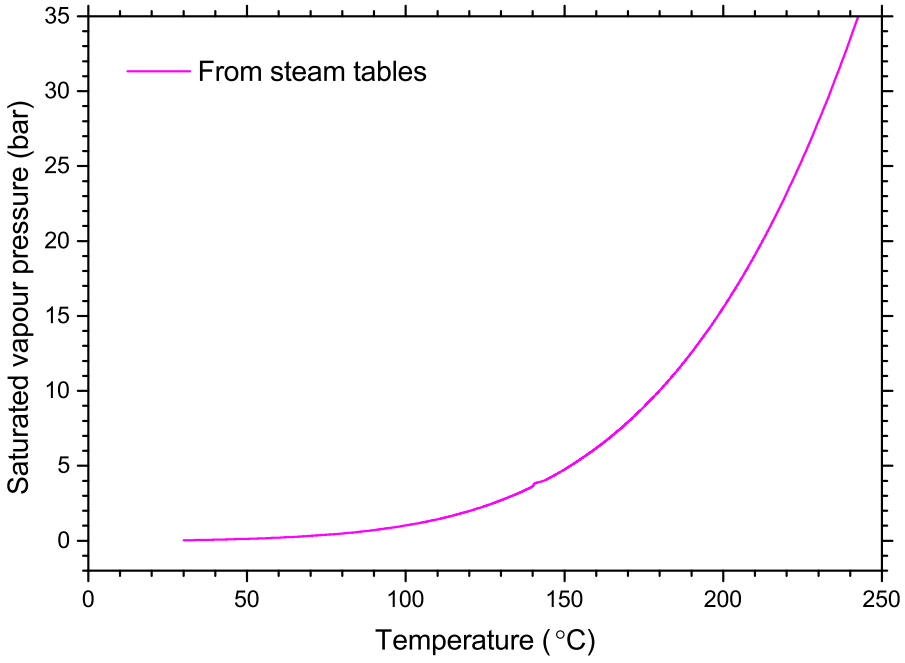

Figure 8.13: Characteristic curve of the vapour pressure versus temperature of water under saturation conditions.

8.3.1 Arguments about the cavity size

The dimensions and shape of the inner cavity determine both the volume of enriched water and the effective heat-transfer surface. There are conflicting requirements concerning the cavity size. Even though $H_2{}^{18}O$ is much less expensive today than it was, say, two decades ago, it is still a significant expense. This results in a stimulus to reduce the cavity size. Unfortunately, a reduction in cavity size also reduces the effective heat-transfer surface, limiting the maximum thermal load that the target can withstand, leading to a reduction in the operational beam current and the subsequent ^{18}F yield that can be obtained in a single production run. The increasing demand for ^{18}F led to a succession of modest increases in the cavity size in recent years. The IBA target that iThemba LABS purchased has a nominal cavity volume of 2.3 mL, the niobium insert of which was marketed as size L (large) at that time. Nowadays this will be considered to be a rather small insert.

To shed light on this issue, it is useful to consider Eq. 8.1 and the results of Fig. 8.12, where the target-water temperature was substituted by the cavity pressure according to the saturation characteristics shown in Fig. 8.13. For the purposes of that calculation, a cooling-water temperature of $T_0 = 30$ °C was assumed and the best fit with the measured data was obtained with $h = 0.49$ W cm^{-2} °C^{-1}, as already mentioned. What can be done to improve the target performance? First, it is interesting to contemplate the overall heat-transfer coefficient, h. Buckley [Buc2006] also reported a value of $h = 0.49$ W cm^{-2} °C^{-1} for their 15 MeV target with a volume of about 0.9 mL (a cylindrical cavity with a 12 mm inner diameter and 8 mm length). This is very reassuring. At the present time, we do not have ideas about how to meaningfully increase the value of h for this kind of target system. Second, one can chill the cooling water (i.e. reduce the value of T_0). One can, for example, decide to use cooling water chilled to 10 °C. If the target is operated at a pressure of 30 bar (a value which we do not want to exceed) the nominal target-water temperature will be about 235 °C. Under these conditions the gain will be less than 10%. Thus, there is not much room for improvement by chilling the cooling water. If one further assumes that the target is operated at or near its optimal proton energy ($\Delta E = 14$ MeV) then the only parameter left that can be adjusted to improve the target performance is the cavity surface, A. As already mentioned, in this simple model we neglect the small differential temperature across the thin Nb wall. In practice, however, the inner surface opposite the wetted outer water-cooled surface is slightly smaller and we take the average between these two surfaces as the "heat-transfer surface". Clearly, a larger surface to remove the heat from is required to increase the maximum operational beam intensity.

Two additional experimental niobium inserts were designed at iThemba LABS but had to be contracted out for CNC machining. The details of all three inserts are presented in Table 8.3 and Fig. 8.14. Insert 1 is the original IBA insert. Insert 2 is an enlarged version of this design but with more than double the volume. The cross sectional areas in the beam direction of Inserts 1 and 2 are circular but in Insert 3 it has a tear shape, which will be described below.

The reason for the tear-shaped inner cavity of Insert 3 was an effort at that time to provide some sort of "reflux cavity" in very close proximity to the "target cavity". It was already our belief that a separate chamber for reflux (not to be confused with the second chamber

Table 8.3: Niobium insert design and performance parameters.

Parameter	Insert 1 (IBA)	Insert 2 (iThemba LABS)	Insert 3 (iThemba LABS)
Inner diameter	11.5 mm	13.0 mm	—
Inner width/height	—	—	13.0 mm / 17.2 mm
Wall thickness	1 mm	1 mm	1 mm
Cavity volume	2.3 mL	5.0 mL	6.2 mL
Heat-transfer surface	7.34 cm^2	15.1 cm^2	17.6 cm^2
h (W cm^{-2} $°C^{-1}$)	0.49	0.32	(0.32)*
Beam current at $P = 30$ bar	41.2 μA	54.3 μA	63.3 μA

*Adopted from measurement on Insert 2.

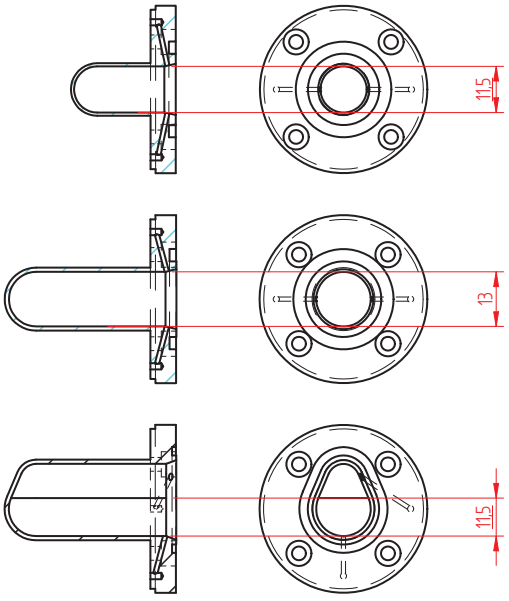

Figure 8.14: The three niobium inserts investigated at iThemba LABS in the enriched water target system. TOP: Insert 1. MIDDLE: Insert 2. BOTTOM: Insert 3. (See also Table 8.3).

in a thermosyphon target, which is water-filled and under an external gas pressure) cannot function on such a small system under violent boiling, as already explained before. Additional space directly above the target chamber, however, might be beneficial. We do not anymore think in terms of a true reflux cavity here (where steam can neatly escape to, condense and the resulting condensate neatly flows back from) but we see the additional space above the target volume more in terms of a free volume for expansion, providing also some modest additional heat-transfer surface as well as a region out of the beam strike where condensation can occur. Manufacturing such a complex design has become much easier with the mainstream availability of 3D printing and CNC machining. Although the overall convective heat-transfer coefficient decreased for the large cavities (see Table 8.3) a strong correlation with available heat-transfer surface is evident.

8.4 Monte Carlo modelling

Extensive radiation transport calculations using the Monte Carlo code MCNPX have been performed for this target system in conjunction with Inserts 1 and 2. Modelling of Insert 3 was not attempted due to its more complex shape, although it is possible in principle. The lack of axial symmetry with Insert 3 would have required significantly more labour to define the geometry while we did not expect to glean much more insight from such an effort than what one would learn from modelling the other two inserts. Calculations were performed with the target cavity filled with liquid water as well as a mixture of water and steam. The latter was modelled as the liquid filled with bubbles (kind of like a foam as the bubbles remained stationary) with a consistency estimated from photographs of contained water under bulk boiling conditions. In this regard, the work of Peeples *et al.* [Pee2012] deserves a special mention. These authors produced a target with optically transparent sides which permitted making video recordings of the bulk boiling process at various beam intensities. Photographs from this work were used to define the "water + bubbles foam" used in our modelling. Other useful studies on the visual observation of boiling water targets were also performed by Heselius *et al.* [Hes1989] and by Hong *et al.* [Hon2011].

Figure 8.15 shows examples of the output generated from mesh tallies on the proton flux in the bombardment of the entire target assembly with a 66 MeV proton beam. The top figure (a) was obtained with the smaller insert (Insert 1) filled with liquid water. The bottom figure (b) is a similar study of the larger insert (Insert 2) filled with water containing steam bubbles.

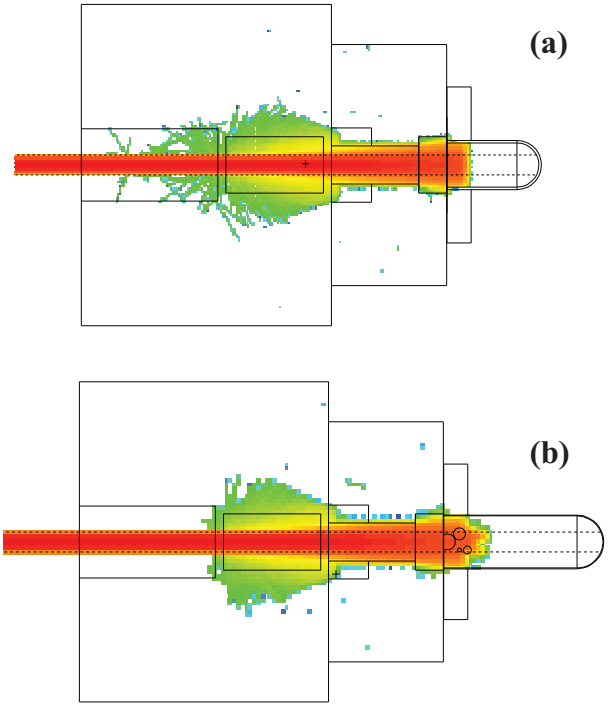

Figure 8.15: MCNPX model of the water-target assembly for the production of ^{18}F at iThemba LABS. (a) Insert 1 (see Table 8.3) containing liquid water. (b) Insert 2 containing a mixture of water and steam bubbles.

It is interesting to compare the measured ratio of beam current on the degrader/collimator assembly and water target with that predicted by the MCNPX modelling. With the modified IBA target assembly in conjunction with the final degrader/collimator unit, a ratio of 20%/80% is typically obtained (e.g. 80% into the target water cavity). For the smaller insert (i.e. Insert 1) the MCNPX calculations predict 19.4%/80.6%. With Insert 2, the corresponding values are 19.7%/80.3%. This level of agreement is very reassuring.

8.5 Conclusion

The target system described above has now been in routine use for the production of ^{18}F at iThemba LABS for a few years. It operates in the boiling regime with the majority of the system at saturation conditions. No yield reduction caused by instabilities due to superheating or any such phenomena which may lead to burn-through have been observed. The use of a 66 MeV primary proton beam delivered by the separated sector cyclotron (SSC) for this purpose is not ideal as the beam energy is much higher than required. Beam time from the SSC is also at a premium. In addition, the use of a degraded beam leads to higher residual activation, more radioactive waste and more radiation damage to targetry components. This arrangement was never envisaged to be a permanent one, however, but rather to stimulate the establishment and use of PET in South Africa. It was foreseen that a dedicated, small PET cyclotron would eventually be established in the Western Cape.

A commercial 11 MeV PET cyclotron has been installed at iThemba LABS and from September 2012 has taken over most of the routine ^{18}F productions. This has freed some much needed beam time on the SSC (about 12 hours of the 54 hours per week allocated for radionuclide production) that are being used for the production of other radionuclides such as the relatively long-lived isotopes ^{22}Na, ^{68}Ge and ^{82}Sr, which remain in high demand. The existing water target system has been retained as a backup and development facility. It is being maintained and is occasionally used for productions, e.g. when maintenance is being done on the PET cyclotron. The year-round provision of ^{18}F has thus been secured.

In conclusion, we would like to explicitly state that there are numerous papers on this topic that have not been referred to, in particular from the collection over many years in the proceedings of the Workshop on Target and Target Chemistry (WTTC) meetings. The aim was not to exhaust this topic, which would have been impossible in one chapter. Instead, the main aim was to communicate the work done at our own laboratory. There is a wealth of information in the literature and it is our belief that the time is right for someone to produce a more recent overview article on the targetry aspects of ^{18}F production. Finally, it may seem as if the thermosyphon targets are criticized here. This is not the case – we appreciate the efforts by those investigators. The benefits of targets employing that concept as compared to the more standard Generation II boiling-cavity targets are just not very obvious, in our opinion. In a similar vain, we question the use of an external gas pressure on a Generation II target as ebullient boiling water enclosed in a cavity self-regulates its own pressure.

Chapter 9

Gas-Cooled Beam Windows

9.1 Introduction

As has already been mentioned in Chapter 2, radionuclide production targets are bombarded outside the cyclotron and beamline vacuum at iThemba LABS (see Sections 2.2.1 and 2.3.3). In addition to preserving the vacuum, the ability to rapidly transfer targets to and from a target station is greatly simplified when the need to break the vacuum and pumping down afterwards have been eliminated. The beamlines of the VBTS, Elephant and Babe target stations have been provided with beam exit windows consisting of two closely-spaced thin metal foils (Havar) cooled by helium flowing between them. These gas-cooled double-foil windows are thin enough to cause minimal energy degradation to the beam but provide a strong enough barrier to maintain the vacuum behind it for extended periods of time. They do have a finite life-time due to radiation damage, however, a window assembly typically lasts many months and at times even a few years.

During the design stage of the VBTS, one of the tasks on the list was to calculate the expected temperature profiles of the beam windows during bombardment, using a new set of beam parameters that take the various facility upgrades into account. An existing FORTRAN code, originally developed for modelling the Elephant windows [Ste1990] more than a decade earlier, was located and implemented on a PC. While the older calculations, as published, could be reproduced without any problems, some unexpected convergence issues plagued the calculations for the VBTS windows. Thus, a task that was not expected to take long prompted several new avenues of investigation. This led to the old code, WINDOW, evolving into the present code, WINHEAT. The changes and additions are discussed in Appendices J through M.

Two further events influenced the new investigation. First, we became aware of the work reported by Chang *et al.* [Cha1995] on heat transfer using submerged single and multiple jets. Second, when the beam was first brought into the newly completed VBTS, the vacuum deteriorated sharply when the beam intensity was increased to values above 150 μA. Initially, the VBTS beam window was suspected and some design changes were suggested. Later, however, the vacuum problem was found to be unrelated to the beam window but not before some design changes had, in fact, been implemented.

In this chapter, the relevant aspects of work on the gas-cooled windows are presented in a

logical order and not the chronological order of events which was, at times, rather fragmented. It is considered appropriate to first discuss the convective heat-transfer coefficient and various schemes from dimensional analysis developed to make predictions for this coefficient. In this regard, we believe that the work by Chang *et al.* [Cha1995] is especially relevant. Next, new measurements of convective heat-transfer coefficients are presented, employing an electrically heated element to simulate the beam. The experiment was not conceived to be a perfect simulation of the beam-window assembly, rather, it was designed to investigate the effect of the geometry of the flow, which will be explained later. Finally, calculated temperature profiles for the windows used on all the radionuclide production bombardment stations at iThemba LABS, under their various operational conditions, are compared. Initial results from modelling the experimental set-up with a commercial CFD code are also presented.

9.2 Convective heat-transfer coefficients

A substantial number of papers dealing with the cooling of thin foils in ion beams have been collected at iThemba LABS over the years. Several of these authors estimated the convective heat-transfer coefficient by considering the foil to be equivalent to a small surface on the inner wall of a circular tube or duct through which the coolant flows. It is not clear when this practice started but the oldest paper in our possession that follows this approach is by Liljenzin [Lil1973], who makes the following statement: *"As a rough approximation, the foil can be thought of as a part of the wall in a circular tube."* Subsequently, Liljenzin used the Dittus-Boelter equation [Dit1930] to estimate the convective heat-transfer coefficient. Derived using the methods of dimensional analysis and correlations with experimental data, the Dittus-Boelter equation is the oldest of several similar approaches to forced convection heat transfer by coolants flowing in tubes or ducts. This equation and several later refinements thereof, such as the Sieder-Tate and Petukhof-Kirilof equations, are still widely employed. The relevant equations as well as aspects of the underlying dimensional analysis are presented in Appendix I. In the following paragraphs, a familiarity with dimensional analysis and basic heat-transfer concepts is assumed, as summarized in Appendices I through M.

At the time when the first bombardment station for radionuclide production was built at iThemba LABS (the Elephant), an experiment was performed to measure convective heat-transfer coefficients for helium flowing in a double-foil window assembly. An experimental assembly was built with the exact dimensions and lay-out of a real beam-window assembly except that the hot beam spots were simulated with electrically heated elements. That work reported significantly higher convective heat-transfer coefficients than predictions based on the Dittus-Boelter, Sieder-Tate and Petukhof-Kirilof equations [Ste1990]. The large discrepancy was finally understood to be related to the neglect of thermal entrance effects. The above-mentioned equations are valid for long pipes (i.e. for a length much longer than the inner diameter of the flow passage) where both the hydrodynamic and thermal boundary layers have become fully developed. Even if the hydrodynamic boundary layer has become fully developed but not the thermal boundary layer, a significant enhancement of the convection heat transfer can be expected. Such effects are seen in the entrance regions of heated tubes through which a coolant is flowing. In fact, the enhancement is most notable in the region where the

length-to-diameter ratio is smaller than unity (i.e. $x/D < 1$), as discussed in Section I.2.7 of Appendix I (see also Fig. I.1). It was argued in [Ste1996] that the small heated areas made by focused beams on window foils cannot be treated as warm areas on the inner walls of tubes unless these hot spots are located in the entrance region of the tube. Predictions of convective heat-transfer coefficients in the thermal entry region can be made using a formalism by Kays and Perkins [Kay1985], amongst others. The measured and predicted convective heat-transfer coefficients using the duct equations are presented in Table 9.1. Also shown in the table is the length-to-diameter ratio at which a prediction using the formalism by Kays and Perkins give the same result as the measured value.

Before discussing the results of Table 9.1, it is prudent to first mention some aspects of the helium cooling system. The bulk temperature of the helium is room temperature and it circulates in a closed loop. The bulk pressure is maintained at nominally 1.25 bar. The type of gas circulating pump in use from the time when the system became operational in the late 1980s until the present remained a Northey single-stage twin-rotor compressor. The laboratory owns a few of them and service them in-house. The system essentially remained unchanged except that nowadays when two bombardment stations are operated simultaneously using split beam, two of these compressors run simultaneously to provide a sufficient flow rate. These compressors are positive displacement pumps with a nominal bulk flow rate of 125 m^3/h each. In the two iThemba LABS papers on beam window cooling [Ste1990, Ste1996] a flow rate of 132 m^3/h was used for purposes of calculations. This value was found by measuring the time to inflate a cylindrical plastic bag with a volume of 2.6 m^3, subsequently used to calibrate an in-line flowmeter. Recently, a similar measurement was performed on a brand new Northey compressor and a somewhat lower value of 117 m^3/h was obtained. For the purposes of this work, the 125 m^3/h specification value has been adopted for calculations, with an understanding that there may be an uncertainty of about $\pm 6\%$ in the bulk flow rate. The hydraulic diameter of a single-port inlet into the double-foil window assemblies used on the Babe and Elephant target stations is 14.27 mm, resulting in a high linear gas velocity of 217 ± 13 m/s in the region of the foils. In the VBTS a multi-jet configuration is used, which will be discussed later.

The results of Table 9.1 show that the Dittus-Boelter, Sieder-Tate and Petukhof-Kirilof equa-

Table 9.1: Convective heat-transfer coefficients relevant to the helium-cooled beam-window assemblies of the horizontal-beam target stations – Elephant and Babe.

Method	h (W cm^{-2} °C^{-1})	x/D
Measured [Ste1990]	0.244	
Dittus-Boelter	0.086	
Sieder-Tate	0.094	
Petukhof-Kirilof	0.078	
Kays and Perkins	0.244	0.42

Helium pressure: 1.25 bar. Bulk flow rate: 125 m^3/h.
Helium inlet temperature: 300 K (room temperature).

tions underestimate the convective heat-transfer coefficient by almost a factor of 3. The average of these three values is $h = 0.086$ W cm^{-2} °C^{-1}, which is the same as the value obtained from the Dittus-Boelter equation. The equations of Kays and Perkins predict the measured value of $h = 0.244$ W cm^{-2} °C^{-1} with a length-to-diameter ratio of 0.42. This value multiplied with the hydraulic diameter of the Babe/Elephant window assemblies gives a value of 6.0 mm. This is of the same order of magnitude as the beam spot size – the heated surfaces in the experimental simulation of an Elephant window were circular with a diameter of 10 mm.

Calculations using the formalism by Kays and Perkins are useful for gaining an understanding of the convection heat transfer in helium-cooled beam windows, especially concerning thermal entrance effects, but it does not provide a means for making better predictions. There simply is no way to reconcile a calculation for a heated annular surface at the entrance of a heated tube with a circular beam spot inside a window assembly.

We only became aware of the existence of the work by Chang *et al.* [Cha1995] at the 13^{th} International Workshop on Targetry and Target Chemistry (WTTC 13) which was held in Roskilde, Denmark, in 2010. During that workshop, a presentation was made by Gagnon, Wilson and McQuarrie [Gag2010] on the modelling of a water-cooled solid cyclotron target using finite element analysis. These authors used the Dittus-Boelter, Sieder-Tate and a formalism by Chang *et al.* to calculate convective heat-transfer coefficients to be used in their model. They also performed measurements of the target temperature at the water/solid boundary for various values of the power deposited by the beam. An important aspect of this target design is that the cooling water enters the target assembly from the back through a single central inlet and that the direction of flow is perpendicular to the heated surface. After impact with the hot surface, the water flows radially outwards towards two outlet ports. It was found that the Dittus-Boelter and Sieder-Tate equations underestimated the convective heat-transfer coefficient considerably, very similar to what we observed for the helium cooling of beam windows. In sharp contrast, the calculations using the formalism of Chang *et al.* gave results in excellent agreement with the experimental measurements. In the original paper by Chang, the coolant is freon and the direction of flow is perpendicular to the heated surface. We found it very interesting that a formulation derived from correlations using freon as coolant would give such good results for convection cooling using water as coolant. A question begged for an immediate answer, namely, what does the formalism of Chang *et al.* predict in the case of forced convection cooling with helium as the coolant?

Chang's approach for single-jet impingement heat transfer has been applied to the helium-cooled window assembly used on the Elephant, however, this calculation has been done in a rather "cold-blooded" fashion as the direction of flow in the window assembly is not perpendicular to the heated surface. In fact, the flow in the window assembly is horizontal to the surface! This, admittedly, is not something that can be ignored. As a point of departure, however, we would like to put this complication on the back burner. Because this value of the convective heat-transfer coefficient is so precious to the discussion that will follow, it is highlighted in a separate table. Table 9.2 is an extension of Table 9.1 and compares the measured value with the value obtained from the formalism of Chang *et al.* The agreement between the measured

Table 9.2: Convective heat-transfer coefficients for the Target Station 1 (Elephant) helium-cooled beam-window assembly at iThemba LABS.

Method	h (W cm^{-2} °C^{-1})
Measured [Ste1990]	0.244
Chang formalism	0.228

Helium pressure: 1.25 bar.
Bulk flow rate: 125 m^3/h.
Helium inlet temperature: 300 K (room temperature).

and calculated values is remarkable. In order to shed light on the configuration issue, i.e. the direction of flow onto the heated surface, it was decided to design an experiment in which the incident angle of the jet could be adjusted between 0° and 90°. In the following sections, the formalism of Chang *et al.* will be described first, followed by the new experimental investigation.

9.3 Chang's formalism for single-jet impingement heat transfer

Chang's experiment employed jets with circular orifices. As is often done, we substituted the diameter in the equations with the hydraulic diameter in cases where the orifice had a shape different from circular (see Appendix I). The following expression gives the Nusselt number at the point of impact (the so-called stagnation point):

$$\mathrm{Nu}(0) = 0.660\,\mathrm{Re}_j^{0.574}\,\mathrm{Pr}^{0.4}\,(z/d_j)^{-0.106}, \tag{9.1}$$

where Re_j is the Reynolds number evaluated with the characteristic length taken as the exit nozzle diameter of the jet, Pr is the Prandtl number, z is the distance from the nozzle exit to the stagnation point, and d_j is the nozzle exit diameter. The dimensionless groups are described in Appendix I but are given here explicitly for the case of a single jet:

$$\mathrm{Nu} = \frac{hd_j}{k};\ \ \mathrm{Re} = \frac{\rho v d_j}{\mu};\ \ \mathrm{Pr} = \frac{c_p\mu}{k}; \tag{9.2}$$

where h is the convective heat-transfer coefficient, k is the thermal conductivity of the coolant, d_j is the exit diameter of the nozzle, ρ is the density (or specific gravity) of the coolant, v is the bulk velocity of the coolant where the jet exits the nozzle, μ is the dynamic viscosity of the coolant, and c_p is the specific heat of the coolant. The Nusselt number is often described as a dimensionless form of the convective heat-transfer coefficient. Once the Nusselt number is known, h can be calculated. In single-jet impingement heat transfer, there is a radial decrease in the value of the Nusselt number away from the stagnation point. A local average Nusselt number for a region within a radius r from the stagnation point is given by

$$\begin{aligned} \frac{\overline{\mathrm{Nu}}(r)}{\mathrm{Nu}(0)} &= [1 + 0.1147\,(r/d_j)^{1.81}]^{-1} \qquad \text{for } r/d_j \le 1.25, \\ \frac{\overline{\mathrm{Nu}}(r)}{\mathrm{Nu}(0)} &= 1.0632\,(r/d_j)^{-0.62} \qquad \text{for } r/d_j > 1.25. \end{aligned} \tag{9.3}$$

The local average convective heat-transfer coefficient is then given by

$$\overline{h}(r) = \frac{\overline{\mathrm{Nu}}(r)k}{d_j}. \tag{9.4}$$

9.4 New experimental measurements

9.4.1 Experimental set-up for single jets

An experiment was designed to measure convective heat-transfer coefficients of a gas incident onto a small heated surface, similar in size to a typical VBTS beam spot. The main aim was to investigate the effect of changing the angle of incidence of the jet onto the heated surface while keeping everything else the same. For the purposes of the experiment, it was not considered essential that the gas had to be helium circulating in a closed loop. In order to simplify the experimental set-up, it was decided to use air at ambient conditions as the coolant. This eliminated the need for a gas-tight, closed-loop system and a heat exchanger. A schematic diagram of the system is shown in Fig. 9.1 with further details in Figs. 9.2 and 9.3

The main aspects of the experimental set-up are as follows: A Northey twin-rotor compressor supplies a bulk flow of up to 125 m^3/h to a 25 L buffer tank. Tubing with a 40 mm inner diameter connects the tank to a heated plate assembly. A commercial electric element (manufactured by Swift Heat & Control: 230 V AC, 400 W) is embedded into the aluminium plate, as shown in Fig. 9.2. The aluminium plate assembly is thermally insulated with mineral wool (supplied by Rockwool) except at the circular gas-cooled surface. The heated surface has a diameter of 36 mm. A k-type thermocouple is used to measure the temperature at the solid/gas interface. The AC voltage can be adjusted with a variac and Fluke instrumentation is used to read out the voltage and current values. All temperature, voltage and current values can also be streamed to a computer in 1 second intervals. A small chamber with a hemispherical shape (or dome) fits over the heated surface. In fact, five of these chambers were constructed with different jet angles but otherwise they are identical. Measurements were performed at jet angles of 0°, 22.5°, 45°, 67.5° and 90°. The surface area adjacent to the heated surface is

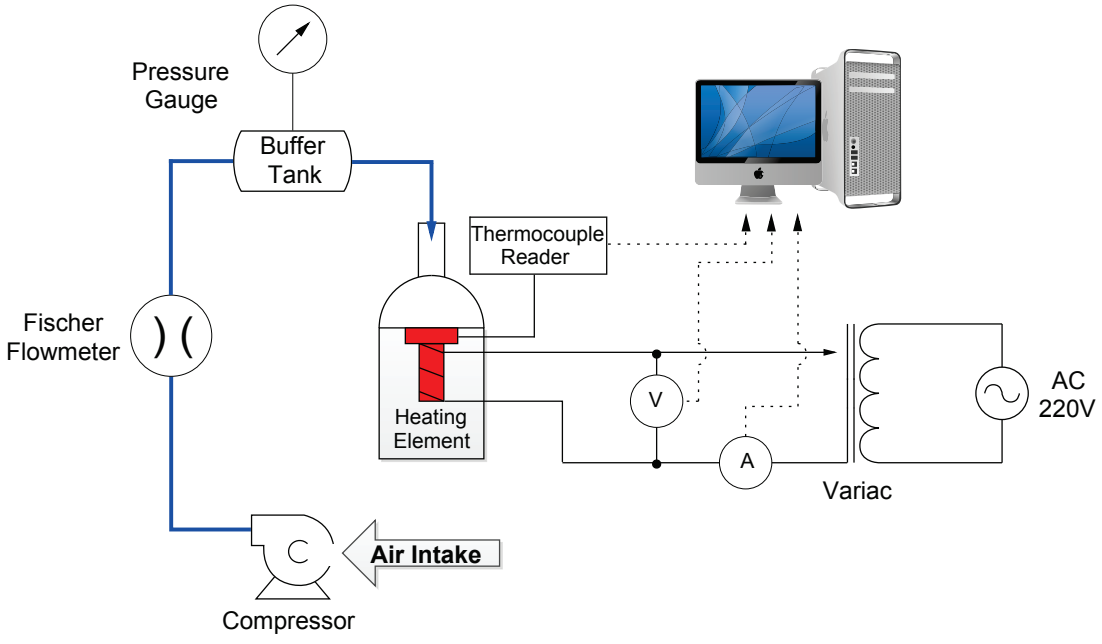

Figure 9.1: Schematic diagram of the experimental set-up to measure convective heat-transfer coefficients for air flowing onto a small heated surface.

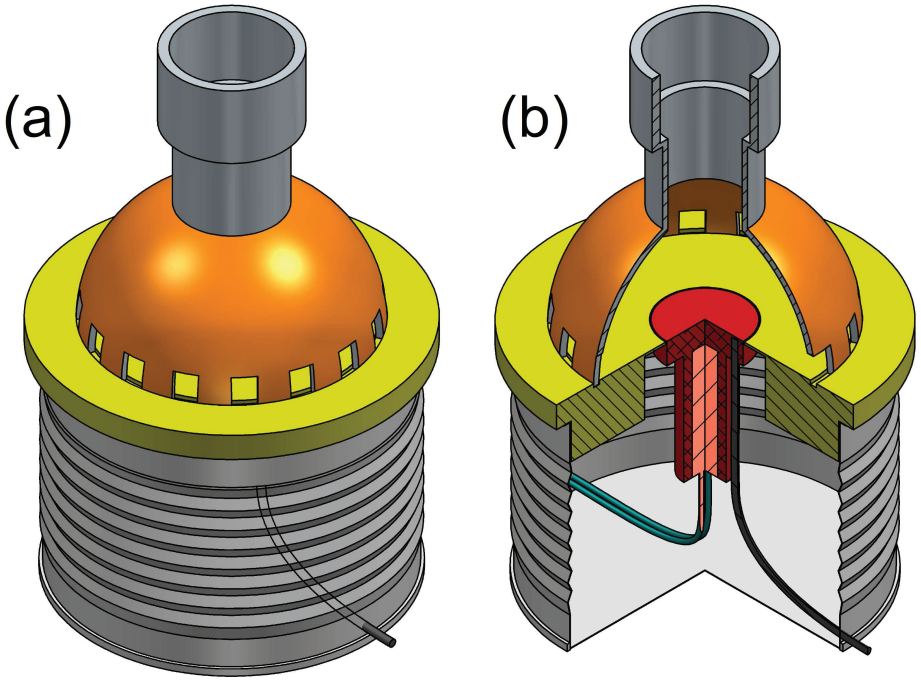

Figure 9.2: (a) 3D view of the hemispherical chamber (or dome) and electrically heated plate assembly. (b) The same view but with a cut-away of the assembly to show the heated surface and single jet.

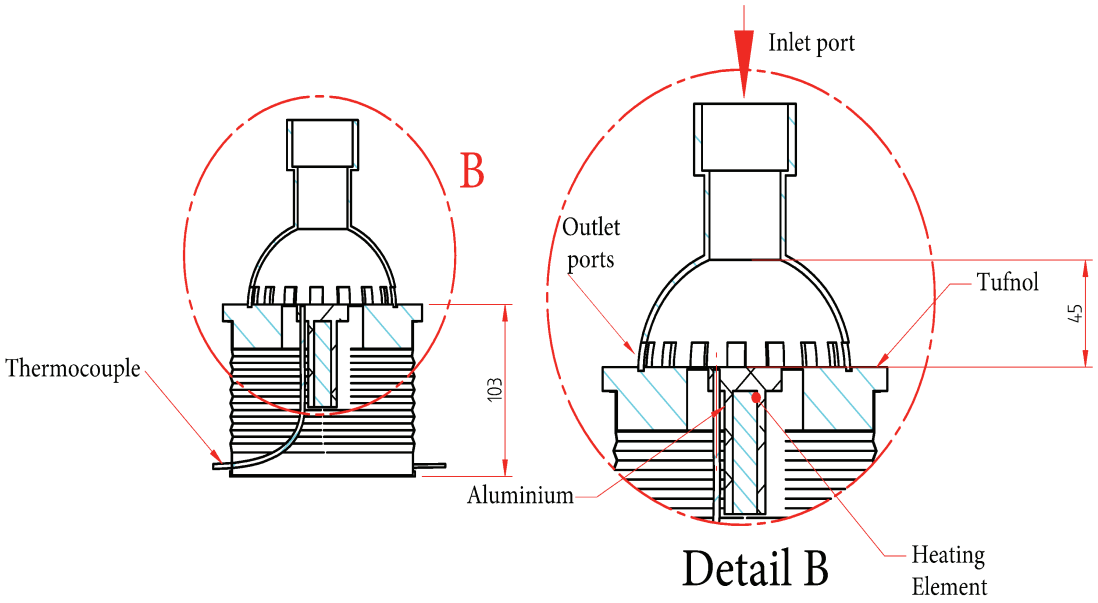

Figure 9.3: Cross-sectional views of the electrically heated plate assembly for measuring convective heat-transfer coefficients with a single jet. Note the single inlet port at the top and several rectangular outlet ports along the bottom edge of the hemispherical chamber.

made of Tufnol, a material with more than two orders of magnitude lower thermal conductivity than aluminium. Also, the Tufnol plate was machined so that the material in contact with the aluminium plate was only 1 mm thick. This provided a single hot surface within a region predominantly at room temperature. Several rectangular apertures along the bottom edge of the dome serve as exit ports for the gas (nine in total, each 10 mm wide and 11 mm high on one side of the dome only, opposite to the inlet side). The differential pressure between the

buffer tank and outside atmosphere never exceeded 15 mbar, thus, for all practical purposes the pressure of the gas in the dome was considered to be at a constant value of 1 bar.

The thermal losses due to mechanisms other than forced convection were determined by covering the heated surface with insulating wool and measuring the electrical power versus temperature characteristics of the system for steady-state conditions without flow. These values were subtracted from the corresponding values obtained with flow. Steady-state cooling power densities (or heat-transfer rates) for forced convection were measured at surface temperatures of 100 °C, 150 °C, 200 °C, 250 °C and 300 °C.

9.4.2 Data analysis

When the values of the power density (q/A) are plotted versus the difference in temperature between the surface and the coolant ($T - T_0$), the convective heat-transfer coefficient is given by the slope of a straight line fitted through the measured data points. A representative example is shown in Fig. 9.4. In this case the jet direction was 0°, i.e. parallel to the heated surface. Note that the adiabatic heating of the gas was determined to be about 14 °C by running the system with the electric element switched off, which raised the coolant temperature somewhat above the room temperature. The uncertainty associated with each h-value determined from the fitting procedure was taken as one standard deviation of the h-values determined from the individual measurements at discrete temperatures.

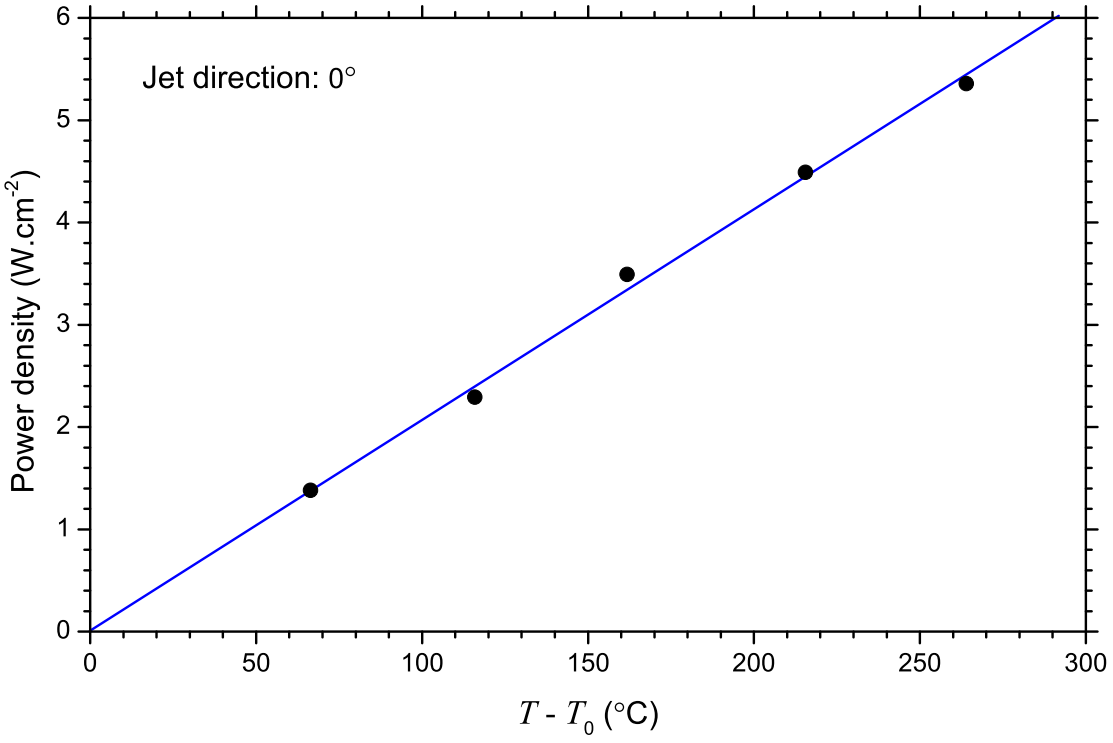

Figure 9.4: Measured power density (q/A) versus the difference in temperature between the surface and the coolant ($T - T_0$) in the case of flow parallel to the heated surface. The coolant was air at a pressure of 1 bar and a flow rate of 125 m^3/h. The diameter of the single jet was 36 mm.

9.4.3 Results and discussion - single jets

The measured convective heat-transfer coefficients are shown in Fig. 9.5 as a function of the jet angle. Also shown in Fig. 9.5 are calculated values according to the Chang, Dittus-Boelter, Sieder-Tate and Petukhof-Kirilov equations. A wall temperature of 300 °C was adopted for the Sieder-Tate calculation. Note that these calculated values are shown as horizontal lines in the figure for purposes of comparison with the measured values, however, they are not to be understood as functions of the jet angle. The two red dashed lines are calculations using the Chang equations for flow rates adjusted by -6% and +6% relative to the nominal value of 125 m^3/h, respectively, as an indication of the measure of uncertainty described above. The small schematic diagrams of the dome at the top of the figure indicate the flow directions. The bulk velocity of the jet was nominally 36 m/s.

This result is rather remarkable. There is very little difference between the measured heat-transfer coefficients except at a jet angle of 45°, where the value is markedly lower. We believe that this result points significantly towards an explanation why the formalism of Chang *et al.*, established for a jet direction of 90°, yields a surprisingly good value also when the jet direction is 0° in a helium-cooled window assembly (see Table 1.2). At least, we can see for ourselves a case where a change in jet direction from 90° to 0° made very little difference to the convection cooling. Before the experiment, we kind of hoped to find a rather weak dependence on jet angle, perhaps a plateau with a slow drop-off towards smaller angles. Instead, we see the largest difference at a jet angle of 45°, which is rather intriguing. It is interesting to compare some of the convective heat-transfer values at 90°: Measured ($h = 0.0212$ W cm^{-2} °C^{-1}); Chang

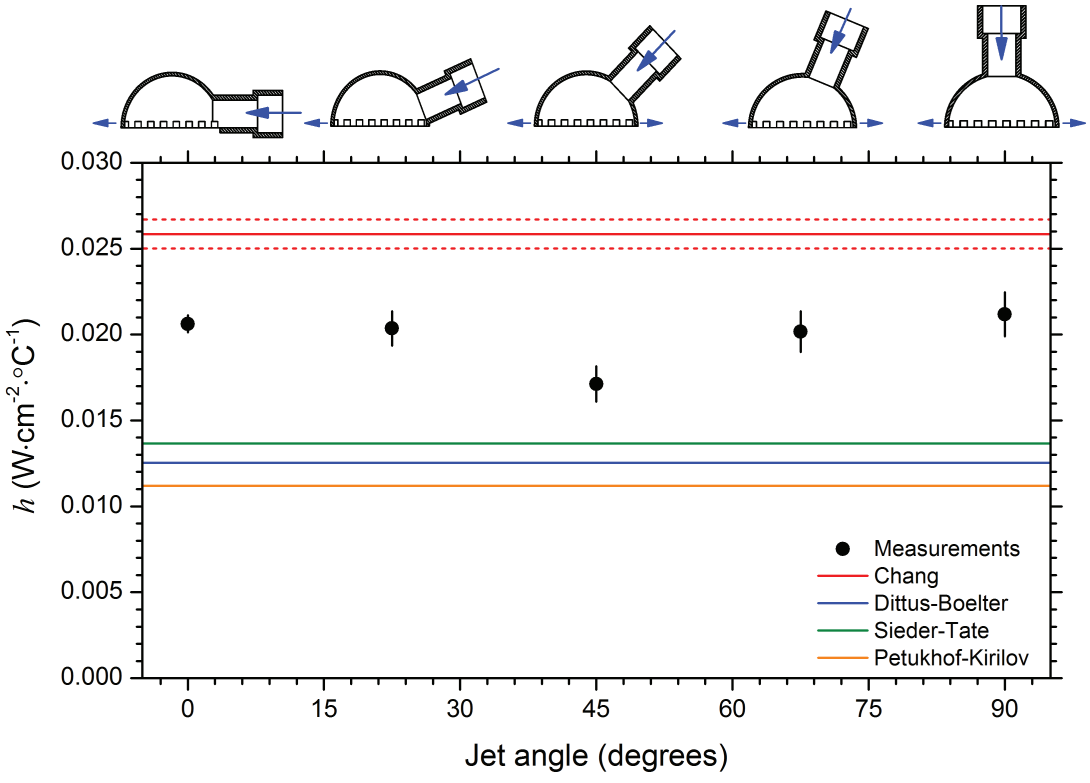

Figure 9.5: Measured convective heat-transfer coefficients versus jet angle. The bulk linear velocity of the air was nominally 36 m/s. Some calculated values are also shown, as indicated. See also caption to Fig. 9.4 for further details.

($h = 0.0258$ W cm^{-2} °C^{-1}); Dittus-Boelter ($h = 0.0125$ W cm^{-2} °C^{-1}). The Chang formalism gives a 21.7% overprediction relative to the measured value. The Dittus-Boelter equation, on the other hand, gives a 69.6% underprediction. Thus, the Chang result is much closer, which is perhaps not so evident from a first glance of Fig. 9.5.

The experimental set-up was found to be very stable. Individual measurements repeated on different days yielded the same results. It seems that if a small heated surface is enclosed inside a compact chamber through which a coolant gas flows at a large flow rate, such that the time for an exchange of the gas from the chamber is small compared to the relaxation time of the system, the exact orientation of the heated surface is of secondary importance. With "relaxation time" we mean the characteristic time to respond to a change of conditions or to recover from a perturbation to the system. With "small" we mean dimensions not significantly larger than that of the jet, or the combined extent of the jets if there are more than one – i.e. the effective cross-sectional extent of the entire "flow stream". This statement is made reservedly and will be gladly changed or rephrased if better insight warrants a better description.

9.4.4 Modelling

As already mentioned, the heated surface was chosen to have an area similar to the expected beam spot on a VBTS target and beam-window assembly. In addition, the heating element was positioned such that the contact area onto the aluminium plate approximately modelled the annular surface of the swept beam. Calculations were performed using the methods discussed in Appendices J and L. A boundary condition was specified that no conduction should occur between the radial edge of the plate and surrounding materials. Heating was from below onto one flat surface and convection cooling was applied on the other flat surface. Relaxation was first performed in the axial direction by allowing conduction in only that direction until a steady-state was obtained. Relaxation was then performed in the radial direction until a steady state was again obtained. This is not, admittedly, what happens in the real world but the approximation is nevertheless expected to give realistic results. The method followed was to adjust the thermal load until the edge temperature of the plate reached a measured value. The power required to achieve this could then be directly compared with the measured electrical power supplied to the heated plate. Generally, excellent agreement was found.

The thickness of the heated plate in the experiment was chosen to be 10 mm, which is rather thick. This was done for a reason, namely, to keep the entire heated surface onto which the convection cooling was applied constant, for all practical purposes. Figure 9.6 shows the radial temperature profile of the heated surface for this case, where the edge temperature was set at 300 °C. The convective heat-transfer coefficient measured at 0° was adopted, namely $h = 0.0206$ W cm^{-2} °C^{-1}. The power required to reach a steady-state with an edge temperature of 300 °C under these conditions is 55.8 W, in good agreement with the corresponding experiment value of 54.5 W. This is very reassuring. As can be seen in the figure, the variation in temperature across the heated surface is less than 2 °C in this case.

Also shown in Fig. 9.6 are radial temperature profiles of the heated surface should the plate be made thinner, as indicated. For these calculations, the thermal load was kept unchanged

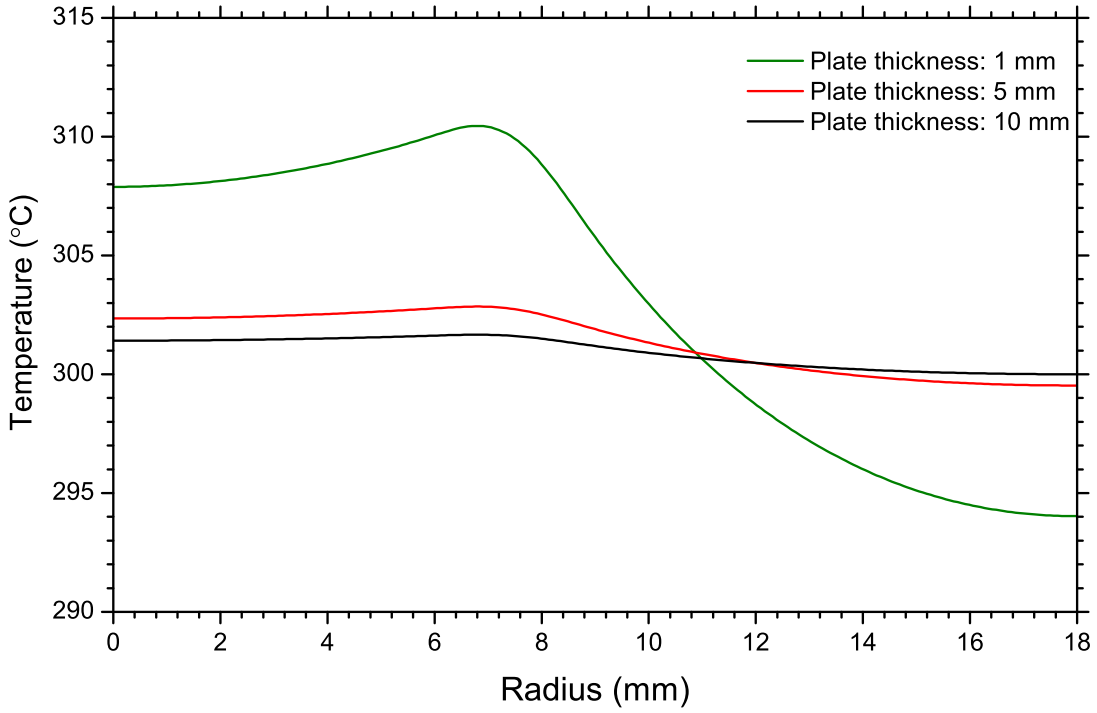

Figure 9.6: Calculated steady-state radial temperature profiles of the heated plate for different plate thicknesses. A convective heat-transfer coefficient of $h = 0.0206$ W cm^{-2} °C^{-1} and a thermal load of 55.8 W (see text) were specified.

at a value of 55.8 W. It is clear that the radial temperature variation increases with decreasing plate thickness. With a plate thickness of 1 mm, the radial temperature variation is slightly more than 17 °C, which would no longer be negligible. This behaviour is to be expected as the cross-sectional area through which the heat has to spread radially by conduction is smaller when the plate becomes thinner. A thin window would have been advantageous from the point of view of the response time of the system, i.e. a steady state would be arrived at sooner after an adjustment to the thermal load. The thicker plate used in the actual experiment made the response somewhat tardy but this was not a disadvantage of any real significance.

9.4.5 Experimental set-up for multiple jets

Multiple-jet cooling seems to be a considerably more complicated topic than single-jet cooling and general descriptions for the convective heat-transfer coefficient do not seem to exist. The different permutations in terms of flow conditions and configurations are probably too numerous. Chang *et al.* [Cha1995], for example, compared a multi-jet configuration (a 5 × 5 square matrix of jets) with their single-jet case and reported some notable enhancement, however, they also reported that their results are not in full agreement with a number of other authors. Chang attempted a description for their multi-jet case as an expansion of their their single-jet description. This multi-jet description, however, seems to be very case specific and not particularly useful to beam-window thermal modelling – at least, this is the conclusion that we ultimately reached.

The present VBTS beam-window assembly utilizes a multi-jet design (ten 4 mm jets per foil with a jet angle of 12°). This was done in an attempt to ensure a better coverage of the helium

onto these larger windows. To be more specific, the original design did indeed utilize a single jet only. Vacuum problems during the first run of the VBTS led to some hasty decisions, one being the change to a multi-jet configuration for the window, which was implemented in less than 48 hours. Quite frankly, we were flying by the seats of our pants at that time and the design change was in all probability not necessary. Nevertheless, we have been operating the VBTS with these multi-jet windows ever since.

Several authors commented on the fact that adjacent jets in a confined flow can interact in a way that enhances the turbulence in the regions away from the stagnation points of the individual jets. This can lead to an overall enhancement of the heat transfer even though the stagnation point heat transfer may be reduced.

After the completion of the single-jet measurements described in the previous section, it was decided to convert the experimental set-up to a multi-jet configuration on the 90° dome. What we wanted to investigate was whether any enhancement could be achieved relative to the single-jet results. The experimental set-up is shown in Fig. 9.7.

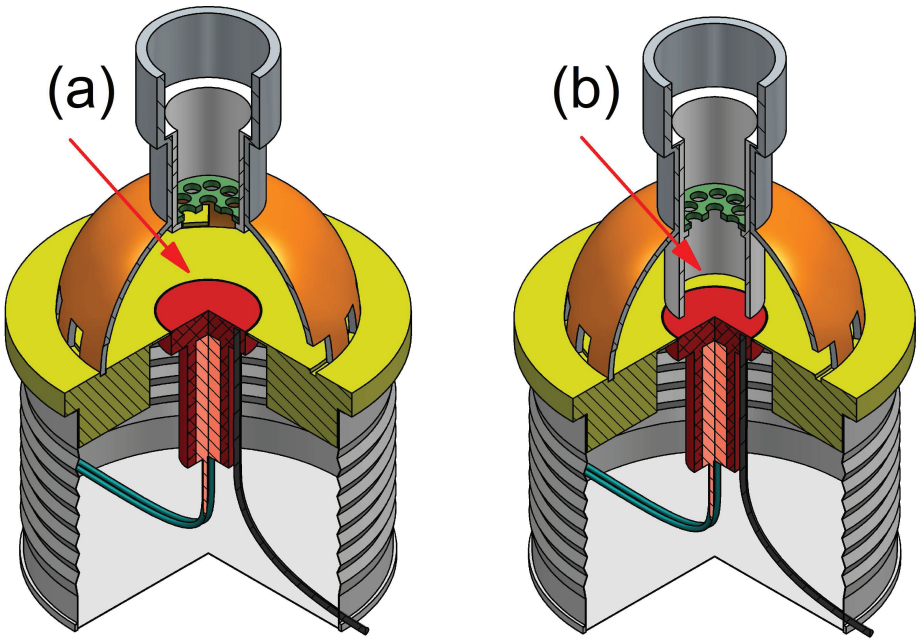

Figure 9.7: (a) 3D view of the 90° hemispherical chamber (or dome) and electrically heated plate assembly with a cut-away to show the heated surface and multiple jets. (b) The same view but with a flow guide installed (see text). The flow direction is perpendicular to the heated surface.

Essentially, the experimental set-up was the same as before except that an insert with holes could be fitted at the top of the dome. Several such inserts were manufactured, each with a different number of holes but the total jet cross-sectional area remained the same. These inserts reduced the free flow area considerably compared to the previous single-jet case. The volume flow rate was therefore reduced for these measurements but the bulk linear velocity was nevertheless increased to 50 m/s (compared to 36 m/s in the case of the single-jet experiment). To be more precise, one of the inserts of the multi-jet experiment also had only one jet: Insert no. 1 (one jet, accurately machined to a diameter of 15.87 mm); Insert no. 2 (three jets,

machined to a diameter of 9.175 mm each); Insert no. 3 (seven jets with a diameter of 6 mm each); Insert no. 4 (ten jets with a diameter of 5 mm each); Insert no. 5 (sixteen jets with a diameter of 4 mm each). In order to ensure that the total free flow areas of all the jet inserts were exactly the same, one of the holes had to be machined slightly larger or smaller than the others in a few cases. The inserts are shown schematically at the top of Fig. 9.8. The idea behind the "flow guide" shown in Fig. 9.7 (b) will be explained below.

9.4.6 Results and discussion - multiple jets

The measured convective heat-transfer coefficients are shown in Fig. 9.8 as a function of the number of jets. Also shown in Fig. 9.8 are calculated values according to the Chang, Dittus-Boelter, Sieder-Tate and Petukhof-Kirilov equations, as before, but for a bulk linear velocity of 50 m/s. A wall temperature of 300 °C was adopted for the Sieder-Tate calculation. Similar to the approach in Fig. 9.5, the calculated values are shown as horizontal lines for purposes of comparison with the measured values, however, they are not to be understood as functions of the number of jets. The two red dashed lines are calculations using the Chang equations for flow rates adjusted by -6% and +6% relative to the nominal value of 35.4 m^3/h (50.0 m/s), respectively, as an indication of the measure of uncertainty described above.

These results are most certainly very case specific. A significant enhancement in the convective heat-transfer coefficient relative to the single-jet value is found only in the three-jet case. There is also a very slight enhancement with seven jets relative to one jet, however, this value is reduced considerably relative to the three-jet value. This falling trend continues

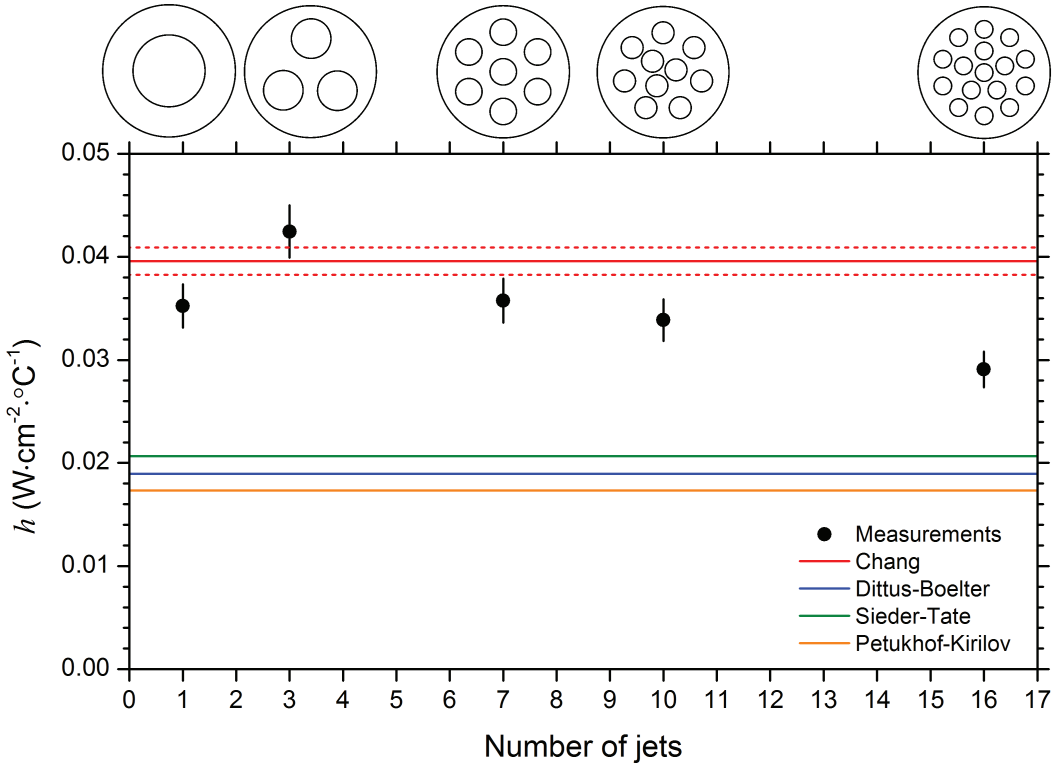

Figure 9.8: Measured convective heat-transfer coefficients versus number of jets. The bulk linear velocity of the air was nominally 50 m/s. Some calculated values are also shown, as indicated.

towards increasing the number of jets. As before, the calculations with the Dittus-Boelter, Sieder-Tate and Petukhof-Kirilov equations calculation underestimate the convection cooling. The calculation with the formalism of Chang *et al.* is much closer to the measured single-jet value but the experimental value is nevertheless lower (Chang: $h = 0.0396$ W cm^{-2} °C^{-1}; Single-jet: $h = 0.0352 \pm 0.0021$ W cm^{-2} °C^{-1}). The measurement with three jets was repeated several times and consistently gave a higher value ($h = 0.0424 \pm 0.0025$ W cm^{-2} °C^{-1}).

It was speculated by Chang *et al.* [Cha1995] that the increased turbulence caused by the interaction of neigbouring jets may reduce the "jet potential core", leading to reduced stagnation point heat transfer but enhanced heat transfer away from the stagnation points. Based on this notion, there was some speculation at iThemba LABS that perhaps this kind of jet interaction may be having a "diverging" effect on the flow, leading to a significant spreading of the impinging coolant onto the uncooled surface adjacent to the heated surface. Such a spreading would then account for the observed reduction of the convective heat-transfer coefficient with increasing number of jets (for jet numbers larger than 3). In order to investigate this notion, a "flow guide" was installed, shown in Fig. 9.7 (b). This is just a piece of tubing below the jet insert up to a distance of 10 mm from the heated surface. Its purpose was to ensure that the bulk of the coolant impinged onto the heated surface and prevent the primary jet from straying onto the adjacent uncooled surface. Measurements with the flow guide installed, however, produced the same results as measurements without it. The flow guide had no significant effect at all!

It is clear that one can obtain an enhancement with a multi-jet configuration but one can also obtain a reduction. Consequently, the rule should be to *use multiple jets with caution!* It seems to be justified only in situations where the pitch-to-jet-diameter ratio has to be rather large, by necessity rather than choice, such as the cooling of relatively large surfaces with a limited amount of coolant. This is not usually the case for relatively small beam spots on thin gas-cooled window foils.

The VBTS beam-window assembly was not changed from its multi-jet configuration as there was not considered any need to. We now believe, however, that a single jet would have sufficed. One cannot at this time know with good certainty what the effective convective heat-transfer coefficient is for helium in that assembly. One can, however, make some estimates: Consider the heated area as determined by the four-sector collimator (36 mm diameter) and partition the surface equally for the 10 jets. If such a partitioned surface section is considered to be spherical with a single jet impinging in its centre, the formalism of Chang *et al.* predicts a value of $h = 0.0234$ W cm^{-2} °C^{-1}. This is quite similar to the measured value pertaining to the Elephant and Babe window assemblies (see Tables 9.1 and 9.2).

9.5 Radial temperature distributions

As mentioned in Section 9.1, the code WINHEAT has evolved by upgrading the old WINDOW code considerably. It was considered necessary to perform some benchmark calculations to evaluate the upgraded code. The work of Votaw and Nickles [Vot89] was found perfect for this purpose. These authors performed calculations for an 11 MeV proton beam with an intensity of 15 μA on Ni foils. They considered the radial intensity distribution to be uniform and the tem-

perature dependence of material properties, such as the thermal conductivity, was neglected. Otherwise, all three modes of heat transfer (forced convection, conduction and radiation) were implemented rigorously. Consequently, we used the calculations of [Vot89] as a benchmark for our WINHEAT predictions. The results are shown in Fig. 9.9. The overall good agreement is very reassuring. As can be seen from Fig. 9.9 (b), the heat transfer by radiation is only a perturbation on window cooling, as also commented on in [Vot89]. Votaw and Nickles employed a much smaller helium flow rate compared to the nominal flow rate at iThemba LABS (more than an order of magnitude lower), the reason for their reduced convective heat-transfer coefficient of $h = 0.04$ W cm^{-2} °C^{-1}. In their application, smaller windows and a lower thermal load by the beam can be matched by a smaller helium cooling system.

It is interesting to compare the radial temperature profiles calculated for the Havar beam-window assemblies of the three target stations under maximum bombardment conditions and typical beam characteristics. Various properties of the beam and window assemblies are summarized in Table 9.3. For the purposes of the comparison, a conservative value for the convective heat-transfer coefficient was adopted, namely $h = 0.20$ W cm^{-2} °C^{-1}. The temperature dependent values of the conductivity and emissivity of Havar from [Ste1990] were employed. Figure 9.10 shows the calculated temperature distributions for Babe (50 μA), the Elephant (100 μA) and the VBTS (300 μA) with typical beam conditions as specified in Table 9.3. It is clear that the window foils of Babe become the hottest as the beam is not swept but the maximum temperature is still below 250 °C, which is relatively cool. Even in the unlikely situation

Table 9.3: Typical properties of the beam and He-cooled window asssemblies.

	VBTS	Elephant	Babe
Beam direction	vertical	horizontal	horizontal
Beam sweep radius	8.5 mm	3 mm	nil (no sweeping)
Beam sweep frequency	3 kHz	450 Hz	–
Beam diameter (2 × FWHM)[a]	13 mm	8 mm	8 mm
Maximum design beam current	300 μA	100 μA	50 μA
Window collimator diameter	36 mm	16 mm	16 mm
Target collimator diameter[b]	none	none	9 mm
Window diameter	50 mm	20 mm	20 mm
Inner window foil thickness	75 μm	25 μm	25 μm
Outer window foil thickness	50 μm	25 μm	25 μm
He bulk pressure	1.25 bar	1.25 bar	1.25 bar
He bulk temperature	25 °C	25 °C	25 °C
He bulk volume flow rate[c]	125 m^3/h	125 m^3/h	125 m^3/h
He-jet flow velocity	138 m/s	217 m/s	217 m/s
Number of jets	10 per foil	1	1
Effective jet exit diameter	4 mm	14.27 mm	14.27 mm

[a] Diameter of the unswept beam, assuming a Gaussian shape of width $2 \times \mathrm{FWHM}$.
[b] Necessary to reshape the degraded beam for the $H_2{}^{18}O$ target;
Not required on the Elephant and VBTS.
[c] Delivered by a positive displacement rotary compressor.

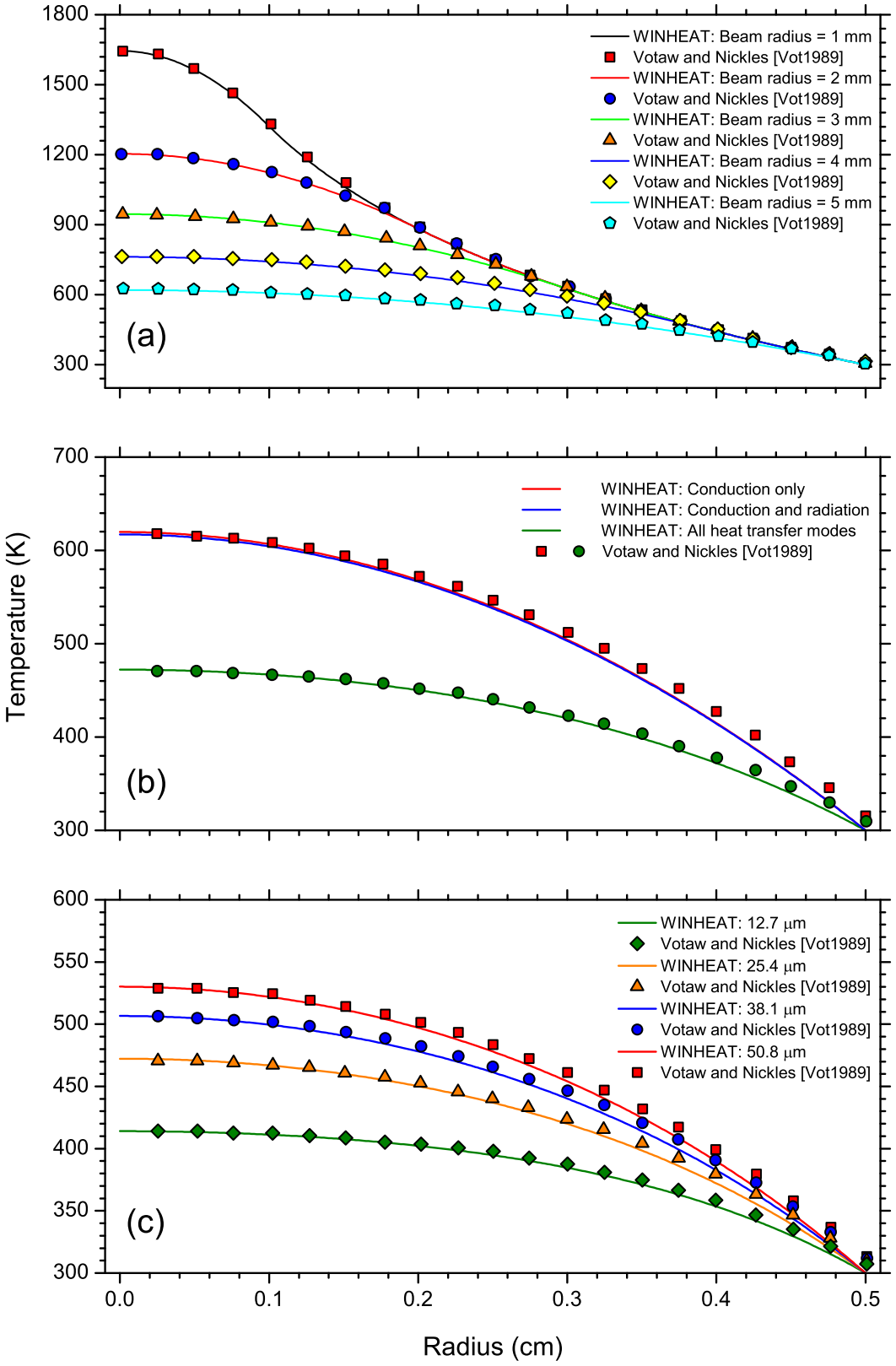

Figure 9.9: Calculated radial temperature profiles for a Ni foil with a diameter of 1 cm under bombardment with an 11 MeV proton beam of 15 μA intensity. (a) Conduction only as the means of heat transport for different beam diameters, as indicated. (b) The upper curves assume conduction and conduction plus radiation as the means to remove heat from the foil. The bottom curve in (b) includes forced convection of helium with $h = 0.04$ W cm^{-2} °C^{-1}. (c) All modes of heat transfer included for different Ni foil thicknesses, as indicated. All symbols: Votaw and Nickles [Vot89]; All curves: WINHEAT – this work.

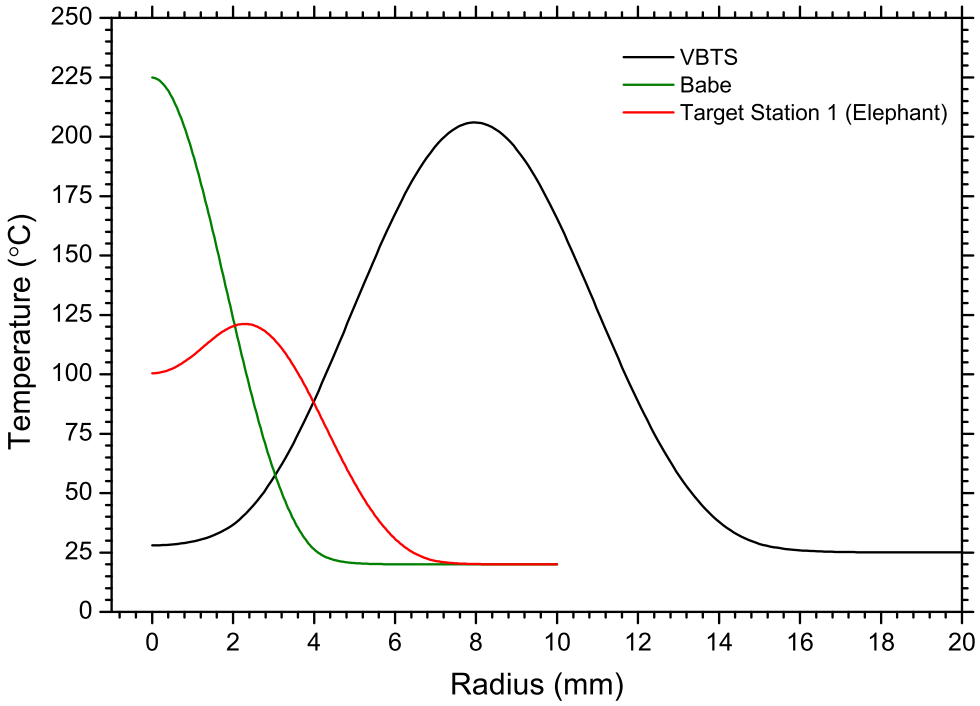

Figure 9.10: Calculated radial temperature profiles for the beam windows used on the target stations for radionuclide production at iThemba LABS under maximum bombardment conditions, as summarized in Table 9.3.

where the convective heat-transfer coefficient has a value of only half of the adopted value, the maximum temperatures will still be well below the maximum safe operating temperature of 700 °C. All indications, therefore, are that these windows operate at safe temperatures during bombardment, well below the normal capabilities of Havar as a window material.

9.6 Different gasses as coolants

It is interesting to compare different gasses as coolants. While we never seriously doubted helium as the coolant of choice for these windows, occasionally this has to be explained. At one such occasion, an argumentative individual told us that "everybody knows that freon is a superior coolant to helium". Figure 9.11 shows the ratios of convective heat-transfer coefficients of various gasses relative to helium under typical flow conditions used in the beam-window assemblies at iThemba LABS. These values have been calculated using the formalism of Chang *et al.* It is evident that the lighter gasses are better for this application. While hydrogen has the best cooling properties of all the gasses, it is considered too dangerous for application in window cooling due to its highly flammable properties. Second to hydrogen, helium has the best cooling properties, significantly better than R22 freon in a gaseous state. Even neon is better than gaseous R22. In addition to its cooling properties, the proton bombardment of helium does not lead to the production of significant activation products. This is not the case with the heavier gasses. In the case of nitrogen, for example, copious quantities of ^{7}Be ($T_{1/2} = 52.2$ d) will be produced. Other nasty radionuclides will be produced if the heavier gasses are used as coolant. The build-up of radioactive activation products in the cooling system is certainly something to avoid. A gas leak, for example, may result in a nasty release of radioactivity. Also,

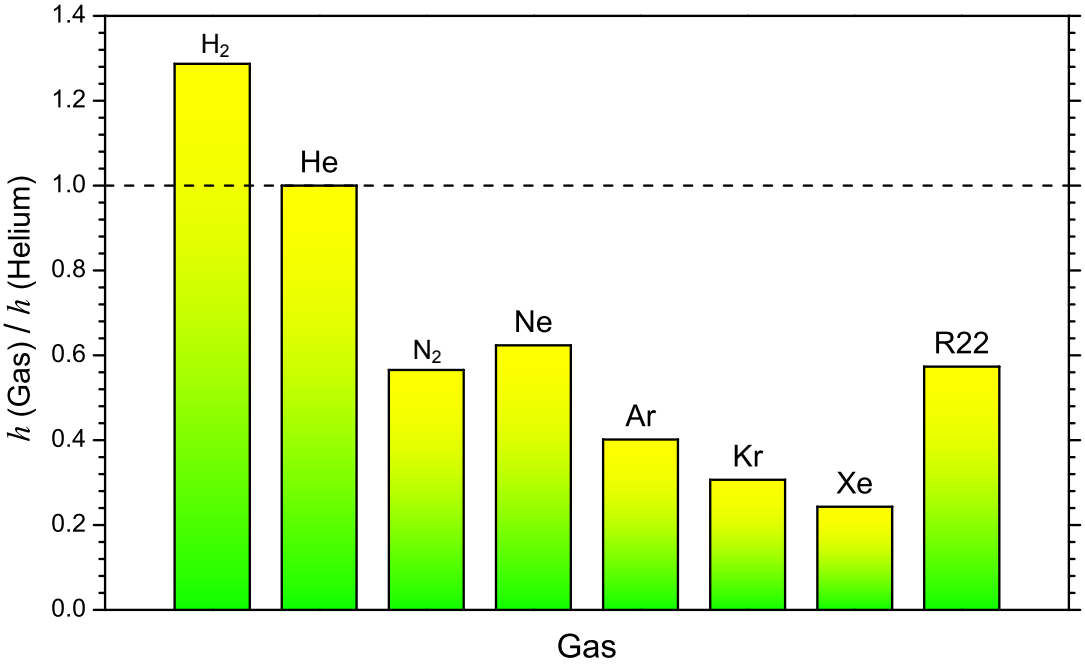

Figure 9.11: Ratios of convective heat-transfer coefficients of various gasses (as coolants) relative to that of helium.

freon consists of composite molecules which will be broken down by the intense radiation. Unfortunately, the cost of helium has increased dramatically in recent years and the world-wide supply of this gas is under threat. This, however, is another issue.

9.7 Transient calculations

Strictly speaking, a steady-state temperature profile can never be obtained with a swept beam. If the sweep frequency is sufficiency high, however, conditions close to a steady state can be obtained. In this work, an approximate method to calculate the transient temperature behaviour of the hottest node on a window foil under bombardment has been implemented in the WINHEAT code. The details of the method is described in Appendix M. In fact, Section 2.3.3 already "borrowed" the method in order to describe key aspects of the beam sweeping in the vertical beamline (also see Fig. 2.13). Here, we would like to revisit the outer window foil of the VBTS beam-window assembly under maximum bombardment conditions with an optimized beam (i.e. a beam diameter of 13 mm, a sweep diameter of 17 mm and a 300 μA intensity of the 66 MeV proton beam). Figure 9.12 compares the results of a steady-state calculation and the corresponding transient calculations for a number of different sweep frequencies. The time period shown is one cycle of the beam at 50 Hz (i.e. 20 ms) starting at a time 0.5 s after the beam intensity reached the 300 μA maximum value. It is clear why the line frequency, which is 50 Hz in South Africa, is not a good choice for the sweep frequency. Perhaps a value as high as 3000 Hz is not strictly necessary but this is what could be achieved at the laboratory with the chosen infrastructure. It is evident that at the highest frequency the thermal behaviour of the window foil is close to a steady state.

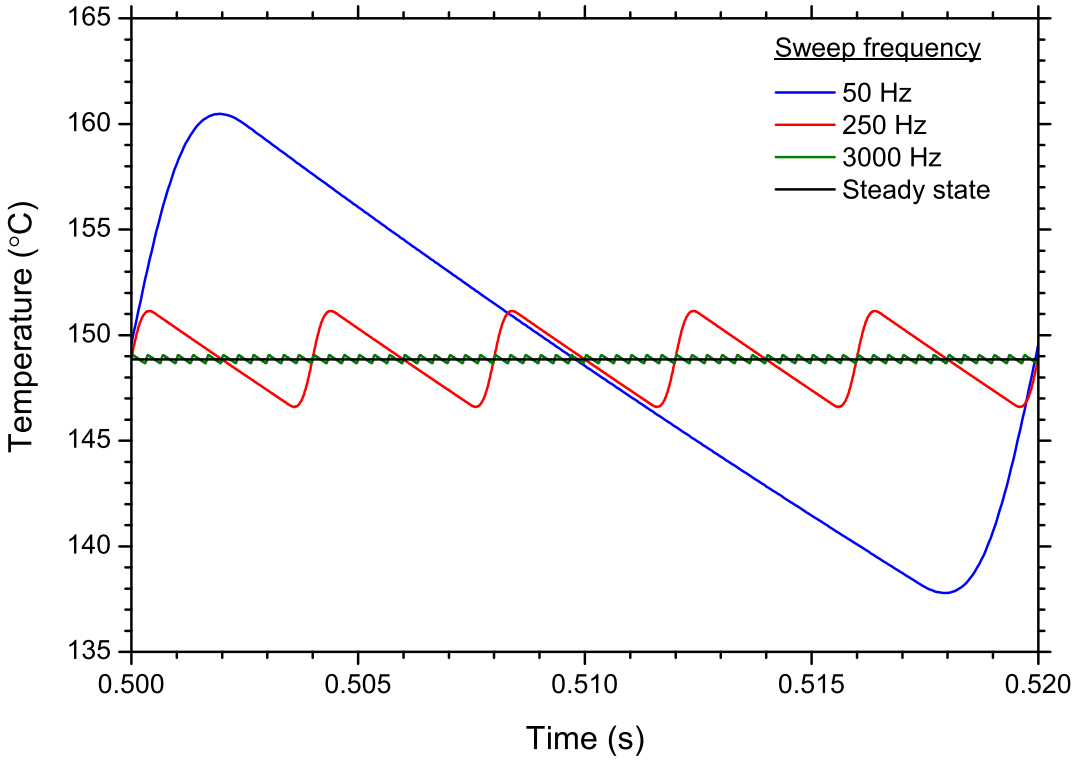

Figure 9.12: Steady-state and transient calculations for the temperature of the hottest node on the outer Havar foil of the VBTS helium-cooled beam-window assembly. Cooling is by forced convection of helium with $h = 0.2$ W cm^{-2} °C^{-1} (see text for details).

9.8 Advanced modelling

From the outset of this thesis project, it was planned to investigate advanced modelling using modern codes in which Computational Fluid Dynamics (CFD) and Finite Element Analysis (FEA) techniques for thermal analysis have been implemented. Such work, however, was to follow initial work using simpler techniques based on the finite difference technique and dimensional analysis. One reason for this decision was to not neglect methods which are computationally simpler but can nevertheless provide good physical insight. A second reason was to avoid a possible situation where too much time was spent on modelling activities using a "black box" commercial code at the expense of learning the basic principles of heat transfer. This was probably the correct decision as both approaches are believed to be useful and important. There was an expectation, perhaps, that more progress would have been made earlier with the advanced modelling codes but this did not happen as more time than expected was spent on the experimental work and development work on the WINHEAT code. Calculations relevant to this thesis project using commercial codes only started rather recently but already the results prove to be rewarding.

The experimental set-up for single-jet cooling, described in Section 9.4.1, was modelled using the program Autodesk Simulation CFD 2014 (formerly called CFDesign). The geometry of the set-up, as designed with the drafting code Solid Edge, was imported via AutoCAD Inventor into the Simulation CFD code and further refined by specifying the various materials, surfaces and flow passages. In this way, models of the geometries with flow at 0°, 45° and 90° relative to

the heated surface were established. It was possible to arrive at the first calculations relatively quickly as the Simulation CFD code has many default options. It is also a reasonably user friendly code with a well-developed user interface to provide the necessary input, such as boundary conditions, mesh sizes and model choices. The coolant was specified as air with a temperature of 25 °C and a bulk flow rate of 125 m^3/h, similar to the actual experiment. A constant heat flux of $q = 5.4$ W·cm^{-2} was specified for the heated surface, which is equivalent to a total thermal load of 55 W. The first calculations were performed mostly using "automatic" selections, allowing the program to determine a mesh size by its own internal algorithms. The user is allowed to alter the mesh size by means of a slider. Since some sensitivity to the choice of mesh size was evident, it was decided to use the finest mesh that the code allowed, which was 0.2 mm for this specific problem. Figure 9.13 shows an example of a velocity magnitude profile for the 45° scenario with a 0.2 mm mesh size. Such a run creates just over 743 000 elements and typically takes several hours to complete on a mid-level PC.

The Simulation CFD 2014 code has 8 built-in turbulence models. The default is the so-called K-epsilon model, which is described as one of the most common turbulence models of CFD. The online literature of the code gives a fairly comprehensive description of each of these models. By discounting those models intended for low Reynolds numbers, transition flow or otherwise not recommended for our type of problem, 5 turbulence models remain. Only two of these have been investigated at the time of writing, namely the default K-epsilon model and the SST K-omega model. A short description on each is given below.

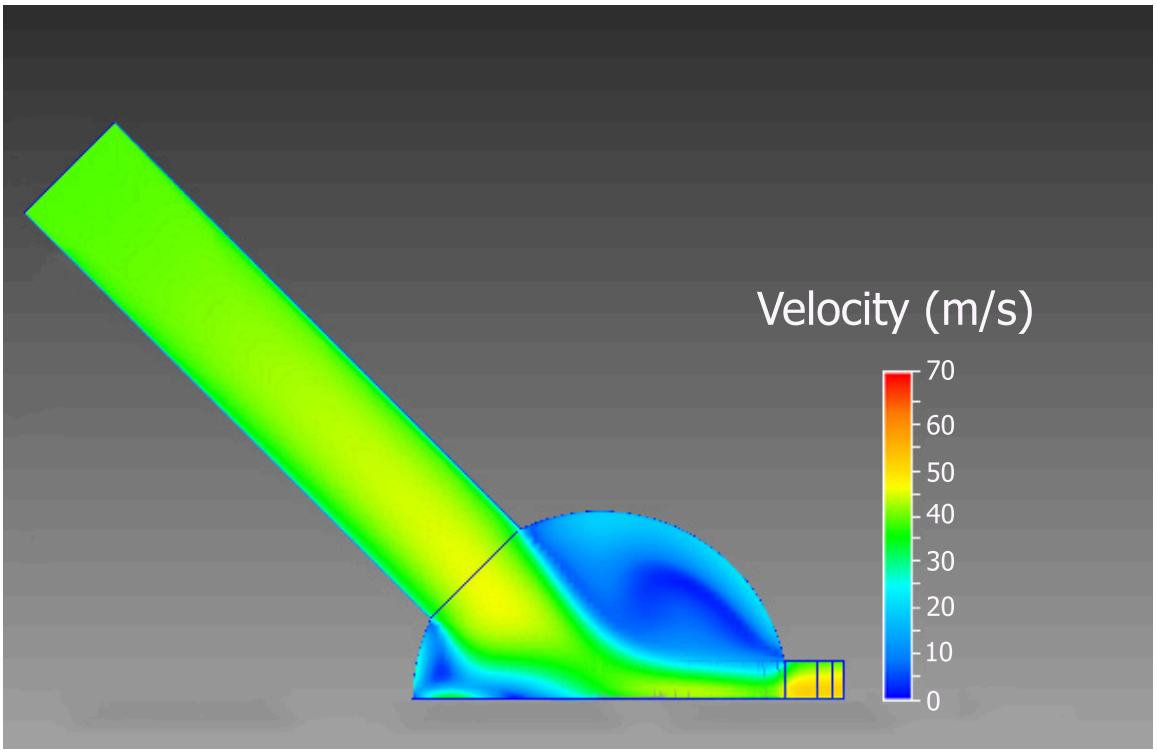

Figure 9.13: A velocity profile for a 45° impingement of the coolant in the experimental set-up as modelled with the code Autodesk Simulation CFD 2014. Note that this is the XY median plane, showing the magnitude of the maximum components of the flow vectors in that plane.

9.8.1 The K-epsilon turbulence model

This is a general purpose model that is reported to perform well across a large number of applications. The first variable, K, determines the kinetic energy in the turbulence and the second variable, ϵ, is the so-called "turbulent dissipation", which describes the scale of the turbulence [Kwo1995]. According to Bardina *et al.* [Bar1997], the K-epsilon model gives good results for wall-bounded and internal flows only in cases where the mean pressure gradients are small. These authors also report that the K-epsilon model would be an inappropriate choice for modelling heat transfer near flow inlets. As already mentioned, the small heated surface of a beam spot in a gas-cooled window assembly can be thought of as a thermal entry-region problem, thus, it is possible that the K-epsilon model may not be the best choice in this particular case. It has been reported that under highly turbulent conditions (i.e. high Reynolds numbers), the K-epsilon model overpredicts the mixing inside the wall boundary layer [Kwo1995], therefore overpredicting the convection heat transfer. A so-called "damping function" or "wall function" is employed to describe the strong attenuation of the normal component of turbulence in the vicinity of the wall. Several such damping functions exist and we could not with certainty determine which is implemented in the code, but it is probably the so-called "standard wall function" (SWF) in the case of the default calculation.

The maximum number of iterations was set to 2000 but convergence was typically reached after 700–800 iterations in all the runs. A run typically lasted between 5 and 6 hours. Except for adjusting the mesh size to the minimum value allowed, no further parameter adjustments were made. We want to stress this point – no fine tuning of any description was attempted by making parameter adjustments. Results for the three impingement angles are shown in Table 9.4. It is evident that the convective heat-transfer coefficients obtained from the CFD calculations are generally significantly higher than the corresponding experimental values. Interestingly, the results for the 0° and 45° jet angles are nearly the same, with some enhancement in the convection heat transfer predicted at 90°.

9.8.2 The SST K-omega turbulence model

The shear stress transport (SST) K-omega model is described as an eddy-viscosity model which has become very popular in recent years. Its behaviour is the same as the K-epsilon model in free stream regions of the flow but the treatment is very different near wall boundaries. It

Table 9.4: Results of Simulation CFD calculations for different impingement angles using the K-epsilon turbulence model.

Jet angle	T_{min} °C	T_{max} °C	$\overline{T}$ °C	h [CFD] (W·cm^{-2}·°C^{-1})	h [measured][a] (W·cm^{-2}·°C^{-1})
0°	207.92	213.56	211.72	0.0289	0.0206 ± 0.0005
45°	207.39	212.94	210.96	0.0290	0.0171 ± 0.0010
90°	165.29	168.98	167.21	0.0380	0.0212 ± 0.0013

[a] Single-jet experimental convective heat-transfer coefficients are shown for purposes of comparison.

does not use any add-hoc damping functions to describe the viscous sub-layer flow near a wall. Instead, it simulates turbulence all the way to the wall boundary but requires a very fine mesh in the boundary layer region. With this choice, one can specify up to ten extra mesh layers in the boundary layer region using the "Mesh Enhancement dialog" of the code. Indeed, in our calculations we selected a value of 10 for this parameter. The price to pay is that any calculation becomes more resource intensive and requires a significantly longer execution time.

The results are shown in Table 9.5. For the 0°-jet case, the agreement between the measured convective heat-transfer coefficient and the corresponding CFD result is almost perfect. At 90°, the CFD result is about 27% higher than the measured value. Interestingly, the CFD result at 90° is in excellent agreement with the prediction by means of the Chang formalism (see Fig. 9.5) – the difference being less than 5%! As can be seen from Table 9.5, the predicted convective heat-transfer coefficients obtained by means of the CFD calculations also do not display a strong dependence on the jet angle, confirming what was observed experimentally. While the curious experimental minimum at 45° was not found in the CFD calculations, by and large the overall agreement between the experimental and CFD results is excellent. This is very reassuring. It is clear that the SST K-omega turbulence model is a better choice than the K-epsilon turbulence model in this regime of heat transfer. From the comments by other authors (e.g. Pattamatta et al. [Pat2012]), this is not unexpected.

Table 9.5: Results of Simulation CFD calculations for different impingement angles using the SST K-omega turbulence model.

Jet angle	T_{min} °C	T_{max} °C	$\overline{T}$ °C	h [CFD] (W·cm^{-2}·°C^{-1})	h [measured][a] (W·cm^{-2}·°C^{-1})
0°	273.43	283.87	281.01	0.0211	0.0206 ± 0.0005
45°	265.05	269.55	268.05	0.0222	0.0171 ± 0.0010
90°	223.57	226.58	225.24	0.0269	0.0212 ± 0.0013

[a] Single-jet experimental convective heat-transfer coefficients are shown for purposes of comparison.

9.9 Conclusion

Forced convection cooling of Havar beam-window foils with fast flowing helium has been part of the modus operandi at iThemba LABS since the start-up of the radionuclide production programme. With the advent of the VBTS, beams of higher intensity and larger targetry, cooling had to be provided for larger and thicker window foils. It is reassuring to discover that VBTS windows become only marginally hotter than those of the Elephant and that, in fact, the Babe windows run at the highest temperature. By and large, all the windows operate at safe temperatures. In fact, they remain relatively cool, even at maximum bombardment conditions provided sufficient interlocks exist for critical parameters such as the sweep radius.

The calorimetric technique in conjunction with an electrically heated surface to simulate beam heating proved yet again to be an invaluable tool to investigate aspects of forced convec-

tion cooling relevant to beam-window assemblies. While some questions have been answered, several issues still require further work. A deeper understanding of multi-jet cooling is certainly one avenue which requires further investigation. It is contemplated to design a new experimental set-up which will be compatible with the existing helium cooling system and to extend the measurements to helium at a high flow rate.

The new data confirm our previous conclusion that the duct equations, such as the Dittus-Boelter, Sieder-Tate and Petukhof-Kirilov equations, are not particularly suited to make estimates for the convective heat-transfer coefficient in this particular application. The fact that air was used as the coolant is not expected to affect the general validity of this statement as the underlying reason is a geometry dependent effect, namely heat transfer in the thermal entrance region of the flow. The formalism of Chang *et al.* for single-phase flow is seen to provide a definitive improvement in this region.

Modelling using a computational fluid dynamics (CFD) code, such as the program Autodesk Simulation CFD 2014, shows much promise. Predictions using the SST K-omega turbulence model are in better agreement with the measurements than those obtained with the default K-epsilon turbulence model. At the time of writing, only the single-jet experimental set-up has been modelled with the CFD code and calculations have been performed only with air as the coolant. Much work still has to be done, including the modelling of the multi-jet experimental set-up as well as the helium-cooled beam-window assemblies. A beginning has been made but this work is clearly still in its infancy at iThemba LABS. We came to realize that the use of a commercial package such as Autodesk Simulation CFD does not protect one from convergence issues! It should also be clarified that, at one stage, it was unclear whether CFD calculations should be included in this thesis at all. The above results were obtained very close to the deadline for submission and the work is continuing.

Chapter 10

Aspects of Target Cooling and Shielding

10.1 Introduction

In Chapters 2 and 9 and several of the appendices, various aspects of the target stations and their ancillary facilities have been addressed. This chapter addresses two additional aspects, both very relevant to the VBTS and the utilization of higher beam intensities, namely target cooling and shielding. Many of the ideas related to the gas cooling of beam windows are equally valid for water cooling. Here, the upper limits in terms of thermal loads on targets and the relevant convective heat-transfer coefficients using water as coolant will be explored. As for the local shielding of the VBTS, the final choice of the adopted shielding configuration will be discussed based on radiation transport calculations using the Monte Carlo code MCNPX.

10.2 Target cooling

It is well known that high heat fluxes (or power densities) limit the operational beam intensity on targets. In other words, when the beam intensity exceeds a certain critical limit, one gets burnout and the target is destroyed. Two questions, which are very often hard to answer, arise: (1) Do we know what the critical limit is? (2) How close to this critical limit can we operate a target with a reasonable chance of a successful bombardment?

The main difficulty in target cooling is the limited surface to cool from. Methods to increase the heat-transfer surface have been developed and implemented for years, depending on the beam energy and intensity regime as well as the type of bombarding particles. Several philosophies exist. A widely used approach at lower energies, where the maximum depth of penetration of the charged particles is not much beyond the surface, is to plate the target material onto a suitable backing material and bombard the target with a small grazing angle (typically less then 10°). The small grazing angle increases the irradiated area considerably. The backing material or substrate is normally a metal with a good thermal conductivity, cooled by means of forced convection with water as the coolant. Very refined targets of this type have been developed. With increasing beam energy and penetration depth, different approaches are often required, e.g. rotating targets, beam sweeping, etc. With proton beams of about 50 MeV and higher, encapsulated targets become attractive. Such targets are usually bombarded with an incidence angle of 90°. This is the regime where beam sweeping becomes most attractive.

In the final analysis, the limiting factor for most targets in terms of their thermal behaviour is the magnitude of the convective heat-transfer coefficient that can be provided. These coefficients (often called h-values) can, for example, be increased by increasing the linear flow velocity. This would normally result in an increase in the differential pressure over the target – another quantity for which a critical value exists. One can increase the pressure only up to some limit, which limits the flow. What else can be done to augment the convective heat-transfer coefficient? What is a realistic value in targetry?

In order to attempt answering some of these questions, the work on swirl-flow cooling by Genis and Rautenbach [Gen1985, Gen1987, Gen1988] is found to be invaluable. Results of that work can be used to set an upper limit on the convective heat-transfer coefficient for a flow system which is far closer to "ideal" than any practical target design can be. The thermal behaviour of a system which has a superior thermal behaviour compared to our targets sets a ceiling on the convective heat-transfer coefficient, beyond which we will find ourselves in "forbidden territory". One can then establish – relying on something more than guesswork – how close to the forbidden region targets can be operated with a reasonable chance of success.

10.2.1 High velocity swirl-flow cooling

A review on passive heat transfer augmentation techniques by Dewan *et al.* [Dew2004] employs the phrase "twisted tape in turbulent flow". Although several other authors also investigated swirl flow by using twisted tape (TT) inserts into the flow passage, the work of Genis and Rautenbach is specifically mentioned for the fact that they investigated high-velocity water flow in short tubes. The reason for studying convection heat transfer in short tubes was precisely because these authors had application in radionuclide production targetry in mind.

Genis and Rautenbach [Gen1985, Gen1987] constructed a Radial Electron Accelerator (REA) which served as the heat source. The REA constituted a 40 kW, 7 kV bombardment system. The cathode and anode formed a concentric, cylindrical dipole configuration in which the inner axial anode also served as the target. These anode/target sections were called "heat transfer targets" by Genis and Rautenbach and constituted simple tubes with a heated length of 65 mm and inside diameter of 4.2 mm. The radially impinging electrons onto an anode/target section provided a homogeneous heat flux. High velocity flow of water through the tube provided forced convection as the main heat-transfer mechanism. Temperature measurements were performed by means of ungrounded k-type thermocouples embedded at various positions into the tube. Twisted strip inserts were used as a passive augmentation method to increase the convection heat transfer by introducing so-called "centrifugal convection". Measurements were performed with and without the twisted strips. The linear flow velocity was varied between 11 and 48 m/s, resulting in Reynolds numbers at bulk flow conditions between 20 000 and 97 000. The temperature difference between the heated wall and the bulk of the coolant was varied between around 21 °C and 113 °C during a series of measurements. An extensive correlation study by means of dimensional analysis was performed and it was found essential to evaluate coolant properties at the film conditions and not the bulk conditions. Measurements were performed well into the regime of subcooled nucleate boiling (see also Section 2.3.4). The rotating flows

induced by the twisted insert is very beneficial in this regime as the centripetal buoyancy force acting on the bubbles can be orders of magnitude larger than the gravitational force which is always present, effectively removing the bubbles from the heat-transfer surface towards the centre of the tube. Even before the onset of local boiling, swirl flow introduces an increased turbulence, a higher velocity with respect to the tube wall for the same mass flow and a thinner boundary layer. This results in an increased convective heat-transfer coefficient. There is a price to pay, however: To maintain a swirl flow generally requires an increased differential pressure as compared to normal axial flow. In fact, the differential pressure increase can be substantial – the downside of using swirl flows.

Genis and Rautenbach reported a maximum heat flux of 2.7 kW/cm^2 under stable operating conditions, which was at that time a kind of new world record. They also showed that the maximum convective heat-transfer coefficient resulting from swirl-flow cooling was about twice the value than when the cooling was obtained with normal axial flow. This is a very significant result! Half of the maximum heat flux obtained from swirl-flow cooling, i.e. 1.35 kW/cm^2, is not far from the maximum of the power density curve shown in Fig. 2.15 for a Ga target under bombardment with a thermal load of 8 kW. Thus, it is evident that the VBTS is already being operated close to the maximum thermal load conditions on the target located in the lower-energy slot.

10.2.2 Estimates based on the duct equations

At iThemba LABS, a few phrases originated concerning the convective water cooling of targets. The phrase “Hadrian’s wall of target cooling” refers to the heat-flux value 1 kW/cm^2. The heat-flux value 1.35 kW/cm^2 is referred to as “the cliff”. The implication is that that danger exists on the other side of Hadrian’s wall – don’t venture too far beyond Hadrian’s wall if you don’t want to fall off the cliff (i.e. target burnout).

To conclude this section, it is interesting to consider the convective heat-transfer coefficients of water according to the Dittus-Boelter, Sieder-Tate, and Petukhof-Kirilov equations for a linear flow velocity of 16 m/s between two flat plates spaced 1 mm from each other. If the separation is small compared to the dimensions of the plates, the hydraulic diameter is twice the separation (i.e. $D_h = 2$ mm). The values are shown in Table 10.1.

Also shown in Table 10.1 are estimated maximum values for the heat flux based on a temperature difference between the heated wall and the bulk coolant temperature of 120 °C. Two points of clarification are required here. First, the boiling point of water increases with pressure. The inlet pressure on a tandem VBTS target is typically of the order of 10 bar with a flow rate of 120 L/min, as already mentioned in Chapter 2. In contrast, the outlet pressure in the return line is not significantly higher than 1 bar, thus, there is a considerable differential pressure across the target. The onset of boiling is therefore more likely nearer the exit ports than the inlet ports inside the target holder. Genis and Rautenbach reported a maximum temperature difference of 113 °C. It is estimated that the return pressure from the VBTS target is somewhat larger than in the experimental set-up of Genis and Rautenbach (due to a larger distance to the pump station), therefore a slightly larger value of 120 °C has been adopted.

(At any rate, a significantly lower or higher value than that of Genis and Rautenbach is not expected). Second, it is known from the work of Genis and Rautenbach, amongst other studies, that in this regime of convection heat transfer the coolant properties should be evaluated at the film temperature. This is the reason for the second result using the Dittus-Boelter equation, evaluated at the film temperature, as shown in Table 10.1. We do not believe that the value obtained using coolant properties evaluated at the bulk temperature is very meaningful in this case.

With the exception of the result obtained from the Dittus-Boelter equation evaluated at the bulk coolant temperature (taken to be 20 °C), the other predictions in Table 10.1 are all in the region of Hadrian's wall or somewhat above this value, but not higher than the "cliff". By and large, the various approaches to estimate a realistic maximum convective heat-transfer coefficient for targetry seem to agree to a large extent, which is very reassuring.

Table 10.1: Convective heat-transfer coefficients for flow in one direction between two flat plates separated by 1 mm.

Equation	h (W cm^{-2} °C^{-1})	Estimated maximum [a] heat flux (kW/cm^2)
Dittus-Boelter (evaluated at bulk temperature)	4.96	0.59
Dittus-Boelter (evaluated at film temperature)	10.70	1.28
Sieder-Tate	8.22	0.99
Petukhof-Kirilov	11.21	1.35

[a]Assuming a maximum differential temperature of 120 °C.

10.3 Local shielding

The advantage of local shielding surrounding targets during radionuclide production bombardments, even though performed inside a bona-fide "vault" having extensive concrete walls and provided with proper neutron attenuation mazes, is often overlooked or underestimated. It is certainly true that for lower energy cyclotrons (such as small PET cyclotrons) it is possible to dispense with, or have some minimal shielding in place as the residual activation of the target surrounds is relatively minimal. At medium proton energies, e.g. above about 60 MeV, the flux of liberated neutrons from the nuclear reactions can be several orders of magnitude larger [Ste1992]. This, in turn, may lead to a much higher dose rate in the vault and considerably more residual activation of the infrastructure located there.

As early as 1985, Weinreich [Wei1985] reported that without local shielding in close proximity to the targets, the polymers inside the radionuclide production vaults at PSI would suffer significant radiation damage within a year from the photon dose alone. That study pertained to a proton beam of 72 MeV and a maximum beam current of 100 μA. The sensitive components include the pneumatics, hoses, cable insulation, etc. The proton beam energy at iThemba

LABS for routine radionuclide production is only marginally lower than at PSI (i.e. 66 MeV) but the beam intensities are significantly higher. The need for local shielding is therefore the same at our laboratory. From the outset, the philosophy at iThemba LABS has been to provide local shielding in close proximity and completely surrounding the target during a bombardment. Moreover, the shielding forms an integral part of a target station, as already discussed in Chapter 2. In addition to the protection of sensitive equipment, local shielding also has huge advantages in terms of limiting the radiation dose to staff. Weinreich [Wei1985] elucidated the fact that maintenance and repairs inside a vault would otherwise require long cooling times, inconsistent with maintaining a production programme. At iThemba LABS, safe access into a vault is possible after about 10 minutes after the end of bombardment (EOB), even after an extensive bombardment with a high intensity proton beam and with the target still located in the bombardment position. This is the time required for one complete exchange of the activated air inside the vault.

In the following paragraphs, the local shielding of the VBTS will be briefly described. This will be followed by a short explanation of the main principles and the relevant properties of each material used in the shield. It has to be said that this shield was designed based on a scaling of the results from a previous study concerning Target Station 1 at iThemba LABS [Ste1992]. A full Monte Carlo simulation with the code MCNPX was only done afterwards. Some of these MCNPX results will be shown to illustrate that the VBTS design is close to the optimum for a three-layer shield but not quite there.

10.3.1 The local shield of the VBTS

The VBTS shield consists of two half cylinders which form a complete cylinder around the target when the station is in a closed state (see Section 2.3). This shield primarily consists of three layers. The inner layer closest to the target consists of Fe with a thickness of 50 cm. This material has a low Mn impurity content (0.1% as compared to 1–2% for mild steel). The middle layer consists of 20 cm thick paraffin wax containing 2.5% boron carbide ($^{nat}B_4C$) by weight. An outer Pb layer of 4 cm thickness completes the shield. Obviously, some structural material have to be present in the design as well. This mainly consists of 5 mm thick mild-steel plate, e.g. for forming cavities into which the paraffin wax was molded.

The inner Fe layer effectively degrades the energy of fast neutrons to intermediate energies via non-elastic nuclear interactions. Some neutrons are obviously absorbed, which leads to residual activation. This is why it is prudent to keep the Mn content low – the residual ^{56}Mn radioactivity produced via neutron capture on the Mn in mild steel is known for a long time to dominate the residual γ-ray dose in the first ~ 8 h after EOB (see e.g. [Att1976]).

In the second layer, the paraffin wax effectively moderates the neutrons to thermal energies. This is mainly by means of elastic scattering with hydrogen nuclei, as paraffin wax has a high hydrogen content. This process, however, only becomes effective towards lower neutron energies (below about 4 MeV). This is because the elastic scattering cross section of neutrons with hydrogen falls almost exponentially with the neutron energy. The non-elastic neutron scattering cross section on Fe, however, reaches a plateau above 4 MeV. Thus, Fe is a good

shielding material for neutrons above about 4 MeV but poor for energies below this value. Exactly the opposite is true for paraffin wax, therefore the two materials in combination can provide an excellent radiation shield in this energy regime. The boron carbide is included in the wax as the ^{10}B content serves to absorb thermal neutrons via its high cross section for thermal neutron capture. This reduces the number of thermal neutrons escaping from the shield into the vault. It also reduces the γ-ray dose rate outside the shield by supressing the 2.23 MeV γ-rays emitted by the capture of thermal neutrons by hydrogen to form deuterium, a process in competition with the production of the softer 0.48 MeV γ-rays produced in the ^{10}B(n,α)^{7}Li reaction.

The outer Pb layer serves to shield photons. Many γ-rays are produced in the inelastic interactions by the neutrons as they traverse the shield layers, as alluded to above.

10.3.2 Shielding calculations

The total thickness of the local shielding of the VBTS was, in part, decided by the amount of space available for it. It is a somewhat thicker shield than that of Target Station 1 (74 cm for the VBTS versus 64 cm for Target Station 1.) That is the reason why a scaling was done from previous shield calculations in the design of the VBTS shield. Previously, calculations were performed using the discrete ordinates radiation transport codes, ANISN and DOT, in conjunction with cross sections from the HILO data library (see [Ste1992] for details). These methods are now largely outdated, having been superseded by Monte Carlo codes such as MCNPX.

The following MCNPX calculations serves both to illustrate the principles of the shield as well as to find the optimum layer thicknesses, in particular those of the inner and middle layers. A circular symmetry was selected to simplify the input. The source is a Cu beamstop for a 66 MeV proton beam, located at the centre of the sphere. Dose attenuation factors were determined by placing a tally at a point 1 m from the shield in the forward direction. The dose attenuation factor (DAF) at the observation point is defined as follows:

$$\text{DAF} = \frac{\text{Transmitted dose rate at the observation point with shield in place}}{\text{Transmitted dose rate at the observation point without a shield}}. \tag{10.1}$$

First, only the inner and middle layers are considered (i.e. with the Pb outer layer absent). The total shield thickness is kept constant at a value of 70 cm but the Fe and wax layer thicknesses are varied. This is equivalent to saying that the interface between the Fe and wax is being moved systematically from the inside (source side) to the outside (observation side). With an Fe/wax-interface position at a value of zero, the entire shield consists of wax. With an Fe/wax-interface position at a value of 70 cm, the entire shield consists of Fe. A bona-fide two-layer Fe/wax shield is defined for any values of the interface position between these two extremes. The MCNPX results for the neutron DAF is shown in Fig. 10.1. From the figure, it is clear that a single-layer Fe and a single-layer wax shield will both significantly underperform in comparison with a proper two-layer Fe/wax shield. An optimum configuration exists for values of about 54 cm for the Fe thickness and 16 cm for the borated wax thickness. For the VBTS

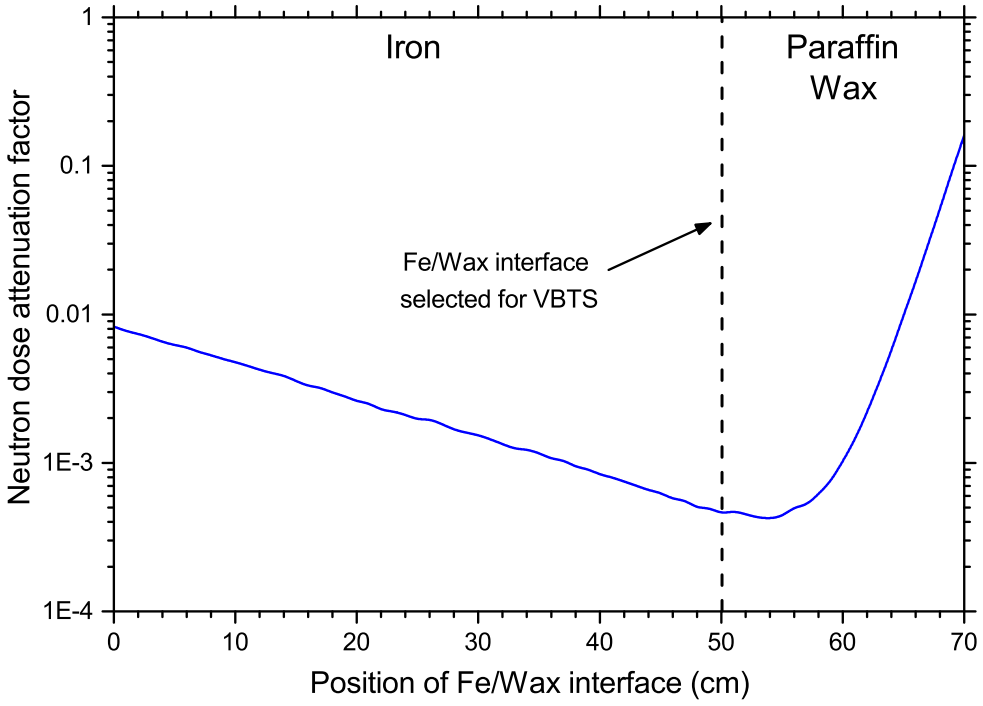

Figure 10.1: Neutron dose attenuation factor (DAF) versus the position of the Fe/wax interface for a two-layer Fe + borated wax local radiation shield, as calculated with the Monte Carlo code MCNPX.

shield, an Fe/wax interface position at 50 cm was selected, which is slightly off the optimum. Nevertheless, this is still considered to be a very good shield and the objective to reduce the neutron dose rate into the vault by three orders of magnitude was comfortably exceeded.

A similar investigation can be done for a three-layer shield. One way to obtain a three-layer shield is to fix the thicknesses of the Fe and borated wax layers to some sensible values, followed by moving both interfaces (i.e. both the the Fe/wax and wax/Fe interfaces systematically from the source side to the observation side through the shield. In this scenario, with an Fe/wax-interface position at a value of zero one obtains a two-layer shield with the wax layer on the inside (source side). With an Fe/wax-interface position at the maximum value selected for the Fe thickness (i.e. 50 cm if the existing VBTS case is considered), another two-layer shield is obtained but with the Fe at the source side. A bona-fide three-layer Fe/wax/Fe shield is defined for any values of the interface position between these two extremes. The MCNPX results for the neutron DAF as well as the "total = neutron + photon" DAF is shown in Fig. 10.2.

From the figure, it is clear that the neutron DAF gets smaller (i.e. enhanced shielding for neutrons) as the position of the Fe/wax interface is moved to the maximum Fe thickness (i.e. all the Fe on the source side) . This is not surprising – a shield with the borated wax layer near the source side makes no sense as the high-energy neutrons will not be attenuated effectively. From the perspective of the neutrons only, the best geometry is the one with all the Fe on the source side and all the borated wax on the outside. The picture is different if one also considers the contribution to the transmitted dose by photons. As can be seen from the figure, the total DAF (i.e. for neutrons + photons) initially follows the same slope as the DAF for neutrons only

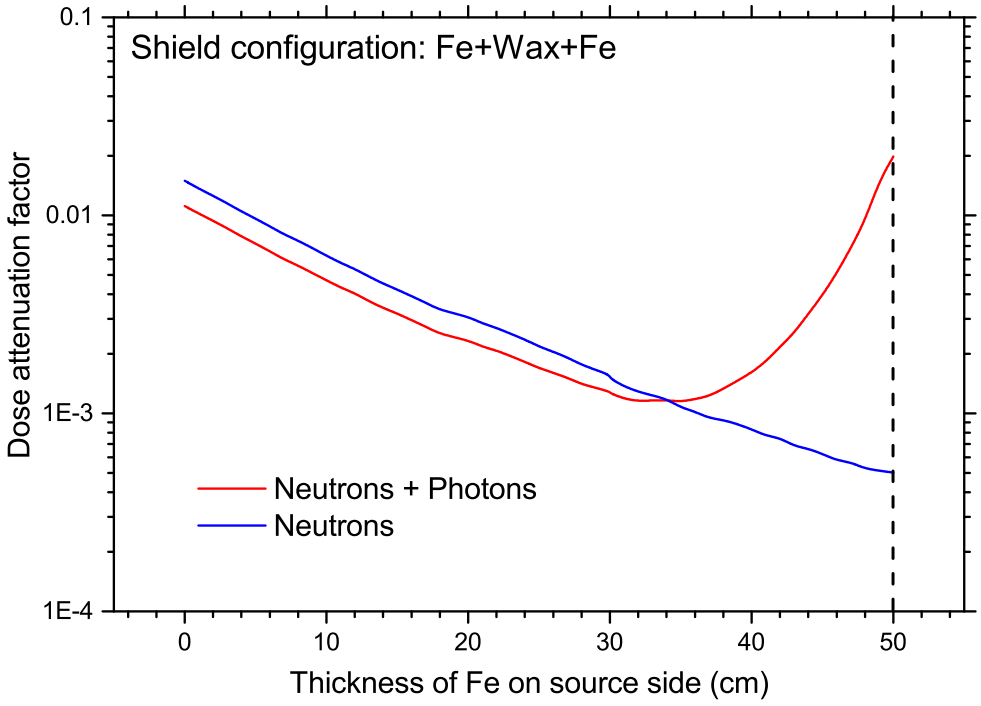

Figure 10.2: Neutron and total dose attenuation factors (DAF) versus the position of the Fe/wax interface for a three-layer Fe/wax/Fe local radiation shield, as calculated with the Monte Carlo code MCNPX. The total Fe thickness is fixed at 50 cm and the borated wax thickness is 20 cm.

but at a value of the Fe/wax interface position of about 33 cm there is a minimum, whereafter the slope turns positive. This is a clear indication that an outer layer to shield the γ-rays is indeed required. An Fe/wax/Fe shield is not, however, the best choice for a three-layer shield, considering that the outer layer is primarily for shielding photons. It makes much more sense to have an outer Pb layer. The philosophy at iThemba LABS was therefore to essentially adapt the two-layer shield designed to attenuate the neutrons by adding to it an outer Pb layer.

To conclude, a statement needs to be made about the choice of modelling the radiation shield as a sphere, rather than a cylinder. In fact, both geometries were extensively investigated in the context of the local radiation shields of the other two target stations, i.e. Target Station 1 (Elephant) and Target Station 2 (Babe) in the masters thesis work of T. G. Kupi [Kup2007]. In that work, no significant difference was found.

Chapter 11

Conclusion

The discipline broadly classified as "targetry" in the field of radionuclide production constitutes a remarkably diverse collection of activities. Various aspects of nuclear reactions have to be taken into consideration, e.g. excitation functions, reaction thresholds, physical yields, a familiarity with the relevant sources of nuclear data, detectors, analysis of measured spectra, etc. Various aspects of mechanical design, manufacturing techniques, material properties, heat transfer calculations, etc., and a familiarity with those sources of information, are required. A familiarity with radiation and the appropriate training to work with high levels of radioactivity are essential. A familiarity with relevant aspects of radiochemistry is highly advantageous. The field is interdisciplinary and the targetry expert has to deal with techniques and sources of information from several fields.

A large proportion of the activities during the past number of years concerned the cyclotron and radionuclide production facility upgrades at iThemba LABS. It was foreseen from the outset that some of this work would be addressed in the thesis in one way or another. Many people contributed towards the upgrade. Chapter 2, therefore, should be seen as a background chapter and not a summary of the author's own efforts – a heavy involvement in the entire VBTS project, its ancillary facilities, new targetry and aspects of the interlocking is, however, undisputed. The same applies to the establishment of a ^{18}F production capability and the beam splitter project under an Innovation Fund Grant from the NRF. Concerning the physics and targetry R&D of the radionuclide production programme at iThemba LABS, the effort narrows down to only two researchers (one, in fact, from another department). Our colleagues in this regard were mainly people from abroad. Strong ties with researchers from ATOMKI, especially concerning the excitation function work, deserves a special mention. Their influence is certainly reflected in these pages.

The concluding remarks below are arranged according to the type of activity, with the aim to highlight contributions made by this work and to identify aspects that need further systematic investigation.

11.1 Development of infrastructure

The VBTS has proved to be as reliable as the two horizontal-beam target stations (Elephant and Babe). The downtime on these stations is generally small, albeit not insignificant. In addition to planned maintenance, episodes of unplanned maintenance do occur. It is, therefore, interesting to ponder over the strengths and weaknesses of our production philosophy and practices and to ask the question: "What should we do the same and what should we do differently if the entire programme can be conceived from scratch?" By and large, the present philosophy will remain in place. Components such as the movable local radiation shields, robot arms for target transfer, target-transport rail system, four-sector collimators in front of the targets, double-foil beam windows, target holders, metal-clad batch targets, etc., will be retained. One will, however, try to achieve a larger measure of standardization across the target stations. Currently, none of the subassemblies are interchangeable between the three stations. The collimator assembly of the Elephant, for example, does not fit onto the VBTS or Babe, and vice versa. The same applies to the window assemblies and various other components. The evolution of the three target stations has been such that each requires its own set of spares. A significantly better approach towards standardization can be imposed if one has the opportunity to conceive the programme from scratch.

It is interesting to ponder what the ideal building should look like. This point is, in actual fact, very relevant to iThemba LABS as the purchase of a dedicated 70 MeV commercial cyclotron is a vital component of the strategic plan for the future of the laboratory, currently under consideration by the National Research Foundation (NRF) and the Department of Science and Technology (DST). Should this become a reality, the new cyclotron will be accommodated in a new building. Without any doubt, we would insist on irradiation vaults with somewhat more interior space. The roofs of the vaults should also be higher to provide space for small overhead cranes (or appropriate lift mechanisms that move on overhead rails). The current vaults are too small to fit such lift devices, which is a drawback as various maintenance tasks can be significantly simplified if such devices are available.

Within the context of the multidisciplinary nature of the separated-sector cyclotron facility of iThemba LABS, the beam splitter makes perfect sense. This was really the only way to significantly increase the radionuclide production capacity without affecting other programmes. While conceptually simple, in practice the beam splitter is quite a complex system. It is also not small. It is dubious whether beam splitters will be justified for new production facilities based on compact, dual-port, commercial 70 MeV cyclotrons. The technology, however, is reliable and it may be something to consider.

One can have a long discussion about the pros and cons of a production beam with a vertical orientation. It is likely that the "pros list" will be remarkably short. In contrast, it is likely that the "cons list" will be significantly longer. Why? The vertical beamline introduced a number of ergonomic problems that we did not foresee. Some components are located in difficult to reach places. Maintenance work on the VBTS is significantly more uncomfortable than on the other stations. The vertical orientation of the beamline is also more vulnerable for the collimator and double-foil window assemblies. Anything that accidentally falls down the beamline while

maintenance work is being performed above can damage them. Indeed, a few such incidents have already occured. In one case, the beam melted the metal support structure of a diagnostic component which became stuck in a misaligned position. The drops of molten metal fell from above onto the window foils, obliterating them. The original idea of a vertical beam was that contained molten target material would remain within the beam strike. This, however, does not appear to be a much of an issue with horizontal beams. Some of us, at least, while considering the VBTS to be a success, will rather base a future facility on horizontal beams only.

Another aspect that requires careful scrutiny is the modularity of components and sub-assemblies and the ease with which they can be exchanged on a target station. Stay times calculated for maintenance tasks preclude certain tasks in the vicinity of highly activated components. There is not enough time, for example, to undo rows of bolts. We therefore utilize quick release couplings wherever possible. A few tasks, however, still prove to remain problematic in terms of exposure to staff. The central region of the VBTS has been redesigned to further reduce exposure during maintenance. The new central structure is currently being assembled and will be installed during a future maintenance shutdown period. During conversations within the group on the lessons learnt over the years of operating radionuclide production facilities, an idea surfaced which requires further investigation. The short way to explain this idea is by asking the question: "Why not make an entire bombardment station modular?" Should enough resources be available, one can conceive of a strategy where a defective target station is removed in its entirety from the vault while its radiation shield remains closed. This station is then left in a dedicated maintenance area where it is allowed to cool sufficiently before maintenance work commences. In the meantime, a new or reconditioned station is in its entirety brought to the vault and connected to the beamline and ancillary facilities. One possibility would be to provide rails on which entire stations can be moved in and out of a vault. In this way, the concept of modularity can be utilized to its fullest extent. Not only will maintenance work on target stations be done outside the irradiation vaults, in a better equipped and less activated environment, but the downtime before beam operations can resume will be shortened considerably.

11.2 Excitation functions and yields

In general, the stacked-foil technique in combination with off-line γ-ray spectrometry produces abundant data. Not all the data extracted in the studies presented here have been included in the thesis; rather, a selection was made in each case to address the main topic of interest. In the case of ^{nat}Gd + p, the main interest was to get some quantitative idea of the reactions and yields relevant to the three members of the radioterbium quadruplet that can be produced with a cyclotron, namely ^{149}Tb, ^{152}Tb and ^{155}Tb; the last member of the quadruplet being ^{161}Tb, which is reactor produced. Since other radioterbiums are potential co-produced contaminants in these productions, cross-section data extracted for all observed radioterbiums have been included. The data set comprises ^{151}Tb, ^{152}Tb, ^{153}Tb, ^{154m2}Tb, ^{155}Tb, ^{156}Tb and ^{160}Tb. An important member of this family of radionuclides could not be observed in ^{nat}Gd + p, namely the therapeutically important radioisotope ^{149}Tb. This is because contributions from the main

reaction for its formation, ^{152}Gd(p,4n)^{149}Tb, suffered from the very low natural abundance of ^{152}Gd (0.20%) in the natural target material. Nevertheless, the study produced a significant set of new data, enabling some predictions relevant to the production of the PET radioisotope ^{152}Tb and the SPECT radioisotope ^{155}Tb. Although the non-observance of ^{149}Tb was somewhat of a disappointment, it was not entirely unexpected and the study pointed to the necessity of locating some enriched ^{152}Gd material for further investigations.

In a follow-up study, some data were measured for the ^{152}Gd(p,4n)^{149}Tb and ^{155}Gd(p,4n)^{152}Tb reactions, utilizing thin targets of enriched ^{152}Gd (30.60%) and ^{155}Gd (99.82%), respectively. These data are not extensive but it is sufficient to constrain the excitation functions and to make sensible yield predictions. Measurements at lower energies, utilizing the stacked-foil technique and a 30 MeV proton beam, are required to complete this data set. Such further experimental work, however, falls outside the scope of this thesis. It is clear that electromagnetic (EM) isotope separation will have to be an integral part of the production regimen for radionuclidically pure ^{149}Tb, regardless of which reactions are utilized. It is speculated that a dedicated facility for its large-scale production, based on a commercial 70 MeV cyclotron and a compact EM isotope separator such as the Ion Source Test Facility (ISTF) at TRIUMF, is not a too far-fetched concept. Such a facility might also be useful to augment the production of ^{152}Tb and ^{155}Tb. In this regard, it will also be interesting to follow developments at the ISOLDE facility of CERN as well as future isotope harvesting operations at FRIB.

The use of mono-isotopic ^{159}Tb targets for the production of ^{155}Tb via the indirect reaction path ^{159}Tb(p,5n)^{155}Dy$\rightarrow$^{155}Tb has been investigated by means of a stacked-foil experiment that included foils of natural Tb metal. The potential yield is high and this production route certainly has some merit for facilities based on the new generation of 70 MeV cyclotrons. The data set includes cross-section measurements for ^{153}Dy, ^{155}Dy, ^{157}Dy, ^{159}Dy, ^{153}Tb, ^{154m}Tb, ^{155}Tb, ^{156}Tb, ^{151}Gd and ^{153}Gd. Except for a few previous measurements by one author on the formation of ^{159}Dy in ^{159}Tb + p below 20 MeV, the entire data set constitutes new results published for the first time. Comments received by the authors during the publication process indicated that this work was timeous and that current interest in the nuclear medicine field on radioterbium-labelled compounds in particular, and the radiolanthanides in general, is large.

At iThemba LABS, the main interest in measuring excitation functions for radionuclides of Zr in ^{93}Nb + p and ^{89}Y + p was to investigate the production regimen of ^{88}Zr for use in ^{88}Zr/^{88}Y generators. Confirmation of the existing data for the production of the medically important radionuclide ^{89}Zr was also an objective. New data measured at iThemba LABS in the energy region 24–66 MeV, in conjunction with new data from other authors at lower energies down to the respective (p,n) reaction thresholds and some older data, resulted in a mature database for ^{93}Nb(p,X)^{86,87,88,89}Zr and ^{89}Y(p,xn)^{86,87,88,89}Zr up to 66 MeV. It was shown that useful quantities of ^{88}Zr can be extracted as a byproduct by processing the Nb capsules used in production targetry of several other radionuclides. Yttrium, however, is the target material of choice for dedicated production purposes (probably in the form Y_2O_3) due to a significantly higher yield.

Colleagues from ATOMKI were more interested in the cross sections for the formation of Nb radionuclides in ^{93}Nb + p as these are relevant to the thin layer activation (TLA) method,

which is extensively employed in Debrecen. It is for this reason that excitation functions for ^{93}Nb(p,X)^{90,91m,92m}Nb were included in this study. For the same reason, extensive data have been measured for ^{nat}Zr + p, both at iThemba LABS and at ATOMKI. These data are not considered to be part of the thesis project except for one result, namely the excitation function for ^{nat}Zr(p,X)^{88}Zr, which has been included in Chapter 5. It was shown Zr has some potential as the higher-energy partner in a tandem Zr/Y_2O_3 target for ^{88}Zr production. In this case, the product need not be carrier free as it is used in a stock solution for a ^{88}Zr/^{88}Y generator, i.e. a few grams of stable Zr can be tolerated. New measurements for the excitation function of the ^{nat}Zr(p,X)^{88}Zr process was one of the main reasons for our interest in a ^{nat}Zr + p stacked-foil experiment at iThemba LABS as the existing data at that time contained serious discrepancies.

In the case of ^{192}Os + p, the rather low cross sections for the ^{192}(p,X)^{186}Re process, which is dominated by the ^{192}(p,α3n)^{186}Re reaction, are rather disappointing. Nevertheless, this remains a potential production route for ^{186}Re production with larger cyclotrons, e.g. the new generation 70 MeV machines. Data for the ^{192}Os(p,xn)^{186,187,188,189,190}Ir reactions that resulted from this study have been published for the first time. In addition, new data for the medically relevant radionuclide ^{192}Ir have been confirmed in the energy region up to 18 MeV and further extended up to 66 MeV.

For the work on ^{18}F production, no excitation-function data needed to be measured as these data are well established. The stacked-foil technique, however, was found to very useful to experimentally determine the average energy of the degraded beam. For this purpose, the standard ^{nat}Cu(p,X)^{65}Zn excitation function published by the IAEA was found to be ideally suited.

11.3 Encapsulated targets

Many of the targets used in batch radionuclide productions at iThemba LABS are encapsulated targets. This is similar to the practice at the radionuclide production facilities of the Los Alamos National Laboratory (LANL) and Brookhaven National Laboratory (BNL), however, the targets at iThemba LABS are generally smaller in size. During the period of this study, new targets were developed for the VBTS. This includes Rb metal encapsulated in 316 stainless steel (tested successfully up to a beam intensity of 300 μA), Ga metal encapsulated in Nb and Mg encapsulated in Nb (both tested up to 250 μA). These targets are for the production of ^{82}Sr, ^{68}Ge and ^{22}Na, respectively. New Elephant targets, specifically developed for studies reported in this thesis, include Y_2O_3 encapsulated in Al (for the production of ^{88}Zr) and LiCl encapsulated in Al (for the production of ^{28}Mg). These targets have been tested in different bombardments by progressively increasing the beam intensity from about 50 μA up to 90 μA.

While most of the work in this thesis concerned proton-induced reactions up to 66 MeV, the production of ^{28}Mg in the bombardment of LiCl targets has been investigated in the energy region 50–200 MeV. It was shown experimentally, as well as by means of Monte Carlo modelling with the code MCNPX, that the total outscattering loss from a stack of 10 targets that cover this entire energy region is surprisingly small. This last-mentioned statement has to be qualified – the individual targets had similar dimensions to the usual targets employed for routine batch

productions on the Elephant and they were manufactured in the same way. While routine production of ^{28}Mg is not envisaged at iThemba LABS at this stage, it has been a topic of interest for some time after requests for its production have been received.

11.4 Target modelling and heat transfer

The gas cooling of beam windows was extensively studied by means of new measurements in an experiment utilizing an electrically heated element in conjunction with an empirical model. In addition, some calculations were performed using a commercial computational fluid dynamics (CFD) code, which incorporates finite element analysis (FEA) techniques for the heat transfer by conduction in solid structural materials. It was found that the SST-omega turbulence model gave results in better agreement with experimental measurements than the K-epsilon turbulence model. Single-jet cooling seems to be better understood than multi-jet cooling at this time. In fact, new experimental work as well as CFD analysis on multi-jet cooling may be a very interesting topic to pursue in future.

By and large, it was shown that the double-foil beam windows on all the target stations operate at safe temperatures if bombardment conditions remain normal. In the cases of Target Station 1 and the VBTS, it is vital that the beam sweeping can be trusted and that the interlock system trips the beam very rapidly if the sweep conditions change.

Monte Carlo radiation transport calculations by means of the code MCNPX were shown to accurately reproduce the beam transmission in targets. In the case of enriched water targets for ^{18}F production, the correct ratio of beam current on the degrader/collimator unit and actual target was predicted with MCNPX for two sizes of niobium inserts. Considering the rather unconventional way that the cooling water is utilized to effect the desired beam energy degradation from 66 MeV down to 18 MeV, this result is very reassuring. In the case of a 200 MeV proton beam incident on a LiCl target stack for ^{28}Mg production, the agreement between MCNPX predictions and experimental observations was equally impressive. This work can be expanded to other targets and/or target systems at iThemba LABS as well. The code is also extremely useful to follow the transmission of neutrons and photons directly produced in the target as well as by secondary processes in surrounding materials. As such, it is a useful tool to study radiation shielding and has been extensively used for this purpose at our laboratory. New results for the VBTS local radiation shield have been presented here for the first time.

At the present time, the water cooling of batch targets at iThemba LABS has only been modelled in an approximate way using empirical calculations. These methods have served the laboratory well for many years and they provide useful insight. The time is right, however, to invest in more advanced modelling. The CFD code utilized in the study of gas cooling should be equally well suited to model water-cooled targets. Such work has been initiated but falls outside the scope of this thesis project.

Appendix A

Excitation Functions: Activation Equation and Methodology

A.1 Introduction

In papers presenting experimental excitation functions measured using the stacked-foil technique, one often finds a sentence such as the following: "The cross sections have been derived using the well-known activation equation", followed by a reference. In several theses and dissertations presenting such work (at least five from iThemba LABS) one finds a write-up of the relevant equations, usually in an appendix. The question then begs whether this thesis should yet again present such a derivation – what purpose would it serve? If it is "well known", why not just suffice with the standard sentence mentioned above and an appropriate reference?

The decision to write this appendix was based one the following observations:

- The usual form of the so-called "activation equation" (see e.g. [Gil2008, Cat2008, Kha2012]) is an approximation. It does not explicitly take the time dependence of certain quantities into account, e.g. possible fluctuations in beam intensity during bombardment, the correct mean value of the counting interval, etc. One sometimes finds that this leads to errors in the literature, in particular those cases where the half-life of the radionuclide of interest is short compared to the bombarding time as well as cases requiring long counting periods, comparable or longer than the half-life, to obtain the desired statistics.

- Publications seldom elaborate on how they handle the above-mentioned problems. Fluctuations in the beam current and even disruptions in the bombardment (e.g. caused by RF trips) can lead to complex beam histories. If the beam history is properly monitored, e.g. in 1 second intervals such as at iThemba LABS in recent times, corrections can be made, but by what procedure? When the RERAME-II chamber was permanently moved from the N-line to the I-line (i.e. the horizontal-beam radionuclide production vault) a few years ago, it was specifically supplied with a new beam monitoring and logging system. The question was how to best use the logged information from the new system.

- In a concise write-up by Buthelezi [But2004], a derivation of the activation equation is given for a constant beam intensity. This is followed by an extension of the arguments

to show how a time-dependent beam history can be accommodated. It was felt, however, that this approach should be reversed. Instead of first deriving the more usual activation equation and then moving on to a more complex scenario by introducing additional arguments, as dictated by some experimental problems, one can from the outset derive the most general form of the activation equation and afterwards apply simplifications as "special conditions", e.g. a constant beam intensity during bombardment.

- It was also felt that the full story on these activation experiments and their analysis can never be found in one place. Rather, for the purpose of describing the analysis in this thesis, it was considered better to provide a reasonably complete account of the procedures followed, instead of referring to multiple previous works which, in a few cases, do not give a consistent description. This does not mean that the sources referred to are considered to be insufficient, merely that there was a desire to produce a single account more suitable to explain the relevant principles and their implementation at iThemba LABS in recent times, as it pertains to this particular project.

A.2 Derivation of the Activation Equation

A.2.1 The thin-target approximation

The thin-target approximation is not only useful in stacked-foil experiments but also a useful way to view thick solid targets, i.e. a thick target can be viewed as a stack of "slices". Consider a foil stack (target) having a number of J foils (slices). Next, we consider an arbitrary single foil or slice in isolation, as shown in Fig. A.1. Let E_j be the average energy of beam particles incident on the j^{th} thin target, $1 \leq j \leq J$. The average energy after traversing the thin target is $E_j - \Delta E_j$. The thin target approximation is fulfilled if $\Delta E_j \ll E_j$. This can be achieved by making the slice thickness, Δx_j, sufficiently small. The incremental thickness, Δx_j, and the incremental energy loss, ΔE_j, are then related to the stopping power $S(E)$ in such a way that it can be considered constant and evaluated at the average beam energy in the thin target:

$$\Delta E_j = S\left(\frac{E_j + E_{j+1}}{2}\right)\Delta x_j, \tag{A.1}$$

where $E_{j+1} = E_j - \Delta E_j$. Let N_j be the number of target nuclei per unit area of the thin target and I_j the number of charged particles per second traversing it. In general, I_j will be a function of time: $I_j = I_j(t)$. The number of residual nuclei of type p produced per second, R_j^p, is given by

$$R_j^p = \sigma_j N_j I_j, \tag{A.2}$$

where σ_j is the production cross section (per definition) and, in general, $R_j^p = R_j^p(t)$. This is sometimes called the production rate. Also, in general, the cross section σ is a function of energy, thus, in the thin-target approximation it is constant for a particular slice or foil:

$$\sigma_j = \sigma\left(\frac{E_j + E_{j+1}}{2}\right). \tag{A.3}$$

The number of target nuclei per unit area is related to the target thickness by

$$N_j = \frac{\rho \Delta x N_a}{A}, \tag{A.4}$$

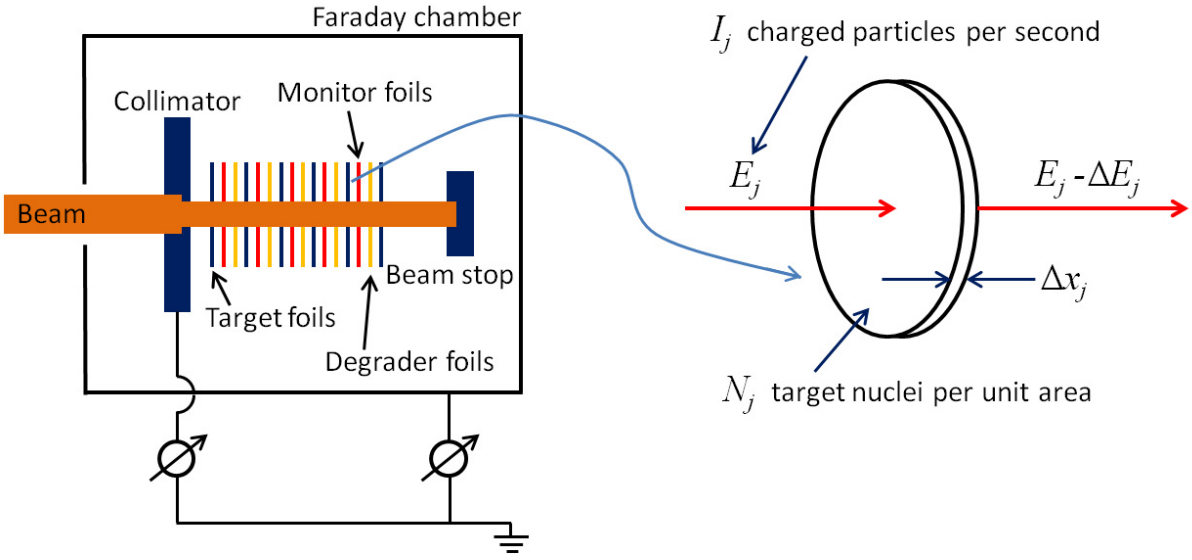

Figure A.1: LEFT: Diagram showing beam penetration through a foil stack. RIGHT: Beam penetration through foil no. j of the foil stack.

where ρ is the density of the target material (or partial density of the target element in the case of compounds), N_a is Avogadro's number and A is the atomic mass (in AMU). Obviously, in the above description foil no. 1 will be the first foil of a particular kind in the stack and foil no. J the last foil of that kind at the back of the stack.

A.2.2 Beam current

Let the bombardment period be denoted by T. The following times are defined:

$t = 0$:	Beginning of bombardment (BOB),
ΔT :	Time increment of current integrator scaler (adjustable 1–10 s),
n :	Total number of incremental time intervals in bombardment period,
$t = T = n\Delta T$:	End of bombardment (EOB).

The end of each time interval is given by

$$t_i = i\Delta T \quad \text{for all} \quad 1 \leq i \leq n. \tag{A.5}$$

Let ΔQ_i be the charge collected during bombardment interval i in units of nano-Coulomb (nC). The mean number of beam particles per second incident on the stack during this interval is given by

$$I_{beam}(t_i) = \frac{\Delta Q_i \times 10^{-9}}{q_e m \Delta T}, \tag{A.6}$$

where $q_e = 1.602177 \times 10^{-19}$ C is the electron charge and m is the charge state of the beam particles ($m = 1$ for protons). The relationship between $I_j(t_i)$ and $I_{beam}(t_i)$ depends on the so-called *non-elastic nuclear interaction probability*, which will be discussed later.

As already mentioned in Chapter 2, the entire RERAME-II chamber is electrically isolated and provided with good electron suppression at the beam entrance to prevent secondary electrons from escaping back down the beamline. This is done with strong permanent magnets

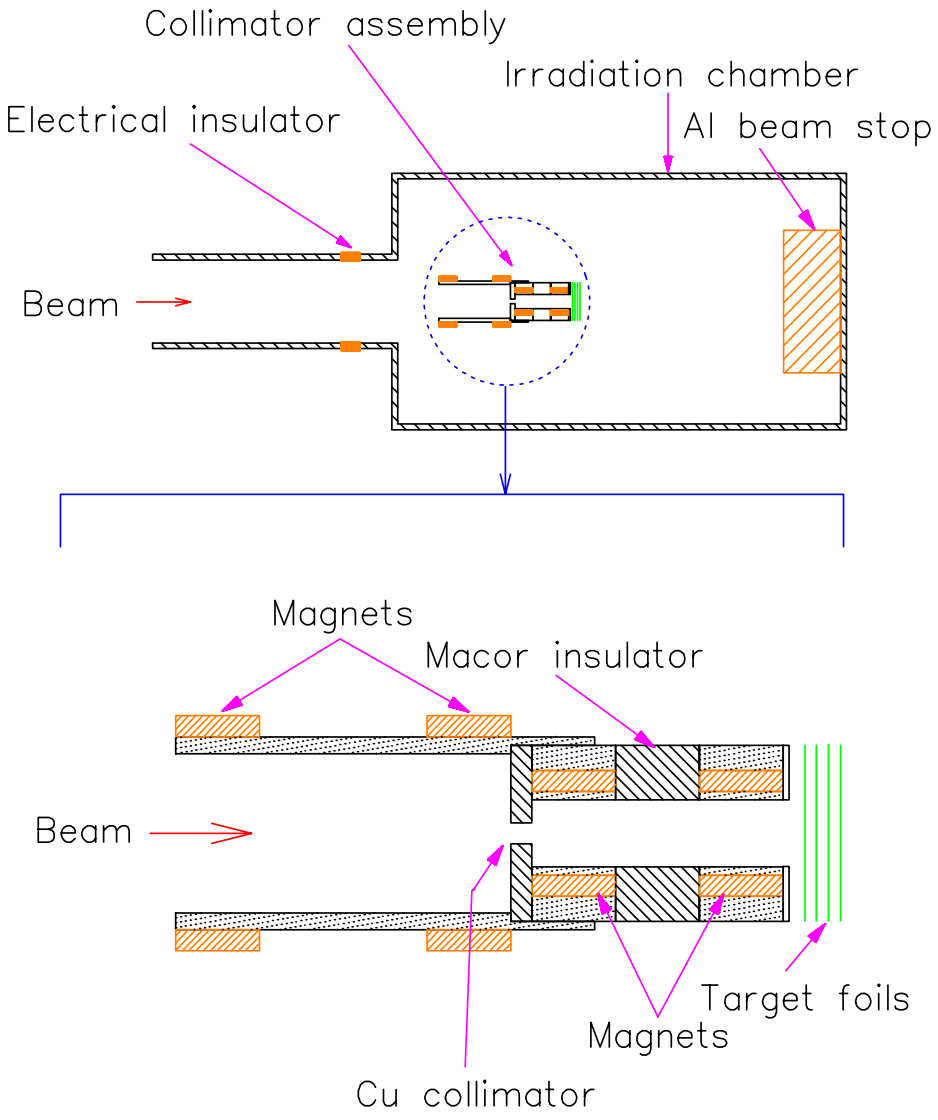

Figure A.2: Diagram showing the modified RERAME-II irradiation chamber (TOP) and an enlarged cross-sectional view of the collimator assembly (BOTTOM).

(samarium-cobalt type) as shown in Fig. A.2. Furthermore, the collimator assembly is electrically isolated independently and also provided with permanent magnets to trap secondary electrons from escaping to the chamber. In this way, the charge intercepted by the collimator and the charge traversing the foil stack or target can be measured independently. The current and integrated charge on the chamber is measured with a Brookhaven Instruments model 1000C current integrator and the current intercepted by the collimator is measured with a Keithley electrometer. The currents of both instruments are logged with a PC-based system running the LabVIEW software. A screenshot of the LabVIEW window, for an actual stacked-foil bombardment, is shown in Fig. A.3. Typically, the focus conditions are adjusted to defocus the beam somewhat so that about 50% is measured on the collimator and 50% on the chamber. This prevents the beam from being too sharply focused but still being well defined on target in a predictable manner.

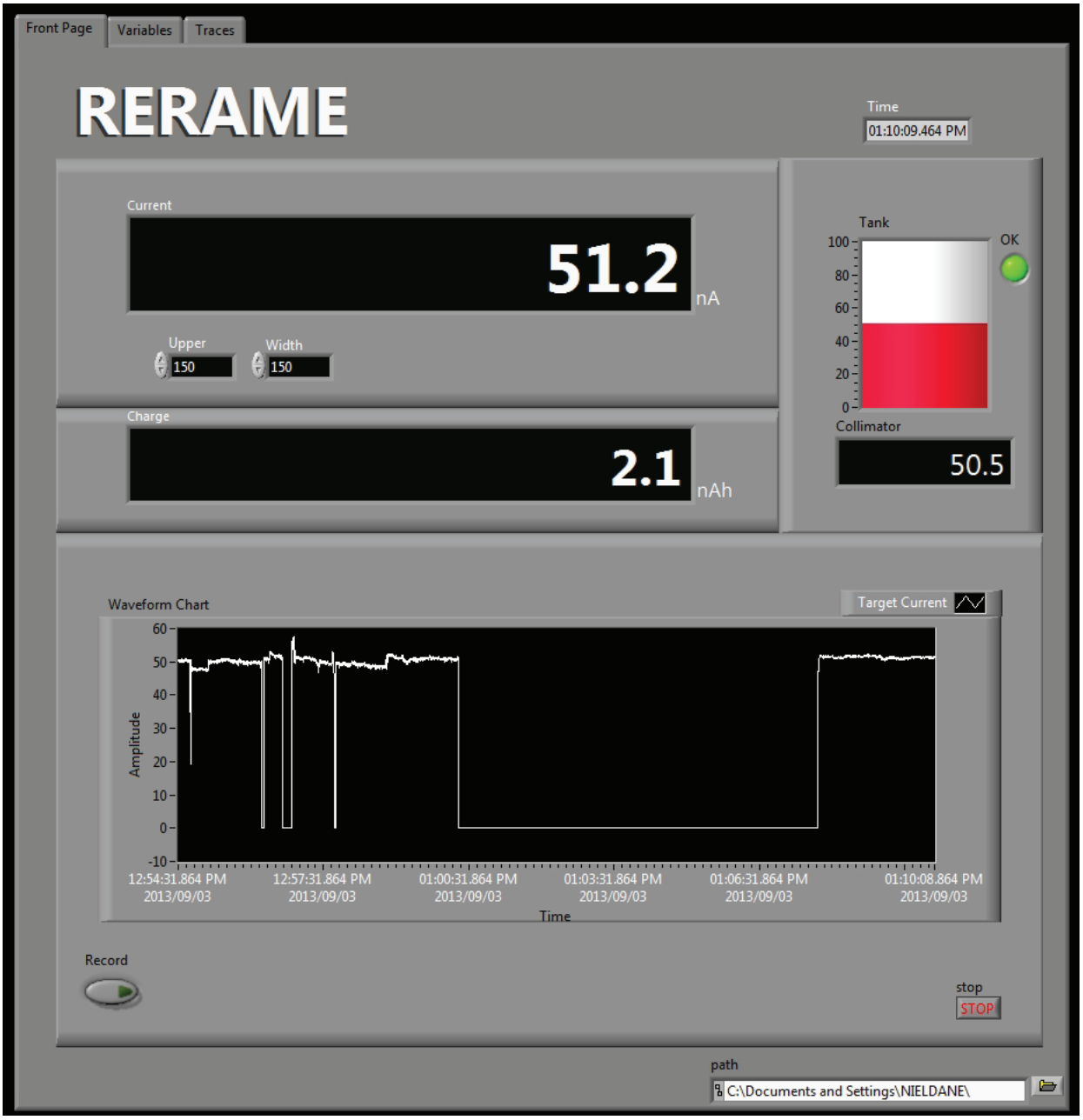

Figure A.3: Screenshot of the LabVIEW window for monitoring the beam in the RERAME-II chamber. Note that the beam fell away several times, the longest interruption being about 6 minutes in this case.

A.2.3 Induced activity

The number of residual nuclei produced in time increment i in thin target j of a nuclide of type p is given by

$$\Delta N_j^p(t_i) = R_j^p(t_i)\Delta T \qquad \text{for all} \quad 1 \leq i \leq n. \tag{A.7}$$

The associated activity if the nuclide is a radionuclide with half-life $T_{1/2}$, at a reference time $t = t_{ref}$ after EOB, is given by

$$\Delta A_j^p(t_{ref}) = \lambda \Delta N_j^p(t_i) \exp[-\lambda(t_{ref} - t_i)], \tag{A.8}$$

where $\lambda = \ln(2)/T_{1/2}$ is the decay constant. Substitution of Eqs. (A.2) and (A.7) into (A.8) gives

$$\Delta A_j^p(t_{ref}) = \lambda N_j \sigma_j I_j(t_i) \Delta T \exp[-\lambda(t_{ref} - t_i)]. \tag{A.9}$$

The total activity at $t = t_{ref}$ is then found by summing:

$$A_j^p(t_{ref}) = \lambda N_j \sigma_j \sum_{i=1}^{n} I_j(t_i) \Delta T \exp[-\lambda(t_{ref} - t_i)]. \tag{A.10}$$

A.2.4 Spectrometric counting

The counting times of target foil j are defined as follows:

$t = t_{Start}$: Beginning of counting period,
$t = t_{Stop}$: End of counting period.

The real time of the spectrometric measurement is then given by

$$\tau_{Real} = t_{Stop} - t_{Start}, \tag{A.11}$$

and the live time by

$$\tau_{Live} = \tau_{Real} - \Delta\tau, \tag{A.12}$$

where $\Delta\tau$ is the dead time of the spectrometry system under those particular measurement conditions. The measured activity of type p is given by

$$A_j^p(t_m) = \frac{A_p}{\tau_{Live}\epsilon_\gamma\epsilon_d}, \tag{A.13}$$

where A_p is the full photo-peak area of a characteristic γ-line, ϵ_γ is the branching ratio of the γ-line, ϵ_d is the detector efficiency for that particular γ-line and t_m is the mean value within the interval (t_{Start}, t_{Stop}) where the actual activity equals the average activity over the entire counting period. Thus

$$A_j^p(t_m) = \frac{1}{(t_{Stop} - t_{Start})} \int_{t_{Start}}^{t_{Stop}} A_j^p(t) dt. \tag{A.14}$$

After integration and rearranging terms, t_m is found to be

$$t_m = -\frac{1}{\lambda} \ln \left[\frac{\exp(-\lambda t_{Start}) - \exp(-\lambda t_{Stop})}{-\lambda(t_{Start} - t_{Stop})} \right]. \tag{A.15}$$

A.2.5 Equating reference and measurement times

By selecting the reference time equal to the measurement mean time, $t_{ref} = t_m$, Eqs. (A.10) and (A.13) should give the same result:

$$A_j^p(t_m) = \lambda N_j \sigma_j \sum_{i=1}^{n} I_j(t_i) \Delta T \exp[-\lambda(t_m - t_i)] = \frac{A_p}{\tau_{Live}\epsilon_\gamma\epsilon_d}. \tag{A.16}$$

By rearranging terms, one finds the general expression for the cross section as follows:

$$\sigma_j = \frac{A_p}{\lambda N_j \tau_{Live}\epsilon_\gamma\epsilon_d \sum_{i=1}^{n} I_j(t_i) \Delta T \exp[-\lambda(t_m - t_i)]}. \tag{A.17}$$

A.2.6 Non-elastic nuclear interactions

All the quantities in Eq. (A.17) are known except the $I_j(t_i)$, which we still need to relate to the measured beam current. As the beam traverses a target or foil stack, the beam intensity is progressively attenuated because of non-elastic nuclear interactions. This reduction in beam intensity is explicitly taken into account:

$$I_j(t_i) = I_{beam}(t_i)[1 - P(E_{beam}, \bar{E}_j)], \tag{A.18}$$

where $I_{beam}(t_i)$ is the number of charged particles per second at time $t = t_i$ incident upon the foil stack. The quantity $P(E_{beam}, \bar{E}_j)$ is the non-elastic nuclear interaction probability for the case where the beam energy, E_{beam}, has been degraded to an average energy of

$$\bar{E}_j = \frac{E_j + E_{j+1}}{2} \qquad \text{for all} \quad 1 \leq j \leq J, \tag{A.19}$$

by the time it reached thin target or foil number j in the stack. The non-elastic nuclear interaction probability will be separately discussed in Appendix B. Substitution of Eq. (A.18) into Eq. (A.17) gives the general expression for the cross section as follows:

$$\sigma_j = \frac{A_p}{\lambda N_j \tau_{Live} \epsilon_\gamma \epsilon_d [1 - P(E_{beam}, \bar{E}_j)] \sum_{i=1}^{n} I_{beam}(t_i) \Delta T \exp[-\lambda(t_m - t_i)]}. \tag{A.20}$$

A.2.7 Constant beam intensity

Equation (A.20) simplifies in the following way when the beam intensity remains constant:

$$\begin{aligned}
\sigma_j &= \frac{A_p}{\lambda N_j \tau_{Live} \epsilon_\gamma \epsilon_d [1 - P(E_{beam}, \bar{E}_j)] \sum_{i=1}^{n} I_{beam}(t_i) \Delta T \exp[-\lambda(t_m - t_i)]}, \\
&= \frac{A_p}{\lambda N_j \tau_{Live} \epsilon_\gamma \epsilon_d [1 - P(E_{beam}, \bar{E}_j)] I_{beam} \sum_{i=1}^{n} \Delta T \exp[-\lambda(t_m - t_i)]}, \\
&= \frac{A_p}{\lambda N_j \tau_{Live} \epsilon_\gamma \epsilon_d [1 - P(E_{beam}, \bar{E}_j)] I_{beam} \int_0^T \exp[-\lambda(t_m - t)] dt}, \\
&= \frac{A_p}{N_j \tau_{Live} \epsilon_\gamma \epsilon_d [1 - P(E_{beam}, \bar{E}_j)] I_{beam} \exp[-\lambda(t_m - T)][1 - \exp(-\lambda T)]}.
\end{aligned} \tag{A.21}$$

A.2.8 Beam attenuation neglected

When beam intensity attenuation is neglected, Eq. (A.21) can be further simplified:

$$\sigma_j = \frac{A_p}{N_j \tau_{Live} \epsilon_\gamma \epsilon_d I_{beam} \exp[-\lambda(t_m - T)][1 - \exp(-\lambda T)]}. \tag{A.22}$$

Equation (A.22) is the form of the activation equation most often found in the literature, e.g. [Gil2008, Kha2012].

A.3 Recoil losses

Recoiling residual nuclei in close proximity to the surface of a target foil may occasionally escape and be collected in an adjacent foil of the stack. It is, therefore, customary to place a foil of a different material behind a target foil to act as as a so-called "catcher foil". This is also done at iThemba LABS, however, these foils often serve as both degrader and/or monitor foils. In general, the fraction of recoil losses is a function of the target/recoiling nucleus combination, the projectile species and energy, as well as the target thickness. Also, the fractional recoil loss increases with decreasing foil thickness, as one would reasonably expect. At any rate, in this work the target foils were relatively thick and the recoil losses found to be negligible. A literature search found rather few precision studies of this phenomenon for proton-induced reactions at energies typical of this work. Sisterson [Sis2008] reported values well below the 1% level in targets of C, Al, Mg and Fe of 125 μm thickness at proton energies of 200 and 500 MeV. Lebeda *et al.* [Leb2012] reported recoil losses of ^{48}V from their rather thin Ti monitor foils (nominally 12 μm thick) not exceeding 2% with a proton beam of 30 MeV. These studies are both in agreement with our findings.

Appendix B

Beam Loss by Nonelastic Nuclear Interactions

As a beam of charged particles traverses a target or foil stack, some particles are lost from the beam due to nonelastic nuclear interactions. While often neglected in studies at lower energies (e.g. protons of ≤ 30 MeV), at higher energies the resulting attenuation in beam intensity, as a function of penetration depth, needs to be be taken into account explicitly. In fact, the stacked-foil experiment remains a good experimental technique only as long as the nonelastic nuclear interaction probability over the energy region of the stack remains relatively small. This may require a compromise between the length of a single stack and the number of primary beams and stacks required to measure an excitation function accurately down to threshold. Shorter stacks and more primary beam energies are usually required as the upper beam energy is increased. Nonelastic nuclear interactions are not taken into account in the continuous slowing-down approximation, by which stopping powers and ranges are calculated (e.g. the Bethe-Block equation). The phrase "beam energy" is actually a misnomer as it refers to the average kinetic energy of a single beam particle which never suffered a nonelastic nuclear interaction, while nonelastic nuclear interactions are treated as an absorptive process which effectively removes a particle from the beam.

Several systematic studies on the nonelastic nuclear interaction probability of protons in various materials were conducted from the early sixties until sometime into the seventies, when synchrocyclotrons were still fashionable machines. It seems that much of the current experimental information comes from that period. One such facility that produced a wealth of information was the CERN Synchrocyclotron (SC) which became operational in 1957 and closed in 1990 (see e.g. [Mea1969] and references therein). The most comprehensive sources of information available, for both elements and compounds, are the two 1982 compilations by Janni [Jan1982]. Figure B.1 (a) shows the nonelastic nuclear interaction probability of protons over their entire pathlength, for a selection of elements, plotted versus the incident proton energy. While not a strong function of mass, it is higher for the lighter elements. The values for a 70 MeV incident proton beam are as follows: Al (6.82%), Cu (5.69%), Nb (5.26%), Tb (4.62%) and Pb (4.35%). The probability for a nonelastic nuclear interaction over a limited energy range,

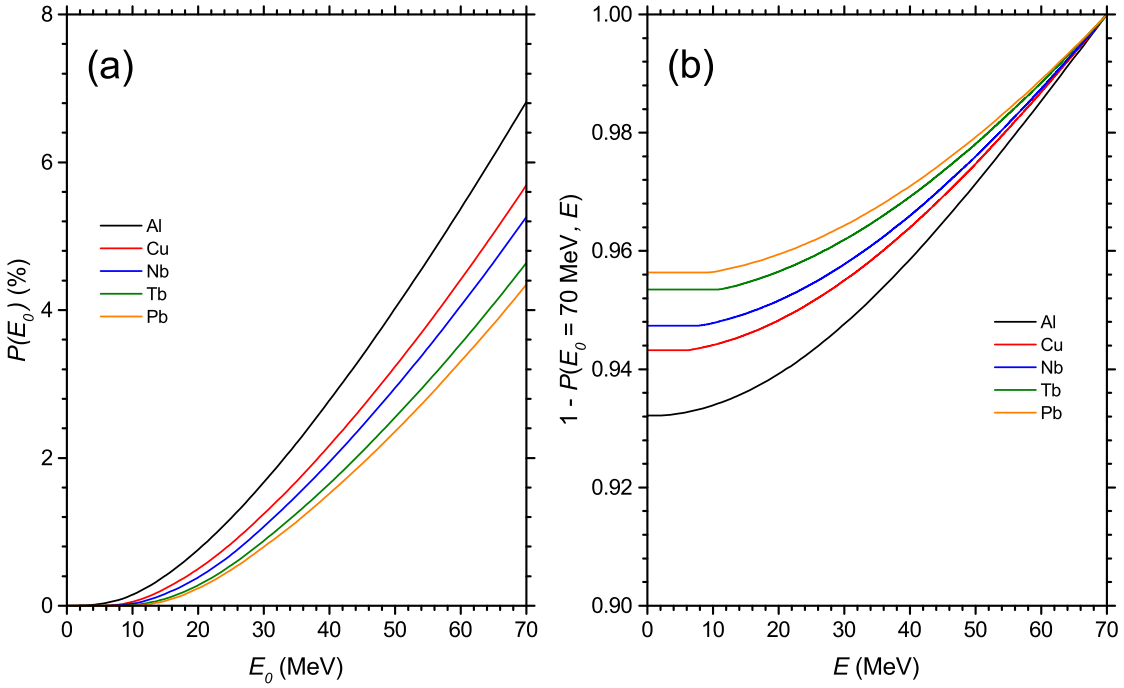

Figure B.1: (a) Nonelastic nuclear interaction probability over the full pathlength, plotted versus incident proton energy for a selection of elements, as indicated. The data have been taken from the tables of Janni [Jan1982]. (b) Beam attenuation factor for a 70 MeV incident proton beam, plotted versus the proton energy at an arbitrary penetration depth (or the exit energy).

instead of over the full pathlength, is given by

$$P(E_0, E) = 1 - \left[\frac{1 - P(E_0)}{1 - P(E)}\right], \tag{B.1}$$

where E_0 is the incident beam energy and E is the average energy at an arbitrary penetration depth inside the target or stack (or the exit energy if the target thickness is smaller than the range). The values of $P(E_0)$ and $P(E)$ can be found from the tables of Janni [Jan1982].

The beam intensity inside the material is given by

$$I(E) = I_0[1 - P(E_0, E)], \tag{B.2}$$

where I_0 is the incident beam intensity and the expression in square brackets is the attenuation factor. The attenuation factor at arbitrary energies for an incident beam of 70 MeV is shown in Fig. B.1 (b) .

Appendix C

Energy Uncertainties

The calculation of energy uncertainties in a stacked-foil experiment takes into account the energy straggling as the beam traverses the stack, the energy uncertainly of the incident beam and the energy uncertainty associated with the foil thickness. These individual uncertainties are summed in quadrature.

C.1 Energy straggling

An unpublished method to compute energy straggling for protons in thick targets and/or foil stacks has been in existence at iThemba LABS for many years. It is based on the work of Tschalär [Tsc68a, Tsc68b]. The theoretical treatment by Tschalär is rather complex and not easy to directly implement in a code. Instead, a parametrization was implemented which reproduces the values of Tschalär within 5% for protons up to 200 MeV, in light and heavy target materials. This scheme uses only two independent parameters: The first is the *mean ionization potential*, I, which is also found in expressions of stopping power. The second parameter, W, was introduced by Tschalär and is related to the energy straggling as follows:

$$W = \frac{[s(\langle E\rangle)]^2}{E_0(E_0 - \langle E\rangle)} \log_{10}(u_0) \left[\frac{\epsilon_p}{\epsilon}\right], \tag{C.1}$$

where E_0 is the incident kinetic energy of the projectile, $\langle E\rangle$ is the mean energy of the projectile traversing the target, and $s(\langle E\rangle)$ is one standard deviation of the energy straggling distribution about a mean energy $\langle E\rangle$. The parameter u_0 is the so-called reduced energy of the beam, given by

$$u_0 = \frac{\epsilon E_0}{I}. \tag{C.2}$$

The parameter ϵ is given by

$$\epsilon = 4\left(\frac{m}{M}\right)\left[1 + \frac{m}{M}\right]^{-2}, \tag{C.3}$$

where m is the electron mass and M is the projectile mass. The parameter ϵ_p in Eq. (C.1) is ϵ for protons, therefore the factor ϵ_p/ϵ becomes 1 in the case of proton beams.

Tschalär presented plots of W as a function of the normalized mean energy $\langle E\rangle/E_0$ for different values of u_0. The parametrization used in this work is based on a set of values extracted from those curves, listed in Table C.1. Unfortunately, the original FORTRAN code was

Table C.1: Values of parameter W from the work of Tschalär [Tsc68a, Tsc68b].

$\langle E\rangle/E_0$	W						
(%)	$u_0 = 10$	$u_0 = 20$	$u_0 = 50$	$u_0 = 100$	$u_0 = 200$	$u_0 = 500$	$u_0 = 1000$
100	4.70	4.70	4.70	4.70	4.70	4.70	4.70
95	4.76	4.77	4.78	4.79	4.80	4.81	4.82
90	4.85	4.88	4.90	4.92	4.93	4.94	4.95
80	5.06	5.09	5.14	5.22	5.24	5.26	5.28
70	5.30	5.46	5.58	5.70	5.76	5.81	5.85
60	5.60	5.96	6.17	6.32	6.40	6.47	6.54
50	5.96	6.56	7.05	7.42	7.60	7.71	7.83
40	6.32	7.60	8.54	9.06	9.41	9.75	10.01
30	6.45	9.02	11.15	12.19	13.05	13.68	14.22
25	6.20	9.91	13.26	14.92	16.29	17.49	18.38
20	5.34	10.93	16.35	19.56	21.79	24.32	25.93
15	3.21	11.28	21.30	28.76	35.41	45.28	49.84

lost some years ago when the mainframe computer on which it resided was decommissioned and the back-ups resided on a medium which no apparatus could read anymore. A new version of the code ESTRAGG was therefore created as part of this work, with the main aim to make a comparison with alternative calculations based on the Monte Carlo code SRIM [Zie2013]. One reason for the comparison is simply because of academic interest; another is because SRIM calculations for an entire foil stack can take a long time because the proton flux has to be tallied at the exit of each foil, added progressively to the stack, resulting in many separate runs which each has to continue until good statistics has been obtained. In contrast, the ESTRAGG code can do the entire calculation in only one run. The region of applicability of the code is $0.15 \leq \langle E\rangle/E_0 \leq 1$. In the original ESTRAGG code, a two-dimensional (surface) cubic spline was used to interpolate for off-grid values, using the tabulated values of Table C.1 as the grid in the spline routine. An alternative approach was used in this work. For each tabulated value of u_0, W was determined as a function $\langle E\rangle/E_0$ by means of a non-linear regression fit using the software package TABLECURVE. The following function was selected for this purpose:

$$W(\langle E\rangle/E_0) = a(u_0) + \frac{b(u_0)}{\langle E\rangle/E_0} + \frac{c(u_0)}{(\langle E\rangle/E_0)^2} + \frac{d(u_0)}{\exp(\langle E\rangle/E_0)}, \tag{C.4}$$

where $a(u_0)$, $b(u_0)$, $c(u_0)$ and $d(u_0)$ are the coefficients from the fitting procedure. A one-dimensional cubic spline is used in the code to obtain W values for off-grid u_0 values, the interpolation being performed using on-grid values calculated from Eq. (C.4). Grid coordinates are taken as $(\log_{10}(u_0), W)$ for purposes of the spline interpolation as this gives a more even grid spacing than the (u_0, W) coordinates. By rearranging Eq. (C.1), one can write down the relevant expression for the energy straggling of protons:

$$\frac{s(\langle E\rangle)}{E_0} = \sqrt{\frac{W}{\log_{10}(u_0)}\left[1 - \frac{\langle E\rangle}{E_0}\right]}. \tag{C.5}$$

In the case of some lighter elements and for protons of higher energies, the value of u_0 may

occasionally exceed 1000 (the highest value included in Table C.1). In these cases, a value of $u_0 = 1000$ is used. This was found to be a good approximation as the function $s(\langle E \rangle)$ changes only slowly with increasing energy. In fact, the above approach leads to a slight overestimation of the straggling, not expected to exceed 5%. Interestingly, a linear extrapolation in u_0 resulted in a slight underestimation of the energy straggling.

In the case of mixtures and compounds, an effective value for the mean ionization potential is calculated using Bragg's additivity rule [Jan1982]:

$$\langle I \rangle = \exp\left[\frac{\sum_i n_i \ln(I_i)}{\sum_i n_i Z_i}\right], \tag{C.6}$$

where n_i is the number of atoms per gram (number density) of constituent element i, Z_i is the atomic number of constituent element i, and I_i is the mean ionization potential of constituent element i. Values for the elemental mean ionization potential were taken from Ziegler [Zie1980].

Figure C.1 shows energy distributions of protons at different penetration depths inside a thick Nb target as calculated with the code SRIM. The 66 MeV incident proton beam (distribution A in the figure) is mono-energetic and therefore a delta function. The other distributions are tallied at different depths as follows: B (1 mm), C (3 mm), D (5.4 mm) and E (6.9 mm). The bin sizes have been adjusted to give similar heights for distributions B through E. These distributions can be fitted satisfactorily with the Gaussian function, even at large penetration depths. The increase in width with increasing penetration depth is evident.

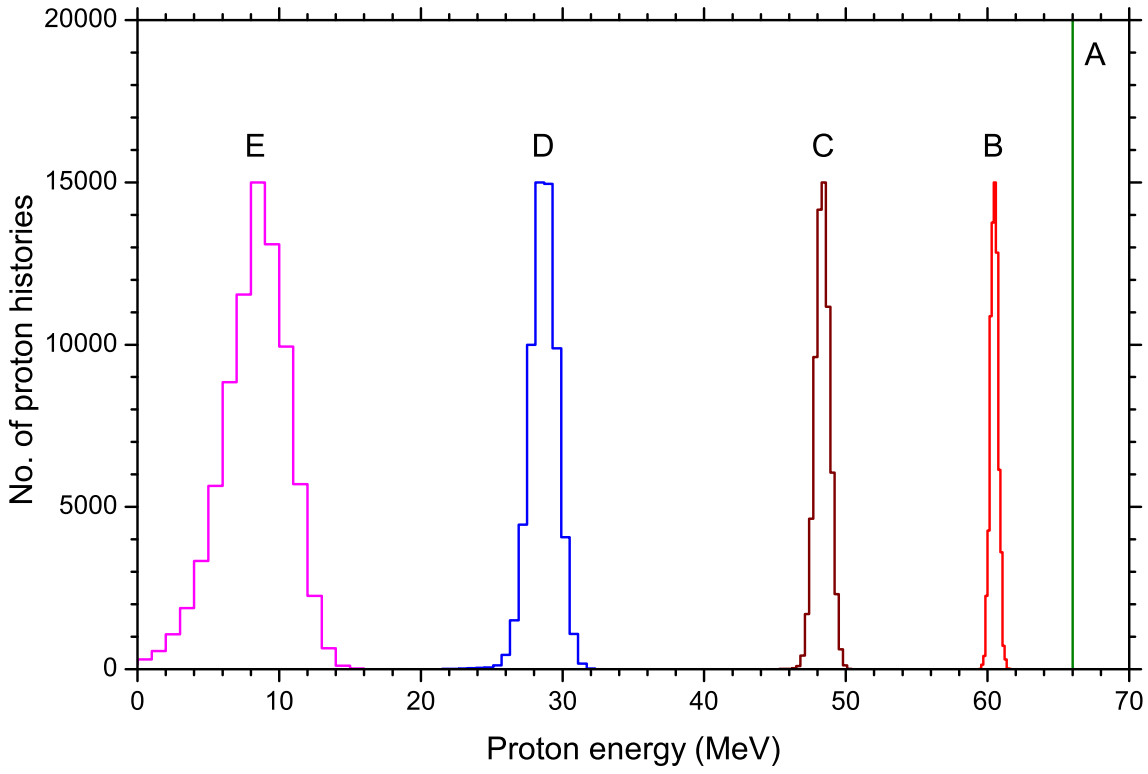

Figure C.1: Energy distributions of protons at different penetration depths inside Nb as calculated with the code SRIM [Zie2013]. The distributions are tallied at penetration depths as follows: A (0 mm), B (1 mm), C (3 mm), D (5.4 mm) and E (6.9 mm). The number of particle histories tracked was 100 000 in each case.

Figure C.2 compares the energy straggling calculations based on the work of Tschalär with those performed with the code SRIM, for thick targets of C, Mg, Nb and Pb under bombardment with 66 MeV protons. Very good agreement is obtained for the lighter elements (C and Mg) but for the heavier elements (Nb and Pb) SRIM predicts somewhat larger values. The mass dependence is depicted in Fig. C.2 (a) and (b) for the SRIM and ESTRAGG calculations, respectively.

C.2 Energy uncertainty

In this work, the energy uncertainty in stacked-foil experiments were calculated as follows:

$$\Delta E = \sqrt{(\Delta E_0)^2 + [s(\langle E \rangle)]^2 + \left(\frac{1}{3}\left[\frac{dE}{dx}\Delta x\right]\right)^2}, \tag{C.7}$$

where ΔE_0 is the energy uncertainty of the incident beam, Δx is the foil thickness and dE/dx is the proton stopping power at energy $\langle E \rangle$. The first two terms under the radical sign pertain to stochastic processes in that there is some indeterminacy in the behaviour of an individual proton in the beam and as it traverses the target material. Collectively, however, these processes are well described by statistical distribution functions – the Gaussian distribution in this case. The individual uncertainties of the incident beam energy and the energy straggling are taken as one standard deviation (i.e. a 1 σ criterion) of their respective Gaussian distributions. Equation (C.7) is then said to provide the *combined standard uncertainty*. For quantities described by the Gaussian distribution, the interval $-1\sigma \rightarrow +1\sigma$ defines an interval having a 68.27% level of confidence (see e.g. Taylor and Kuyatt [Tay1994]). This fact is important as it sheds light on the third term under the radical sign of Eq. (C.7). Because the foils used in stacked-foil experiments have finite thicknesses, an energy uncertainty associated with the foil thickness is introduced. In contrast to the uncertainties associated with the incident beam energy and energy straggling, which result from stochastic processes, the foil thickness is a deterministic quantity. The interval $-1/3\Delta x \times dE/dx \rightarrow +1/3\Delta x \times dE/dx$ corresponds to two thirds of the deterministic quantity $\Delta x \times dE/dx$. This represents a $\sim 66.67\%$ interval, compatible with the 68.27% confidence interval associated with standard uncertainties, for all practical purposes.

It was finally decided to use SRIM calculations for purposes of estimating the energy uncertainties for the stacked-foil results presented in this work. In some cases, the calculations have been re-done and may differ slightly from our published values. A further approximation was introduced, namely to consider the entire stack as a homogeneous mixture of its constituent elements. This reduces the amount of work considerably without any significant compromise to the results.

As a final comment, the new ESTRAGG code may be useful in calculations for gaseous targets. Ziegler [Zie1980] presented different mean ionization potentials for solids and gasses, for all the elements. Both sets have been implemented in the code. Generally, the potentials are somewhat higher for solids than for gasses because the outer atomic electrons are more tightly bound in solids than in gasses.

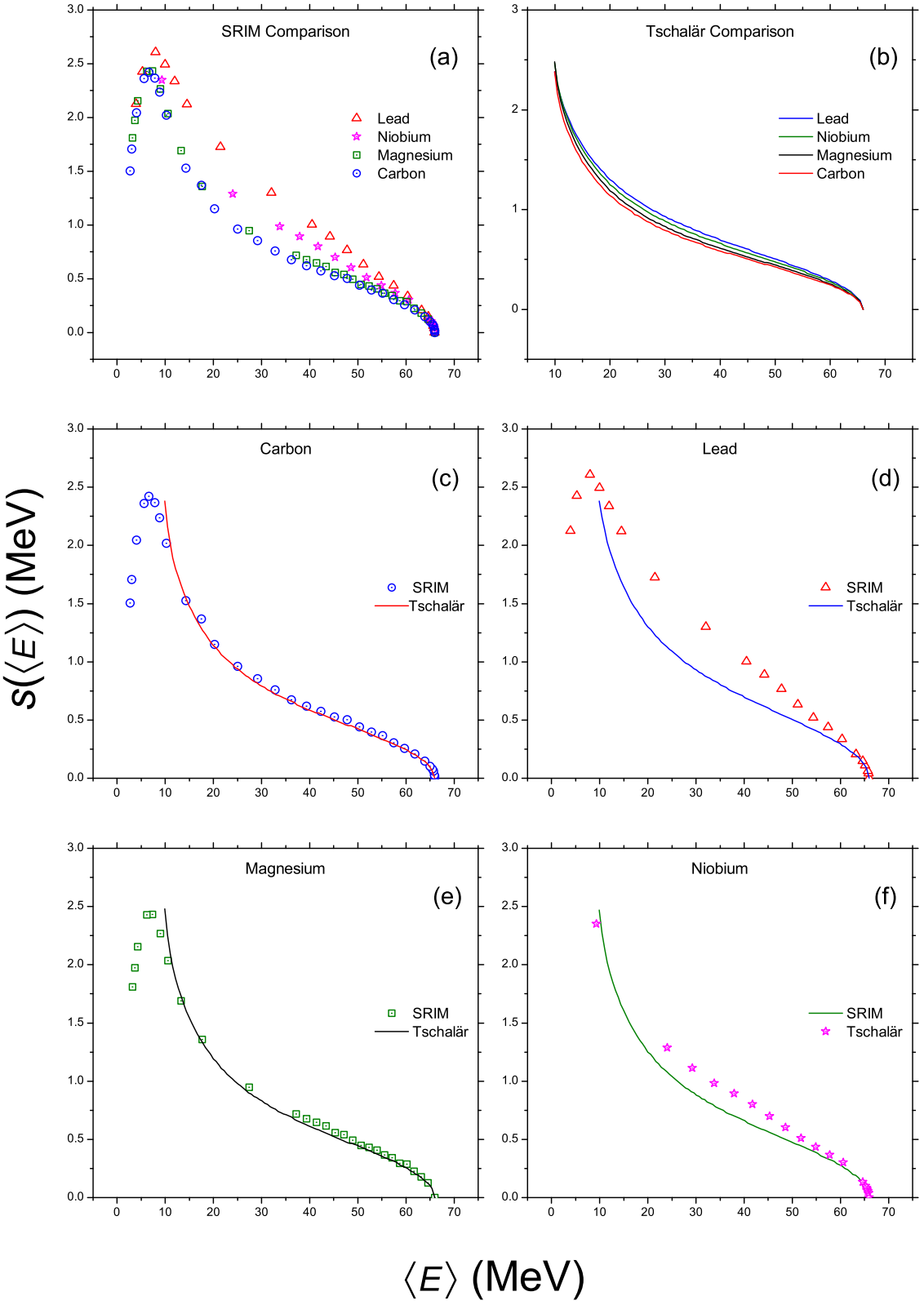

Figure C.2: Energy straggling calculations for a 66 MeV mono-energetic proton beam on thick targets of Pb, Nb, Mg and C. One standard deviation (1σ) of the energy distribution is plotted versus the mean proton energy as the beam traverses the target. The SRIM calculations for all four targets are compared in (a) and the corresponding calculations based on the work of Tschalär [Tsc68a, Tsc68b] in (b). The SRIM and Tschalär results are compared for the individual targets in (c) through (f).

Appendix D

ALICE/ASH nuclear model calculations

D.1 Overview

In this work, the focus is primarily on proton-induced reactions in the energy region up to 70 MeV (with the exception of the ^{28}Mg study at 200 MeV) and those nuclear processes which dominate the formation of radionuclides. The so-called semi-classical pre-equilibrium-evaporation models [Gul2001] are the theoretical formalisms which are most useful for predicting the formation cross sections of heavy target-like residues. Direct reaction mechanisms only play a very minor role in the formation of radionuclides (which can be viewed in this context as the residues remaining after the relevant nuclear reactions have run their cause) and their contributions are therefore usually neglected. The reasons for this will be clarified in the paragraphs below.

The main classes of reaction mechanisms are briefly revisited for the purposes of the present discussion. Consider a typical inclusive spectrum of protons emitted from a thin target during bombardment with protons. Such an experiment is shown diagrammatically in Fig. D.1, where a particle detector of appropriate type is utilized to measure the energy of emitted protons at a forward scattering angle, θ. The measured emission spectrum of this inclusive (p,p′) reaction can be expressed in the form a double-differential cross section, as shown in Fig. D.2 (a). The same data can also be displayed as an excitation energy spectrum, which is depicted in Fig. D2 (b). Here, E^* is the energy available for the excitation of the nucleus. The emission and excitation energy spectra are virtually mirror images of each other. Different reaction mechanisms can be associated with various characteristic features of these spectra.

The *direct reactions* take place on a time scale comparable with the time it takes the projectile to traverse the target nucleus, typically of the order of 10^{-22} s. The simplest direct reaction is *elastic scattering*, which leaves the target nucleus in its ground state (i.e. $E^* = 0$). *Inelastic scattering* (i.e. scattering where $E^* > 0$) typically excites the target nucleus to a low lying discrete state which has a simple structural relationship with the ground state. In these reactions, the energy transferred from the projectile to the target nucleus is relatively small and an ejectile with properties very similar to the projectile can be observed. Particle emission following the reaction is unlikely and the nucleus will usually de-excite by γ-emission until it reaches the ground state. Other processes such as giant resonances may be excited, which are more likely

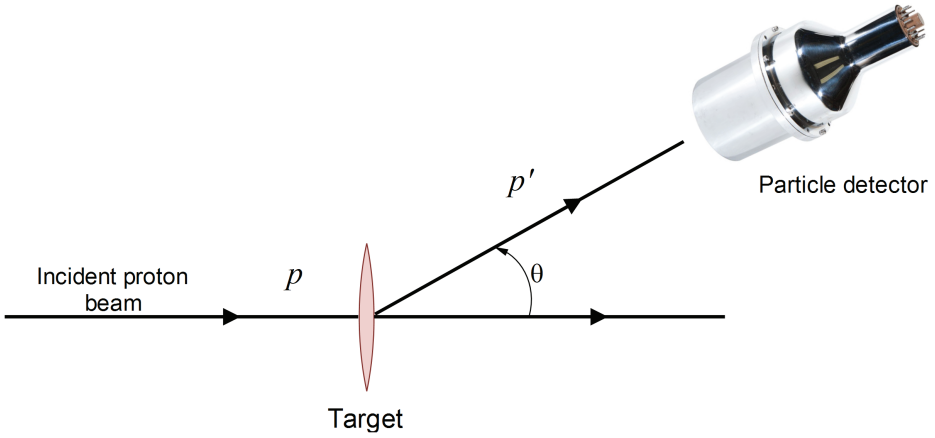

Figure D.1: Typical experimental set-up to measure the inclusive emission spectrum of protons emitted from a thin target under bombardment with a proton beam.

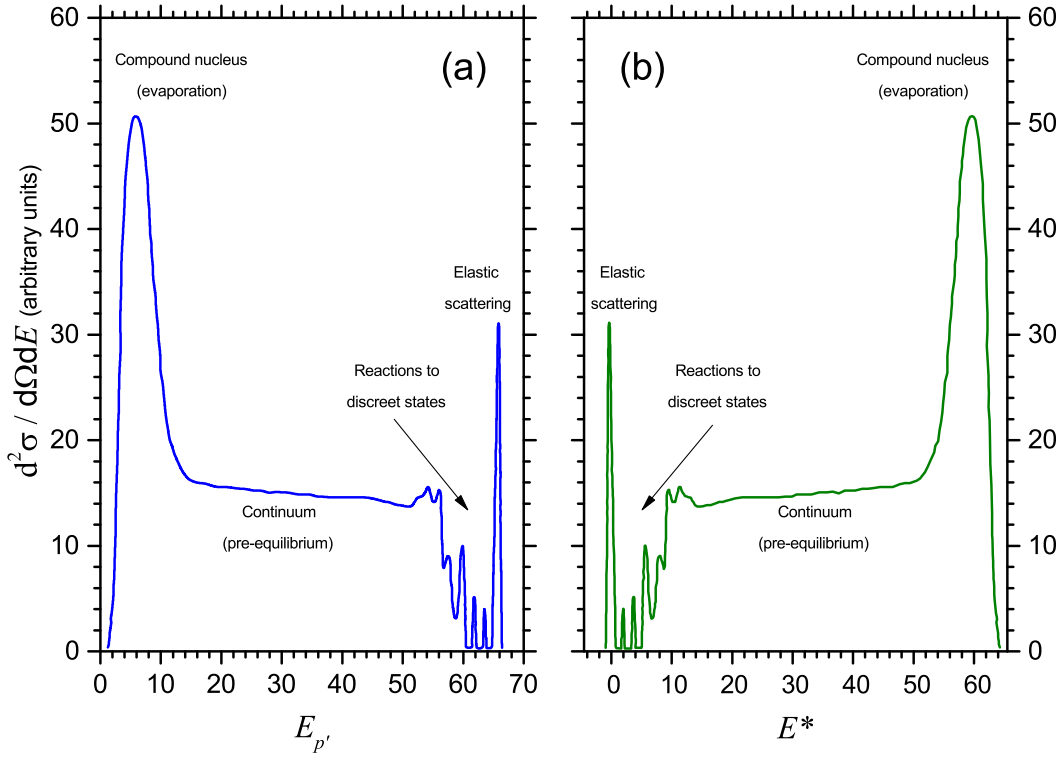

Figure D.2: (a) Inclusive emission spectrum of protons emitted from a thin target under bombardment with a proton beam. (b) The same data presented as an excitation energy spectrum. (Idea of figure developed from a similar sketch in [Gad1992] by Gadioli and Hodgson.)

to decay by particle emission. These processes, however, do not occur with a high probability.

The so-called *compound nucleus reactions* occupy the other extreme of the excitation energy scale (i.e. $E^* >> 0$). In these reactions, the projectile is absorbed by the target nucleus and the excitation energy is shared amongst all the nucleons by means of successive two-body nucleon-nucleon collisions until the compound nucleus reaches a state of statistical equilibrium. Because of the rapid sharing of excitation energy amongst many nucleons during the

initial stages of the reaction, a situation is quickly reached where the individual nucleons do not have enough energy to readily escape. Thus, as the emission probability decreases sharply during the evolution of the reaction, the time scale of compound nucleus reactions increases dramatically compared to that of direct reactions. The characteristic time for an evaporation event is typically 10^6–10^7 times longer than the projectile transit time. The emission of particles becomes a statistical process with characteristics similar to the *evaporation* of molecules from a heated liquid drop. Purely by chance, as a result of statistical fluctuations due to the many intra-nuclear collisions that occur, a nucleon (or a cluster of nucleons) near the nuclear surface may occasionally receive enough energy to escape. Figure D.2 shows the broad evaporation peak with a Maxwellian shape towards the low-energy side of the emission spectrum and the high-energy side of the excitation energy spectrum, in contrast to the sharp peaks which characterize elastic scattering and inelastic reactions to discrete states.

The direct reactions are fast and lead to the emission of particles with relatively high kinetic energies. In contrast, compound nucleus reactions are slow and lead to the emission of particles with relatively low kinetic energies. Between these two extremes, a third class of reaction mechanisms represents processes which are neither direct, nor compound. These so-called *pre-equilibrium reactions* (also sometimes called pre-compound reactions) occur at characteristic times which are longer than the projectile transit time, yet much shorter than for compound nucleus formation. In this case, the emission of particles occurs before statistical equilibrium of the nucleus is reached. Their energies are therefore higher than observed for evaporated particles but lower than for particles emitted during direct reactions. A characteristic of the pre-equilibrium part of the spectrum is that it is flat and featureless, as shown in Fig. D.2.

The relative contributions to the *total cross section* of these various reaction mechanisms is important. In the mass and energy region relevant to the present study, elastic scattering and direct reactions contribute about 2–3% to the total cross section. The contribution from evaporation is not expected to exceed 20%. Thus, the contribution from pre-equilibrium reactions is of the order of 80%. The compound and pre-equilibrium reactions lead to high excitation of the target nucleus and to significant particle emission, thus they dominate the formation of heavy residues different from the target species. The probability of particle emission following a direct reaction is considerably smaller, thus their contribution to produce radionuclides is very much inhibited. It is therefore justified to neglect them.

D.2 The ALICE-ASH computer code

A number of computer codes based on compound and pre-equilibrium nuclear reaction mechanisms exist which can be employed to predict the formation cross sections of heavy residues in a nuclear reaction (e.g. STAPRE, ALICE, GNASH, TALYS, etc. [Gul2001]) Although the underlying physics of these codes is similar, they differ largely in the complexity of implementation and input preparation (mainly due to the level of approximations made to simplify computation). Consequently, the required computing time of these codes vary dramatically. For very detailed calculations of the properties of nuclear reactions where one needs information on each participating channel, codes like STAPRE and GNASH are often employed. The downside

is that calculations for a whole family of excitation functions of a particular nuclear reaction become a formidable task. The ALICE code is much faster, require much less input and is more user friendly. It is usually sufficient to estimate optimum bombarding energies for many proton induced reactions [Gul2001] and often generate predictions which are by and large not inferior to predictions by the larger codes. The ALICE code has been written to be versatile, yet easy to be used by non-nuclear specialists [Oka1998]. For these reasons, it has become one of the workhorses for theoretical predictions by the radionuclide production community; another being TALYS. Extensive TALYS calculations for many reactions have been performed and are being published online as the TENDL library [Kon2012]. It is useful to compare the TENDL library values for particular reactions, if they exist, with the ALICE calculations, as an additional consistency check. This approach has been followed for the bulk of the current excitation function work.

Various evolutions of the ALICE code appeared since the early seventies. One of the latest versions, ALICE/ASH (developed at Forschungszentrum Karlsruhe) is an advanced version of the ALICE-91 code originally developed by Marshall Blann [Bla1991] and is built on the ALICE-IPPE code developed at Obninsk. The ALICE codes perform equilibrium decay (evaporation) calculations using the *W*eisskopf-Ewing formalism. Pre-equilibrium decay is treated using the *G*eometry Dependant Hybrid (GDH) model approach. This version of the code includes the Generalized Superfluid model of Ignatyuk and co-workers [Ign1993] as an option for calculating nuclear level densities. Furthermore, the ALICE/ASH code incorporates improved models for the description of pre-compound cluster emission, fast γ-ray emission as well as different parameter-selectable approaches for the calculation of nuclear level densities and fission fragment yields. In the following section, a short description is given of the main concepts.

D.3 The Hybrid and Geometry Dependant Hybrid models

The Hybrid model is largely based on an approach first published by Griffin [Gr1966] for calculating the excited particle populations during equilibration in an excited nucleus, which led to the development of the so-called Exciton models. The Hybrid model differs from the standard Exciton model in that the intra-nuclear transition rates are determined from calculations of the mean free paths of nucleons in nuclear matter [Bla1971]. It is assumed that the projectile fuses with the target nucleus and remains bound in an intermediate nucleus which is far from statistical equilibrium. It is further assumed that equilibration of this intermediate nucleus is achieved by a succession of two-body nucleon-nucleon interactions – the so-called *intra-nuclear cascade*. Thus, as the reaction proceeds, the nucleus is progressively excited to more and more complex states, each of which is characterized by the number of excited particles (p) above the Fermi energy plus holes (h) below the Fermi energy. The number $n = p + h$ is called the *exciton number*. Collectively, the particles above and holes below the Fermi energy (ε_f) are referred to as *excitons*.

This process is diagrammatically depicted in Fig. D.3, where a proton with energy E above the Fermi energy is incident upon a target nucleus in its ground state. Before any nuclear interaction takes place, one can view the system as having an exciton number of $n = 1$. In

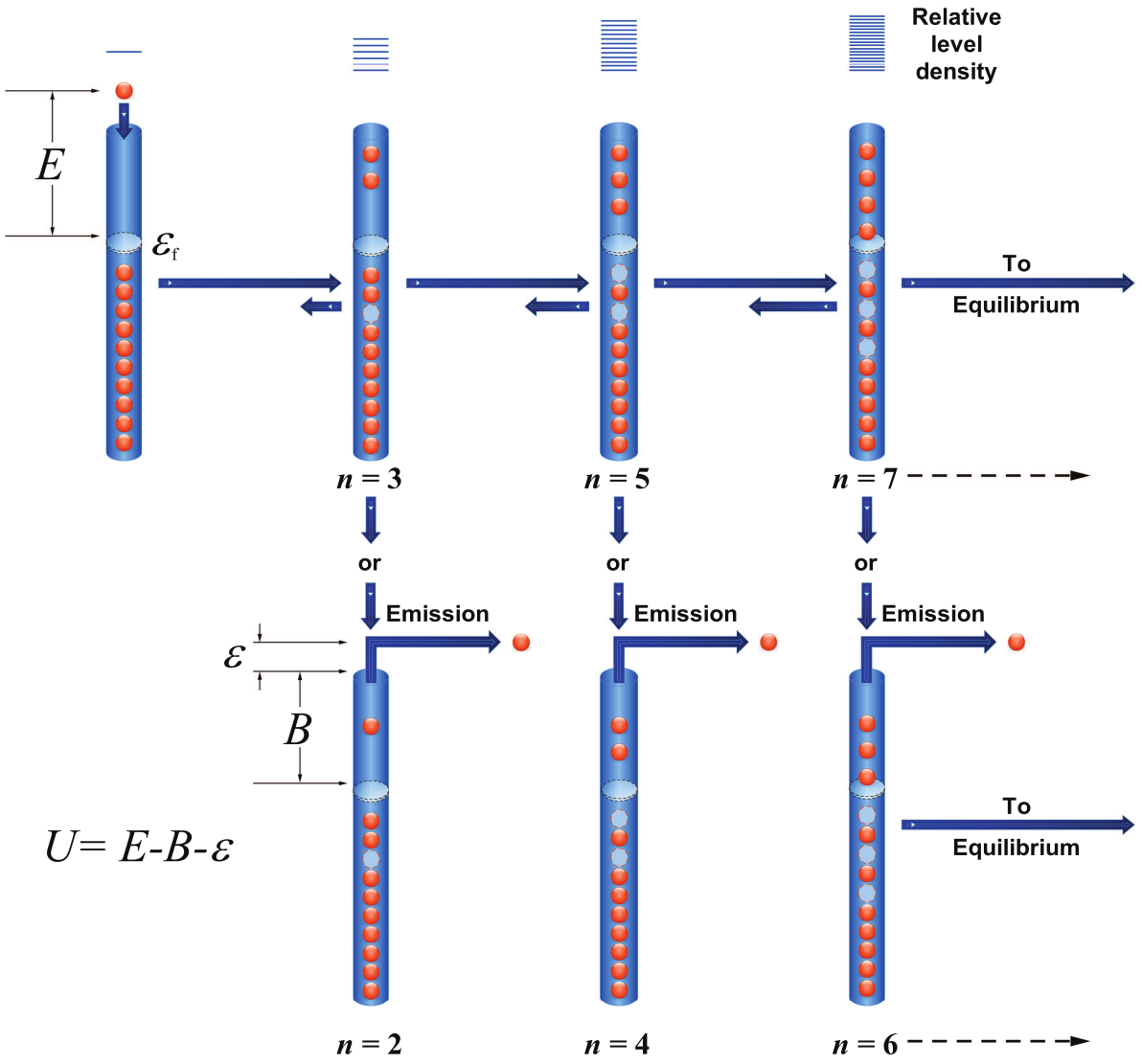

Figure D.3: Schematic representation of the first few stages of a nucleon-induced reaction in the Exciton, Hybrid or GDH models. The red spheres represent single nucleons in discrete energy levels in a nuclear potential well. The incident energy of the projectile nucleon, as measured from the Fermi energy ε_f, is denoted by E. The average nucleon binding energy is denoted by B and an escaping nucleon has an emission energy ε. (Idea of figure developed from description in [Gad1992] by Gadioli and Hodgson.)

the first nucleon-nucleon interaction, the projectile proton becomes bound by exciting a target nucleon above the Fermi energy. The resulting nucleus is now in a $2p$-$1h$ state, thus the exciton number increases to $n = 3$. A further nucleon-nucleon interaction may lead to a $3p$-$2h$ state, taking the exciton number to $n = 5$. In principle, this process can continue until the nucleus achieves statistical equilibrium, always increasing the exciton number by $\Delta n = +2$ in each successive interaction. However, provision for the emission of particles must still be included. Particle emission has a finite probability at each stage of the interaction chain. In the Hybrid model, if any nucleon obtains enough energy to become unbound, it has a finite probability to escape and thus be emitted into the continuum. Thus, for each exciton number (or exciton configuration) there is competition between emission and a further interaction which will increase the complexity of the nuclear state. Note, however, that this last statement is only approximately true, as energetically it is always possible that a further step may reduce the exciton number by 2 (i.e. a decay process with $\Delta n = -2$ which takes the nuclear system back

to a less complex state). This, however, is rather improbable, especially for states which still have low exciton numbers. The "never come back" approximation is therefore often enforced in the application of the theory, which only allows for Δn to be positive except when particles or particle clusters are emitted. The density of states of p excited particles and h holes (called a partial state density) also rapidly increases as the exciton number increases. This is because the number of possible configurations of the nuclear system rapidly increases with increasing exciton number. All the states of a given exciton configuration are also assumed to be equally probable.

In order to calculate the excitation functions of heavy residues in a nuclear reaction, it is necessary to keep track of the number and type of emissions from the combined nuclear system (projectile plus target nucleus) as well as the energy carried away by these emissions. If, for the moment, the pre-equilibrium (PE) decay is considered to involve only individual protons and neutrons (neglecting clusters of protons and neutrons), the PE decay probability [Gad1992] in the Hybrid model and in the Geometry Dependent Hybrid model (a later enhanced version of the Hybrid model) can be written, respectively, as

$$P_x(\varepsilon_x)d\varepsilon_x = \sum_{n=n_o}^{\bar{n}} \left[R_x(n) \frac{\omega(p-1,h,U)}{\omega(p,h,E)} g d\varepsilon_x \right] \left[\frac{\lambda_c^x(\varepsilon_x)}{\lambda_c^x(\varepsilon_x) + \lambda_+^x(\varepsilon_x)} \right] D_n, \tag{D.1}$$

and

$$P_x(\varepsilon_x)d\varepsilon_x = K \sum_{l=o}^{l_{max}} (2l+1) T_l \sum_{n=n_o}^{\bar{n}} \left[R_x(n) \frac{\omega(p-1,h,U)}{\omega(p,h,E)} g d\varepsilon_x \right] \left[\frac{\lambda_c^x(\varepsilon_x)}{\lambda_c^x(\varepsilon_x) + \lambda_+^x(\varepsilon_x)} \right] D_n. \tag{D.2}$$

The PE energy differential cross section (angle integrated) is then given by

$$\frac{d\sigma_x^{PE}}{d\varepsilon_x} = \sigma_R P_x(\varepsilon_x). \tag{D.3}$$

Note the similarity between Eq. (D.1) and the second summation in Eq. (D.2), which we will discuss first: This summation is over the exciton number n, from an initial exciton number n_0 (which is 3 for a nucleon-induced reaction) in increments of $\Delta n = 2$ up to an upper value $\bar{n}$, which should be selected large enough so that it may be assumed that the nucleus has reached statistical equilibrium. (A value of $\bar{n}$ between 20 and 30 is usually sufficient). $R_x(n)$ is the number of particles of type x (either protons or neutrons) in the n-exciton state. The quantity $\omega(p,h,E)$ is the density of n-exciton states (having p particles and h holes) at an excitation energy E. This definition applies similarly to $\omega(p-1,h,U)$, where $U = E - B - \varepsilon_x$ is the residual excitation energy for sharing amongst $n-1$ remaining excitons should a particle which had a binding energy B be emitted with energy ε_x. The quantity g is the single-particle level density, while $d\varepsilon_x$ is an energy increment. (An energy bin size of 0.5 MeV was typically used in calculations presented in this work.) Thus, the expression in the first set of square brackets gives the number of particles of type x in an n-exciton state that are in an unbound level with energy between ε_x and $\varepsilon_x + d\varepsilon_x$ in the continuum. The second expression in square brackets gives the fraction of those particles at energy ε_x which are emitted into the continuum, rather than interacting in a way that leads to a transition to a $n+2$ exciton state. Here, $\lambda_c^x(\varepsilon_x)$ is the particle

decay rate to the continuum while $\lambda_+^x(\varepsilon_x)$ is the intra-nuclear collision probability per unit time. (Note that the denominator $\lambda_c^x(\varepsilon_x) + \lambda_+^x(\varepsilon_x)$ is the total particle decay rate). The quantity D_n is the so-called depletion factor for the n-exciton state, representing the fraction of the particle population surviving from simpler exciton states. Since the details of the calculation of all these quantities are rather voluminous, we will constrain the present discussion by mentioning that the densities of exciton states (or partial state densities) are calculated according to the Strutinski-Ericson formalism.

In the ALICE/ASH code [Bro2006], one can specify whether the calculations should be performed according to the standard Hybrid model or the Geometry Dependent Hybrid model. In the standard Hybrid model, the effect of different impact parameters is not explicitly considered but rather averaged over the nucleus as a whole. In the GDH, the diffuse surface of the nucleus, which is preferentially sampled in collisions at higher impact parameters, is explicitly incorporated. The different possible trajectories of the incident projectile relative to the target nucleus translate into different values of the entrance channel orbital angular momentum. The higher the impact parameter, the larger the orbital angular momentum and the more peripheral (i.e. confined to the nuclear surface) the interaction becomes. This is the reason why in Eq. (D.2) for the GDH, the first summation is over the orbital angular momentum. This summation is from $l = 0$, which represent the most central collisions, becoming progressively more peripheral as l increases, up to a sufficiently large cut-off value $l = l_{max}$, above which a nuclear interaction becomes unlikely. The quantity T_l is the transmission coefficient, calculated using the Optical model. The GDH model is thus built on the basic idea that the nucleus has a density distribution that can affect pre-equilibrium decay in two ways [Bla1972]. Firstly, the mean free path of a nucleon in the diffuse nuclear surface is expected to be longer. Secondly, there is a density dependant limit to the hole depth in the approximation of local density. This last statement is obvious, as intuitively one can understand that the allowed hole depth in the nuclear interior should be larger than at a radius where the nuclear density is, say, only one tenth of that of the interior.

To conclude this section, Eq. (D.3) should still be explained. The energy differential cross section of emitted pre-equilibrium nucleons of type x is just a partitioning of the *r*eaction cross section, σ_R, by multiplying it with the probability, $P_x(\varepsilon_x)$, for those kinds of pre-equilibrium events at an emission energy ε_x. The reaction cross section is inclusive of all reaction channels except the entrance channel, thus it is the same as the total cross section for all possible nuclear interactions excluding elastic scattering (i.e. $\sigma_R = \sigma_T - \sigma_{el}$).

D.4 Further refinements, multi-particle and cluster emission

The ALICE/ASH and its predecessor, ALICE-IPPE differ from ALICE-91 in that pre-equilibrium cluster emission has been incorporated in the code. For this purpose, additional expressions remarkably similar in form to Eq. (D.2) have been formulated, with summations over orbital angular momenta and exciton numbers appropriate for the clusters. For pre-equilibrium deuteron emission, a nucleon pick-up is assumed prior to the emission. In a similar fashion, triton and ^{3}He emission spectra are incorporated according to the *coalescence pick-up model* of Sato,

Iwamoto and Harada [Iwa1982, Sat1983]. In the case of α-particle emission, both coalescence pick-up and knock-out processes have been incorporated. In the case of knock-out, the emission rates of pre-formed α-clusters according to Oblozinský and Ribanski [Obl1978] were used. It is beyond the scope of this thesis to present the details.

The multiple pre-equilibrium nucleon emission of previous versions of the ALICE code has been retained. Let P_n and P_p denote the emission probabilities for neutrons and protons, respectively, from a particular n-exciton configuration. The probability for emission of both a neutron and a proton from the same exciton state is then given by $P_{np} = P_n P_p$. The emission of two neutrons is given by $P_{nn} = P_n P_n/2$.

In previous versions of the ALICE code, single particle level densities were calculated using a Fermi gas model. Starting with ALICE-IPPE and also in ALICE/ASH, the option has been included to calculate the level densities according to the Generalized Superfluid model (GSM) [Ign1993, Blo1985].

D.5 Calculations

The ALICE/ASH calculations presented in this work were performed using the recommended values of the input parameters according to the comments in the preamble to the code. No attempt was made to fine-tune the calculations in order to obtain better agreement for individual residual nuclides. Level densities were calculated according to the Generalized Superfluid model. The normal pairing shift was selected. Experimental nuclidic masses were used where available, else calculated using the built-in Myers and Swiatecki mass formula of the code. The energy bin size was normally taken as 0.5 MeV but sometimes varied between 0.4 and 0.6 MeV. The evaporated particles included protons, neutrons, deuterons and α-particles.

D.6 Input parameters used in calculations

Some parameter values are not listed, e.g. those specifying target nuclei and projectiles, parameters relevant to fission (which was not required in this work) and parameters that specify the output format. The table below contains the subset of parameters that was used throughout.

D.7 Comments in conclusion

The GDH model is quite successful in reproducing the angle-integrated emission spectra of nucleons emitted into the continuum. A shortcoming of the code is that the Hauser-Feshbach theory used to describe the evaporation does not explicitly take the conservation of angular momentum into account, thus it does not accurately predict angular distributions, nor does it predict the excitation functions of residues formed in long-lived isomeric states. In this work, such cases were either scaled or added incoherently with the ground state, for purposes of comparison with the ALICE/ASH predictions.

Table D.1: Values of important parameters specified in the input to the ALICE/ASH code.

Parameter	Value	Description
MC	10	The mass option. Myers and Swiatecki (MSL) semi-empirical mass formula including shell corrections selected. Tabled experimental masses are substituted where available.
MP	3	The pairing option. Normal pairing shift selected; zero for odd-even nuclei, delta added for odd-odd nuclei.
LDOPT	2	Level density option. Level densities are calculated according to the Generalized Superfluid nuclear model (GSM).
INVER	0	Method of inverse cross section calculation. The optical model is selected.
ED	0.4 – 0.6	Energy bin mesh size. If sensitivity to the choice of bin size was not problematic, a value of ED = 0.5 MeV was used.
PLD	9	Level density parameter. This is the default value recommended in the preamble to the code.
M3	4	Emitted particles include protons, neutrons, α-particles and deuterons.
RCSS	0	Reaction cross sections to be internally generated by the optical model subroutine for incident protons.
JCAL	1	Weisskopf-Ewing evaporation calculation selected.
TD	1	Initial exciton number.
TMX	1	The Geometry Dependent Hybrid (GDH) model is selected for calculations of pre-equilibrium emission.
AV	0	Together with choice TD = 1, nucleon-nucleon mean free paths are used in GDH calculations.
Other	blank	Other Card 4 parameters assume the default values when left blank. This is in accordance with the recommendations in the preamble to the code.

Appendix E

Integral Yields

E.1 The physical yield

Let $\sigma(E)$ be a known excitation function with units in mb. Let $S(E)$ be the stopping power function of a target material in units of MeV·(g/cm^2)$^{-1}$. The more general case of the target material being a compound is considered. The integral physical yield in units of Bq/μAh is given by

$$Y_P(E') = K \int_{E_{threshold}}^{E'} \frac{\sigma(E)}{S(E)} dE. \tag{E.1}$$

The factor K is given by

$$K = \lambda \left(\frac{N_A \eta}{A}\right) \left(\frac{3.6 \times 10^{-3}}{e}\right) \left(1 \times 10^{-27}\right), \tag{E.2}$$

where N_A is Avogadro's number, A is the molar mass of the target material in atomic mass units (amu), η is the number of target atoms of the desired species per molecule of the target material, and e is the charge of the projectile (1.602×10^{-19} C for protons). Note that the number of protons corresponding to 1 μAh of accumulated charge is ($3.6 \times 10^{-3}/e$) and (1×10^{-27}) is the conversion factor for mb to cm^2.

In the case of an elemental target material, A in Eq. (E.2) becomes the atomic mass (in amu) and $\eta = 1$. The integral physical yield represents an upper limit as it neglects all losses, such as decay losses and beam attenuation losses.

E.2 The production yield at EOB

The relationship between the production yield at the end of bombardment (EOB) and the physical yield can be derived by first subdividing the bombardment period, T, into a large number, n, of infinitesimal time intervals of duration Δt:

$$T = n\Delta t. \tag{E.3}$$

Assume that R radioactive nuclei of the type described by the excitation function are formed per second in the target during bombardment with a beam of energy E'. The total number of radioactive nuclei formed during the bombardment is then

$$N_{total} = RT = Rn\Delta t. \tag{E.4}$$

This is, however, not the number at EOB as some would have decayed before the bombardment ended. Thus, we know that N_{EOB} must be smaller than N_{total}. The relationship between N_{EOB} and N_{total} is found by summing over all time intervals and including decay:

$$\begin{aligned} N_{EOB} &= \sum_{i=1}^{n} R\Delta t \, \exp[-\lambda(T - i\Delta t)], \\ &= R\sum_{i=1}^{n} \exp[-\lambda(T - i\Delta t)]\Delta t, \\ &= R\int_{0}^{T} \exp[-\lambda(T - i\Delta t)]dt, \quad \text{in the limit where } \Delta t \to 0 \\ &= R\left[\frac{\exp(-\lambda T)}{\lambda}[\exp(\lambda T) - 1]\right], \\ &= R\left[\frac{1 - \exp(-\lambda T)}{\lambda}\right]. \end{aligned} \tag{E.5}$$

It is convenient to multiply both the numerator and denominator in Eq. (E.5) with T:

$$\begin{aligned} N_{EOB} &= RT\left[\frac{1 - \exp(-\lambda T)}{\lambda T}\right], \\ &= N_{total}\left[\frac{1 - \exp(-\lambda T)}{\lambda T}\right]. \end{aligned} \tag{E.6}$$

The factor in square brackets of Eq. (E.6) relates the total number of nuclei formed during the bombardment to the number that is left at EOB. The relevant activities are found by multiplying both sides of the equal sign with λ, while the yields can be obtained by dividing both sides of the equal sign by the accumulated charge, Q:

$$\begin{aligned} \left(\frac{\lambda}{Q}\right) N_{EOB} &= \left(\frac{\lambda}{Q}\right) N_{total}\left[\frac{1 - \exp(-\lambda T)}{\lambda T}\right], \\ \therefore Y_{EOB}(E') &= Y_P(E')\left[\frac{1 - \exp(-\lambda T)}{\lambda T}\right]. \end{aligned} \tag{E.7}$$

In this work, values of $Y_P(E)$ and $Y_{EOB}(E)$ for $E_{threshold} \leq E \leq E'$ were performed using a small FORTRAN code. This code uses Simpson's rule to perform the integration in Eq. (E.1). A spline fit through a set of discrete cross-section values is used to interpolate for off-grid $\sigma(E)$ values and a polynomial fit is used to represent $S(E)$ in the code. Equation (E.7) does not yet correct for beam attenuation losses. Normally, it is sufficient to make an estimate as follows:

$$Y_{EOB}(E') = Y_P(E')\left[\frac{1 - \exp(-\lambda T)}{\lambda T}\right]\left[1 - \bar{P}\right], \tag{E.8}$$

where $\bar{P}$ is a mean nonelastic nuclear interaction probability for the energy window of the target. Thus, $[1 - \bar{P}]$ can be seen as an effective beam attenuation factor. For an energy window (E_{in}, E_{out}) where both E_{in} and E_{out} are larger than $E_{threshold}$, the following rule applies:

$$Y_P(E_{in}, E_{out}) = Y_P(E_{in}) - Y_P(E_{out}). \tag{E.9}$$

Appendix F

Problems in Calculations for (p,n) Reactions

Unexpectedly large scatter was found for ALICE/ASH calculations [Bro2006] in the case of ^{192}Os + p. This was most notable for the ^{192}Os(p,n)^{192}Ir reaction, especially in the high-energy "tail" region of the excitation function. It has been known for many years that some scatter is occasionally evident in the calculated results from successive versions of the ALICE code. In this particular case the level of scatter of about 30% is considered to be unusually large. The scatter was much smaller for the predictions of the other (p,xn) reactions on ^{192}Os.

In order to study this phenomenon further, the sensitivity of the output to small adjustments of the input parameters was systematically investigated. A large effect was traced to only one parameter, namely *ED*, which is the energy bin mesh size for numerical integration of the emitted particle spectra. It was found that small adjustments to the value of *ED*, even on the level of a few 10s of keV, can cause large changes in the excitation function for the (p,n) reaction, while the other (p,xn) reactions remain almost unaffected. Stable behaviour for the (p,n) reaction was eventually obtained by performing sets of calculations, varying the energy bin size, followed by taking the arithmetic average over all sets. The following scheme was adopted: A first calculation was done with $ED = 0.5$ MeV. If scattering seemed to be a problem, a set of calculations were performed where *ED* was adjusted from 0.4 to 0.6 MeV in steps of 0.01 MeV, followed by taking the arithmetic average. A selection of such results are shown in Fig. F.1 for the ^{192}Os(p,n)^{192}Ir reaction.

The maximum number of energy bins allowed by the ALICE/ASH code is 300. In order to comply with this limit, the following rule is applied:

$$\frac{EP + QVAL}{ED} < 300, \tag{F.1}$$

where *EP* is the projectile energy in MeV and *QVAL* is the separation energy of the projectile from the compound nucleus, i.e.

$$QVAL = AP + AT - A_{compound}, \tag{F.2}$$

where *AP* is the mass of the projectile, *AT* is the mass of the target nucleus and $A_{compound}$ is the mass of the compound nucleus. Here we used the nomenclature according to the preamble to the code. Note that in older versions of the code, the energy bin size was fixed at a value of 1 MeV. It is variable only in fairly recent versions of the code.

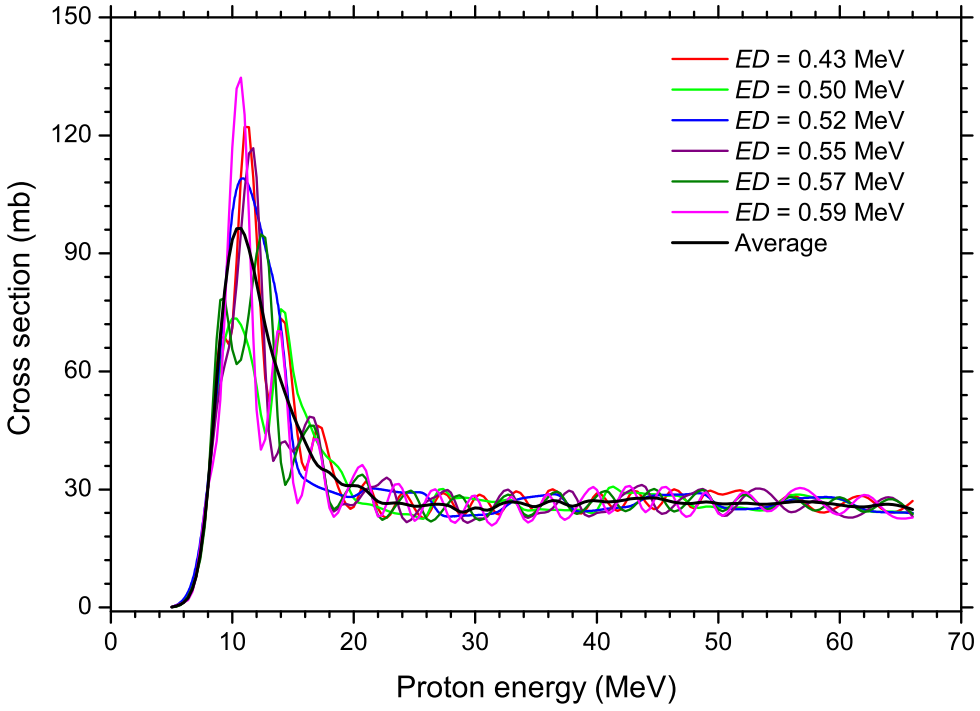

Figure F.1: Excitation function calculated with the ALICE/ASH code for the ^{192}Os(p,n)^{192}Ir reaction with a selection of values for the parameter *ED*, as indicated. The curve labelled "Average" has been obtained by taking the arithmetic mean of the twenty-one results with *ED* values ranging from 0.4 to 0.6 MeV in steps of 0.01 MeV (see text).

We do not know the reason for this behaviour but we have reported it. The procedure outlined above yielded essentially the same results for the other (p,xn) reactions obtained using a fixed value of $ED = 0.5$ MeV but reduced the fluctuations in the case of the (p,n) reaction. Admittedly, this is not seen as a way to solve the problem, rather, the point of the exercise is to illustrate the sensitivity to the choice of the energy bin size and to show that the average over a region of energy reduces the scatter, which we reported in [Sze2010].

In the case of TENDL-2012, a different problem seems to manifest, namely a spurious second maximum. This is illustrated in Fig. F.2 for a selection of (p,n) reactions in the mass region $141 \leq A \leq 181$. This effect is particularly large for the ^{160}Gd(p,n)^{160}Tb reaction, shown in Fig. F.2 (c). Note that the data in TENDL-2012 are based on theoretical calculations, produced using the TALYS code [Kon2012, Kon2013]. Thus, something strange seems to have happened in those calculations. Note that the (p,n) reaction on all nuclei, except the very lightest ones, show a single peak and a featureless tail towards higher energies, such as for the ^{141}Pr(p,n)^{141}Nd reaction shown in Fig. F.2 (a). This is the only excitation function of the six presented in the figure that shows normal behaviour. Second maxima are not observed experimentally. At all masses below $A = 144$, the TENDL-2012 excitation functions for the (p,n) reaction seem to have the expected shape. The spurious second maxima seem to be a universal feature at masses above this value, up to the spontaneous fission region.

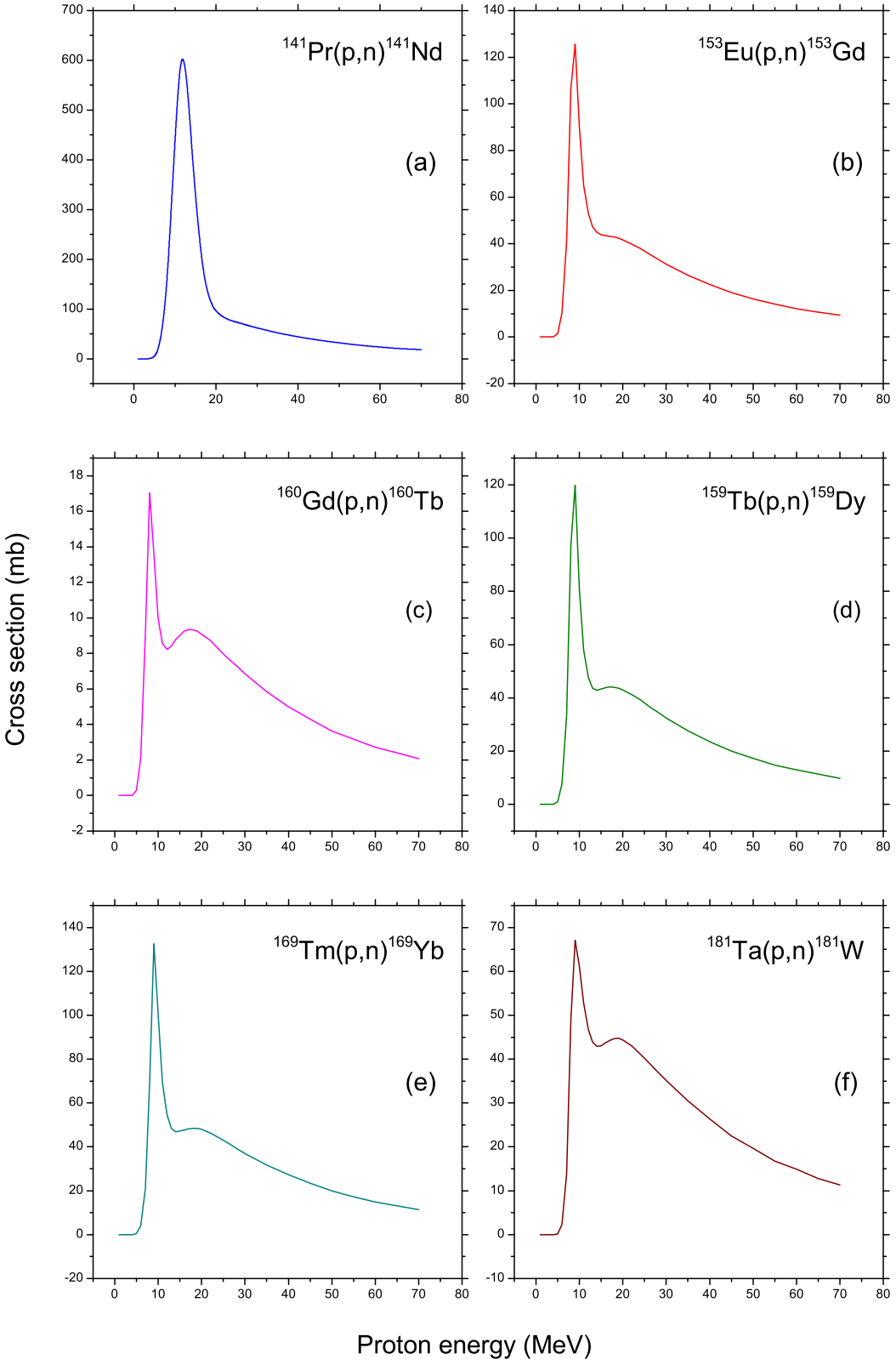

Figure F.2: Excitation functions of selected (p,n) reactions from the TENDL-2012 library.

Appendix G

Growth and Decay Curves

Let $A_m(t)$ and $A_d(t)$ denote the mother and daughter activities, respectively, of a pair of appropriate radionuclides, such as ^{155}Dy and ^{155}Tb. Let $t = 0$ be chosen such that $A_m(0) > 0$ and $A_d(0) = 0$, i.e. a time where a certain quantity of the precursor has been isolated but no significant feeding to the daughter radionuclide has yet happened. The growth and decay curve is defined as

$$H(t) = \frac{A_d(t)}{A_m(0)}. \tag{G.1}$$

The time $t = 0$ may, for example, denote the time of the end of a chemical separation of the mother radionuclide from an irradiated target, or at least a fraction thereof, depending on the relative half-lives of the mother and daughter radionuclides. If a two-stage chemical separation procedure is to be followed in order to recover the daughter radionuclide, the second separation would typically be performed at or near the time where $H(t)$ reaches a maximum.

Let $t = T_{end}$ denote a conveniently chosen "end time" for following the growth and decay of the daughter activity. Let N_{inc} be the number of small time increments of duration Δt such that

$$\Delta t = \frac{T_{end}}{N_{inc}}. \tag{G.2}$$

Let i be an index such that $1 \leq i \leq N_{inc} + 1$ maps the time interval $0 \leq t \leq T_{end}$ as follows:

$$t_i = (i-1)\Delta t \quad \text{for all} \quad 1 \leq i \leq N_{inc} + 1. \tag{G.3}$$

Let $N_m(t)$ and $N_d(t)$ denote the number of mother and daughter nuclei present at time t, and let $\Delta N_d(i\Delta t)$ be the number of daughter nuclei formed in the time increment Δt ending at $t = t_{i+1}$, for all $1 \leq i \leq N_{inc}$. Then

$$\begin{aligned} \Delta N_d(i\Delta t) &= \epsilon_b[N_m(i\Delta t) - N_m([i+1]\Delta t)] \quad \text{for all} \quad 1 \leq i \leq N_{inc}, \\ &= \epsilon_b[N_m(0)\exp(-\lambda_m i\Delta t) - N_m(0)\exp(-\lambda_m(i+1)\Delta t)], \\ &= \epsilon_b N_m(0)\exp(-\lambda_m i\Delta t)[1 - \exp(-\lambda_m \Delta t)], \end{aligned} \tag{G.4}$$

where λ_m is the decay constant of the mother radionuclide and ϵ_b is the branching ratio applicable to the formation of the daughter radionuclide. Note that Δt should be sufficiently small for decay of the daughter radionuclide during this interval to be negligible. Thus, by summing

over all preceding intervals and incorporating daughter decay from all these intervals, one gets

$$\begin{aligned} N_d(i\Delta t) &= \sum_{j=1}^{i} \Delta N_d(j\Delta t)\exp[-\lambda_d(i-j)\Delta t], \\ &= \epsilon_b N_m(0)[1-\exp(-\lambda_m\Delta t)]\sum_{j=1}^{i}\exp(-\lambda_m j\Delta t)\exp[-\lambda_d(i-j)\Delta t], \\ &= \epsilon_b N_m(0)[1-\exp(-\lambda_m\Delta t)]\sum_{j=1}^{i}\exp[-\lambda_m j\Delta t-\lambda_d(i-j)\Delta t]. \end{aligned} \tag{G.5}$$

By multiplying both sides of the equal sign with $\lambda_m\lambda_d$ and rearranging variables, one can write

$$\lambda_m[\lambda_d N_d(i\Delta t)] = \lambda_d[\lambda_m N_m(0)]\epsilon_b[1-\exp(-\lambda_m\Delta t]\sum_{j=1}^{i}\exp[-\lambda_m j\Delta t-\lambda_d(i-j)\Delta t], \tag{G.6}$$

from which follows that

$$\frac{A_d(i\Delta t)}{A_m(0)} = \frac{\lambda_d}{\lambda_m}\epsilon_b[1-\exp(-\lambda_m\Delta t)]\sum_{j=1}^{i}\exp[-\lambda_m j\Delta t-\lambda_d(i-j)\Delta t]. \tag{G.7}$$

Equation (G.7) can easily be computed numerically. One must ensure that the time interval Δt is small enough for daughter decay of new growth during this interval to be insignificant. One can improve this approximation by allowing the new growth to decay from the centre of each time interval instead of from its end. This leads to

$$H(i\Delta t) = \frac{A_d(i\Delta t)}{A_m(0)} = \frac{\lambda_d}{\lambda_m}\epsilon_b[1-\exp(-\lambda_m\Delta t)]\sum_{j=1}^{i}\exp[-\lambda_m j\Delta t-\lambda_d(i-j+1/2)\Delta t]. \tag{G.8}$$

In practice, it is unimportant whether Eq. (G.7) or Eq. (G.8) is employed. With a value of $\Delta t = 1$ s, for example, both equations give the same results, for all practical purposes, for all the radionuclides relevant to the present study. Several relevant cases of Tb radionuclides formed via the decay of their Dy precursors are shown in Fig. G.1.

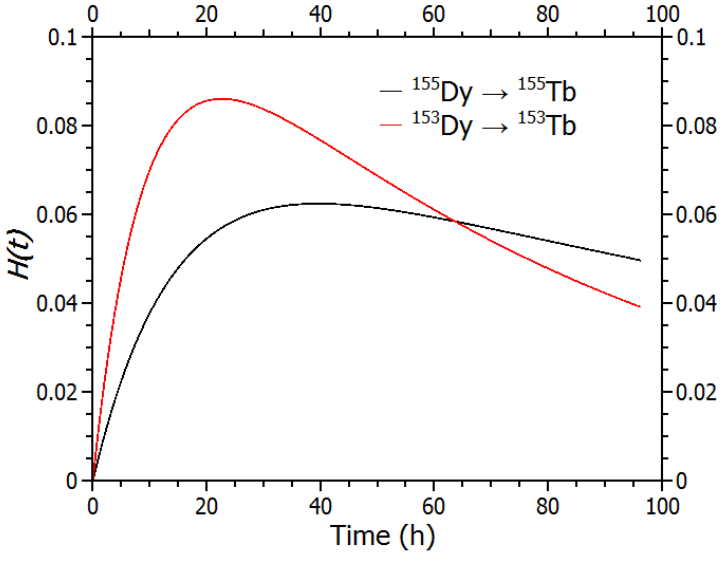

Figure G.1: Growth and decay curves for selected Tb radionuclides formed in precursor decay.

Appendix H

Final Activities of Tb Radionuclides Formed Via Dy Precursor Decay

The necessary equations to calculate the activity that will be obtained at a reference time after completion of the two-stage chemical separation procedure for ^{155}Tb produced from a ^{159}Tb target are derived. It can also be applied to all the other Tb radionuclides produced via Dy precursor decay in order to calculate the radionuclidic purity of the final product. Radiochemical losses are assumed to be negligible but can easily be introduced at the end – this will be discussed later.

Let R be the integral physical yield (production rate) of a mother Dy radionuclide in a target with an energy window $E_{in} \rightarrow E_{out}$. In general, $R = R(E_{in}, E_{out}) = R(E_{in}) - R(E_{out})$. In the following paragraphs, units of MBq/μAh are assumed for the integral yield.

Let H be the fraction of $m \rightarrow d$ decay, as given by the growth and decay curve (see Appendix G). In general, $H = H(t)$.

Let I_0 be the beam current in units of μA.

Various times are defined as follows:

1. $t = 0$: Beginning of bombardment (BOB),
2. $t = T$: End of bombardment (EOB),
3. $t = t_1^{beg}$: Effective start of the first chemical separation,
4. $t = t_1^{end}$: Effective end of the first chemical separation,
5. $t = t_2^{beg}$: Effective start of the second chemical separation,
6. $t = t_2^{end}$: Effective end of the second chemical separation,
7. $t = t_{ref}$: Reference time,

where $0 < T < t_1^{beg} < t_1^{end} < t_2^{beg} < t_2^{end} < t_{ref}$.

Thus, there are several important time periods:

1. T : Bombardment time,
2. $t_1^w = t_1^{beg} - T$: Waiting time 1,
3. $t_1^{chem} = t_1^{end} - t_1^{beg}$: Chemical separation 1,
4. $t_2^w = t_2^{beg} - t_1^{end}$: Waiting time 2,
5. $t_2^{chem} = t_2^{end} - t_2^{beg}$: Chemical separation 2,
6. $t_3^w = t_{ref} - t_2^{end}$: Waiting time 3.

Two more times are required:

1. $t = t_1^{(j)}$: Effective end of the first chemical separation of a fraction (j) of the mother solution, where j is an index, $1 \leq j \leq J$ and $t_1^{beg} \leq t_1^{(j)} \leq t_1^{end}$;
2. $t = t_2^{(k)}$: Effective end of the second chemical separation of a fraction (k) of the relevant second solution, where k is an index, $1 \leq k \leq K$ and $t_2^{beg} \leq t_2^{(k)} \leq t_2^{end}$.

J and K are integer numbers which should be sufficiently large. They represent the number of discrete fractions into which the relevant solutions are divided for purposes of the calculation. This aspect needs some careful explanation: First, the mother solution contains the entire target (now dissolved) as well as all the various radionuclides produced. Separating the Dy out from the mother solution does not happen instantaneously but takes place over a period of time. Here we model this separation by assuming that all the Dy from an incremental volume of the mother solution is effectively separated out at a specific time within this period of separation and that the entire process proceeds linearly. Thus, different completion times are associated with different fractions of the mother solution (moving, for example, through an ion-exchange column at a constant flow speed). Also, note that the “effective separation time" may be quite different from the total time of the chemical separation procedure. The first step in the chemistry may, for example, be the dissolution of the target. No separation takes place during this step, thus it falls outside the time interval t_1^{chem} above. Similar arguments apply to the second chemical separation.

In the following paragraphs, the relevant equations pertaining to each of the essential time periods are derived:

1. The bombardment period

Divide the bombardment period into N small time increments of length Δt. Let i be an index such that $0 \leq i\Delta t \leq T$ is mapped by $0 \leq i \leq N$. The mother (m) activity at the end of bombardment is given by the sum of the individual contributions during each time increment:

$$A_m(T) = \sum_{i=1}^{N} \Delta A_m \exp[-\lambda_m(T - i\Delta t)], \tag{H.1}$$

where

$$\Delta A_m = RI_0 \Delta t. \tag{H.2}$$

I_0 is the beam current, which is taken to be a constant to simplify the expressions.

$$\therefore A_m(T) = RI_0 \sum_{j=1}^{N} \exp[-\lambda_m(T - j\Delta t)]\Delta t. \tag{H.3}$$

In the limit where $\Delta \to 0$, the summation can be replaced by an integration:

$$\begin{aligned}
\therefore A_m(T) &= RI_0 \int_0^T \exp[-\lambda_m(T-t)]dt \\
&= RI_0 \exp(-\lambda_m T) \int_0^T \exp(-\lambda_m t)dt \\
&= \frac{RI_0 \exp(-\lambda_m T)}{\lambda_m} \exp(-\lambda_m t)\Big|_0^T \\
&= \frac{RI_0 \exp(-\lambda_m T)}{\lambda_m} \left[\exp(\lambda_m T) - 1\right] \\
&= \frac{RI_0}{\lambda_m} \left[1 - \exp(-\lambda_m T)\right].
\end{aligned} \tag{H.4}$$

2. Waiting time 1

The m activity after EOB is given by

$$A_m(t) = \frac{RI_0}{\lambda_m} \left[1 - \exp(-\lambda_m T)\right] \exp[-\lambda_m(t - T)], \tag{H.5}$$

where $t \geq T$.

3. Chemical separation 1

At the beginning of chemical separation 1, the activity of the mother radionuclide fractions is given by [using Eq. (H.5)]

$$\Delta A_m(t_1^{beg}) = \frac{A_m(t_1^{beg})}{J} = \frac{RI_0}{\lambda_m J} \left[1 - \exp(-\lambda_m T)\right] \exp[-\lambda_m(t_1^{beg} - T)]. \tag{H.6}$$

At this stage, all fractions have the same activity. At the effective end of the first chemical separation of fraction (j), its m activity is given by

$$\Delta A_m^{(j)} = \frac{RI_0}{\lambda_m J} \left[1 - \exp(-\lambda_m T)\right] \exp[-\lambda_m(t_1^{(j)} - T)]. \tag{H.7}$$

The associated daughter (d) activity of fraction (j) at the end of chemical separation 1 is given by

$$\Delta A_{1d}^{(j)} = \Delta A_m^{(j)} H(t_1^{end} - t_1^{(j)}). \tag{H.8}$$

The total d activity at the end of chemical separation 1 is obtained by summing:

$$\begin{aligned} A_{1d}(t_1^{end}) &= \sum_{j=1}^{J} \Delta A_{1d}^{(j)} \\ &= \frac{RI_0}{\lambda_m J}\Big[1-\exp(-\lambda_m T)\Big] \sum_{j=1}^{J} H(t_1^{end}-t_1^{(j)})\,\exp[-\lambda_m(t_1^{(j)}-T)]. \end{aligned} \tag{H.9}$$

Note that for ^{155}Dy$\rightarrow^{155}$Tb, the daughter activity given by Eq. (H.9) only constitutes a very small fraction of the final daughter activity. The bulk of the final daughter activity comes from decay of the mother activity during waiting period 2.

4. Waiting time 2 and Chemical separation 2

It is possible to relate the daughter Tb activities, formed during waiting time 2 and up to the end of the second chemical separation, to the mother Dy activities in the final solution obtained at the end of the first chemical separation. Similar to the first chemical separation, one can divide the solution into K fractions of equal size:

$$\Delta A_m(t_1^{end}) = \frac{A_m(t_1^{end})}{K} = \frac{RI_0}{\lambda_m K}\Big[1-\exp(-\lambda_m T)\Big]\,\exp[-\lambda_m(t_1^{end}-T)]. \tag{H.10}$$

The daughter (d) activity of fraction (k) at the effective end of chemical separation 2 is given by

$$\Delta A_{2d}^{(k)} = \Delta A_m(t_1^{end}) H(t_2^{(k)}-t_1^{end}). \tag{H.11}$$

The total d activity at the end of chemical separation 2 is obtained by summing:

$$\begin{aligned} A_{2d}(t_2^{end}) &= \sum_{k=1}^{K} \Delta A_{2d}^{(k)} \\ &= \frac{RI_0}{\lambda_m K}\Big[1-\exp(-\lambda_m T)\Big]\exp[-\lambda_m(t_1^{end}-T)] \sum_{k=1}^{K} H(t_2^{(k)}-t_1^{end})\,\exp[-\lambda_d(t_2^{end}-t_2^{(k)})]. \end{aligned} \tag{H.12}$$

5. Waiting time 3

The total daughter activity at the end of waiting time 3 is given by Eqs. (H.9) and (H.12), with inclusion of the decay up to $t = t_{ref}$:

$$A_d = \Big[A_{1d}(t_1^{end})\exp[-\lambda_d(t_{ref}-t_1^{end})] + A_{2d}(t_2^{end})\exp[-\lambda_d(t_{ref}-t_2^{end})]\Big] \tag{H.13}$$

In order to take radiochemical losses into account, Eq. (H.13) can be written as follows:

$$A_d = \Big[F_1 A_{1d}(t_1^{end})\exp[-\lambda_d(t_{ref}-t_1^{end})] + F_1 F_2 A_{2d}(t_2^{end})\exp[-\lambda_d(t_{ref}-t_2^{end})]\Big], \tag{H.14}$$

where

$$F_1 = \left[1-\frac{P_1^{loss}}{100}\right], \tag{H.15}$$

and

$$F_2 = \left[1-\frac{P_2^{loss}}{100}\right], \tag{H.16}$$

with P_1^{loss} and P_2^{loss} the percentage radiochemical losses of chemical separations 1 and 2, respectively.

Appendix I

Dimensionless Groups in Forced Convection Heat Transfer

I.1 Dimensional analysis and Bridgman's principle

The objective of this appendix is to introduce a number of useful expressions which describe forced convection heat transfer for the case of turbulent flow of a coolant in a tube or pipe. This sheds light on a number of principles which are also relevant to other flow geometries, e.g. target holders and beam window assemblies. Some aspects of dimensional analysis are important here, including Bridgman's principle. Formally, it is called *Bridgman's principle of absolute significance of relative magnitude* [Son2001], which will be described shortly. From a personal experience, a measure of discomfort was felt for a long time when using semi-empirical heat transfer equations as they do not seem to be derived in a logical way from first principles. This changed after becoming aware of Bridgman's fascinating principle. Dimensional analysis, as a mathematical subject, can be introduced very formally. Here we would like to avoid that and rather introduce the relevant aspects by way of examples of simple physical systems.

So-called *dimensionless groups* often arise quite naturally in the development of a theory for a physical system. Radioactive decay, for example, obeys an exponential law:

$$N(t) = N(0)\exp(-\lambda t), \tag{I.1}$$

where $N(0)$ is the number of radioactive nuclei of the same species at an arbitrary time $t = 0$, $N(t)$ is the remaining number at any other time $t > 0$ and $\lambda = \ln(2)/T_{1/2}$ is the decay constant. Here λt is a dimensionless group. It is essential that λt should be dimensionless. A requirement of any equation in physics, without exception, is that it should be *dimensionally homogeneous*, i.e. both sides of the equation must have the same dimension. This also implies that wherever a sum of quantities appears, all the terms must have the same dimension. In Eq. (I.1) both $N(t)$ and $N(0)$ are just dimensionless numbers, thus, the exponential function must be dimensionless too in order to preserve dimensional homogeneity. Generally, all arguments of exponentials, logarithmic functions, trigonometric functions, power laws, etc., must be dimensionless in order for a theorem to be physically meaningful. Note that dimensionless quantities are also sometimes referred to as *quantities of dimension one*.

Very often, even in quite complex problems, the number of quantities with different dimensions are rather few. The subsets amongst them that can combine to form dimensionless groups are even fewer. If this would not have been the case, dimensional analysis as a tool would probably not have been very useful. Dimensionless groups can often be found by inspection. If, for example, a researcher determines that the quantities relevant in a particular experiment happen to be displacement (x), speed (v) and time (t), it does not take much mental effort to conclude that vt/x is a dimensionless group and that no other combinations exist except its inverse.

An important theorem in dimensional analysis is Buckingham's π theorem [Son2001]. The basis for this theorem, which will be described shortly, is that the laws of physics are not contingent upon any specific system of units. Physical laws should remain valid, regardless of the choice of units. A consequence of this is that any physical law can be expressed as an identity that involves only dimensionless combinations (ratios or products) of the variables linked by the law. These dimensionless combinations remain dimensionless when the system of units is changed. If this would not have been the case, the equation expressing the law would not be an identity and the physical law would fall apart.

Buckingham's π theorem of dimensional analysis states that when a complete relationship exists between n variables, of which a subset of k variables has independent dimensions, the functional form can be reduced and expressed as an identity consisting of $n - k$ dimensionless quantities. Different systems which share the same description in terms of dimensionless quantities are said to be *equivalent*. In practice, the application of Buckingham's theorem lends itself to the introduction of conditions and/or criteria, which can be very powerful in experimental situations. To illustrate this, a "thought" experiment that involves Newton's second law of motion will be described (which can actually be performed in real life). Newton's second law states that the acceleration of a body is directly proportional to, and in the same direction as, the net force acting on the body, and inversely proportional to its mass. For the sake of simplicity, linear motion is selected to simplify the vector equation to a scalar equation:

$$F = ma, \tag{I.2}$$

where, F is the force, m is the mass and a is the acceleration. In terms of dimensionless quantities, Eq. (I.2) can be written as follows:

$$\frac{F}{ma} = 1. \tag{I.3}$$

Nobody prevents us from giving the dimensionless group in Eq. (I.3) a name. Let it be called "Newton's number" and denoted by R_N. Newton's second law can then be written as

$$R_N = 1, \tag{I.4}$$

where R_N is defined by

$$R_N = \frac{F}{ma}. \tag{I.5}$$

So far, the exercise may seem trivial but note that Eq. (I.4) is an identity, which may or may not turn out to be true for a given situation, while Eq. (I.5) is a general equation, which does

not place any restriction on what value the dependent variable R_N may assume. Equation (I.4) is still Newton's law but Eq. (I.5) is something else (a definition, which by its nature always remains true). Next, let's refine the definition of R_N by insisting that the mass in the equation is the rest mass of the body. An experiment is now conceived which can be performed on a section of a linac. Consider a section of a linac that consists of a passive drift tube, followed by a single accelerating gap, followed by another passive drift tube. Time-of-flight capability is provided on each drift tube by means of two capacitive probes, spaced a sufficient distance from each other so that the velocity of a passing ion can be accurately determined experimentally. Thus, provision is made to measure the velocity of a passing bunch of ions both before and after the accelerating gap. In practice, this can be achieved by measuring the time difference between successive signals from the capacitive probes on an oscilloscope and since the distances between the probes are known, the velocity can be calculated. If both the velocity before and after the accelerating gap is known, the acceleration can be calculated. Since the charge state of the ions as well as the electric field across the gap is accurately known during the time that the bunch passes through, the force on an ion is also known accurately. (It is just the Lorenz force.) The rest mass of the ion is also known accurately and can be found from standard data tables. Independently, therefore, values for F, a and m_0 can be found and R_N can be calculated from Eq. (I.5). If Newton's law holds, a value of one (1) should be found within the experimental uncertainties. Values significantly larger than 1 would indicate that Newton's law no longer holds, in all probability an indication that relativistic effects are becoming important. This is because an ion with a relativistically increased mass will be more difficult to accelerate, leading to smaller values of a in Eq. (I.5).

Certain criteria can now be imposed on the interpretation of the results from the experiment, depending on the experimental uncertainties. This may be something like the following:

- $0.98 \leq R_N \leq 1.02$: Newton's law holds. Classical mechanics will be appropriate.
- $1.02 \leq R_N \leq 1.08$: Classical mechanics is likely to be a good approximation.
- $1.08 \leq R_N < 1.2$: Take care. Classical mechanics may be inappropriate.
- $R_N > 1.2$: Relativistic kinematics are required.
- $R_N < 0.9$: The experiment probably failed. Please repeat the measurement.

In this rather trivial example, there are $n = 3$ variables of which $k = 2$ have independent dimensions and we found $n-k = 1$ independent dimensionless group. Buckingham's π theorem holds. Newton's law was used here just for the sake of illustration and, in practice, there may be no compelling reason to deal with it in such a manner. In more complex problems that contain many more variables, but which are nevertheless well understood in terms of an exact formalism with solvable equations and boundary conditions, Buckingham's π theorem may be useful to reduce the number of independent variables, simplify the formalism and to reveal similarity with different physical systems.

The full power of dimensional analysis, however, comes into its own in complex problems where an exact and solvable mathematical formalism remains elusive. This may be because

of boundary conditions that are not completely articulated and/or the sheer difficulty of dealing with complex dynamics in an exact manner. In such cases, where the equations and/or boundary conditions are not well known, Bridgman's principle may be useful.

Bridgman's principle of absolute significance of relative magnitude states the following: A number obtained from a quantity Q by inserting the numerical values of base quantities into a formula shows it to be a physical quantity only if the ratio of two samples of it remains constant when base unit sizes are changed. A monomial formula satisfies the principle of absolute significance of relative magnitude if and only if it has the power-law form:

$$Q = \alpha A^a B^b C^c \cdots \tag{I.6}$$

where Q is a derived quantity, A, B, C, etc., are base quantities (i.e. their dimensions are base units) and the coefficient α as well as the exponents a, b, c, etc., are real numbers. Derived quantities are physical quantities if and only if they have this power-law form; no other form represents a physical quantity. The consequence of this is that in any physical theorem, variables that represent quantities with dimension other than one can only appear on their own as a base in a power-law function. In any other situation, they can appear only in combination with other variables which combine to form dimensionless groups, e.g. in arguments of trigonometric functions, exponential functions, etc. (i.e. reduction to pure numbers). In any physical description, whether theoretical or empirical, once calculations are being performed by inserting numerical values into the variables, the description will eventually reduce into a power law regardless of how complex the original description was.

It is hard to overemphasize the importance of Bridgman's principle. Dimensionless groups always constitute derived quantities as no base quantity can be dimensionless. A dimensionless group can be constructed by the multiplication and/or ratio of base quantities as well as other derived quantities, however, multiplications and ratios of power-law functions again yield a power-law function.

According to Sonin [Son2001], a debate raged for years over the theoretical-philosophical underpinnings of dimensional analysis. While most applications of dimensional analysis were not in question, some mathematicians found the basic arguments to lack rigor. Note that Bridgman introduced the principle of absolute significance of relative magnitude in 1931 only as a postulate. It was rigorously proved mathematically only much later (by Grigory Isaakovich Barenblatt). This finally validated dimensional analysis as a *bona fide* branch of mathematics.

I.2 Forced convection in tubes and pipes

In the description of forced convection heat transfer, three particular dimensionless groups are very often involved. They are the Nusselt number (Nu), Reynolds number (Re) and Prandtl number (Pr). The simplest kind of empirical relation to describe the heat transfer between a fluid flowing in a pipe and the wall of the pipe is the following [Hol2013]:

$$\mathrm{Nu} = C\mathrm{Re}^m\mathrm{Pr}^n, \tag{I.7}$$

where C, m and n are constants (real numbers) to be determined experimentally. The form of Eq. (I.7) clearly satisfies Bridgman's principle. Various different relationships based on Eq. (I.7) have been developed and are widely used. Three of them will be introduced here, after discussing the underlying dimensionless groups individually.

I.2.1 The Nusselt number

The Nusselt number [Hol2013] is a dimensionless group given by

$$\mathrm{Nu} = \frac{hx}{k}, \tag{I.8}$$

where h is the convective heat-transfer coefficient, k is the thermal conductivity of the coolant medium and x is a characteristic length, depending on the geometry of the flow system for its definition. By convention, x is taken as the inner diameter in the case of flow in round tubes and pipes. If the flow channel is not of circular cross section, x is taken as the so-called "hydraulic diameter", given by

$$x = D_H = \frac{4A}{P}, \tag{I.9}$$

where A is the cross-sectional area and P is the wetted perimeter of the flow passage. For circular tubes, the hydraulic diameter and inner diameter is the same. The dimension of h is typically [W cm^{-2} °C^{-1}], thus, for x it has to be [cm] and for k it has to be [W cm^{-1} °C^{-1}]. The Nusselt number is usually thought of as nothing more than a convenient dimensionless form of the heat-transfer coefficient. It is, however, proportional to the ratio of convective to conductive heat transfer across a boundary. As such, an increase in convective heat transfer relative to conductive heat transfer will lead to larger Nusselt numbers, and vice versa. It thus gives a measure of the relative importance of these two types of heat transfer for given flow conditions.

I.2.2 The Reynolds number

The Reynolds number [Hol2013] is a dimensionless group given by

$$\mathrm{Re} = \frac{\rho v x}{\mu}, \tag{I.10}$$

where ρ is the density (specific gravity) of the coolant, v is the bulk velocity of the coolant, μ is the dynamic viscosity of the coolant, and x is again a characteristic length, taken as the hydraulic diameter for tubes and pipes. The Reynolds number is a measure of the ratio of inertial forces to viscous forces for given flow conditions. This can easily be seen by multiplying both the numerator an denominator in Eq (I.10) by v (v/v = 1) and rearranging variables:

$$\mathrm{Re} = \frac{\rho v^2}{\mu v / x}. \tag{I.11}$$

The numerator in Eq. (I.11) is proportional to the inertial force of the flowing coolant while the denominator is proportional to the viscous shear stress in the fluid. As a result, the Reynolds number is a useful measure to characterize different flow regimes. Laminar (smooth) flow occurs at low Reynolds numbers, where the viscous forces are dominant. Laminar flow can be viewed as flow where individual molecules of the fluid travel in the direction of bulk flow in lamina with constant speed. Turbulent flow occurs at high Reynolds numbers, where the

inertial forces are dominant. Such flow is characterized by chaotic flow instabilities such as eddies, vortices and swirls. In this case, macroscopic "chunks" of fluid molecules can briefly have very different behaviour than the bulk behaviour of the fluid – such correlations develop and decay all the time.

The flow is usually laminar when the Reynolds number is below 2000. For values above 4000, the flow is usually turbulent. Somewhere in the region $2000 < \mathrm{Re} < 4000$ a transition between laminar flow and turbulent flow is likely. The transition point is influenced by factors such as the roughness of the tube walls, impurities in the fluid, etc.

I.2.3 The Prandtl number

The Prandtl number [Hol2013] is a dimensionless group given by

$$\mathrm{Pr} = \frac{\nu}{\alpha} = \frac{\text{viscous diffusion rate}}{\text{thermal diffusion rate}}, \tag{I.12}$$

where ν is the kinematic viscosity and α is the thermal diffusivity of the coolant medium. The kinematic viscosity is a measure of the rate at which momentum may diffuse through a fluid as a result of molecular motion and the thermal diffusivity is a measure of the rate at which thermal energy may diffuse through a fluid by the same molecular motion. Both the kinematic viscosity and thermal diffusivity can be explained qualitatively in terms of the concept of a *boundary layer*. For the sake of argument, consider a semi-infinite volume of fluid flowing in a certain direction. Somewhere in this system is a solid/fluid boundary but most of the fluid remains far away from this boundary. The solid also has a different temperature than the fluid. An observer inside the fluid approaches the boundary from a large distance away. At first, the observer is not aware of the existence of the boundary because of the sufficient distance away from the wall. However, as the distance to the wall gets smaller, at some point its presence will be felt. The observer will either detect a change in temperature or a change in momentum (velocity). Ultimately, as the distance to the wall gets progressively smaller, both effects will be felt. The larger the value of the kinematic viscosity, the further away from the solid/fluid boundary the effect of viscous forces on the wall is still felt. This is equivalent to saying that the larger the value of the kinematic viscosity, the thicker the hydrodynamic boundary layer becomes (i.e. the effective thickness of the layer of fluid affected by the presence of the wall). Similarly, the larger the value of the thermal diffusivity, the further away from the solid/fluid boundary the effect of the different surface temperature will be felt. This is equivalent to saying that the larger the value of the thermal diffusivity, the thicker the thermal boundary layer becomes. The Prandtl number can therefore also be defined as the ratio of the hydrodynamic boundary layer thickness and the thermal boundary layer thickness. Note that close to the wall, the flow always becomes laminar, even if the bulk flow is turbulent. This region of flow is often referred to as the laminar sublayer or viscous sublayer.

The above paragraph provides an appropriate basis for introducing the concept of "film". The film is the region near the solid/fluid boundary where the fluid properties differ appreciably from the bulk of the fluid. So-called "bulk properties" are distinguished from so-called "film properties", which will be discussed later. To conclude the discussion on the Prandtl number,

it is useful to compare a liquid like mercury to a liquid like water. Typical values at room temperature (20 °C) are Pr =0.015 for mercury and Pr =7 for water. For mercury, thermal conduction is much more effective as a means for transferring energy than convection. In the case of water, the opposite is true and convection is the dominant mechanism to transfer energy. When Pr $<<$ 1, thermal diffusivity dominates. When Pr $>>$ 1, momentum diffusivity (i.e. convection) dominates.

The Prandtl number is often written as follows:

$$\mathrm{Pr} = \frac{c_p \mu}{k}, \tag{I.13}$$

where c_p is the specific heat of the coolant, with k and μ the thermal conductivity and dynamic viscosity, respectively, as already introduced. The relationship between the kinematic viscosity and dynamic viscosity is given by

$$\nu = \frac{\mu}{\rho}. \tag{I.14}$$

The thermal diffusivity and thermal conductivity is related by

$$\alpha = \frac{k}{\rho c_p}. \tag{I.15}$$

I.2.4 The Dittus-Boelter equation

The Dittus-Boelter equation [Hol2013] for fully developed turbulent flow in smooth tubes is given by

$$\mathrm{Nu} = 0.023\,\mathrm{Re}^{0.8}\mathrm{Pr}^{n}. \tag{I.16}$$

The properties of the fluid should be evaluated at the bulk temperature. The following conditions should be satisfied:

- $n = 0.3$ for cooling and $n = 0.4$ for heating,
- $10\,000 < \mathrm{Re} < 120\,000$,
- $0.7 < \mathrm{Pr} < 100$,
- $L/D_H > 60$, where L is the length of the tube.

Note that it takes a length of several tube diameters for the flow to become fully developed. Dittus and Boelter formulated Eq. (I.16) in 1930 by correlating the logarithm of the Nusselt number with the logarithms of the Reynolds and Prandtl numbers for a range of flow conditions in smooth tubes. Their method essentially searched for linear relationships in log-log plots of the measured data [Dit1930]. It does not apply to the entrance region of a tube. Entrance effects can be large, as will be discussed in a subsequent appendix.

I.2.5 The Sieder-Tate equation

The Dittus-Boelter equation [Hol2013] works well for moderate temperature differences between wall and bulk fluid conditions. For high heat fluxes, the temperature difference between

the wall and bulk of the fluid may become large, leading to different fluid properties in the central and near-surface regions, in particular the viscosity. The Sieder-Tate equation includes a correction for this. For cooling, the Sieder-Tate equation is given by

$$\mathrm{Nu} = 0.027\,\mathrm{Re}^{0.8}\mathrm{Pr}^{1/3}\left(\frac{\mu_b}{\mu_w}\right)^{0.14}, \tag{I.17}$$

where μ_b and μ_w are the dynamic viscosities evaluated at the bulk temperature and the wall temperature, respectively. All other fluid properties are evaluated at the bulk temperature.

I.2.6 The Pethukhof-Kirilov equation

According to Holman [Hol2013], the Dittus-Boelter and Sieder-Tate equations offer simplicity of computation but uncertainties of the order of $\pm$ 25% are not uncommon. Petukhof and Kirilov (see e.g. [Pet1974] and references therein) developed a more accurate description for forced convection heat transfer in tubes:

$$\mathrm{Nu} = \frac{(f/8)\,\mathrm{Re}\,\mathrm{Pr}}{1.07 + 12.7(f/8)^{1/2}(\mathrm{Pr}^{2/3} - 1)}\left[\frac{\mu_b}{\mu_w}\right]^n, \tag{I.18}$$

where f is the so-called friction factor, which can be calculated for smooth tubes from the relevant Darcy-Weisbach friction factor expression [Hol2013]:

$$f = (1.82\log_{10}\mathrm{Re} - 1.64)^{-2}. \tag{I.19}$$

The following ranges apply to Eq. (I.18):

- $n = 0.11$ for cooling ($T_w > T_b$),
- $n = 0.25$ for heating ($T_w < T_b$),
- $n = 0$ for constant heat fluxes and for gasses,
- $0.5 < \mathrm{Pr} < 2000$,
- $10^4 < \mathrm{Re} < 5 \times 10^6$,
- $0 < \mu_b/\mu_w < 40$.

Except for μ_b and μ_w, all fluid properties are evaluated at the so-called film temperature, given by

$$T_f = \frac{(T_w - T_b)}{2}. \tag{I.20}$$

In the region $0.5 < \mathrm{Pr} < 200$, the Petukhof-Kirilov equation is reported to give an accuracy of 6%. The accuracy is 10% in the region $200 < \mathrm{Pr} < 2000$.

I.2.7 The thermal entrance region

The Dittus-Boelter, Sieder-Tate and Petukhof-Kirilof equations are valid for fully developed flow in tubes and ducts. In the case of tubes with a constant wall temperature, it takes a length of several diameters (perhaps 10 or more) for the temperature and velocity profiles of the coolant to become fully developed. The behaviour of the fluid in the entrance region is different, leading

to generally larger local Nusselt numbers. The length of tube in the entrance region where the flow is still developing is called the "entry length". In this region, the convection heat transfer is generally enhanced. Fortunately, the entrance region of round tubes at a constant temperature has been investigated for forced convection cooling by several authors. In this work, we will take advantage of a formulation by Kays and Perkins [Kay1985] who actually elaborated on the much older work by Sleicher and Tribus [Sle1957].

A round tube with a constant wall temperature is considered. A coolant enters the tube with a fully developed velocity profile (this is possible, for example, if an unheated connecting hose has the same inner diameter as the heated tube). Let $x = 0$ denote the tube entrance, therefore, at this point the temperature profile of the coolant will be uniform (constant). Let the flow be in the positive x direction. The radial temperature profile will now develop with increasing values of x in such a way that the fluid is hotter at the wall than in the centre of the tube. For values of x larger than the entry length, the temperature profile will no longer change – at this point the thermal boundary layer has become fully developed. It is this layer of hotter water at the inner surface of the tube that reduces the convective heat transfer coefficient (i.e. reducing the Nusselt number). This can be understood by remembering that the mechanism by which heat is transferred across the solid/fluid interface is, in fact, conduction. In other words, in the entry region of the tube the differential temperature across the solid/fluid boundary is larger than at distances larger than the entry length, and heat transfer by conduction is directly proportional to the temperature gradient. The mean Nusselt number [Kay1985] from the entrance of the tube to a particular value of x is given by

$$\overline{\mathrm{Nu}} = \frac{1}{2x^+} \ln \left(\left[8 \sum_{n=0}^{\infty} \frac{G_n}{\lambda_n^2 \exp(-\lambda_n^2 x^+)} \right]^{-1} \right), \tag{I.21}$$

where G_n and λ_n are coefficients (the majority of which are determined by correlations with experimental data) and x^+ is the so-called non-dimensional tube length, given by

$$x^+ = \frac{2x/D}{\mathrm{Re}\,\mathrm{Pr}}, \tag{I.22}$$

with x the tube length and D the tube inner diameter. The series in Eq. (I.21) becomes rapidly convergent with increasing x^+ and for large values of x^+, only the first term ($n = 0$) is significant. In this case, the mean Nusselt number approaches the local Nusselt number at a long distance from the entrance asymptotically:

$$\overline{\mathrm{Nu}} \to \mathrm{Nu}_\infty = \frac{\lambda_0^2}{2}. \tag{I.23}$$

Tabulated values of the λ_n^2 and G_n are available for different Prandtl and Reynolds numbers but the data seem to be rather limited. The approach of [Ste1996] is followed here to calculate the coefficients. From Eq. (I.23) it is clear that if Nu_∞ is known, a value for λ_0^2 can be calculated. The question is: does similar relationships exist for the other λ_n^2? It was shown that in the turbulent regime, up to $\mathrm{Re} = 100\,000$, such a relationship does exist to a good approximation. This is because the various ratios between the λ_n^2 for different n remain approximately constant for different values of the Reynolds number. The G_n coefficients behave in precisely the same way. This is true, however, only for a constant Prandtl number. This rather fortunate situation

can be expressed as follows:

$$\begin{aligned} \lambda_n^2 &= a_n \mathrm{Nu}_\infty, \\ G_n &= b_n \mathrm{Nu}_\infty, \end{aligned} \tag{I.24}$$

where the values for a_n and b_n are listed in Table I.1. The tabled values have been determined by calculating averages from the known data in the turbulent regime for the case $\mathrm{Pr} = 0.7$ and are slightly different than the values of [Ste1996].

Table I.1: Coefficients for forced convection heat transfer calculations in the thermal entrance region for a circular tube at a constant temperature[a].

n^a	a_n	b_n
0	2.0	0.244
1	22.3	0.0462
2	63.5	0.0296

[a]For $\mathrm{Pr} = 0.7$.
[b]Truncation of the series at 3 terms is in accordance with [Kay1985].

Figure I.1 shows a calculation of $\overline{\mathrm{Nu}}/\mathrm{Nu}_\infty$ versus x/D for helium at a pressure of 1.25 bar (typical for the bombardment stations at iThemba LABS) and a Reynolds number of $\mathrm{Re} = 20\,000$. The Prandtl number is $\mathrm{Pr} = 0.685$ under these conditions, therefore the use of the data in Table I.1 is justified. The enhancement of the Nusselt number in the entrance region is evident, in particular when the length-to-diameter ratio is smaller than 1.

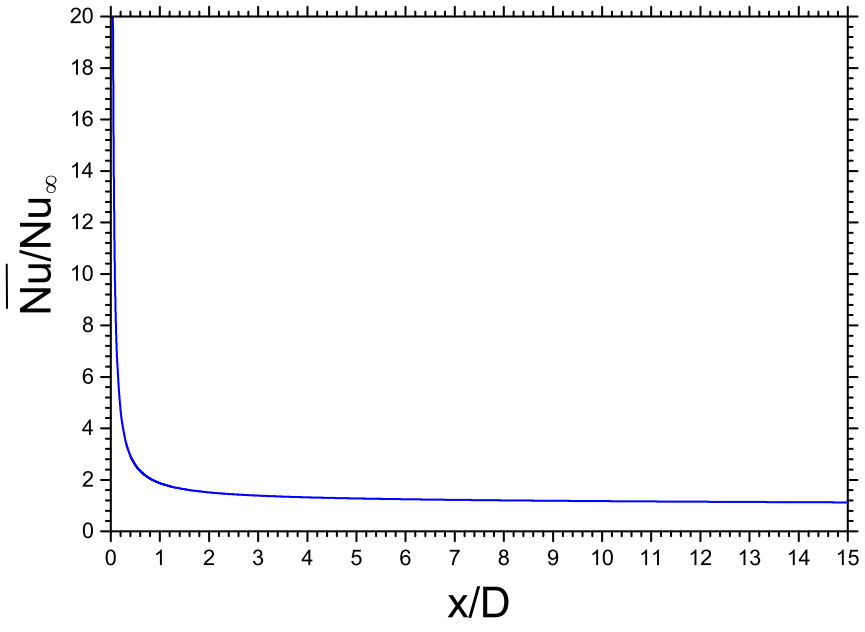

Figure I.1: Ratio of the mean Nusselt number and the Nusselt number at a large distance from the entrance of a round tube, plotted against the length-to-inner-diameter ratio of the tube (see text). The wall temperature is constant. The coolant is He with a Reynolds number of $\mathrm{Re} = 20\,000$.

Appendix J

Beam Windows: Steady-state Temperature Profiles – Finite Difference Method

J.1 Introduction

Some simplifications as well as some additions have been made to the code WINDOW [Ste1990]. The simplifications were necessary to circumvent convergence problems. The implementation in new code, renamed WINHEAT, are discussed here for steady-state calculations.

Consider a thin circular foil window as shown in Fig. J.1. The beam and window foil are both considered to have a radial symmetry. With "thin" we mean that the axial temperature difference across any part of the foil is insignificant and can be neglected. This will usually be true if the beam energy degradation is sufficiently small (i.e. $\Delta E_{beam} << E_{beam}$). Similar notation as in [Ste1990] will be used, however, the treatment of suppression of radiation from inner surfaces in the case of double-foil windows will be simplified considerably, albeit with the introduction of another approximation. The rationale for this simplification will be discussed later. The notation is introduced in Fig. J.1.

It is convenient to use a finite-difference approach to calculate the radial beam profile. Let the foil have a radius R and consider it to be divided into N concentric radial nodal elements, constrained by equispaced radial nodes. Let the numbering of the nodes (i.e. their indices) increase with increasing radius. A set of N nodal elements (numbered from 1 to N) will therefore be constrained by $N+1$ radii, r_i where $1 \leq i \leq N+1$. Two boundary conditions are immediately evident:

$$r_1 = 0 \text{ and } r_{N+1} = R. \tag{J.1}$$

The radial increment is given by

$$\Delta R = R/N. \tag{J.2}$$

One can also assign an average radius or "representative" radius for each nodal element, which is used in the source term description:

$$\overline{r}_i = \frac{r_i + r_{i+1}}{2}. \tag{J.3}$$

The area of each concentric nodal element is given by

$$A_i = \pi(r_{i+1}^2 - r_i^2), \text{ where } 1 \leq i \leq N. \tag{J.4}$$

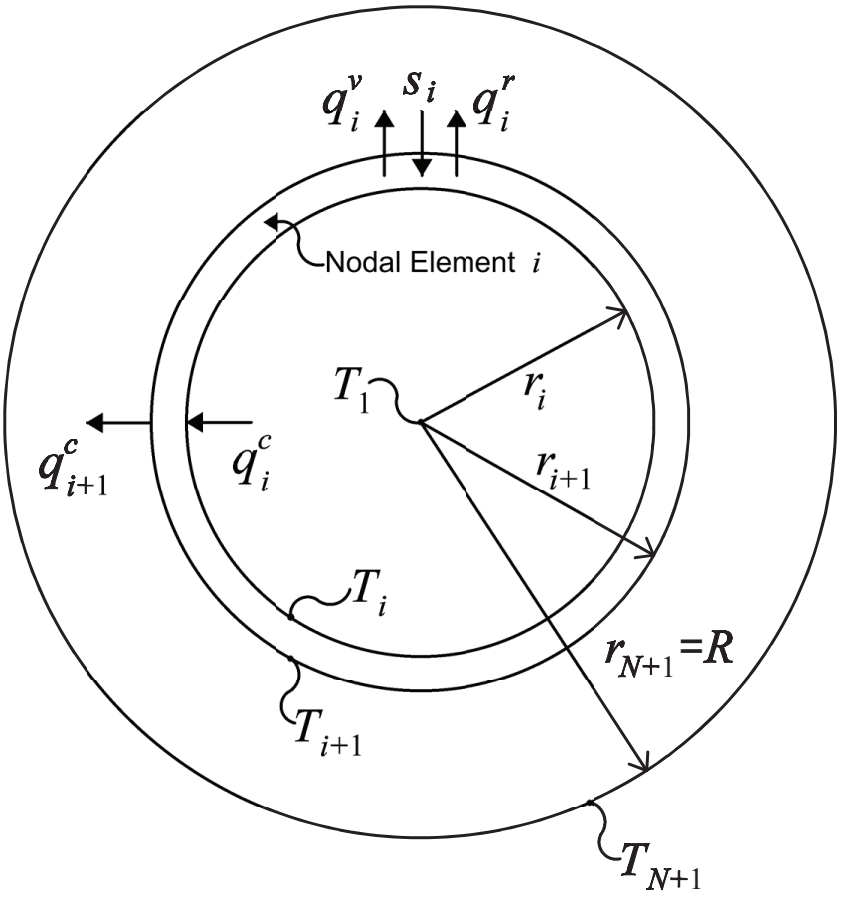

Figure J.1: Notation used for the numerical analysis of a thin circular foil window.

Nodal temperatures are defined similarly by T_i such that the radial temperature difference across each element is given by

$$\Delta T_i = T_i - T_{i+1}, \text{ where } 1 \leq i \leq N.. \tag{J.5}$$

The temperature of each nodal element is considered to be constant with a value taken to be the arithmetic average of the temperatures of its constraining nodes:

$$\overline{T}_i = \frac{T_i + T_{i+1}}{2}. \tag{J.6}$$

The material properties of each nodal element is evaluated at this temperature. Thus, the calculation provides a stepwise temperature distribution with discrete temperature jumps at the nodes. Consider the i^{th} nodal element as shown in Fig. J.1. Let the source term, corresponding to the beam heating, be denoted by s_i. These values will be positive for in-beam nodal elements and zero when out of the beam. Let the term q_i^r represent radiation heat transfer and have a positive value for emission (thus, by implication, negative for absorption). Let the term q_i^v represent convection heat transfer and have a positive value when removing heat from the element. (In principle, the coolant can be hotter than the window and warms it up, rather than cool it down. In such an unlikely case, the q_i^v may have negative values.) Two radial thermal conduction terms are required to describe the heat transfer of the nodal element completely; q_i^c at radial boundary r_i and q_{i+1}^c and radial boundary r_{i+1} Let these quantities have positive

values if heat is conducted away from the centre node (i.e. negative for heat flow in the direction of the centre node). The energy balance on nodal element i can therefore be written as follows:

$$q_{i+1}^c = q_i^c + s_i - q_i^r - q_i^v, \tag{J.7}$$

with a boundary condition

$$q_1^c = 0. \tag{J.8}$$

This last boundary condition simply states that no heat is transferred by conduction into or out of the centre node, which is a point, unlike the other nodes at finite radii that have associated cross-sectional areas through which conduction can take place. Typically, the number of nodes N will be chosen large enough so that the ΔT_i are sufficiently small; one should have $T_{i+1} \approx T_i$. Under such conditions, it is justified to consider the temperature of each nodal element to be constant over its entire surface, simplifying the calculations of the heat removed by convection and radiation.

In the following sections, the terms of the energy balance equation – Eq. (J.7) – will be discussed individually.

J.2 The source term

In principle, any radial beam profile can easily be included in the code (WINHEAT) but only the following three have been implemented:

1. Gaussian beam profile;
2. Uniform (flat) beam profile;
3. Time integrated average of a rotating Gaussian beam (i.e. a swept beam profile).

J.2.1 Gaussian beam profile

A typical 66 MeV proton beam at iThemba LABS has a truncated Gaussian radial profile (see section 2.3.3 and Fig. 2.11). As the Gauss function extends to infinity, a cut-off parameter is required to constrain it. Let the cut-off parameter be denoted by K. Let the total beam power loss (for a constant beam intensity) be denoted by Q and let $G(r)$ denote the Gaussian function without normalization:

$$G(r) = \exp\left(\frac{-r^2}{2\sigma^2}\right). \tag{J.9}$$

Then

$$\begin{aligned} s_i &= \left[\frac{[G(\overline{r}_i) - G(K\sigma)]\,\overline{r}_i \Delta r}{\sum_{j=1}^{N} [G(\overline{r}_j) - G(K\sigma)]\,\overline{r}_j \Delta r}\right] Q \qquad \text{for } i \leq \frac{K\sigma}{\Delta r}, \\ &= 0 \qquad\qquad\qquad\qquad\qquad\quad \text{for } \frac{K\sigma}{\Delta r} < i \leq N. \end{aligned} \tag{J.10}$$

The cut-off parameter, K, is now a variable parameter in the code. As shown in Chapter 2, excellent agreement with measured beam profiles is obtained when the beam width is considered

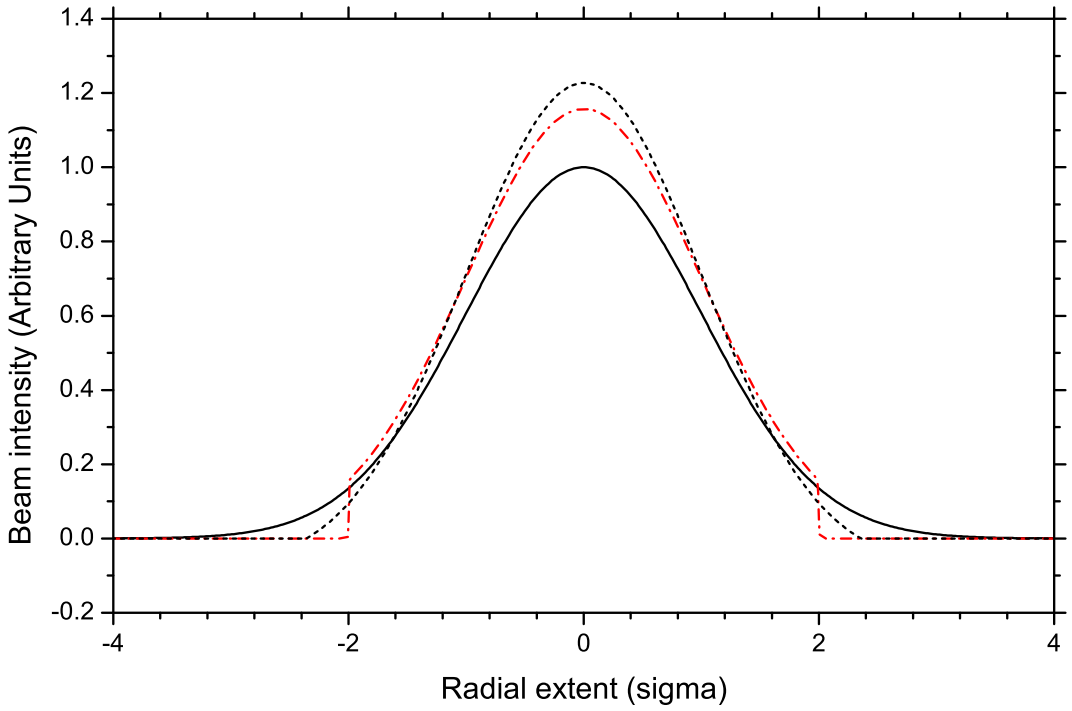

Figure J.2: Cross section through a radial beam profile. The solid black curve is a standard Gaussian. The red dot-dash curve is a Gaussian truncated by a "cookie cutter" at $r = 2\sigma$. The black dotted curve is a Gaussian truncated to give a beam width of $2 \times$ FWHM, using Eq. (J.10). Both truncated Gaussians have been renormalized to have the same radial volume integral as the untruncated Gaussian.

to be twice the full width at half maximum (i.e. $W = 2 \times$ FWHM). This is equivalent to a beam width of $4.70964\,\sigma$ or a cut-off parameter of $K = 2.35482$.

The Gaussian truncation in the new WINHEAT code is handled a bit differently than in the original versions of the WINDOW code. In the original code, the truncation was done at a radius of $r = 2\sigma$ (i.e. $K = 2$) and the truncated Gaussian was renormalized so that its radial volume integral was unity. This led to a discontinuity at $r = 2\sigma$. In WINHEAT this step discontinuity has been removed, as shown in Fig. J.2. This gives a slightly more realistic source term.

J.2.2 Uniform beam profile

Let the beam width be denoted by W. The source term is given by

$$\begin{aligned} s_i &= \left[\frac{1}{\pi(W/2)^2}\right] Q \qquad \text{for } \bar{r}_i \leq W/2, \\ &= 0 \qquad\qquad\quad \text{for } \bar{r}_i > W/2. \end{aligned} \tag{J.11}$$

J.2.3 Other radially symmetric beam profiles

In general, any radially symmetric beam profile can be implemented with relative ease. Let this profile be denoted by $F(r)$. The cumulative source term at a specific radius r_s is given by

$$H(r_s) = \left[C_n \int_0^{r_s} F(r) r dr\right] Q, \tag{J.12}$$

where the normalization factor C_n must be such that the factor in square brackets becomes unity at radii exceeding the beam radius $W/2$. The source term for any concentric element

constrained by arbitrary radii r_1 and r_2 is then given by

$$s(r_1, r_2) = H(r_2) - H(r_1), \text{ where } r_2 > r_1. \tag{J.13}$$

By discretizing the radius, the integration is replaced by a summation in Eq. J.12. Details of how $F(r)$ is obtained for a rotating Gaussian will be discussed in a separate Appendix which gives details of a transient calculation for swept beams.

J.3 The convection term

The model considers forced convection cooling from only one surface of the window foil. The rate of heat transfer by convection is calculated by applying Newton's law of cooling to each nodal element:

$$q_i^v = h_i A_i (T_i - T_c), \tag{J.14}$$

where $h_i = h_i(T_i)$ is the temperature dependent convection heat transfer coefficient and T_c is the bulk temperature of the coolant medium. The temperature dependence of the heat transfer coefficient is usually well described by a simple first or second order polynomial.

J.4 The radiation term

This part of the calculation has been simplified significantly. In a double-foil window assembly, the outer surfaces can readily radiate to a colder environment. This is, however, not possible for the two inner surfaces facing each other. In the program WINDOW, the complete matrix of radiation shape factors describing the emission and absorption of radiation between nodal elements on adjacent foils was calculated. While that algebra is interesting, in practice radiation heat transfer is negligible on all the convection-cooled windows of interest in the targetry of this work. The iterative process used to find the appropriate energy balance on each nodal element and simultaneously satisfy all the boundary conditions, was found to be more complicated by this part of the calculation. When applying the WINDOW code to helium-cooled windows for the VBTS, convergence issues were experienced under certain conditions. After a brief struggle to understand the lack of convergence, it was decided to rather simplify the code. This could be done without compromising its predictive power except, perhaps, for very hot windows where radiation is the dominant mode of cooling.

The radiation from the outer surface of each nodal element of a window foil can be calculated from the Stefan-Boltzmann law:

$$q_i^{r(out)} = c_b \epsilon_i A_i (T_i^4 - T_\infty^4), \tag{J.15}$$

where c_b is the Stefan-Boltzmann constant, $\epsilon_i = \epsilon(T_i)$ is the temperature dependent emissivity of the foil material and T_∞ is the temperature of the environment around the foil assembly. The dependence on temperature to the power of 4, as well as the temperature dependence of the emissivity, contributes to the highly non-linear nature of the total heat-transfer problem.

The radiation from the inner surface of each nodal element is considered to be impeded, either completely or to some degree, by the presence of a second hot foil in its vicinity. This is

modelled only approximately in the new code (WINHEAT) by assuming a similar form as for the outer foil but multiplied by a scale factor, P:

$$q_i^{r(in)} = c_b \epsilon_i A_i P (T_i^4 - T_\infty^4), \tag{J.16}$$

where $0 \leq P \leq 1$.

The condition $P = 0$ corresponds to complete suppression of radiation to the environment from an inner surface and $P = 1$ implies unimpeded radiation to the environment. It is more useful to perform two calculations for double-foil windows (with $P = 0$ and with $P = 1$) and to compare their difference, than to guess some value for P in between. Most often, the results depend very little on the value of P.

The radiation term in the energy balance equation (Eq. J.7) is given by

$$q_i^r = q_i^{r(out)} + q_i^{r(in)}. \tag{J.17}$$

J.5 The conduction terms

The energy balance as expressed by Eq. (J.7) states that the heat conduction out of a nodal element is equal to the heat conduction into that nodal element plus the beam heating source term minus convection and radiation losses. Starting from the innermost node, that equation can now be repeatedly applied. Indeed, it is possible to relate the relevant nodal temperatures to the conduction terms by applying Fourier's law of thermal conduction, which can be rewritten in the following explicit form:

$$T_{1+1} = T_i - \frac{q_i^c \Delta r}{2\pi \bar{r}_i t k_i} \text{ for } 1 \leq i \leq N, \tag{J.18}$$

where t is the foil thickness and $k_i = k(T_i)$ is the temperature dependent thermal conductivity of the window material. Equation (J.13) clearly states that T_{i+1} can only be calculated if T_i is known. Thus, the calculation can only commence from a concrete value of the centre node temperature, T_1. Generally, however, this temperature is not known. The approach followed here is to make an initial "guess" of the centre node temperature. This allows one to calculate a whole set of nodal temperatures $\{T_i, 1 \leq i \leq N+1\}_1$ and to use some criterion to judge how good this set is. In all probability, this first attempt (or first iteration) will not be very successful. The value of the centre node temperature must then either be increased or decreased, in a constrained manner, before starting the second iteration. The same criterion should then be applied again to judge this subsequent nodal temperature set, $\{T_i, 1 \leq i \leq N+1\}_2$. This process should be allowed to continue until convergence is reached, i.e. $\{T_i, 1 \leq i \leq N+1\}_m$ is found, where m is the number of the iteration which leads to all the boundary conditions being met to the desired precision. This iterative search for the centre node temperature is performed by using the numerical method of bisection, described below.

J.5.1 The method of bisection

The method of bisection is simple but extremely powerful. In this particular case we would like to use this method to find the value of the centre node temperature to a particular degree of

accuracy. In order for the method to yield a successful convergence, one must correctly specify two limiting temperature values, T_{min} and T_{max}, so that the true centre node temperature is constrained by these two values. Some physical insight helps with this choice. This can be described means of an example:

Consider a helium-cooled Havar foil window assembly, where both the helium and window assembly are both at room temperature. The edge of the foil is kept at a constant temperature, which is the same as the inlet helium coolant temperature, thus

$$T_{edge} = T_{\infty} \leftarrow T_{N+1}, \tag{J.19}$$

where T_{∞} is the temperature of the environment, taken as room temperature.

As a convergence criterion, an accuracy for the edge temperature to within a value of α is most appropriate in this case, thus α is the desired precision. For example, one may specify the edge temperature to be 25 °C (298.16 K) and the desired precision to be $\alpha = 0.01$°C. As no part of the window under bombardment can ever be cooler than the edge temperature, one may specify T_{min} to be marginally lower than the desired edge temperature including its precision. For this reason, the minimum temperature is usually specified to be

$$T_{min} = T_{edge} - 2\alpha. \tag{J.20}$$

This value for T_{min} will always be a constraining minimum. Let us further assume that we have knowledge that the Havar material can withstand the bombardment, i.e. that it will not melt. The melting point of Havar may therefore be a good choice for T_{max}. At any rate, two appropriate values must be specified for the minimum and maximum temperatures.

Next, one must decide on a starting temperature for the centre node to "kick off" the calculation. This can be any value between T_{min} and T_{max} but it is customary to use their bisection value:

$$T_1^{(n)} = \frac{T_{min} + T_{max}}{2}, \tag{J.21}$$

where $n = 1$ denotes the first iteration. If this starting temperature for the first iteration is too low, one will end up having a too low temperature of the edge node, i.e. $T_{N+1} < T_{edge} - \alpha$. On the other hand, if the starting temperature is too high, one will end up having a too high temperature for the edge node, i.e. $T_{N+1} < T_{edge} + \alpha$. It usually takes several tens of iterations to achieve convergence. Also, the thermal conductivity and emissivity values generally are temperature dependent. In principle, the convection heat-transfer coefficient can also have a temperature dependence. These values are recalculated for each node as the iteration progresses. Let the temperature dependent set of material and coolant properties be denoted by $\{k_i, \epsilon_i, h_i; 1 \leq i \leq N\}$. These quantities must be recalculated during each iteration. In the real world, thus, based on the outcome of the test for convergence, either T_{min} or T_{max} will be adjusted to $T_1^{(n)}$, where (n) denotes the n^{th} iteration. If it turns out that the starting temperature $T_1^{(n)}$ was too low, T_{min} will be adjusted to that value of $T_1^{(n)}$ for the next iteration. However, if it turns out that $T_1^{(n)}$ was too high, T_{max} will be adjusted to that value of $T_1^{(n)}$ for the next iteration. Thus, in this iterative process, the values of T_{min} and T_{max} are repeatedly adjusted, using the bisection value from Eq. (J.21) as the centre node temperature to "kick off" each successive iteration. Successive values of $T_1^{(n)}$ will be ever more closely constrained by T_{min} and

T_{max}, which will progressively approach each other as (n) increases. Thus, the temperature interval in which we search for convergence is progressively becoming smaller and smaller. Convergence will finally be obtained when

$$(T_{edge} - \alpha) < T_{N+1}^{(n)} < (T_{edge} + \alpha). \tag{J.22}$$

In the code WINHEAT, as the calculation of nodal temperatures progresses from the inner to the outer nodes, each new value is tested whether it falls within the allowed temperature region (T_{min}, T_{max}). The first value to violate this condition terminates that particular iteration and initiates the next iteration.

J.6 Comments in conclusion

This is, perhaps, a kind of "brute force" method but it works amazingly well. It is perfectly suited to include the temperature dependence of material or fluid properties, values which depend on the very temperatures which we would like to calculate. Equations like these cannot be solved in a closed form as they are transcendental. Numerical solutions, however, can easily be found.

Appendix K

Beam Windows: Steady-state Temperature Profiles – Neglecting Conduction

K.1 Introduction

There are two situations where it is useful to neglect conduction when calculating temperature profiles for beam windows. First, the method explained in Appendix J may give convergence problems if the thermal conductivity values of nodal elements become very small. Second, even for materials with good thermal conductivity, one may start getting convergence issues if the window becomes extremely thin (sub-micron thicknesses). This is because the available surface through which heat can conduct radially becomes so small that compared to the heat transfer by radiation and convection, conduction becomes negligible. Essentially, when the conduction terms in Eq. (J.7) become negligible compared to the other terms, heat is no longer redistributed radially across the nodal elements.

Care should be taken when comparing the relative contributions of the three mechanisms of heat transfer (i.e. conduction, radiation and convection). For example, one finds that for a typical VBTS Havar window of 75 μm thickness, the amount of heat reaching the window edge is negligible and that 100% of the total heat is removed by convection and radiation only (mainly convection). This does not mean that conduction can be ignored or is unimportant. What happens is that heat conducts radially towards the window edge, redistributing across many nodal elements, but just never reaches the edge before radiation and convection takes care of effectively removing it. This redistribution of heat by conduction is nevertheless important as it changes the overall radial temperature profile. The radial spreading of heat by conduction effectively increases the surface from which convection and radiation can effectively remove the heat. In contrast, heat removal by conduction from the window happens only if it conducts out of the window edge. Thus, even if this amount is negligible, conduction between nodal elements at smaller radii can significantly enhance the effectiveness of the other two heat-transfer mechanisms.

As explained in the first paragraph, there are genuine cases where one would like to do a calculation that neglects conduction. But if one makes the thermal conductivity values zero, subroutine PROFIL in WINHEAT will “crash”. Subroutine PROFIL2 does the proper calculation

for this case. Consider again the energy balance equation on nodal element i (Eq. J.7). With the conduction terms vanishing, one gets:

$$s_i = q_i^v + q_i^r. \tag{K.1}$$

The nodal elements are now completely decoupled and one must find, for each element separately, the temperature that satisfies Eq. (K.1). It is quite simple. One again uses the method of bisection but with a different convergence criterion:

$$|T_i^{(n)} - T_i^{(n+1)}| < \alpha \text{ for all } 1 \leq i \leq N, \tag{K.2}$$

where (n) denotes the number of the iteration. In subroutine PROFIL2, the change in the value of T_i from one iteration to the next is used as convergence criterion. The decision on whether to adjust T_{min} or T_{max} to the nodal temperature $T_i^{(n)}$ for the subsequent iteration $(n+1)$ is made based on whether $s_i - q_i^v - q_i^r > 0$ or $s_i - q_i^v - q_i^r < 0$, respectively. There is one boundary condition which must be independently satisfied, namely that

$$T_{N+1} = T_{edge}. \tag{K.3}$$

The effect of heat redistribution by conduction for a VBTS Havar window is shown in Fig. (K.1). In both calculations, no heat was removed from the window by conduction. However, the normal calculation clearly shows the beneficial effect of radial redistribution of heat by conduction even though the temperature reaches T_{edge} at a radius much smaller than the window radius.

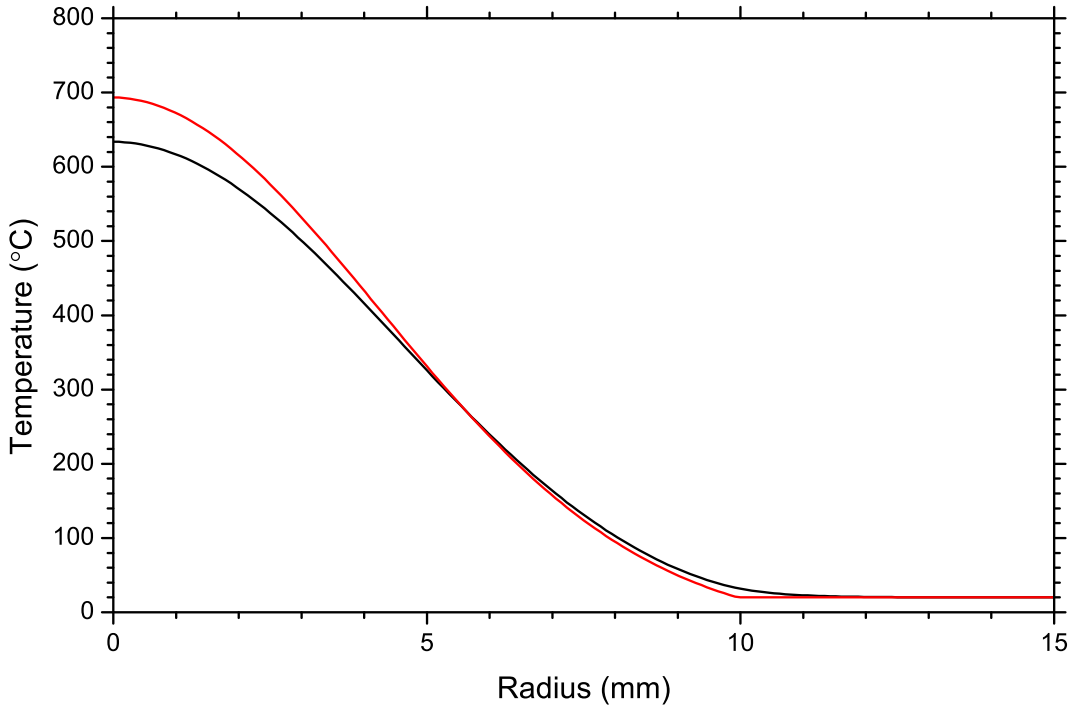

Figure K.1: Radial temperature profiles for a VBTS Havar window. The beam is Gaussian with an intensity of 300 μA. The beam width is 20 mm. The window width is 50 mm and its thickness is 75 μm. The black curve is the standard calculation discussed in Appendix J. The red curve neglects conduction. The black curve peaks at 633 °C and the red curve at 694 °C. The room temperature is 20 °C.

Appendix L

Beam Windows: Steady-state Temperature Profiles – Axial Temperature Difference

L.1 Introduction

This appendix should be read in conjunction with Appendices J and K. The word "window", in the context of targetry, carries the connotation of something which is "thin" to the beam which it should allow through. Windows should be a barrier for cooling water, helium, etc., or protect the cyclotron or beamline vacuum, while degrading the beam as little as possible. For Havar windows, which are typically only a few tens of micron thick in radionuclide applications at iThemba LABS, the beam energy degradation is minimal for a 66 MeV proton beam. The maximum temperature difference in the axial direction typically does not exceed 2 °C and is usually much less. This is why only radial nodes have initially been defined in the code WINHEAT (i.e. no axial nodes). The method of finite difference can be used to model thicker discs, using so-called relaxation techniques to solve the energy balance on volume elements which extend in both the axial and radial directions. This, however, is considered to be outside the scope of the WINHEAT code at this stage. Something is required, however, to test the assumption of "thin", i.e. whether axial temperature differences across the nodal elements are small enough to be neglected. One may want to know whether, say, a 1 mm or 2 mm thick aluminium water-cooled window can be considered thin enough to model with WINHEAT. There is a simple way to make an estimate of the axial temperature differences across nodal elements. It is guaranteed to provide an upper limit for each nodal element.

In the method described below, the radial temperature profile is first calculated as per usual, under the assumptions that the window is thin and the usual methods of WINHEAT are valid. This temperature profile is then considered to be the axial boundary condition on one of the two large surfaces of the window, at the surface which is convection cooled. Next, the window is partitioned into a discrete number of axial layers. Let us denote this number by M. The source terms are likewise partitioned so that

$$s_{ij} = \left(\frac{M-j-1}{M}\right) s_j \quad \text{for all} \quad 1 \leq j \leq M \ \text{ and } \ 1 \leq i \leq N. \tag{L.1}$$

Conduction is now only considered in the axial direction. One knows that the nodal temperatures will be lower at the cooled surface than at the uncooled surface, i.e. that heat will

flow from the uncooled surface to the cooled surface and into the cooling medium. Let the index $j = 1$ denote the axial layer containing the convection-cooled outer surface and similarly $j = M$ will denote the layer containing the uncooled outer surface. It is a simple matter to apply Fourier's law of thermal conduction to calculate the axial temperature difference across each axial layer for each nodal element i. The total axial temperature difference is then simply their sum (i.e. the sum over all j for each i). Consider nodal element i. The axial temperature difference across that element is given by

$$\Delta T_i = \sum_{j=1}^{M} \left(\frac{t}{M k_i A_i} \right) s_{ji}, \tag{L.2}$$

where t is the window thickness, A_i is the radial surface of nodal element i and k_i is the nodal thermal conductivity, as previously defined in Appendix J. These axial temperature differences are calculated neglecting any further radial dispersion of heat, thus, they are expected to yield true upper limits. Care must be taken into their correct interpretation. If these values are small (i.e. $\Delta T_i << T_i$) then one knows with certainty that the WINHEAT code can be trusted. If this is not the case, the window may be too thick to model with WINHEAT. Perhaps, and with caution, one may consider the set

$$\{T_i + \Delta T_i\} \tag{L.3}$$

to be a more appropriate set of nodal temperatures than the $\{T_i\}$ for situations in between. In the code WINHEAT, these calculations are performed by subroutine PROFIL3. (The type of calculations to include in the output is selected by the values of parameters *NC* and *ND* (see preamble comments to the code).

Two examples are given below, for a helium-cooled VBTS Havar window of 75 μm thickness and for a water-cooled aluminium VBTS target-holder window of 2 mm thickness. In both cases, the beam has a Gaussian profile with a width of 20 mm (2 $\times$ FWHM) with no sweeping. The beam intensity is 300 μA.

Havar window

This is the same calculation showed in Fig. K.1 of Appendix K. The temperature at the centre node, for a normal calculation, is 633.79 °C. With the estimate of the axial heat flow included, one gets a value of 635.85 °C. Thus, the condition $\Delta T_1 << T_1$ is certainly true. The difference between the two values is much less than 1%. Clearly, even for thick Havar windows (75 μm is thick for beam windows) and a beam current higher than typically used, the axial temperature difference is negligible. With a typical swept beam profile, this difference is even smaller.

Aluminium window

The temperature at the centre node, according to the usual calculation, is 121.06 °C. With the estimate of the axial heat flow included, one gets a value of 190.40 °C. Clearly, the condition $\Delta T_1 << T_1$ is no longer true. Neither will one consider a 2 mm aluminium window to be thin. Normally, WINHEAT is not the right tool for such a calculation. Nevertheless, one knows the truth is lying somewhere between these two values. Furthermore, even the higher of the two values is indicative of a fairly "cold" window. This is very reassuring. The boiling point of water

is 181 °C at 10 bar. A fast flow of cooling water is therefore necessary to suppress possible surface boiling.

This example shows that the code WINHEAT can successfully be applied to windows that are not strictly thin, however, care should be taken in the interpretation of the results. In the above example, one should remember that the larger value, 190.40 °C, is to be interpreted as an upper limit. It is way below the melting point of aluminium and considerably colder than some of the other target surfaces inside the target holder. To conclude, a VBTS target-holder window is not in trouble with a Gaussian beam with an intensity of 300 μA if its width is of the order of 20 mm.

Appendix M

Beam Windows: Swept Gaussian Beams and Transient Calculation for Hottest Node

M.1 Time-averaged source terms

This appendix should be read in conjunction with Appendices J, K and L. This appendix has two objectives: (1) Calculation of the time-averaged source terms of a swept Gaussian beam, and (2) calculation of the transient temperature behaviour of the hottest nodal element during bombardment with a swept Gaussian beam. The window foil and beam are both considered to be radially symmetric, as before, however, the beam is now off-centre and rotating around the centre node with a sweep frequency f_s. The sweep frequency is 450 Hz on the Elephant and 3000 Hz on the VBTS. Let the beam radius be denoted by r_b, the sweep radius by r_s and the window radius by R (see Fig. M.1). As before, we divide the window into discrete, equispaced radii r_i where $1 \leq i \leq N+1$, $r_1 = 0$ and $r_{N+1} = R$. This gives a number of $N+1$ radial nodes and N concentric nodal elements.

It is convenient, from a mathematical point of view, to choose a coordinate system in which the beam stays stationary and the window spins around its centre (i.e. the centre node) with an angular velocity defined by the sweep frequency. Since the beam has a radial symmetry, the resulting movement of the beam on the window foil will be exactly the same to that of the real case (i.e. stationary window and moving beam). Furthermore, we can place the beam at any convenient position in our frame of reference, thus we choose to place it so that its centre is located on the x-axis, as shown in Fig. M.1. Next, we place the centre of the window at the origin of the frame of reference and spin the window like a wheel around an axis perpendicular to the x and y axes (i.e. the z-axis).

In order to describe the motion of the spinning target foil, it is necessary to revert to polar coordinates and from a computational point of view, to discretize the polar angle. Let us consider one full rotation through 360 degrees. Consider a number of J discrete equispaced angles given by

$$\theta_j \quad \text{for} \quad 1 \leq j \leq J+1, \tag{M.1}$$

so that $\theta_1 = 0$ and $\theta_{J+1} = 2\pi$. The radial increment is given (as before) by

$$\Delta r = r_{i+1} - r_i = \frac{R}{N}. \tag{M.2}$$

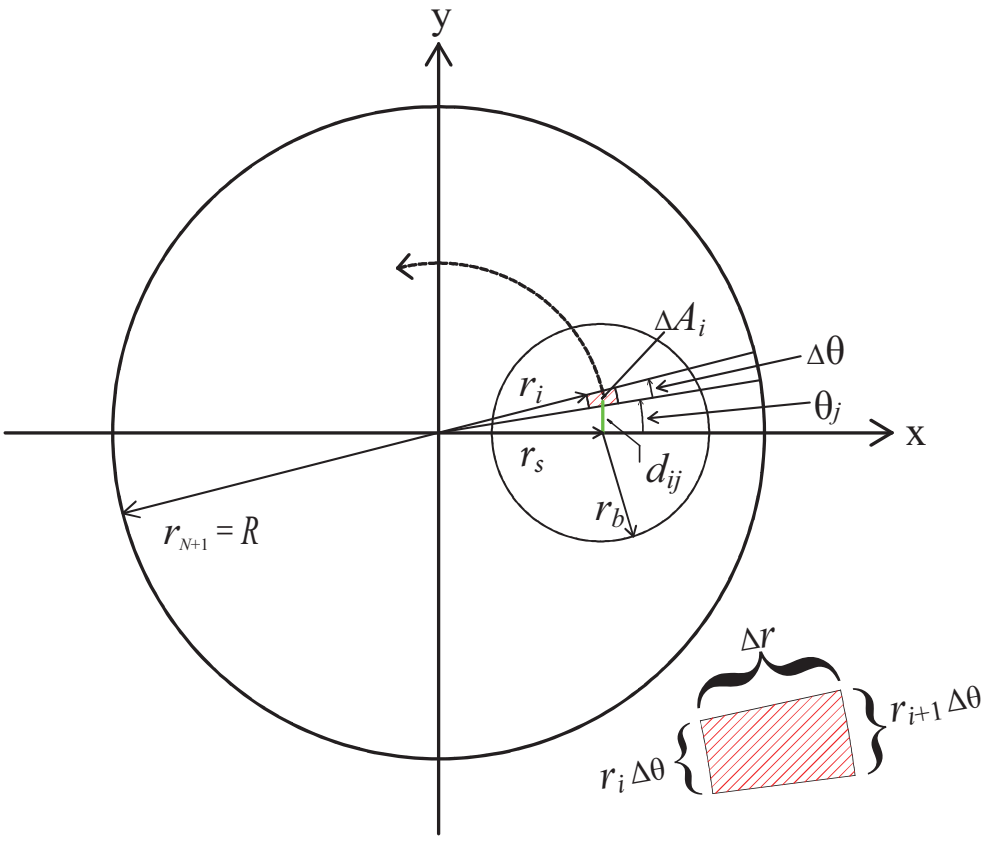

Figure M.1: Diagram showing a circular window foil and an off-centre beam as well as the notation used in the heat transfer equations.

The angular increment is given by

$$\Delta\theta = \theta_{j+1} - \theta_j = \frac{2\pi}{J}. \tag{M.3}$$

As shown in the figure, incremental surface elements are defined on the window by discretizing the radius and the angle. Consider the incremental surface element constrained by the radii r_i and r_{i+1} as well as the angles θ_j and θ_{j+1}, as shown in the figure. The polar coordinates of the corners are (r_i, θ_j), (r_{i+1}, θ_j), (r_i, θ_{j+1}) and (r_{i+1}, θ_{j+1}). It is convenient to consider N and J to be large enough so that the location of each incremental surface element can be sufficiently defined by a single polar coordinate $(\overline{r}_i, \overline{\theta}_j)$ where

$$\overline{r}_i = \frac{r_{i+1} + r_i}{2}, \tag{M.4}$$

and

$$\overline{\theta}_j = \frac{\theta_{j+1} + \theta_j}{2}. \tag{M.5}$$

Its surface is given by

$$\Delta A_i \approx \overline{r}_i \Delta r \Delta\theta = \frac{A_i}{J}, \tag{M.6}$$

where A_i is the area of nodal element i, as defined in Appendix J.

What we would like to do now is to rotate the window through one full revolution and calculate the distance between the coordinate defining the incremental surface element and the coordinate defining the centre of the beam. Let this distance be denoted by d_{ij} as shown in

the figure. The beam centre is located at $(r_s, 0)$ and the incremental surface element at $(\overline{r}_i, \overline{\theta}_j)$, thus elementary trigonometry can be used to get the distance between them. Converting to Cartesian coordinates, one has the coordinates $(r_s, 0)$ for the beam centre and $(\overline{r}_i \cos\overline{\theta}_j, \overline{r}_i \sin\overline{\theta}_j)$ for the incremental surface element. The distance between any two points (x_1, y_1) and (x_2, y_2) in Cartesian coordinates is given by

$$d = \sqrt{(x_1 - x_2)^2 + (y_1 - y_2)^2}. \tag{M.7}$$

Thus

$$d_{ij} = \sqrt{(\overline{r}_i \cos\overline{\theta}_j - r_s)^2 + (\overline{r}_i \sin\overline{\theta}_j)^2}. \tag{M.8}$$

When $d_{ij} \leq r_s$, the elemental surface is heated by the beam, however, the moment $d_{ij} > r_s$, the elemental surface will be outside the beam and consequently no longer heated by it. Partial source terms are now defined such that

$$\begin{aligned} \Delta s_{ij} &= [G(d_{ij}) - G(K\sigma)]\, \overline{r}_i \Delta r \qquad \text{for} \quad d_{ij} \leq r_s, \\ &= 0 \qquad\qquad\qquad\qquad\quad \text{for} \quad d_{ij} > r_s. \end{aligned} \tag{M.9}$$

where G is the Gaussian function defined by Eq. (J.9) in Appendix J. The time averaged source term will be directly proportional to the sum of partial source terms for one full revolution:

$$s_i \propto \sum_{j=1}^{J} \Delta s_{ij}. \tag{M.10}$$

The normalization still has to be done, as discussed in Appendix J – see Eqs. (J.10) and (J.12):

$$s_i = \left[\frac{\sum_{j=1}^{J} \Delta s_{ij}}{\sum_{i=1}^{N} \sum_{j=1}^{J} \Delta s_{ij}} \right] Q, \tag{M.11}$$

where Q is the total beam power loss in the window, as previously described in Appendix J. An example of the application of Eq. (M.11) has already been shown in Fig. 2.11, together with the results from an autoradiogram of VBTS beam made by means of Gaßcromic film.

M.2 The transient behaviour of the nodal element with highest temperature

Discretization of time

It was decided to investigate the transient behaviour of only the nodal element that becomes hottest during beam operations. Any steady-state calculation in WINHEAT stores the relevant information needed by the transient calculation, if required, including which nodal element becomes the hottest. What we would like to do is to follow the heating of an incremental surface element of the hottest nodal element as a function of time, i.e. to calculate a "snapshot" of the transient thermal behaviour.

As with the radius and angle, it is necessary to discretize time when doing transient calculations numerically. The duration of one revolution of the beam on target is given by

$$t_s = \frac{1}{f_s}, \tag{M.12}$$

where f_s is the sweep frequency. However, that one revolution is also discretized into a number of J angles. One can picture that revolution as making a number of J discrete "jumps" instead of rotating in a continuous way (almost as if the window foil is connected to a stepper motor). There is, therefore, a minimum discrete time interval in the transient calculation, given by

$$\Delta t_s = \frac{1}{f_s J} = \frac{t_s}{J}, \tag{M.13}$$

which is the time to complete one discrete "angular jump" or discrete "frame" of rotation. Time is therefore only defined, or has meaning, in integer multiples of Δt_s.

Decoupling of the incremental surface element

Consider a small part of a nodal element, such as shown in Fig. M.1. Furthermore, consider this to be from the hottest nodal element of the window as determined from a steady-state calculation. To simplify the generally quite complex transient calculation, it would be very convenient if this element could be decoupled from the rest of the window. We found that such an approximation is indeed possible but only for a rather special case. First, we know that for practical convection-cooled windows, the heat transferred by radiation is minimal (less than 1% of the total heat transferred by convection for Elephant, Babe and VBTS windows). Radiation will therefore be neglected, thus, the transient calculations described here will only be valid in cases where radiation is negligible. Second, conduction connects the incremental surface element to the rest of the window. The only way to decouple it will be if there is some or other simple relationship between conduction losses and convection losses from this element, so that conduction losses can be expressed in terms of the convection losses (by, e.g. a polynomial). It turns out that this can be achieved quite easily for the hottest nodal element.

As already seen in Appendix J, the amount of heat removed from the window by conduction is negligible. Instead, conduction helps to redistribute heat to colder parts of the window, from where convection takes care of the removal. It turns out, by doing a large number of steady-state calculations for several typical windows, that the ratio of heat removed from the hottest nodal element by conduction and by convection remains nearly constant, for different thermal. This is, perhaps, not such a big surprise as both mechanisms of heat transfer are linearly dependent on temperature. This means that one can make an approximation which removes the necessity to take both radiation and conduction into account explicitly. From the relevant steady-state calculation, we can express the total heat loss from the hottest nodal element as some factor times the heat loss by convection:

$$q_i^{total} = H_{const} q_i^v. \tag{M.14}$$

Since convection heat transfer from any part of the window can always be calculated independently from what happens on the rest of the window, Eq. (M.14) gives the desired decoupling.

The role of the specific heat

We can now proceed to write down the rest of the relevant equations. From here onwards, let $i = i_{max}$ denote the index of the hottest node. We follow a small part of that nodal element as

it rotates. An incremental element such as shown in Fig. M.1, with a surface area as given by Eq. (M.6), will consequently be used in the calculations. Its mass is given by

$$\Delta m = \rho t \Delta A_i, \tag{M.15}$$

where ρ is the density of the window material and t is the foil thickness. From Eqs. (M.9) to (M.11) one can write down the partial source terms, properly normalized, as follows:

$$\Delta s'_{ij} = \left[\frac{\Delta s_{ij}}{\sum_{i=1}^{N} \sum_{j=1}^{J} \Delta s_{ij}} \right] Q. \tag{M.16}$$

One more ingredient is required, namely the *starting temperature* of the calculation, T_{start}. This can be any legitimate temperature between T_{edge} and the steady-state maximum temperature of the nodal element. Thus, one will calculate "snap shots" of the transient thermal behaviour of the window at the radius where it reaches a maximum temperature, starting at the value of T_{start}. The window is now rotated, angle by angle, through many revolutions. For the sake of the calculation, let L be the number of time intervals to follow. Typically, L would be chosen to be a much larger number than J. Let the temperature of the incremental surface element be denoted by T_l . The heat dissipated by the beam in the incremental element during time increment l is

$$\Delta q_{beam} = \Delta s'_{il} \Delta t_s, \tag{M.17}$$

The corresponding amount of heat lost during this time increment is given by

$$\Delta q_{lost} = H_{const} h(T_l) \Delta A_i (T_l - T_c) \Delta t_s, \tag{M.18}$$

where $h(T_l)$ is the convection heat transfer coefficient at temperature T_l and T_c is the temperature of the coolant medium (see Eq. (J.14) of Appendix J). Thus, the amount of heat gained by the incremental element is given by

$$\Delta q_{gain} = \Delta q_{beam} - \Delta q_{lost}. \tag{M.19}$$

The temperature increase during time increment l is given by

$$\Delta T_l = \frac{\Delta q_{gain}}{c_p \Delta m}, \tag{M.20}$$

where c_p is the specific heat (also called "heat capacity" or "specific heat capacity") of the window material. Equation (M.20) shows that the larger the specific heat of a material, the longer it will take to heat it to a specific temperature. The final temperature after heating during time increment l is given by

$$T_l = T_{start} + \sum_{k=1}^{l} \Delta T_k. \tag{M.21}$$

The set of transient temperatures $\{T_l,\ 1 \leq l \leq L\}$ is a snapshot of the temperature as a function of time, starting at a value of T_{start} and followed for a duration of $L\Delta t_s$. The current version of WINHEAT allows for values of L up to 100 000 and values of J up to 600.

Figures (M.2) and (M.3) show examples for the Elephant window with a sweep frequency of 50 Hz and a beam current of 90 μA. Note the rapid temperature increase in Fig. (M.2). It takes only about 200 ms to reach the stage where the temperature fluctuates around the steady state value, shown in Fig. (M.3). These examples show why a sweep frequency larger than the line frequency of 50 Hz is required.

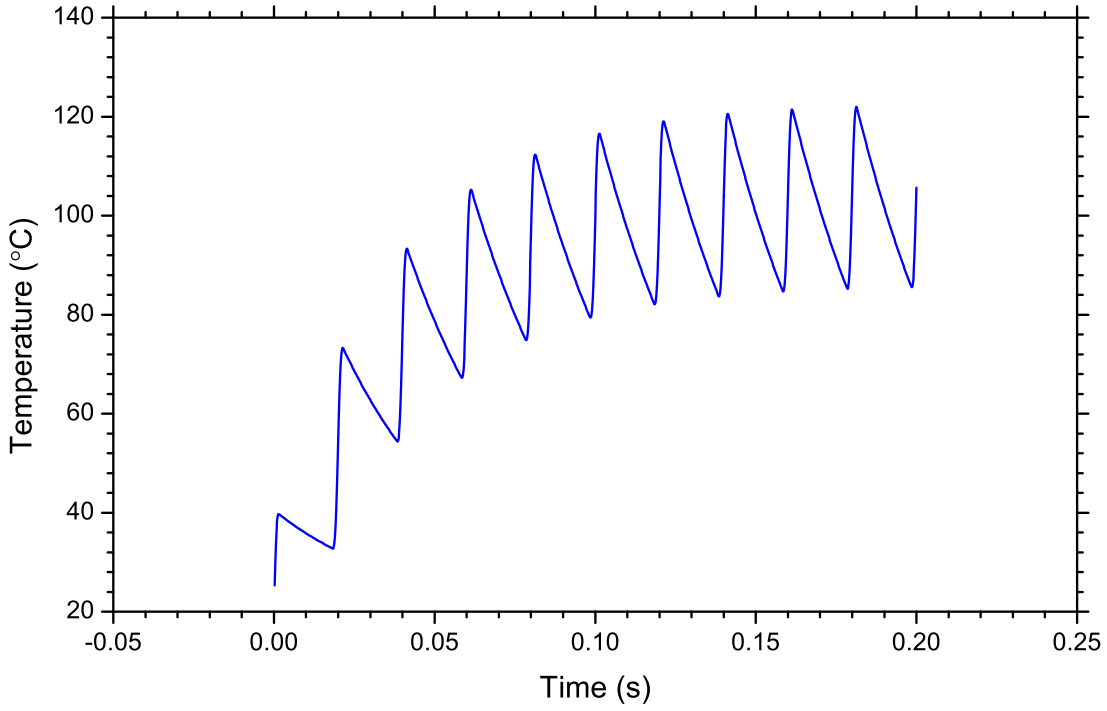

Figure M.2: Temperature as a function of time for the hottest node on a 25 μm thick Havar Elephant window, followed from room temperature at time $t = 0$ for a time period of 200 ms. The sweep radius and beam diameter are both 5 mm. The sweep frequency is 50 Hz. The beam current is 90 μA. The beam profile is a Gaussian truncated at a width of 2 $\times$ FWHM.

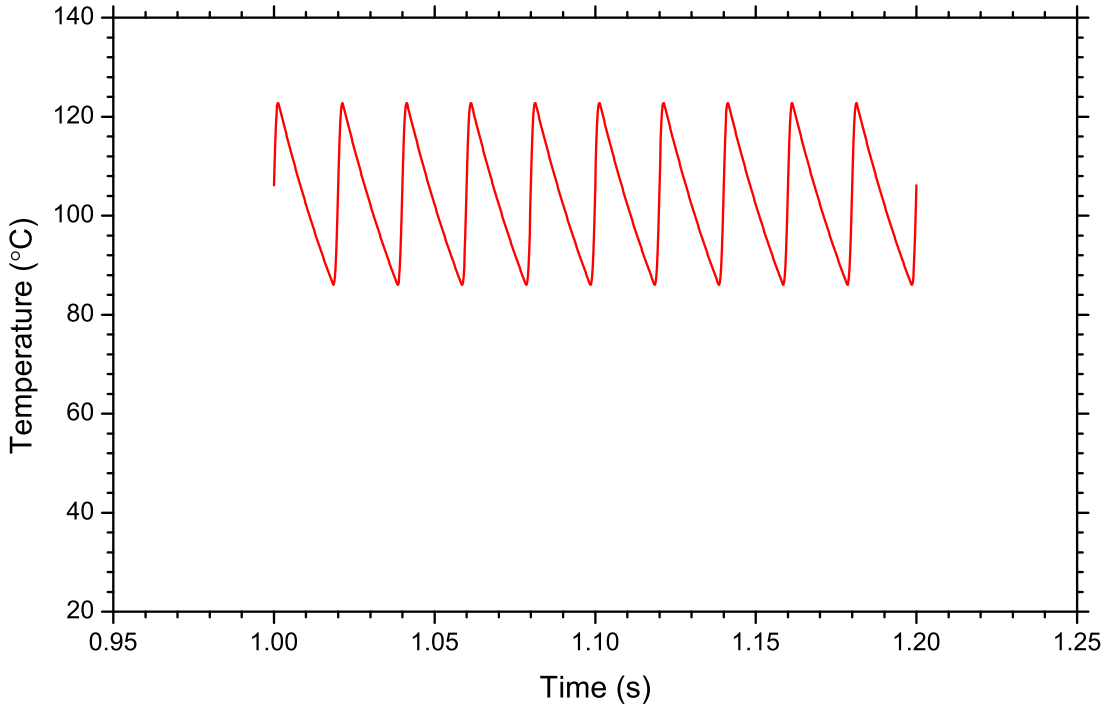

Figure M.3: Temperature as a function of time for the hottest node on a 25 μm thick Havar Elephant window during the period 1 to 1.2 seconds after the bombardment started. The sweep radius and beam diameter are both 5 mm. The sweep frequency is 50 Hz. The beam current is 90 μA. The beam profile is a Gaussian truncated at a width of 2 $\times$ FWHM.

Bibliography

[Abb2000] S. M. A. Abbas Rizvi, S. Sarkar, G. Goozee, B. J. Allen, Radioimmunoconjugates for targeted [alpha] therapy of malignant melanoma. Melanoma Research 10 (2000) 281–289.

[All1996] B. J. Allen, N. Blagojevic, Alpha- and beta-emitting radiolanthanides in targeted cancer therapy: The potential use of terbium-149. Nucl. Med. Comm. 17 (1996) 40–47.

[All2001] B. J. Allen, G. Goozee, S. Sarkar, G. Beyer, C. Morel, A. P. Byrne, Production of terbium-152 by heavy ion reactions and proton induced spallation. Appl. Radiat. and Isot. 54 (2001) 53–58.

[Alv2008] C. W. Alvord, A. E. Ruggles and C. D. West, Calculation of attainable superheats and predicted embryonic flux rates in commercial water isotope targets. Appl. Radiat. and Isot. 66 (2008) 1781–1787.

[And1977] H. H. Anderson, J. F. Ziegler, Hydrogen stopping powers and ranges in all elements. In: *The stopping and Ranges of Ions in Matter*, Vol. 3 (ed. J. F. Ziegler), Pergamon, New York, 1977, p. 1.

[Att1976] F. H. Attix, R. B. Theus, G. E. Miller, Attenuation measurements of a fast neutron radiotherapy beam. Phys. Med. Biol. 21 (1976) 530-546.

[Avi2006] M. A. Avila-Rodriguez, R. G. Selwyn, A. K. Converse, R. J. Nickles, ^{86}Y and ^{89}Zr as PET Imaging Surrogates for ^{90}Y : A Comparative Study. AIP Conf. Proc. 854 (2006) 45.

[Avi2008] M. A. Avila-Rodriguez, J. S. Wilson, M. J. Schueller, S. A. McQuarrie, Measurement of the activation cross section for the (p,xn) reactions in niobium with potential applications as monitor reactions. Nucl. Instr. and Meth. B 266 (2008) 3353–3358.

[Bac2013] H. T. Bach, T. N. Claytor, J. F. Hunter, E. R. Olivas, C. T. Kelsey, J. W. Engle, M. A. Connors, F. M. Nortier, W. H. Runde, C. Moddrell, J. W. Lenz, K. D. John, Improving the survivability of Nb-encapsulated Ga targets for the production of ^{68}Ge. Nucl. Instr. and Meth. B 299 (2013) 32–41.

[Bai2005] D. L. Bailey, D. W. Townsend, P. E. Valk, M. N. Maisey, Positron Emission Tomography. Springer-Verlag, London, 2005.

[Bar1997] J. E. Bardina, P. G. Huang, T. J. Coakley, Turbulence Modeling Validation, Testing, and Development. NASA Technical Memorandum 110446, 1997.

[Bec1985] V. Bechtold, R. J. Nickles, Target foils. In: *Proc. 1st Int. Workshop on Targetry and Target Chemistry* (WTTC 1, 1985, Heidelberg, Germany), pp. 5–8. Available from URL: http://wttc.triumf.ca. Printed version: eds. F. Helus, T. J. Ruth, DKFZ Press Department, Heidelberg, 1987, pp. 5–8.

[Bec2004] C. F. W. Becker, D. Clayton, G. Shapovalov, H. A. Lester, G. G. Kochendoerfer, On-resin assembly of a linkerless lanthanide(III)-based luminescence label and its application to the total synthesis of site-specifically labelled mechanosensitive channels. Bioconjugate Chem. 15 (2004) 1118–1124.

[Ber2004] M. J. Berger, J. S. Coursey, M. A. Zucker, J. Chang, Stopping-Power and Range Tables for Electrons, Protons and Helium Ions. Last update, August 2004. Available from URL: http://physics.nist.gov/Star.

[Bey2004] G. J. Beyer, M. Miederer, S. Vranješ-Durić, J. J. Čomor, G. Künzi, O. Hartley, R. Senekowitsch-Schmidtke, D. Soloviev, F. Buchegger, Targeted alpha therapy in vivo: direct evidence for single cancer cell kill using ^{149}Tb-rituximab. Eur. J. Nucl. Med. Biol. Imaging 31 (2004) 547–554.

[Bir1973] C. Birattari, E. Gadioli, E. Gadioli Erba, A. M. Grassi Strini, G. Strini, G. Tagliaferri, Pre-equilibrium processes in (p,n) reactions. Nucl. Phys. A 201 (1973) 579–592.

[Bla1971] M. Blann, Hybrid model for pre-equilibrium decay in nuclear reaction. Phys. Rev. Lett. 27 (1971) 337–340.

[Bla1972] M. Blann, Importance of nuclear density distribution on pre-equilibrium decay. Phys. Rev. Lett. 28 (1972) 757–759.

[Bla1991] M. Blann, Recent progress and current status of preequilibrium reaction theories and computer code ALICE. Lawrence Livermore National Laboratory Reports, UCRL-JC-109052, Lawrence Livermore National Laboratory, Livermore, California, USA, 1991.

[Ble1986] G. Blessing, H. H. Coenen, K. Franken, S. M. Qaim, Production of [^{18}F]F_2, H^{18}F and $^{18}F^-_{aq}$ using the ^{20}Ne(d,α)^{18}F process. Appl. Radiat. and Isot. 37 (1986) 1135–1139.

[Blo1985] A. I. Blokhin, A. V. Ignatyuk, A. B. Pashchenko, Yu. V. Sokolov, Yu. N. Shubin, Analysis of threshold reaction excitation functions in frame of unified superfluid model. Comm. Acad. of Science of USSR 49 (1985) 962.

[Boh2003] T. Bohn, Magnesium Absorption in Humans. PhD. Thesis, ETH Zürich, Switzerland, 2003.

[Bon1998] M. Bonardi, C. Birattari, M. Gallorini, F. Groppi, D. Arginelli, L. Gini, Cyclotron production, radiochemical separation and quality control of platinum radiotracers for toxicological studies. J. Radioanal. Nucl. Chem. 236 (1998) 159–164.

[Bro2006] C. H. M. Broeders, A. Yu. Konobeyev, Yu. A. Korovin, V. P. Lunev, M. Blann, ALICE/ASH - Pre-compound and Evaporation Model Code System for Calculation of Excitation Functions, Energy and Angular Distributions of Emitted Particles in Nuclear Reac-

tions at Intermediate Energies. Wissenschaftliche Berichte FZKA 7183, Forschungzentrum Karlsruhe GmbH, Karlsruhe, Germany, 2006.

[Buc2006] K. Buckley, ^{18}O Water target design for production of 18F. TRIUMF Design Note, TRI-DN-06-07 (2006) (TRIUMF, Vancouver, Canada) pp 1–6.

[But2004] E. Z. Buthelezi, Near-target and other heavy residues in the interaction of ^{12}C and ^{16}O with ^{103}Rh. PhD Thesis, University of Stellenbosch, South Africa, 2004. Available from URL: http://library.sun.ac.za.

[Cas1980] V. Casella, T. Ido, A. P. Wolf, J. S. Fowler, R. R. MacGregor, T. J. Ruth, Anhydrous F-18 labelled elemental fluorine for radiopharmaceutical preparation. J. Nucl. Med. 21 (1980) 750–757.

[Cat2008] I. Cata-Danil, M. Ivascu, T. Glodariu, N. V. Zamfir, D. Bucurescu, D. Filipescu, G. Cata-Danil, L. Stroe, C. Mihai, D. Ghita, G. Suliman, T. Sava, Measurement of cross-sections and thick target yields for (α, γ) process on ^{63}Cu. Romanian Reports Phys. 60 (2008) 555–561.

[Cel1992] C. P. Celata, M. Cumo, Burnout at very high heat fluxes. Wärme- und Stoffübertragung 27 (1992) 233–244.

[Cel2000] P. J. Celliers, A. H. Botha, J. L. Conradie, P. M. Cronje, J. L. G. Delsink, J. G. de Villiers, H. du Plessis, J. S. du Toit, Z. B. du Toit, D. T. Fourie, M. E. Hogan, H. N. Jungwirth, A. Müller, P. F. Rohwer, H. A. Smit, P. J. Theron, M. J. van Niekerk, Present status and new developments at NAC. In: *Proc. 17th European Particle Accelerator Conf.* (EPAC 2000, Vienna, Austria), p. 533–535. Available from URL: http://accelconf.web.cern.ch/accelconf/e00.

[CERN2013] Terbium: a new “Swiss army knife” for nuclear medicine. In: *CERN Courier* (ed. C. Sutton), January, 2013. Available from URL: http://cerncourier.com.

[Cha1995] C. T. Chang, G. Kojasoy, F. Landis, S. Downing, Confined single- and multiple-jet impingement heat transfer – I. Turbulent submerged liquid jets. Int. J. Heat Mass Transfer 38 (1995) 833–842.

[Cha2001] S. Chakrabarty, B. S. Tomar, A. Goswami, V. A. Raman, S. B. Manohar, Preparation of thin osmium targets by electrodeposition. Nucl. Instr. and Meth. B 174 (2001) 212–214.

[Cha2006] A. Chatwin-Davies, R. Pavan and K. Buckley, An [^{18}O]H_2O target design and thermal model with vapour reflux volume, TRIUMF Design Note, TRI-DN-06-09 (2006) (TRIUMF, Vancouver, Canada) pp 1–24.

[Cha2007] M. B. Challan, G. S. Moawad, M. A. Abou-Zeid, M. N. H. Comsan, Excitation functions of radionuclides produced by proton induced reactions on gadolinium targets. In: *Proc. 6th Int. Conf. on Nuclear and Particle Physics* (2007, Luxor, Egypt, ed. M. N. H. Comsan), pp. 159–168.

[Cla1966] J. C. Clark, D. J. Silvester, A cyclotron method for the production of flourine-18. Appl. Radiat. and Isot. 17 (1966) 151–154.

[Con2005] J. L. Conradie, P. J. Celliers, J. P. A. Crafford, J. L. G. Delsink, J. G. de Villiers, H. du Plessis, R. E. F. Fenemore, D. T. Fourie, Z. Kormany, Y. E. Manjoo, G. S. Muller, G. S. Price, P. F. Rohwer, J. F. Sharpey-Schafer, G. F. Steyn, J. T. van der Walt, T. N. van der Walt, M. J. van Niekerk, J. Dietrich, I. Mohos, Cyclotrons at iThemba LABS. In: *Proc. 17th Int. Conf. on Cyclotrons and their Applications* (2004, Tokyo, Japan), Particle Accelerator Society of Japan, 2005, pp. 105–109.

[Con2006] J. L. Conradie, P. F. Rohwer, P. J. Celliers, M. J. van Niekerk, D. T. Fourie, P. T. Mansfield, J. L. G. Delsink, A. H. Botha, J. Dietrich, I. Mohos, Beam phase measurement in a 200 MeV cyclotron. In: *Proc. 10th European Particle Accelerator Conf.* (EPAC 2006, Edinburgh, Scotland), pp. 1187–1189. Available from URL: http://accelconf.web.cern.ch/accelconf/e06.

[Con2007] J. L. Conradie, P. J. Celliers, J. G. de Villiers, J. L. G. Delsink, H. du Plessis, J. S. du Toit, R. E. F. Fenemore, D. T. Fourie, I. H. Kohler, C. Lussi, P. T. Mansfield, H. Mostert, G. S. Muller, G. S. Price, P.F. Rohwer, M. Sakildien, R. W. Thomae, M. J. van Niekerk, P. A. van Schalkwyk, Z. Kormány, J. Dietrich, T. Weis, S. Adam, D. Goetz, P. A. Schmelzbach, Improvements to the iThemba LABS cyclotron facilities. In: *Proc. 18th Int. Conf. on Cyclotrons and their Applications* (2007, Giardini Naxos, Italy), pp. 140–142. Available from URL: http://accelconf.web.cern.ch/accelconf/c07.

[Con2010] J. L. Conradie, L. S. Anthony, A. H. Botha, M. A. Crombie, J. G. de Villiers, J. L. G. Delsink, W. Duckitt, D. T. Fourie, M. E. Hogan, I. H. Kohler, C. Lussi, R. H. McAlister, H. W. Mostert, S. S. Ntshangase, J. V. Pilcher, P. F. Rohwer, M. Sakildien, N. Stodart, R. W. Thomae, M. J. van Niekerk, P. A. van Schalkwyk, D. de Villiers, C. Böhme, J. Dietrich, Z. Kormány, Current status and future projects of the iThemba LABS cyclotron facilities. In: *Proc. 19th Int. Conf. on Cyclotrons and their Applications* (CYCLOTRONS 2010, Lanzhou, China), pp. 42–44. Available from URL: http://accelconf.web.cern.ch/accelconf/Cyclotrons2010/index.htm.

[Cro1978] C. Crouzel, D. Comar, Production of carrier-free ^{18}F-hydrofluoric acid. Appl. Radiat. and Isot. 29 (1978) 407–408.

[Cun2012] J. Cugnon, A short introduction to spallation reactions. Few-Body Syst. 53 (2012) 143–149.

[Dah1983] J. R. Dahl, R. Lee, R. E. Bigler, B. Schmall, J. E. Aber, A new target system for the preparation of no-carrier-added ^{18}F-fluorinating compounds. Appl. Radiat. and Isot. 34 (1983) 693–700.

[DAu2013] J. M. D'Auria, R. Keller, K. Ladouceur, S. E. Lapi, T. J. Ruth, P. Schmor, An alternate approach to the production of radioisotopes for nuclear medicine applications. Rev. Sci. Instr. 84 (2013) 034705-1 – 034705-4.

[Del2013] K. Delobbe-Lussier, Density of Molten Elements and Representative Salts. In: *CRC Handbook of Chemistry and Physics 94th Edition* (ed. Haynes W. M.), CRC Press, Taylor and Francis, Boca Raton, Florida, USA, 2013.

[Dem2000] J. F. Dempsey, D. A. Low, S. Mutic, J. Markman, A. S. Kirov, G. H. Nussbaum, J. F. Williamson, Validation of a precision radiochromic film dosimetry system for quantitative two-dimensional imaging of acute exposure dose distributions. Med. Phys. 27 (2000) 2462–2475.

[deV2005] J. G. de Villiers, J. L. Conradie, M. J. van Niekerk, R. E. F. Fenemore, H. du Plessis, G. S. Price, G. S. Muller, J. P. A. Crafford, J. van der Walt, J. L. G. Delsink, A. H. Botha, A flat-topping system for the separated-sector cyclotron at iThemba LABS. In: *Proc. 17th Int. Conf. on Cyclotrons and their Applications* (2004, Tokyo, Japan), Particle Accelerator Society of Japan, 2005, pp. 344–346.

[Dew2004] A. Dewan, P. Mahanta, K. Sumithra Raju, P. Suresh Kumar, Review of passive heat transfer augmentation techniques. Proc. Instn Mech. Engrs Part A: J. Power and Energy 218 (2004) 509–527.

[Die2004] J. Dietrich, I. Mohos, A. H. Botha, J. L. Conradie, J. L. G. Delsink, P. F. Rohwer, Beam position monitor development for iThemba LABS cyclotron beamlines. In: *Proc. 9th European Particle Accelerator Conf.* (EPAC 2004, Lucerne, Switzerland), pp. 2589–2591. Available from URL: http://accelconf.web.cern.ch/accelconf/e04.

[Die2008] J. Dietrich, C. Boehme, T. Weis, L. Anthony, A. H. Botha, J. L. Conradie, J. A. Crombie, J. L. G. Delsink, J. G. de Villiers, J. H. du Toit, D. T. Fourie, H. Mostert, P. F. Rohwer, P. A. van Schalkwyk, Non-destructive beam position and profile measurements using light emitted by residual gas in a cyclotron beam line. In: *Proc. 11th European Particle Accelerator Conf.* (EPAC 2008, Genoa, Italy), pp. 1095–1097. Available from URL: http://accelconf.web.cern.ch/accelconf/e08.

[Dit1930] F. W. Dittus, L. M. K. Boelter, Pub. Eng. 2 (1930) 443.

[Dit2006] F. Ditrói, S. Takács, F. Tárkányi, M. Reichel, M. Scherge, A. Gervé, Thin layer activation of large areas for wear study. Wear 261 (2006) 1397–1400.

[Dit2008] F. Ditrói, S. Takács, F. Tárkányi, M. Baba, E. Corniani, Yu. N. Shubin, Study of proton induced reactions on niobium targets up to 70 MeV. Nucl. Instr. and Meth. B 266 (2008) 5087–5100.

[Dit2009] F. Ditrói, A. Hermanne, E. Corniani, S. Takács, F. Tárkányi, J. Csikai, Yu. N. Shubin, Investigation of proton induced reactions on niobium at low and medium energies. Nucl. Instr. and Meth. B 267 (2009) 3364–3374.

[Dmi1989] P. P. Dmitriev, G. A. Molin, Z. P. Dmitrieva, The production of ^{155}Tb for nuclear medicine by ^{155}Gd(p,n), ^{156}Gd(p,2n), ^{155}Gd(d,2n). Atomnaya Énergiya 66 (1989) 419–421.

[Dos2008] J. M. Doster, New cyclotron targetry to enhance F-18 clinical positron emission tomography. Final Technical Report, OSTI ID: 945375, North Carolina State University, Raleigh, NC, USA, 2008, pp 1–52. Available from URL: http://www.osti.gov/scitech/servlets/purl/945375

[Faß2004] M. Faßbender, F. M. Nortier, D. R. Phillips, V. T. Hamilton, R. C. Heaton, D. J. Jamriska, J. J. Kitten, L. R. Pitt, L. L. Salazar, F. O. Valdez, E. J. Peterson, Some nuclear chemical aspects of medical generator nuclide production at the Los Alamos hot cell facility. Radiochim. Acta 92 (2004) 237–243.

[Fir2004] R. B. Firestone, L. P. Ecktröm, WWW Table of Radioactive Isotopes, Version 2.1, January 2004. Available from URL: http://ie.lbl.gov/toi.

[Fit1977] J. Fitschen, R. Beckmann, U. Holm, H. Neuert, Yield and production of ^{18}F by ^{3}He irradiation of water. Appl. Radiat. and Isot. 28 (1977) 781–784.

[Fou2005] D. T. Fourie, J. L. Conradie, J. L. G. Delsink, P. F. Rohwer, J. G. de Villiers, C. Lussi, J. S. du Toit, A. H. Botha, New beam lines for the production of radioisotopes at iThemba LABS. In: *Proc. 17th Int. Conf. on Cyclotrons and their Applications* (2004, Tokyo, Japan), Particle Accelerator Society of Japan, 2005, pp. 492–494.

[Fre1994] R. Fresca Fantoni, E. Gadioli, P. Guazzoni, P. Vergani, L. Zetta, P.L. Dellera, F. Tomasi, V. Campagna, G. Ciavola, C. Marchetta, RERAME: A facility for investigating heavy ion reactions with activation techniques. Appl. Radiat. and Isot. 45 (1994) 325–334.

[Gad1992] E. Gadioli, P. E. Hodgson, Oxford Studies in Nuclear Physics Vol.15: Pre-equilibrium Nuclear Reactions, Clarendon Press, Oxford, 1992, p. 218.

[Gag2010] K. Gagnon, J. S. Wilson, S. A. McQuarrie, Thermal modelling of a solid cyclotron target using finite element analysis: An experimental validation. In: *Proc. 13th Int. Workshop on Targetry and Target Chemistry* (WTTC 13, 2010, Roskilde, Denmark), paper 011. Available from URL: http://wttc.triumf.ca.

[Gay1996] R. E. Gayoso, A. A. Sonzogni, S. J. Nassiff, (α,pxn) Reactions on natural gadolinium. Radiochim. Acta 72 (1996) 55–60.

[Gen1985] G. J. Genis, The generation of intense heat fluxes by electron bombardment to evaluate the use of swirl flow in the cooling of accelerator targets. PhD Thesis, University of Stellenbosch, South Africa, 1985. Available from URL: http://library.sun.ac.za.

[Gen1987] G. J. Genis, W. L. Rautenbach, High heat flux, forced convection heat transfer for tubes with twisted tape inserts. Trans. ASME, J. Heat Transfer 68 (1987) 1–9.

[Gen1988] G. J. Genis, W. L. Rautenbach, The development of a technique for the construction of small-diameter, large-L/D thermocouple placement holes in high-heat-flux environments. J. Phys. D: Appl. Phys. 21 (1988) 1537–1539.

[Gil2008] G. R. Gilmore, Practical Gamma-ray Spectrometry, 2nd Edition. John Wiley & Sons, Est Sussex, England, 2008, p. 20.

[Gol2010] S. J. Goldsmith, Radioimmunotherapy of lymphoma: Bexxar and Zevalin. Semin. Nucl. Med. 40 (2010) 122–135.

[Gol2013] R. Golestani, C. J. Zeebregts, A. G. Terwisscha van Scheltinga, M. N. Lub-de Hooge, G. M. van Dam, A. W. Glaudemans, R. A. Dierckx, R. A. Tio, A. J. Suurmeijer, H. H. Boersma, W. B. Nagengast, R. H. Slart, Feasibility of vascular endothelial growth factor imaging in human atherosclerotic plaque using ^{89}Zr-bevacizumab positron emission tomography. Molecular Imaging 12 (2013) 235–243.

[Gr1966] J. J. Griffin, Statistical model of intermediate structure. Phys. Rev. Lett. 17 (1966) 478–481.

[Gui1991] M. Guillaume, A. Luxen, B. Nebeling, M. Argentini, J. C. Clark, V. W. Pike, Recommendations for fluorine-18 production. Appl. Radiat. and Isot. 42 (1991) 749–762.

[Gul2001] K. Gul, A. Hermanne, M. G. Mustafa, F. M. Nortier, P. Obložinský, S. M. Qaim, B. Scholten, Y. Shubin, S. Takács, F. T. Tárkányi and Z. Zhuang, Charged particle cross-section database for medical radioisotope production: diagnostic radioisotopes and monitor reactions. IAEA-Tecdoc-1211, IAEA, Vienna, May 2001. Available from URL: http://www-nds.iaea.org/medical/. (last updated 2007).

[Haa1992] F. J. Haasbroek, P. Andersen, A. R. Eatwell, S. J. Mills, F. M. Nortier, D. du T. Rossouw, G. F. Steyn, Radionculide production with a 66 MeV proton beam, shared with neutron therapy, at a multidisciplinary cyclotron facility. In: *Proc. 4th Int. Symp. on the Synthesis and Applications of Isotopes and Isotopically Labelled Compounds* (1991, Toronto, Canada, eds. E. Buncel, G. W. Kabalka), Elsevier Science Publishers, 1992, pp. 640–643.

[Has2007] H. E. Hassan, F. S. Al-Saleh, K. F. Hassan, A. Sayed, Z. A. Saleh, Proton induced reactions on Tb-159 and La-139 for producing Dy-159 and Ce-139. In: *Proc. 6th Int. Conf. on Nuclear and Particle Physics* (2007, Luxor, Egypt, ed. M. N. H. Comsan), pp. 209–217.

[Hei1996] M. L. Heijnen, G. J. van den Berg, A. C. Beynen, Dietary raw versus retrograded resistant starch enhances apparent but not true magnesium absorption in rats. J. Nutr. 126 (1996) 2253–2259.

[Hes1989] S.-J. Heselius, D. J. Schlyer, A. P. Wolf, A diagnostic study of proton-beam irradiated water targets. Appl. Radiat. and Isot. 40 (1989) 663–669.

[Hil2005] K. Hilgers, S. Sudár, S. M. Qaim, Experimental study and nuclear model calculations on the ^{192}Os(p,n)^{192}Ir reaction: Comparison of reactor and cyclotron production of the therapeutic radionuclide ^{192}Ir. Appl. Radiat. and Isot. 63 (2005) 93–98.

[Hol2013] J. P. Holman, Heat Transfer, Tenth Edition. McGraw Hill, 2013.

[Hon2011] B. H. Hong, T. G. Yang, I. S. Jung, Y. S. Park, H. H. Cho, Visualization experiment of 30 MeV proton beam irradiated water target. Nucl. Instr. and Meth. A 655 (2011) 103–107.

[Hus1985] I. Huszár, R. Weinreich, Production of ^{18}F with an ^{18}O enriched water target. J. Radioanal. Nucl. Chem. 93 (1985) 349–354.

[IAEA2006] IAEA, Directory of Cyclotrons used for Radionuclide Production in Member States. IAEA Tech. Rep. IAEA-DCRP/2006, Vienna, 2006.

[Ign1993] A. V. Ignatyuk, J. L. Weil, S. Raman, S. Kahane, Density of discrete levels in ^{116}Sn. Phys. Rev. C 47 (1993) 1504–1513.

[ISO1995] Guide to the expression of uncertainty in measurements. International Organization for Standardization (ISO), Geneva, ISBN 92-67-10188-9, 1995.

[Iwa1982] A. Iwamoto, K. Harada, Mechanism of cluster emission in nucleon-induced preequilibrium reactions. Phys. Rev. C 26 (1982) 1821–1834.

[Iwa1992] R. Iwata, M. Kawamura, T. Ido, S. Kimura, 1992. Chromatographic purification of no-carrier-added magnesium-28 for biological studies. J. Radioanal. Nucl. Chem. 159 (1992) 233–237.

[Jan1982] J. F. Janni, Proton range-energy tables: Part 1. At. Data Nucl. Data Tables 27 (1982) 142–339. Proton range-energy tables: Part 2. At. Data Nucl. Data Tables 27 (1982) 341–529.

[Kay1985] W. M. Kays, H. C. Perkins, Forced convection, Internal flows in ducts. In: *Handbook of Heat Transfer Fundamentals.* Second Edition. (eds. W. M. Rohsenhow, J. P. Hartnett, E. N. Ganić), McGraw Hill, 1985, pp. 7-1 – 7-23.

[Kha2009] M. U. Khandaker, K. Kim, M.-W. Lee, K.-S. Kim, G. N. Kim, Y. S. Cho, Y. O. Lee, Experimental determination of proton-induced cross sections on natural zirconium. Appl. Radiat. and Isot. 67 (2009) 1341–1347.

[Kha2012] M. U. Khandaker, K. Kim, M.-W. Lee, K.-S. Kim, G. Kim, N. Otsuka, Investigations of ^{89}Y(p,x)^{86,88,89g}Zr, $^{86m+g,87g,87m,88g}$Y, ^{85g}Sr, and ^{84g}Rb nuclear processes up to 42 MeV. Nucl. Instr. and Meth. B 271 (2012) 72–81.

[Kil1985] M. R. Kilbourn, P. A. Jerabeck, M. J. Welch, An improved [^{18}O]water target for [^{18}F]fluoride production. Appl. Radiat. and Isot. 36 (1985) 327–328.

[Kin1996] R. R. Kinsey, C. L. Dunford, J. K. Tuli, T. W. Burrows, The NUDAT/PCNUDAT program for nuclear data. In: *Proc. 9th Int. Symp. on capture gamma-ray spectroscopy and related topics* (1996, Budapest, Hungary, eds. G. L. Molnar, T. Belgya, Zs. Revay). Available from URL: http://www.nndc.bnl.gov/nudat2/

[Kir2012] M. F. Kircher, H. Hricak, S. M. Larson, Molecular imaging for personalised cancer care. Molecular Oncology 6 (2012) 182–195.

[Kni1972] J. C. Kniffen, C. E. Roessler, G. S. Roessler, B. G. Dunuvant, D. T. Quick, Whole body counter determination of ^{28}Mg retention in humans. In: *Radioaktive Isotope in Klinik und Forschung* (eds. K. Fellinger, R. Höfer), Urban & Schwarzenberg, München, 1972, pp. 231–244.

[Knu1983] E. J. Knust, H. J. Machulla, High yield production of ^{18}F in a water target via the ^{16}O(^{3}He,p)^{18}F reaction. Appl. Radiat. and Isot. 34 (1983) 1627–1628.

[Kon2012] A. J. Koning, D. Rochman, Modern nuclear data evaluation with the TALYS code system. Nuclear Data Sheets 113 (2012) 2841–2934.

[Kon2013] A. J. Koning, D. Rochman, S. van der Marck, J. Kopecky, J. Ch. Sublet, S. Pomp, H. Sjostrand, R. Forrest, E. Bauge, H. Henriksson, TENDL-2012: TALYS-based evaluated nuclear data library, version 5. Released on 11 January 2013. Available from URL: http://www.talys.eu/tendl-2012.html.

[Kor1994] Z. Kormány, A new method and apparatus for measuring the mean energy of cyclotron beams. Nucl. Instr. and Meth. A 337 (1994) 258–264.

[Kor2008] Z. Kormány, K. Juhász, J. L. Conradie, J. L. G. Delsink, D. T. Fourie, J. V. Pilcher, P. F. Rohwer, Development of non-destructive beam current measurement for the iThemba LABS cyclotrons. In: *Proc. 11th European Particle Accelerator Conf.* (EPAC 2008, Genoa, Italy), pp. 1089–1091. Available from URL: http://accelconf.web.cern.ch/accelconf/e08.

[Kup2007] T. G. Kupi, Radiation Shield Design Verification and Optimisation for Two Radionuclide Production Beam Target Stations, using Monte Carlo Radiation Transport Code, MCNPX. Masters Thesis, North West University, South Africa, 2007.

[Kwo1995] O. Kwon, F. E. Ames, Advanced k-epsilon Modeling of Heat Transfer. NASA Contractor Report 4679, NASA Scientific and Technical Information Program, 1995.

[Lap2010] S. E. Lapi, K. Ladouceur, T. J. Ruth, J. M. D'Auria, The MORE Project: An alternative route to the production of high specific activity ^{99}Mo. In: *Proc. Int. Symp. on Technetium and Other Radiometals in Chemistry and Medicine* (Terachem 2010, Bressanone, Bolzano, Italy, ed. U. Mazzi), SG Editoriali, Padova, 2010, pp. 435–436.

[Leb2012] O. Lebeda, V. Lozza, P. Schrock, J. Štursa, K. Zuber, Excitation functions of proton-induced reactions on natural Nd in the 10–30 MeV energy range, and production of radionuclides relevant for double-β decay. Phys. Rev. C 85 (2012) 014602-1 – 014602-12.

[Leh2011] S. Lehenberger, C. Barkhausen, S. Cohrs, E. Fischer, J. Grünberg, A. Horn, U. Köster, R. Schibli, A. Türler, K. Zhernosekov, The low-energy β^- and electron emitter ^{161}Tb as an alternative to ^{177}Lu for targeted radionuclide therapy. Nucl. Med. Biol. 38 (2011) 917–924.

[Lev1981] V. I. Levin, A. B. Malanin, I. N. Tronova, Production of radionuclides by photonuclear reactions. I. Production of terbium-155 and thulium-167 using the electron accelerator EA-25. Radiochem. Radioanal. Lett. 49 (1981) 111-118.

[Lev1991] V. N. Levkovskij, Activation cross section nuclides of average masses (A = 40–100) by protons and alpha-particles with average energies (E = 10–50 MeV): Experiment and systematics. Inter-Vesi, Moscow, USSR, 1991.

[Lew2012] D. M. Lewis, U. Zetterberg, Medical-isotope cyclotron designs go full circle, CERN Courier, March 27, 2012.

[Lil1973] J. O. Liljenzin, The temperature of thin foils in ion beams. Lawrence Berkeley Laboratory Report LBL-1912, Berkeley, California, USA, 1973.

[Lin1973] L. Lindner, T. H. G. A. Suér, G. A. Brinkman, J. Th. Veenboer, A dynamic "loop"-target for the in-cyclotron production of ^{18}F by the ^{16}O(α,d)^{18}F reaction on water. Appl. Radiat. and Isot. 24 (1973) 124–126.

[Lit1968] G. M. Litton, J. Lyman, C. Tobias, Penetration of high-energy heavy ions, with the inclusion of Coulomb, nuclear and other stochastic processes. University of California Radiation Laboratory Report UCRL-17392, Berkeley, California, USA, 1968.

[Lun1979] H. Lundqvist, P. Malmborg, Production of carrier-free ^{28}Mg and ^{24}Na by 50–180 MeV protons on Si, P, S, Cl, Ar and K: Excitation functions and chemical separation. Appl. Radiat. and Isot. 30 (1979) 33–37.

[Ma1996] D. Ma, A. R. Ketring, G. J. Ehrhardt, W. Jia, Production of radiolanthanides and radiotherapy research at MURR. Radional. Nucl. Chem. 206 (1996) 119–126.

[Mar1962] H. E. Martin, F. K. Bauer, Magnesium-28 studies in the cirrhotic and alcoholic. Proc. R. Soc. Med. 55 (1962) 912–914.

[Mau1983] L. F. Mausner, P. Richards, The production of spallation radionuclides for medical applications at BLIP. IEEE Transactions on Nuclear Science, NS-30 (1983) 1793–1796.

[Mau1984] L. F. Mausner, T. Prach, T. Ku, P. Richards, Production of Mg-28 for medical applications by spallation. J. Nucl. Med. 25 (1984) 120.

[Mau1990] L. F. Mausner, S. Mirzadeh, H. Schnakenberg, S. C. Srivastava, The design and operation of the upgraded BLIP facility for radionuclide research and production. Appl. Radiat. and Isot. 41 (1990) 367–374.

[Mea1969] D. F. Measday, C. Richard-Serre, The loss of protons by inelastic interactions in various materials. Nucl. Instr. and Meth.76 (1969) 45–54.

[Med2012] D. G. Medvedev, S. V. Smith, L. F. Mausner, Recovery and irradiation of isotopically pure ^{68}Zn and ^{86}Sr at the Brookhaven Linac Isotope Producer. In: *Proc. 14th Int. Workshop on Targetry and Target Chemistry* (WTTC 14, 2012, Playa del Carmen, Mexico), AIP. Conf. Proc. 1509 (2012) 218–222.

[Men1965] J. H. Mendelson, B. Barnes, C. Mayman, M. Victor, The determination of exchangeable magnesium in alcoholic patients. Metabolism: Clinical and Experimental 14 (1965) 88–98.

[Mic1997] R. Michel, R. Bodemann, H. Busemann, R. Daunke, M. Gloris, H.-J. Lange, B. Klug, A. Krins, I. Leya, M. Lüpke, S. Neumann, H. Reinhardt, M. Schnatz-Büttgen, U. Herpers, Th. Schiekel, F. Sudbrock, B. Holmqvist, H. Condé, P. Malmborg, M. Suter, B. Dittrich-Hannen, P.-W .Kubik, H.-A. Synal, D. Filges, Cross sections for the production of residual

nuclides by low- and medium-energy protons from the target elements C, N, O, Mg, Al, Si, Ca, Ti, V, Mn, Fe, Co, Ni, Cu, Sr, Y, Zr, Nb, Ba and Au. Nucl. Instr. and Meth. B 129 (1997) 153–193.

[Mil1989] S. J. Mills, F. M. Nortier, W. L. Rautenbach, H. A. Smit, G. F. Steyn, A multi-purpose target station for radioisotope production at medium energies. In: *Proc. 12th Int. Conf. on Cyclotrons and their Applications* (1989, Berlin, Germany, eds. B. Martin, K. Ziegler), World Scientific, 1989, pp. 527–530.

[Mül2012] C. Müller, K. Zhernosekov, U. Köster, K. Johnston, A. Hohn, T. N. van der Walt, A. Türler, R. Schibli, A unique matched quadruplet of terbium radioisotopes for PET and SPECT and for α- and β^--radionuclide therapy: An in vivo proof-of-concept study with a new receptor-targeted folate derivative. J. Nucl. Med. 53 (2012) 1951–1959.

[Mus1998] M. G. Mustafa, H. I. West Jr., H. O. OḂrien, R. G. Lanier, M. Benhamou, T. Tamura, Measurements and a direct-reaction–plus–Hauser-Feshbach analysis of ^{89}Y(p,n)^{89}Zr, ^{89}Y(p,2n)^{88}Zr, and ^{89}Y(p,pn)^{88}Y reactions up to 40 MeV. Phys. Rev. C 38 (1988) 1624–1637.

[Nca2005] N. J. Ncapayi, P. J. Celliers, J. L. Conradie, J. P. A. Crafford, J. L. G. Delsink, J. G. de Villiers, D. de Villiers, J. Dietrich, H. du Plessis, R. E. F. Fenemore, D. T. Fourie, Z. Kormány, I. Mohos, G. S. Muller, G. S. Price, P. F. Rohwer, G. F. Steyn, J. T. van der Walt, M. J. van Niekerk, Upgrading of accelerator facilities at iThemba LABS to increase the production of radionuclides. In: *Proc. Int. Symp. on Utilization of Accelerators* (2005, Dubrovnik, Croatia), IAEA-CN-115, 2005, Paper no. 56, pp. 1–8. Available from URL: http://www-pub.iaea.org/MTCD/Publications/PDF/P1251-cd.

[Nic1984] R. J. Nickles, M. E. Daube, T. J. Ruth, An $^{18}O_2$ target for the production of [^{18}F]F_2. Appl. Radiat. and Isot. 35 (1984) 117–122.

[Nit1976] J. M. Nitschke, A high intensity heavy-ion recoil-target system. Nucl. Instr. and Meth. 138 (1976) 393–406.

[Nor1995] F. M. Nortier, N. R. Stevenson, W. Z. Gelbart, Investigation of the thermal performance of solid targets for radioisotope production. Nucl. Instr. and Meth. A 355 (1995) 236–241.

[Nor1996] F. M. Nortier, F. J. Haasbroek, J. H. Langenhoven, E. Vorster, Neon gas target and synthesis system for the production of 2-[F-18]Fluoro-2-deoxy-D-glucose with a 66 MeV proton beam. In: *Proc. 6th Int. Workshop on Targetry and Target Chemistry* (WTTC 6, 1995, Vancouver, Canada), TRIUMF Reports, 1996, p. 68. Available from URL: http://wttc.triumf.ca.

[Nor1999] F. M. Nortier, P. J. Binns, J. Hanekom, M. A. Penny, R. E. Quantrill, H. A. Smit, T. J. van Rooyen, V. M. P. Xulubana, A second target station for the bombardment of semi-permanent targets at the NAC. In: *Proc. 8th Int. Workshop on Targetry and Target Chemistry* (WTTC 8, 1999, St. Louis, Missouri, USA), p. 22. Available from URL: http://wttc.triumf.ca.

[Nor2004] F. M. Nortier, M. DeJohn, M. E. Fassbender, V. T. Hamilton, R. C. Heaton, D. J. Jamriska, J. J. Kitten, J. W. Lenz, C. E. Lowe, C. F. Moddrell, L. M. McCurdy, E. J. Peterson, L. R. Pitt, D. R. Phillips, L. L. Salazar, P. A. Smith, F. O. Valdez, Targetry at the LANL 100 MeV isotope production facility: lessons learned from facility commissioning. In: *Proc. Americas Nuclear Enery Symp.* (ANES 2004, Miami Beach, Florida, USA), LA-UR-04-6421, 2004, pp. 1–8.

[Nor2007] F. M. Nortier, J. W. Lenz, P. A. Smith, Large-scale isotope production with an intense 100 MeV proton beam: recent target performance experience. In: *Proc. 18th Int. Conf. on Cyclotrons and their Applications* (2007, Giardini Naxos, Italy), pp. 257–259. Available from URL: http://accelconf.web.cern.ch/accelconf/c07.

[Noz1968] T. Nozaki, Y. Tanaka, A. Shimamura, T. Karasawa, The Preparation of Anhydrous HF^{18}. Appl. Radiat. and Isot. 19 (1968) 27–32.

[Obl1978] P. Oblozinský, I. Ribanský, Emission rate of preformed α-particles in preequilibrium decay. Phys. Lett. B 74 (1978) 6–8.

[Oka1998] K. Okamoto (Ed.), Proceedings of the IAEA Consultants' Meeting on Data Requirements for Medical Radioisotope Production. International Nuclear Data Committee (INDC) Report INDC(NDS)-195/GZ, IAEA Nuclear Data Section, Vienna, 1988, p. 115.

[Oma2009] H. M. Omara, K. F. Hassan, S. A. Kandil, F. E. Hegazy, Z. A. Saleh, Proton induced reactions on ^{89}Y with particular reference to the production of the medically interesting radionuclide ^{89}Zr. Radiochim. Acta 97 (2009) 467–471.

[Par1991] D. J. Parker, P. Vergani, E. Gadioli, J. J. Hogan, F. Vettori, E. Gadioli-Erba, E. Fabrici, M. Galmarini, Recoil range study of incomplete fusion of C with Au at 10 MeV/nucleon. Phys. Rev. C 44 (1991) 1528–1540.

[Pat2012] A. Pattamatta, G. Singh, Assessment of turbulence models in the prediction of flow field and thermal characteristics of wall jet. Frontiers in Heat and Mass Transfer (FHMT) 3 (2012) 023005-1 – 023005-11.

[Pee2012] J. L. Peeples, M. H. Stokely, M. C. Poorman, M. Magerl, B. W. Wieland, Visual observation of boiling in high power liquid target. In: *Proc. 14th Int. Workshop on Targetry and Target Chemistry* (WTTC 14, 2012, Playa del Carmen, Mexico), AIP. Conf. Proc. 1509 (2012) 76–80.

[Pel2011a] D. B. Pelowitz (ed.), MCNPX User's Manual Version 2.7.0. Los Alamos National Laboratory Report LA-CP-07-1473, Los Alamos, 2011.

[Pel2011b] D. B. Pelowitz, J. W. Durkee, J. S. Elson, M. L. Fensin, J. S. Hendricks, M. R. James, R. C. Johns, G. W. McKinney, S. G. Mashnik, J. M. Verbeke, L. S. Waters, T. A. Wilcox, MCNPX 2.7.E Extensions, LA-UR-11-01502, Los Alamos, March 2011.

[Pet1974] B. S. Petukhof, Turbulent heat transfer in tubes with variable fluid properties. In: Heat exchangers: Design and Theory Sourcebook (eds. N. H. Afgan, E. U. Schlünder) McGraw Hill, 1974.

[Pil2003] M. R. A. Pillai, S. Chakraborty, T. Das, M. Venkatesh, N. Ramamoorthy, Production logistics of ^{177}Lu for radionuclide therapy. Appl. Radiat. and Isot. 59 (2003) 109–118.

[Pri2012] B. Pritychenko, A. Sonzogni, A Q-value Calculator (QCalc). NNDC, Brookhaven National Laboratory. Available from URL: http://www.nndc.bnl.gov/qcalc/.

[Qai2009] S. M. Qaim, K. Hilgers, S. Sudár, H. H. Coenen, Excitation function of the ^{192}Os(^{3}He,4n)-reaction for production of ^{191}Pt. Appl. Radiat. and Isot. 67 (2009) 1074–1077.

[Rös1993] F. Rösch, S. M. Qaim, G. Stöcklin, Nuclear data relevant to the production of the positron emitting radioisotope ^{86}Y via the ^{86}Sr(p,n) and ^{nat}Rb(^{3}He,xn)-processes. Radiochim. Acta 61 (1993) 1–8.

[Rös2000] F. Rösch, J. Brockman, N. A. Lebedev, S. M. Qaim, Production and radiochemical separation of Auger electron emitter ^{140}Nd. Acta Oncologica 39 (2000) 727–730.

[Rös2007] F. Rösch, Radiolanthanides in endoradiotherapy: an overview. Radiochim. Acta 95 (2007) 303–311.

[Rut1979] T. J. Ruth, A. P. Wolf, Absolute cross-sections for the production of ^{18}F via the ^{18}O(p,n)^{18}F reaction. Radiochim. Acta 26 (1979) 21–24.

[Sah1966] G. B. Saha, N. T. Porile, L. Yaffe, (p,xn) and (p,pxn) reactions of yttrium-89 with 5–85 MeV protons. Phys. Rev. 144 (1966) 962–971.

[Sat1983] K. Sato, A. Iwamoto, H. Harada, Pre-equilibrium emission of light composite particles in the framework of the exciton model. Phys. Rev. C 28 (1983) 1527.

[Sch1973] C. Schimansky, Investigations on translocation of magnesium (^{28}Mg) in sunflower plants. Z. Pflanzenernährung und Bodenkunde 136 (1973) 68–82.

[Sch1981] R. Schwartz, E. M. Wien, R. A. Wentworth, Use of nonabsorbable markers for gastrointestinal contents in in-vivo measurement of magnesium bioavailablility. J. Nutr. 111 (1981) 219–225.

[Sch2008] D. J. Schlyer, P. Van den Winkel, T. J. Ruth, M. M. Vora, M. R. A. Pillai, M. Haji-Saeid (eds.), Cyclotron Produced Radionuclides: Principles and Practice. IAEA Technical Reports Series no. 465, Vienna, Austria, 2008.

[Sch2009] D. J. Schlyer, M. R. A. Pillai, M. Haji-Saeid (eds.), Cyclotron Produced Radionuclides: Physical Characteristics and Production Methods. IAEA Technical Reports Series no. 468, Vienna, Austria, 2009.

[Sch2011] P. Schmor, Review of cyclotrons for the production of radioactive isotopes for medical and industrial applications. Rev. Accl. Sci. Tech. 4 (2011) 103–116.

[Sch2012] D. Schlyer, M. Haji-Saeid (eds.), Cyclotron Produced Radionuclides: Operation and Maintenance of Gas and Liquid Targets, IAEA Radioisotopes and Radiopharmaceuticals Series no. 4, Vienna, Austria, 2012, p. 11.

[She1953] R. K. Sheline, N. R. Johnson, New long-lived magnesium-28 isotope. Phys. Rev. 89 (1953) 520–521.

[Shu1988] Yu. N. Shubin, V. P. Lunev, A. Yu. Konobeyev, A. I. Dityuk, MENDL-2P: proton reaction data library for nuclear activation (Medium Energy Nuclear Data Library). IAEA-NDS-204, Nuclear Data Section, IAEA, Vienna, 1988.

[Sis2008] J. M. Sisterson. Measurement of recoil nuclei losses for proton-induced reactions in Al, Si, Mg and Fe at 200 and 500 MeV. Nucl. Instr. and Meth. B 266 (2008) 3913–3918.

[Sle1957] C. A. Sleicher, M. Tribus, Heat transfer in a pipe with turbulent flow and arbitrary wall-temperature distribution. Trans. ASME 79 (1957) 789–796.

[Son2001] A. A. Sonin, The Physical Basis of Dimensional Analysis, Second edition. Department of Mechanical Engineering, MIT, MA 02139, Massachusetts, USA, 2001.

[Ste1994] N. R. Stevenson, F. M. Nortier, W. Z. Gelbart, R. Bloemhard, R. van den Elzen, C. Hunt, J. Lofvendahl, J. Orzechowski, Pushing beam currents to the limit. In: *Proc. 5th Int. Workshop on Targetry and Target Chemistry* (WTTC 5, 1993, Brookhaven, Upton, New York, USA), Report BNL-61149, 1994, pp. 5–11. Available from URL: http://wttc.triumf.ca.

[Ste1990] G. F. Steyn, F. M. Nortier, S. J. Mills, Helium cooling of a double-foil window for external cyclotron beams. Nucl. Instr. and Meth. A 292 (1990) 35–44.

[Ste1990a] G. F. Steyn, Bombardment facilities for radioisotope production at the NAC and the production of Iron-52, Iron-55 and Rubidium-81. PhD Thesis, University of Stellenbosch, South Africa, 1990.

[Ste1992] G. F. Steyn, T. J. van Rooyen, P. J. Binns, J. H. Hough, F. M. Nortier, S. J. Mills, Design calculations for a local radiation shield of a radioisotope production target bombardment station. Nucl. Instr. and Meth. A 316 (1992) 128–113.

[Ste1996] G. F. Steyn, C. J. Stevens, The importance of thermal entrance effects in gas-cooled beam windows for radioisotope production targets. Nucl. Instr. and Meth. A 373 (1996) 10–17.

[Ste2004] G. F. Steyn, C. Vermeulen, R. Quantrill, J. P. A. Crafford, J. L. G. Delsink, A vertical-beam target station for radionuclide production with high-intensity proton beams. In: *Proc. 10th Int. Workshop on Targetry and Target Chemistry* (WTTC 10, 2004, Madison, Wisconsin, USA). Available from URL: http://wttc.triumf.ca.

[Ste2006] G. F. Steyn, C. Vermeulen, F. M. Nortier, F. Szelecsényi, Z. Kovácz, S. M. Qaim, Production of no-carrier-added ^{139}Pr via precursor decay in the proton bombardment of ^{nat}Pr. Nucl. Instr. and Meth. B 252 (2006) 149–159.

[Ste2008a] G. F. Steyn, C. Vermeulen, E. Isaacs, S. DeWindt, D. Saal, H. P. Burger, C. van Rooyen, F. C. de Beer, H. Knox, J. Isobe, Development of tandem targets for a vertical beam target station. In: *Proc. 12th Int. Workshop on Targetry and Target Chemistry* (WTTC 12, 2008, Seattle, Washington, USA), pp. 51–53. Available from URL: http://wttc.triumf.ca.

[Ste2008b] G. F. Steyn, N. P. van der Meulen, T. N. van der Walt, C. Vermeulen, Production of carrier-free ^{28}Mg by 50–200 MeV protons on ^{nat}Cl: Excitation function and target optimization. In: *Proc. Int. Conf. on Nuclear Data for Science and Technology* (ND2007, Nice, France, eds. O. Bersillon, F. Gunsing, E. Bauge, R. Jacqmin, S. Leray), DOI: 10.1051/ndata:07186, EDP Sciences, CEA, 2008, pp. 1391–1394.

[Ste2011] G. F. Steyn, C. Vermeulen, F. Szelecsényi, Z. Kovács, K. Suzuki, T. Fukumura, K. Nagatsu, Excitation functions of proton-induced reactions on ^{89}Y and ^{93}Nb with empasis on the production of selected radio-zirconiums. J. Korean Phys. Soc. 59 (2011) 1991–1994.

[Ste2012] G. F. Steyn, C. Vermeulen, Confinement single- and multiple-jet impingement heat transfer in helium-cooled beam window assemblies at a cyclotron facility. In: *Proc. 57th Annual Conf. of the South African Institute of Physics* (SAIP2012, Pretoria, South Africa), in press. Series available from URL: http://www.saip.org.za.

[Ste2013] G. F. Steyn, C. Vermeulen, A. H. Botha, J. L. Conradie, J. P. A. Crafford, J. L. G. Delsink, J. Dietrich, H. du Plessis, D. T. Fourie, Z. Kormány, M. J. van Niekerk, P. F. Rohwer, N. P. Stodart, J. G. de Villiers, A vertical-beam target station and high-power targetry for the cyclotron production of radionuclides with medium energy protons. Nucl. Instr. and Meth. A 727 (2013) 131–144.

[Steam2013] The Steam Tables. Available from URL: http://www.thermexcel.com.

[Sto2010] M. Stokely, B. Wieland, M. P. Dehnel and T. M. Stewart, A high current PET target and compact beamline. In: *Proc. 23rd Particle Accelerator Conference* (PAC09, TRIUMF, Vancouver, Canada), 2010, pp 2808–2810.

[Stu1983] A. E. Stuchbery, Electrodeposition of Pt and Os targets for nuclear reaction experiments. Nucl. Instr. and Meth. 211 (1983) 293–295.

[Sug2013] A. Sugyo, A. B. Tsuji, H. Sudo, K. Nagatsu, M. Koizumi, Y. Ukai, G. Kurosawa, M.-R. Zhang, Y. Kurosawa, T. Saga, Evaluation of ^{89}Zr-labelled human anti-CD147 monoclonal antibody as a positron emission tomography probe in a mouse model of pancreatic cancer. PLOS ONE 8 (2013) e61230-1 – e61230-9. Available from URL: http://www.plosone.org.

[Sze1985] G. Sz/'ekely, FGM–a flexible gamma-spectrum analysis program for a small computer. Computer Phys. Commun. 34 (1985) 313-Ű319.

[Sze2005] F. Szelecsényi, G. F. Steyn, Z. Kovácz, C. Vermeulen, N. P. van der Meulen, S. G. Dolley, T. N. van der Walt, K. Suzuki, K. Mukai, Investigation of the ^{66}Zn(p,2pn)^{64}Cu and ^{68}Zn(p,x)^{64}Cu nuclear processes up to 100 MeV: Production of ^{64}Cu. Nucl. Instr. and Meth. B 240 (2005) 625–637.

[Sze2009a] F. Szelecsényi, G. F. Steyn, Z. Kovács, K. Aardaneh, C. Vermeulen, T. N. van der Walt, Production possibility of ^{186}Re via the ^{192}Os(p,α3n)^{186}Re nuclear reaction. J. Radioanal. Nucl. Chem. 282 (2009) 261–263.

[Sze2009b] F. Szelecsényi, G. F. Steyn, S. G. Dolley, Z. Kovács, C. Vermeulen, T. N. van der Walt, Investigation of the ^{68}Zn(p,2p)^{67}Cu nuclear reaction: new measurements up to 40 MeV and compilation up to 100 MeV. Nucl. Instr. and Meth. B 267 (2009) 1877–1881.

[Sze2010] F. Szelecsényi, C. Vermeulen, G. F. Steyn, Z. Kovács, K. Aardaneh, T. N. van der Walt, Excitation functions of ^{186,187,188,189,190,192}Ir formed in proton-induced reactions on highly enriched ^{192}Os up to 66 MeV. Nucl. Instr. and Meth. B 268 (2010) 3306–3314.

[Tak2003] S. Takács, F. Tárkányi, A Hermanne, R. Paviotti de Corcuera, Validation and upgrading of the recommended cross section data of charged particle reactions used for production of PET radioisotopes. Nucl. Instr. and Meth. B 211 (2003) 169–189.

[Tar2003] F. Tárkányi, S. Takács, F. Szelecsényi, F. Ditrói, A. Hermanne, M. Sonck, Excitation functions of deuteron induced nuclear reactions on natural tungsten up to 50 MeV. Nucl. Instr. and Meth. B 211 (2003) 319–330.

[Tar2005] F. Tárkányi, F. Ditrói, S. Takács, J. Csikai, I. Mahunka, M. S. Uddin, M. Hagiwara, M. Baba, T. Ido, A. Hermanne, M. Sonck, Yu. N. Shubin, A. I. Dityuk, Excitation functions for production of ^{88}Zr and ^{88}Y by proton and deuteron irradiation of Mo, Nb, Zr and Y. In: *Proc. Int. Conf. on nuclear data for science and technology* (ND2004, Santa Fe, USA, Sept. 2004, eds. R. C. Haight, M. B. Chadwick, T. Kawano, P. Talou), AIP 0-7354-0254-X, 769 Vol. 2 (2005) pp. 1658–1661.

[Tar2006] F. Tárkányi, S. Takács, F. Szelecsényi, F. Ditrói, A. Hermanne, M. Sonck, Excitation functions of proton induced nuclear reactions on natural tungsten up to 34 MeV. Nucl. Instr. and Meth. B 252 (2006) 160–174.

[Tar2007a] F. Tárkányi, A. Hermanne, S. Takács, F. Ditrói, F. Kovalev, A. V. Ignatyuk, New measurement and evaluation of the excitation function of the ^{186}W(p,n) nuclear reaction for production of the therapeutic radioisotope ^{186}Re. Appl. Radiat. and Isot. 264 (2007) 389–394.

[Tar2007b] F. Tárkányi, A. Hermanne, S. Takács, K. Hilgers, S. F. Kovalev, A. V. Ignatyuk, S. M. Qaim, Study of the ^{192}Os(d,2n) reaction for production of the therapeutic radionuclide ^{192}Ir in no-carrier added form. Appl. Radiat. and Isot. 65 (2007) 1215–1220.

[Tay1991] W. A. Taylor, A. N. Herring, R. M. Lopez, D. C. Moody, D. R. Phillips, R. C. Staroski, Production of Mono-isotopic ^{88}Y from the decay of ^{88}Zr. Appl. Radiat. and Isot. 42 (1991) 208–209.

[Tay1994] B. N. Taylor, C. E. Kuyatt, Guidelines for evaluating and expressing the uncertainty of NIST measurement results. NIST Technical Note 1297, Physics Laboratory, National Institute of Standards and Technology, Gaithersburg, Maryland, USA, 1994.

[Tin1991] N. D. Tinker, J. Zweit, H. L. Sharma, S. Downey, C. A. McAuliffe, Production of no-carrier-added ^{191}Pt, a radiolabel for the synthesis and biological investigations of platinum anti-tumor compounds. Radiochim. Acta 54 (1991) 29–34.

[Tit2011] Yu. E. Titarenko, V. F. Batyaev, A. Yu. Titarenko, M. A. Butko, K. V. Pavlov, S. N. Florya, R. S. Tikhonov, V. M. Zhivun, A. V. Ignatyuk, S. G. Mashnik, S. Leray, A. Boudard, J. Cugnon, D. Mancusi, Y. Yariv, K. Nishihara, N. Matsuda, H. Kumawat, G. Mank, W. Gudowski, Measurement and simulation of the cross sections for nuclide production in Nb-93 and Ni-nat targets irradiated with 0.04- to 2.6-GeV protons. Phys. Atom. Nucl. 74 (2011) 537–550.

[Tsc68a] Tschalär C. Straggling distributions of large energy losses. Nucl. Instr. and Meth. 61 (1968) 141–156.

[Tsc68b] Tschalär C. Straggling distributions of extremely large energy losses. Nucl. Instr. and Meth. 64 (1968) 237–243.

[Udd2005] M. S. Uddin, M. Hagiwara, M. Baba, F. Tárkányi, F. Ditrói, Experimental studies on excitation functions of the proton-induced activation reactions on yttrium. Appl. Radiat. and Isot. 63 (2005) 367–374.

[Udd2008] M. S. Uddin, M. U. Khandaker, K. S. Kim, Y. S. Lee, M. W. Lee, G. N. Kim, Excitation functions of the proton induced nuclear reactions on natural zirconium. Nucl. Instr. and Meth. B 266 (2008) 13–20.

[Uus2006] H. Uusijärvi, P. Bernhardt, F. Rösch, H. R. Maecke, E. Forssell-Aronsson, Electron- and positron-emitting radiolanthanides for therapy: aspects of dosimetry and production. J. Nucl. Med. 47 (2006) 807–814.

[vdM2008] N. P. van der Meulen, The cyclotron production of selected radionuclides using medium energy protons. PhD Thesis, University of Stellenbosch, South Africa, 2008. Available from URL: http://library.sun.ac.za.

[vdM2011] N. P. van der Meulen, S. G. Dolley, G. F. Steyn, T. N. van der Walt, H. G. Raubenheimer, The use of selective volatilization in the separation of ^{68}Ge from irradiated Ga targets. Appl. Radiat. and Isot. 69 (2011) 727–731.

[vdM2013] N. P. van der Meulen, T. N. van der Walt, G. F. Steyn, H. G. Raubenheimer, The production of ^{82}Sr using larger format RbCl targets. Appl. Radiat. and Isot. 72 (2013) 96–99.

[Ver1988] H. Vera Ruiz, Report of an International Atomic Energy Agency's consultants meeting on fluorine 18: Reactor production and utilization. Appl. Radiat. and Isot. 39 (1988) 31–39.

[Ver2002] M. Verhas, V. de la Guéronnière, J. M. Grognet, J. Paternot, A. Hermanne, P. van den Winkel, R. Gheldof, P. Martin, M. Fantino, Y. Rayssiguier, Magnesium bioavailability from mineral water. A study in adult men. Eur. J. Clin. Nutr. 56 (2002) 442–449.

[Ver2003] I. Verel, G. W. M. Visser, R. Boellaard, O. C. Boerman, J. van Eerd, G. B. Snow, A. A. Lammertsma, G. A. M. S. van Dongen, Quantitative ^{89}Zr immuno-PET for in-vivo scouting of ^{90}Y-labelled monoclonal antibodies in xenograft-bearing nude mice. J. Nucl. Med. 44 (2003) 1663–1670.

[Ver2006] C. Vermeulen, G. F. Steyn, D. Saal, C. Naidoo, J. C. Crafford, Degrading and reshaping a 66 MeV proton beam to match targetry for producing ^{18}F in commercially viable quantities. In: *Proc. 11th Int. Workshop on Targetry and Target Chemistry* (WTTC 11, 2006, University of Cambridge, UK), p. 120. Available from URL: http://wttc.triumf.ca.

[Ver2012] C. Vermeulen, G. F. Steyn, F. Szelecsényi, Z. Kovács, K. Suzuki, K. Nagatsu, A. Hohn, T. N. van der Walt, Cross sections of proton-induced reactions on ^{nat}Gd with special emphasis on the production possibilities of ^{152}Tb and ^{155}Tb. Nucl. Instr. and Meth. B 275 (2012) 24–32.

[Vot89] J. R. Votaw, R. J. Nickles, A theoretical description of the beam induced heating of accelerator target foils. Nucl. Instr. and Meth. A 281 (1989) 216–223.

[Wat1979] W. S. Watson, T. E. Hilditch, P. W. Horton, D. L. Davies, R. Lindsay, Magnesium metabolism in blood and the whole body in man using ^{28}Mg. Metabolism: Clinical and Experimental 28 (1979) 90–95.

[Wei1985] R. Weinreich, Production of positron emitters at the SIN cyclotron facilities. In: *Proc. 1st Int. Workshop on Targetry and Target Chemistry* (WTTC 1, 1985, Heidelberg, Germany), pp. 86–91. Available from URL: http://wttc.triumf.ca. Printed version: eds. F. Helus, T. J. Ruth, DKFZ Press Department, Heidelberg, 1987, pp. 86–91.

[Wei2001] R. E. Weiner, M. L. Thakur, Radiolabelled peptides in diagnosos and therapy. Semin. Nucl. Med. 31 (2001) 296–311.

[Wes1993] H. I. West Jr. (ed.),R. G. Lanier, M. G. Mustafa, R .M. Nuckolls, R. J. Nagle, H. O'Brien, J. Frehaut, A. Adam, C. Philis, Some light-ion excitation-function measurements on titanium, yttrium and europium, and associated results. Lawrence Livermore National Laboratory Report UCRL-ID-115738, Lawrence Livermore National Laboratory, Livermore, California, USA, 1993.

[Woo2013] A. L. Wooten, E. Madrid, G. D. Schweitzer, L. A. Lawrence, E. Mebrahtu, B. C. Lewis, S. E. Lapi, Routine production of ^{89}Zr using an automated module. Appl. Sci. 3 (2013) 593–613.

[Zai2003] N. G. Zaitseva, S. N. Dmitriev, O. D. Maslov, L. G. Molokanova, G. Ya. Starodub, S. V. Shishkin, T. V. Shishkina, G. J. Beyer, Terbium-149 for nuclear medicine. The production of ^{149}Tb via heavy ions induced nuclear reactions. Czech. J. Phys. 53 (2003) A455–A458.

[Zei1999] S. K. Zeisler, D. W. Becker, A new method for PET imaging of tumours: human serum albumin labelled withthe long-lived Nd-140/Pr-140 in vivo radionuclide generator. Clin. Pos. Imaging 2 (1999) 324.

[Zhu1997] Z. H. Zhu, X. Y. Wang, Y. H. Wu, Y. F. Liu, An improved Re/W separation protocol for preparation of carrier-free ^{186}Re. J. Radioanal. Nucl. Chem. 221 (1997) 199–201.

[Zie1980] J. F. Ziegler, Stopping cross-sections for energetic ions in all elements. In: *The Stopping and Ranges of Ions in Matter*, Vol. 5, Pergamon, New York, 1980.

[Zie2006] J. F. Ziegler, J. P. Biersack, The Stopping and Range of Ions in Matter (SRIM-2006) version 2006.01. Available from URL: http://www.srim.org/.

[Zie2013] J. Ziegler, SRIM – the Stopping and Range of Ions in Matter. Available from URL: http://www.srim.org.